Modeling forcings and responses in the global carbon cycle-climate system: Past, present and future

Inauguraldissertation

der Philosophisch–naturwissenschaftlichen Fakultät
der Universität Bern

vorgelegt von

Raphael Roth

aus Basel (BS)

Leiter der Arbeit:

Prof. Dr. Fortunat Joos

Abteilung für Klima– und Umweltphysik
Physikalisches Institut der Universität Bern

Modeling forcings and responses in the global carbon cycle-climate system: Past, present and future

Inauguraldissertation

der Philosophisch–naturwissenschaftlichen Fakultät
der Universität Bern

vorgelegt von

Raphael Roth

aus Basel (BS)

Leiter der Arbeit:

Prof. Dr. Fortunat Joos

Abteilung für Klima– und Umweltphysik
Physikalisches Institut der Universität Bern

Von der Philosophisch–naturwissenschaftlichen Fakultät angenommen.

Der Dekan
Bern, 12. Dezember 2013   Prof. Dr. Silvio Decurtins

Thesis overview and summary

This thesis investigates the interactions within the coupled carbon cycle-climate system. It addresses questions regarding both its past and future evolution using a computationally efficient carbon cycle-climate model. Therefore, no specific single topic or mechanism is studied, but a suite of applications is presented in the following.

The cycling of carbon in the Earth system is driven by a complex interplay between physical, biological and chemical processes in the major carbon reservoirs: atmosphere, land, ocean, sediments and lithosphere. Of primary interest is the net exchange of carbon dioxide (CO_2) from/to the atmosphere, as this is the process that ultimately influences Earth's climate, as CO_2 absorbs electromagnetic radiation. Carbon fluxes on decadal timescales are controlled by the interactions between atmosphere, surface ocean and living biomass on land. On longer timescales, atmospheric CO_2 concentrations are driven by the oceanic carbon cycle, which is influenced both by changes in ocean circulation, marine biology, seawater chemistry and sediment interactions. On geological timescales, atmospheric CO_2 stabilization is primarily a result of balancing igneous rock weathering, volcanism and seafloor burial rates. The tool invoked in this theses to study these interactions on different timescales is a cost-efficient Earth system model of intermediate complexity: the Bern3D-LPJ model. This model does not only simulate the cycling of carbon, but also tracks isotopes ^{13}C and ^{14}C (radiocarbon), thus helping to understand the complex nature of the global carbon cycle.

The **introductory chapter** of this thesis gives an overview on the global carbon cycle, with a focus on carbon-climate interactions and isotopes. It emphasizes paleoclimatic investigations and benchmarking to strengthen our understanding of current and future human-driven climate change. Moreover, the most important concepts and methods are introduced as a basis for the subsequent chapters.

In **Chapter 2**, the Bern3D-LPJ carbon cycle-climate model is shortly described. In addition, a summary of changes incorporated in the recently updated ocean component is given. A special focus is set on the adjustment of biogeochemical parameters in order to improve the modeled distribution of dissolved carbon, alkalinity and nutrients. In a final step, the model's preindustrial solution, i.e. ocean circulation, tracer distributions and global fluxes is presented and discussed in the light of the latest datasets available.

Chapter 3 consists of a study published in *Earth and Planetary Science Letters* in which a recent hypothesis is tested, namely whether the deglacial retreat of Northern Hemisphere ice sheets triggered enhanced deglacial volcanic activity in these regions. As volcanoes release carbon stored in Earth's mantle as they erupt, this process may considerably contributed to the observed glacial-interglacial CO_2 variation of $\sim$100 parts per million (ppm).

In order to test the implications of the proposed mechanism, we apply a range of 40 kyr volcanic emission scenarios of carbon, ^{13}C and ^{14}C to the Bern3D model. We find a CO_2 increase of 46 ppm for the central scenario, peaking at around 6 kyr before present (BP). By comparing the modeled response in the atmosphere-ocean-sediment system to a range of ice-core and marine proxy records, we show that the proposed mechanism cannot be rejected: the uncertainties in

the emission history as well as in other processes involved in deglacial and early Holocene CO_2 dynamics prevent a firm conclusion. One of the drawbacks is that carbon isotopes serve as a weak constraint here, because i) magma $\delta^{13}C$ does not differ significantly from the signature of the contemporary atmosphere and ii) the $\Delta^{14}C$ decrease induced by a weakening of the geomagnetic shield and outgassing of old oceanic carbon may screen the $\Delta^{14}C$ decline induced by old volcanic CO_2. On the other hand, the pronounced CO_2 increase in the early Holocene resulting from the central and high scenarios is in conflict with the observed CO_2 decline during this period. We therefore conclude that the volcanic feedback to deglaciation is small.

Chapter 4 focuses on ^{14}C and its application as a proxy for solar activity. By running simulations with the Bern3D-LPJ model from 20 kyr BP to 1950 AD with prescribed atmospheric $\Delta^{14}C$ from the IntCal09 and SHCal04 records, the Holocene radiocarbon budget is solved for atmospheric production (Q). We do not only consider past changes in $\Delta^{14}C$, but also take into account changes in CO_2 and its radiative forcing, continental ice-sheet extent, sea level, dust flux, shallow-water carbonate deposition and anthropogenic landuse change. The results of these experiments are summarized in a study published in *Climate of the Past*. With these experiments, we partially resolve the discrepancy between carbon-cycle and particle-simulation based estimates of the contemporary production rate; our estimate of Q is in line with the results of the most recent production-model estimates. We do not only reconstruct Q for the first time with a 3-D model over the past 10 kyr, but Q is also applied as a proxy for the solar modulation potential and total solar irradiance (TSI) using published methodologies. We show that linking past TSI to instrumental records is problematic, both because i) early instrumental records are prone to considerable uncertainty and ii) humans disturb the natural ^{14}C cycle not only by atomic bomb testing, but also by the combustion of fossil fuels and landuse emissions, both introducing uncertainty in the radiocarbon budget and thus our Q reconstructions. Our best-guess normalization of the solar activity record suggests a high, but not exceptionally high contemporary solar activity compared to the past 10 kyr. We also show that a bias is introduced by globally applying the Northern Hemisphere record (IntCal09) as done in past studies. Beside the solar activity reconstruction, Chapter 4 also includes results on pre-Holocene ^{14}C dynamics. For the past 50 kyr, ^{10}Be and paleointensity-based Q reconstructions are prescribed to the Bern3D model in order to simulate atmospheric $\Delta^{14}C$. We find that most of the reconstructions of Q are in conflict with high glacial $\Delta^{14}C$ levels as preserved in natural archives; past carbon cycle changes are probably too small to explain the remaining offset.

In **Chapter 5**, we present the results of a multi-model effort to determine the response of the carbon cycle-climate system to a pulse-release of CO_2. In this study, which we published in *Atmospheric Chemistry and Physics*, fifteen models ran the same CO_2 pulse-emission experiments under contemporary CO_2 conditions (389 ppm). On a time horizon of decades to centuries, atmospheric CO_2 and therefore its radiative impact is controlled by how much of the (excess) CO_2 is taken up the by ocean and land carbon reservoirs. The evolution of atmospheric CO_2 can then be represented by impulse response functions (IRF_{CO_2}). IRF_{CO_2} serves as a basis for the computation of the global warming potential (GWP), a metric to compare the radiative effect of emissions of different greenhouse gases. We provide an updated estimate (and uncertainty range) of the absolute GWP of CO_2 at e.g. year 100 of 92.5 (68–117) $\times 10^{-15}$ yr W m^{-2} per kg CO_2. Further, we set up numerous sensitivity experiments with the Bern3D-LPJ model in order to quantitatively estimate the influence of the pulse size, the chosen background scenario and carbon-climate feedbacks. In addition to analyzing the response in atmospheric CO_2 levels, the model responses in air-sea and air-biosphere fluxes, atmospheric temperature, sea level rise and ocean heat content are quantified and fitted by analytical functions. As an extension to the published study, a simple representation of the continental weathering feedback is implemented in the Bern3D and its influence on IRF_{CO_2} quantified in terms of a pulse-release of CO_2 under preindustrial conditions.

In **Chapter 6**, the feedback of the terrestrial biosphere under global warming scenarios is

explored. In a study published in *Nature Climate Change*, we i) reconcile the observed 20th century increase in atmospheric N_2O and CH_4 levels and ii) quantify the terrestrial response to CO_2 increase and climate change in terms of feedback parameters. The feedbacks of N_2O and CH_4 are not well understood so far, as most current Earth system models do not simulate the cycling of these compounds. By running numerous experiments with the Bern3D-LPJ model applying the extended Representative Concentration Pathway (RCP) emission scenarios, we separate feedbacks arising from snow-albedo changes as well as changes in CO_2, N_2O and CH_4 fluxes. Our results show that under RCP8.5 (a business-as-usual scenario), the land biosphere likely turns into a net source of CO_2 by 2100 AD. We find that by the year 2300 AD, N_2O and CH_4 feedbacks add another 0.4–0.5 °C on top of the 0.8–1.0 °C caused by the albedo and carbon cycle feedbacks.

Chapter 7 outlines how the Bern3D-LPJ model can be applied in the future, for example by modeling the response of multiple greenhouse gases (CO_2, N_2O, CH_4) during abrupt climate events or by applying inverse modeling methods to paleoclimatic questions. In the **appendices**, supplementary material is given, mainly related to the Bern3D-LPJ model but also containing additional material to the multi-model IRF_{CO_2} study.

Contents

Chapter 1

Introduction

1.1 Motivation

Humans have emitted $\sim$550 gigatons[1] (Gt) of carbon (C) into the atmosphere since 1750 AD (Ciais et al., 2013). As a consequence, the concentration of carbon dioxide (CO_2) and its radiative forcing (RF) have increased more than an order of magnitude faster than any sustained change during the past 22 thousand years (kyr) (Joos & Spahni, 2008; Masson-Delmotte et al., 2013). Atmospheric CO_2 concentrations have recently exceeded[2] 400 parts per million[3] (ppm) for the first time since at least 800 kyr ago (Siegenthaler et al., 2005; Lüthi et al., 2008). Not only CO_2, but also other well-mixed greenhouse gases (GHGs) including methane (CH_4) and nitrous oxide (N_2O) increase at a rate not seen in the past 22 kyr. This anthropogenic perturbation of the carbon cycle has considerably altered Earth's energy budget as GHGs absorb outgoing thermal longwave radiation (greenhouse effect). In the fifth assessment report (AR5), the Intergovernmental Panel on Climate Change (IPCC) concludes that it is extreme likely that human influence has been the dominant cause of the global warming since the mid-20th century (IPCC, 2013).

The anthropogenic perturbation calls for a more comprehensive understanding of the processes driving the carbon cycle-climate system and their interactions in order to predict their future impacts. In the recent decades, the modeling of the carbon cycle has evolved from using simple box models to the application of comprehensive Earth system models (ESMs), i.e. atmosphere-ocean general circulation models (AOGCMs) including a representation of global biogeochemical cycles such as the carbon and nitrogen (N) cycles. Earth system models of intermediate complexity (EMICs), i.e. models based on simplified physics and a reduced number of included processes, close the gap between these box models and ESMs, some example of which are probabilistic applications (Steinacher et al., 2013) or simulations over extended timescales (Ritz et al., 2011; Brovkin et al., 2012; Menviel & Joos, 2012).

But how do we know that such models correctly represent the relevant processes of the carbon cycle? Information on the past carbon cycle state as reconstructed from air trapped in polar ice or preserved in ocean sediments provide a benchmark for models (Schmidt et al., 2013). The cooperative work between modelers and experimentalists is therefore of utmost importance to understand and disentangle the complex chain of forcings and feedbacks in the past and therefore also the future carbon cycle-climate system.

---

[1] 1 gigaton $= 10^9$ tons $= 10^{15}$ g
[2] http://www.esrl.noaa.gov/gmd/ccgg/trends/
[3] The ratio of the number of gas molecules to the total number of molecules of dry air.

1.2 The global carbon cycle

Although the greenhouse effect of CO_2 and CH_4 is directly linked to the atmospheric concentrations, carbon is found in many different reservoirs on Earth, namely the land, ocean (including sediments) and lithosphere. In fact, the atmospheric carbon inventory is small (in comparison with the ocean/land) and due to the rigorous exchange with the surface ocean and land biosphere, its CO_2 concentration is largely controlled by the ocean and land reservoirs. In order to understand how atmospheric CO_2 reacts to changes in the global carbon cycle or the climate, a holistic understanding of the participating reservoirs is essential. Present day fluxes and inventories (as well as the anthropogenic perturbation thereof) are sketched in Fig. 1.1. In the following section, these reservoirs and their interactions are explained in more detail.

adapted from IPCC AR5, chapter 8, final draft
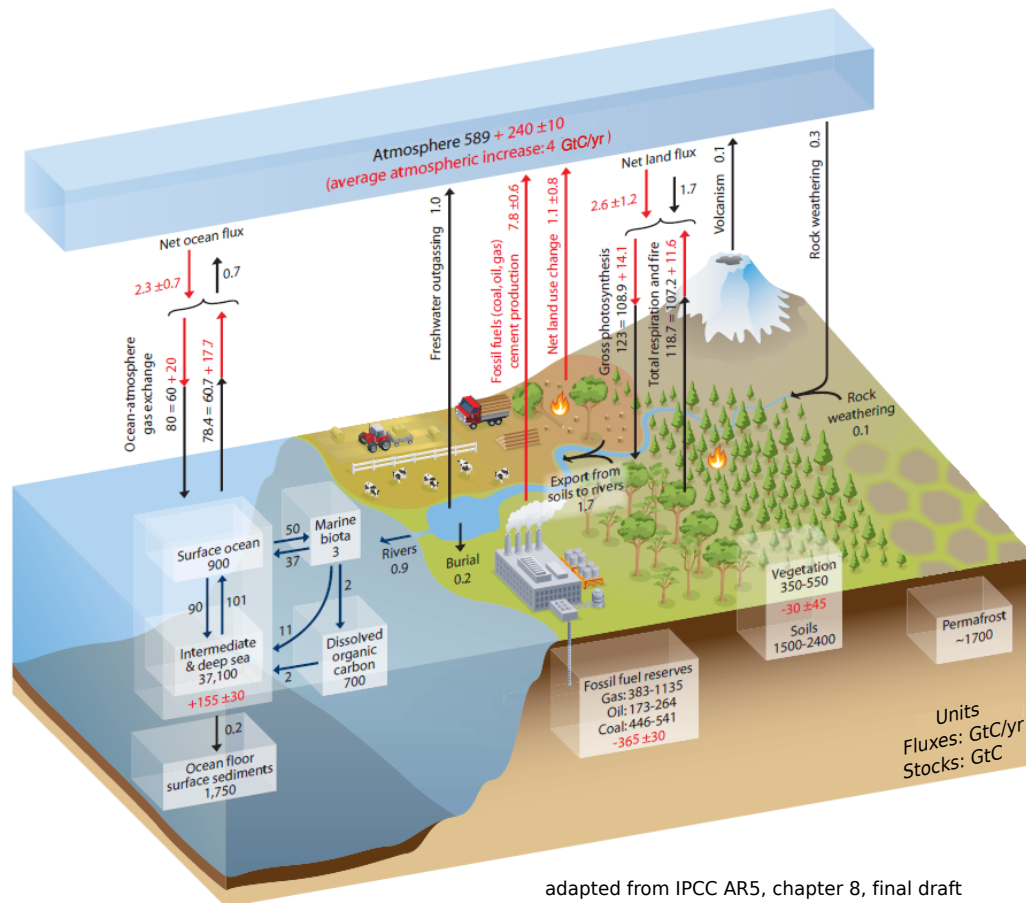
Figure 1.1: Schematic overview on the global carbon cycle. Preindustrial (1750 AD), i.e. "natural" inventories and fluxes (black numbers and arrows) are reported in Gt C and Gt C yr^{-1} respectively ($1\,\text{Gt} = 10^{15}\,\text{g}$). The main carbon reservoirs, including the atmosphere, land, ocean (and sediments) and lithosphere, exchange carbon on many different timescales ranging from $0.2\,\text{Gt C yr}^{-1}$ (weathering-burial cycle) to $120\,\text{Gt C yr}^{-1}$ (gross atmosphere-vegetation exchange). Red arrows and numbers indicate annual "anthropogenic" fluxes averaged over the last decade (2000–2009). The atmospheric CO_2 increase of $240 \pm 10\,\text{Gt C}$ ($113 \pm 5\,\text{ppm}$) as a result of anthropogenic emissions from the combustion of fossil fuels, cement production and landuse change have been considerably buffered by an increase in net ocean and land fluxes such that $155 \pm 30\,\text{Gt C}$ and $150 \pm 90\,\text{Gt C}$ have been stored in the ocean and land sinks. The figure is adapted from Ciais et al. (2013).

1.2.1 Atmosphere

Though the smallest carbon reservoir with a preindustrial inventory of $\sim$590 Gt C, the atmosphere is of special importance for two reasons: firstly, the atmosphere connects both the land and

surface ocean carbon reservoirs almost instantaneously with a turnover timescale of only a few years. Secondly, the atmospheric carbon, mostly in the form of CO_2 and to a minor portion CH_4, directly influences Earth's climate due its ability to absorb longwave radiation. The influence of greenhouse gases on climate is further discussed in Sec. 1.3. Atmospheric carbon is often reported as a concentration, the burden can then be calculated using the conversion factor of $2.12\,\mathrm{Gt\,C\,ppm^{-1}}$ (Prather et al., 2012) assuming that the atmosphere is well mixed.

1.2.2   Ocean

Most of the carbon in the ocean is found to be in the form of dissolved inorganic carbon (DIC, $\sim$38'000 Gt C), only $\sim$700 Gt C is stored as dissolved organic carbon (DOC) (Hansell et al., 2009). The marine biota pool, consisting of e.g. phytoplankton, is comparatively small ($\sim$3 Gt C). Due to the large carbon inventory and a turnover timescale of $\sim$600 yr, the ocean is the most important driver for carbon fluxes on timescales of centuries to millennia, also because of its ability to absorb/emit a large amount of CO_2 from/to the atmosphere. The ocean's capability to store a large amount of carbon is primarily a consequence of the inorganic carbonate chemistry, which is discussed in the following in more detail.

Inorganic carbonate chemistry in seawater

In equilibrium, concentration of dissolved CO_2, which is chemically not separable from the sum of aqueous carbon dioxide ($CO_2(aq)$) and carbonic acid (H_2CO_3), is given by Henry's law:

$$[CO_2(aq) + H_2CO_3] \equiv [CO_2] = K_0 \cdot pCO_2, \tag{1.1}$$

where K_0 is the temperature- and salinity-dependent solubility constant (Weiss, 1974). Once dissolved, CO_2 reacts with H_2O to form HCO_3^- (bicarbonate) and CO_3^{2-} (carbonate) ions:

$$CO_2 + H_2O \overset{K_1}{\rightleftharpoons} HCO_3^- + H^+ \overset{K_2}{\rightleftharpoons} CO_3^{2-} + 2H^+, \tag{1.2}$$
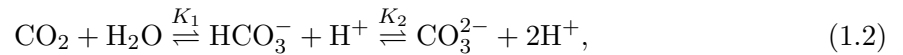
where the pressure, temperature and salinity-dependent stochoimetric equilibrium constants are defined as:

$$K_1 = \frac{[HCO_3^-][H^+]}{[CO_2]} \quad \text{and} \quad K_2 = \frac{[CO_3^{2-}][H^+]}{[HCO_3^-]}. \tag{1.3}$$

DIC (sometimes denoted ΣCO_2 or TCO_2) is then defined as the sum of these species:

$$DIC = [CO_2] + [HCO_3^-] + [CO_3^{2-}], \tag{1.4}$$

where in the modern ocean most (86.5%) of the carbon is the form of HCO_3^-, followed by CO_3^{2-} (13%), and the abundance of CO_2 is only $\sim$0.5%. An important concept in chemical oceanography is the seawater alkalinity (Alk), which can be understood as a charge balance and is given by:

$$Alk = [HCO_3^-] + 2[CO_3^{2-}] + [B(OH)_4^-] - [H^+] + \text{minor compounds.} \tag{1.5}$$

Alk can be approximated by the so-called carbonate alkalinity $Alk \approx CA = [HCO_3^-] + 2[CO_3^{2-}]$. CO_3^{2-} is therefore approximately $Alk - DIC$, but in reality also depends weakly on local phosphate (PO_4^{3-}) and silicic acid (SiO_2) concentrations. As the carbonate system is over-determined, it is not necessary to transport all carbon species as tracers. Normally, at least DIC and Alk are transported in biogeochemical ocean components (e.g. Najjar et al., 1999; Orr & Najjar, 1999).

The calculations of the dissociation constants K_i need be performed at least for the ocean surface in order to obtain surface water pCO_2 and therefore air-sea fluxes (F_{as}) of CO_2. The net flux of CO_2 across the air-sea interface (subscripts a and s) is then given by [4] :

$$F_{as} = k_w \cdot ([CO_2]_a - [CO_2]_s) = k_w \cdot K_0 \cdot (pCO_{2,a} - pCO_{2,s}), \qquad (1.6)$$

where the piston-velocity k_w is commonly parametrized as function of wind speed (Wanninkhof, 1992) and sea-ice cover (e.g. Steiner et al., 2013).

But what is the influence of DIC and Alk on surface ocean pCO_2 and thus atmospheric pCO_2 in equilibrium conditions? This can be well approximated as

$$pCO_2 \approx \frac{K_2}{K_0 \cdot K_1} \frac{(2 \cdot DIC - Alk)^2}{Alk - DIC}, \qquad (1.7)$$

This relationship clearly demonstrates that the concentration of DIC alone does not drive atmospheric pCO_2, it is rather the combination of Alk and DIC. As a rule of thumb, changes in pCO_2 are given by $\Delta pCO_2 \propto \Delta DIC - 1.22 \cdot \Delta Alk$ for a PI surface ocean (i.e. the addition of DIC and Alk in a 1:1 ratio increases pCO_2 only marginally).

One of the most important characteristics of the ocean's inorganic carbon cycle is its ability to buffer atmospheric CO_2 changes, e.g. due to fossil fuel emissions. As Alk is conserved during ocean CO_2 uptake (because CO_2 is not charged), DIC increases and thus CO_3^{2-} decreases (as well as pH). However, the change in DIC is not proportional to the change in $[CO_2]$ as ocean DIC only increases by $\sim 10\%$ for a doubling of atmospheric CO_2. The sensitivity of pCO_2 to changes in DIC is expressed by the so-called buffer-factor or Revelle-factor (Revelle, 1957). The Revelle-factor is defined as $\frac{d[CO_2]}{CO_2} / \frac{d[DIC]}{[DIC]}$ and varies spatially from $\sim$8–15 (Sabine et al., 2004).

What controls the DIC and Alk gradients in the ocean?

Besides ocean mixing, the three key processes influencing the gradients of DIC and Alk in the water column are summarized in Fig. 1.2. For DIC, all of these processes referred to as carbon "pumps", tend to redistribute DIC from the surface ocean to the deep (without these processes, DIC and Alk would be uniformly distributed within the ocean): the **solubility pump**, or the gradient of DIC induced by air-sea gas exchange, leads to higher DIC concentrations in the deep ocean because areas of deepwater formation tend to be cold and therefore its waters have a higher-than-average CO_2 solubility.

The surface-dwelling phytoplanktion form particulate organic matter (POM) from CO_2 by photosynthesis. The rate of this primary production depends on the availability of macronutrients PO_4 and nitrate (NO_3^-), micronutrients as iron (Fe), light and water temperature. As these organisms settle to the deep as they die, they significantly alter DIC (and to a minor part Alk[5]) during the remineralization[6] of the organic matter. This process is termed **organic matter pump** or soft-tissue pump. Most of the organic matter is remineralized within the uppermost 300 m, such that only a tiny fraction is eventually deposited on the ocean sediments (Martin et al., 1987; Sarmiento & Gruber, 2006; Buesseler et al., 2007).

The last pump, referred to as the **carbonate pump**, denotes the water-column component of the calcium carbonate ($CaCO_3$) cycle. The production (and subsequent dissolution) of calcite

---

[4] Actually the fugacity of CO_2 (fCO_2) is the quantity to consider here, but as CO_2 behaves almost like an ideal gas, the deviation of pCO_2 from fCO_2 is negligible.

[5] For each mol of carbon bound in organic matter Alk is **increased** by $\sim 16/117$ mol

[6] Remineralization denotes the reverse process of photosynthesis, i.e. the liberation of carbon, alkalinity and nutrients from POM under the consumption of oxygen.
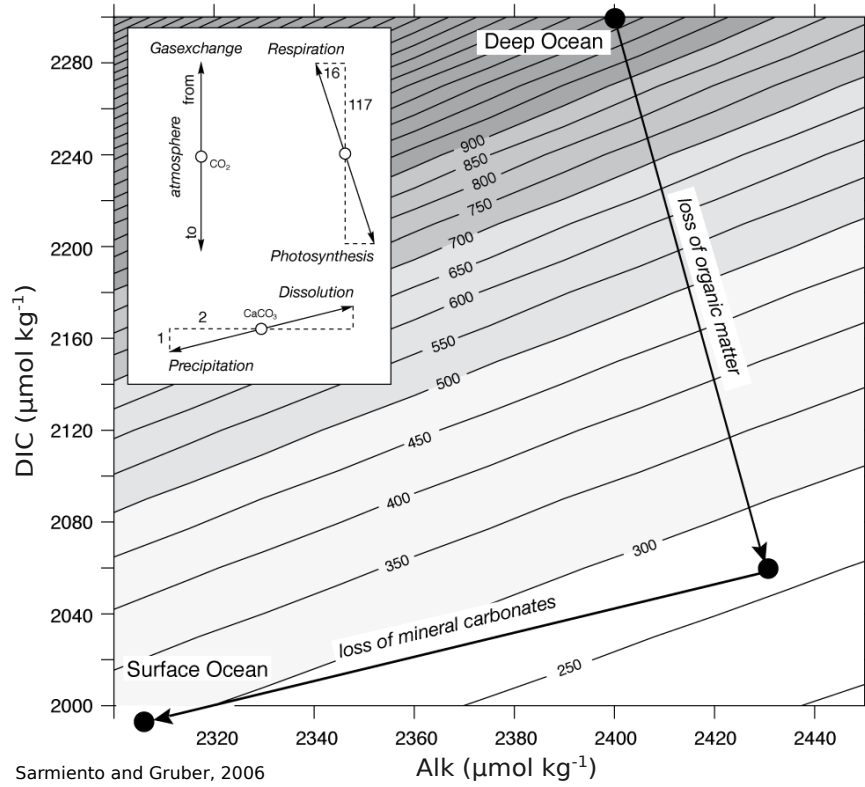
Figure 1.2: Biologically and physically driven changes in the ocean's Alk and DIC concentrations (horizontal and vertical axes) and the resulting changes in $p\mathrm{CO_2}$ (contours) for typical ocean temperature and salinity values. The organic matter pump, i.e. surface ocean photosynthesis and remineralization in the deep, induces changes primarily in affecting the vertical distribution of DIC. On the other hand, the carbonate pump ($\mathrm{CaCO_3}$ precipitation at the surface and redissolution in the deep) largely controls the Alk distribution in the water column as calcium carbonate as a Alk to DIC ratio of 2:1. Note that organic matter export reduces $p\mathrm{CO_2}$, while $\mathrm{CaCO_3}$ export increases $p\mathrm{CO_2}$ at the surface. Gas exchange does not affect Alk as $\mathrm{CO_2}$ is not electrically charged. The net effect of these processes is a decreased Alk:DIC ratio in the deep ocean with an elevated $p\mathrm{CO_2}$ compared to typical surface waters. The figure is adapted from Sarmiento & Gruber (2006).

shells by calcifying organism such as coccolithophores, i.e. the reactions (see e.g. Sarmiento & Gruber, 2006; Gattuso & Hansson, 2011):

$$\mathrm{Ca^{2+} + CO_3^{2-} \rightleftharpoons CaCO_3} \quad \text{and} \quad \mathrm{Ca^{2+} + 2\,HCO_3^{-} \rightleftharpoons CaCO_3 + CO_2 + H_2O} \qquad (1.8)$$

actually liberate $\mathrm{CO_2}$ (surface ocean $p\mathrm{CO_2}$ is increased) during $\mathrm{CaCO_3}$ formation, as the removal of $\mathrm{CO_3^{2-}}$ leads to the dissociation of $\mathrm{HCO_3^{-}}$ (DIC and Alk are consumed in a 2:1 ratio). Therefore it is also known as the carbonate "counter-pump".

Of special importance here is $\mathrm{CO_3^{2-}}$, because it defines the degree of seawater saturation w.r.t. to $\mathrm{CaCO_3}$: $\Delta[\mathrm{CO_3^{2-}}] = [\mathrm{CO_3^{2-}}] - [\mathrm{CO_3^{2-}}]_{\mathrm{sat}}$, i.e. the deviation from the local concentration to the saturation concentration determines whether, and at what rate, $\mathrm{CaCO_3}$ is preserved or dissolved. The degree of $\mathrm{CaCO_3}$ saturation w.r.t. calcite is often reported as a dimensionless parameter Ω [7].

Due to the strong pressure-dependence of $[\mathrm{CO_3^{2-}}]_{\mathrm{sat}}$, the upper ocean is oversaturated and the deep ocean ($\lesssim 3000\,\mathrm{m}$) undersaturated w.r.t. calcite. Due to this depth-dependence of Ω, calcite is slowly dissolved while sinking to the deep ocean, eventually reaching the seafloor. There the calcite shells are deposited on the sediment layer and preserved if the local water is oversaturated.

---

[7] $\Omega = \frac{[\mathrm{CO_3^{2-}}][\mathrm{Ca^{2+}}]}{[\mathrm{CO_3^{2-}}]_{\mathrm{sat}}[\mathrm{Ca^{2+}}]_{\mathrm{sat}}}$ such that for $\Omega > 1$, $\mathrm{CaCO_3}$ is preserved while for $\Omega < 1$, $\mathrm{CaCO_3}$ is dissolved.

1.2.3   Sediments

Although the flux of particulate matter (e.g. $CaCO_3$, POM and opal[8]) to the ocean floor is small with an corresponding net carbon flux of only $\sim 0.2\,\mathrm{Gt\,C\,yr^{-1}}$, the ocean sediment is an important carbon reservoir, especially on timescales longer than $1000\,\mathrm{yr}$.

The actual amount of carbon stored in the sediments is difficult to constrain, mainly because its definition can range from the upper few centimeters to the entire lithosphere. The "diagenetically active zone" of the seafloor sediments, i.e. the portion of the sediments that is still subject to bioturbation and exchange with the ocean (uppermost $\sim 10\,\mathrm{cm}$) contains $\sim 1750\,\mathrm{Gt\,C}$ (Ciais et al., 2013).

The $CaCO_3$ stored in this surface sediment reservoir is of special interest as it stabilizes seawater CO_3^{2-}. This process know as "carbonate compensation" and works as follows given rising DIC concentrations, e.g. due to a transient increase in atmospheric CO_2: as Alk is not affected by air-sea fluxes of CO_2, whole-ocean CO_3^{2-} decreases as a result of this process, leading to a decrease in the calcite saturation state. The lysocline, i.e. depth where $\Omega = 1$, shoals such that $CaCO_3$ in the now undersaturated zone dissolve, adding Alk and DIC in a 2:1 ratio to the surrounding water. This flux increases CO_3^{2-}, thereby restoring the depth of the lysocline. The net effect of this process is to increase to ocean's Alk/DIC-ratio and therefore lower atmospheric $p CO_2$.

In the long run, deposition fluxes of POM and $CaCO_3$ exceed redissolution/remineralization fluxes, leading to a net burial (i.e. loss) of carbon from the atmosphere-ocean-sediment system. This carbon enters the geologic reservoir (i.e. the lithosphere) and eventually re-enters the ocean-atmosphere system by volcanic outgassing or the weathering of silicate and carbonate rocks. This weathering-burial cycle is of special importance on timescales of several millennia to millions of years, as it stabilizes the carbon cycle (and therefore atmospheric $p CO_2$) on these geological timescales (e.g. Berner, 2003).

Fossil fuels as coal and oil are also considered as a part of this geologic reservoir. It is clear that the rate of CO_2 liberation by the excessive combustion of these fuels largely exceeds natural volcanic and weathering fluxes ($8.6\,\mathrm{Gt\,C\,yr^{-1}}$ vs $0.2\,\mathrm{Gt\,C\,yr^{-1}}$ in 2012), considerably disturbing the natural carbon balance between these reservoirs; this is discussed in Sec. 1.4.

1.2.4   Terrestrial biosphere

The storage of carbon in biomass on land is more difficult to quantify due to the significantly inhomogeneous carbon density distribution, further complicating the estimation of global inventories. Ciais et al. (2013) estimates that 450–$650\,\mathrm{Gt\,C}$ is stored in living biomass, i.e. organic carbon built from atmospheric CO_2 through carbon fixation (photosynthesis). This flux is referred to as gross primary production (GPP) and is approximately $120\,\mathrm{Gt\,C\,yr^{-1}}$. About half of this carbon is used by the plants for maintenance and growth, the so-called autotrophic respiration. The remaining flux is called net primary production (NPP) and is of great importance, but its quantification is difficult. The effect of changing ambient CO_2 levels on NPP, know as "CO_2 fertilization" of photosynthesis, is not yet well understood. Free-air CO_2 enrichment (FACE) experiments yield differing results depending on the studied ecosystem (Leuzinger & Hättenschwiler, 2013, and references therein). Although a $\sim$logarithmic increase in NPP is used in dynamic global vegetation models (DGVMs) (Sitch et al., 2008), the long-term effect on (global) carbon pools is not clear, especially when taking into account limiting nutrients, e.g. N-dynamics (Sokolov et al., 2008; Thornton et al., 2009). The net flux of carbon between the terrestrial biosphere and the atmosphere is denoted as net ecosystem production (NEP).

---

[8]Opal is a hydrated amorphous form of silica: $SiO_2 \cdot n H_2O$.

Despite the $\sim$constant terrestrial carbon storage during the preindustrial epoch, NEP shows a considerable inter-annual variability of $\sim 3\,\mathrm{Gt\,C\,yr^{-1}}$.

In addition to the relatively fast exchanging pool of living biomass, 1500–2400 Gt C is stored in (dead) litter and soils (Ciais et al., 2013). This carbon may be decomposed by bacterial activity (heterotrophic respiration) and the associated carbon returned to the atmosphere. Even more isolated are $\sim$2500 Gt of "old" carbon assumed to be stored in permafrost regions and peatlands (Tarnocai et al., 2009; Yu et al., 2010; Spahni et al., 2013), i.e. regions where organic matter accumulates due to low respiration rates. It is currently a field of active research how e.g. northern hemisphere (NH) peatlands behave in response to waxing and waning of continental ice sheets and thus contribute to observed CO_2 changes (Sec. 1.4). Although limited in the amount, the carbon stored on land has the potential to influence atmospheric CO_2 on different timescales, corresponding to the temporal variability of the interactions of the various carbon reservoirs.

1.2.5 Isotopes in the carbon cycle

Although much less abundant than ^{12}C, the carbon isotopes ^{13}C and ^{14}C play a major role in the current process of understanding global carbon cycle dynamics. Both isotopes take part in the global carbon cycle, and most of the processes explained above apply also for carbon isotopes, though their cycling differs in an important aspects these processes involve fractionation.

Stable carbon isotope

Approximately 1% of the global carbon is the form of the stable isotope ^{13}C. It is transported along the same pathways as ^{12}C but is fractionated mainly during photosynthesis (Hubick & Farquhar, 1989) and air-sea gas exchange (Mook, 1986). During photosynthesis, plants prefer "light" carbon, i.e. carbon having a low $^{13}R = {}^{13}\mathrm{C}/{}^{12}\mathrm{C}$. Expressed in terms of the isotopic signature, i.e.:

$$\delta^{13}\mathrm{C} = 1000 \cdot \left(\frac{^{13}R}{^{13}R_{\mathrm{std}}} - 1\right), \tag{1.9}$$

with $^{13}R_{\mathrm{std}} = 1.12372{\cdot}10^{-2}$ being a standard ratio, the terrestrial biomass is depleted in ^{13}C with $\delta^{13}\mathrm{C} \approx -25‰$ compared to the preindustrial atmosphere, which had a $\delta^{13}\mathrm{C}$ of approximately –6.4‰.

Oceanic δ^{13}C of DIC is primarily controlled by temperature-dependent kinetic fractionation during air-sea gas exchange, in which carbon enriched in ^{13}C is preferentially dissolved, such that the average ocean δ^{13}C is close to 0‰ for the preindustrial atmosphere (Schmittner et al., 2013). Within the water column, the fixation of CO_2 in POM during photosynthesis favors light carbon, inducing a surface-to-deep gradient of $\sim$2–3‰ as light organic matter remineralizes in the deep. For oceanographers, δ^{13}C of DIC as recorded in sediment cores is therefore a valuable proxy for ocean stratification, and ocean circulation. On multi-millennia timescales, atmospheric δ^{13}C of CO_2 is stabilized through the weathering-burial cycle of ^{13}C, with the lithospheric carbon having a δ^{13}C of $\sim -5‰$ (Deines, 2002).

In summary, δ^{13}C of atmospheric CO_2 can be used as a proxy both for the amount of biomass stored on land as well as for ocean circulation (and temperature) changes.

Radiocarbon

The radioactive carbon isotope ^{14}C (radiocarbon) behaves much like ^{13}C except for some major differences: i) it is produced in the upper atmosphere by the secondary neutron flux resulting from the spallation reaction $^{14}\mathrm{N} + \mathrm{n} \rightarrow {}^{14}\mathrm{C} + \mathrm{p}$, triggered by incoming galactic cosmic rays (GCRs). ^{14}C is produced at a rate (Q) of $\sim$1.5–2.5 atoms cm^{-2} s^{-1} (Damon & Sternberg, 1989; Masarik & Beer, 1999; Usoskin & Kromer, 2005; Masarik & Beer, 2009; Kovaltsov et al., 2012). ii)

^{14}C decays with a half-life of $t_{1/2} = 5730 \pm 40\,\mathrm{yr}$ (Godwin, 1962), or alternatively expressed by the mean lifetime $\tau = t_{1/2} \cdot \ln(2)^{-1} = \lambda^{-1} = 8267 \pm 58\,\mathrm{yr}$ (λ being the *decay constant*). iii) As a consequence of its mass, the fractionation is twice as large as that of compounds containing ^{13}C[9].

As the rate of radiocarbon production is small compared to the rate of its radioactive decay, the preindustrial atmosphere contains only a tiny fraction of ^{14}C, namely approximately $^{14}R_{\mathrm{std}}$ $= [^{14}\mathrm{C}/^{12}\mathrm{C}\,]_{\mathrm{std}} = 1.176 \cdot 10^{-12}$. Analogous to ^{13}C, radiocarbon concentrations are reported in terms of a per-mil deviation from this standard ratio (Stuiver & Polach, 1977):

$$\delta^{14}\mathrm{C} = 1000 \cdot \left(\frac{^{14}R}{^{14}R_{\mathrm{std}}} - 1\right). \tag{1.10}$$

Alternatively, ^{14}R may be expressed by the activity of a given sample. The half-life of radiocarbon makes it ideally suitable as an age tracer, and this is how it is mainly used in paleoclimatology: as ^{14}C enters the global carbon cycle after production (in the atmosphere), it is incorporated into living biomass on land (e.g. trees) as well as into $CaCO_3$-shells of marine biota, eventually deposited in deep-sea sediments. Given the possibility to reconstruct the ^{14}C concentration of the environment where these organisms grew, their ^{14}C activity is directly linked to the time when they last exchanged carbon with their environment (i.e. their death).

A common way to express ^{14}C abundances is in terms of δ^{14}C corrected for fractionation, for which δ^{13}C of the sample must be known, is as follows:

$$\Delta^{14}\mathrm{C} = \delta^{14}\mathrm{C} - 2 \cdot (\delta^{13}\mathrm{C} + 25\text{‰}) \cdot \left(1 + \frac{\delta^{14}\mathrm{C}}{1000}\right). \tag{1.11}$$

The 25‰ in numerator of the correction term is motivated by the reconstruction of ^{14}C from dead biomass (trees) having a $\delta^{13}\mathrm{C} \approx -25\text{‰}$[10]. Alternatively, measured radiocarbon data is reported in terms of radiocarbon-ages (see e.g. Stuiver & Polach, 1977), i.e. the age of the sample assuming that the atmosphere was always fixed at 0‰. In other words: if the radiocarbon age is lower than the calendar age (which has to be determined by an independent method) in a given sample, then the past atmospheric Δ^{14}C signature was higher than 0‰. Given the calendar age and the radiocarbon age, past Δ^{14}C is given by:

$$\Delta^{14}\mathrm{C} = \mathrm{e}^{\frac{\text{radiocarbon-age}}{-8033\,\mathrm{yr}}} \cdot \mathrm{e}^{\frac{\text{calendar-age}}{8267\,\mathrm{yr}}}. \tag{1.12}$$

In addition to its application as a proxy for "age", the production rate of ^{14}C (as well as of others cosmogenic radionuclides) can also be used as a proxy for GCR influx, which in turn is modulated by solar activity. The rational behind this is briefly outlined in the following and sketched in Fig. 1.3a and detailed in a recent review by Usoskin (2013) : Q is modulated both by changes in the geomagnetic as well as magnetic fields enclosed in the regions enclosed by solar wind hitting Earth's magnetosphere. Both components of the magnetic field shield Earth's atmosphere from incident high-energy GCR, the prerequisite of spallation-reactions with N to produce ^{14}C. The solar activity may therefore be defined as so-called a solar modulation parameter Φ (e.g. Castagnoli & Lal, 1980), such that changes in Q (and thus atmospheric Δ^{14}C) are inversely related to solar activity: the higher the solar activity, the lower the value of Q. Particle simulations are needed in order to derive a quantitative relationship between Q, Φ and the strength of the geomagnetic field as expressed by its virtual axis dipole moment (VADM) (Masarik & Beer, 1999, 2009; Kovaltsov et al., 2012). The result of such a simulation is shown in Fig. 1.3b.

---

[9]This theoretical consideration is based on the fact that the mass difference to ^{12}C is twice as large for ^{14}C as for ^{13}C. Southon (2011) recently questioned this simple assumption.

[10]As a consequence: $\delta^{14}\mathrm{C} \approx \Delta^{14}\mathrm{C}$ for organic carbon.
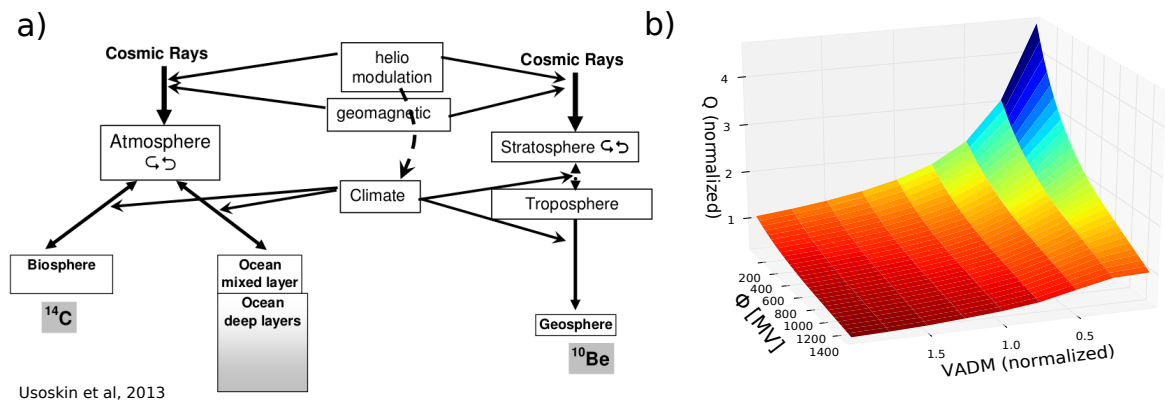
Figure 1.3: **(a)** The production and cycling of cosmogenic radionuclides ^{14}C (left) and ^{10}Be (right). The production of these isotopes is controlled both by the solar and geomagnetic modulation of the cosmic ray influx. While ^{10}Be is removed from the atmosphere within a few years, ^{14}C enters the global carbon cycle as ^{14}CO$_2$. Solar activity influences both the production of ^{14}C as well its distribution in the carbon cycle as mediated by climate-carbon feedbacks. This figure is taken from Usoskin (2013). **(b)** The rate of ^{14}C production (Q) from Masarik & Beer (1999) is shown as a function of the solar modulation potential (Φ) and the geomagnetic field, expressed as the virtual axis dipole moment (VADM). Both Q and VADM are normalized to a reference value.

The qualitative link between variations in Q and variations in atmospheric Δ^{14}C is trivial. Nevertheless, because the observed Δ^{14}C is the result of the entire past history of Q, they can only be related to each other in a quantitative way using a carbon cycle model (e.g. Muscheler et al., 2004; Usoskin & Kromer, 2005). In addition to a reconstruction of Δ^{14}C, the time evolution of past geomagnetic-field changes must also be known in order to isolate the solar signal.

A state-of-the-art reconstruction of decadal variations in Q over the past 10 kyr is presented in this thesis (see Chap. 4 and Roth & Joos (2013)). On the basis of this new production record, published methods and the newest available VADM history were used to infer past variations in Φ and total solar irradiance (TSI).

1.3 Carbon-cycle dynamics and interferences with the climate system

Reconstructions of past state variables of the carbon cycle, e.g. GHG concentrations, indicate a tight coupling between the global carbon cycle and the Earth's climate system. The high correlation between biogeochemical variables in the atmosphere (CO$_2$, CH$_4$, N$_2$O, ...) with physical quantities (temperature, ice volume) alone does not allow for the separation of cause and effect of the processes, as lead-lag questions are hard to answer given the timescales of some fast feedbacks and uncertainties in the age-models of proxy-data reconstruction.

To determine the ways in which the carbon cycle and the climate system interact, it is first necessary to understand the underlying processes. Only with the collaboration of modelers and people working on paleo-proxy measurements it is possible to disentangle the different interactions and feedbacks in the carbon cycle-climate system.

A key problem when using paleo data is the fact the they represent the state of the entire (coupled) carbon cycle-climate system, making it difficult to separate forcing and response. Therefore, coupled carbon cycle-climate models (e.g. the CMPI5 and C^{4}MIP ensembles[11]) play a

---

[11]CMIP5 – Coupled Model Intercomparison Project Phase 5; C^{4}MIP– Coupled Carbon Cycle Climate Model Intercomparison Project

special role in answering these questions, as they allow to couple/uncouple different model components which is a prerequisite to disentangle the cause-reaction chain and feedback loops in this complex system. The interferences between the carbon-cycle can be separated in three groups of interactions, briefly presented in the following:

Carbon-climate interactions: the effect of the carbon cycle on climate is probably the best understood process, although considerable uncertainties remain. This interaction is dominated by the radiative effect of airborne GHGs, including CO_2, and to a lesser extent CH_4. As the upward outgoing thermal (longwave) radiation is partially absorbed by these gases, they perturb Earth's energy balance. This radiative perturbation is expressed by the so-called radiative forcing (RF) and reported in units of $W\,m^{-2}$. The RF effect of CO_2 can be approximated by (Myhre et al., 1998):

$$\mathrm{RF}(CO_2) = 5.35\,\mathrm{W\,m^{-2}} \cdot \ln\left(\frac{CO_2}{CO_{2,0}}\right), \qquad (1.13)$$

where $CO_{2,0}$ is a (preindustrial) reference concentration. The radiative forcing of CH_4 can be expressed by a similar expression (Ramaswamy et al., 2001). This radiative perturbation leads to an increase of the global mean surface atmospheric temperature (ΔT) and triggers a series of physical feedbacks[12]. The top-of-atmosphere (TOA) radiation is balanced again (i.e. $\mathrm{TOA} = 0\,\mathrm{W\,m^{-2}}$ in the global average) once the feedbacks compensate the RF. The new equilibrium is given for $\Delta T > 0\,\mathrm{K}$ and is normally expressed by the equilibrium climate sensitivity (ECS), i.e. the equilibrium temperature increase for a doubling of atmospheric CO_2, and is estimated to be 1.5–4.5 K (Myhre et al., 2013), not including slow feedbacks such as the response of continental ice sheets.

The impact of various GHGs on climate is difficult to quantify, not only because of their different "strengths" (expressed by the radiative efficiency) but also because of their differing lifetimes. Several metrics exist to compare different GHGs quantitatively (e.g. Azar & Johansson, 2012); the most widely used are the global warming potential (GWP) and the global temperature potential (GTP). The GWP quantifies the integrated radiative forcing induced by a unit emission of a substance, while the GTP quantifies its induced temperature change. Both these metrics are expressed relative to CO_2, which serves as a reference substance (Joos et al., 2013). To overcome challenges created by the interaction of different lifetimes, a time horizon must be chosen on which different forcing agents are to be compared. The choice of the time horizon has a dominating influence on weighting of different GHGs with respect to CO_2 (Joos et al., 2013).

The radiative effect of GHGs is not the only way the carbon cycle influences climate. Changes in the terrestrial biosphere can for example alter the surface albedo and therefore directly influence climate. The importance of the land vegetation in the global hydrological cycle has also the potential to influence climate either by influencing evapotranspiration and/or changing the atmospheric dust load.

We have seen that the carbon cycle has the potential to influence climate. What is it then that drives changes in the carbon cycle itself? These effects can be separated in two fundamentally different classes:

Carbon-carbon interactions are the processes triggered in the carbon cycle when a certain variable, e.g. atmospheric CO_2, is altered and can be expressed in terms of flux-based carbon-concentration feedback parameters β_O and β_L for the ocean and land, respectively (Friedlingstein et al., 2006; Arora et al., 2013). β is expressed as a change in the integrated exchange flux of carbon for an unit change in CO_2 (i.e. reported as $\mathrm{Gt\,C\ ppm^{-1}}$). β is positive for both ocean and land, meaning that a certain portion of a sudden increase in atmospheric CO_2 is absorbed by the ocean and land carbon reservoirs (Archer et al., 2009; Joos et al., 2013). The physical

---

[12]e.g. the Planck, albedo, lapse-rate and could feedbacks (see e.g. Andrews et al., 2012).

absorption of carbon by the ocean is relatively well know as it is a consequence of carbonate chemistry, but uncertainties in certain aspects remain, e.g. in the response of the biological pump. Land carbon also increases in these models under increased CO_2 levels due to the fertilization effect of CO_2 during photosynthesis; but the overall response of the terrestrial biosphere is quite different between models in future CO_2 emission scenarios, depending on whether or not they represent the cycling of limiting nutrients. In the most recent analysis of the CMIP5 ensemble, β_O is estimated to be $0.8\,\mathrm{Gt\,C\,ppm}^{-1}$ and $\beta_L = 0.92\,\mathrm{Gt\,C\,ppm}^{-1}$ with a considerable spread, especially in the land response (Arora et al., 2013).

Often not captured by comprehensive ESMs is the slow sediment feedback to atmospheric CO_2 changes (denoted as β_S in Fig. 1.4), i.e. the neutralization of excess carbon taken up by the ocean due to seafloor $CaCO_3$ dissolution. The sediment feedback on CO_2 is negative, as dissolving $CaCO_3$ increases the seawater Alk:DIC ratio thus enabling the ocean to absorb more CO_2. Archer et al. (2009) show that for a 5000 GtC pulse, sediment interactions neutralize $\sim$800 Gt C after 10 kyr. In the β-notation, the sediment feedback has the same sign as β_O even though the sediment carbon stock decreases, but the dissolution of $CaCO_3$ leads to an increase in the integrated air-sea flux of carbon.

Carbon-carbon feedbacks generally involve many different timescales as illustrated in the example of a pulse release of carbon into the atmosphere and listed in Tab. 1.1 and detailed in e.g. Archer (2005); Archer & Brovkin (2008); Archer et al. (2009): as the carbon pulse increases atmospheric CO_2, photosynthesis on land reacts within years to centuries, taking up a fraction of the excess CO_2 by elevated NPP; the same is true for CO_2 buffering of the surface ocean and subsequent sequestration in the deep ocean. As ocean $[CO_3^{2-}]$ decreases, $CaCO_3$ stored in ocean sediments dissolves and partially restores the ocean's buffer-capacity ("$CaCO_3$ neutralization"). This process takes approximately $10^3 - 10^4$ yr. On longer timescales, higher CO_2 levels increase the rate at which silicate rocks weather, a process which ultimately restores the state of the atmosphere-ocean system on timescales of $> 10^4$ yr.

The time-evolution of the airborne fraction of CO_2 is referred to as the CO_2 impulse response function (IRF_{CO_2}) and not only includes carbon-carbon feedbacks, but also takes into account that increases in CO_2 levels lead to a rise in global temperatures, which in turn have an effect on the carbon cycle. In Chapter 5, a multi-model approach to deduce IRF_{CO_2} is presented both for preindustrial and present-day background conditions. The relevant interactions between the climate and the carbon cycle are discussed next.

Climate-carbon interactions are climate-driven changes in the carbon cycle. The sensitivity of the carbon inventory in the ocean and on land can again be expressed as sensitivity parameters γ_O and γ_L, respectively. γ is then the carbon inventory change per degree Kelvin of global temperature increase ($\mathrm{Gt\,C\,K}^{-1}$). In contrast to β, γ has been found to be negative both for the ocean and land reservoirs, that is, carbon is lost under rising atmospheric temperatures. Again, the uncertainty in the land response dominates the overall response of the carbon cycle. In the ocean, the loss of carbon is relatively predictable as the temperature-dependency of the CO_2 solubility is well understood, at least for present-day and near-future conditions. On land, the

Reservoir	Process	Timescale (yr)	Chemical reactions
Land	Photosynthesis – respiration	1–10^2	$6CO_2+6H_2O+\text{photons}\rightarrow C_6H_{12}O_6+6O_6$ $C_6H_{12}O_6+6O_6\rightarrow 6CO_2+6H_2O+\text{heat}$
Ocean	Seawater buffer	10–10^3	$CO_2+CO_3^{2-}+H_2O\rightleftharpoons 2HCO_3^-$
Sediments	$CaCO_3$ neutralization	10^3–10^4	$CO_2+CaCO_3+H_2O\rightarrow Ca^{2+}+2HCO_3^-$
Lithosphere	Silicate weathering	10^4–10^6	$CO_2+CaSiO_3+H_2O\rightarrow CaCO_3+SiO_2$

Table 1.1: Processes removing CO_2 from the atmosphere operate on different timescales. The table is based on Archer et al. (2009) and Ciais et al. (2013).

responses are much more regionally distinct and partially offsetting, such that the confidence on the land response is relatively low. Arora et al. (2013) estimates γ_O and γ_L from CMIP5 ESMs of -7.9 Gt C K^{-1} and -58.4 Gt C K^{-1} respectively, with an especially large spread for the land response.

The climate-carbon feedback can also be determined from data, e.g. by comparing past temperatures to CO_2 variations. Frank et al. (2010) estimate that atmospheric CO_2 increases 7.7 ppm for every 1 °C of warming (i.e. $\gamma_L + \gamma_O \approx -16$ Gt C K^{-1}) for the last the 1000 years. More recently, Bauska et al. (2013) used high resolution measurements $\delta^{13}C$ of CO_2 in order to reconstruct changes in the land carbon stock. Using simple regression with temperature reconstructions, they estimated $\gamma_L \approx -65$ Gt C K^{-1}, compatible with the CMIP5-based estimate.

One caveat of these feedback quantifications is that they apply to preindustrial/present-day or near-future global warming scenarios and may differ for a different background state of the carbon cycle-climate system, e.g. during ice ages. In addition, timescales in paleoclimate research are often longer, such that feedback factors as deduced from global warming scenarios cannot be applied to these processes. Also, strong/abrupt changes in for example the ocean circulation, ice sheets, wind speed and sea-ice cover not captured by these models ensembles may lead to different sensitivities, as different processes are involved.

Gregory et al. (2009) proposed an alternative framework to express feedback factors, namely the expression of the abovementioned processes as an additional radiative feedback (λ_i). This feedback by a certain process i is can then be reported as radiative forcing per degree of global warming (i.e. in units of W m^{-2} K^{-1}). This has the advantage that these feedback factors can be more easily compared to physical feedbacks as well as to feedbacks of CH_4 or N_2O, for example. This methodology is used in Chap. 6 in order to quantify (and compare) the land feedback of multiple greenhouse gases (e.g. λ_{CH_4}, λ_{N_2O},...) under global warming scenarios. See Sec. 6.2 for a more in-detail description of how these feedback factors can be calculated.

1.4 Manifestation of carbon-climate interactions in the past, present and future

For several decades, direct instrumental measurements of ambient air have allowed scientists to track changes in atmospheric composition, for example the rise in atmospheric CO_2 and coincident decline in $\delta^{13}C$ as a result of the combustion of (organic) fossil fuels ("Suess effect"). The measurement of seawater by ships allows the mapping of the distribution of temperature, salt, alkalinity, carbon and other trace elements in the modern ocean with a high spatial coverage (e.g. Key et al., 2004). More recently, satellites have revolutionized modern climatology by enabling us to map properties of the Earth's surface such as temperature, albedo, clouds, glaciers and sea ice cover with an unprecedented precision.

But perhaps one of the most important aspects of modern climatology is the possibility to draw on a large archive of paleo-climatic variables and link these to present-day instrumental measurements. Timeseries of past atmospheric trace gases and their isotopic ratios as conserved in polar ice cores and firn both allow the reconstruction of GHG forcing as well as the climate system's response. Although GHGs can be directly measured from the air trapped in the ice, climate variables such as temperature are more difficult to reconstruct, as they have to be determined by the use of so-called climate proxies, i.e conserved physical characteristics. For example, δD of H_2O (i.e. the ice) is a proxy for atmospheric temperature. Similarly, most climate proxies are based on isotopic signatures of compounds, as their fractionation factors are temperature-dependent. Compared to the direct measurement of trace gases, the relation of such proxies to climatological quantities such as temperature is more complex and uncertain in terms of absolute values.
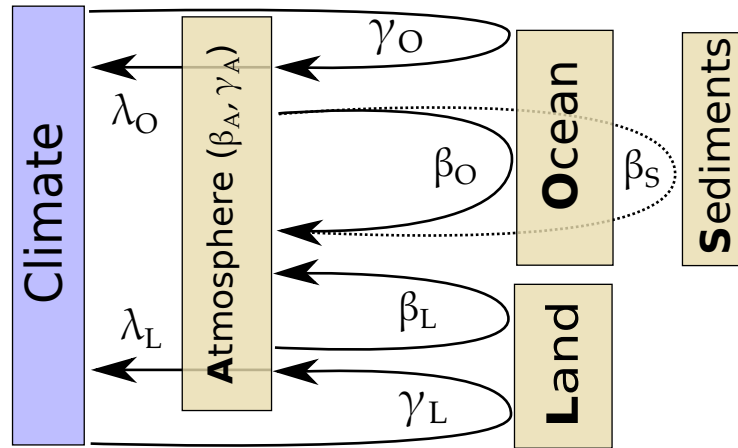
Figure 1.4: Conceptual illustration of metrics for quantifying the interaction within the carbon cycle between the carbon cycle and the climate system. The sensitivity of the land and ocean carbon stocks to atmospheric CO_2 can be expressed by carbon-concentration feedback parameters β_i , which are generally positive for modern carbon-cycle conditions: as atmospheric CO_2 increases, a considerable fraction of this carbon is taken up by the ocean and land sinks. The feedback of ocean sediments to CO_2 (dashed line), that is, the neutralization of CO_2 by $CaCO_3$ is often not included in comprehensive ESMs, as it is only important for timescales longer than $\sim 1000\,yr$. This feedback is denoted as β_S and is already included in β_O, as a CO_2 perturbation is first mitigated through the ocean before this feedback is triggered. On the other hand, climate-induced changes in these reservoirs, expressed by γ_i, tend to trigger the loss of carbon, especially on land. Note that $\beta_A = -(\beta_O + \beta_L)$ and $\gamma_A = -(\gamma_O + \gamma_L)$ follows from the conservation of carbon. The net of effect of carbon-cycle feedbacks on climate (λ_i) can be expressed in the framework of Gregory et al. (2009), where climate-induced changes in the ocean and land carbon cycle are translated into atmospheric concentration changes and subsequently reported as a radiative forcing. In general, these feedbacks operate on different timescales.

Regarding the reconstruction of the past state of the ocean's physical and chemical properties from sediment cores, a series of proxies has been developed, these includes: i) proxies for ocean circulation ($\Delta^{14}C$, Nd, $^{231}Pa/^{230}Th$, $\delta^{13}C$), water temperature (alkenone, Mg/Ca) and sea level ($\delta^{18}O$) and ii) carbon-related proxies for past chemical composition of seawater (e.g. CO_3^{2-} from B/Ca, depth of the lysocline from $\%CaCO_3$) and proxies for the biological pump such as paleo-productivity ($\delta^{13}C$, species abundances).

In the ocean, the coupling of circulation and carbon-cycle changes is considerable, such that it can be difficult to attribute changes in e.g. $[CO_3^{2-}]$ to ocean-atmosphere repartitioning of CO_2 alone. In addition, signals recorded by individual sediment cores can be strongly site-dependent, that is, they reflect only a very local signal. Therefore, robust conclusions can only be drawn from multi-site, multi-proxy reconstructions as applied e.g. by the MARGO Project Members (2009).

As important as the reconstruction of past changes in the Earth system is the knowledge of past forcings in order to obtain a process-based cause-reaction understanding of the climate system. The interplay between forcings and responses is difficult to disentangle from past archives due to the strong correlation of many climatic variables. In addition, many responses in the climate system are themselves forcings, depending on the point of view. For example: a climate modeler may say that knowing the evolution of past 800 kyr of GHG variations is a good constraint on the radiative forcing of the climate system, while a carbon-cycle modeler sees these GHG variations as a response of the carbon cycle to an even more fundamental, external forcing.

Ultimately, the external driver for the Earth's climate is insolation, i.e. the slowly varying spatial distribution of radiation (obliquity, precession) and the total amount of radiation given by orbital eccentricity. In addition to this so-called orbital forcing, the energetic output of the Sun, i.e. TSI, also varies on shorter timescales (e.g. Steinhilber et al., 2012; Roth & Joos, 2013) and influences climate, although the amplitude of TSI variations (Schmidt et al., 2012) and its influence on climate are still uncertain (Gray et al., 2010). The ultimate goal Earth-system

modeling would therefore be to reproduce past observed changes only by applying these external forcings, everything else being the response internal to the Earth system.

Some of the most prominent past changes in the carbon cycle-climate system are discussed next. The **Quaternary glacial cycles** denote the cyclic change between cold (glacials) and warm states (interglacials) of the climate system with a period of $\sim$120 kyr. Already soon after their discovery, it was proposed that the orbital forcing must be the cause of these variations (Milankovic theory). Conceptual models of glacial-interglacial (G-IG) changes have been successfully applied, but it is still not possible to model these cycles with process-based models such as ESMs.

The continental ice-sheet dynamics have been identified as the key element (Abe-Ouchi et al., 2013) in generating these sawtooth-like patterns in temperature and greenhouse gases (see Fig. 1.5). The basic mechanism is that ice sheets grow until they reach a critical size, making them labile w.r.t. external perturbations. Their collapse (glacial terminations), presumably triggered by high-latitude summer-insolation maxima, initiate a complex chain of reactions (Clark et al., 2012). The main feedbacks involved in these cycles are the ocean circulation response to abrupt freshwater relocation and albedo-feedback both from ice sheets, sea-ice and snow as well as the RF of well mixed GHGs.

There have, however, also been abrupt climate events during relatively stable glacial periods. Dansgaard-Oescher (DO) events are characterized by abrupt NH warmings of $\sim$10 °C and are assumed to be linked to instabilities in the global thermohaline circulation. On the other hand, Heinrich events have been identified as changes in the North Atlantic freshwater balance, probably induced by the stimulated export of icebergs as indicated by the observed peak in ice-rafted debris (IRD) in sediment cores.

Also the GHGs and their responses to climate forcings contribute considerably to the total radiative forcing in G-IG cycles, but the biogeochemical processes leading to their variations are still poorly quantified (Sigman & Boyle, 2000; Archer et al., 2000). Several hypothesis have been discussed to explain the $\sim$100 ppm drawdown during the LGM in atmospheric CO_2 (Lüthi et al., 2008); these include: changes in the ocean's biological pump, e.g. by changes in its strength as modulated by the availability of nutrients, changes in the rain ratio or remineralization rates, ocean temperature, circulation and stratification changes. A rather novel hypothesis on the cause/amplification of G-IG changes in CO_2 is the increased outgassing of volcanic CO_2 as a result of continental ice-sheet retreat (Huybers & Langmuir, 2009). The implication of hypothesis has been "tested" by Roth & Joos (2012) and is presented in Chap. 3.

The carbon storage on land can probably not explain the observed changes, as model results (Joos et al., 2004; Spahni et al., 2013) even indicate a lower glacial carbon storage of $\sim$500–800 Gt C, mainly due to the negative CO_2 fertilization feedback and deglacial built-up of peatlands. The observed CO_2 history is assumed to be a combination of the aforementioned mechanisms, although it remains challenging to explain the full amplitude and timing of CO_2 variations with EMICs (Brovkin et al., 2012; Menviel et al., 2012). The physical mechanisms that transferred carbon from the ocean to the atmosphere as recorded by deep-ocean $[CO_3^{2-}]$ (Yu et al., 2013) and ice-core records during the deglaciations is still a matter of debate, but there is a scientific consensus that the Southern Ocean has played a key role in this process, as a large portion of deepwater is formed there, and all ocean basins are connected through the Antarctic circumpolar current (ACC).

The greenhouse gases CH_4 and N_2O covaried with CO_2 as shown in Fig. 1.5. While CH_4 is assumed to be primarily driven by NH land-temperature changes, N_2O may be driven both by ocean and land biogeochemistry changes.

Although the current interglacial (Holocene), i.e. the last $\sim$11 kyr, has been characterized by relatively stable climatic conditions, CO_2 has risen by approximately 20 ppm, the cause of
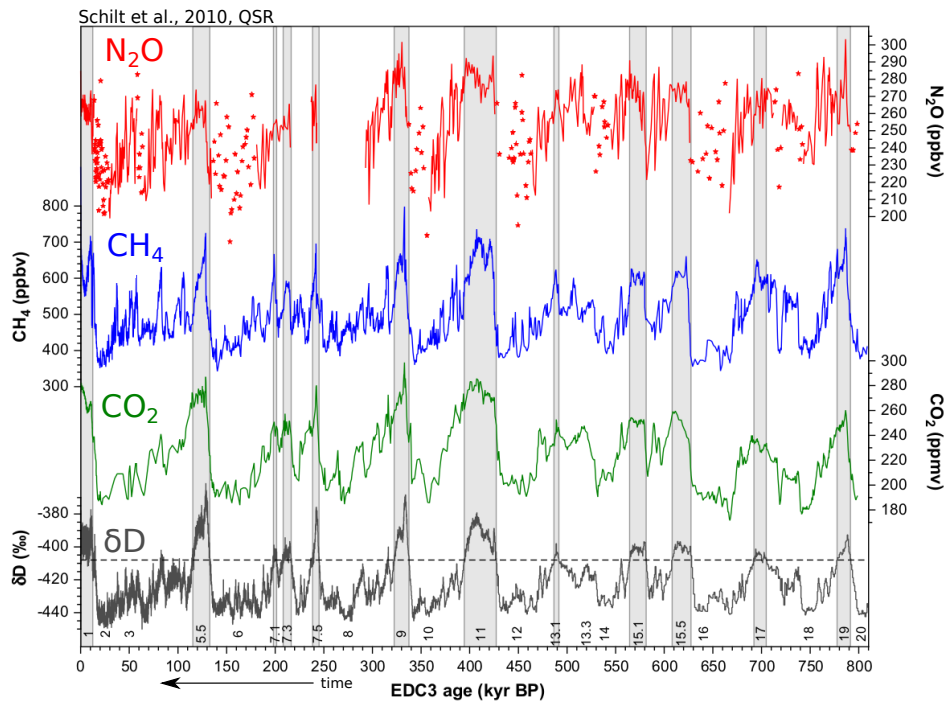
Figure 1.5: Imprint of Quaternary glacial cycles on the well-mixed atmospheric GHGs N_2O (red), CH_4 (blue)
and CO_2 (green) as reconstructed from ancient air trapped in polar ice (for individual references for the data, see
Schilt et al., 2010). Obviously, Earth's climate system and biogeochemical cycles were tightly coupled in the past
as indicated by the high correlation with δD, a proxy for Antarctic temperature over the last 800 kyr. On these
timescales, the carbon and nitrogen cycles act as positive feedbacks as concentrations and radiative forcing of
these gases have a minimum during cold periods (glacials) and peak during warm periods (interglacials). CO_2
varies with an amplitude of $\sim$100 ppm, which can so far not be reconciled with 3 dimensional carbon cycle-climate
models. It is generally assumed that many different physical and biogeochemical processes are involved in order to
transfer carbon from the atmosphere in the ocean (Sigman & Boyle, 2000; Brovkin et al., 2012; Menviel et al.,
2012). The scientific understanding on glacial-interglacial CH_4 and N_2O variations is even lower. The figure is
adapted from Schilt et al. (2010).

which is still a matter of debate. Late deglacial changes in sea-level and thus an increase in
shallow-water carbonate deposition is supposed to have partially contributed to this CO_2 rise in
combination with land-biosphere carbon dynamics (Kleinen et al., 2010; Menviel & Joos, 2012).
In addition, slow feedbacks such as ocean carbonate compensation still relaxing from previous
carbon-cycle changes induced by the circulation-driven Bølling-Allerød (BA) warm and Younger
Dryas (YD) cold events, may play a role. Because this rise in CO_2 is unique to the current
interglacial, some studies attribute it to early human-induced changes, such as landuse and
land-cover change (LULCC) (Ruddiman, 2007; Ruddiman et al., 2011).

In resolving these questions, reconstructions of past isotopic compositions of atmospheric and
seawater tracers have become a standard tool in the field of reconstructing the carbon cycle in
the past. In particular, records of past atmospheric $\Delta^{14}C$ (Reimer et al., 2013) and $\delta^{13}C$ (Elsig
et al., 2009; Schmitt et al., 2012) of CO_2 provide powerful constraints on past carbon-cycle
changes.

The anthropogenic perturbation and future scenarios

Since the industrial revolution ($\sim$1750 AD), humans have superseded external factors in driving
current climate by extracting and emitting carbon from the geologic reservoir, widespread
LULCC and the emission of non-CO_2 forcing agents. Our actions have led to an unprecedented
rate of changes as well as absolute levels of the most important GHGs, including CO_2, CH_4 and

N_2O since at least 22 kyr ago. At the same time, globally averaged land and ocean surface temperatures have risen by $\sim 0.85°C$. It has recently been stated that these human influences are extremely likely to be the dominant cause of the observed warming since the mid-20th century (IPCC, 2013). The strongest human-induced radiative forcing is given by atmospheric CO_2, followed by other well mixed GHGs as summarized in Fig. 1.6. Some man-made forcing agents such as aerosols have a negative RF (i.e. they cool the Earth's surface) but the scientific understanding of their direct and indirect effects on climate is comparably low.
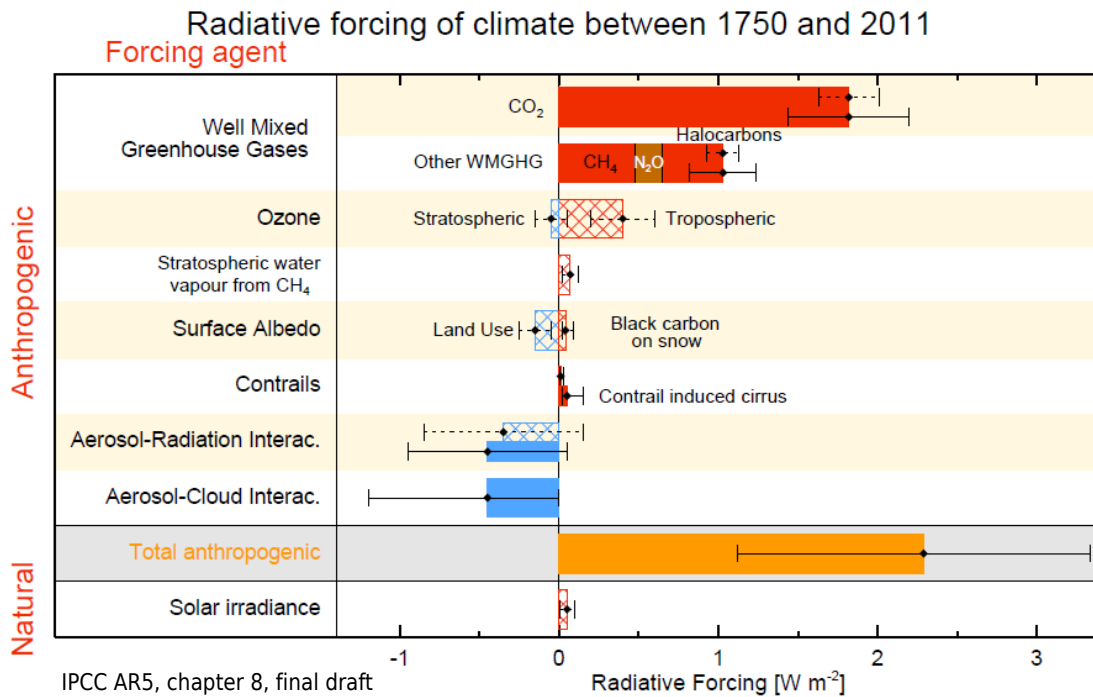
Figure 1.6: Radiative forcing of different anthropogenic forcing agents, where the positive forcing is dominated by CO_2 and other well mixed greenhouse gases. There are also anthropogenic components with a negative contribution to the radiation balance (i.e. they cool) such as landuse-induced albedo changes and aerosols (including their interaction with clouds). Total anthropogenic radiative forcing since preindustrial times is $2.3\,(1.1$ to $3.3)\,W\,m^{-2}$. On the other hand, natural variations in the total solar irradiance account only for 0.0 to $0.1\,W\,m^{-2}$. The figure is taken from Myhre et al. (2013).

In contrast to natural climate variations which are ultimately driven by physical mechanisms (insolation) and subsequently amplified by physical and climate-carbon cycle feedbacks, the impact of the anthropogenic perturbation is primarily a question of carbon-climate and carbon-carbon interactions and feedbacks. It is therefore crucial to (quantitatively) understand how the ocean and land carbon reservoirs react to the concurrent increase in CO_2 concentration (β), as the fraction of CO_2 not taken up by these reservoirs remains airborne and leads to carbon-climate feedbacks, i.e. an increase in RF and temperature. The carbon budget over the industrial period has been estimated (Le Quéré et al., 2013; Ciais et al., 2013) by measured atmospheric CO_2 concentrations and ocean DIC changes; the remainder, referred to as the "missing sink", is assumed to have accumulated in the biomass on land. Since 1750 humans have emitted 545 ± 85 Gt of carbon, from which 240 ± 10 Gt C have remained in the atmosphere. The ocean has stored 155 ± 30 Gt C and land not affected by LULCC 150 ± 90 Gt C[13].

How will the Earth system react to past and future carbon emissions? Will the land and ocean sinks continue to absorb fossil CO_2 under sustained carbon emissions? To separate socio-economic and physical uncertainties, four different future representative concentration

---

[13]The land carbon stocks have remained $\sim$constant considering the emissions of 180 ± 90 Gt C from LULCC

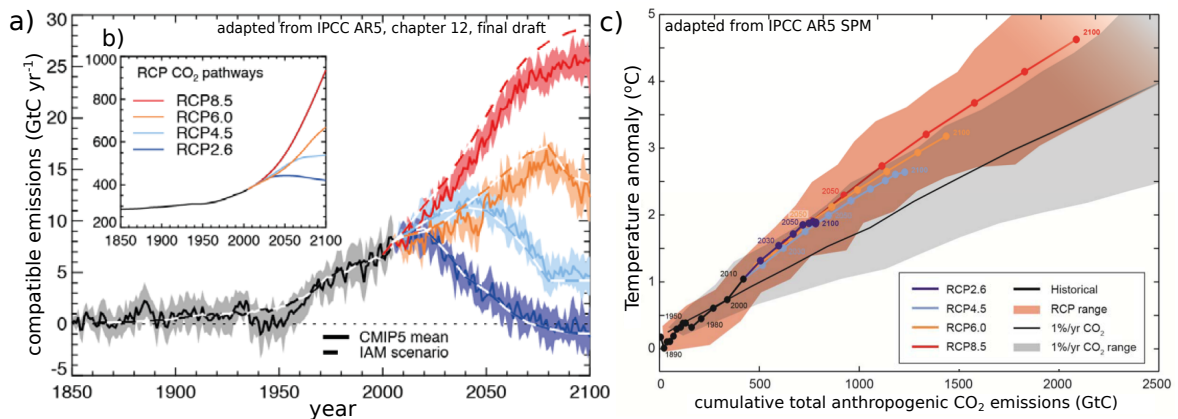**Figure 1.7: (a)** Four representative concentration pathways (RCPs) have been selected to be used in the latest assessment report from the IPCC. These result from different integrated-assessment models and different assumptions on future energy consumption and political climate mitigation actions (van Vuuren et al., 2011). The RCPs can either be used as emission scenarios (a, dashed lines) or concentration scenarios (**b**). Earth system models are normally run in a concentration-driven setup, and compatible carbon emissions are diagnosed. The figure is modified from Collins et al. (2013). **(c)** Global temperature increase as a function of cumulative CO_2 emissions shows an approximately linear behavior, independent of the RCP scenario (colored lines and red shading). Temperature increase, and cumulative emissions are w.r.t. 1870. Note that the RCPs also include non-CO_2 forcings. In a CO_2-only experiment (1% increase per year), the slope in this relationship is slightly reduced (black line and gray shading). In order to limit global warming to $2\,°C$ since preindustrial times, approximately $1000\,\mathrm{Gt\,C}$ can be emitted, whereof $\sim550\,\mathrm{Gt\,C}$ have already been emitted by now. The figure is adapted from IPCC (2013).

pathways (RCPs) have been developed for AR5, representing the future emissions of CO_2 and non-CO_2 GHGs and landuse (van Vuuren et al., 2011). The underlying emission scenarios are an output of different integrated assessment models (IAMs) under different future human behaviors, ranging from a scenario with strong emission reduction in the near future (RCP2.6) to a business-as-usual scenario (RCP8.5). These four emission scenarios have been translated into concentration scenarios by the MAGICC6[14] model (see Fig. 1.7b) in order to perform concentration-driven simulations for models without a representation of the global carbon-cycle. Earth system models with a carbon-cycle component can either perform concentration-driven simulations where *compatible emissions* are diagnosed (see Fig. 1.7a), or they directly apply the emission scenarios from the IAMs and predict future GHG concentrations.

Global mean temperatures for 2081–2100 are projected to rise between 0.3 and $4.8\,°C$ relative to 1986–2005 (IPCC, 2013), where the given range covers both scenario and climate-model uncertainties. Although the four RCPs yield completely different temperature responses by the end of this century, the relationship between global warming and cumulative CO_2 emissions (Fig. 1.7c) is astonishingly linear (Collins et al., 2013). But how does the global carbon cycle react to our current and future actions? The basic behavior of the carbon pools to rising temperature and CO_2 have already been indicated in Sec. 1.3 and shown in Fig. 1.4. Certainly, ocean acidification will continue as a result of the oceanic uptake of fossil CO_2 and subsequent shift in seawater chemistry to lower $[CO_3^{2-}]$ and pH. This is a possible threat to calcifying organisms and ultimately to the entire marine foodweb. Ocean productivity and export is expected to decrease in the global integral with increasing temperatures as ocean stratification limits the availability of nutrients in the euphotic zone (Steinacher et al., 2010). The reduced export of $CaCO_3$ due a decreased surface ocean supersaturation may act here as a (small) negative feedback to the CO_2 rise (Gangstø et al., 2011). Ocean stratification is, together with the non-linearity in the carbonate system, the main reason why future oceanic CO_2 uptake may be weakened.

The vegetation on land is supposed to be strongly affected by global warming, as higher

---

[14]A rather simple carbon cycle-climate model described in Meinshausen et al. (2011).

temperatures allow the treeline to shift polewards. At the same time, turnover rates in the soil increase, resulting in a reduced carbon storage. In addition, the response of carbon stored in soil subject to permafrost (e.g. MacDougall et al., 2012) as well as wetland CH_4 dynamics are among the most uncertain but probably also some of the most important future feedbacks.

In summary, both land and ocean responses and future warming scenarios show complex, partial offsetting responses on a very diverse spatial domain. The scientific understanding of many biogeochemical processes (yet to be incorporated in ESMs) is still comparably low and need further improvement. This is of special importance as both ocean and land-based food production is probably threatened by rising CO_2 and warmer climate conditions. But ultimately, the evolution of future climate and carbon cycle depends primarily on if (and how) we humans change our current lifestyle regarding the consumption of fossil energy.

Bibliography

Abe-Ouchi, A., Saito, F., Kawamura, K., Raymo, M. E., Okuno, J., Takahashi, K., & Blatter, H., 2013. Insolation-driven 100,000-year glacial cycles and hysteresis of ice-sheet volume, *Nature*, 500(7461), 190–193.

Andrews, T., Gregory, J. M., Webb, M. J., & Taylor, K. E., 2012. Forcing, feedbacks and climate sensitivity in cmip5 coupled atmosphere-ocean climate models, *Geophys. Res. Lett.*, 39(9), n/a–n/a.

Archer, D., 2005. Fate of fossil fuel CO_2 in geologic time, *J. Geophys. Res.*, 110(C9), C09S05.

Archer, D. & Brovkin, V., 2008. The millennial atmospheric lifetime of anthropogenic CO_2, *Climatic Change*, 90, 283–297.

Archer, D., Winguth, A., Lea, D., & Mahowald, N., 2000. What caused the glacial/interglacial atmospheric pCO_2 cycles?, *Rev. Geophys.*, 38(2), 159–189.

Archer, D., Eby, M., Brovkin, V., Ridgwell, A., Cao, L., Mikolajewicz, U., Caldeira, K., Matsumoto, K., Munhoven, G., Montenegro, A., & Tokos, K., 2009. Atmospheric Lifetime of Fossil Fuel Carbon Dioxide, *Ann. Rev. Earth and Planet. Sci.*, 37(1), 117–134.

Arora, V. K., Boer, G. J., Friedlingstein, P., Eby, M., Jones, C. D., Christian, J. R., Bonan, G., Bopp, L., Brovkin, V., Cadule, P., Hajima, T., Ilyina, T., Lindsay, K., Tjiputra, J. F., & Wu, T., 2013. Carbon–Concentration and Carbon–Climate Feedbacks in CMIP5 Earth System Models, *J. Climate*, 26(15), 5289–5314.

Azar, C. & Johansson, D. J. A., 2012. On the relationship between metrics to compare greenhouse gases – the case of IGTP, GWP and SGTP, *Earth Syst. Dynam.*, 3(2), 139–147.

Bauska, T., Joos, F., Roth, R., J., A., Mix, A., & Brook, E., 2013. Pre-industrial atmospheric carbon dioxide controlled by land carbon during the last millennium, *in prep*.

Berner, R. A., 2003. The long-term carbon cycle, fossil fuels and atmospheric composition, *Nature*, 426(6964), 323–326.

Brovkin, V., Ganopolski, A., Archer, D., & Munhoven, G., 2012. Glacial CO_2 cycle as a succession of key physical and biogeochemical processes, *Clim. Past*, 8(1), 251–264.

Buesseler, K. O., Lamborg, C. H., Boyd, P. W., Lam, P. J., Trull, T. W., Bidigare, R. R., Bishop, J. K. B., Casciotti, K. L., Dehairs, F., Elskens, M., Honda, M., Karl, D. M., Siegel, D. A., Silver, M. W., Steinberg, D. K., Valdes, J., Van Mooy, B., & Wilson, S., 2007. Revisiting carbon flux through the ocean's twilight zone, *Science*, 316(5824), 567–570.

Castagnoli, G. & Lal, D., 1980. Solar Modulation Effects in Terrestrial Production of Carbon-14, *Radiocarbon*, 22, 133–158.

Ciais, P., Sabine, C., Bala, G., Bopp, L., Brovkin, V., Canadell, J., A., C., DeFries, R., J., G., Heimann, M., Jones, C., Le Quéré, C., Myneni, R., S., P., & Thornton, P., 2013. Chapter 6: Carbon and Other Biogeochemical Cycles, in *Climate Change 2013: The Physical Science Basis. Working Group I Contribution to the Fifth Assessment Report of the Intergovernmental Panel on Climate Change*, Final Draft, 7. June 2013.

Clark, P. U., Shakun, J. D., Baker, P. A., Bartlein, P. J., Brewer, S., Brook, E., Carlson, A. E., Cheng, H., Kaufman, D. S., Liu, Z., Marchitto, T. M., Mix, A. C., Morrill, C., Otto-Bliesner, B. L., Pahnke, K., Russell, J. M., Whitlock, C., Adkins, J. F., Blois, J. L., Clark, J., Colman, S. M., Curry, W. B., Flower, B. P., He, F., Johnson, T. C., Lynch-Stieglitz, J., Markgraf, V., McManus, J., Mitrovica, J. X., Moreno, P. I., & Williams, J. W., 2012. Global climate evolution during the last deglaciation, *P. Natl. Acad. Sci. USA*, 109(19), E1134–E1142.

Collins, M., R., K., Arblaster, J., Dufresne, J.-L., Fichefet, T., Friedlingstein, P., Gao, X., Gutowski Jr., W., Johns, T., Krinner, G., Shongwe, M., Tebaldi, C., Weaver, A., & M., W., 2013. Chapter 12: Long-term Climate Change: Projections, Commitments and Irreversibility, in *Climate Change 2013: The Physical Science Basis. Working Group I Contribution to the Fifth Assessment Report of the Intergovernmental Panel on Climate Change*, Final Draft, 7. June 2013.

Damon, P. E. & Sternberg, R. E., 1989. Global production and decay of radiocarbon, *Radiocarbon*, 31(3), 697–703.

Deines, P., 2002. The carbon isotope geochemistry of mantle xenoliths, *Earth-Sci. Rev.*, 58(3–4), 247–278.

Elsig, J., Schmitt, J., Leuenberger, D., Schneider, R., Eyer, M., Leuenberger, M., Joos, F., Fischer, H., & Stocker, T. F., 2009. Stable isotope constraints on Holocene carbon cycle changes from an Antarctic ice core, *Nature*, 461, 507–510.

Frank, D. C., Esper, J., Raible, C. C., Büntgen, U., Trouet, V., Stocker, B., & Joos, F., 2010. Ensemble reconstruction constraints on the global carbon cycle sensitivity to climate, *Nature*, 463, 527–530.

Friedlingstein, P., Cox, P., Betts, R., Bopp, L., von Bloh, W., Brovkin, V., Cadule, P., Doney, S., Eby, M., Fung, I., Bala, G., John, J., Jones, C., Joos, F., Kato, T., Kawamiya, M., Knorr, W., Lindsay, K., Matthews, H. D., Raddatz, T., Rayner, P., Reick, C., Roeckner, E., Schnitzler, K.-G., Schnur, R., Strassmann, K., Weaver, A. J., Yoshikawa, C., & Zeng, N., 2006. Climate-carbon cycle feedback analysis: Results from the c4mip model intercomparison, *J. Climate*, 19(14), 3337–3353.

Gangstø, R., Joos, F., & Gehlen, M., 2011. Sensitivity of pelagic calcification to ocean acidification, *Biogeosciences*, 8(2), 433–458.

eds Gattuso, J.-P. & Hansson, L., 2011. *Ocean Acidification*, Oxford University Press, New York, USA.

Godwin, H., 1962. Half-life of radiocarbon, *Nature*, 195(4845), 984–984.

Gray, L. J., Beer, J., Geller, M., Haigh, J. D., Lockwood, M., Matthes, K., Cubasch, U., Fleitmann, D., Harrison, G., Hood, L., Luterbacher, J., Meehl, G. A., Shindell, D., van Geel, B., & White, W., 2010. Solar Influences on Climate, *Rev. Geophys.*, 48(4), RG4001.

Gregory, J. M., Jones, C. D., Cadule, P., & Friedlingstein, P., 2009. Quantifying carbon cycle feedbacks, *J. Climate*, 22(19), 5232–5250.

Hansell, D. A., Carlson, C. A., Repeta, D. J., & Schlitzer, R., 2009. Dissolved organic matter in the ocean a controversy stimulates new insights, *Oceanography*, 22(4), 202–211.

Hubick, K. & Farquhar, G., 1989. carbon isotope discrimination and the ratio of carbon gained to water lost in barley cultivars, *Plant Cell Environ.*, 12(8), 795–804.

Huybers, P. & Langmuir, C., 2009. Feedback between deglaciation, volcanism, and atmospheric CO_2, *Earth Planet. Sci. Lett.*, 286(3–4), 479–491.

IPCC, 2013. Summary for Policymakers. In: Climate Change 2013: The Physical Science Basis. Contribution of Working Group 1 to the Fith Assessment Report of the Intergovernmental Panel on Climate Change.

Joos, F. & Spahni, R., 2008. Rates of change in natural and anthropogenic radiative forcing over the past 20,000 years, *P. Natl. Acad. Sci. USA*, 105(5), 1425–1430.

Joos, F., Gerber, S., Prentice, I. C., Otto-Bliesner, B. L., & Valdes, P. J., 2004. Transient simulations of Holocene atmospheric carbon dioxide and terrestrial carbon since the Last Glacial Maximum, *Global Biogeochem. Cy.*, 18(GB2002).

Joos, F., Roth, R., Fuglestvedt, J. S., Peters, G. P., Enting, I. G., von Bloh, W., Brovkin, V., Burke, E. J., Eby, M., Edwards, N. R., Friedrich, T., Frölicher, T. L., Halloran, P. R., Holden, P. B., Jones, C., Kleinen, T., Mackenzie, F. T., Matsumoto, K., Meinshausen, M., Plattner, G.-K., Reisinger, A., Segschneider, J., Shaffer, G., Steinacher, M., Strassmann, K., Tanaka, K., Timmermann, A., & Weaver, A. J., 2013. Carbon dioxide and climate impulse response functions for the computation of greenhouse gas metrics: a multi-model analysis, *Atmos. Chem. Phys.*, 13(5), 2793–2825.

Key, R. M., Kozyr, A., Sabine, C. L., Lee, K., Wanninkhof, R., Bullister, J. L., Feely, R. A., Millero, F. J., Mordy, C., & Peng, T.-H., 2004. A global ocean carbon climatology: Results from Global Data Analysis Project (GLODAP), *Global Biogeochem. Cy.*, 18(4), GB4031.

Kleinen, T., Brovkin, V., von Bloh, W., Archer, D., & Munhoven, G., 2010. Holocene carbon cycle dynamics, *Geophys. Res. Lett.*, 37, L02705.

Kovaltsov, G. A., Mishev, A., & Usoskin, I. G., 2012. A new model of cosmogenic production of radiocarbon ^{14}C in the atmosphere, *Earth Planet. Sci. Lett.*, 337–338(0), 114–120.

Le Quéré, C., Andres, R. J., Boden, T., Conway, T., Houghton, R. A., House, J. I., Marland, G., Peters, G. P., van der Werf, G. R., Ahlström, A., Andrew, R. M., Bopp, L., Canadell, J. G., Ciais, P., Doney, S. C., Enright, C., Friedlingstein, P., Huntingford, C., Jain, A. K., Jourdain, C., Kato, E., Keeling, R. F., Klein Goldewijk, K., Levis, S., Levy, P., Lomas, M., Poulter, B., Raupach, M. R., Schwinger, J., Sitch, S., Stocker, B. D., Viovy, N., Zaehle, S., & Zeng, N., 2013. The global carbon budget 1959-2011, *Earth Syst. Sci. Data*, 5(1), 165–185.

Leuzinger, S. & Hättenschwiler, S., 2013. Beyond global change: lessons from 25 years of CO_2 research, *Oecologia*, 171(3), 639–651.

Lüthi, D., Le Floch, M., Bereiter, B., Blunier, T., Barnola, J.-M., Siegenthaler, U., Raynaud, D., Jouzel, J., Fischer, H., Kawamura, K., & Stocker, T. F., 2008. High-resolution carbon dioxide concentration record 650,000-800,000 years before present, *Nature*, 453, 379–382.

MacDougall, A. H., Avis, C. A., & Weaver, A. J., 2012. Significant contribution to climate warming from the permafrost carbon feedback, *Nature Geosci.*, 5(10), 719–721.

MARGO Project Members, 2009. Constraints on the magnitude and patterns of ocean cooling at the last glacial maximum, *Nature Geosci.*, 2, 127–132.

Martin, J. H., Knauer, G. A., Karl, D. M., & Broenkow, W., 1987. VERTEX: Carbon cycling in the northeast Pacific.

Masarik, J. & Beer, J., 1999. Simulation of particle fluxes and cosmogenic nuclide production in the Earth's atmosphere, *J. Geophys. Res.*, 104, 12099–12111.

Masarik, J. & Beer, J., 2009. An updated simulation of particle fluxes and cosmogenic nuclide production in the Earth's atmosphere, *J. Geophys. Res.*, 114, D11103.

Masson-Delmotte, V., M., S., Abe-Ouchi, A., J., B., A., G., González Rouco, J., Jansen, E., K., L., Luterbacher, J., Naish, T., Osborn, T., Otto-Bliesner, B., Quinn, T., Ramesh, R., Rojas, M., Shao, X., & Timmermann, A., 2013. Chapter 5: Information from Paleoclimate Archives, in *Climate Change 2013: The Physical Science Basis. Working Group I Contribution to the Fifth Assessment Report of the Intergovernmental Panel on Climate Change*, Final Draft, 7. June 2013.

Meinshausen, M., Raper, S. C. B., & Wigley, T. M. L., 2011. Emulating coupled atmosphere-ocean and carbon cycle models with a simpler model, MAGICC6 – Part 1: Model description and calibration, *Atmos. Chem. Phys.*, 11(4), 1417–1456.

Menviel, L. & Joos, F., 2012. Toward explaining the Holocene carbon dioxide and carbon isotope records: Results from transient ocean carbon cycle-climate simulations, *Paleoceanography*, 27, PA1207.

Menviel, L., Joos, F., & Ritz, S., 2012. Simulating atmospheric CO_2, ^{13}C and the marine carbon cycle during the Last Glacial-Interglacial cycle: possible role for a deepening of the mean remineralization depth and an increase in the oceanic nutrient inventory, *Quaternary Sci. Rev.*, 56(0), 46–68.

Mook, W., 1986. ^{13}C in atmospheric CO_2, *Neth. J. Sea Res.*, 20(2–3), 211–223.

Muscheler, R., Beer, J., Wagner, G., Laj, C., Kissel, C., Raisbeck, G. M., Yiou, F., & Kubik, P. W., 2004. Changes in the carbon cycle during the last deglaciation as indicated by the comparison of ^{10}Be and ^{14}C records, *Earth Planet. Sci. Lett.*, 219(3–4), 325–340.

Myhre, G., Highwood, E. J., Shine, K. P., & Stordal, F., 1998. New estimates of radiative forcing due to well mixed greenhouse gases, *Geophys. Res. Lett.*, 25(14), 2715–2718.

Myhre, G., Shindell, D., Bréon, F.-M., Collins, W., Fuglestvedt, J., Huang, J., Koch, D., Lamarque, J.-F., Lee, D., Mendoza, B., Nakajima, T., Robock, A., G., S., Takemura, T., & Zhang, H., 2013. Chapter 8: Anthropogenic and Natural Radiative Forcing, in *Climate Change 2013: The Physical Science Basis. Working Group I Contribution to the Fifth Assessment Report of the Intergovernmental Panel on Climate Change*, Final Draft, 7. June 2013.

Najjar, R. G., Orr, J., Sabine, C. L., & Joos, F., 1999. Biotic-HOWTO. Internal OCMIP Report, Tech. rep., LSCE/CEA Saclay, Gif-sur-Yvette, France.

Orr, J. & Najjar, R. G., 1999. Abiotic-HOWTO. Internal OCMIP Report, Tech. rep., LSCE/CEA Saclay, Gif-sur-Yvette, France.

Prather, M. J., Holmes, C. D., & Hsu, J., 2012. Reactive greenhouse gas scenarios: Systematic exploration of uncertainties and the role of atmospheric chemistry, *Geophys. Res. Lett.*, 39(9), L09803.

Ramaswamy, V., Boucher, O., Haigh, J., Hauglustaine, D., Haywood, J., Myhre, G., Nakajima, T., Shi, G. Y., & Solomon, S., 2001. Radiative forcing of climate change, in *Climate Change 2001: The Scientific Basis. Contribution of Working Group I to the Third Assessment Report of the Intergovernmental Panel on Climate Change*, pp. 349–416, eds Houghton, J. T., Ding, Y., Griggs, D., Noguer, M., van der Linden, P., Dai, X., Maskell, K., & Johnson, C. A., Cambridge University Press, Cambridge, United Kingdom and New York, NY, USA.

Reimer, P., Bard, E., Bayliss, A., Beck, J., Blackwell, P., Ramsey, C. B., Grootes, P., Guilderson, T., Haflidason, H., Hajdas, I., Hatté, C., Heaton, T., Hoffmann, D., Hogg, A., Hughen, K., Kaiser, K., Kromer, B., Manning, S., Niu, M., Reimer, R., Richards, D., Scott, E., Southon, J., Staff, R., Turney, C., & van der Plicht, J., 2013. IntCal13 and Marine13 Radiocarbon Age Calibration Curves 0–50,000 Years cal BP, *Radiocarbon*, 55(4).

Revelle, Rogerand Suess, H. E., 1957. Carbon Dioxide Exchange Between Atmosphere and Ocean and the Question of an Increase of Atmospheric CO_2 during the Past Decades, *Tellus*, 9(1), 18–27.

Ritz, S. P., Stocker, T. F., & Joos, F., 2011. A coupled dynamical ocean-energy balance atmosphere model for paleoclimate studies, *J. Climate*, 24(2), 349–75.

Roth, R. & Joos, F., 2012. Model limits on the role of volcanic carbon emissions in regulating glacial-interglacial CO_2 variations, *Earth Planet. Sci. Lett.*, 329–330(0), 141–149.

Roth, R. & Joos, F., 2013. A reconstruction of radiocarbon production and total solar irradiance from the Holocene ^{14}C and CO_2 records: implications of data and model uncertainties, *Clim. Past*, 9(4), 1879–1909.

Ruddiman, W., Kutzbach, J., & Vavrus, S., 2011. Can natural or anthropogenic explanations of late-Holocene CO_2 and CH_4 increases be falsified?, *The Holocene*, 21(5), 865–8879.

Ruddiman, W. F., 2007. The early anthropogenic hypothesis: Challenges and responses, *Rev. Geophys.*, 45(4), RG4001.

Sabine, C. L., Feely, R. A., Gruber, N., Key, R. M., Lee, K., Bullister, J. L., Wanninkhof, R., Wong, C. S., Wallace, D. W. R., Tilbrook, B., Millero, F. J., Peng, T. H., Kozyr, A., Ono, T., & Rios, A. F., 2004. The oceanic sink for anthropogenic CO_2, *Science*, 305(5682), 367–371.

Sarmiento, J. L. & Gruber, N., 2006. *Ocean biogeochemical dynamics*, Princeton University Press.

Schilt, A., Baumgartner, M., Blunier, T., Schwander, J., Spahni, R., Fischer, H., & Stocker, T. F., 2010. Glacial-interglacial and millennial-scale variations in the atmospheric nitrous oxide concentration during the last 800,000 years, *Quaternary Sci. Rev.*, 29(1-2, SI), 182–192.

Schmidt, G. A., Jungclaus, J. H., Ammann, C. M., Bard, E., Braconnot, P., Crowley, T. J., Delaygue, G., Joos, F., Krivova, N. A., Muscheler, R., Otto-Bliesner, B. L., Pongratz, J., Shindell, D. T., Solanki, S. K., Steinhilber, F., & Vieira, L. E. A., 2012. Climate forcing reconstructions for use in PMIP simulations of the Last Millennium (v1.1), *Geosci. Model Dev.*, 5(1), 185–191.

Schmidt, G. A., Annan, J. D., Bartlein, P. J., Cook, B. I., Guilyardi, E., Hargreaves, J. C., Harrison, S. P., Kageyama, M., LeGrande, A. N., Konecky, B., Lovejoy, S., Mann, M. E., Masson-Delmotte, V., Risi, C., Thompson, D., Timmermann, A., Tremblay, L.-B., & Yiou, P., 2013. Using paleo-climate comparisons to constrain future projections in CMIP5, *Clim. Past Discuss.*, 9(1), 775–835.

Schmitt, J., Schneider, R., Elsig, J., Leuenberger, D., Lourantou, A., Chappellaz, J., Köhler, P., Joos, F., Stocker, T. F., Leuenberger, M., & Fischer, H., 2012. Carbon isotope constraints on the deglacial CO_2 rise from ice cores, *Science*, 336(6082), 711–714.

Schmittner, A., Gruber, N., Mix, A. C., Key, R. M., Tagliabue, A., & Westberry, T. K., 2013. Biology and air–sea gas exchange controls on the distribution of carbon isotope ratios (δ^{13}C) in the ocean, *Biogeosciences*, 10(9), 5793–5816.

Siegenthaler, U., Stocker, T. F., Monnin, E., Lüthi, D., Schwander, J., Stauffer, B., Raynaud, D., Barnola, J.-M., Fischer, H., Masson-Delmotte, V., & Jouzel, J., 2005. Stable Carbon Cycle–Climate Relationship During the Late Pleistocene, *Science*, 310(5752), 1313–1317.

Sigman, D. M. & Boyle, E. A., 2000. Glacial/interglacial variations in atmospheric carbon dioxide, *Nature*, 407(6806), 859–869.

Sitch, S., Huntingford, C., Gedney, N., Levy, P. E., Lomas, M., Piao, S. L., Betts, R., Ciais, P., Cox, P., Friedlingstein, P., Jones, C. D., PrenticE, I. C., & Woodward, F. I., 2008. Evaluation of the terrestrial carbon cycle, future plant geography and climate-carbon cycle feedbacks using five Dynamic Global Vegetation Models (DGVMs), *Glob. Change Biol.*, 14(9), 2015–2039.

Sokolov, A. P., Kicklighter, D. W., Melillo, J. M., Felzer, B. S., Schlosser, C. A., & Cronin, T. W., 2008. Consequences of considering carbon-nitrogen interactions on the feedbacks between climate and the terrestrial carbon cycle, *J. Climate*, 21(15), 3776–3796.

Southon, J., 2011. Are the Fractionation Corrections Correct: Are the Isotopic Shifts for $^{14}C/^{12}C$ Ratios in Physical Processes and Chemical Reactions Really Twice Those for $^{13}C/^{12}C$?, *Radiocarbon*, 53(4).

Spahni, R., Joos, F., Stocker, B. D., Steinacher, M., & Yu, Z. C., 2013. Transient simulations of the carbon and nitrogen dynamics in northern peatlands: from the Last Glacial Maximum to the 21st century, *Clim. Past*, 9, 1287–1308.

Steinacher, M., Joos, F., Frölicher, T. L., Bopp, L., Cadule, P., Cocco, V., Doney, S. C., Gehlen, M., Lindsay, K., Moore, J. K., Schneider, B., & Segschneider, J., 2010. Projected 21st century decrease in marine productivity: a multi-model analysis, *Biogeosciences*, 7(3), 979–1005.

Steinacher, M., Joos, F., & Stocker, T. F., 2013. Allowable carbon emissions lowered by multiple climate targets, *Nature*, 499, 197–201.

Steiner, N. S., Lee, W. G., & Christian, J. R., 2013. Enhanced gas fluxes in small sea ice leads and cracks: Effects on CO_2 exchange and ocean acidification, *J. Geophys. Res.-Oceans*, 118(3), 1195–1205.

Steinhilber, F., Abreu, J. A., Beer, J., Brunner, I., Christl, M., Fischer, H., Heikkilä, U., Kubik, P. W., Mann, M., McCracken, K. G., Miller, H., Miyahara, H., Oerter, H., & Wilhelms, F., 2012. 9,400 years of cosmic radiation and solar activity from ice cores and tree rings, *J. Geophys. Res.-Oceans*, 109, 5967–5971.

Stuiver, M. & Polach, H. A., 1977. Discussion: Reporting of ^{14}C data, *Radiocarbon*, 3, 355–363.

Tarnocai, C., Canadell, J. G., Schuur, E. A. G., Kuhry, P., Mazhitova, G., & Zimov, S., 2009. Soil organic carbon pools in the northern circumpolar permafrost region, *Global Biogeochem. Cy.*, 23(2), GB2023.

Thornton, P. E., Doney, S. C., Lindsay, K., Moore, J. K., Mahowald, N., Randerson, J. T., Fung, I., Lamarque, J.-F., Feddema, J. J., & Lee, Y.-H., 2009. Carbon-nitrogen interactions regulate climate-carbon cycle feedbacks: results from an atmosphere-ocean general circulation model, *Biogeosciences*, 6(10), 2099–2120.

Usoskin, I. & Kromer, B., 2005. Reconstruction of the C-14 production rate from measured relative abundance, *Radiocarbon*, 47(1), 31–37.

Usoskin, I. G., 2013. A History of Solar Activity over Millennia, *Living Rev. Solar Phys*, 10(1).

van Vuuren, D., Edmonds, J., Kainuma, M., Riahi, K., Thomson, A., Hibbard, K., Hurtt, G., Kram, T., Krey, V., Lamarque, J.-F., Masui, T., Meinshausen, M., Nakicenovic, N., Smith, S., & Rose, S., 2011. The representative concentration pathways: an overview, *Climatic Change*, 109, 5–31, 10.1007/s10584-011-0148-z.

Wanninkhof, R., 1992. Relationship between wind–speed and gas–exchange over the ocean, *J. Geophys. Res.-Oceans*, 97(C5), 7373–7382.

Weiss, R. F., 1974. Carbon dioxide in water and seawater: The solubility of a non-ideal gas, *Mar. Chem.*, 2, 203–215.

Yu, J., Anderson, R. F., Jin, Z., Rae, J. W., Opdyke, B. N., & Eggins, S. M., 2013. Responses of the deep ocean carbonate system to carbon reorganization during the Last Glacial–interglacial cycle, *Quaternary Sci. Rev.*, 76(0), 39 – 52.

Yu, Z., Loisel, J., Brosseau, D. P., Beilman, D. W., & Hunt, S. J., 2010. Global peatland dynamics since the Last Glacial Maximum, *Geophys. Res. Lett.*, 37, L13402.

Chapter 2

Methods

2.1 The Bern3D-LPJ carbon cycle-climate model

The tool used during this thesis is the Bern3D-LPJ model. The Bern3D-LPJ model is only the latest version of the "Bern"-model series (see Tab. 2.1) and was born by the development of a 3-D ocean component, the GOLDSTEIN[1] around year 1998. Since then, the Bern3D has been improved and extended as sketched in Fig. 2.1. In the latest major step, the Bern3D was extended with an energy-balance model (EBM) and got coupled to the LPJ dynamical global vegetation model (DGVM) in 2010. At the same time, the seafloor sediment diagenesis model was added. Therefore, the Bern3D-LPJ is now a fully featured Earth-system model of intermediate complexity (EMIC).

The main focus of the family of models developed in Bern was at first the modeling of the carbon cycle, starting from a simple multi-box model. Today, the Bern3D-LPJ includes both a climate and a carbon cycle component in order to take into account the strong interactions between climate and the carbon cycle. As typical for an EMIC, this model is based on simplified physics and the parametrization or neglect of many processes as e.g. a dynamical atmosphere. On the other hand, these simplified models allow different kind of experiments (such as probabilistic or very long simulations) due to their computational efficiency. Therefore EMICs are not less valuable than comprehensive atmosphere-ocean general circulation models but cover a different scope. Taken together, EMICs and AOGCMs complement each other in answering scientific questions.

As of 2013, the complete Bern3D-LPJ model code consists of ∼120 thousand lines of code written in Fortran, whereof ∼1/3 belong to the LPJ subroutine. The code has been managed by the subversion (SVN) code management software since 2002 in order to allow multiple modelers to work on the code simultaneously, and to track changes. This system also allows to reproduce past simulations if the revision number of the used code is known and if the input files are still available.

model name	IPCC	atm	sea ice	ocean	land
Bern	SAR	0D		multi-box (HILDA)	4-box biosphere
BernCC-LPJ	TAR	0D		multi-box (HILDA)	DGVM (LPJ)
Bern2.5D-LPJ	AR4	1D EBM	1D	zonally averaged (3 basins)	DGVM (LPJ)
Bern3D-LPX	AR5	2D EBM	2D	3D (GOLDSTEIN)	DGVM (LPX)

Table 2.1: Overview on the main versions of the "Bern"-model as cited in the last five IPCC assessment reports. This is only a selection as many other combinations of model components have been used in the past.

---

[1]GOLDSTEIN: Global Ocean Linear Drag Salt and Temperature Equation Integrator
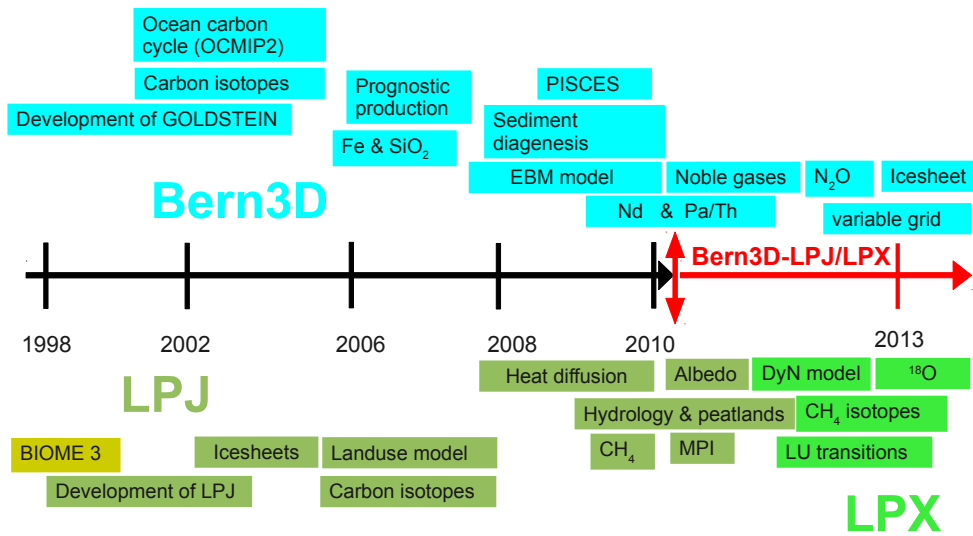
Figure 2.1: The development of the Bern3D-LPJ model: starting from 1998, many different components and features have been added to the model. With the coupling of the LPJ in 2010, the Bern3D-LPJ has become a fully featured EMIC which includes all major carbon reservoirs.

2.1.1   Model components

Due to the long time of continuous model development and simultaneous application of the Bern3D-LPJ the documentation of the individual model components is distributed over many papers, theses and internal documents (available through the SVN repository). In the following subsections, the different model components are briefly described in a qualitative form. In order to avoid repeating all the underlying analytical formulations, references are given for the documented governing equations whenever possible. During this thesis, several different setups of the model were used, therefore the actual details may slightly differ from chapter to chapter.

Note also that this description comprises only the model components that were used in this thesis. Other model components, such as the neodymium or the noble gases implementations, are described elsewhere (Rempfer et al., 2011; Ritz et al., 2011b).

Atmosphere

The atmosphere is represented by a 2-D energy and moisture balance model with the same horizontal resolution as the ocean (Ritz et al., 2011a). Following Weaver et al. (2001), outgoing longwave radiative fluxes are parametrized after Thompson & Warren (1982) with additional radiative forcings due to CO_2, other greenhouse gases, volcanic aerosols. Note that due this atmospheric model is not capable to explicitly calculate the vertical radiative transfer, therefore the effect of CO_2 is parametrized according to Myhre et al. (1998). A feedback parameter is introduced to produce an equilibrium climate sensitivity of 3°C for a nominal doubling of CO_2 under preindustrial conditions. The past extent of Northern Hemisphere ice sheets is prescribed following the ICE4G and ICE5G models (Peltier, 1994, 2004) as described in Ritz et al. (2011a) and updated in Ritz et al. (2011b) and Ritz (2013).

Simplified formulations have recently been added for the atmospheric chemistry of CH_4, N_2O and tropospheric O_3 (Joos et al., 2001) to convert fluxes from the land and ocean module to concentrations and subsequently to a radiative forcing to as e.g. used in Stocker et al. (2013).

Ocean

The geostrophic-frictional balance 3-D ocean component is based on Edwards & Marsh (2005) and as further improved by Müller et al. (2006). It includes an isopycnal diffusion scheme and Gent-McWilliams parametrization for eddy-induced transport (Griffies, 1998).

The horizontal resolution is 36×36 gridboxes with a regular longitudinal grid ($10°$ spacing) and a constraint that the latitudinal grid spacing must be proportional to the sine of the latitude (such that all boxes have the same area). Recently, the model has been modified to overcome these constraints and currently a resolution of 41×40 is used for future projects (see next section). The "classic" setup in terms of horizontal resolution is henceforth referred as the 36×36 version, while the new, "variable grid"-setup is referred as the 41×40 version. In all setups, 32 logarithmically spaced layers in the vertical are used where the surface box is $39\,\mathrm{m}$ thick and the lowest box almost $400\,\mathrm{m}$. Wind stress is prescribed according to the monthly climatology from NCEP/NCAR[2] (Kalnay et al., 1996). Thus, changes in ocean circulation in response to changes in wind stress under varying climate are usually not simulated.

The calculation of the 3-D flowfield as a result of windstress, friction, topography and density gradients is the principal task of the physical core of the model and is shortly outlined in the following: First, the barotropic streamfunction Ψ_B (i.e. the vertically averaged transport) is calculated by considering topographic features, seasonal windstress, Coriolis force and drag (friction). This calculation becomes non-trivial when multiple islands (i.e. landmasses) are to be considered. The so-called "Island Rule" (Godfrey, 1989) is applied[3] to determine the constant value of Ψ_B at the island boundaries while a value of $\Psi_B=0$ is assigned to the main-land without loss of generality. Applying the Island Rule leads then to a solution for Ψ_B. The baroclinic velocity $\mathbf{u}_B$ can be calculated be eliminating the pressure-term in the geostrophic equations using hydrostatic balance and then integrating over depth. The complete procedure how the equations are discretizerd and solved is detailed in Ritz (2013). Note that the calculation of Ψ_B has to be conducted only once as the windstress (and the drag) terms do normally not change between years. For the study presented in Chap. 4, this has been changed to allow windstress to be scaled during transient simulations

The marine biogeochemical module computes the cycling of carbon, alkalinity (Alk), phosphate, iron, oxygen, silica, and of the carbon isotopes. Carbon is represented as dissolved inorganic carbon (DIC) and labile dissolved organic carbon (DOC). Prognostic formulations link marine productivity and dissolved organic matter (DOM) to available nutrients (PO_4, Fe, SiO_2), temperature, sea ice and light using Michaelis-Menten limiting terms (Doney et al., 2006) in the euphotic zone (uppermost $75\,\mathrm{m}$) described in Parekh et al. (2008); Tschumi et al. (2011) and detailed in Parekh (2006); Tschumi (2007). Particulate organic matter (POM) is exported from the euphotic zone as a constant fraction of new production. The export between $CaCO_3$ and POM ("rain ratio") is constant unless silicic acid is abundant; in this case diatom growth is favored at the expense of calcifer growth[4]. This is primarily the case in the Southern Ocean upwelling regions. The downward particle flux (POM, $CaCO_3$ and opal) is instantaneously remineralized/dissolved in the water column following predefined profiles. The remaining material reaching the seafloor is then remineralized or, if the sediment model is activated, deposited on the seafloor sediment diagenesis layer (see below). The export and remineralization of particulate

---

[2]NCEP: The National Centers for Environmental Prediction
  NCAR: The National Center for Atmospheric Research
[3]The depth-averaged momentum-equation around the island must be zero.
[4]The rain ratio is therefore not globally uniform, but its upper limit is fixed.

matter leads to a vertical gradient in DIC and Alk as carbon is removed from the surface and transported to the deep as sketched in Fig. 2.2. The basic fluxes in the model are expressed in terms of PO_4 fluxes, the other elements being linked using empirical observed elemental ratios in organic matter, the so-called Redfield ratios (Sarmiento & Gruber, 2006).

As the Bern3D is a rigid-lid ocean model, the dilution/concentration effect of evaporation and precipitation is parameterized as virtual tracer fluxes according to the OCMIP-2 protocol. Virtual fluxes do not lead to real changes in the global ocean mean tracer concentrations (and thus inventories) unless the oceanic salt content changes. This is e.g. the case in simulation on glacial-interglacial (G-IG) timescales when sealevel-changes are taken into account by removing/adding salt to the ocean. In such cases, global mean tracer concentrations need to be multiplied with a "virtual" ocean volume according to the mean salt content in order to calculate inventories.

Carbon isotopes are implemented as tracers DIC-13, DIC-14, DOC-13, DOC-14, POC-13, POC-14, $CaCO_3$-13 and $CaCO_3$-14 as described in Müller (2007). ^{13}C is fractionated during photosynthesis and $CaCO_3$ formation while ^{14}C is not subject to fractionation.

Air-sea gas exchange for CO_2 and ^{14}C is implemented according to the OCMIP-2 protocol (Orr & Najjar, 1999; Najjar et al., 1999). $^{14}CO_2$ is not fractionated during air-sea gas exchange while ^{13}C is fractionated as a function of temperature and carbonate chemistry as detailed in Müller (2007). In order to calculate ^{14}C inventories, DIC-14 und DOC-14 must be corrected for fractionation (offline) using $\delta^{13}C$ of DIC and DOC (Müller, 2007). The global mean air-sea transfer rate is reduced by 19% compared to OCMIP-2 to match observation-based estimates of natural and bomb-produced radiocarbon (Müller et al., 2008) and in agreement with other studies (Sweeney et al., 2007; Krakauer et al., 2006; Naegler & Levin, 2006). In addition, the gas-transfer velocity ("piston velocity") k_w now scales linear (instead of a quadratic dependence) with wind speed following Krakauer et al. (2006). To ensure the global conservation of the rate of gas exchange w.r.t. the OCMIP-2 formulation, the following formulation is currently used in the model:

$$k_w = k_{\text{scale}}^{\text{gas}} \cdot (1 - F_{\text{ice}}) \cdot \underbrace{\left(0.337 \cdot \frac{\overline{\text{xKw}_{\text{OCMIP}})}}{\overline{|u|_{\text{NCEP}}}} \right)}_{\text{normalization factor} = 7.798 \cdot 10^{-6}} \cdot |u|_{\text{NCEP}} \cdot \left(\frac{\text{Sc}}{660} \right)^{-\frac{1}{2}}. \qquad (2.1)$$

Here, the overlined variables denote spatially and temporally averaged values (i.e. scalars). $\text{xKw}_{\text{OCMIP}} = X_{\text{conv}} \cdot (u^2 + v)$ is the climatology provided[5] by OCMIP, where $X_{conv} = 1/(3.6 \cdot 10^5)$ is a constant factor to convert the piston velocity from cm hr^{-1} to m s^{-1} and v the variance of instantanous wind speed. This climatology has been replaced by a climatology for monthly mean absolute wind speeds from NCEP/NCAR[6] ($|u|_{\text{NCEP}}$). The normalization factor in Eq. 2.1 ensures the conservation of the globally integrated rate of annual mean gas transfer w.r.t. the original OCMIP formulation. F_{ice} is the sea-ice concentration as calculate by the EBM[7]. This implies that there is no gas transfer if the sea-ice concentration is 100%, e.g. fluxes through small leads and cracks (Steiner et al., 2013) are neglected in the default setup. $k_{\text{scale}}^{\text{gas}} = 0.81$ is the abovementioned scaling factor (Müller et al., 2008) and Sc the Schmidt number as calculated by the modelled seawater temperature.

A simple model of N_2O production similar to the model described in Goldstein et al. (2003), i.e. a parametrization of N_2O production based on oxygen consumption and local oxygen levels, has been added in 2013 (Bourquin, 2013). Solubilities of N_2O are taken from Wanninkhof (1992). In

---

[5] `http://ocmip5.ipsl.jussieu.fr/OCMIP/phase2/simulations/CFC/boundcond/gasx_ocmip2.nc.gz`
[6] In the 36×36 setup of the model, the cross-calibrated, multi-platform (CCMP) ocean 10 m surface wind fields from the Physical Oceanography Distributed Active Archive Center (PO.DACC) is used instead.
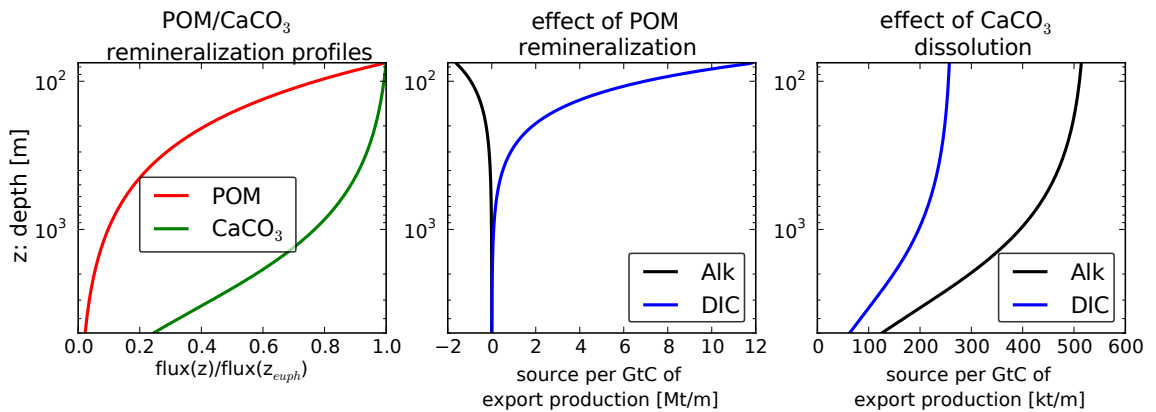[7] F_{ice} is set to 0 if $F_{\text{ice}} < 0.2$

Figure 2.2: The simple representation of the biological pump in the Bern3D ocean component: the particulate matter leaving the euphotic zone (at 75 m depth) is instantaneously remineralized according to simple profiles leading to depth-dependent sources and sinks of DIC and Alk in the ocean interior. The numbers expressed here for an hypothetical POM export flux of 1 Gt C per unit area and a rain-ratio of 0.07.

the current version, half of the N_2O production is associated with oxygen consumption using the Redfield ratio $\mathcal{R}_{N_2O:O_2} = 6 \cdot 10^{-5}$, i.e. one molecule of N_2O is produced for 16'667 molecules of O_2 consumed during remineralization. The other half of the production is associated with low oxygen levels.

Sediment

A 10-layer sediment diagenesis model (Heinze et al., 1999; Gehlen et al., 2006) with the same horizontal resolution as the ocean model is coupled to the ocean floor, dynamically calculating the advection, remineralization/redissolution and bioturbation of solid material ($CaCO_3$, POM, opal and clay) deposited on the top 10 cm of the seafloor as well as pore-water chemistry and diffusion as described in detail in Tschumi (2009); Tschumi et al. (2011). The model assumes conservation of volume, i.e. the entire column of the sediments is pushed downwards if deposition exceeds redissolution. The POM redissolution flux is primarily a function of local oxygen levels while the local CO_3^{2-} concentration determines whether, and at which rate, $CaCO_3$ dissolves. The latter mechanism is crucial for simulating the "carbonate compensation", the most important coupling between ocean and sediment reservoirs on multi-millennial timescales. Isotopes are transported (without fractionation) as $Ca^{13}CO_3$, $Ca^{14}CO_3$, POC-13, POC-14 and in dissolved form as DIC-13 and DIC-14.

To compensate the loss of tracer due to sedimentation, a weathering flux has to be prescribed at the surface ocean. These weathering fluxes of DIC, DIC-13, Alk, PO_4 and SiO_2 are diagnosed during a spinup as to compensate for the burial fluxes of particulate matter as to conserve global inventories. Optionally, a simple model of weathering feedback following Colbourn et al. (2013) can be activated as demonstrated in Sect. 5.3. In a steady-state, the burial-weathering cycle does only slightly change ocean tracer distribution, the DIC, Alk and PO_4 gradients are slightly flattened.

The addition of such a sediment module also implies that the model is now "open" concerning the cycling of carbon and nutrients. In contrast to when using the ocean-atmosphere only version of the Bern3D, tracer inventories are not conserved anymore as there may be a transient imbalance of weathering and burial fluxes.

Land

For the land component, two different options were used in this thesis.

The more sophisticated land component is based on the Lund-Potsdam-Jena (LPJ) dynamic global vegetation as used by Joos et al. (2001); Gerber et al. (2003); Joos et al. (2004) and described in detail in Sitch et al. (2003). The resolution is variable; normally a resolution of $3.75° \times 2.5°$ is used for paleo-simulations and probabilistic approaches (Roth & Joos, 2013; Steinacher et al., 2013) or $1° \times 1°$ (Stocker et al., 2013) for less cost-intensive applications. The model consists of independent gridboxes driven by external climate fields and CO_2 forcings.

The cells are divided into different landuse-classes (i.e. natural, cropland, pastures...) on which different plant functional types (PFTs) may grow. The fact that the gridboxes are independent from each other makes the LPJ ideal for parallelization (see below). The fertilization of PFTs by CO_2 during photosynthesis is calculated according to the modified Farquhar scheme (Farquhar et al., 1980). A land-use conversion module has been added to take into account anthropogenic land cover change (ALCC) (Strassmann et al., 2008; Stocker et al., 2011). Recently, a dynamic nitrogen (DyN) model from Xu-Ri & Prentice (2008) has been incorporated allowing for modeling N-limitation and prognostic land N_2O emissions.

The hydrology scheme (Gerten et al., 2004; Wania et al., 2009) solves heat and moisture dynamics in the soil (top $2\,m$) at 8 different depths. Built-up on this, permafrost, Northern Hemisphere peatlands CH_4 dynamics have been added as used in Spahni et al. (2013); Zürcher et al. (2013); Stocker et al. (2013). A simplified scheme with only 2 layers may be used to reduce computational costs. In this case, the permafrost- and peatland models can not be used.

Land surface albedo is calculated from vegetation cover, vegetation type, and snow cover after Otto et al. (2011) and communicated to the Bern3D by the means of mass-conserving remapping as detailed in Steinacher (2011).

^{14}C is implemented following the implementation of ^{13}C (Scholze et al., 2003) and taking into account radioactive decay. Fractionation is twice as large for ^{14}C as for ^{13}C. Fractionation during assimilation depends on the photosynthesis pathways (C3 versus C4) and on stomatal conductance. No fractionation is associated with the transfer of carbon between the different pools in vegetation and soils.

Due to the many developments and extensions, the LPJ version used here in Bern is either called LPJ-Bern or LPX (**L**and surface **P**rocesses and e**X**changes) since the addition of the DyN module as indicated in Fig. 2.1.

The computational more efficient option is a simple 4-box representation according to Siegenthaler & Oeschger (1987) which includes the cycling of ^{13}C and ^{14}C. Starting from a version with fixed carbon stocks, two simple formulations were added as used in Chap. 3: a stimulation of NPP by elevated CO_2 using a logarithmic dependency of NPP on atmospheric CO_2. Soil and litter turnover rates are taken to vary with global mean surface air temperature. The parameters have been tuned towards the response of the LPJ model.

Coupling of the components

The coupling of the Bern3D-LPJ is sketched in Fig. 2.3. As the ocean biogeochemical model is run on the same grid as the ocean model, the coupling is relatively trivial. The same is true for atmosphere and sediment model which share the same horizontal grid as the ocean model. For the coupling of the Bern3D and the LPJ model, a separate coupler routine was developed to handle calculation of CO_2, CH_4 and N_2O and the remapping of albedo fields (Steinacher, 2011). Note that the LPJ was coupled to the Bern3D by the means of a pattern-scaling approach: only a scalar temperature change ΔT is communicated to LPJ where then a pattern[8] of "global warming" is then scaled and applied accordingly. The direct exchange of monthly 2-D temperature and precipitation fields has been implemented later as part of this thesis. This extension allows one

---

[8]i.e. temperature-, precipitation- and cloud cover-anomaly fields taken from a GCM
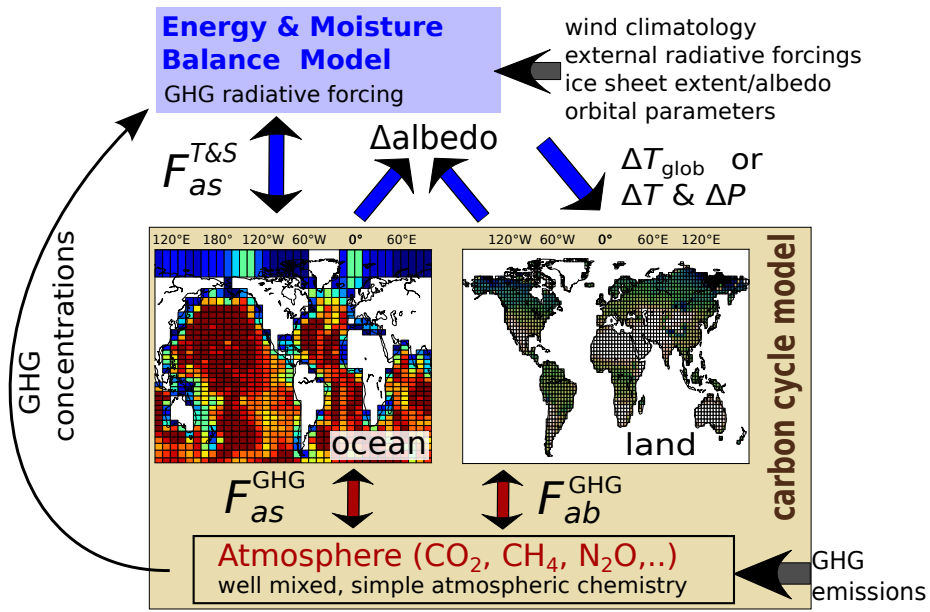
Figure 2.3: A cartoon of the coupled Bern3D-LPJ setup. The atmospheric component (blue box) is forced by a wind climatology, orbital parameters, ice-sheet mask and radiative forcing of agents not simulated by the model (i.e. aerosols). Driven by atmospheric boundary conditions as simulated by the energy balance model (EBM), the ocean component is forced with temperature (T) and salt (S) fluxes. The land component is either driven by a pattern-scaling approach (see main text) or by the direct exchange of remapped temperature and precipitation anomalies. Albedo changes (Δalbedo) from the sea-ice and land components are fed back to the EBM. The air-sea (F_{as}) and atmosphere-biosphere (F_{ab}) fluxes of greenhouse gases (GHG) calculated by carbon cycle (brown box) are then fed back to the well-mixed atmosphere where concentrations and radiative forcings of GHGs are updated.

to use the fully coupled model for e.g. freshwater experiments where the pattern of climate change is different from that of global warming.

The coupling of the model components is done sequentially, i.e. by default one model component after the other is executed. The complete flowchart of subroutine calls is shown in the Appendix A. Strongly simplified, the steps of the model integration are the following ones:

- The ocean velocity field is deduced.

- The LPJ is called and atmosphere-biosphere fluxes of greenhouse gases and land-albedo changes are calculated (F_{ab}^{GHG}).

- The EBM is run and air-sea change fluxes of temperature and salt are calculated ($F_{as}^{T\&S}$).

- The ocean biogeochemistry is updated and vertical[9] fluxes as well as air-sea gas exchange of greenhouse gases (F_{as}^{GHG}) are calculated.

- The ocean tracer transport is performed: advection, diffusion and source-minus-sink (SMS) terms.

- The sediment model is run: calculation of burial and weathering fluxes.

When using the Bern3D together with the LPJ model, the model can be run in a parallel mode (open MPI standard) by distributing the model on $N+1$ CPU cores: 1 core (the master task) is used to run the atmosphere-ocean-sediment model while N cores are used to run the LPJ at the same time (Steinacher, 2011).

---

[9]Fluxes within the water column.

CPU demand

The computational cost of the different model components is listen in Tab. 2.2 both for the `36×36` version and the new `41×40` version. For the ocean model, the computational cost increases almost linearly with the number of tracers which are transported in addition to temperature and salt. To reduce computation time, the number of tracers can be reduced from the standard value of 14, e.g by disabling carbon isotopes.

The computational cost of the LPJ model varies considerably with the horizontal resolution, the number of soil layers (2 or 8), the number of biogeochemical processes taken into account and the number of land-use-classes. For example the DyN module requires a daily timestep (δt) which makes the model more costly. Two extreme cases are listed in Tab. 2.2. As noted above, the LPJ can be run in MPI mode and therefore the listed times can be divided by N cores (for small N). When using the MPI mode for the coupled model it is useful to check the computation time for different N to find the optimum for a given setup of the LPJ and Bern3D. As a guidance, N=3–5 should be suitable for the 3.75°×2.5° and N=6–10 for the 1°×1° setup, depending on the chosen LPJ features.

In addition to the model setup, the compiler's optimization options have a considerable influence on computation time[10]. Our standard compiler flags have been chosen by searching for the fastest option which exactly reproduces the numeric results of the model compiled with `-O1`.

model components / resolution	36×36 (δt=1/48 yr)	41×40 (δt=1/96 yr)
ocean physics + EBM atmosphere	01 m 12 s	03 m 28 s
ocean biology and biogeochemistry	03 m 45 s	09 m 45 s
seafloor sediments	01 m 17 s	02 m 05 s
total	06 m 14 s	15 m 32 s
	3.75°×2.5° - min. processes	1°×1° - max. processes
terrestrial biosphere (LPJ)	~30 s	~10m

Table 2.2: CPU time demand for 100 model years on a single Intel i7 CPU clocked at 3.2 GHz and the compiler optimization flags: `-O3 -fast -Mnovect`. Note the different timestep (δt) in the two model versions.

2.1.2 The variable-grid version of the Bern3D model

Recently, the physical core of the Bern3D ocean component underwent some major changes. Before 2012, only grids with a latitudinal spacing proportional to the sine of the latitude were possible, such that the surface area of all gridboxes is equal. Based on this constraint, many equations were simplified in the original GOLDSTEIN model as gridcell areas were omitted in the equations. Another problem was that the equations appearing in their discretized form were not properly documented[11].

During 2012 and early 2013, all equations were generalized to be used with arbitrary rectangular grids. At the same time, all equations got documented including their discretization (Ritz, 2013). In addition to the horizontal resolution, some minor changes were incorporated in the ocean and EBM modules. The optimization of the new model as well as the necessary adaptation of the biogeochemical components of the model are documented in this thesis. Despite the fact that the old version was applied for all publications included in this thesis, the new version is documented here with a focus on the oceanc's biogeochemistry. This may be useful for future PhD and Master students. Also, much of the following is also applicable to the old model as the underlying formulations did not change.

---

[10]Between `-O1` and `-O3` there is almost a factor of 2 in computation time.
[11]Physical core of the ocean model almost like a "black box" to us modelers.
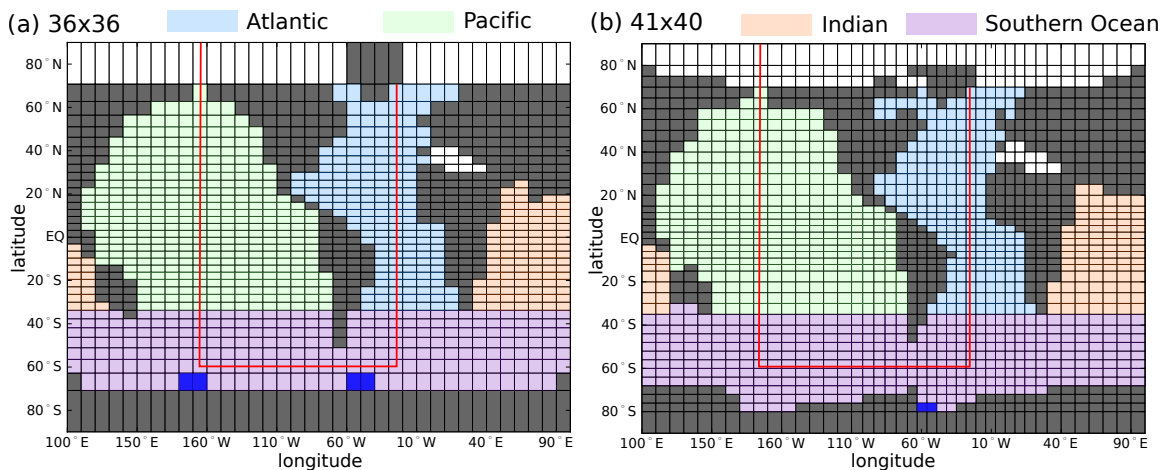
Figure 2.4: Comparison of the horizontal grid for the "old" (36×36) **(a)** and the "new" (41×40) **(b)** version of the Bern3D ocean model. Latitudinal resolution near the equator remained largely unchanged while resolution was increased in the high-latitude. Note that the ocean, atmosphere and sediment models share the same horizontal grid. The red line shows the path of the transect plot used in this thesis. The blue colored cells indicate the locations of freshwater removal (i.e. the addition of salt) to stimulate deepwater formation. The light colors depict the definition of ocean basins as used to calculate depth gradients and zonal means.

Note that several horizontal grid configurations were tested in an early stage. Our group then decided to proceed with the 41×40 configuration which has a higher latitudinal resolution in the Southern Ocean as well as an increased longitudinal resolution in the Atlantic (see Fig. 2.4b). A more detailed overview on the grid is given in Appendix B. Although the number of boxes only modestly increased, the timestep (δt) had to be decreased by a factor of two in order to maintain numerical stability.

Only the 41×40 configuration is discussed here, even though other grids a relatively easy to generate (see Ritz (2013) for a HOW-TO). The following changes were made for this setup (w.r.t. the 36×36 setup used in the most recent publications):

- new grid with 41×40 gridboxes in the horizontal.

- Ocean:

    - new parameter set (see Tab. 2.3)

    - new time step: 96 timesteps per year (instead of 48 timesteps per year in the old version)

    - max. isopycnal slope has been increased to prevent spatial oscillations of the tracer fields in the Southern Ocean

    - shuffling convection is now applied for all tracers (instead of only to T & S).

- Atmosphere:

    - new parameter set (see Tab. 2.3)

    - updated input fields

    - no Atlantic-to-Pacific freshwater correction flux

    - zonal resolved winds are now used for moisture and heat advection

    - zonal eddy-diffusive transport of heat is now a function of latitude (see Tab. 2.3)

    - moisture advection is now reduced by a scaling factor $\beta_{\mathrm{moist}} = 0.5$

- land albedo changes through snow is now taken into account by default. Changes in snow albedo calculated by the snow albedo parametrization of Ritz et al. (2011b) are accounted for as anomalies to the fixed surface albedo. Minimum snow albedo is the MODIS[12] land surface albedo from which the snow contribution has been removed
- wind stress is reduced by a factor of $(1 - F_{\text{ice}}^2)$ at the presence of sea ice.

- Sea ice:

  - sea ice is solved with a separate time-stepping: 10 steps per atmospheric time step
  - sea-ice advection is reduced to 0.3 times the surface ocean current for better consistency with ERA–40[13] sea-ice fields
  - sea-ice diffusion has been increased (see parameters table)

- Ice sheet:

  - new ice-sheet parametrization: Greenland and Antarctica are now assumed to have temporally constant ice sheet cover. Due to this, the climate is no longer affected when ice sheets are activated at a present day state (albedo of Greenland and Antarctica remain at the values of the MODIS climatology)
  - updated ice-sheet mask (Peltier, 2004)

- Ocean biogeochemistry:

  - new (absolute) windspeed climatology (from NCEP instead of PO.DACC) for the gas exchange formulation.
  - new parameter set (see Tab. 2.4)
  - new dust input fields from Mahowald et al. (2006)
  - virtual fluxes are now applied to all biogeochemical tracers.

- Sediment:

  - new parameter set (see Tab. 2.4)
  - weathering input is now distributed along the coastline
  - organic matter denitrification disabled per default.

In the 41×40 version, the key ocean parameters remained largely unchanged with the exception of an ad-hoc doubling of diapycnal diffusivity (k_D) from $10^{-5}\,\mathrm{m}^2\mathrm{s}^{-1}$ to $2 \cdot 10^{-5}\,\mathrm{m}^2\mathrm{s}^{-1}$. This change was motivated by the lower-than-observed rates of anthropogenic CO_2 uptake in the old model version (Gerber & Joos, 2013). Despite some effort to optimize these parameters, no convincingly better parameter set could be found in a 1000 member ensemble exercise constrained by temperature, salt, $\Delta^{14}C$ and trichlorofluoromethane (CFC-11). The result of this exercise can be found in Appendix C. The preindustrial ocean circulation from the new model is visualized in Figs. 2.9a-d and 2.10. Deepwater formation is discussed and visualized in Appendix D. For the 36×36 version's preindustrial solution see e.g. Tschumi (2009); Tschumi et al. (2011); Ritz et al. (2011a).

---

[12]The Moderate Resolution Imaging Spectroradiometer
[13]European Centre for Medium-Range Weather Forecasts (ECMWF) 40 year re-analysis

module	parameter	new value	Description
OCN	k_D	$2 \times 10^{-5} \, \mathrm{m^2 \, s^{-1}}$	diapycnal diffusivity
OCN	$\mathrm{fw_{SO}}$	$0.07 \, \mathrm{Sv}$	Weddell sea freshwater removal
OCN	$\mathrm{fw_{Atl\text{-}Pac}}$	$0.0 \, \mathrm{Sv}$	Atlantic to Pacific freshwater flux correction
OCN	$\mathrm{ss_{max}}$	40	slope limitation of isopycnals
EBM	ε_l	1.00	reference land emissivity
EBM	G_{cl}	0.219	fraction of shortwave radiation that is reflected by the atmosphere in the standard case for clear sky conditions
EBM	G_{ov}	0.379	fraction of shortwave radiation that is reflected by the atmosphere in the standard case for overcast conditions
EBM	λ_{rad}	0.641	ratio between the total transmissivity in overcast and clear-sky conditions for the standard cases
EBM	$r_{h,precip}$	0.85	relative humidity after precipitation
EBM	K_φ	$2.0 \times 10^5 + (2.0 \times 10^7 - 2.0 \times 10^5) \times \cos^4 \vartheta \, \mathrm{m^2}$	zonal eddy-diffusivity of heat
EBM	K_ϑ	$1.2 \times 10^6 + 0.6 \times 10^6 \frac{\vartheta + \pi/2}{\pi} + 2.5 \times 10^6 \cos^2 \vartheta \, \mathrm{m^2 \, s^{-1}}$	meridional eddy-diffusivity of heat
EBM	β_{moist}	0.5	scaling coefficient for moisture advection
EBM	λ_{lw_rad}	$-0.71 \, \mathrm{W \, m^{-2} \, K^{-1}}$	Feedback parameter
EBM	K_i	$1.5 \times 10^4 \, \mathrm{m^2 \, s^{-1}}$	sea-ice diffusion coefficient
EBM	β_{ice}	0.3	scaling coefficient for sea-ice advection
EBM	α_{seaice}	0.65	sea-ice albedo
EBM	$\alpha_{icesheet}$	0.7	ice-sheet albedo
EBM	α_{snow}^{max}	0.75	maximum snow albedo
EBM	H_0	$0.05 \, \mathrm{m}$	minimal ice thickness

Table 2.3: Parameters in the ocean and atmosphere module that changed with respect to the parameters listed in Ritz et al. (2011a).

Tuning of the biogeochemical component

As the new grid configuration of the updated physical model of the new Bern3D lead to significant changes in ocean circulation, the biogeochemical parameters needed some adjustment. As most of the ocean parameters in the old model were taken from Doney et al. (2006) without optimization, some improvement could be expected. Especially the alkalinity distribution was rather poor in the old model. Note that the following discussion is based on an experimental setup which includes the sediment module. The boundary conditions are set to 1765 AD unless mentioned otherwise.

In a first step, the Fe-cycle needed to be re-calibrated as new modern aeolian dust deposition fields are applied in the new model (taken from Mahowald et al. (2006) instead from Luo et al. (2003)) leading to too high dissolved Fe concentrations and disturbed patterns of Fe-limitation. This tuning was done first because the dissolved Fe concentration influences the primary production and thus the entire biological pump. Fe solubility (β) and total ligand concentrations (L_{tot}) were adjusted to match the sparse observational data especially at the surface but also in the deep. Equivalently, the fraction of Fe in dust could have been adjusted instead of β. The resulting distribution is compared to the compilation of Tagliabue et al. (2009) and presented in Fig. 2.5a. Patterns of nutrient limitation now compare well with Moore et al. (2001) given the simplicity of our model (Fig. 2.5b).

One of the main problems with the given formulations for elemental ratios, fraction of $CaCO_3$ to POM export and remineralization characteristics is the fact that they are globally uniform, which is not the case in the real ocean (e.g. Martin et al., 1987; Buesseler et al., 2007; Lam et al., 2011; Martiny et al., 2013). As the biological pump primarily alters the water column distribution of carbon and nutrients, it makes sense to first analyze the effect of some key parameters to globally
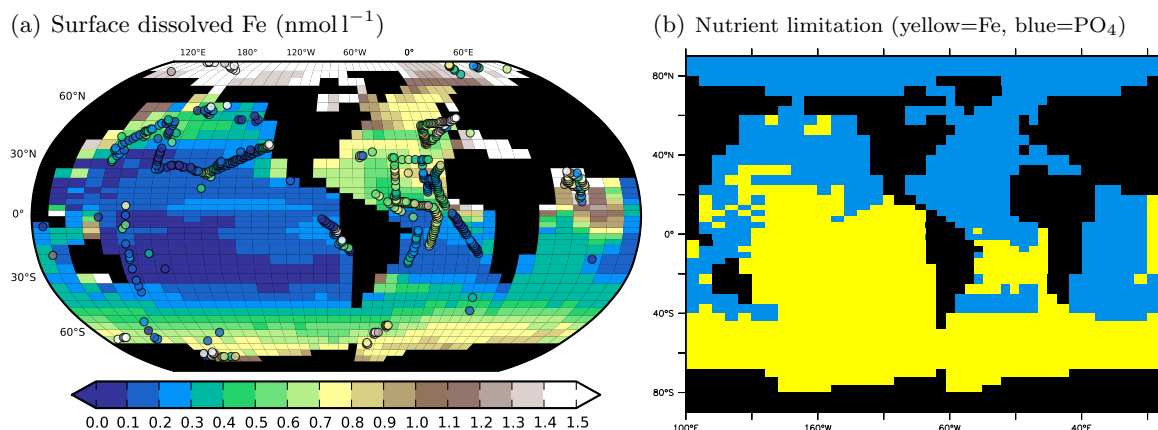
Figure 2.5: (a) Modeled surface dissolved Fe compared to the dataset of Tagliabue et al. (2009) (overlaid with dots). **(b)** Pattern of nutrient limitation: colored in yellow are regions where the limitation-term of Fe dominates w.r.t. PO_4, while blue colored areas are primarily limited by PO_4.

averaged depth profiles. In sensitivity experiments, 7 parameters were perturbed and the effect on gradients quantified by subtracting a control run. Changes in elemental ratios (Redfield ratio) were not considered in this exercise. The results of 4 out of 7 parameters are shown in Fig. 2.6 (the other 3 having only a minor effects), these are: the exponent in the remineralization profile of POM (α), the length-scale of $CaCO_3$ dissolution (l_{CaCO_3}), the maximum fraction of $CaCO_3$ production (M_{CaCO_3}, this determines the rain ratio) and the fraction of the primary production transferred in the DOC pool (σ). As a perturbation, an arbitrary reduction of 20% w.r.t. the original value was used with a fixed atmospheric CO_2 concentration of 278 ppm.

To control the global gradients of DIC and Alk, α is an especially powerful tuning "knob" because it determines the rain ratio in the deep and alters the DIC and Alk gradients in opposite directions (the other parameters altering the gradients in the same direction). These profiles are then compared to model-data biases to find optimal parameters. As a side-constraint, global export, deposition and burial fluxes of organic and inorganic carbon should fall within observational ranges.

To adjust the burial fluxes, sediment pore-water reaction rates and the terrestrial clay flux had to be adjusted. Note that due to the long equilibration time of the ocean-sediment system, the tuning is rather time consuming. As a final step, the N_2O production formulation was tuned in order to match observational data (Bange et al., 2009) of dissolved N_2O and estimates global integrated N_2O emissions (Denman et al., 2007)

A satisfying solution could be found using the parameters listed in Tab. 2.4. Using this updated parameter set lead to a significantly better agreement with data compared to the original set taken from the old model, as summarized in the Taylor diagram shown in Fig. 2.7. The improvement in Alk and pH is noteworthy. The new optimized solution also shows a considerably smaller discrepancy between many model variables and observations as compared to the old model. The reason for this may be a more realistic circulation in combination with a more careful choice of biogeochemical parameters.

The resulting present-day distribution of tracers as well as globally integrated fluxes are discussed next.
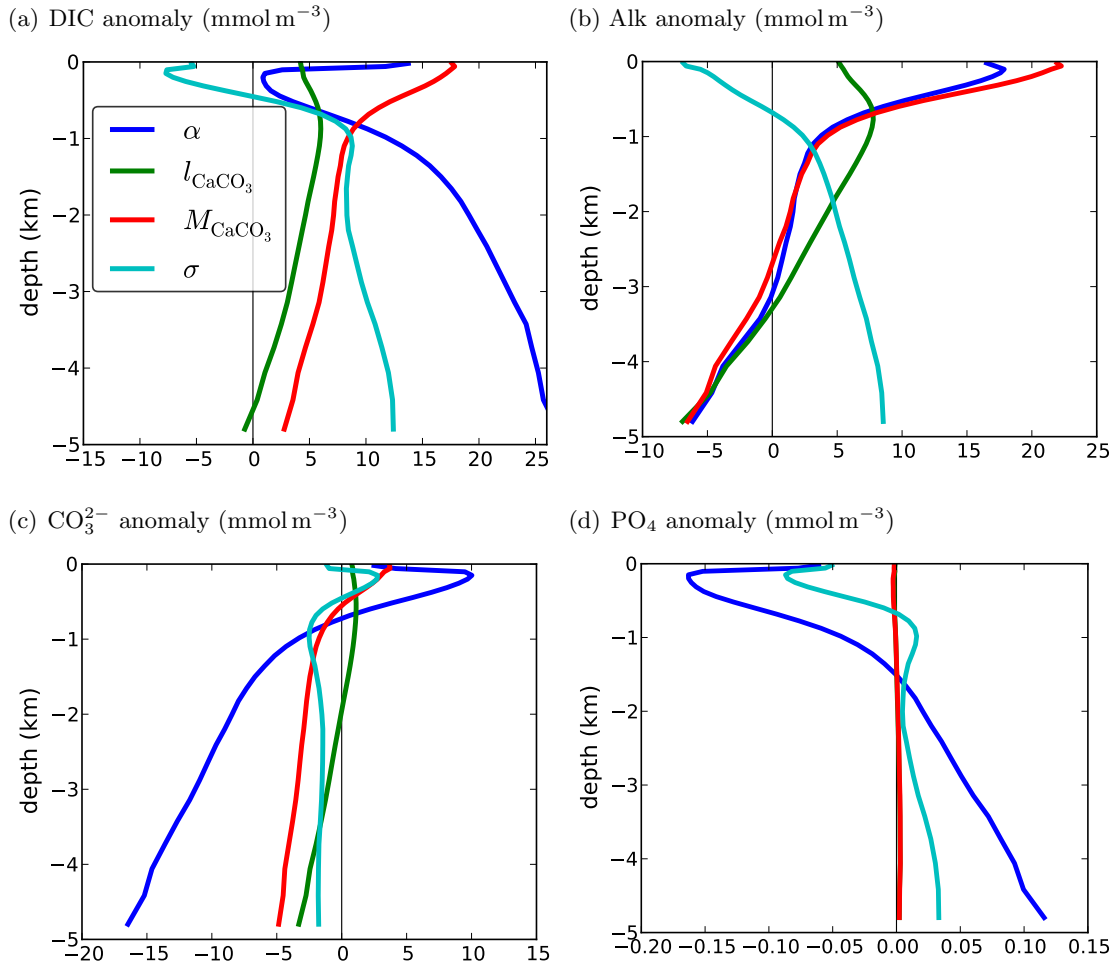
Figure 2.6: (a-d) Change in Alk, DIC, CO_3^{2-} and PO_4 for a 20% reduction in different key parameters w.r.t. a control run. The atmospheric CO_2 was held constant at a concentration of 278 ppm.

Module	parameter	old value	new value	units	description
BGC	$\mathcal{R}_{\text{Alk:P}}$	−16	−17	-	Redfield ratio Alk:P for organic matter
BGC	Alk_{init}	2409	2429	mol m^{-3}	initial Alk concentration
BGC	σ	0.67	0.68	-	DOM fraction of new production
BGC	M_{CaCO_3}	0.30	0.25	-	maximum $CaCO_3$ production relative to POM
BGC	l_{CaCO_3}	3500	2900	m	$CaCO_3$ dissolution length-scale
BGC	α	0.92	0.83	-	exponent for Martin curve (POM remineralization)
BGC	β	0.01	0.0018	-	Fe solubility
BGC	L_{tot}	$1.0 \cdot 10^{-6}$	$1.2 \cdot 10^{-6}$	mol m^{-3}	total ligand concentration
SED	$\mathcal{R}_{\text{Alk:P}}$	−18	−17	-	Redfield ratio Alk:P for organic matter
SED	F_{clay}	1.0	0.8	$\text{g m}^{-2} \text{yr}^{-1}$	terrestrial clay flux
SED	r_{oxy}	50	100	$\text{l mol}^{-1} \text{yr}^{-1}$	reactivity for POC/O_2
SED	r_{denit}	50	0	$\text{l mol}^{-1} \text{yr}^{-1}$	reactivity for POC/NO_3 (denitrification)
SED	$[O_2]_{\text{crit}}$	1	0	$\mu\text{mol l}^{-1}$	O_2 threshold for denitrification

Table 2.4: Overview on optimized parameters in the 41×40 setup of the ocean biogeochemistry (BGC) and sediment (SED) modules.
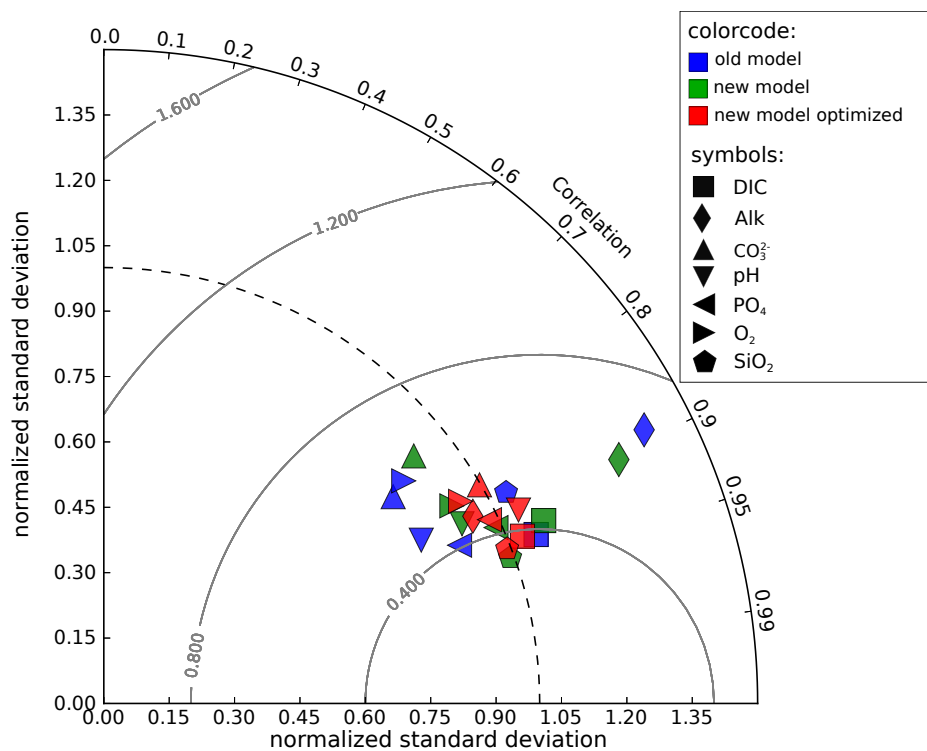
Figure 2.7: Taylor-diagram showing normalized standard deviation and correlation for the old (36×36) version of the Bern3D model (blue), the new version (41×40, green) with the same BGC-parameters as the old version and the new version with the final set of parameters (red). The statistics are computed by comparing a preindustrial (1765 AD) equilibrium simulation with gridded natural carbon data derived from the GLODAP dataset (Key et al., 2004) and WOA09 nutrient and oxygen products (Garcia et al., 2010b,a). Global tracer fields were used to generate the statistics where tracer concentrations where weighted by gridbox volumes.

The modern solution

A series of model-data comparison plots is given in this section. Tracer fields are compared by the means of horizontal plots (atmosphere and ocean surface), in a transect through the Atlantic, Southern Ocean and Pacific (indicated by the red line in Fig. 2.4) and by basin-averaged depth-profiles. The basins are defined as follows: the Atlantic and Pacific go from 70°N to 35°S where the circumpolar Southern Ocean begins. 35°S is therefore also the southern boundary for the Indian basin. The basins extent is depicted in Fig. 2.4.

The experimental setup for the model is the following: the model is spun up under 1765 AD conditions and weathering fluxes then set to constant values equal to the steady-sate burial rates. A transient simulation from 1765–2011 AD is performed using prescribed atmospheric CO_2 (RCP database, 2009), the radiative effect of volcanic eruptions as well as anthropogenic aerosol forcing according to Eby et al. (2013). Atmospheric $\Delta^{14}C$ is taken from Reimer et al. (2009) and Orr & Najjar (1999) while $\delta^{13}C$ boundary conditions are taken from an inhouse compilation of ice core, firn and air measurements.

The model output is then averaged over the period over which the observations have been collected. The observations shown here include the products from the World Ocean Atlas 2009 (WOA09) (Antonov et al., 2010; Locarnini et al., 2010; Garcia et al., 2010b,a) and the ERA–40 reanalysis (Uppala et al., 2005). Ocean carbon data taken from GLODAP (Key et al., 2004) is converted from $mmol\,kg^{-1}$ to $mol\,m^{-3}$ using the potential density calculated from the WOA09 data using the UNESCO-formula for seawater density. Modeled preindustrial carbon is compared to natural DIC as computed from GLODAP's products TCO2 and TCO2_ANTH, the same procedure was used for radiocarbon. A small correction deduced by a transient simulation (with the default parameter set only) was applied to the modeled $\Delta^{14}C$ distribution in order to account for the Holocene history of atmospheric $\Delta^{14}C$ which was not taken into account in this setup.

No complete description and interpretation of the results is given here in the following, only strong biases and/or improvements compared to the 36×36 version are highlighted.

Atmosphere and sea ice:

Annual mean fields as simulated by the EBM are shown in Fig. 2.8. Surface atmospheric temperature (SAT) is simulated reasonably well despite some local biases: over the North Atlantic region as well as over Africa the modeled SAT is too cold, while the North Pacific and North America are generally too warm. Simulated freshwater fluxes have considerably improved compared to the old model due to the zonally resolved winds, but the equatorial precipitation belt is still too weak. Sea-ice concentration is now simulated in much more detail due to the higher resolution around the poles in the new model.

Ocean ventilation:

The annual mean preindustrial overturning and barotropic streamfunctions are shown in Fig. 2.9. Barotropic velocity averaged over 3 different depth intervals is given in Fig. 2.10. One of the striking changes in the new version is the more vigorous Antarctic Circumpolar Current (AAC) with a Drake-Passage throughflow of $\sim$110 Sv[14] compared to $\sim$40 Sv, presumably due to the reduced friction (Drake Passage is now 5 cells wide instead of 3) and the choice of a different integration-path (for the Island Rule) around Antarctica. The annual mean maximum of the Atlantic meridional overturning circulation (AMOC) is 17.3 Sv, but North Atlantic Deep Water (NADW) is still formed too far south (see Fig. D.1). The southern sourced Antarctic bottom water (AABW) tongue is still weak in the Atlantic with only $\sim$2 Sv. Simulated potential temperature is captured well by the new model. The most pronounced biases can be found in

---

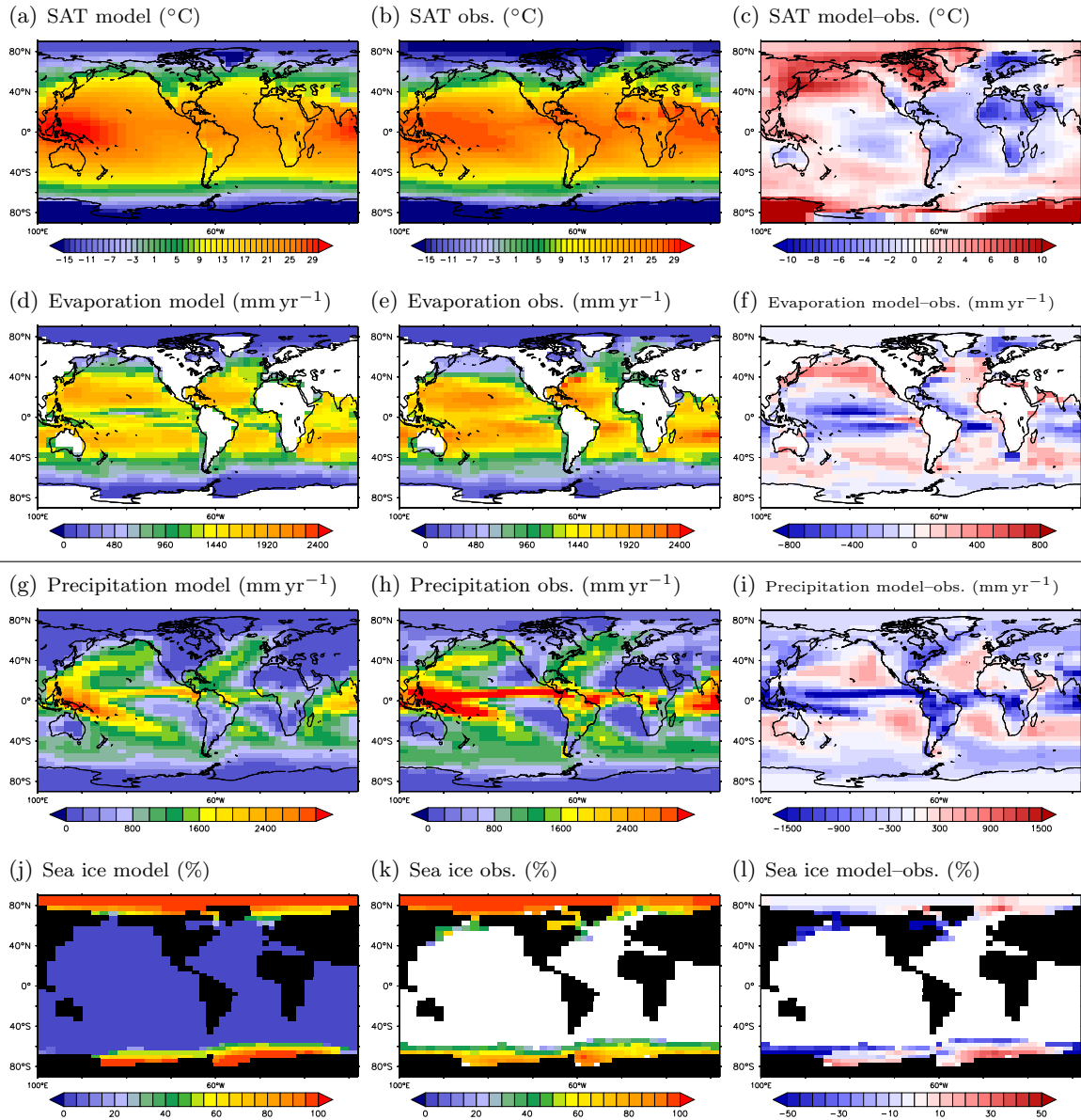[14]1 Sverdrup (Sv) $= 10^6\,m^3\,s^{-1}$

Figure 2.8: (a-l) Key modeled atmospheric (annual mean) fields compared to the ERA–40 reanalysis (Uppala et al., 2005). Sea ice is reported as fractional sea-ice cover ("sea-ice concentration").

North Pacific where surface waters are too warm as well as the too warm mid-depth Atlantic. The latter could be explained by the too warm SST in the region where NADW is formed (Fig. D.1). Salinity distribution is not satisfying, independent of the horizontal resolution. Generally, the surface ocean is too fresh while the NADW is too saline. The reason for this could be attributed to the simple atmospheric model combined with the generally small observed spatial variations of only ∼1 psu.

Ocean ventilation timescales are reproduced well by the model as indicated by the tracers natural $\Delta^{14}C$ and O_2 with the exception of the deep North Atlantic which is too old in the model, probably linked to the too weak AABW. Surface ocean ventilation shows only some regional biases compared to observation.

Also the decadal rates ocean uptake of anthropogenic CO_2 is well within estimates from Canadell et al. (2007) with a cumulative uptake from 1765–2011 AD of 156 Gt C compared to observational estimates of 155 ± 30 Gt C (Ciais et al., 2013).
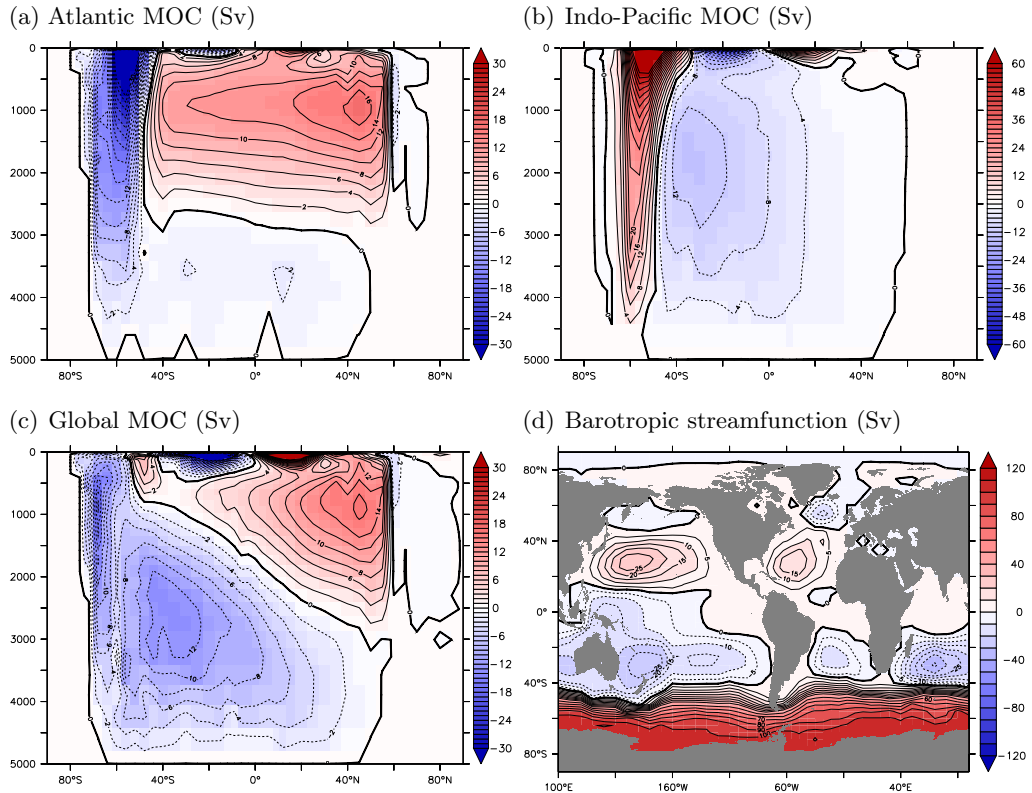
Figure 2.9: (a-c) Annual mean streamfunction of the meridional overturning circulation (MOC) for different regions. The depth-integrated flow as represented by the barotropic streamfunction (Ψ_B) is depicted in **(d)**. Note the non-equidistant contour lines. Negative numbers (blue) denote a counter-clockwise flow while positive number (red) indicate a clockwise flow.
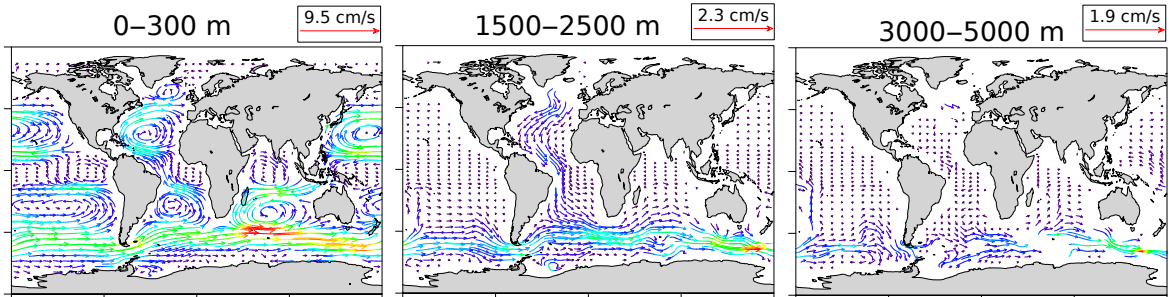
Figure 2.10: Streamlines for the barotropic velocity component averaged over 3 different depths intervals (note the different scaling of the vectors) from left to right: mean velocity from 0–300 m, 1500–2500 m and 3000–5000 m.

period:	1959–2006 ($GtC\,yr^{-1}$)	1970–1999 ($GtC\,yr^{-1}$)	1990–1999 ($GtC\,yr^{-1}$)	2000–2006 ($GtC\,yr^{-1}$)	cumulative 1765–2011 (GtC)
observations	1.9 ± 0.4^a	2.0 ± 0.4^a	2.2 ± 0.4^a	2.2 ± 0.4^a	155 ± 30^b
model	1.6	1.7	2.0	2.2	156

a: Canadell et al. (2007) b: Ciais et al. (2013)

Table 2.5: CO_2 uptake rates diagnosed in a transient simulation from 1765–2011 with prescribed atmospheric CO_2 (RCP database, 2009) compared to independent estimates of Canadell et al. (2007) and Ciais et al. (2013).

Figure 2.11: Modeled ocean temperature **(a-g)** and salinity **(h-n)** compared to observations from the WOA09 dataset (Locarnini et al., 2010; Antonov et al., 2010).

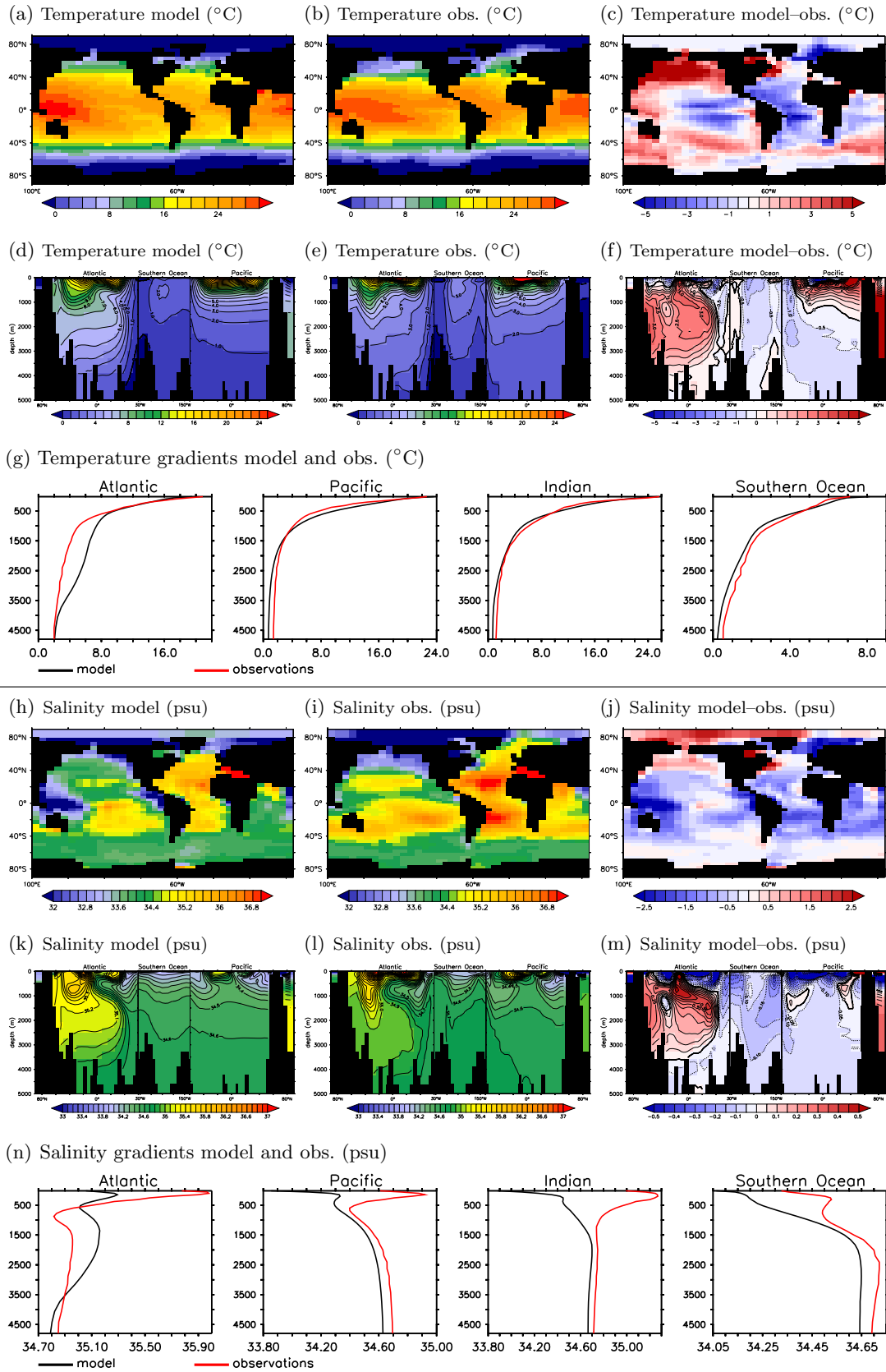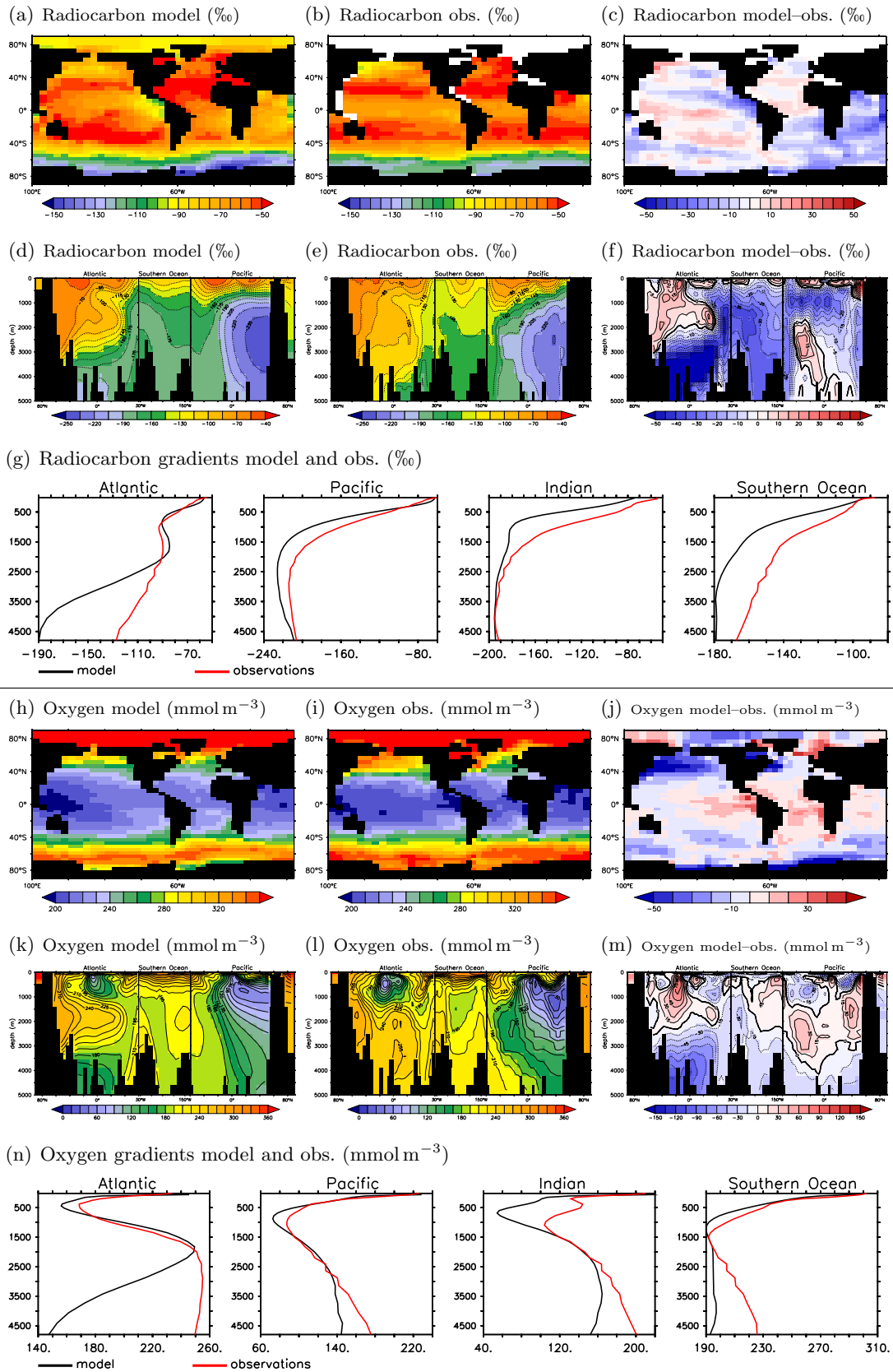**Figure 2.12:** Biogeochemical tracers both strongly influenced by ventilation timescales: modeled natural Δ^{14}C of DIC **(a-g)** and oxygen **(h-n)** compared to observations from GLODAP (Key et al., 2004) and WOA09 (Garcia et al., 2010a).

Biological pump and carbon cycling:

Next, the tracers related to the cycling of carbon are discussed. Figs. 2.13a-c show the modeled organic matter export (ePOM) out of the euphotic zone compared to data-based estimate of Schlitzer (2004). The model captures the peaks in export production in the equatorial and Southern Ocean upwelling regions and accounts for $11.7\,\mathrm{Gt\,C\,yr^{-1}}$ in the global integral. The same pattern applies to the calcite export with the exception of the Southern Ocean where diatoms grow in favor of calcifying organisms (not shown). Note that the estimation of export production based on satellite-based chlorophyll data is fraught with considerable uncertainty. The saturation horizon of CO_3^{2-} w.r.t. calcite, i.e. the depth where $\Omega_c = 1$, is shown in Figs. 2.13a-c and compared to data-derived estimates which agree well except for the North Pacific.

Whole ocean carbon inventory and export, deposition and burial fluxes are summarized in Tab. 2.6. Especially the particulate matter flux estimates are rather uncertain and mostly stem from sediment-trap data and global budget considerations. These estimates only serve as a weak constraint for the model.
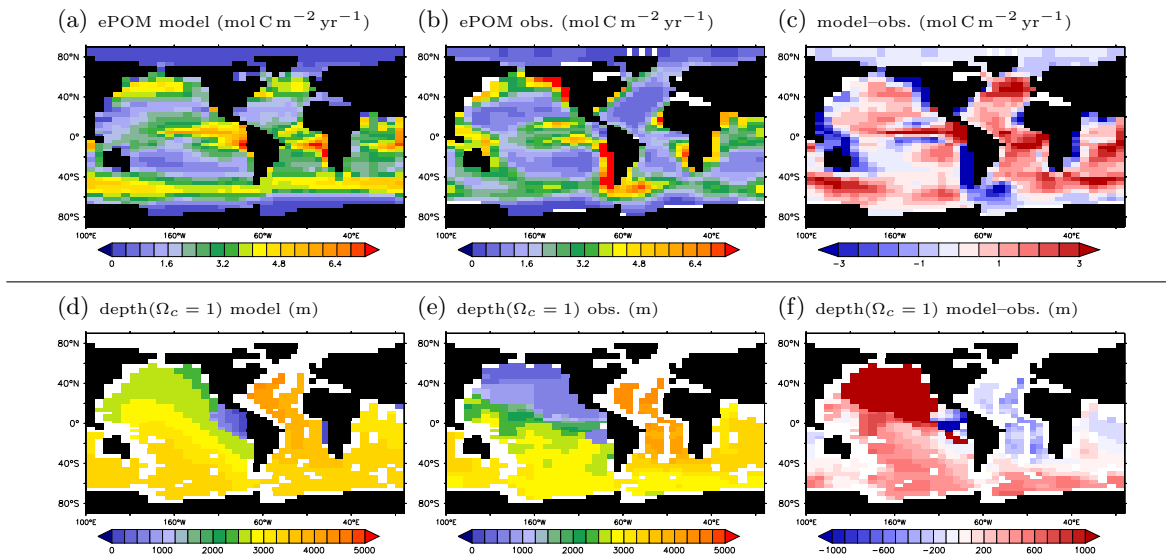

Figure 2.13: (a-c) Modeled POM export flux compared to the dataset of Schlitzer (2004). **(d-e)** Modeled versus data-derived (GLODAP & WOA09) depth of the calcite saturation horizon.

Modeled distributions of DIC and Alk are shown in Figs. 2.14a-n and are compared to natural DIC and Alk from GLODAP (Key et al., 2004). Gradients of DIC closely follow the observed gradients in the global average. Although the earlier discussed ventilation-bias in the deep Atlantic is also visible here as carbon accumulates in the deep (the same is true for alkalinity). The high DIC concentration in the North Pacific can not quite be reproduced in magnitude. Although the Alk-cycle is still challenging to model within the given ocean biology framework, the new model preforms considerably better in this respect.

Stable carbon isotope $\delta^{13}C$ of DIC is displayed in Fig. 2.15. The model shows a global bias of $\sim +0.2\permil$ at the surface as well as in the deep. As the shape of the vertical gradients are well captured by the model, this offsets points to a bias in the (local) rate of gas exchange rather than in the biological pump (for a discussion see e.g. Schmittner et al. (2013)). The higher-than-observed $\delta^{13}C$ in the Bern3D points to a too fast air-sea gas exchange. Note that for the surface data of $\delta^{13}C$ shown in Fig. 2.15a were collected from 1990 to 2005 AD, a period where atmospheric $\delta^{13}C$ of CO_2 decreased. This introduces some uncertainty in the data. The model output was taken from 1997 which is centered in this interval.

Distributions of nutrients PO_4 and SiO_2 are shown in Figs. 2.16a-n, despite the expected bias in

variable	units	value	range of estimates
DIC inventory	$Gt\,C$	37370	37510^a
$CaCO_3$ export	$Gt\,C\,yr^{-1}$	0.872	0.8–1.2^b
opal export	$Tmol\,Si\,yr^{-1}$	101	102–178^b
POM export	$Gt\,C\,yr^{-1}$	11.7	6.5–13.1^c
$CaCO_3$ deposition	$Gt\,C\,yr^{-1}$	0.273	0.5^g
opal deposition	$Tmol\,Si\,yr^{-1}$	70.2	13–47^e
POM deposition	$Gt\,C\,yr^{-1}$	0.630	1.7–3.3^c
$CaCO_3$ burial	$Gt\,C\,yr^{-1}$	0.0934	0.10–0.14^d
opal burial	$Tmol\,Si\,yr^{-1}$	2.19	5.3–8.9^e
POM burial	$Gt\,C\,yr^{-1}$	0.181	0.12–0.26^c
N_2O emissions	$Tg\,N\,yr^{-1}$	3.66	1.8–5.8^f

[a] based on the GLODAP and WOA09 datasets; [b] Jin et al. (2006) ; [c] Sarmiento & Gruber (2006); [d] Feely et al. (2004) (excluding continental shelf areas) ; [e] Tréguer et al. (1995); [f] Denman et al. (2007) ; [g] Milliman & Droxler (1996)

Table 2.6: Overview on globally integrated fluxes of particulate matter and oceanic N_2O emission for a preindustrial equilibrium simulation.

the deep Atlantic, the simulated tracer distributions compare reasonably well with the WOA09 dataset (Garcia et al., 2010b). A notable bias can be found though in the North Pacific where both PO_4 and SiO_2 concentrations are highly underestimated by the model, which is partly linked to the circulation bias in this region and maybe to an underestimated local riverine nutrient influx.

In order to further characterize the models biological activity, apparent oxygen utilization (AOU) is computed following Sarmiento & Gruber (2006) from the saturation concentration of oxygen (O_2^{sat}) using the solubilities given by García & Louis (1992) and the actual observed/modeled dissolved concentration ($O_2^{observed}$):

$$AOU = O_2^{sat} - O_2^{observed}. \tag{2.2}$$

AOU is a measure of biological activity in the water column as remineralization of settling organic particles consumes oxygen under oxic conditions and is shown in Figs. 2.17a-c. In the deep Atlantic, the model shows an increased AOU which is not observed in the data. This seems again to be linked to the too slow ventilation in the deep Atlantic where oxygen is consumed during remineralization while not enough oxygen-rich water is entering to replace this water.

In addition to AOU, we also infer the preformed concentration of PO_4:

$$PO_4^{pre} = PO_4^{observed} + \frac{AOU}{\mathcal{R}_{O_2:P}}, \tag{2.3}$$

that is, the nutrient concentration stemming from sinking water masses without being used during photosynthesis. PO_4^{pre} is therefore a measure of the missed opportunity of the biological pump to sequester carbon in the deep and therefore strongly influences atmospheric CO_2 (see e.g. Ito & Follows, 2005). Figs 2.17d-f show the fraction of PO_4^{pre} w.r.t. the total PO_4. Note that the separation into preformed and regenerated nutrients does not hold true for water column denitrification. Although the Bern3D model does not include denitrification, the observations do contain this signal.
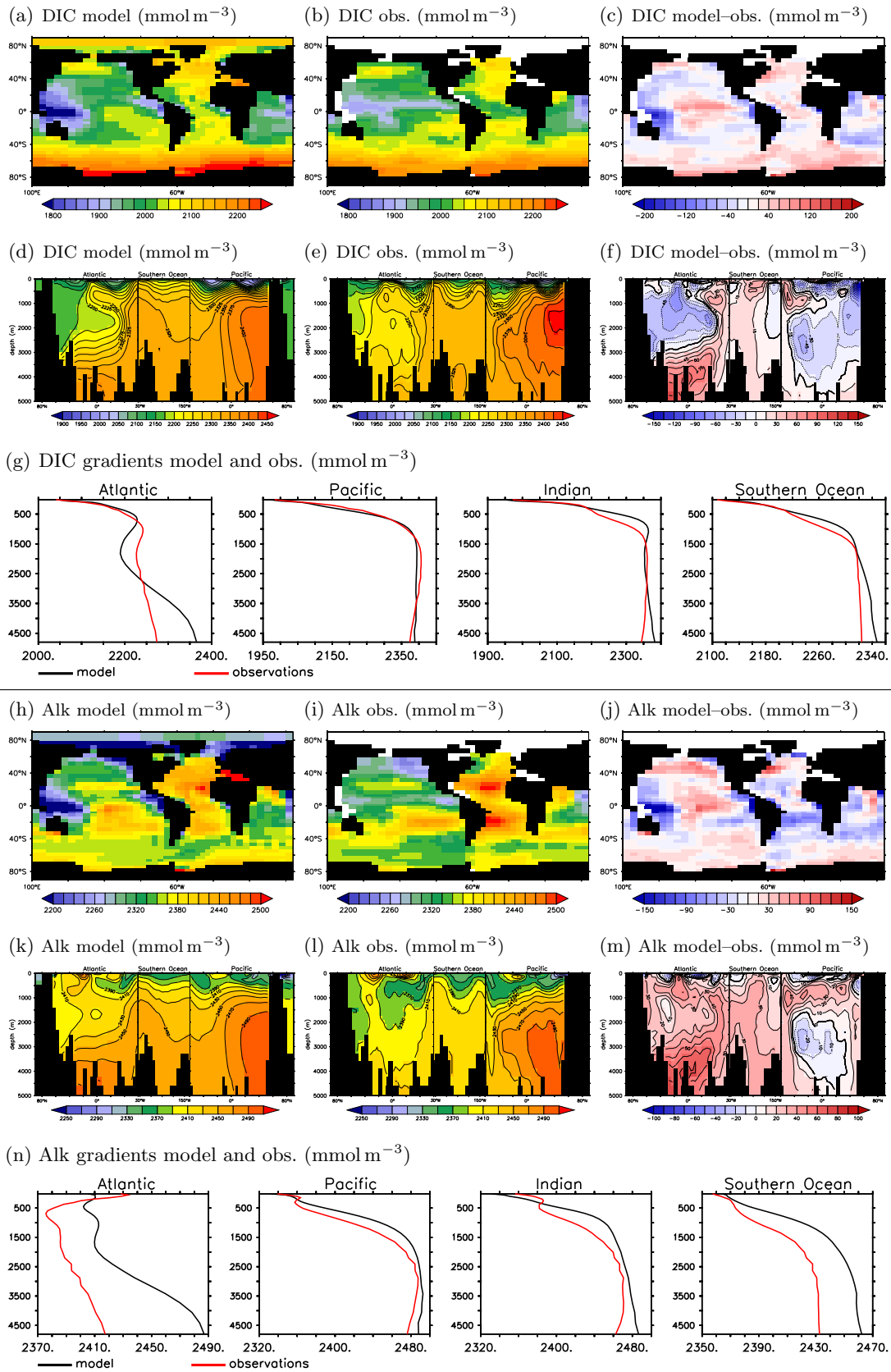
Figure 2.14: Modeled natural DIC **(a-g)** and Alk **(h-n)** compared to observations from GLODAP (Key et al., 2004).

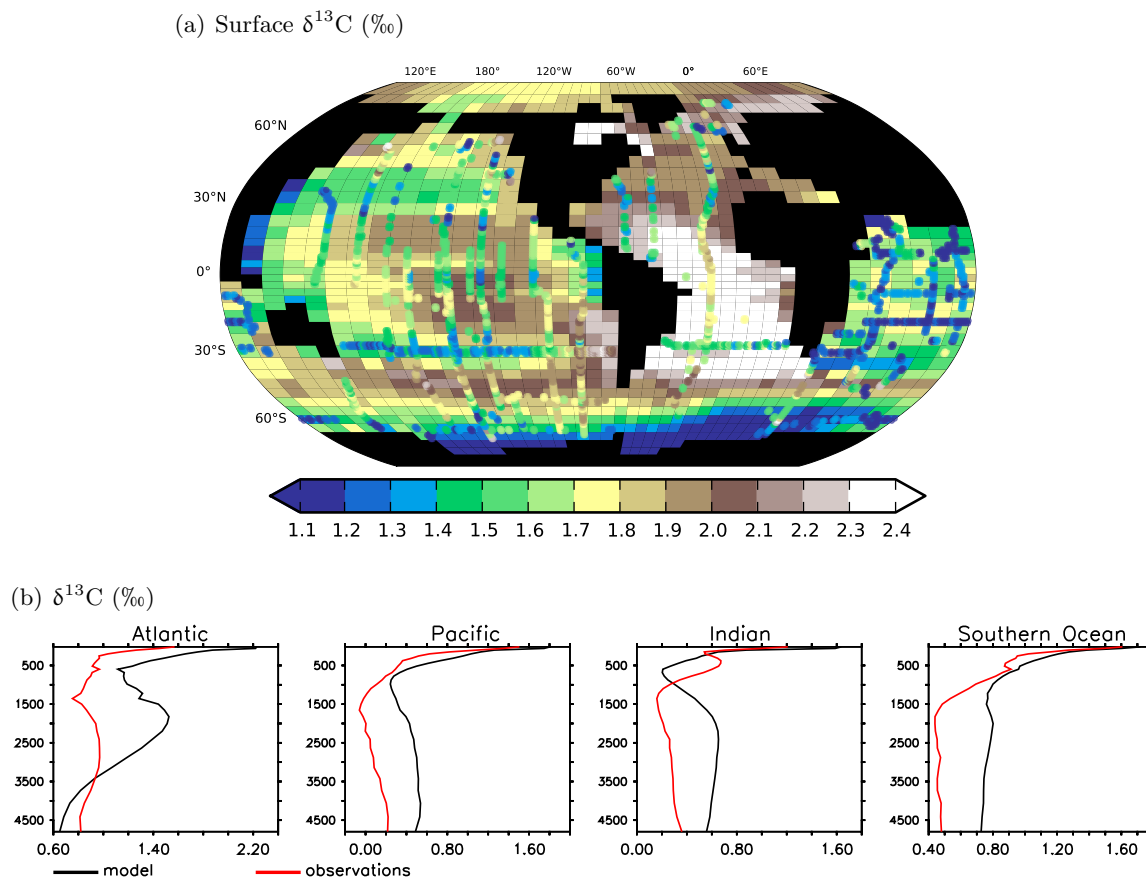(a) Surface δ^{13}C (‰)

(b) δ^{13}C (‰)

Figure 2.15: (a) Surface (0–50 m) and **(b)** vertical profiles of modeled δ^{13}C of DIC compared to the dataset of Schmittner et al. (2013). The model output was taken for year 1997 while the observations were collected between 1990–2005.

As a last tracer, dissolved N_2O is discussed (Fig. 2.18), which is compared to the data taken from a premilinary version of the MEMENTO[15] database (Bange et al., 2009). As the sources of this tracer are a simple function of remineralization and local oxygen levels (besides gas exchange), it also shares potential biases from modeled O_2. The surface N_2O is primarily a function of the temperature-dependent solubility and therefore reasonably well captured. In the deep, the distribution of N_2O captures the pronounced peak around 500 m (oxygen minimum zones). In the current configuration the oceanic production, and therefore net outgassing, is $3.66\,\mathrm{Tg\,N\,yr^{-1}}$ in the global integral.

Summary and conclusions: the Bern3D ocean component does a reasonable job in capturing the observed large-scale features in the distribution of physical and biogeochemical tracers. Local biases are linked to the simplified 2-D atmosphere (evaporation, precipitation) and the simple hydrological scheme on land (e.g. continental runoff). In addition, deep ocean circulation seems to be too slow in general, especially in the deep northern Atlantic as visible in the distribution of ventilation-sensitive tracers O_2 and Δ^{14}C. This is probably linked to the coarese resolution in the deep as well as the simplistic formulations of friction. The seawater carbon chemistry has been considerable improved by re-tuning the relevant parameters controlling biological export and redissolution profiles. Local biases are not an big issue in this case as the Bern3D model is used to address questions on a basin-wide (or even global) scale.

---

[15]**M**arin**E M**ethan**E** and **N**i**T**rous **O**xide database – `http://memento.geomar.de/`
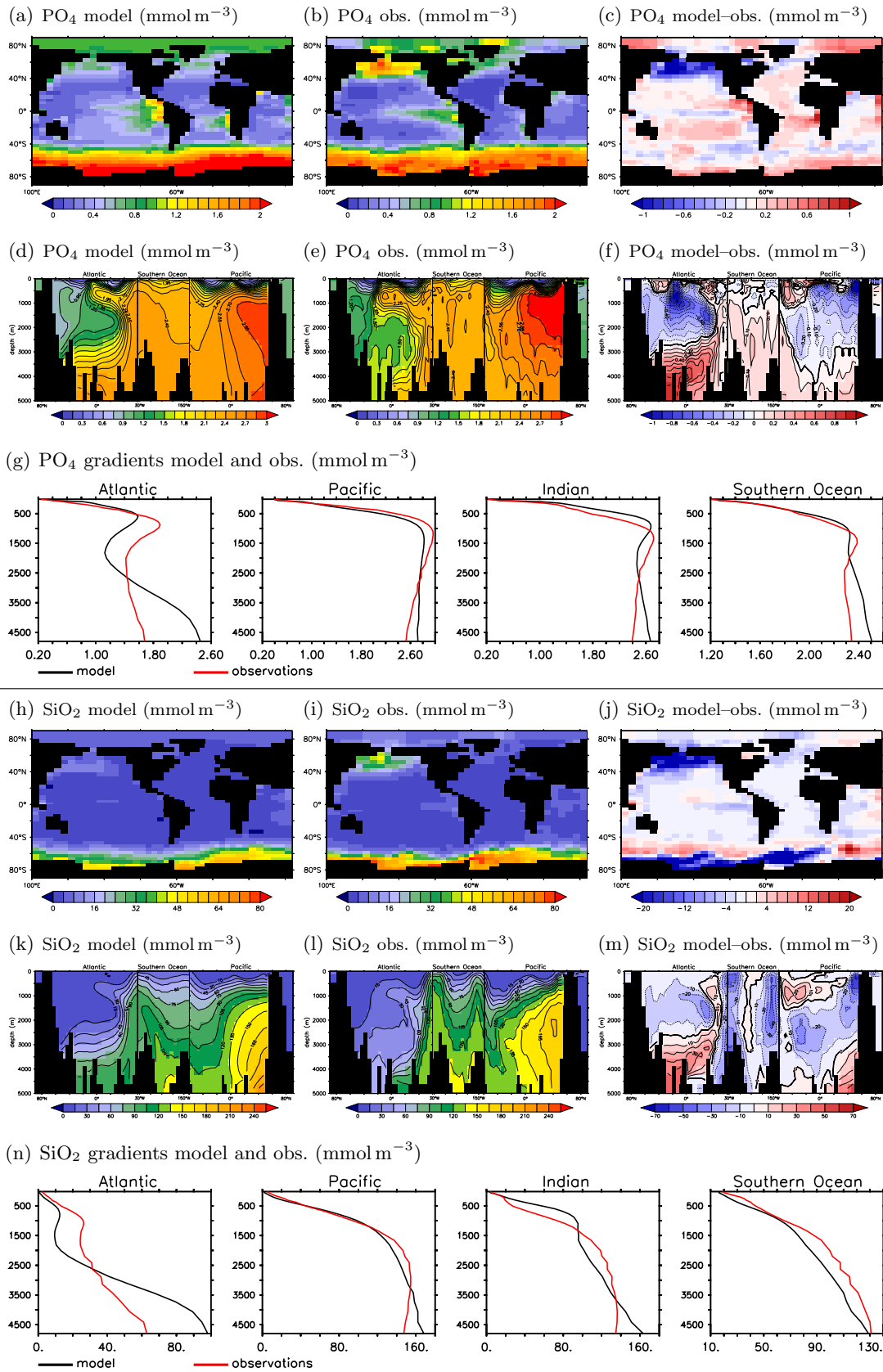
Figure 2.16: Modeled PO$_4$ **(a-g)** and SiO$_2$ **(h-n)** compared to observations (WOA09, Garcia et al. (2010b)).

(a) AOU model (mmol m^{-3})　　(b) AOU obs. (mmol m^{-3})　　(c) AOU model–obs. (mmol m^{-3})

(d) PO$_4^{pre}$/PO$_4$ model (%)　　(e) PO$_4^{pre}$/PO$_4$ obs. (%)　　(f) PO$_4^{pre}$/PO$_4$ model–obs. (%)
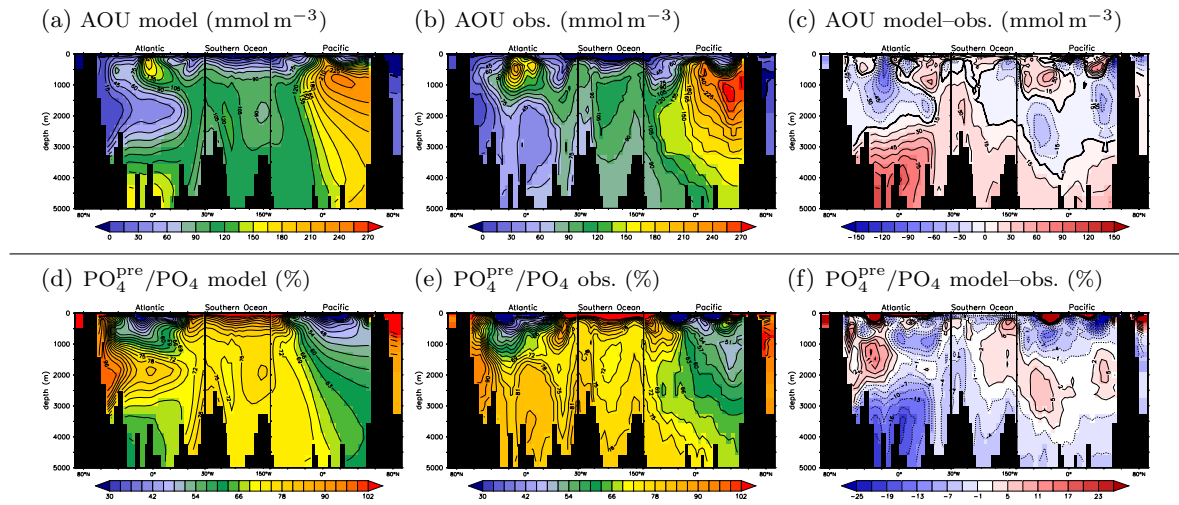
Figure 2.17: (a-c) Apparent oxygen utilization (AOU) computed from the difference between the dissolved and equilibrium saturation concentrations (García & Louis, 1992) based on modeled/observed seawater properties (temperature and salinity). **(d-f)** Percent fraction of the preformed nutrient concentration (observations are based on Garcia et al. (2010b)).

(a) Surface dissolved N$_2$O (µmol l^{-1})

(b) dissolved N$_2$O (µmol l^{-1})
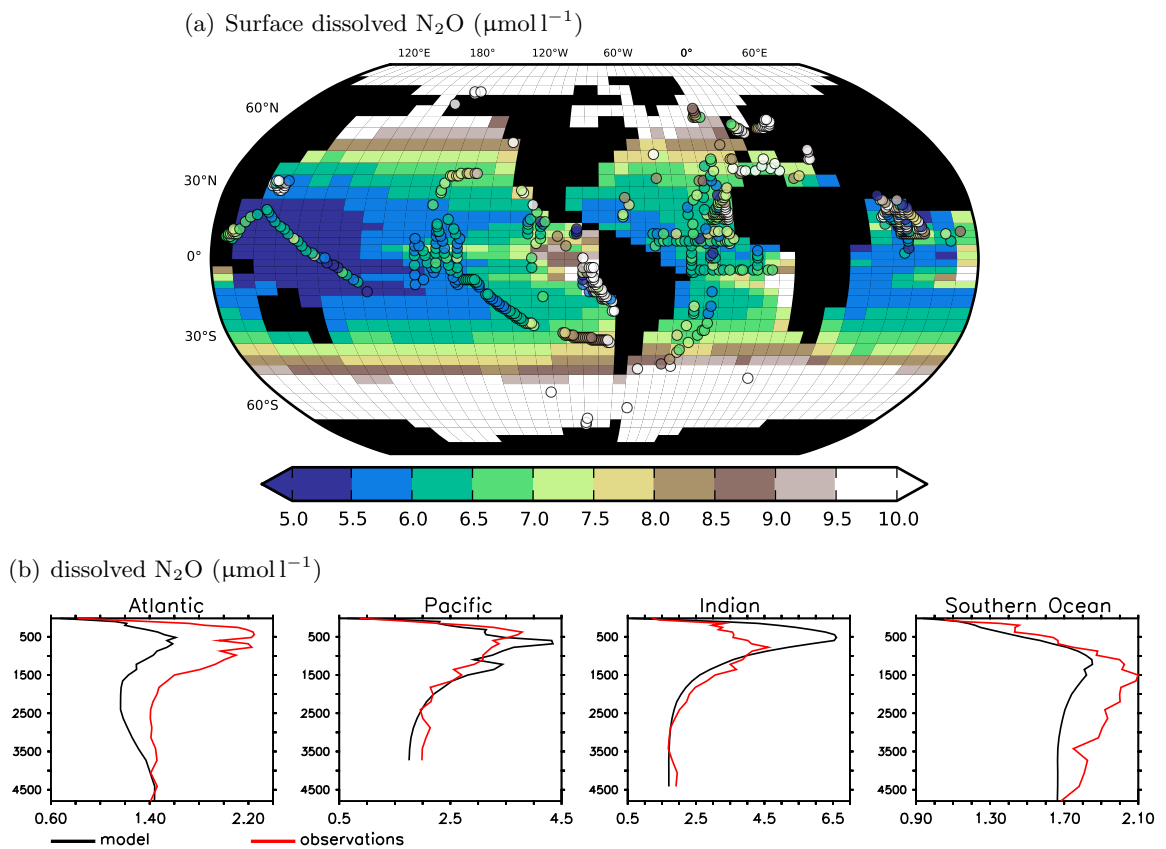
Figure 2.18: (a) Modeled surface and **(b)** vertical profiles of dissolved N$_2$O compared the data of the MEMENTO database (Bange et al., 2009).

Bibliography

Antonov, J. I., Seidov, D., Boyer, T. P., Locarnini, R. A., Mishonov, A. V., Garcia, H. E., Baranova, O. K., Zweng, M. M., & R., J. D., 2010. World Ocean Atlas 2009, Volume 2: Salinity, NOAA Atlas NESDIS 69, U.S. Government Printing Office, Washington, D.C.

Bange, H. W., Bell, T. G., Cornejo, M., Freing, A., Uher, G., Upstill-Goddard, R. C., & Zhang, G., 2009. MEMENTO: a proposal to develop a database of marine nitrous oxide and methane measurements, *Environ. Chem.*, 6(3), 195–197.

Bourquin, Y., 2013. *Modelling marine sources of the greenhouse gas nitrous oxide*, Master thesis, University of Bern.

Buesseler, K. O., Lamborg, C. H., Boyd, P. W., Lam, P. J., Trull, T. W., Bidigare, R. R., Bishop, J. K. B., Casciotti, K. L., Dehairs, F., Elskens, M., Honda, M., Karl, D. M., Siegel, D. A., Silver, M. W., Steinberg, D. K., Valdes, J., Van Mooy, B., & Wilson, S., 2007. Revisiting carbon flux through the ocean's twilight zone, *Science*, 316(5824), 567–570.

Canadell, J. G., Le Quere, C., Raupach, M. R., Field, C. B., Buitenhuis, E. T., Ciais, P., Conway, T. J., Gillett, N. P., Houghton, R. A., & Marland, G., 2007. Contributions to accelerating atmospheric CO_2 growth from economic activity, carbon intensity, and efficiency of natural sinks, *P. Natl. Acad. Sci. USA*, 104(47), 18866–18870.

Ciais, P., Sabine, C., Bala, G., Bopp, L., Brovkin, V., Canadell, J., A., C., DeFries, R., J., G., Heimann, M., Jones, C., Le Quéré, C., Myneni, R., S., P., & Thornton, P., 2013. Chapter 6: Carbon and Other Biogeochemical Cycles, in *Climate Change 2013: The Physical Science Basis. Working Group I Contribution to the Fifth Assessment Report of the Intergovernmental Panel on Climate Change*, Final Draft, 7. June 2013.

Colbourn, G., Ridgwell, A., & Lenton, T. M., 2013. The Rock Geochemical Model (RokGeM) v0.9, *Geosci. Model Dev.*, 6(5), 1543–1573.

Denman, K. L., Brasseur, G., Chidthaisong, A., Ciais, P., Cox, P. M., Dickinson, R. E., Hauglustaine, D., Heinze, C., Holland, E., Jacob, D., Lohmann, U., Ramachandran, S., da Silva Dias, P. L., Wofsy, S. C., & Zhang, X., 2007. Couplings between changes in the climate system and biogeochemistry, in *Climate Change 2007: The Physical Science Basis. Working Group I Contribution to the Fourth Assessment Report of the Intergovernmental Panel on Climate Change*, pp. 499–588, eds Solomon, S., Qin, D., Manning, M., Chen, Z., Marquis, M., Averyt, K. B., Tignor, M., & Miller, H. L., Cambridge University Press, Cambridge, United Kingdom and New York, NY, USA.

Doney, S. C., Lindsay, K., Fung, I., & John, J., 2006. Natural variability in a stable, 1000-yr global coupled climate–carbon cycle simulation, *J. Climate*, 19(13), 3033–3054.

Eby, M., Weaver, A. J., Alexander, K., Zickfeld, K., Abe-Ouchi, A., Cimatoribus, A. A., Crespin, E., Drijfhout, S. S., Edwards, N. R., Eliseev, A. V., Feulner, G., Fichefet, T., Forest, C. E., Goosse, H., Holden, P. B., Joos, F., Kawamiya, M., Kicklighter, D., Kienert, H., Matsumoto, K., Mokhov, I. I., Monier, E., Olsen, S. M., Pedersen, J. O. P., Perrette, M., Philippon-Berthier, G., Ridgwell, A., Schlosser, A., Schneider von Deimling, T., Shaffer, G., Smith, R. S., Spahni, R., Sokolov, A. P., Steinacher, M., Tachiiri, K., Tokos, K., Yoshimori, M., Zeng, N., & Zhao, F., 2013. Historical and idealized climate model experiments: an intercomparison of Earth system models of intermediate complexity, *Clim. Past*, 9(3), 1111–1140.

Edwards, N. R. & Marsh, R., 2005. Uncertainties due to transport-parameter sensitivity in an efficient 3-d ocean-climate model, *Clim. Dynam.*, 24(4), 415–433.

Farquhar, G. D., Caemmerer, S. V., & Berry, J. A., 1980. A biochemical-model of photosynthetic co_2 assimilation in leaves of C-3 species, *Planta*, 149(1), 78–90.

Feely, R., Sabine, C., Lee, K., Berelson, W., Kleypas, J., Fabry, V., & Millero, F., 2004. Impact of Anthropogenic CO_2 on the $CaCO_3$ System in the Oceans, *Science*, 305(5682), 362–366.

García, H. & Louis, G., 1992. Oxygen solubility in seawater: Better fitting equations, *Limnol. Oceanogr.*, 37, 1307–1312.

Garcia, H. E., Locarnini, R. A., Boyer, T. P., Antonov, J. I., Baranova, O. K., Zweng, M. M., , & Johnson, D. R., 2010a. World Ocean Atlas 2009, Volume 3: Dissolved Oxygen, Apparent Oxygen Utilization, and Oxygen Saturation, NOAA Atlas NESDIS 70, U.S. Government Printing Office, Washington, D.C.

Garcia, H. E., Locarnini, R. A., Boyer, T. P., Antonov, J. I., Zweng, M. M., Baranova, O. K., & R., J. D., 2010b. World Ocean Atlas 2009, Volume 4: Nutrients (phosphate, nitrate, silicate), NOAA Atlas NESDIS 71, U.S. Government Printing Office, Washington, D.C.

Gehlen, M., Bopp, L., Emprin, N., Aumont, O., Heinze, C., & Ragueneau, O., 2006. Reconciling surface ocean productivity, export fluxes and sediment composition in a global biogeochemical ocean model, *Biogeosciences*, 3(4), 521–537.

Gerber, M. & Joos, F., 2013. An Ensemble Kalman Filter multi-tracer assimilation: Determining uncertain ocean model parameters for improved climate-carbon cycle projections, *Ocean Model.*, 64, 29–45.

Gerber, S., Joos, F., Brugger, P., Stocker, T. F., Mann, M. E., Sitch, S., & Scholze, M., 2003. Constraining temperature variations over the last millennium by comparing simulated and observed atmospheric CO_2, *Clim. Dynam.*, 20(2–3), 281–299.

Gerten, D., Schaphoff, S., Haberlandt, U., Lucht, W., & Sitch, S., 2004. Terrestrial vegetation and water balance–hydrological evaluation of a dynamic global vegetation model, *J. Hydrol.*, 286(1–4), 249 – 270.

Godfrey, J., 1989. A Sverdrup Model of the Depth-Integrated Flow for the World Ocean allowing for Island Circulation, *Geophys. Astro. Fluid.*, 45(1-2), 89–112.

Goldstein, B., Joos, F., & Stocker, T. F., 2003. A modeling study of oceanic nitrous nitrous oxide during the Younger Dryas cold period, *Geophys. Res. Lett.*, 30(2), 1092.

Griffies, S. M., 1998. The Gent–McWilliams Skew Flux, *J. Phys. Oceanogr.*, 28(5), 831–841.

Heinze, C., Maier-Reimer, E., Winguth, A. M. E., & Archer, D., 1999. A global oceanic sediment model for long-term climate studies, *Global Biogeochem. Cy.*, 13(1), 221–250.

Ito, T. & Follows, M., 2005. Preformed phosphate, soft tissue pump and atmospheric CO_2, *J. Marine Res.*, 63(4), 813–839.

Jin, X., Gruber, N., Dunne, J. P., Sarmiento, J. L., & Armstrong, R. A., 2006. Diagnosing the contribution of phytoplankton functional groups to the production and export of particulate organic carbon, caco3, and opal from global nutrient and alkalinity distributions, *Global Biogeochem. Cy.*, 20(2), n/a–n/a.

Joos, F., Prentice, I. C., Sitch, S., Meyer, R., Hooss, G., Plattner, G.-K., Gerber, S., & Hasselmann, K., 2001. Global warming feedbacks on terrestrial carbon uptake under the Intergovernmental Panel on Climate Change (IPCC) emission scenarios, *Global Biogeochem. Cy.*, 15(4), 891–907.

Joos, F., Gerber, S., Prentice, I. C., Otto-Bliesner, B. L., & Valdes, P. J., 2004. Transient simulations of Holocene atmospheric carbon dioxide and terrestrial carbon since the Last Glacial Maximum, *Global Biogeochem. Cy.*, 18(GB2002).

Kalnay, E., Kanamitsu, M., Kistler, R., Collins, W., Deaven, D., Gandin, L., Iredell, M., Saha, S., White, G., Woollen, J., Zhu, Y., Chelliah, M., Ebisuzaki, W., Higgins, W., Janowiak, J., Mo, K., Ropelewski, C., Wang, J., Leetmaa, A., Reynolds, R., Jenne, R., & Joseph, D., 1996. The NCEP/NCAR 40-year reanalysis project, *B. Am. Meteorol. Soc.*, 77(3), 437–471.

Key, R. M., Kozyr, A., Sabine, C. L., Lee, K., Wanninkhof, R., Bullister, J. L., Feely, R. A., Millero, F. J., Mordy, C., & Peng, T.-H., 2004. A global ocean carbon climatology: Results from Global Data Analysis Project (GLODAP), *Global Biogeochem. Cy.*, 18(4), GB4031.

Krakauer, N. Y., Randerson, J. T., Primeau, F. W., Gruber, N., & Menemenlis, D., 2006. Carbon isotope evidence for the latitudinal distribution and wind speed dependence of the air-sea gas transfer velocity, *Tellus B*, 58(5), 390–417, 7th International Carbon Dioxide Conference (CO_2), Boulder, CO, SEP 25-30, 2005.

Lam, P. J., Doney, S. C., & Bishop, J. K. B., 2011. The dynamic ocean biological pump: Insights from a global compilation of particulate organic carbon, $CaCO_3$, and opal concentration profiles from the mesopelagic, *Global Biogeochem. Cy.*, 25(3), GB3009.

Locarnini, R. A., Mishonov, A. V., Antonov, J. I., Boyer, T. P., Garcia, H. E., Baranova, O. K. Zweng, M. M., & Johnson, D. R., 2010. World Ocean Atlas 2009, Volume 1: Temperature, NOAA Atlas NESDIS 68, U.S. Government Printing Office, Washington, D.C.

Luo, C., Mahowald, N. M., & del Corral, J., 2003. Sensitivity study of meteorological parameters on mineral aerosol mobilization, transport, and distribution, *J. Geophys. Res.*, 108(D15), 4447.

Mahowald, N. M., Muhs, D. R., Levis, S., Rasch, P. J., Yoshioka, M., Zender, C. S., & Luo, C., 2006. Change in atmospheric mineral aerosols in response to climate: Last glacial period, preindustrial, modern, and doubled carbon dioxide climates, *J. Geophys. Res.*, 111, D10202.

Martin, J. H., Knauer, G. A., Karl, D. M., & Broenkow, W., 1987. VERTEX: Carbon cycling in the northeast Pacific.

Martiny, A. C., Pham, C. T. A., Primeau, F. W., Vrugt, J. A., Moore, J. K., Levin, S. A., & Lomas, M. W., 2013. Strong latitudinal patterns in the elemental ratios of marine plankton and organic matter, *Nature Geosci.*, 6(4), 279–283.

Milliman, J. & Droxler, A., 1996. Neritic and pelagic carbonate sedimentation in the marine environment: Ignorance is not bliss, *Geologische Rundschau*, 85(3), 496–504.

Moore, J., Doney, S. C., Glover, D. M., & Fung, I. Y., 2001. Iron cycling and nutrient-limitation patterns in surface waters of the world ocean, *Deep-Sea Res. Pt. 2*, 49(1–3), 463 – 507.

Müller, S., 2007. *Large-scale ocean circulation, air-sea gas exchange, and carbon isotopes in a three-dimensional, computationally efficient ocean model*, PhD thesis, University of Bern.

Müller, S. A., Joos, F., Edwards, N. R., & Stocker, T. F., 2006. Water mass distribution and ventilation time scales in a cost-efficient, three-dimensional ocean model, *J. Climate*, 19(21), 5479–5499.

Müller, S. A., Joos, F., Edwards, N. R., & Stocker, T. F., 2008. Modeled natural and excess radiocarbon: Sensitivities to the gas exchange formulation and ocean transport strength, *Global Biogeochem. Cy.*, 22(GB3011), 14 pp.

Myhre, G., Highwood, E. J., Shine, K. P., & Stordal, F., 1998. New estimates of radiative forcing due to well mixed greenhouse gases, *Geophys. Res. Lett.*, 25(14), 2715–2718.

Naegler, T. & Levin, I., 2006. Closing the global radiocarbon budget 1945-2005, *J. Geophys. Res.-Atmos.*, 111(D12).

Najjar, R. G., Orr, J., Sabine, C. L., & Joos, F., 1999. Biotic-HOWTO. Internal OCMIP Report, Tech. rep., LSCE/CEA Saclay, Gif-sur-Yvette, France.

Orr, J. & Najjar, R. G., 1999. Abiotic-HOWTO. Internal OCMIP Report, Tech. rep., LSCE/CEA Saclay, Gif-sur-Yvette, France.

Otto, J., Raddatz, T., & Claussen, M., 2011. Strength of forest-albedo feedback in mid-holocene climate simulations, *Clim. Past Discuss.*, 7, 809–840.

Parekh, P., 2006. Bern 3D model: Addition of a prognostic formulation of new production and iron chemistry, Tech. rep., Climate and Environmental Physics, Physics Institute, University of Bern.

Parekh, P., Joos, F., & Müller, S. A., 2008. A modeling assessment of the interplay between aeolian iron fluxes and iron-binding ligands in controlling carbon dioxide fluctuations during Antarctic warm events, *Paleoceanography*, 23, PA4202.

Peltier, W. R., 1994. Ice age paleotopography, *Science*, 265, 195–201.

Peltier, W. R., 2004. Global Glacial Isostasy and the Surface of the Ice-Age Earth: The ICE-5G (VM2) Model and GRACE, *Ann. Rev. Earth and Planet. Sci.*, 32, 111–149.

RCP database, 2009. RCP database, version 2.0.5, Website, Available from http://www.iiasa.ac.at/web-apps/tnt/RcpDb/ accessed 27/10/2011.

Reimer, P. J., Baillie, M. G. L., Bard, E., Bayliss, A., Beck, J. W., Blackwell, P. G., Ramsey, C. B., Buck, C. E., Burr, G. S., Edwards, R. L., Friedrich, M., Grootes, P. M., Guilderson, T. P., Hajdas, I., Heaton, T. J., Hogg, A. G., Hughen, K. A., Kaiser, K. F., Kromer, B., McCormac, F. G., Manning, S. W., Reimer, R. W., Richards, D. A., Southon, J. R., Talamo, S., Turney, C. S. M., van der Plicht, J., & Weyhenmeye, C. E., 2009. IntCal09 and Marine09 radiocarbon age calibration curves, 0–50,000 years cal BP, *Radiocarbon*, 51(4), 1111–1150.

Rempfer, J., Stocker, T. F., Joos, F., Dutay, J.-C., & Siddall, M., 2011. Modelling Nd-isotopes with a coarse resolution ocean circulation model: Sensitivities to model parameters and source/sink distributions, *Geochim. Cosmochim. Ac.*, 75, 5927–5950.

Ritz, S., 2013. The Bern3D Coupled Ocean–Atmosphere Climate Model: Documentation of the Physical Core, Tech. rep., Climate and Environmental Physics, Physics Institute, University of Bern.

Ritz, S. P., Stocker, T. F., & Joos, F., 2011a. A coupled dynamical ocean-energy balance atmosphere model for paleoclimate studies, *J. Climate*, 24(2), 349–75.

Ritz, S. P., Stocker, T. F., & Severinghaus, J. P., 2011b. Noble gases as proxies of mean ocean temperature: sensitivity studies using a climate model of reduced complexity, *Quaternary Sci. Rev.*, 30(25-26), 3728–3741.

Roth, R. & Joos, F., 2013. A reconstruction of radiocarbon production and total solar irradiance from the Holocene ^{14}C and CO_2 records: implications of data and model uncertainties, *Clim. Past*, 9(4), 1879–1909.

Sarmiento, J. L. & Gruber, N., 2006. *Ocean biogeochemical dynamics*, Princeton University Press.

Schlitzer, R., 2004. Export Production in the Equatorial and North Pacific Derived from Dissolved Oxygen, Nutrient and Carbon Data, *J. Oceanograph.*, 60, 53–62.

Schmittner, A., Gruber, N., Mix, A. C., Key, R. M., Tagliabue, A., & Westberry, T. K., 2013. Biology and air–sea gas exchange controls on the distribution of carbon isotope ratios (δ^{13}C) in the ocean, *Biogeosciences*, 10(9), 5793–5816.

Scholze, M., Kaplan, J. O., Knorr, W., & Heimann, M., 2003. Climate and interannual variability of the atmosphere-biosphere $^{13}CO_2$ flux, *Geophys. Res. Lett.*, 30(2).

Siegenthaler, U. & Oeschger, H., 1987. Biospheric CO_2 emissions during the past 200 years reconstructed by deconvolution of ice core data, *Tellus B*, 39B(1–2), 140–154.

Sitch, S., Smith, B., Prentice, I., Arneth, A., Bondeau, A., Cramer, W., Kaplan, J., Levis, S., Lucht, W., Sykes, M., Thonicke, K., & Venevsky, S., 2003. Evaluation of ecosystem dynamics, plant geography and terrestrial carbon cycling in the LPJ dynamic global vegetation model, *Glob. Change Biol.*, 9(2), 161–185.

Spahni, R., Joos, F., Stocker, B. D., Steinacher, M., & Yu, Z. C., 2013. Transient simulations of the carbon and nitrogen dynamics in northern peatlands: from the Last Glacial Maximum to the 21st century, *Clim. Past*, 9, 1287–1308.

Steinacher, M., 2011. *Modeling changes in the global carbon cycle-climate system*, PhD thesis, University of Bern.

Steinacher, M., Joos, F., & Stocker, T. F., 2013. Allowable carbon emissions lowered by multiple climate targets, *Nature*, 499, 197–201.

Steiner, N. S., Lee, W. G., & Christian, J. R., 2013. Enhanced gas fluxes in small sea ice leads and cracks: Effects on CO_2 exchange and ocean acidification, *J. Geophys. Res.-Oceans*, 118(3), 1195–1205.

Stocker, B. D., Strassmann, K., & Joos, F., 2011. Sensitivity of Holocene atmospheric CO_2 and the modern carbon budget to early human land use: analyses with a process-based model, *Biogeosciences*, 8(1), 69–88.

Stocker, B. D., Roth, R., Joos, F., Spahni, R., Steinacher, M., Zaehle, S., Bouwman, L., Xu-Ri, & Prentice, I. C., 2013. Multiple greenhouse-gas feedbacks from the land biosphere under future climate change scenarios, *Nature Clim. Change*, 3(7), 666–672.

Strassmann, K. M., Joos, F., & Fischer, G., 2008. Simulating effects of land use changes on carbon fluxes: past contributions to atmospheric CO_2 increases and future commitments due to losses of terrestrial sink capacity, *Tellus B*, 60(4), 583–603.

Sweeney, C., Gloor, E., Jacobson, A. R., Key, R. M., McKinley, G., Sarmiento, J. L., & Wanninkhof, R., 2007. Constraining global air-sea gas exchange for CO_2 with recent bomb ^{14}C measurements, *Global Biogeochem. Cy.*, 21(2).

Tagliabue, A., Bopp, L., Roche, D. M., Bouttes, N., Dutay, J.-C., Alkama, R., Kageyama, M., Michel, E., & Paillard, D., 2009. Quantifying the roles of ocean circulation and biogeochemistry in governing ocean carbon-13 and atmospheric carbon dioxide at the last glacial maximum, *Clim. Past*, 5(4), 695–706.

Thompson, S. L. & Warren, S. G., 1982. Parameterization of outgoing infrared radiation derived from detailed radiative calculations, *J. Atmos. Sci.*, 39(12), 2667–2680.

Tréguer, P., Nelson, D. M., Van Bennekom, A. J., DeMaster, D. J., Leynaert, A., & Quéguiner, B., 1995. The Silica Balance in the World Ocean: A Reestimate, *Science*, 268(5209), 375–379.

Tschumi, T., 2007. Prognostic formulation for calcite- and opal-production in the Bern3D-model, Tech. rep., Climate and Environmental Physics, Physics Institute, University of Bern.

Tschumi, T., 2009. *Modeling the Ocean's Contribution to Past and Future Changes in Global Carbon Cycling*, PhD thesis, University of Bern.

Tschumi, T., Joos, F., Gehlen, M., & Heinze, C., 2011. Deep ocean ventilation, carbon isotopes, marine sedimentation and the deglacial CO_2 rise, *Clim. Past*, 7(3), 771–800.

Uppala, S. M., Kallberg, P. W., Simmons, A. J., Andrae, U., Bechtold, V. D. C., Fiorino, M., Gibson, J. K., Haseler, J., Hernandez, A., Kelly, G. A., Li, X., Onogi, K., Saarinen, S., Sokka, N., Allan, R. P., Andersson, E., Arpe, K., Balmaseda, M. A., Beljaars, A. C. M., Berg, L. V. D., Bidlot, J., Bormann, N., Caires, S., Chevallier, F., Dethof, A., Dragosavac, M., Fisher, M., Fuentes, M., Hagemann, S., Holm, E., Hoskins, B. J., Isaksen, L., Janssen, P. A. E. M., Jenne, R., Mcnally, A. P., Mahfouf, J.-F., Morcrette, J.-J., Rayner, N. A., Saunders, R. W., Simon, P., Sterl, A., Trenberth, K. E., Untch, A., Vasiljevic, D., Viterbo, P., & Woollen, J., 2005. The era–40 re-analysis, *Q.J.R. Meteorol. Soc.*, 131(612), 2961–3012.

Wania, R., Ross, I., & Prentice, I. C., 2009. Integrating peatlands and permafrost into a dynamic global vegetation model: 1. evaluation and sensitivity of physical land surface processes, *Global Biogeochem. Cy.*, 23(3), GB3014–.

Wanninkhof, R., 1992. Relationship between wind–speed and gas–exchange over the ocean, *J. Geophys. Res.-Oceans*, 97(C5), 7373–7382.

Weaver, A. J., Eby, M., Wiebe, E. C., Bitz, C. M., Duffy, P. B., Ewen, T. L., Fanning, A. F., Holland, M. M., MacFadyen, A., Wang, H. X., & Yoshimori, M., 2001. The UVic Earth System Climate Model: Model description, climatology, and applications to past, present and future climates, *Atmos. Ocean*, 39(4), 361–428.

Xu-Ri & Prentice, I. C., 2008. Terrestrial nitrogen cycle simulation with a dynamic global vegetation model, *Glob. Change Biol.*, 14(8), 1745–1764.

Zürcher, S., Spahni, R., Joos, F., Steinacher, M., & Fischer, H., 2013. Impact of an abrupt cooling event on interglacial methane emissions in northern peatlands, *Biogeosciences*, 10(3), 1963–1981.

Chapter 3

Glacial-interglacial CO_2 changes

3.1 Model limits on the role of volcanic carbon emissions in regulating glacial-interglacial CO_2 variations

Raphael Roth and Fortunat Joos

Model limits on the role of volcanic carbon emissions in regulating glacial–interglacial CO$_2$ variations

Raphael Roth *, Fortunat Joos

Climate and Environmental Physics, Physics Institute, University of Bern, Bern, Switzerland
Oeschger Centre for Climate Change Research, University of Bern, Bern, Switzerland

ARTICLE INFO

ABSTRACT

Huybers and Langmuir (2009) proposed that an increase in volcanic activity provoked by ice sheet melting contributed substantially to the deglacial CO$_2$ increase. Here, their hypothesis is evaluated by prescribing their central, high, and low volcanic CO$_2$ emission scenarios in the Bern3D carbon cycle-climate model as a perturbation. Reconstructed emissions increase mainly between 15 and 11 ka BP, remain high in the early Holocene and drop after 7 ka BP in all scenarios with total emissions between 181 and 2011 GtC. Simulated increase of atmospheric CO$_2$ peaks around 6 ka BP at 46 ppm for the central scenario and with a range between 13 and 142 ppm. Modeled carbonate ion concentration in the deep ocean decreases and the calcite saturation horizon shoals on global average by 440 m (150 to 1500 m). Simulated changes in δ^{13}C and Δ^{14}C isotopic signatures are small compared to reconstructed, proxy-based changes over the deglacial period. The comparison of our model results and available proxy evidence suggests a small role for volcanic carbon emissions in regulating glacial–interglacial CO$_2$ variations, but uncertainties prevent a firm conclusion. A problem with the volcanic emission hypothesis is in the timing of emissions which peak in the early Holocene, a period of decreasing atmospheric CO$_2$.

1. Introduction

Many hypotheses (see e.g., Jansen et al. (2007); Köhler et al. (2005)) have been proposed to explain the variations in atmospheric CO$_2$ concentration of order 100 ppm (parts per million) between glacial and interglacial climate states (Lüthi et al., 2008; Monnin et al., 2004; Petit et al., 1999). Typically, changes in the marine carbon cycle and related ocean–sediment interactions are invoked to explain the CO$_2$ increase from the Last Glacial Maximum (LGM) to the current warm period. In contrast to this view, Huybers and Langmuir (2009) suggest that an increase in global volcanic activity caused by deglacial ice sheet removal and related changes in pressure could be a major driver for the reconstructed deglacial CO$_2$ increase.

The goal of this study is to investigate the plausibility of the volcanic CO$_2$ release hypothesis by Huybers and Langmuir (2009) in the context of available proxy evidence. Specifically, we prescribe their central, low, and high deglacial CO$_2$ emission scenarios in the Bern3D Earth System Model of Intermediate Complexity and analyze simulated changes in atmospheric CO$_2$ and its ^{13}C and ^{14}C isotopic signatures as well as the spatio-temporal evolution of carbonate ion concentration, alkalinity, and δ^{13}C and Δ^{14}C of dissolved inorganic carbon in the deep ocean. Results are compared to proxy data.

The conventional hypotheses to explain glacial–interglacial CO$_2$ variations rely on marine mechanisms and suggest a repartitioning of carbon between the atmosphere, the ocean and ocean sediments, and vegetation and soils. The ocean stores much more carbon than vegetation and soils on land and is by far the largest of the three relatively fast (<1000 years) exchanging carbon reservoirs (atmosphere–ocean–land biosphere). Carbon storage on land is thought to have increased by several hundreds of gigatons of carbon (GtC) from Last Glacial Maximum (LGM) to the current warm period and can thus not explain the LGM to Holocene CO$_2$ increase. A broad range of proxies, including for example the stable carbon isotope ^{13}C signature of atmospheric CO$_2$ (Elsig et al., 2009; Lourantou et al., 2010), the ^{13}C and radiocarbon (^{14}C) signature of dissolved inorganic carbon (e.g. Duplessy et al., 1988; Oliver et al., 2010; Robinson et al., 2005; Sarnthein et al., 1994), or the carbonate ion concentration in the deep ocean (Yu et al., 2010), indicates large scale changes in ocean circulation, temperature, water mass distribution, and ocean biogeochemistry over glacial–interglacial cycles. However, no consensus has yet emerged on the explanation of the coeval CO$_2$ changes. The challenge remains to quantify the contribution of identified physical and biogeochemical mechanisms to the CO$_2$ transient consistent with available proxy information.

Despite the importance of volcanic outgassing of CO$_2$ on the carbon cycle on geological timescales and early suggestions on their role in regulating glacial–interglacial climate variations (Arrhenius, 1896), changes in global volcanic activity were until recently not considered to explain CO$_2$ variations on the multi-millennial timescales of glacial–

* Corresponding author.
  E-mail address: roth@climate.unibe.ch (R. Roth).

interglacial (G/IG) cycles. Several studies addressed changes in local volcanic activity. Tephra-measurements in Antarctica (Narcisi et al. (2010) and references therein) for example reveal past variations in volcanic activity from nearby Antarctic regions. For Iceland, Maclennan et al. (2002) found a pronounced peak in volcanic activity around ~12 kyr ago, exceeding modern rates by a factor of 100. Also for France and Germany, such a relationship could be shown (Nowell et al., 2006). Difficulties for the extrapolation of local records to the globe are the spatio-temporal variability of volcanic activity and, more important, that the quality of the records decreases when going back in time. The available data on volcanic eruptions show a marked observational bias with 80% of the dated eruptions occurring in the last 1000 years (e.g. Fig. 1 in Huybers and Langmuir (2009)). A further step adding additional uncertainty is to estimate CO$_2$ emissions from estimated volcanic activity. These issues are thoroughly discussed by Huybers and Langmuir (2009).

Huybers and Langmuir (2009) in their stimulating study estimate the global flux-variation of subaerial volcanic carbon over the last 40 kyr by evaluating historical eruption data-sets covering more than 5000 individual volcanic events. Eruption frequencies in regions which are subject to deglacial processes such as ice sheet retreat (especially in the northern hemisphere) are compared to those of regions presumably free of deglacial influences in an attempt to remove observational biases. A considerable increase in volcanic activity of two to six times above background level between 12 kyr and 7 kyr is identified and linearly translated into a corresponding increase in CO$_2$ flux. Using a box model approach, these authors estimate an increase in atmospheric CO$_2$ of 60 ppm during the second half of the last deglaciation due to volcanism alone (uncertainty range: 25–130 ppm).

The reason for the strong increase in volcanic activity is thought to have emerged from the retreat of the northern hemisphere ice sheet provoking magma production due to depressurization (Sigmundsson et al., 2010). If the proposed volcanic emission peak during deglaciations is real, volcanism would mediate a positive feedback between increasing atmospheric CO$_2$, warming, and ice sheet melting. This volcanic deglacial CO$_2$ scenario is different from the hypotheses that propose a repartitioning of carbon between the atmosphere, ocean, and land biosphere to explain the glacial-to-interglacial CO$_2$ increase. It involves the net addition of carbon to the atmosphere–ocean–land biosphere system from the earth's upper mantle, a pool that is currently exchanging only little carbon with these other reservoirs.

2. Method

2.1. Model description

Simulations were performed with the Bern3D Earth System Model of Intermediate Complexity (EMIC). The ocean component is a three-dimensional frictional-geostrophic balance ocean model based on Edwards et al. (1998) and further described in Müller et al. (2006). It is run with a horizontal resolution of 36×36 grid boxes, with 32 logarithmically spaced layers, and with a time-step of 48^{-1} yr. Here, the Bering Strait is open and there is a flow of 21 Sv $\left(1 \, Sv = 10^6 m^3 s^{-1}\right)$ through the Indonesian Passage from the Pacific to the Indian Ocean.

The 2D energy balance model of the atmosphere, described in detail in Ritz et al. (2011), has the same horizontal resolution as the ocean. Zonal uniform diffusivities are applied to simulate horizontal heat and water fluxes. The model distinguishes between shortwave and longwave fluxes between atmosphere–ocean, atmosphere–sea ice and atmosphere–land boundaries. Atmospheric trace gases are considered to be well mixed. The equilibrium climate sensitivity has been tuned toward 3 °C for a doubling of atmospheric CO$_2$.

The biogeochemical (BGC) component consists of a prognostic representation of the marine carbon cycle, partly following the OCMIP-II protocol (Najjar et al., 1999; Orr and Najjar, 1999), but with prognostic formulations for export production of organic carbon and featuring competition between calcite and opal-producer according to Maier-Reimer

(1993) with Michaelis–Menten formulation of the limiting production terms (Tschumi et al., 2008). A prognostic iron-cycle is included in the model as described in Parekh et al. (2008). In total 14 oceanic tracers are transported.

A 10-layer sediment-diagenesis model (Gehlen et al., 2006; Heinze et al., 1999) is coupled to the ocean as described in detail by Tschumi et al. (2011). It dynamically calculates bioturbation, oxidation, denitrification, dissolution and pore-water diffusion. Modeled solid components which are subject to sediment burial are opal, particulate organic matter (POM), calcite and clay.

We do not model weathering of silicate and carbonate rocks explicitly and assume that weathering of carbonate and silicate rocks remained constant over the past 20,000 years. This assumption appears justified given the large uncertainties and conflicting suggestions on glacial–interglacial changes in weathering (e.g., Munhoven, 2002; Vance et al., 2009) and, more important, by the small potential of weathering to affect atmospheric CO$_2$ and isotopes on the millennial time scales considered in this study. Technically, the weathering-burial cycle is treated in the following way. Carbon and ^{13}C, alkalinity (Alk) and nutrients are lost from the model system by the burial flux of calcium carbonate, opal, and organic matter leaving reactive sediments and entering the lithosphere. This loss is balanced by a corresponding riverine input flux assumed to result from the weathering of silicate and carbonate rocks during model spin-up. The steady-state weathering input flux, diagnosed at the end of the spin-up, is 0.401 GtC yr^{-1} and has an isotopic ^{13}C signature of $-8.5‰$ and a carbon to alkalinity molar ratio close to 1. This flux is kept constant throughout the simulation.

A simple 4-box representation of the terrestrial biosphere according to Siegenthaler and Oeschger (1987) is coupled to the atmosphere. A stimulation of net primary productivity (NPP) by elevated CO$_2$ is parameterized using a logarithmic dependency of NPP on atmospheric CO$_2$ $(NPP(CO_2)) = NPP(CO_{2,0} \times (1 + \beta \times \ln(CO_2/CO_{2,0})))$. Soil and litter turnover rates, k, are taken to vary with global mean surface air temperature, T according to $k(T) = k_{10} \times Q_{10}^{(T - 10°C)/10°C}$. The response to changing atmospheric CO$_2$ and temperature has been tuned toward the Lund-Potsdam-Jena dynamic global vegetation model (DGVM) (Sitch et al., 2003). The fertilization factor β is set to 0.3, NPP is 60 GtC yr^{-1}, $CO_{2,0}$ concentration is 278 ppm, and Q_{10} is 1.3. Carbon isotopes ^{14}C and ^{13}C are represented in all model components (Tschumi et al., 2011).

For the simulation presented here, we use a perturbation approach. The realistic simulation of the transient deglacial CO$_2$ evolution is beyond the scope of this study. The model is spun up following a similar procedure as described in Tschumi et al. (2011). A relatively well-constrained and documented preindustrial initial state (with 278 ppm atmospheric CO$_2$) is obtained which is then perturbed with the volcanic forcing. The choice of a preindustrial state as a starting point for our volcanic perturbation experiments seems justified as most of the applied volcanic CO$_2$ is released during the late termination and the Holocene, a period where atmospheric CO$_2$ is generally well above ~240 ppm and closer to late Holocene than Last Glacial Maximum concentrations. Using an initial steady state with boundary conditions typically for the Last Glacial Maximum would probably lead to a higher oceanic carbon uptake than the preindustrial steady state as the Revelle factor is lower under lower CO$_2$ (higher buffering capacity).

The remaining drift in a 40 kyr control simulation is 95×10^{-3} ppm kyr^{-1} for CO$_2$, $2.0 \times 10^{-4}‰$ kyr^{-1} for δ^{13}C and $2.3 \times 10^{-2}‰$ kyr^{-1} for Δ^{14}C. All results presented are corrected for this slight drift.

Model performance is discussed for a range of water mass, biogeochemical, and ventilation tracers in earlier publications for the ocean only model (Müller et al., 2006; Parekh et al., 2008; Tschumi et al., 2008, 2011) and for the coupled ocean-EBM model (Ritz et al., 2011). Marine biogeochemical properties and tracer distributions are similar for the ocean only and the coupled model. Here, we present in addition a comparison between the simulated and data-based distribution of carbonate ion concentrations (Fig. 1); concentrations are expressed as deviations from the saturation concentration relative to calcite, ΔCO_3^{2-}.
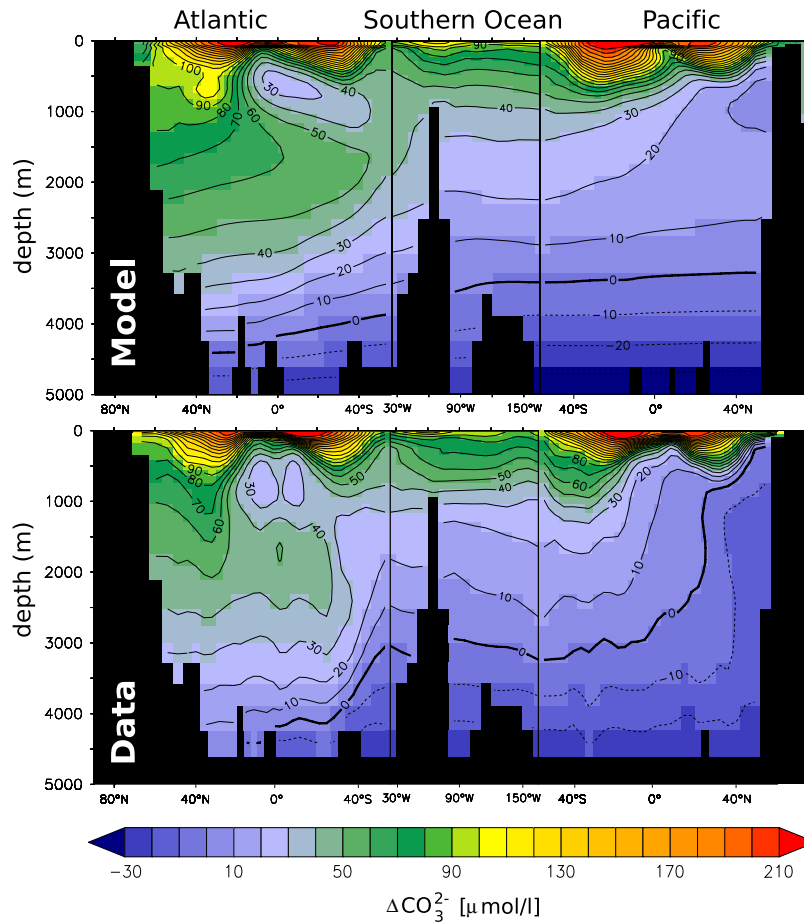
Fig. 1. Modern distribution of the carbonate ion concentration relative to the saturation concentration with respect to calcite, ΔCO_3^{2-}, along a transect through the Atlantic, Southern Ocean and Pacific. The upper panel shows the model steady-state for preindustrial conditions, while the lower panel shows preindustrial values derived from the GLODAP/WOCE data.

The model is able to represent the large-scale gradients in ΔCO_3^{2-}, major water masses, and the calcite saturation horizon ($\Delta CO_3^{2-} = 0$) which separates water masses that are over- and undersaturated with respect to calcite. A major data-model misfit is in the North Pacific where the model overestimates ΔCO_3^{2-} and where the simulated saturation horizon is much deeper than observed. This is linked to modeled low surface productivity and organic matter export in the North Pacific and correspondingly low nutrient and high ΔCO_3^{2-} concentrations at depth.

2.2. Experimental setup

The release of CO$_2$ and ^{13}C by volcanoes is prescribed as input into the atmosphere.

Following the procedure described in Huybers and Langmuir (2009) 10,000 realizations of volcanic activity (relative to modern) histories are randomly computed. Upper and lower estimates are derived from these timeseries by requiring that 90% of the data points for each time-interval (2 kyr) fall within the upper and lower estimates. The mean-activity scenario is defined as the average over all realizations (Fig. 2A). Now these 3 timeseries are multiplied with the best estimate (34.1 MtC yr^{-1}) for the modern subaerial CO$_2$ flux (dark gray range in Fig. 2B) and their high and low estimates with a

high (40.9 MtC yr^{-1}) and low (27.3 MtC yr^{-1}) estimate for the modern subaerial volcanic flux (light gray shading in Fig. 2B). The applied range of modern volcanic CO$_2$ fluxes of 34.1 $\pm$ 6.8 MtC yr^{-1} corresponds to 125 $\pm$ 25 MtCO$_2$, as proposed by Huybers and Langmuir (2009). A possible, but likely small reduction in submarine carbon fluxes from volcanism in response to rising sea level is not taken into account.

In total, 181, 226, 717, 1695, and 2011 GtC are released in these five scenarios between 40 and 0 ka BP in the Bern3D model. For the period 20–0 ka BP, for which results are discussed in this study, the emissions are 249, 312, 721, 1558 and 1870 GtC. We note that the use of these five scenarios in the Bern3D is a simplification compared to a full Monte Carlo approach with 10,000 individual emissions histories. The upper and lower bound scenarios constrain the emissions consistent with the approach of Huybers and Langmuir (2009) for any given time interval and therefore to some extent also the CO$_2$ change within this time interval. This approach seems justified as the upper, lower and central CO$_2$ evolution shown by Huybers and Langmuir (2009) and obtained from 10,000 simulations are close to our results.

The stable isotopic signature of volcanic emissions is uncertain. It depends on the relative mixing ratio of different magma types such as MORB-type basalts, marine limestone and organic sediments and
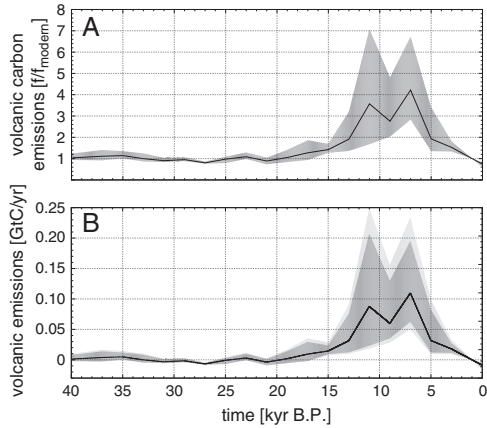
Fig. 2. A) Estimated temporal variation of the relative (to modern) volcanic CO$_2$ outgassing over the last 40 kyr by Huybers and Langmuir (2009). B) Volcanic CO$_2$ emission anomalies relative to present. Lower, upper and central estimates of relative emissions, shown in panel a, are combined with low (27.3 MtC yr^{-1}), central (34.1 MtC yr^{-1}), and high (40.9 MtC yr^{-1}) estimates of contemporary volcanic CO$_2$ emissions to yield five scenarios corresponding to the envelopes of the dark and light gray shaded areas and the solid line, respectively. Total emissions are 181, 226, 717, 1695, and 2011 GtC for the five scenarios.

measured isotopic signals vary considerably between different sources. For examples, Sano and Marty (1995) found the range of δ^{13}C signatures of tropical volcanoes to be -4.4 ± 2.2‰, while in a more recent compilation studied by Deines (2002), corresponding δ^{13}C values scatter around -5‰. No explicit measurements for volcanoes in high latitudes are available to us. To take into account this uncertainty in volcanic δ^{13}C, we apply an isotopic signature of the volcanic CO$_2$ flux of -2.0‰, -5.0‰ or -8.0‰ together with each of the five carbon emission scenarios. Volcanic emissions are free of radiocarbon as the mean life time of 8267 yr is short compared to the residence time of carbon in the lithosphere.

Explosive volcanic eruptions have an effect of a net cooling of the lower atmosphere for the duration of a few years to decades. This cooling is due to sulfur emissions and formation of sulfate aerosols in the stratosphere. The cooling and related climate changes causes a, likely small, positive carbon cycle-climate feedback by a reduction in atmospheric CO$_2$ forcing (Frölicher et al., 2011) and a redistribution of carbon between the land biosphere, the ocean and the atmosphere. However, sulfate aerosols are largely removed from the stratosphere within years, but the CO$_2$ transferred from the lithosphere to the atmosphere alters atmospheric CO$_2$ and its radiative forcing over many millennia. Here, we account for the radiative forcing by this additional CO$_2$, but do neglect radiative forcing by sulfate aerosols. We also neglect the potential influence of volcanic induced iron input on marine biogeochemical cycles and related feedbacks. All other boundary conditions, including the weathering fluxes, are kept at preindustrial conditions.

3. Results

Modeled atmospheric CO$_2$ increases over the glacial termination (18 to 11 ka BP) and the early Holocene to reach a peak value around 6 ka BP (Fig. 3A). Thereafter, CO$_2$ decreases slowly due to the strong decrease in emissions and the multi-millennial response time of ocean carbonate sediment compensation. The mid-Holocene peak anomaly is 46 ppm for the central scenario and the range is 13 to 142 ppm for the five volcanic carbon emission scenarios. Slightly lower changes are found when climate was kept constant in the simulations. The airborne fraction is 12% at the end of the simulations. These low airborne fractions reflect the millennial time scale of the
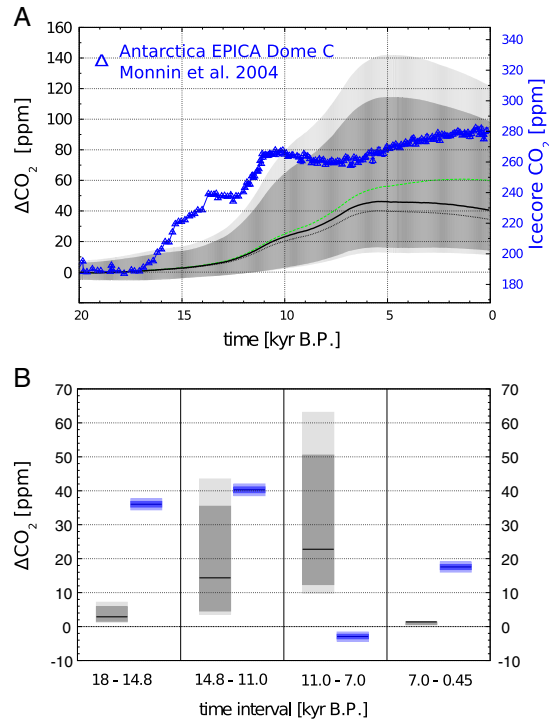

Fig. 3. A) Simulated changes in atmospheric CO$_2$ for the past 20 kyr in response to prescribed volcanic CO$_2$ outgassing for the five scenarios shown in Fig. 2B (shaded areas and solid line). In addition, changes are also given for a simulations without the ocean sediment module (dashed green), and a simulation without climate change (dotted line; radiative forcing by CO$_2$ set to zero). The ice core CO$_2$ record from Dome C, Antarctica (Monnin et al., 2004) is shown by blue symbols. B) Atmospheric CO$_2$ changes for 4 key time intervals. Gray: modeled volcanic contribution, blue: ice core data (Monnin et al., 2004) with blue shading indicating one standard deviation and two standard deviations.

volcanic emissions permitting that most of the volcanic emissions are removed from the atmosphere by the ocean and ocean–sediment interactions. The simulated CO$_2$ changes are substantial compared to the magnitude of the reconstructed increase of 100 ppm from the LGM to the late Holocene.

Simulated atmospheric CO$_2$ changes would be larger without ocean–sediment interactions. The atmospheric CO$_2$ increase by the end of the simulation is 60 ppm in a run without the sediment module compared to 40 ppm simulated in the standard setup and for the central scenario. The influence of sediment–ocean interaction emerges in the early Holocene and becomes particularly large during the late Holocene in accordance with the typical response time of about 7 kyr for sediment carbonate compensation in our model (Fig. 3, green dashed and solid lines).

Sediment carbonate compensation may be briefly described in the following way. CO$_2$ is a weak acid and CO$_2$ uptake by the ocean causes, through acid–base equilibria between dissolved CO$_2$ and bicarbonate and carbonate ion $\left(CO_3^{2-}\right)$, a decrease in pH and in CO_3^{2-}. In turn, the saturation state of water with respect to calcium carbonate (CaCO$_3$) is lowered and the saturation horizon separating oversaturated from undersaturated water with respect to CaCO$_3$ shoals. This shoaling triggers the dissolution of CaCO$_3$ sediments, previously bathed in oversaturated water, into calcium ions and CO_3^{2-}. The release of CO_3^{2-} increases alkalinity twice as much as DIC and

provokes a decrease in dissolved CO_2 which then allows the ocean to take up additional CO_2 from the atmosphere by air–sea gas exchange. In the long run and in the absence of emissions or any other forcings, the saturation horizon relaxes back to its initial location such that the loss of $CaCO_3$ by sediment burial is balanced again by the input of DIC and alkalinity by the weathering flux.

In the following, oceanic changes are discussed as anomalies between 20 ka BP and the late Holocene (i.e. 0 ka BP). The uptake of volcanic CO_2 from the atmosphere raises the dissolved inorganic carbon (DIC) pool and forces deep ocean pH to decrease by 0.06 (0.02 to 0.16) units. CO_3^{2-} is simulated to decrease by about 9 µmol l^{-1} (4 to 20 µmol l^{-1}) in our model (Figs. 5A and 6A). The saturation horizon shoals on global average by about 440 m (150 to 1500 m). The modeled upward shift for the central scenario is larger in the Pacific (520 m) than in the Atlantic (280 m, Fig. 5A). The $CaCO_3$ content in surface sediments decreases considerably near the lysocline. Simulated dissolution of $CaCO_3$ amounts to 120 GtC (40 to 270 GtC) until the end of the simulation and whole-ocean alkalinity increases by 41 µeq l^{-1} (Fig. 5C). In conclusion, the chemistry of the deep ocean and ocean sediments gets perturbed considerably by the assumed volcanic emissions.

Simulated changes in $\delta^{13}C$ of atmospheric CO_2 are small compared to the reconstructed variations for the past 20 kyr of order 0.3‰ (Fig. 4A). $\delta^{13}C$ varies by less than 0.02‰ for the central scenario. Simulated changes are between −0.13‰ and +0.12‰ for the fifteen simulations. This range is caused about equally by the spread in the prescribed isotopic signature of volcanic emissions and by the range in carbon emissions. Small changes are also simulated for the $\delta^{13}C$ signature of DIC in the ocean (Figs. 5B and 6B). The global ocean average $\delta^{13}C$ of DIC is within a range of ±0.14 for the range of simulations.

The small $\delta^{13}C$ changes in response to volcanic emissions are caused by small differences between the isotopic signatures of the relevant fluxes and reservoirs. Small positive $\delta^{13}C$ anomalies for atmospheric CO_2 and whole ocean DIC are simulated for an assumed volcanic signature of −2‰ and small negative anomalies for a signature of −8‰ and explained as follows.

$\delta^{13}C$ of volcanic emissions (-5 ± 3‰) is intermediate between the initial atmospheric signature (−6.3‰) and the mean initial signature of the ocean–atmosphere–land carbon inventory (−0.9‰ in the Bern3D model). Addition of volcanic carbon tends to increase the atmospheric signature to less negative values, whereas it tends to decrease the mean signature of the coupled atmosphere–ocean–land biosphere system on decadal-to-multi century time scales. The net growth of land vegetation of 50 GtC (12 to 130 GtC) as a response to elevated CO_2 increases atmospheric $\delta^{13}C$. On millennial-time scales, carbonate sediments with a slightly higher $\delta^{13}C$ than DIC in the deep ocean (2.9 vs 0.5‰), are dissolved. The effect of the dissolution of isotopically heavy calcium carbonate causes the development of a positive $\delta^{13}C$ anomaly in the deep ocean (Fig. 5B) and tends to increase $\delta^{13}C$ in the ocean and atmosphere. In brief, the sign of the $\delta^{13}C$ anomalies depends on the complex temporal interplay between the different carbon reservoirs and the assumed signature of the volcanic emissions.

Simulated changes in atmospheric $\Delta^{14}C$ are small compared to the reconstructed decrease of 400‰ from the LGM to the late Holocene. The addition of carbon in the form of ^{12}C and ^{13}C, but free of ^{14}C, forces a decrease in the ^{14}C to ^{12}C isotopic ratio. Simulated atmospheric $\Delta^{14}C$ decreases by about 26‰ (10 to 69‰) during the period from 15 to 6 ka BP and stays approximately constant thereafter. In the same time interval, the decrease in whole ocean $\Delta^{14}C$ of DIC is smaller and about 12‰ (6 to 30‰) in the central scenario. The average decrease of 17‰ in the atmosphere–ocean–land system corresponds roughly to the increase in carbon by volcanic input of 717 GtC compared to the initial modeled inventory of 39,100 GtC: 717/39,100 ≈ 18‰.

4. Comparison with proxy records, discussion, and conclusion

The goal of this section is to compare the model results with available proxy data and to discuss the implication for the volcanic carbon emission hypothesis.

Volcanic emissions provoke substantial changes in the carbonate ion concentration and in the lysocline depth. Suitable reconstructions could potentially provide therefore a constraint on the volcanic emission hypothesis. However, as noted by Chiu and Broecker (2008) reconstruction of paleocarbonate is challenging because the existing paleo-CO_3^{2-} indices have limitations. Furthermore, other processes, such as changes in terrestrial storage or coral reef growth, of uncertain magnitude could mask a CO_3^{2-} signal from volcanic emissions.

Many studies indicate a better preservation of calcite and similar or higher concentrations of CO_3^{2-} or alkalinity during the LGM than today in the deep Pacific (Broecker and Clark, 2001). Broecker et al. (1999, 2001) found enhanced calcite preservation, a deglacial preservation peak, in the interval from 13 ka BP to 7 ka BP in the western deep Atlantic and the equatorial deep Pacific. Marchitto et al. (2005) reconstructed for the equatorial deep Pacific a CO_3^{2-} peak of 25–30 µmol kg^{-1} during the termination I with the CO_3^{2-} rise preceding ice sheet melting. Yu et al. (2010) find a maxima in CO_3^{2-} during the termination at 3.4 km depth and little change at 2.3 km in the equatorial Pacific (Fig. 6A).

Results for the difference in CO_3^{2-} concentration and lysocline depth between the LGM and today vary across studies and seem conflicting (Zeebe and Marchitto (2010) and references therein). For example, Farrell and Prell (1989) reconstructed deeper lysocline depth by 400 to 800 m compared to today for the last nine glacials and from cores drilled in the equatorial Pacific. In contrast, Wu et al. (1991) used percent carbonate content to infer a 1 km shallower lysocline for the LGM than today. Rickaby et al. (2010) state that the deep waters in the Weddell Sea experienced elevated alkalinity by ~25 µmol kg^{-1} during the cool period of each glacial cycle and that this signal of less corrosive deep water emanating from the Southern ocean likely accounts for the
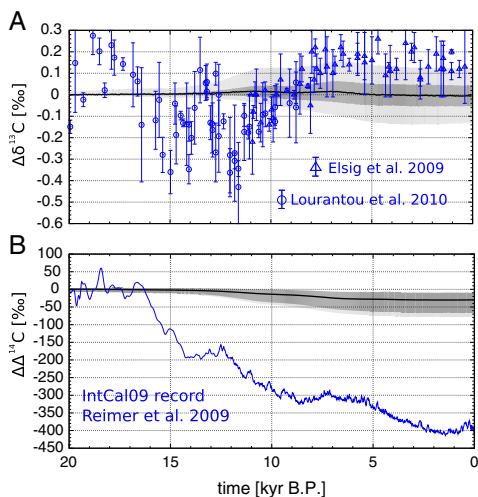

Fig. 4. A) Simulated changes in (A) $\delta^{13}C$ and (B) $\Delta^{14}C$ of atmospheric CO_2 for the past 20 kyr in response to volcanic CO_2 emissions. In panel a, the light gray area spans the results from simulations where CO_2 emissions are from the highest (2011 GtC) scenario combined with low (−8‰) and high (−2‰) estimates of their $\delta^{13}C$ signature; results for the central CO_2 emission scenario (717 GtC) with low, central (−5‰), and high estimates of the $\delta^{13}C$ signature are shown by the dark gray area and the solid line. Ice core data from Elsig et al. (2009) and Lourantou et al. (2010) is shown in blue. The two records were shifted relative to each other by 0.15‰ such that they overlap between 11 and 9 kyr and the data are given as anomalies relative to 20 kyr BP for better comparison. In panel b, gray shadings and the solid line indicate $\Delta^{14}C$ results for the five CO_2 emission scenarios shown in Fig. 2; volcanic CO_2 emissions are free of radiocarbon. IntCal09 data (blue line) (Reimer et al., 2009) are shown as anomalies relative to 20 kyr BP.
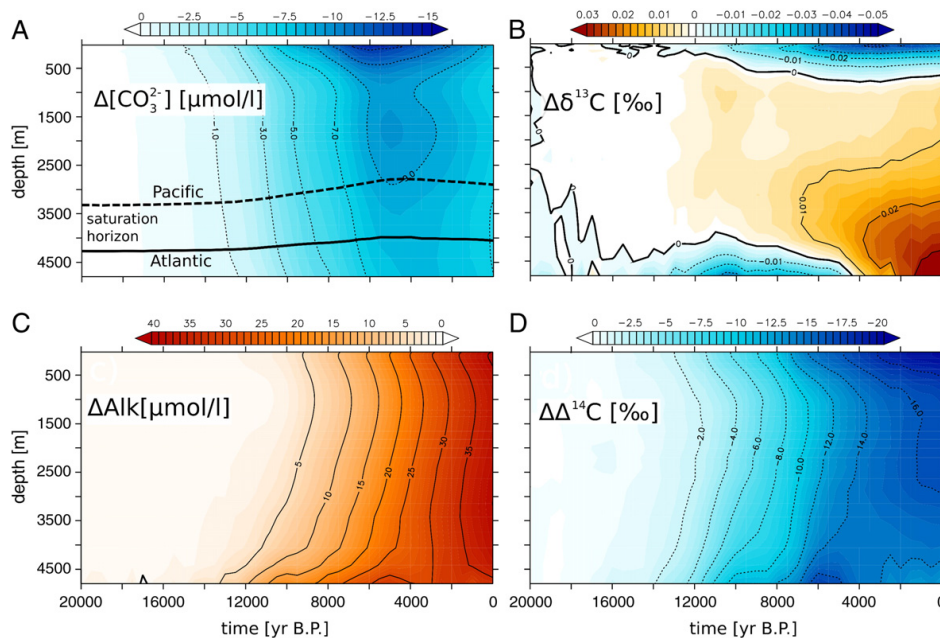
Fig. 5. Depth-resolved time-evolution of changes in A) carbonate ion concentration, B) alkalinity, C) $\delta^{13}C$ of DIC, and D) $\Delta^{14}C$ of DIC. Shown are averages over all basins and for the central emission scenario with total emissions of 717 GtC and $\delta^{13}C$ of $-5‰$. The evolution of the saturation horizon (with respect to calcite) is shown for the Atlantic (solid) and the Pacific (dash) in panel A. Dissolution of calcite results in a positive deep ocean $\delta^{13}C$ anomaly as visible in panel B.

higher carbonate accumulation seen across the glacial Southern and Pacific Ocean. Anderson and Archer (2002) found little change in the CO_3^{2-} gradient during the LGM in comparison to today for the Atlantic, Pacific, and Indian Ocean. On the other hand, Fehrenbacher and Martin (2011) suggest that CO_3^{2-} was on average 7–27 μmol kg^{-1} lower

Fig. 6. A) Model results for the anomaly in carbonate ion concentration in the intermediate equatorial Pacific compared to sediment core proxies (Marchitto et al., 2005; Yu et al., 2010). B) Change in global ocean $\delta^{13}C$ of DIC in the deep and intermediate depths compared to the benthic $\delta^{13}C$ compilation of Oliver et al. (2010) representing averages over available records (blue).

between 2.5 and 4.0 km in the western equatorial Pacific implying more undersaturated waters in the deep Pacific during the LGM and a ~1 km or more shoaling of the lysocline relative to the modern.

The volcanic emission hypothesis yields small CO_3^{2-} changes over the early phase of the termination and the past 5 ka and a nearly uniform whole ocean decrease of 8 μmol kg^{-1} (4 to 17 μmol kg^{-1}) from 14 ka BP to 5 ka BP (Figs. 5A and 6A). Thus, the volcanic hypothesis cannot explain the reconstructed deglacial peak in CO_3^{2-} and may appear in conflict with the enhanced calcite preservation reconstructed by Broecker et al. (1999) and Broecker et al. (2001) for the early Holocene. Whatever caused the deglacial CO_3^{2-} peak, one expects that the carbonate system and deep ocean CO_3^{2-} relax toward its state before the perturbation to achieve balance between weathering input and burial. A decline in CO_3^{2-} after the peak appears thus to be a natural consequence of the initial perturbation causing the peak. There are other known processes that affect the CO_3^{2-} evolution during the termination and the Holocene such as enhanced shallow water carbonate deposition related to sea level rise or the sediment compensation of a deglacial uptake of CO_2 by the land biosphere (Broecker et al., 1999; Kleypas, 1997; Vecsei and Berger, 2004). This makes it difficult to draw firm conclusions from this proxy.

Next, we discuss the volcanic emission hypothesis in the context of the ice core CO_2 record and related studies. We distinguish for simplicity four time periods, namely the early part of the last glacial termination from 18 to 14.8 ka BP, the second part of the termination from 14.8 to 11 ka BP, the early Holocene from 11 to 7 ka BP and the late Holocene (after 7 ka BP), and focus on results from the central scenario (Fig. 3B). As noted above, simulated changes in $\delta^{13}C$ and $\Delta^{14}C$ are small compared to reconstructed isotopic variations. Carbon cycle processes other than volcanic emissions must explain the isotopic variations and volcanic emissions cannot explain all deglacial carbon cycle changes.

Atmospheric CO_2 increased by almost 40 ppm in the early part of the termination. Volcanic emissions hardly do contribute to the initial CO_2 rise at the start of the termination and explain, according to the emission reconstructions of Huybers and Langmuir (2009), only a contribution of
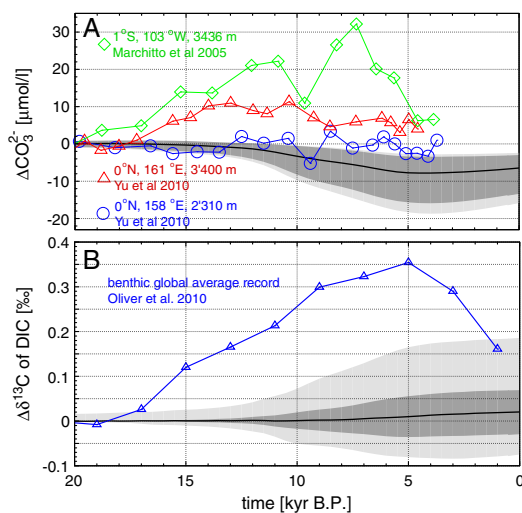
3.5 ppm by 14.8 ka BP. It is very likely that other mechanisms than volcanic emissions were responsible for the onset of the deglaciation and the CO$_2$ rise in the early part of the termination as already noted by Huybers and Langmuir (2009).

Similarly, simulated CO$_2$ differences between 7 ka and the preindustrial period (1750 AD) remain small for the range of volcanic emissions scenarios; there is an increase of about 5 ppm from 7 ka to 6 ka BP and a decrease of the same magnitude in the past 6 ka for the central emission scenario. In contrast, atmospheric CO$_2$ increased by 20 ppm during the last 7 kyr before the industrialization. Again, other processes must be responsible for this late Holocene CO$_2$ increase.

Atmospheric CO$_2$ rose by another 40 ppm until the onset of the Holocene. The simulated CO$_2$ increase over the period from 14.8 to 11 ka BP is about half of the reconstructed increase for the central scenario. Then, other processes are needed to explain the atmospheric CO$_2$ record and the simulated isotopic changes and changes in CO_3^{2-}. A significant contribution by volcanic emissions during the second part of the termination as stipulated by Huybers and Langmuir (2009) appears not in conflict with available evidence as a range of processes likely influenced atmospheric CO$_2$, carbon isotopes, CO_3^{2-}, and the carbon cycle over the termination.

Atmospheric CO$_2$ decreased by about 5 ppm in the early Holocene (11 to 7 ka BP). The reconstructed decrease is in strong contrast to the simulated CO$_2$ increase of 22 ppm during the same period and for the standard volcanic emission model setup. This implies that a strong additional carbon sink, offsetting the difference of 27 ppm, must have operated if volcanic emissions were indeed as large as postulated.

The land biosphere could have been such a sink. Ice core data of $\delta^{13}CO_2$ as well as analyses of peat carbon (Yu, 2011) indicate that the terrestrial land biosphere acted as a carbon sink during the early Holocene. Quantitative analyses of the ice core $\delta^{13}C$ and CO$_2$ records yield a terrestrial uptake of about 224 ± 35 GtC (Elsig et al., 2009) and a related atmospheric CO$_2$ decrease of about 15 ppm during the period 11 to 7 ka BP (Elsig et al., 2009).

There are known carbon sources to the atmosphere in the early Holocene (Menviel and Joos, 2012). These include coral reef build-up and other shallow water carbonate deposition (SWCD) (Ridgwell et al., 2003; Vecsei and Berger, 2004) in the wake of deglacial sea level rise and carbonate compensation of land uptake during the glacial termination (18 to 11 ka BP) (Joos et al., 2004) as well as minor contributions from other sediment–ocean interactions and sea surface temperature changes. Goodwin et al. (2011) also suggest in addition that a weakening of the marine biological cycle contributed to the CO$_2$ increase. On the other hand, no major oceanic sink has yet been identified for the early Holocene period. Menviel and Joos (2012) reproduced the Holocene records of atmospheric CO$_2$ and $\delta^{13}C$ as well as the spatio-temporal evolution of $\delta^{13}C$ and carbonate ion concentration in the deep sea by applying published scenarios for coral reef build-up and atmosphere–land biosphere fluxes and orbital and ice sheet forcings in the Bern3D model. These authors quantify early Holocene source processes to be equivalent to a CO$_2$ increase of 10 ppm between 11 and 7 ka BP.

Accordingly, the land biosphere being the only relevant sink for atmospheric CO$_2$ in the early Holocene, vegetation growth and volcanic emissions together must result in an early Holocene CO$_2$ decrease of at least ~5 ppm CO$_2$ to be consistent with the ice core data.

To asses to the compatibility of these two forcings, additional simulations were carried out applying both the proposed volcanic emission scenarios and the Holocene land-uptake history by Elsig et al. (2009). In addition, a simulation forced by the Elsig land uptake history alone, without volcanic emissions, was performed to further distinguish the influence of the two forcings. The prescribed land-scenario and net emissions are shown in Fig. 7A while the results of atmospheric CO$_2$ and $\delta^{13}CO_2$ anomalies in the time interval from 13 ka to 4 ka BP are shown in Fig. 7B and C. To facilitate the comparison within this time-period, simulated ΔCO_2 have been set to 0 ppm for all scenarios at
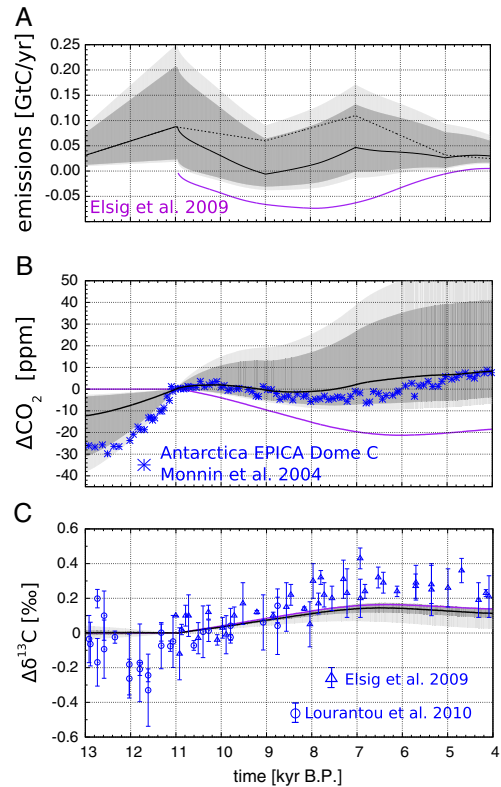

Fig. 7. A) Prescribed net carbon flux into the atmosphere and B) simulated changes in atmospheric CO$_2$ and c) $\delta^{13}C$ for scenarios including volcanic carbon emissions and terrestrial carbon uptake. Simulated changes are relative to 11 kyr BP. Volcanic emissions are as in Fig. 2B. Land-to-atmosphere fluxes are prescribed following Elsig et al. (2009) in all simulations (purple line in panel A). The solid black lines and shadings are for the central and bounding volcanic emission cases combined with the Elsig land uptake scenario. The purple lines in panel B and C are from a simulation with land uptake as the only forcing. The dashed line in panel A indicates volcanic emissions for the central scenario. Ice core data are given by blue symbols (Elsig et al., 2009; Lourantou et al., 2010).

11 ka BP. Any other processes that could had increased atmospheric CO$_2$, including earlier changes in land biosphere carbon inventory, are neglected in these simulations. The comparison of simulated and ice core CO$_2$ provides thus a likely upper bound case for the influence of volcanic emissions on CO$_2$ during this period.

Forcing the model with the land scenario only yields a CO$_2$ decrease of almost 20 ppm. Applying the lowest up to the central volcanic scenario in combination with Holocene land uptake indeed yields a small CO$_2$ decrease after 11 ka BP (3 ppm in the central scenario). This decrease mainly results from the ocean-uptake of the preceding volcanic emission peak which is also centered at 11 ka BP, tending to lower atmospheric CO$_2$ as the atmosphere–ocean–sediment system relaxes as net emissions tend to vanish at ~9 ka BP, as shown in Fig. 7A. For the higher scenarios, the measured CO$_2$ drawdown becomes more and more difficult to explain, at least with the land biosphere scenario from Elsig et al. (2009).

Next, we discuss to which extent volcanic emissions influence the $\delta^{13}C$ evolution in combination with the land uptake and thus earlier interpretations of the $\delta^{13}C$ record. As in Menviel and Joos (2012), the simulated atmospheric $\delta^{13}C$ increase due to Holocene land forcing alone

explains about half of the measured early Holocene δ^{13}C increase (Fig. 7C). More important in the current context, simulated atmospheric δ^{13}C evolutions for the scenarios with or without volcanic emissions are very similar; the δ^{13}C change is less than 0.02‰ smaller for the combined land and central volcanic emission history than for the land only scenario (Fig. 7C). In other words, volcanic emissions in combination with other plausible forcings do hardly affect the evolution of atmospheric δ^{13}C over the Holocene.

In conclusion, the ice core CO$_2$ and δ^{13}C records (Elsig et al., 2009) and reconstructions of shallow water carbonate deposition for the early Holocene (Ridgwell et al., 2003; Vecsei and Berger, 2004) appear incompatible with the central and higher volcanic CO$_2$ emission range of Huybers and Langmuir (2009) during the early Holocene. Volcanic emissions situated between the lower and the central scenario may be compatible with available proxy data, as uncertainties in our understanding of Holocene carbon sources and sink processes and in their timing remain.

The problem with the volcanic scenarios is apparently in the timing of the emissions which peak in the early Holocene, a period of decreasing atmospheric CO$_2$. This timing seems to be an inevitable consequence of the mechanism, depressurization and increased magma production due to ice melting, proposed by Huybers and Langmuir (2009) and the known pace of ice sheet retreat. Ice sheet melting lags the CO$_2$ rise in atmospheric CO$_2$ over the termination (Shackleton, 2000). A much earlier start of volcanic emissions by this mechanism than reconstructed by Huybers and Langmuir (2009) thus appears unlikely, although uncertainties remain as there are volcanic regions that have experienced deglaciation near 12 ka BP (Huybers and Langmuir, 2009). A later peak in emissions could have contributed to the late Holocene CO$_2$ rise, but would not help to explain the CO$_2$ increase over the glacial termination from 18 to 11 ka BP. In summary, our results suggest that volcanic emissions do not play a dominant role in regulating glacial–interglacial CO$_2$ variations.

Acknowledgments

References

Anderson, D.M., Archer, D., 2002. Glacial–interglacial stability of ocean pH inferred from foraminifer dissolution rates. Nature 416, 70–73.

Arrhenius, S., 1896. On the influence of carbonic acid in the air upon the temperature of the ground. Philos. Mag. J. Sci 41, 237–276.

Broecker, W.S., Clark, E., 2001. Glacial-to-Holocene redistribution of carbonate ion in the deep sea. Science 294, 2152–2155.

Broecker, W.S., Clark, E., McCorkle, D.C., Peng, T.H., Hajdas, I., Bonani, G., 1999. Evidence for a reduction in the carbonate ion content of the deep sea during the course of the Holocene. Paleoceanography 14, 744–752.

Broecker, W.S., Lynch-Stieglitz, J., Clark, E., Hajdas, I., Bonani, G., 2001. What caused the atmosphere's CO$_2$ content to rise during the last 8000 years? Geochem. Geophys. Geosyst. 2, 1062–1074.

Chiu, T.C., Broecker, W.S., 2008. Toward better paleocarbonate ion reconstructions: new insights regarding the CaCO$_3$ size index. Paleoceanography 23, PA2216.

Deines, P., 2002. The carbon isotope geochemistry of mantle xenoliths. Earth Sci. Rev. 58, 247–278.

Duplessy, J., Shackleton, N., Fairbanks, R., Labeyrie, L., Oppo, D., Kallel, N., 1988. Deepwater source variations during the last climatic cycle and their impact on the global deepwater circulation. Paleoceanography 3, 343–360.

Edwards, N.R., Willmott, A.J., Killworth, P.D., 1998. On the role of topography and wind stress on the stability of the thermohaline circulation. J. Phys. Oceanogr. 28, 756–778.

Elsig, J., Schmitt, J., Leuenberger, D., Schneider, R., Eyer, M., Leuenberger, M., Joos, F., Fischer, H., Stocker, T.F., 2009. Stable isotope constraints on Holocene carbon cycle changes from an Antarctic ice core. Nature 461, 507–510.

Farrell, J.W., Prell, W.L., 1989. Climatic change and CaCO$_3$ preservation: an 800,000 year bathymetric reconstruction from the Central Equatorial Pacific Ocean. Paleoceanography 4, 447–466.

Fehrenbacher, J., Martin, P., 2011. Western equatorial Pacific deep water carbonate chemistry during the Last Glacial Maximum and deglaciation: using planktic foraminiferal Mg/Ca

to reconstruct sea surface temperature and seafloor dissolution. Paleoceanography 26, PA2225.

Frölicher, T.L., Joos, F., Raible, C.C., 2011. Sensitivity of atmospheric CO$_2$ and climate to explosive volcanic eruptions. Biogeosci. Discuss. 8, 2957–3007.

Gehlen, M., Bopp, L., Emprin, N., Aumont, O., Heinze, C., Ragueneau, O., 2006. Reconciling surface ocean productivity, export fluxes and sediment composition in a global biogeochemical ocean model. Biogeosciences 3, 521–537.

Goodwin, P., Oliver, K.I.C., Lenton, T.M., 2011. Observational constraints on the causes of Holocene CO$_2$ change. Glob. Biogeochem. Cycles 25, GB3011.

Heinze, C., Maier-Reimer, E., Winguth, A.M.E., Archer, D., 1999. A global oceanic sediment model for long-term climate studies. Glob. Biogeochem. Cycles 13, 221–250.

Huybers, P., Langmuir, C., 2009. Feedback between deglaciation, volcanism, and atmospheric CO$_2$. Earth Planet. Sci. Lett. 286, 479–491.

Jansen, E., Overpeck, J., Briffa, K.R., Duplessy, J.C., Joos, F., Masson-Delmotte, V., Olago, D., Otto-Bliesner, B., Peltier, W.R., Rahmstorf, S., Ramesh, R., Raynaud, D., Rind, D., Solomina, O., Villalba, R., Zhang, D., 2007. Palaeoclimate. In: Solomon, S., Qin, D., Manning, M., Chen, Z., Marquis, M., Averyt, K.B., Tignor, M., Miller, H.L. (Eds.), Climate Change 2007: the physical science basis. : Working Group I Contribution to the Fourth Assessment Report of the Intergovernmental Panel on Climate Change. Cambridge University Press, pp. 433–497.

Joos, F., Gerber, S., Prentice, I.C., Otto-Bliesner, B.L., Valdes, P.J., 2004. Transient simulations of Holocene atmospheric carbon dioxide and terrestrial carbon since the Last Glacial Maximum. Global Biogeochem. Cycles 18.

Kleypas, J.A., 1997. Modeled estimates of global reef habitat and carbonate production since the Last Glacial Maximum. Paleoceanography 12, 533–545.

Köhler, P., Fischer, H., Munhoven, G., Zeebe, R., 2005. Quantitative interpretation of atmospheric carbon records over the last glacial termination. Glob. Biogeochem. Cycles 19, GB4020.

Lourantou, A., Lavric, J.V., Köhler, P., Barnola, J.M., Paillard, D., Michel, E., Raynaud, D., Chappellaz, J., 2010. Constraint of the CO$_2$ rise by new atmospheric carbon isotopic measurements during the last deglaciation. Glob. Biogeochem. Cycles 24, GB2015.

Lüthi, D., Le Floch, M., Bereiter, B., Blunier, T., Barnola, J.M., Siegenthaler, U., Raynaud, D., Jouzel, J., Fischer, H., Kawamura, K., Stocker, T.F., 2008. High-resolution carbon dioxide concentration record 650,000–800,000 years before present. Nature 453, 379–382.

Maclennan, J., Jull, M., McKenzie, D., Slater, L., Grönvold, K., 2002. The link between volcanism and deglaciation in Iceland. Geochem. Geophys. Geosyst. 3, 1062–1078.

Maier-Reimer, E., 1993. Geochemical cycles in an ocean general circulation model. Preindustrial tracer distributions. Glob. Biogeochem. Cycles 7, 645–677.

Marchitto, T.M., Lynch-Stieglitz, J., Hemming, S.R., 2005. Deep Pacific CaCO$_3$ compensation and glacial–interglacial atmospheric CO$_2$. Earth Planet. Sci. Lett. 231, 317–336.

Menviel, L., Joos, F., 2012. Towards explaining the Holocene carbon dioxide and carbon isotope records: Results from transient ocean carbon cycle-climate simulations. Paleoceanography 24/PA1207.

Monnin, E., Steig, E.J., Siegenthaler, U., Kawamura, K., Schwander, J., Stauffer, B., Stocker, T.F., Morse, D.L., Barnola, J.M., Bellier, B., Raynaud, D., Fischer, H., 2004. Evidence for substantial accumulation rate variability in Antarctica during the Holocene, through synchronization of CO$_2$ in the Taylor Dome, Dome C and DML ice cores. Earth Planet. Sci. Lett. 224, 45–54.

Müller, S.A., Joos, F., Edwards, N.R., Stocker, T.F., 2006. Water mass distribution and ventilation time scales in a cost-efficient, three-dimensional ocean model. J. Climate 19, 5479–5499.

Munhoven, G., 2002. Glacial–interglacial changes of continental weathering: estimates of the related CO$_2$ and HCO$_3^-$ flux variations and their uncertainties. Global Planet. Change 33, 155–176.

Najjar, R.G., Orr, J., Sabine, C.L., Joos, F., 1999. Biotic-HOWTO. Internal OCMIP Report. Technical Report. LSCE/CEA Saclay, Gif-sur-Yvette, France.

Narcisi, B., Petit, J.R., Chappellaz, J., 2010. A 70 ka record of explosive eruptions from the TALDICE ice core (Talos Dome, East Antarctic plateau). J. Quatern. Sci. 25, 844–849.

Nowell, D.A.G., Jones, M.C., Pyle, D.M., 2006. Episodic quaternary volcanism in France and Germany. J. Quat. Sci. 21, 645–675.

Oliver, K.I.C., Hoogakker, B.A.A., Crowhurst, S., Henderson, G.M., Rickaby, R.E.M., Edwards, N.R., Elderfield, H., 2010. A synthesis of marine sediment core δ^{13}C data over the last 150 000 years. Clim. Past 6, 645–673.

Orr, J., Najjar, R.G., 1999. Abiotic-HOWTO. Internal OCMIP Report. Technical Report. LSCE/CEA Saclay, Gif-sur-Yvette, France.

Parekh, P., Joos, F., Müller, S.A., 2008. A modeling assessment of the interplay between aeolian iron fluxes and iron-binding ligands in controlling carbon dioxide fluctuations during Antarctic warm events. Paleoceanography 23, PA4202.

Petit, J.R., Jouzel, J., Raynaud, D., Barkov, N.I., Barnola, J.M., Basile, I., Bender, M., Chappellaz, J., Davis, M., Delaygue, G., Delmotte, M., Kotlyakov, V.M., Legrand, M., Lipenkov, V.Y., Lorius, C., PÉpin, L., Ritz, C., Saltzman, E., Stievenard, M., 1999. Climate and atmospheric history of the past 420,000 years from the Vostok ice core, Antarctica. Nature 399, 429–436.

Reimer, P.J., Baillie, M.G.L., Bard, E., Bayliss, A., Beck, J.W., Blackwell, P.G., Ramsey, C.B., Buck, C.E., Burr, G.S., Edwards, R.L., Friedrich, M., Grootes, P.M., Guilderson, T.P., Hajdas, I., Heaton, T.J., Hogg, A.G., Hughen, K.A., Kaiser, K.F., Kromer, B., McCormac, F.G., Manning, S.W., Reimer, R.W., Richards, D.A., Southon, J.R., Talamo, S., Turney, C.S.M., van der Plicht, J., Weyhenmeye, C.E., 2009. IntCal09 and Marine09 radiocarbon age calibration curves, 0–50,000 years cal BP. Radiocarbon 51, 1111–1150.

Rickaby, R.E.M., Elderfield, H., Roberts, N., Hillenbrand, C.D., Mackensen, A., 2010. Evidence for elevated alkalinity in the glacial Southern Ocean. Paleoceanography 25, PA1209.

Ridgwell, A.J., Watson, A.J., Maslin, M.A., Kaplan, J.O., 2003. Implications of coral reef buildup for the controls on atmospheric CO$_2$ since the Last Glacial Maximum. Paleoceanography 18, 1083.

Ritz, S.P., Stocker, T.F., Joos, F., 2011. A coupled dynamical ocean energy balance atmosphere model for paleoclimate studies. J. Climate 24, 349–375.

Robinson, L.F., Adkins, J.F., Keigwin, L.D., Southon, J., Fernandez, D.P., Wang, S.L., Scheirer, D.S., 2005. Radiocarbon variability in the Western North Atlantic during the last deglaciation. Science 310, 1469–1473.

Sano, Y., Marty, B., 1995. Origin of carbon in fumarolic gas from island arcs. Chem. Geol. 119, 265–274.

Sarnthein, M., Winn, K., Jung, S.J.A., Duplessy, J.C., Labeyrie, L., Erlenkeuser, H., Ganssen, G., 1994. Changes in east Atlantic deepwater circulation over the last 30,000 years: eight time slice reconstructions. Paleoceanography 9, 209–267.

Shackleton, N.J., 2000. The 100,000-year ice-age cycle identified and found to lag temperature, carbon dioxide, and orbital eccentricity. Science 289, 1897–1902.

Siegenthaler, U., Oeschger, H., 1987. Biospheric CO$_2$ emissions during the past 200 years reconstructed by deconvolution of ice core data. Tellus B 39B, 140–154.

Sigmundsson, F., Pinel, V., Lund, B., Albino, F., Pagli, C., Geirsson, H., Sturkell, E., 2010. Climate effects on volcanism: influence on magmatic systems of loading and unloading from ice mass variations, with examples from Iceland. Philos. Trans. R. Soc. A 368, 2519–2534.

Sitch, S., Smith, B., Prentice, I., Arneth, A., Bondeau, A., Cramer, W., Kaplan, J., Levis, S., Lucht, W., Sykes, M., Thonicke, K., Venevsky, S., 2003. Evaluation of ecosystem dynamics, plant geography and terrestrial carbon cycling in the LPJ dynamic global vegetation model. Glob. Change Biol. 9, 161–185.

Tschumi, T., Joos, F., Parekh, P., 2008. How important are Southern Hemisphere wind changes for low glacial carbon dioxide? A model study. Paleoceanography 23, PA4208.

Tschumi, T., Joos, F., Gehlen, M., Heinze, C., 2011. Deep ocean ventilation, carbon isotopes, marine sedimentation and the deglacial CO$_2$ rise. Clim. Past 7, 771–800.

Vance, D., Teagle, D.A.H., Foster, G.L., 2009. Variable Quaternary chemical weathering fluxes and imbalances in marine geochemical budgets. Nature 458, 493–496.

Vecsei, A., Berger, W.H., 2004. Increase of atmospheric CO$_2$ during deglaciation: constraints on the coral reef hypothesis from patterns of deposition. Glob. Biogeochem. Cycles 18, GB1035.

Wu, G., Yasuda, M., Berger, W., 1991. Late Pleistocene carbonate stratigraphy on Ontong–Java Plateau in the western equatorial Pacific. Mar. Geol. 99, 135–150.

Yu, Z., 2011. Holocene carbon flux histories of the world's peatlands: global carbon-cycle implications. Holocene 21, 761–774.

Yu, J., Broecker, W.S., Elderfield, H., Jin, Z., McManus, J., Zhang, F., 2010. Loss of carbon from the deep sea since the Last Glacial Maximum. Science 330, 1084–1087.

Zeebe, R.E., Marchitto, T.M., 2010. Glacial cycles: atmosphere and ocean chemistry. Nat. Geosci. 3, 386–387.

Chapter 4

Radiocarbon and its application as a proxy for solar activity

4.1   A reconstruction of radiocarbon production and total solar irradiance from the Holocene ^{14}C and CO_2 records: implications of data and model uncertainties

Raphael Roth and Fortunat Joos

Climate
of the Past

Open Access

A reconstruction of radiocarbon production and total solar irradiance from the Holocene ^{14}C and CO_2 records: implications of data and model uncertainties

R. Roth and F. Joos

Climate and Environmental Physics, Physics Institute, University of Bern, Bern, Switzerland

Oeschger Centre for Climate Change Research, University of Bern, Bern, Switzerland

Correspondence to: R. Roth (roth@climate.unibe.ch)

Abstract. Radiocarbon production, solar activity, total solar irradiance (TSI) and solar-induced climate change are reconstructed for the Holocene (10 to 0 kyr BP), and TSI is predicted for the next centuries. The IntCal09/SHCal04 radiocarbon and ice core CO_2 records, reconstructions of the geomagnetic dipole, and instrumental data of solar activity are applied in the Bern3D-LPJ, a fully featured Earth system model of intermediate complexity including a 3-D dynamic ocean, ocean sediments, and a dynamic vegetation model, and in formulations linking radiocarbon production, the solar modulation potential, and TSI. Uncertainties are assessed using Monte Carlo simulations and bounding scenarios. Transient climate simulations span the past 21 thousand years, thereby considering the time lags and uncertainties associated with the last glacial termination.

Our carbon-cycle-based modern estimate of radiocarbon production of 1.7 atoms $cm^{-2} s^{-1}$ is lower than previously reported for the cosmogenic nuclide production model by Masarik and Beer (2009) and is more in-line with Kovaltsov et al. (2012). In contrast to earlier studies, periods of high solar activity were quite common not only in recent millennia, but throughout the Holocene. Notable deviations compared to earlier reconstructions are also found on decadal to centennial timescales. We show that earlier Holocene reconstructions, not accounting for the interhemispheric gradients in radiocarbon, are biased low. Solar activity is during 28 % of the time higher than the modern average (650 MeV), but the absolute values remain weakly constrained due to uncertainties in the normalisation of the solar modulation to instrumental data. A recently published solar activity–TSI relationship yields small changes in Holocene TSI of the order of 1 W m^{-2} with a Maunder Minimum irradiance reduction of 0.85 ± 0.16 W m^{-2}. Related solar-induced variations in global mean surface air temperature are simulated to be within 0.1 K. Autoregressive modelling suggests a declining trend of solar activity in the 21st century towards average Holocene conditions.

1 Introduction

Solar insolation is the driver of the climate system of the earth (e.g. Gray et al., 2010; Lockwood, 2012). Variations in total solar irradiance (TSI) have the potential to significantly modify the energy balance of the earth (Crowley, 2000; Ammann et al., 2007; Jungclaus et al., 2010). However, the magnitude of variations in TSI (Schmidt et al., 2011, 2012; Shapiro et al., 2011; Lockwood, 2012) and its temporal evolution (Solanki et al., 2004; Muscheler et al., 2005b; Schmidt et al., 2011) remain uncertain and are debated. Solar activity and TSI were reconstructed from the Holocene radiocarbon record. These reconstructions relied on box models of the ocean and land carbon cycle or on a 2-D representation of the ocean (Solanki et al., 2004; Marchal, 2005; Usoskin and Kromer, 2005; Vieira et al., 2011; Steinhilber et al., 2012).

However, a quantification of how past changes in climate and the carbon cycle affect reconstructions of radiocarbon production and solar activity is yet missing. Aspects neglected in earlier studies include (i) changes in the climate–carbon-cycle system over the last glacial termination ($\sim$ 18 to

11 kyr BP), (ii) variations in Holocene and last millennium climate, (iii) changes in ocean sediments, and (iv) changes in vegetation dynamics and in anthropogenic land use.

The goal of this study is to reconstruct Holocene radiocarbon production, solar modulation potential to characterise the open solar magnetic field, TSI, and the influence of TSI changes on Holocene climate from the proxy records of atmospheric $\Delta^{14}C$ (McCormac et al., 2004; Reimer et al., 2009) and CO_2 and a recent reconstruction of the geomagnetic field (Korte et al., 2011). The TSI reconstruction is extended into the future to year 2300 based on its spectral properties. We apply the Bern3D-LPJ Earth system model of intermediate complexity that features a 3-D dynamic ocean, reactive ocean sediments, a dynamic global vegetation model, an energy–moisture balance atmosphere, and cycling of carbon and carbon isotopes. The model is forced by changes in orbital parameters, explosive volcanic eruptions, well-mixed greenhouse gases (CO_2, CH_4, N_2O), aerosols, ice cover and land-use area changes. Bounding scenarios for deglacial radiocarbon changes and Monte Carlo techniques are applied to comprehensively quantify uncertainties.

TSI reconstructions that extend beyond the satellite record must rely on proxy information. ^{14}C and ^{10}Be are two proxies that are particularly well suited (Beer et al., 1983; Muscheler et al., 2008; Steinhilber et al., 2012); their production by cosmic particles is directly modulated by the strength of the solar magnetic field and they are conserved in ice cores (^{10}Be) and tree rings (^{14}C). The redistributions of ^{10}Be and ^{14}C within the climate system follow very different pathways, and thus the two isotopes can provide independent information. The ^{10}Be and ^{14}C proxy records yield in general consistent reconstructions of isotope production and solar activity with correlations exceeding 0.8 (Bard et al., 1997; Lockwood and Owens, 2011). Important caveats, however, and differences in detail remain. After production, ^{10}Be is attached to aerosols, and variations in atmospheric transport and dry and wet deposition of ^{10}Be and incorporation into the ice archive lead to noise and uncertainties. This is highlighted by the opposite, and not yet understood, 20th century trends in ^{10}Be in Greenland versus Antarctic ice cores (Muscheler et al., 2007; Steinhilber et al., 2012). Thus, taken at face value, Greenland and Antarctic ^{10}Be records suggest opposite trends in solar activity in the second half of the 20th century.

^{14}C is oxidised after production and becomes as $^{14}CO_2$ part of the global carbon cycle. It enters the ocean, sediments, and the land biosphere and is removed from the climate system by radioactive decay, with an average lifetime of $5730\,\text{yr}/\ln(2) = 8267\,\text{yr}$, and to a minor part by seafloor sediment burial. Atmospheric ^{14}C is influenced not only by short-term production variations, but also by variations of the coupled carbon-cycle–climate system, and their evolutions due to the long timescales governing radioactive decay and carbon overturning in the land and ocean.

The conversion of the radiocarbon proxy record (McCormac et al., 2004; Reimer et al., 2009) to TSI involves several steps. First a carbon cycle model is applied to infer radiocarbon production by deconvolving the atmospheric radiocarbon budget. Radiocarbon production is equal to the prescribed changes in the atmospheric radiocarbon inventory and decay in the atmosphere plus the modelled net air-to-sea and net air-to-land ^{14}C fluxes. The radiocarbon signature of a flux or a reservoir is commonly reported in the $\Delta^{14}C$ notation, i.e. as the fractionation-corrected per mil deviation of $^{14}R = {}^{14}C/^{12}C$ from a given standard defined as $^{14}R_{std} = 1.176 \times 10^{-12}$ (Stuiver and Polach, 1977). ^{14}C production depends on the magnitude of the shielding of the earth's atmosphere by the geomagnetic and the open solar magnetic fields. Reconstructions of the geomagnetic field can thus be combined with a physical cosmogenic isotope production model (Masarik and Beer, 1999, 2009; Kovaltsov et al., 2012) to infer the strength of the magnetic field enclosed in solar winds as expressed by the so-called solar modulation potential, Φ. Finally, Φ is translated into variations in TSI.

Each of these steps has distinct uncertainties and challenges. Deglacial carbon cycle changes are large, and atmospheric CO_2 increased from 180 ppm at the Last Glacial Maximum (LGM) to 265 ppm 11 kyr BP. These variations are thought to be driven by physical and biogeochemical reorganisations of the ocean (e.g. Brovkin et al., 2012; Menviel et al., 2012). They may influence the ^{14}C evolution in the Holocene and the deconvolution for the ^{14}C production, but were not considered in previous studies. Many earlier studies (Marchal, 2005; Muscheler et al., 2005a; Usoskin and Kromer, 2005; Vonmoos et al., 2006; Steinhilber et al., 2012) deconvolving the ^{14}C record relied on simplified box models using a perturbation approach (Oeschger et al., 1975; Siegenthaler, 1983) where the natural marine carbon cycle is not simulated and climate and ocean circulations as well as land carbon turnover are kept constant. In the perturbation approach, the ocean carbon and radiocarbon inventory is underestimated by design as the concentration of dissolved inorganic carbon is set to its surface concentration. ^{12}C and ^{14}C are not transported as separate tracers but combined into a single tracer, the $^{14}C/^{12}C$ ratio. These shortcomings, however, can be overcome by applying a spatially resolved coupled carbon-cycle–climate model that includes the natural carbon cycle and its anthropogenic perturbation, and where ^{12}C and ^{14}C are distinguished.

A key target dataset is the data of the Global Ocean Data Analysis Project (GLODAP) that includes station data and gridded data of dissolved inorganic carbon and its ^{14}C signature (Key et al., 2004). This permits the quantification of the oceanic radiocarbon inventory, by far the largest radiocarbon inventory on earth. Together with data-based estimates of the carbon inventory on land, in the atmosphere, and in reactive sediment and their signatures, the global radiocarbon inventory and thus the long-term average ^{14}C production can be

reliably estimated. Further, the spatial carbon and ^{14}C distribution within the oceans is a yard stick to gauge the performance of any ocean circulation and carbon cycle model. ^{14}C permits the quantification of the overturning timescales within the ocean (e.g. Müller et al., 2006) and of the magnitude of the air–sea carbon exchange rate (e.g. Naegler and Levin, 2006; Sweeney et al., 2007; Müller et al., 2008).

The conversion of the radiocarbon production record into Φ requires knowledge on the strength of the geomagnetic field, which together with the open solar magnetic field contributes to the shielding of the earth's atmosphere from the cosmic ray flux. Recently, updated reconstructions of the earth magnetic field have become available (Knudsen et al., 2008; Korte et al., 2011). The palaeo-proxy record of Φ should be consistent with instrumental observations. The deconvolution of the atmospheric ^{14}C history for natural production variations is only possible up to about 1950 AD. Afterwards, the atmospheric ^{14}C content almost doubled due to atomic bomb tests in the fifties and early sixties of the 20th century and uncertainties in this artificial ^{14}C production are larger than natural production variations. This limits the overlap of the ^{14}C-derived palaeo-proxy record of Φ with reconstructions of Φ based on balloon-borne measurements and adds uncertainty to the normalisation of the palaeo-proxy record to recent data. How variations in cosmogenic isotope production and in Φ are related to TSI is unclear and there is a lack of understanding of the mechanisms. This is also reflected in the large spread in past and recent reconstructions of TSI variability on multi-decadal to centennial timescales (e.g. Bard et al., 2000; Lean, 2000; Wang et al., 2005; Steinhilber et al., 2009; Steinhilber et al., 2012; Shapiro et al., 2011; Schrijver et al., 2011). Recent reconstructions based on the decadal-scale trend found in the TSI satellite record reveal small amplitude variations in TSI of the order of $1\,\mathrm{W\,m^{-2}}$ over past millennia (Steinhilber et al., 2009), whereas others based on observations of the most quiet area on the present sun suggest that TSI variations are of the order of $6\,\mathrm{W\,m^{-2}}$ or even more (Shapiro et al., 2011).

The outline of this study is as follows. Next, we will describe the carbon cycle model and methods applied. In the results Sect. 3, we apply sinusoidal variations in atmospheric ^{14}C with frequencies between $1/(5\,\mathrm{yr})$ to $1/(1000\,\mathrm{yr})$. The results characterise the model response to a given radiocarbon time series as any time series can be described by its power spectrum using Fourier transformation.

In Sect. 3.2, we discuss the radiocarbon and carbon inventory and distribution in the model in comparison with observations (Sect. 3.1), before turning to the time evolution of the carbon fluxes, the atmospheric carbon budget, and radiocarbon production in Sect. 3.2. In Sects. 3.3 to 3.5 results are presented for the solar activity, TSI, and simulated, solar-driven changes in global mean surface air temperature over the Holocene and extrapolated TSI variations up to year 2300. Discussion and conclusions follow in Sect. 4 and the

Appendix presents error calculations for ^{14}C production, solar modulation, and TSI in greater detail.

2   Methodology

2.1   Carbon cycle model description

The Bern3D-LPJ climate–carbon-cycle model is an Earth system model of intermediate complexity and includes an energy and moisture balance atmosphere and sea ice model (Ritz et al., 2011), a 3-D dynamic ocean (Müller et al., 2006), a marine biogeochemical cycle (Tschumi et al., 2008; Parekh et al., 2008), an ocean sediment model (Tschumi et al., 2011), and a dynamic global vegetation model (Sitch et al., 2003) (Fig. 1). Total carbon and the stable isotope ^{13}C and the radioactive isotope ^{14}C are transported individually as tracers in the atmosphere–ocean-sediment–land biosphere system.

The geostrophic-frictional balance 3-D ocean component is based on Edwards and Marsh (2005) and as further improved by Müller et al. (2006). It includes an isopycnal diffusion scheme and Gent-McWilliams parametrisation for eddy-induced transport (Griffies, 1998). Here, a horizontal resolution of 36×36 grid boxes and 32 layers in the vertical is used. Wind stress is prescribed according to the monthly climatology from NCEP/NCAR (Kalnay et al., 1996). Thus, changes in ocean circulation in response to changes in wind stress under varying climate are not simulated.

The atmosphere is represented by a 2-D energy and moisture balance model with the same horizontal resolution as the ocean (Ritz et al., 2011). Following Weaver et al. (2001), outgoing long-wave radiative fluxes are parametrised after Thompson and Warren (1982) with additional radiative forcings due to CO_2, other greenhouse gases, volcanic aerosols, and a feedback parameter, chosen to produce an equilibrium climate sensitivity of $3\,^\circ\mathrm{C}$ for a nominal doubling of CO_2. The past extent of Northern Hemisphere ice sheets is prescribed following the ICE4G model (Peltier, 1994) as described in Ritz et al. (2011).

The marine biogeochemical cycling of carbon, alkalinity, phosphate, oxygen, silica, and of the carbon isotopes is detailed by Parekh et al. (2008) and Tschumi et al. (2011). Remineralisation of organic matter in the water column as well as air–sea gas exchange is implemented according to the OCMIP-2 protocol (Orr and Najjar, 1999; Najjar et al., 1999). However, the piston velocity now scales linear (instead of a quadratic dependence) with wind speed following Krakauer et al. (2006). The global mean air–sea transfer rate is reduced by 17 % compared to OCMIP-2 to match observation-based estimates of natural and bomb-produced radiocarbon (Müller et al., 2008), and is in agreement with other studies (Sweeney et al., 2007; Krakauer et al., 2006; Naegler and Levin, 2006). As fractionation of $^{14}CO_2$ is not taken into account during air–sea gas exchange, the air–sea fluxes are corrected in postprocessing using ^{13}C, for which
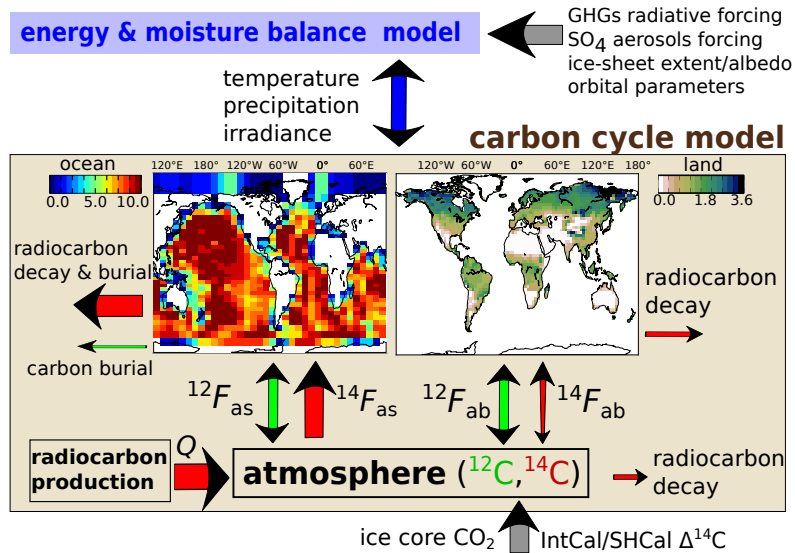
Fig. 1. Setup of the Bern3D-LPJ carbon-cycle–climate model. Grey arrows denote externally applied forcings resulting from variations in greenhouse gas concentrations and aerosol loading, orbital parameters, ice sheet extent, sea level and atmospheric CO_2 and $\Delta^{14}C$. The atmospheric energy and moisture balance model (blue box and arrows) communicates interactively the calculated temperature, precipitation and irradiance to the carbon cycle model (light brown box). The production and exchange fluxes of radiocarbon (red) and carbon (green) within the carbon cycle model are sketched by arrows, where the width of the arrows indicates the magnitude of the corresponding fluxes in a preindustrial steady state. The two maps show the depth-integrated inventories of the preindustrial ^{14}C content in the ocean and land modules in units of $10^3 \, \mathrm{mol}^{14}\mathrm{C} \, \mathrm{m}^{-2}/^{14}R_{\mathrm{std}}$.

the fractionation is explicitly calculated in the model. Prognostic formulations link marine productivity and export production of particulate and dissolved organic matter (POM, DOM) to available nutrients (P, Fe, Si), temperature, and light in the euphotic zone. Carbon is represented as tracers of dissolved inorganic carbon (DIC), DIC-13 and DIC-14, and labile dissolved organic carbon (DOC), DOC-13 and DOC-14. Particulate matter (POM and $CaCO_3$) is remineralised/dissolved in the water column applying a Martin-type power-law curve.

A 10-layer sediment diagenesis model (Heinze et al., 1999; Gehlen et al., 2006) is coupled to the ocean floor, dynamically calculating the advection, remineralisation/redissolution and bioturbation of solid material in the top 10 cm ($CaCO_3$, POM, opal and clay), as well as porewater chemistry and diffusion as described in detail in Tschumi et al. (2011). In contrast to the setup in Tschumi et al. (2011), the initial alkalinity inventory in the ocean is increased from 2350 to 2460 µmol kg^{-1} in order to get a realistic present-day DIC inventory (Key et al., 2004).

The land biosphere model is based on the Lund–Potsdam–Jena (LPJ) dynamic global vegetation model with a resolution of $3.75° \times 2.5°$ as used in Joos et al. (2001), Gerber et al. (2003), Joos et al. (2004) and described in detail in Sitch et al. (2003). The fertilisation of plants by CO_2

is calculated according to the modified Farquhar scheme (Farquhar et al., 1980). A land-use conversion module has been added to take into account anthropogenic land cover change (Strassmann et al., 2008; Stocker et al., 2011). ^{14}C is implemented following the implementation of ^{13}C (Scholze et al., 2003) and taking into account radioactive decay using a mean lifetime of 8267 yr. Fractionation is twice as large for ^{14}C than for ^{13}C. Fractionation during assimilation depends on the photosynthesis pathways (C3 versus C4) and on stomatal conductance. No fractionation is associated with the transfer of carbon between the different pools in vegetation and soils.

2.2 Experimental protocol

The transient simulations are started at 21 kyr BP well before the analysis period for the production (10 to 0 kyr BP) to account for memory effects associated with the long lifetime of radiocarbon (8267 yr) and the millennial timescales of ocean sediment interactions.

The model is initialised as follows. (i) The ocean–atmosphere system is brought into preindustrial (PI) steady state (Ritz et al., 2011). (ii) The ocean's biogeochemical and sediment component is spun up over 50 kyr. During this spin-up phase, the loss of tracers due to solid material seafloor burial is compensated by spatially uniform weathering fluxes
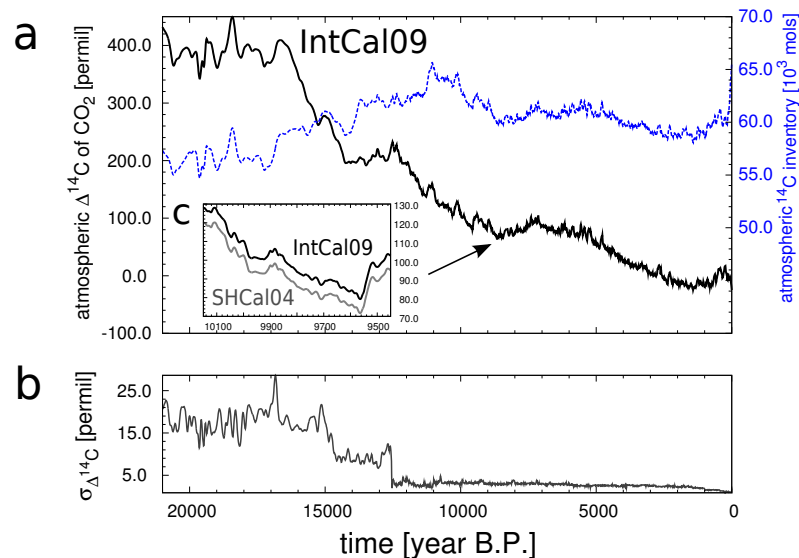
Fig. 2. (a) Reconstructed atmospheric Δ^{14}C of CO$_2$ (black, left axis) and the atmospheric radiocarbon inventory (blue, right axis) over the past 21 kyr. From 21 to 11 kyr BP, radiocarbon data are from IntCal09 (Reimer et al., 2009). Afterward, we use IntCal09 data for the Northern Hemisphere and SHCal04 (McCormac et al., 2004) for the Southern Hemisphere, thereby taking into account the interhemispheric gradient of approximately 8 ‰ and hemisphere-specific anthropogenic depletion of ^{14}C during the industrial period. The two records are not distinguishable in this figure because of their proximity – see **(c)** for a zoom-in. The atmospheric radiocarbon inventory is computed from the Δ^{14}C records and the CO$_2$ record from Monnin et al. (2004). **(b)** The 1σ error assigned to the Δ^{14}C record and used as input for the Monte Carlo uncertainty analysis.

to the surface ocean. These weathering input fluxes are diagnosed at the end of the sediment spin-up and kept constant thereafter. (iii) The coupled model is forced into a LGM state by applying corresponding orbital settings, GHG radiative forcing, freshwater relocation from the ocean to the ice sheets and a LGM dust influx field. Atmospheric trace gases CO$_2$ (185 ppm), δ^{13}C (-6.4 ‰) and Δ^{14}C (432 ‰) are prescribed. The model is then allowed to re-equilibrate for 50 kyr.

Next, the model is integrated forward in time from 21 kyr BP until 1950 AD using the following natural and anthropogenic external forcings (Figs. 2, 3 and 4): atmospheric CO$_2$ as compiled by Joos and Spahni (2008), ^{13}CO$_2$ (Francey et al., 1999; Elsig et al., 2009; Schmitt et al., 2012), Δ^{14}C of CO$_2$ (McCormac et al., 2004; Reimer et al., 2009), orbital parameters (Berger, 1978), radiative forcing due to GHGs CO$_2$, CH$_4$ and N$_2$O (Joos and Spahni, 2008). Iron fertilisation is taken into account by interpolating LGM (Mahowald et al., 2006) and modern dust forcing (Luo et al., 2003) following a spline-fit to the EPICA Dome C (EDC) dust record (Lambert et al., 2008). Shallow water carbonate deposition history is taken from Vecsei and Berger (2004). The ice sheet extent (including freshwater relocation and albedo changes) during the deglaciation is scaled between LGM and modern fields of Peltier (1994) using the benthic δ^{18}O stack of Lisiecki

and Raymo (2005) which was low-pass filtered with a cutoff period of 10 kyr. From 850 to 1950 AD, volcanic aerosols (based on Crowley, 2000, prepared by UVic), sulfate aerosol forcing applying the method by Reader and Boer (1998) detailed by Steinacher (2011), total solar irradiance forcing from PMIP3/CMIP5 (Wang et al., 2005; Delaygue and Bard, 2011) and carbon emissions from fossil fuel and cement production are taken into account (Andres et al., 1999).

The land module is forced by a 31 yr monthly Climatic Research Unit (CRU) climatology for temperature, precipitation and cloud cover. On this CRU-baseline climatology, we superpose interpolated anomalies from snapshot simulations performed with the HadCM3 model (Singarayer and Valdes, 2010). In addition, global mean temperature deviations with respect to 850 AD are used to scale climate anomaly fields obtained from global warming simulations with the NCAR AOGCM from 850 to 1950 AD applying a linear pattern scaling approach (Joos et al., 2001). Changes in sea level and ice sheet extent influence the number and locations of grid cells available for plant growth and carbon storage; we apply interpolated land masks from the ICE5G-VM2 model (Peltier, 2004). Anthropogenic land cover change during the Holocene is prescribed following the HYDE 3.1 dataset (Klein Goldewijk, 2001; Klein Goldewijk and van Drecht, 2006).
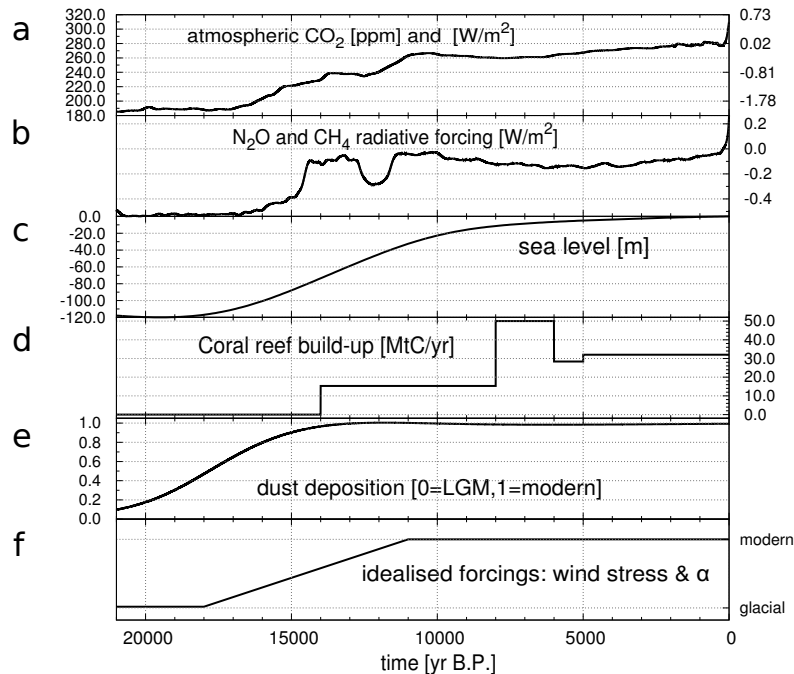
Fig. 3. Main forcings affecting the (preindustrial) Holocene carbon cycle. For completeness, the time series are shown starting from the LGM, i.e. the starting point of our transient simulations. **(a)** Atmospheric CO_2 used both for the radiative forcing as well as for the biogeochemical code, **(b)** radiative forcing of CH_4 and N_2O reported as deviation from preindustrial values, **(c)** sea level record, **(d)** shallow water carbonate deposition, **(e)** (smoothed and normalised) EDC dust record to interpolate between LGM and modern dust deposition fields, and **(f)** hypothetical wind stress/remineralisation depth exponent (α) forcings used for experiments CIRC/BIO. The reader is referred to the main text for details and references to the individual forcing components.

In all transient simulations, the model's atmosphere is forced with the IntCal09 (21 kyr BP to 1950 AD, Reimer et al., 2009) and SHCal04 (11 kyr BP to 1950 AD, McCormac et al., 2004) records for the Northern and Southern Hemisphere, respectively (Fig. 2a). For the equatorial region (20° N to 20° S), we use the arithmetic mean of these two records. Since SHCal04 does not reach as far back in time as the IntCal09 record, we use IntCal09 data for both hemispheres before 11 kyr BP. Between the 5 yr spaced datapoints given by these records, cubic interpolation is applied.

The Earth system underwent a major reorganisation during the last glacial termination as evidenced by warming, ice sheet retreat, sea level rise and an increase in CO_2 and other GHGs (Shackleton, 2001; Clark et al., 2012). Memory effects associated with the long lifetime of radiocarbon (8267 yr) and the long timescales involved in ocean sediment interactions imply that processes during the last glacial termination (ca. 18 to 11 kyr BP) influence the evolution of carbon and radiocarbon during the Holocene (Menviel and Joos, 2012). Although many hypotheses are discussed in the literature on the mechanism governing the deglacial CO_2 rise (e.g. Köhler et al., 2005; Brovkin et al., 2007; Tagliabue

et al., 2009; Bouttes et al., 2011; Menviel et al., 2012), it remains unclear how individual processes have quantitatively contributed to the reconstructed changes in CO_2 and $^{14}CO_2$ over the termination. The identified processes may be distinguished into three classes: (i) relatively well-known mechanisms such as changes in temperature, salinity, an expansion of North Atlantic Deep Water, sea ice retreat, a reduction in iron input and carbon accumulation on land as also represented in our standard model setup; (ii) an increase in deep ocean ventilation over the termination as suggested by a range of proxy data (e.g. Franois et al., 1997; Adkins et al., 2002; Hodell et al., 2003; Galbraith et al., 2007; Anderson et al., 2009; Schmitt et al., 2012; Burke and Robinson, 2012) and modelling work (e.g. Tschumi et al., 2011); (iii) a range of mechanisms associated with changes in the marine biological cycling of organic carbon, calcium carbonate, and opal in addition to those included in (i).

The relatively well-known forcings implemented in our standard setup explain only about half of the reconstructed CO_2 increase over the termination (Menviel et al., 2012). This indicates that the model misses important processes or feedbacks concerning the cycling of carbon in the ocean. To
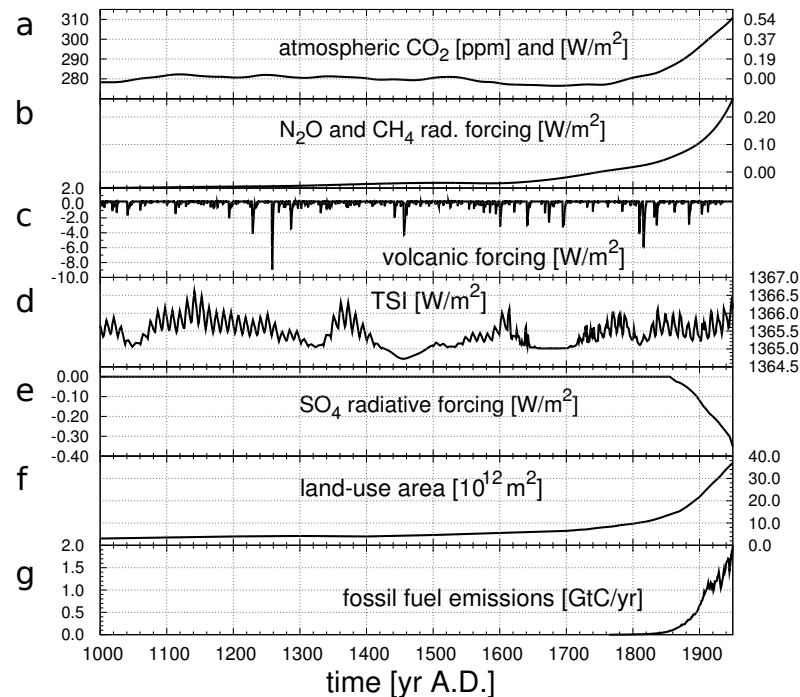
Fig. 4. Forcings for the last millennium including the industrial period: **(a)** atmospheric CO_2 used both for the radiative forcing as well as for the biogeochemical code, **(b)** radiative forcing of CH_4 and N_2O reported as deviation from preindustrial values, **(c)** volcanic forcing, **(d)** solar forcing, **(e)** SO_4 radiative forcing, **(f)** anthropogenic land-use area and **(g)** carbon emissions from fossil fuel use (including cement production). The reader is referred to the main text for details and references to the individual forcing components.

this end, we apply two idealised scenarios for this missing mechanism, regarded as bounding cases in terms of their impacts on atmospheric Δ^{14}C. In the first scenario, termed CIRC, the atmospheric carbon budget over the termination is approximately closed by forcing changes in deep ocean ventilation. In the second, termed BIO, the carbon budget is closed by imposing changes in the biological cycling of carbon.

^{14}C in the atmosphere and the deep ocean is sensitive to the surface-to-deep transport of ^{14}C. This ^{14}C transport is dominated by physical transport (advection, diffusion, convection), whereas biological fluxes play a small role. Consequently, processes reducing the thermohaline circulation (THC), the surface-to-deep transport rate, and deep ocean ventilation tend to increase Δ^{14}C of atmospheric CO_2 and to decrease Δ^{14}C of DIC in the deep. Recently, a range of observational studies addressed deglacial changes in radiocarbon and deep ocean ventilation. Some authors report extremely high ventilation ages up to 5000 yr (Marchitto et al., 2007; Bryan et al., 2010; Skinner et al., 2010; Thornalley et al., 2011), while others find no evidence for such an old abyssal water mass (De Pol-Holz et al., 2010). In contrast, changes in processes related to the biologic cycle of carbon

such as changes in export production or the remineralisation of organic carbon hardly affect Δ^{14}C of DIC and CO_2, despite their potentially strong impact on atmospheric CO_2 (e.g. Tschumi et al., 2011).

Technically, these two bounding cases are realised as follows. In the experiment BIO, we imply (in addition to all other forcings) a change in the depth where exported particulate organic matter is remineralised; the exponent (α) in the power law describing the vertical POM flux profile (Martin curve) is increased during the termination from a low glacial value (Fig. 3f). A decrease in the average remineralisation depth over the termination leads to an increase in atmospheric CO_2 (Matsumoto, 2007; Kwon et al., 2009; Menviel et al., 2012), but does not substantially affect Δ^{14}C. α is increased from 0.8 to 1.0 during the termination in BIO, while in the other experiments α is set to 0.9. In the experiment CIRC, ocean circulation is strongly reduced at the LGM by reducing the wind stress globally by 50 % relative to modern values. The wind stress is then linearly relaxed to modern values over the termination (18 to 11 kyr BP, Fig. 3f). This leads to a transfer of old carbon from the deep ocean to the atmosphere, raising atmospheric CO_2 and lowering Δ^{14}C of CO_2 (Tschumi et al., 2011). We stress that changes

in wind stress and remineralisation depth are used here as tuning knobs and not considered as realistic.

To further assess the sensitivity of the diagnosed radiocarbon production on the cycling of carbon and climate, we perform a control simulation (CTL) where all forcings except atmospheric CO_2 (and isotopes) are kept constant at PI values. This setup corresponds to earlier box model studies where the Holocene climate was assumed to be constant.

As noted, the transient evolution of atmospheric CO_2 and $\Delta^{14}C$ over the glacial termination is prescribed in all three setups (CTL, CIRC, BIO). Thus, the influence of changing conditions over the last glacial termination on Holocene ^{14}C dynamics is taken into account, at least to a first order, in each of the three setups.

2.3 The production rate of radiocarbon, Q

The ^{14}C production rate Q is diagnosed by solving the atmospheric ^{14}C budget equation in the model. The model calculates the net fluxes from the atmosphere to the land biosphere ($^{14}F_{ab}$) and to the ocean ($^{14}F_{as}$) under prescribed $^{14}CO_2$ for a given carbon-cycle/climate state. Equivalently, the changes in ^{14}C inventory and ^{14}C decay of individual land and ocean carbon reservoirs are computed. Data-based estimates for the ocean and land inventory are used to match preindustrial radiocarbon inventories as closely as possible. The production rate is then given at any time t by:

$$Q(t) = \frac{I_{\mathrm{atm,data}}(t)}{\tau} + \frac{dI_{\mathrm{atm,data}}(t)}{dt} + {}^{14}F_{\mathrm{budget}}(t)$$
$$\left. \begin{array}{l} + \frac{I_{\mathrm{ocn,model}}(t)}{\tau} + \frac{dI_{\mathrm{ocn,model}}(t)}{dt} + \frac{\Delta I_{\mathrm{ocn,data\text{-}model}}(t=t_0)}{\tau} \\ + \frac{I_{\mathrm{sed,model}}(t)}{\tau} + \frac{dI_{\mathrm{sed,model}}(t)}{dt} + {}^{14}F_{\mathrm{burial}}(t) \end{array} \right\} = {}^{14}F_{\mathrm{as}}$$
$$+ \frac{I_{\mathrm{lnd,model}}(t)}{\tau} + \frac{dI_{\mathrm{lnd,model}}(t)}{dt} + \frac{\Delta I_{\mathrm{lnd,data\text{-}model}}(t=t_0)}{\tau} = {}^{14}F_{\mathrm{ab}}. \quad (1)$$

Here, I and F denote ^{14}C inventories and fluxes, and τ (8267 yr) is the mean ^{14}C lifetime with respect to radioactive decay. Subscripts atm, ocn, sed, and lnd refer to the atmosphere, the ocean, reactive ocean sediments, and the land biosphere, respectively. Subscript data indicates that terms are prescribed from reconstructions and subscript model that values are calculated with the model. $^{14}F_{\mathrm{burial}}$ is the net loss of ^{14}C associated with the weathering/burial carbon fluxes. $\Delta I_{\mathrm{ocn,data\text{-}model}}(t=t_0)$ represents a (constant) correction, defined as the difference between the modelled and observation-based inventory of $DI^{14}C$ in the ocean plus an estimate of the ^{14}C inventory associated with refractory DOM not represented in our model. In analogue, $\Delta I_{\mathrm{lnd,data\text{-}model}}(t=t_0)$ denotes a constant ^{14}C decay rate associated with terrestrial carbon pools not simulated in our model. $^{14}F_{\mathrm{budget}}$ is a correction associated with the carbon flux diagnosed to close remaining imbalances in the atmospheric CO_2 budget.

2.3.1 Observation-based versus simulated ocean radiocarbon inventory

The global ocean inorganic radiocarbon inventory is estimated using the gridded data provided by GLODAP for the preindustrial state (Key et al., 2004) and in situ density calculated from World Ocean Atlas 2009 (WOA09) temperature and salinity fields (Antonov et al., 2010; Locarnini et al., 2010). Since the entire ocean is not covered by the GLODAP data, we fill these gaps by assuming the global mean ^{14}C concentration in these regions (e.g. in the Arctic Ocean). The result of this exercise is 3.27×10^6 mol of $DI^{14}C$. Hansell et al. (2009) estimated a global refractory DOC inventory of 624 Gt C. $\Delta^{14}C$ of DOC measurements are rare, but data in the central North Pacific (Bauer et al., 1992) suggest high radiocarbon ages of ~ 6000 yr, corresponding to a $\Delta^{14}C$ value of $\sim -530\,\text{‰}$. Taking this value as representative yields an additional 2.9×10^4 mol ^{14}C. The preindustrial ^{14}C inventory associated with labile DOM is estimated from our model results to be 1.3×10^3 mol ^{14}C. This yields a data-based radiocarbon inventory associated with DIC and labile and refractory DOM in the ocean of 3.30×10^6 mol. The corresponding preindustrial modelled ocean inventory yields 3.05×10^6 mol for BIO, 3.32×10^6 mol for CIRC and 3.10×10^6 mol for CTL. Thus, the correction $\Delta I_{\mathrm{ocn,data\text{-}model}}(t=t_0)$ is less than 8 % in the case of BIO and less than 1 % for CIRC and CTL.

2.3.2 Observation-based versus simulated terrestrial radiocarbon inventory

As our model for the terrestrial biosphere does not include carbon stored as peatlands and permafrost soils. We estimate this pool to contain approximately 1000 Gt C of old carbon with a isotopic signature of $-400\,\text{‰}$ (thus roughly one half-life old). Although small compared to the uncertainty in the oceanic inventory, we include these 5.9×10^4 mol of ^{14}C in our budget as a constant correction $\Delta I_{\mathrm{lnd,data\text{-}model}}(t=t_0)$.

2.3.3 Closing the atmospheric CO_2 budget

The atmospheric carbon budget is closed in the transient simulations by diagnosing an additional carbon flux F_{budget}:

$$F_{\mathrm{budget}} = -\frac{dN_{\mathrm{atm,data}}}{dt} - E + F_{\mathrm{as}} + F_{\mathrm{ab}} \quad (2)$$

where the change in the atmospheric carbon inventory (dN_{atm}/dt) is prescribed from ice core data, E are fossil fuel carbon emissions, and F_{as} and F_{ab} the net carbon fluxes into the ocean and the land biosphere. The magnitude of this inferred emission indicates the discrepancy between modelled and ice core CO_2 and provides a measure of how well the model is able to simulate the reconstructed CO_2 evolution. We assign to this flux (of unknown origin) a $\Delta^{14}C$ equal the contemporary atmosphere and an associated uncertainty in

Δ^{14}C of ± 200‰. This is not critical as F_{budget} and associated uncertainties in the ^{14}C budget are generally small over the Holocene for simulations CIRC and BIO (see Appendix Fig. A1e).

The production rate is either reported as $\mathrm{mol\,yr^{-1}}$ or alternatively atoms $\mathrm{cm^{-2}\,s^{-1}}$. The atmospheric area is set to $5.10 \times 10^{14}\,\mathrm{m^2}$ in our model, therefore the two quantities are related as $1\,\mathrm{atom\,cm^{-2}\,s^{-1}} = 267.0\,\mathrm{mol\,yr^{-1}}$.

2.4 Solar activity

Radiocarbon, as other cosmogenic radionuclides, are primarily produced at high latitudes of earth's upper atmosphere due to nuclear reactions induced by high-energy galactic cosmic rays (GCR). Far away from the solar system, this flux is to a good approximation constant in time, but the intensity reaching the earth is modulated by two mechanism: (i) the shielding effect of the geomagnetic dipole field and (ii) the modulation due to the magnetic field enclosed in the solar wind. By knowing the past history of the geomagnetic dipole moment and the production rate of radionuclides, the "strength" of solar activity can therefore be calculated.

The sun's activity is parametrised by a scalar parameter in the force field approximation, the so-called solar modulation potential Φ (Gleeson and Axford, 1968). This parameter describes the modulation of the local interstellar spectrum (LIS) at 1 AU. A high solar activity (i.e. a high value of Φ) leads to a stronger magnetic shielding of GCR and thus lowers the production rate of cosmogenic radionuclides. Similarly, the production rate decreases with a higher geomagnetic shielding, expressed as the virtual axis dipole moment (VADM).

The calculation of the normalised (relative to modern) Q for a given VADM and Φ is based on particle simulations performed by Masarik and Beer (1999). This is the standard approach to convert cosmogenic radionuclide production rates into solar activity as applied by Muscheler et al. (2007), Steinhilber et al. (2008) and Steinhilber et al. (2012), but differs from the model to reconstruct TSI recently used by Vieira et al. (2011).

The GCR flux entering the solar system is assumed to remain constant within this approach, even though Miyake et al. (2012) found recently evidence for a short-term spike in annual Δ^{14}C. The cause of this spike (Hambaryan and Neuhäuser, 2013; Usoskin et al., 2013) is currently debated in the literature.

At the time of writing, three reconstructions of the past geomagnetic field are available to us spanning the past 10 kyr (Yang et al., 2000; Knudsen et al., 2008; Korte et al., 2011), shown in Fig. 11 together with the VADM value of $8.22 \times 10^{22}\,\mathrm{Am^{-2}}$ for the period 1840–1990 estimated by Jackson et al. (2000). The reconstructions by Yang et al. (2000) and Knudsen et al. (2008), relying both on the same database (GEOMAGIA 50), were extensively used in the past for solar activity reconstructions (Muscheler et al., 2007; Steinhilber et al., 2008; Vieira et al., 2011; Steinhilber et al.,

2012). We use the most recently published reconstruction by Korte et al. (2011) for our calculations.

For conversion from Φ into TSI, we follow the procedure outlined in Steinhilber et al. (2009); Steinhilber et al. (2010) which consists of two individual steps. First, the radial component of the interplanetary magnetic field, B_r, is expressed as a function of Φ:

$$|B_r(t)| = 0.56\,B_{\mathrm{IMF},0} \times \left(\frac{\Phi(t)\,v_{\mathrm{SW},0}}{\Phi_0\,v_{\mathrm{SW}}(t)} \right)^{1/\alpha}$$
$$\times \left[1 + \left(\frac{R_{\mathrm{SE}}\,\omega\,\cos\Psi}{v_{\mathrm{SW}}(t)} \right)^2 \right]^{-\frac{1}{2}}, \qquad (3)$$

where v_{SW} is the (time-dependent) solar wind speed (Steinhilber et al., 2010); $B_{\mathrm{IMF},0}$, Φ_0, $v_{\mathrm{SW},0}$ are normalisation factors; R_{SE} is the mean Sun–Earth distance; ω the angular solar rotation rate; and Ψ the heliographic latitude. The factor 0.56 has been introduced to adjust the field obtained from the Parker theory with observations. The exponent is set to be in the range $\alpha = 1.7 \pm 0.3$ as in Steinhilber et al. (2009).

Second, the B_r–TSI relationship derived by Fröhlich (2009) is used to calculate the total solar irradiance:

$$\mathrm{TSI} = (1364.64 \pm 0.40)\,\mathrm{W\,m^{-2}} + B_r \cdot (0.38 \pm 0.17)\,\mathrm{W\,m^{-2}\,nT^{-1}}. \quad (4)$$

This model of converting B_r (here in units of nanotesla) into TSI is not physically based, but results from a fit to observations for the relatively short epoch where high-quality observational data is available. Note that the B_r–TSI relationship is only valid for solar cycle minima, therefore an artificial sinusoidal solar cycle (with zero mean) has to be added to the (solar-cycle averaged) Φ before applying Eqs. (3) and (4). In the results section, we show for simplicity solar cycle averages (i.e. without the artificial 11 yr solar cycle).

A point to stress is that the amplitude of low-frequency TSI variations is limited by Eq. (4) and small. This is a consequence of the assumption underlying Eq. (4) that recent satellite data, which show a limited decadal-scale variability in TSI, can be extrapolated to past centuries and millennia. Small long-term variations in TSI are in agreement with a range of recent reconstructions (Schmidt et al., 2011), but in conflict with Shapiro et al. (2011), who report much larger TSI variations.

3 Results

3.1 Sensitivity experiments

We start the discussion by analysing the response of the Bern3D-LPJ model to regular sinusoidal changes in the atmospheric radiocarbon ratio. The theoretical background is that any time series can be translated into its power spectrum using Fourier transformation. Thus, the response of the model to perturbations with different frequencies characterises the model for a given state (climate, CO_2, land-use

area, etc.). The experimental setup for this sensitivity simulation is as follows. $\Delta^{14}C$ is varied according to a sine wave with an amplitude of 10‰ and distinct period. The sine wave is repeated until the model response is at equilibrium. Periods between 5 and 1000 yr are selected. Atmospheric CO_2 (278 ppm), climate and all other boundary conditions are kept fixed at preindustrial values. The natural carbon cycle acts like a smoothing filter and changes in atmospheric $\Delta^{14}C$ arising from variations in Q are attenuated and delayed (Fig. 5a). That is the relative variations in $\Delta^{14}C$ are smaller than the relative variations in Q. Here, we are interested in inverting this natural process and diagnosing Q from reconstructed variations in radiocarbon. Consequently, we analyse not the attenuation of the radiocarbon signal, but the amplification of Q for a given variation in atmospheric radiocarbon. Figure 5a shows the amplification in Q, defined as the relative change in Q divided by the relative change in the radiocarbon to carbon ratio, ^{14}R. For example, an amplification of 10 means that if ^{14}R oscillates by 1 %, then Q oscillates by 10 % around its mean value. The amplification is largest for high-frequency variations and decreases from above 100 for a period of 5 yr to around 10 for a period of 1000 yr and to 2 for a period of 10 000 yr. High-frequency variations in the ^{14}C reconstruction arising from uncertainties in the radiocarbon measurements may thus translate into significant uncertainties in Q. We will address this problem in the following sections by applying a Monte Carlo procedure to vary $\Delta^{14}C$ measurements within their uncertainties (see Appendix A1).

The atmospheric radiocarbon anomaly induced by variation in production is partly mitigated through radiocarbon uptake by the ocean and the land. The relative importance of land versus ocean uptake of the perturbation depends strongly on the timescale of the perturbation (Fig. 5b). For annual- to decadal-scale perturbations, the ocean and the land uptake are roughly of equal importance. This can be understood by considering that the net primary productivity on land (60 Gt C per year) is of similar magnitude as the gross air-to-sea flux of CO_2 (57 Gt C per year) into the ocean. Thus, these fluxes carry approximately the same amount of radiocarbon away from the atmosphere. On the other hand, if the perturbation in production is varying slower than the typical overturning timescales of the ocean and the land biosphere, then the radiocarbon perturbation in the ratio is distributed roughly proportional to the carbon inventory of the different reservoirs (or to the steady-state radiocarbon flux to the ocean and the land, i.e. 430 vs. 29.1 mol yr^{-1}). Consequently, the ratio between the ^{14}C flux anomalies into ocean and land, $\Delta F_{as} : \Delta F_{ab}$ (with respect to an unperturbed state), is the higher the lower frequency of the applied perturbation (Fig. 5b). Note that these results are largely independent of the magnitude in the applied $\Delta^{14}C$ variations; we run these experiments with amplitudes of ± 10 and ± 100‰. Assuming a constant carbon cycle and climate, Q can be calculated
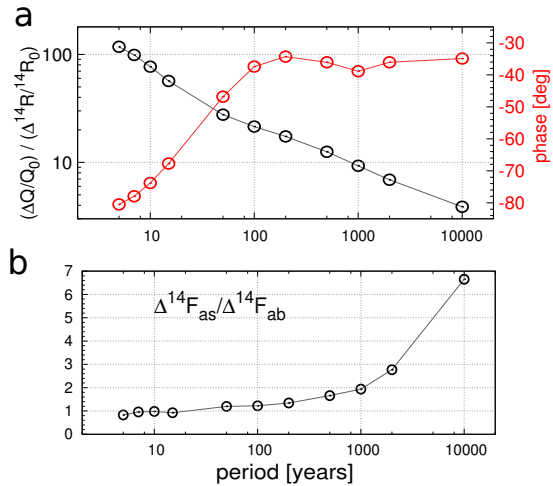

Fig. 5. Response of the Bern3D-LPJ model to periodic sinusoidal variations in the atmospheric radiocarbon ratio (^{14}R) with an amplitude of 10‰ (in units of $\Delta^{14}C$). **(a)** Relative change in production rate, Q, divided by the relative change in ^{14}R (with respect to a PI steady state; black) and the phase shift between Q and ^{14}R (red, left axis); Q is always leading atmospheric ^{14}R. **(b)** Relative changes in the net atmosphere-to-sea (F_{as}) and the net atmosphere-to-land biosphere (F_{ab}) fluxes of ^{14}C for the same simulations.

by replacing the carbon-cycle–climate model by the model-derived Fourier filter (Fig. 5a) (Usoskin and Kromer, 2005).

Preindustrial carbon and radiocarbon inventories

The loss of ^{14}C is driven by the radioactive decay flux in the different reservoirs. The base level of this flux is proportional to the ^{14}C inventory and a reasonable representation of these inventories is thus a prerequisite to estimate ^{14}C production rates. In the following, modelled and observation-based carbon and radiocarbon inventories before the onset of industrialisation are compared (Table 1) and briefly discussed.

The atmospheric ^{14}C inventory is given by the CO_2 and $\Delta^{14}C$ input data and therefore fully determined by the forcing and their uncertainty. The ocean model represents the observation-based estimate of the global ocean ^{14}C inventory within 1 % for the setup CIRC and within 8 % for the setup BIO. These deviations are within the uncertainty of the observational data. Nevertheless, this offset is corrected for when Q is calculated (see Eq. 1).

The model is also able to represent the observation-based spatial distribution of ^{14}C in the ocean (Fig. 7). Both observation and model results show the highest ^{14}C concentrations in the thermocline of the Atlantic Ocean and the lowest concentrations in the deep North Pacific. Deviations between modelled and reconstructed concentrations are less than 5 % and typically less than 2 %. The model shows in general too-high

Table 1. Preindustrial model versus data-based carbon and ^{14}C inventory estimates. The model-based oceanic inventories are calculated as the average of the experiments BIO and CIRC.

	Bern3D-LPJ		Data	
	Carbon [Gt C]	^{14}C [10^5 mol]	Carbon [Gt C]	^{14}C [10^5 mol]
ATM	593	0.591	593[a]	0.591[b]
LND	1930	1.79	2500–3500[c]	
OCN	38 070	32.0	38 200[d]	33.00[d]
	Carbon [Gt C yr^{-1}]	^{14}C [mol yr^{-1}]	Carbon [Gt C yr^{-1}]	^{14}C [mol yr^{-1}]
SED	0.501	52	0.22–0.4[e]	

[a] MacFarling Meure et al. (2006); [b] McCormac et al. (2004); Reimer et al. (2009); [c] Watson (2000); Tarnocai et al. (2009); Yu et al. (2010); [d] Key et al. (2004); Hansell et al. (2009); [e] Sarmiento and Gruber (2006); Feely et al. (2004).

radiocarbon concentrations in the upper 1000 m, while the concentration is lower than indicated by the GLODAP data at depth.

Modelled loss of radiocarbon by sedimentary processes, namely burial of POM and $CaCO_3$ into the diagenetically consolidated zone and particle and dissolution fluxes from/to the ocean, accounts for 52 mol yr^{-1} (or roughly 11 % of the total ^{14}C sink). This model estimate may be on the high side as the ocean-to-sediment net flux in the Bern3D-LPJ model of 0.5 Gt C yr^{-1} is slightly higher than independent estimates in the range of 0.2 to 0.4 Gt C yr^{-1}.

The total simulated carbon stored in living biomass and soils is 1930 Gt C. As discussed above, this is order 1000 Gt C lower than best estimates, mainly because peat and permafrost dynamics (Yu et al., 2010; Spahni et al., 2012) are not explicitly simulated in the LPJ version applied here. The model–data discrepancy in carbon is less than 3 % of the total carbon inventory in ocean, land, and atmosphere. It translates into 5.9×10^5 mol of ^{14}C when assuming a Δ^{14}C of -400 ‰ for this old biomass. This is well within the uncertainty range of the total ^{14}C inventory.

3.2 Transient results for the carbon budget and deep ocean ventilation

Next, we discuss how global mean temperature, deep ocean ventilation, and the carbon budget evolved over the past 21 kyr in our two bounding simulations (CIRC and BIO). Global average surface air temperature (SAT, Fig. 6a) and sea surface temperature (SST, not shown) are simulated to increase by $\sim 0.8\,°C$ over the Holocene. In experiment CIRC, the global energy balance over the termination is strongly influenced by the enforced change in wind stress and the simulated deglacial increase in SAT is almost twice as large in experiment CIRC than in BIO. This is a consequence of a much larger sea ice cover and a higher planetary albedo at LGM in experiment CIRC than BIO. Circulation is slow under the prescribed low glacial wind stress and less heat is transported to high latitudes and less ice is exported from the Southern Ocean to lower latitudes in CIRC than BIO. In other words, the sea-ice–albedo feedback is much larger in CIRC than BIO.

Deep ocean ventilation evolves very differently in CIRC than in BIO (Fig. 6b). Here, we analyse the global average ^{14}C age difference of the deep ocean (i.e. waters below 2000 m depth) relative to the overlying surface ocean. The surface-to-deep age difference is recorded in ocean sediments as ^{14}C age offset between shells of benthic and planktonic (B-P) species. Results from the CTL experiment with time-invariant ocean ventilation show that this "proxy" is not an ideal age tracer; the B-P age difference is additionally influenced by transient atmospheric Δ^{14}C changes and varies between 600 and 1100 yr in CTL.

The wind-stress forcing applied in experiment CIRC leads to an almost complete shutdown of the THC during the LGM and a recovery to Holocene values over the termination. Simulated B-P age increases from 2000 yr at LGM to peak at 2900 yr by 16.5 kyr BP. A slight and after 12 kyr BP a more pronounced decrease follows to the late Holocene B-P age of about 1000 yr. B-P variations are much smaller in simulation BIO, as no changes in wind stress are applied; B-P age varies between 1000 and 1700 yr.

$\Delta\Delta^{14}$C, i.e. the global mean difference in Δ^{14}C between the deep ocean and the atmosphere is -500 ‰ in CIRC until Heinrich Stadial 1 (HS1) (-350 ‰ in BIO), followed by a sharp increase of approximately 150–200 ‰ and a slow relaxation to late-Holocene values (~ -170 ‰). This behaviour is also present in recently analysed sediment cores, see e.g. Burke and Robinson (2012) and references therein. The sharp increase in $\Delta\Delta^{14}$C following HS1 is mainly driven by the prescribed fast atmospheric drop (Broecker and Barker, 2007).

The forcings prescribed in our bounding experiments CIRC and BIO are broadly sufficient to reproduce the reconstructed deglacial CO_2 increase. This is evidenced by an analysis of the atmospheric carbon budget (Fig. 6d and f). In the control simulation (CTL) an addition of 1700 Gt C is required to close the budget. In contrast, the mismatch in the budget is close to zero for BIO and about -100 Gt C for CIRC at the end of the simulation. In other words, only small emissions from unknown origin have to be applied on average to close the budget. Both experiments need a CO_2 sink in the early Holocene as indicated by the negative missing emissions. Such a sink could have been the carbon uptake of Northern Hemisphere peatlands (Yu et al., 2010), as peatland dynamics are not included in this model version. In summary, simulation CIRC corresponds to the picture of a slowly ventilated ocean during the LGM, whereas deep ocean ventilation changes remain small in BIO and are absent in the CTL simulation. The atmospheric carbon budget is approximately
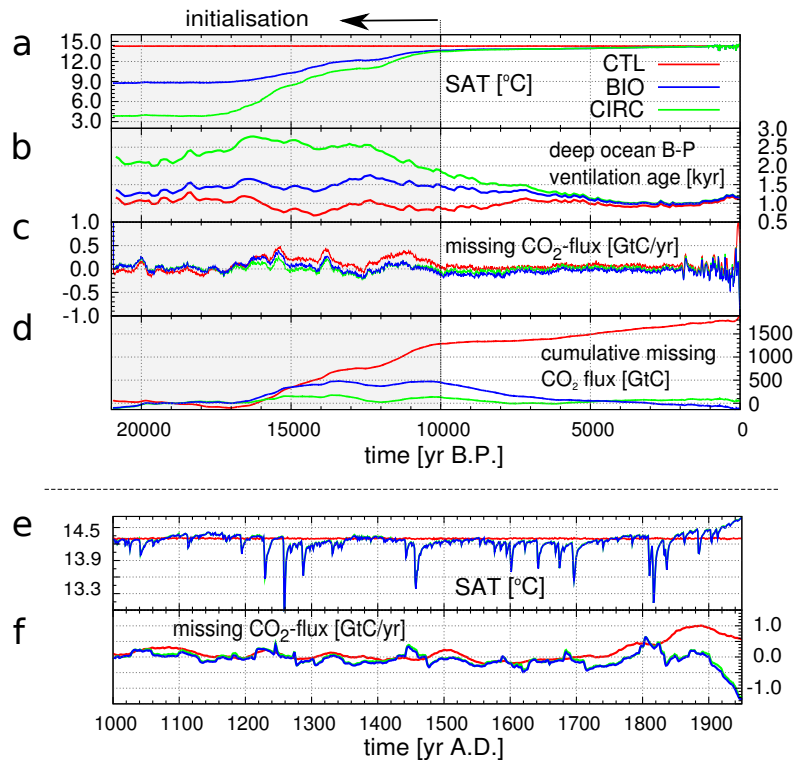
Fig. 6. Transient model response during the past 21 kyr of **(a)** global mean surface air temperature (SAT), **(b)** globally averaged benthic-planktonic (surface-deep) reservoir age calculated as ^{14}C age offset from the global ocean below 2000 m relative to the surface ocean, **(c)** implied carbon flux to solve the atmospheric budget (F_{budget}) and **(d)** cumulative sum thereof for the experiments BIO, CIRC and the control run CTL. For the last millennium, SAT and F_{budget} is shown in detail in the lower two panels **(e, f)**. The grey shaded area indicates the period used to initialise the model. The radiocarbon production rate is diagnosed only for the last 10 kyr.

closed in simulations CIRC and BIO, whereas a substantial external carbon input is required in simulation CTL. These three simulations provide thus three radically different evolutions of the carbon cycle over the past 21 kyr and will serve us to assess uncertainties in inferred radiocarbon production rates due to our incomplete understanding of the past carbon cycle.

3.2.1 Time evolution of the radiocarbon production rate

Total inferred radiocarbon production, Q, varies between 350 and 650 mol yr^{-1} during the Holocene (Fig. 8d). Variations on multi-decadal to centennial timescales are typically within 100 mol yr^{-1}. The differences in Q in the early Holocene between the model setups CIRC, BIO, and CTL are mainly explained by offsets in the absolute value of Q, while the timing and magnitude of multi-decadal to centennial variations are very similar for the three setups. The absolute value of Q is about 40 mol yr^{-1} higher in CIRC than in BIO and about 60 mol yr^{-1} higher in CIRC than in CTL

at 10 kyr BP. This difference becomes very small in the late Holocene and results are almost identical for CIRC and BIO after 4 kyr BP. Note that the absolute (preindustrial) value of the production rate is equal in all three setups per definition (see Eq. 1).

The inferred Q is assigned according to Eq. (1) to individual contributions from a net ^{14}C flux from the atmosphere to the ocean ($^{14}F_{\text{as}}$), a net flux to the land ($^{14}F_{\text{ab}}$), and atmospheric loss terms (Fig. 8). Variations in these three terms contribute about equally to variations in Q on decadal to centennial timescales, whereas millennial-scale variations in Q are almost entirely attributed to changes in $^{14}F_{\text{as}}$. This is in agreement with the results from the Fourier analysis presented in Sect. 3.1. Holocene and preindustrial mean fluxes and their temporal variance are listed in Table 2.

The oceanic component entering the calculation of Q is threefold (Fig. 9): (i) the compensation of the DI^{14}C (and a small contribution of DO^{14}C) decay proportional to its inventory, (ii) changes in the inventory of ^{14}C itself mainly driven by F_{as} and (iii) the export, rain and subsequent burial
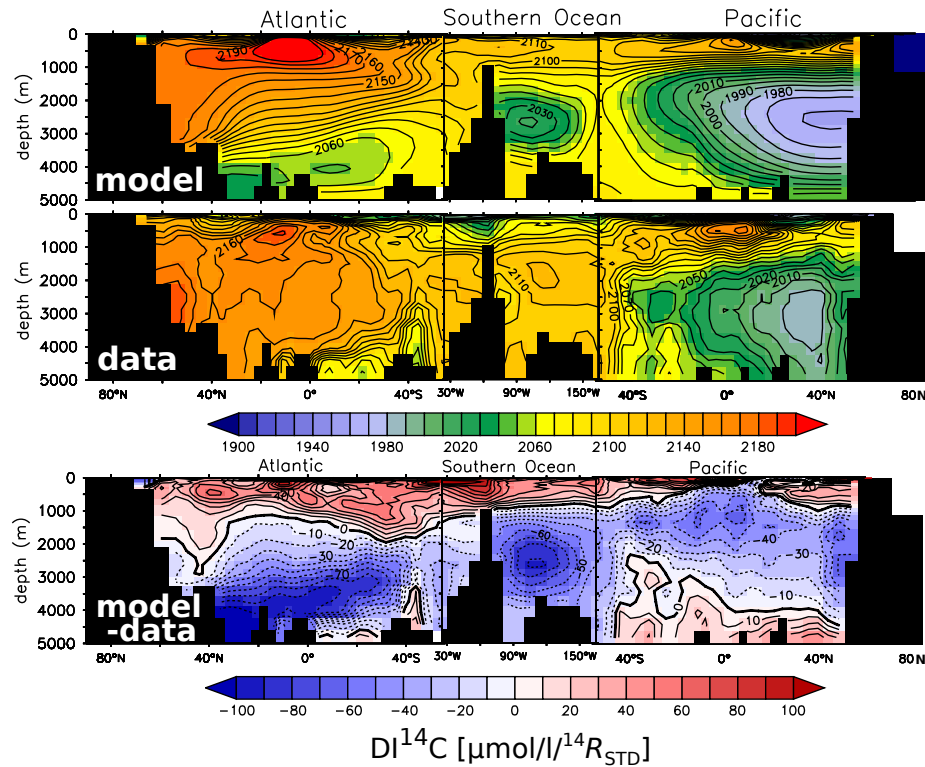
Fig. 7. Comparison of modern modelled and data-based (GLODAP,WOA09) oceanic distribution of ^{14}C in its dominant form of dissolved inorganic carbon (DI^{14}C) along a transect through the Atlantic, Southern Ocean and Pacific. The lowest panel shows the model–data difference.

Table 2. The atmospheric radiocarbon budget (positive numbers: loss of ^{14}C) averaged over the last 10 kyr and for preindustrial times (1750–1900 AD). The statistical uncertainty becomes negligible due to the averaging over hundreds of datapoints and is not given here. Instead, we report $\sqrt{\text{VAR}}$ (where VAR is the variance in time) to quantify the temporal variability of the corresponding fluxes. The bulk uncertainty in the time-averaged fluxes can be estimated by the uncertainty in the corresponding radiocarbon reservoirs and is of the order of 15 % (1σ), except for the atmospheric component which is tightly constrained by data.

^{14}C loss [mol yr^{-1}]	Holocene (10–0 kyr BP)		Preindustrial (1750–1900 AD)	
	Best guess	$\sqrt{\text{VAR}}$	Best guess	$\sqrt{\text{VAR}}$
$^{14}F_{as}$	436	27	451	33
$^{14}F_{ab}$	25	25	−6.9	47
ATM	11	23	24	44
Total	472	57	468	35

of Ca^{14}CO$_3$ and PO^{14}C. Thus, the mentioned offset in $^{14}F_{as}$ between CIRC and BIO at the early Holocene are the result of differences in the dynamical evolution of the whole-ocean DIC inventories and its Δ^{14}C signature. During LGM conditions, the oceanic ^{14}C inventory is larger for BIO than CIRC as the deep ocean is more depleted in the slowly overturning ocean of setup CIRC. Accordingly the decay of ^{14}C and $^{14}F_{as}$ is higher in simulation BIO than in CIRC (Fig. 9). The simulated oceanic ^{14}C inventory decreases both in CIRC and BIO as the (prescribed) atmospheric Δ^{14}C decreases. However, this decrease is smaller in CIRC than in BIO as the enforced increase in the THC and in ocean ventilation in CIRC leads to an additional ^{14}C flux into the ocean. In addition, the strengthened ventilation leads to a peak in organic matter export and burial while the reduced remineralisation depth in BIO leads to the opposite effect (as less POM is reaching the seafloor). In total, the higher oceanic radiocarbon decay in BIO is overcompensated by the (negative) change of the oceanic inventory. Enhanced sedimentary loss of ^{14}C in CIRC further increases the offset, finally leading to a higher Q at 10 kyr BP of ~ 40 mol yr^{-1} in CIRC than in BIO. This
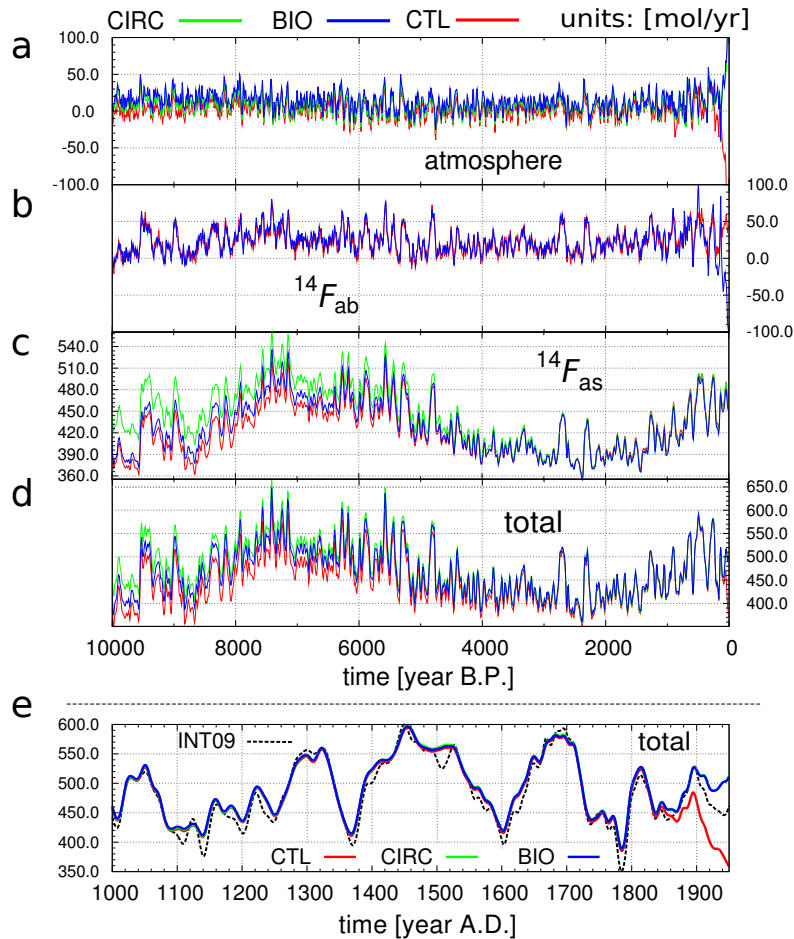
Fig. 8. Holocene ^{14}C fluxes in mol ^{14}C yr^{-1} for the different experiments: **(a)** changes and decay of the atmospheric inventory (including F_{budget}), **(b)** air–biosphere flux (F_{ab}), **(c)** air–sea flux (F_{as}) and **(d)** the sum of these contributions yielding the total production rate Q. **(e)** shows the last 1000 yr in greater detail together with an experiment (INT09) where the entire globe is forced with the Northern Hemisphere dataset IntCal09 (dashed line), thereby neglecting the interhemispheric gradient in Δ^{14}C. Note that the time series shown in **(a)** and **(b)** have been smoothed with a cutoff of 40 yr (only for the visualisation) while **(c)**–**(e)** show 20 yr smoothed data as described in the main text.

offset has vanished almost completely at 7 kyr BP, apart from a small contribution from sedimentary processes.

In general, the influence of climate induced carbon cycle changes is modest in the Holocene. This is indicated by the very similar Q in the CTL experiment. The biggest discrepancy between results from CTL versus those from CIRC and BIO emerge during the industrial period. Q drops rapidly in CTL as the combustion of the radiocarbon-depleted fossil fuel is not explicitly included.

In a further sensitivity run, the influence of the interhemispheric Δ^{14}C gradient on Q is explored (Fig. 8e; dashed line). In simulation INT09 the Northern Hemisphere dataset IntCal09 is applied globally and all other forcings are as in

BIO. Differences in Q between CIRC/BIO and INT09 are generally smaller than 20 mol yr^{-1}, but grow to 50 mol yr^{-1} from 1900 to 1950 AD. The reason is the different slopes in the last decades of the Northern and Southern Hemisphere records. This mid-20th century difference has important consequences for the reconstruction of solar modulation as described in Sect. 3.3. This sensitivity experiment demonstrates that spatial gradients in atmospheric Δ^{14}C and in resulting radiocarbon fluxes should be taken into account, at least for the industrial period.

In conclusion, inferred Holocene values of Q and in particular decadal to centennial variation in Q are only weakly sensitive to the details of the carbon cycle evolution over the
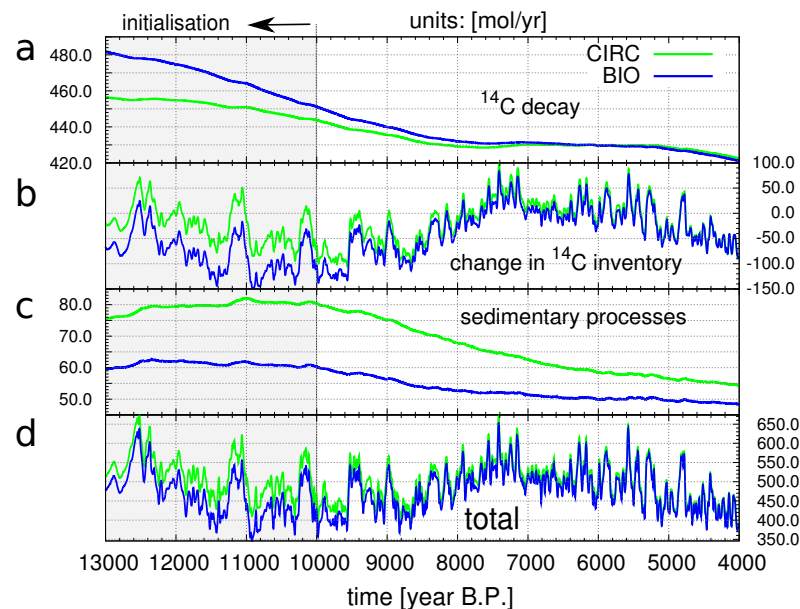
Fig. 9. The oceanic ^{14}C budget for the experiments BIO and CIRC for the period 13 to 4 kyr BP. **(a)** Decay of the data-normalised inventory of ^{14}C in the form of inorganic and organic carbon, **(b)** changes in whole ocean radiocarbon inventory, and **(c)** contribution from sediments (burial flux and decay of ^{14}C within the active sediment layer). **(d)** After 4 kyr BP, the two experiments do not show significant differences in the total ocean and sediment ^{14}C loss.

glacial termination. On the other hand spatial gradients in atmospheric Δ^{14}C and carbon emissions from fossil fuel burning should be explicitly included to estimate radiocarbon production in the industrial period. In the following, we will use the arithmetic mean of BIO and CIRC as our best estimate for Q (Fig. 10). The final record is filtered using smoothing splines (Enting, 1987) with a cutoff period of 20 yr in order to remove high-frequency noise.

Total ± 1 standard deviation (1σ) uncertainties in Q (Fig. 10, grey band) are estimated to be around 6 % at 10 kyr BP and to slowly diminish to around ± 1–2 % by 1800 AD (Appendix Fig. A1f). Overall uncertainty in Q increases over the industrial period and is estimated to be ± 6 % by 1950 AD. The difference in Q between BIO and CIRC is assumed to reflect the uncertainty range due to our incomplete understanding of the deglacial CO_2 evolution. Uncertainties in the Δ^{14}C input data, the air–sea gas exchange rate and the gross primary production (GPP) of the land biosphere are taken into account using a Monte Carlo approach and based on further sensitivity simulations (see Sect. A1 for details of the error estimation).

The radiocarbon production records from Usoskin and Kromer (2005) and from the Marmod09 box model (http://www.radiocarbon.org/IntCal09%20files/marmod09.csv; model described in Hughen et al., 2004) show similar variations on timescales of decades to millennia (Fig. 10).

These include maxima in Q during the well-documented solar minima of the last millennium, generally low production, pointing to high solar activity during the Roman period, as well as a broad maximum around 7.5 kyr BP. However, the production estimates of Usoskin and Kromer (2005) and Marmod09 are about 10 % lower during the entire Holocene and are in general outside our uncertainty range. If we can rely on our data-based estimates of the total radiocarbon inventory in the Earth system, then the lower average production rate in the Usoskin and Kromer (2005) and Marmod09 records suggest that the radiocarbon inventory is underestimated in their setups.

In the industrial period, the Marmod09 production rate displays a drop in Q by almost a factor of two. This reconstruction is intended to provide the surface age of the ocean for the Holocene for calibration of marine samples from that time period. Data after 1850 AD are not to be considered as the authors purposely do not include a fossil fuel correction. Similarly, Usoskin and Kromer (2005) do not provide data after 1900 AD.

3.2.2 A reference radiocarbon production rate

Next, we discuss the absolute value of Q in more detail. Averaged over the Holocene, our simulations yield a ^{14}C production of $Q = 472\,\mathrm{mol\,yr^{-1}}$ ($1.77\,\mathrm{atoms\,cm^{-2}\,s^{-1}}$), as listed in Table 2. Independent calculations of particle fluxes
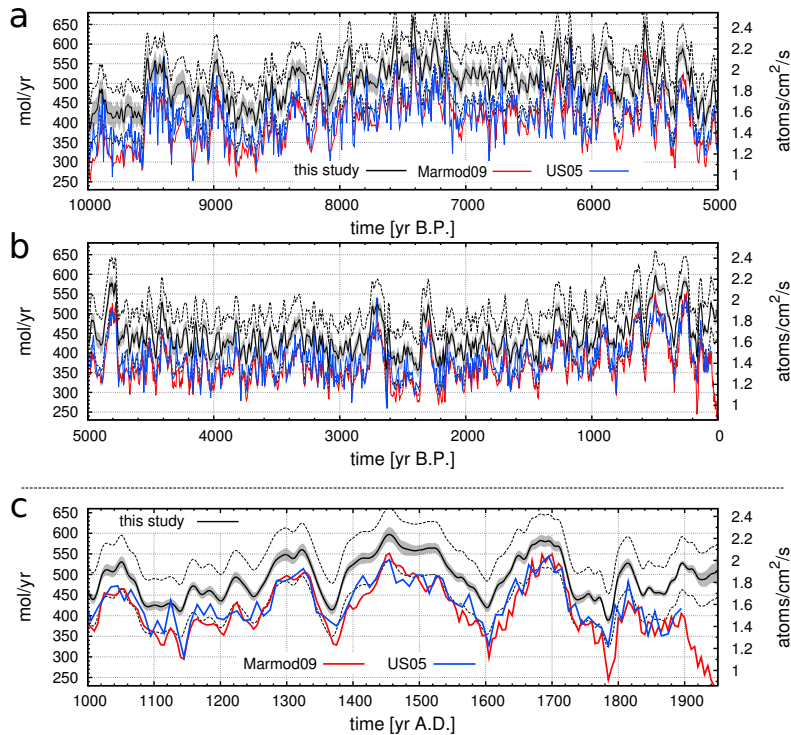
Fig. 10. (a, b) Total ^{14}C production rate from this study (black line with grey 1σ shading) and the reconstructions from Usoskin and Kromer (2005) (blue) and the output of the Marmod09 box model (red). The grey shading indicates $\pm 1\sigma$ uncertainty as computed from statistical uncertainties in the atmospheric Δ^{14}C records and in the processes governing the deglacial CO_2 increase, air–sea gas transfer rate and global primary production on land (see Appendix and Fig. A1). **(c)** Shows the last 1000 yr of the production record in more detail. The two dashed lines indicate the potential offset of our best guess production rate due to the $\sim$15 % (1σ) uncertainty in the data-based radiocarbon inventory.

and cosmogenic radionuclide production rates (Masarik and Beer, 1999, 2009) estimate $Q = 2.05$ atoms $cm^{-2} s^{-1}$ (they state an uncertainty of 10 %) for a solar modulation potential of $\Phi = 550$ MeV. As already visible from Fig. 10, Usoskin and Kromer (2005) obtained a lower Holocene mean Q of 1.506 atoms $cm^{-2} s^{-1}$. Recently, Kovaltsov et al. (2012) presented an alternative production model and reported an average production rate of 1.88 atoms $cm^{-2} s^{-1}$ for the period 1750–1900 AD. This is higher than our estimate for the same period of 1.75 atoms $cm^{-2} s^{-1}$. We compare absolute numbers of Q for different values of Φ (see next section) and the geomagnetic dipole moment (Fig. 13). To determine Q for any given VADM and Φ is not without problems because the probability that the modelled evolution hits any point in the (VADM,Φ)-space is small (Fig. 13). In addition, the value depends on the calculation and normalisation of Φ, which introduces another source of error.

For the present-day VADM and $\Phi = 550$ MeV (see Sect. 3.3), our carbon cycle based estimate of Q is ~ 1.71 atoms $cm^{-2} s^{-1}$ and thus lower than the value reported by Masarik and Beer (2009). Note that the statistical

uncertainty in our reconstruction becomes negligible in the calculation of the time-averaged Q. Systematic and structural uncertainties in the preindustrial data-based ocean radiocarbon inventory of approximately 15 % (1σ) (Key et al., 2004; R. Key, personal communication, May 2013) dominates the uncertainty in the mean production rate, while uncertainties in the terrestrial ^{14}C sink are of minor relevance. Therefore we estimate the total uncertainty of the base level of our production rate to be of the order of 15 %.

3.3 Results for the solar activity reconstruction

Next, we combine our production record Q with estimates of VADM to compute the solar modulation potential Φ with the help of the model output from Masarik and Beer (1999) which gives the slope in the $Q - \Phi$ space for a given value of VADM (we do not use their absolute values of Q). Uncertainties in Φ are again assessed using a Monte Carlo approach (see Appendix A2 for details on the different sources of uncertainty in Φ and TSI).

R. Roth and F. Joos: A reconstruction of radiocarbon production and total solar irradiance   **1895**

One key problem is the normalisation of Φ, i.e. how Φ is aligned to observational data (Muscheler et al., 2007). The period of overlap of the Q record with ground-based measurements is very limited as uncertainties in the atmospheric injection of radiocarbon from atomic bomb tests hinders the determination of Q from the Δ^{14}C record after 1950 AD. Forbush ground-based ionisation chamber (IC) data recently reanalysed by Usoskin et al. (2011) (US11) are characterised by large uncertainties and only cover roughly one solar cycle (mid 1936–1950 AD). The considerable uncertainties both in Q and Φ in this period make it difficult to connect reconstructions of past solar activity to the recent epoch. Still, we choose to use these monthly data to normalise our reconstruction. Converting the LIS used for US11 to the one used by Castagnoli and Lal (1980) (which we use throughout this study) according to Herbst et al. (2010) yields an average solar modulation potential of $\Phi = 403$ MeV during our calibration epoch 1937–1950 AD. Accordingly, we normalise our Q record such that (the Monte Carlo mean) Φ equals 403 MeV for the present-day VADM and the period 1937 to 1950 AD. In this time period, the uncertainty in the IC data is ~ 130 MeV. In addition, the error due to uncertainties in Q is approximately 70 MeV. This makes it difficult to draw firm conclusion on the reliability of the normalisation. Thus, the absolute magnitude of our reconstructed Φ remains uncertain.

We linearly blend the Q based Φ with an 11 yr running mean of the monthly data from US11 in the overlap period 1937–1950 AD and extend the reconstruction up to 2005 AD. Smoothing splines with a cutoff period of 10 yr are applied to remove high-frequency noise, e.g. as introduced by the Monte Carlo ensemble averaging and the blending. This blending with instrumental data slightly changes the average Φ in 1937–1950 AD from 403 to ~ 415 MeV.

Φ varies during the Holocene between 100 and 1200 MeV on decadal to centennial timescales (Fig. 12) with a median value of approximately 565 MeV (see histogram in Fig. 13). Millennial-scale variations of Φ during the Holocene appear small (Fig. 12). This suggests that the millennial-scale variations in the radiocarbon production Q (Fig. 10) appear to be mainly driven by variations in the magnetic field of the earth (Fig. 11). The millennial-scale modulation of Q is not completely removed when applying VADM of Korte et al. (2011). It is difficult to state whether the remaining long-term modulation, recently interpreted as a solar cycle (Xapsos and Burke, 2009), is of solar origin or rather related to uncertainties in reconstructed VADM.

Values around 670 MeV in the last 50 yr of our reconstruction (1955–2005 AD) indicate a high solar activity compared to the average Holocene conditions. However, such high values are not exceptional. Multiple periods with peak-to-peak variations of 400–600 MeV occur throughout the last 10 000 yr, induced by so-called grand solar minima and maxima. The sun's present state can be characterised by a grand
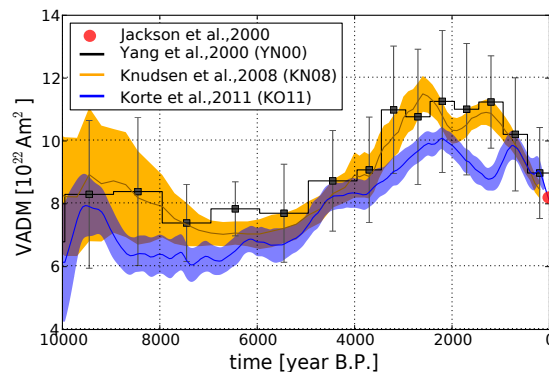

Fig. 11. Reconstructions of the virtual axis dipole moment (VADM) of the geomagnetic field for the Holocene. Black: Yang et al. (2000), orange: Knudsen et al. (2008), blue: Korte et al. (2011). For the most recent epoch, the estimate of Jackson et al. (2000) yields 8.22×10^{22} Am^2 (red dot). In the present study, the data of Korte et al. (2011) is used.

solar maximum (modern maximum) with its peak in 1985 (Lockwood, 2010).

To check to which degree our results depend on the choice of the ^{14}C production model, we apply also the newer model of Kovaltsov et al. (2012) to our Q time series. The result is given for the last millennium in Fig. 12c (dotted line). Obviously, the two models yield very similar result as we normalise in both cases to the same observational dataset.

Our reconstruction of Φ is compared with those of Usoskin et al. (2007) (US07, converted to GM75 LIS), of Muscheler et al. (2007) (MEA07) and with the reconstruction of Steinhilber et al. (2008) (SEA08), who used the ice core record of ^{10}Be instead of radiocarbon data (Fig. 12). Overall, the agreement between the the ^{10}Be and the ^{14}C-based reconstructions points toward the quality of these proxies for solar reconstructions. In detail, differences remain. For example, the ^{14}C-based reconstructions show a increase in Φ in the second half of the 17th century, whereas the ^{10}Be-derived record suggests a decrease in Φ during this period.

In difference to SEA08, which is based on ^{10}Be ice core records, our Φ is always positive and non-zero and thus within the physically plausible range.

Solanki et al. (2004) suggests that solar activity is unusually high during recent decades compared to the values reconstructed for the entire Holocene. Our reconstruction does not point to an exceptionally high solar activity in recent decades, in agreement with the conclusions of Muscheler et al. (2007). The relatively higher modern values inferred by Solanki et al. (2004) are eventually related to their application of a Northern Hemisphere Δ^{14}C dataset (IntCal98) only. Thus, these authors neglected the influence of interhemispheric differences in Δ^{14}C. We calculated Φ from results of our sensitivity simulation INT09, where the IntCal09
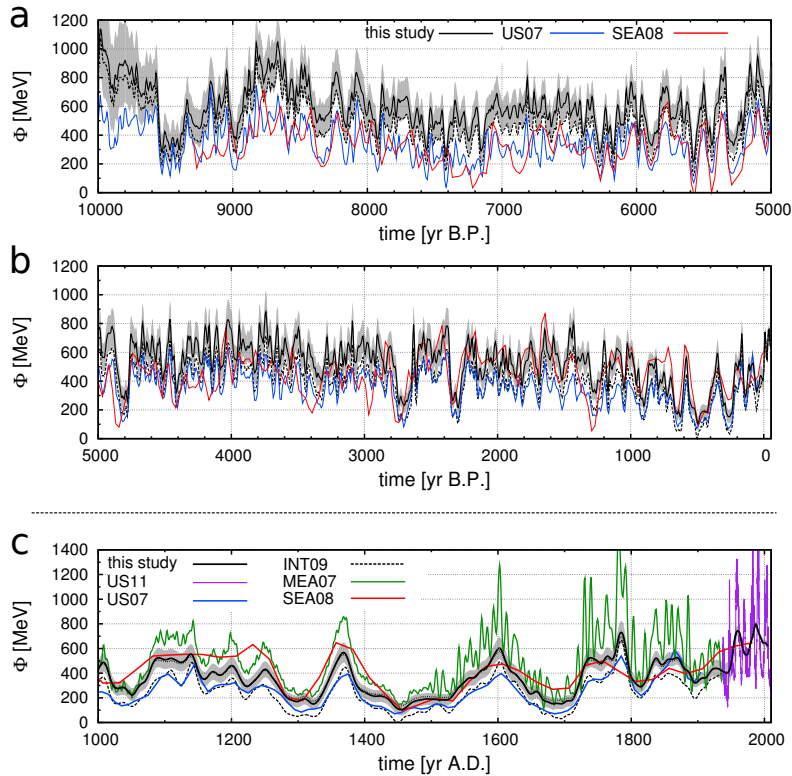
Fig. 12. (a, b) Solid black line and grey shading: solar modulation potential Φ (with 1σ uncertainty) based on our new radiocarbon production reconstruction and the VADM history of Korte et al. (2011) using the production model of Masarik and Beer (1999). The dashed line shows Φ as calculated from the northern hemispheric record only (experiment INT09). The Φ histories of Usoskin et al. (2007) (US07, blue) and of Steinhilber et al. (2008) (SEA08, red) are additionally shown. For the last millennium **(c)**, we include the Φ record from Muscheler et al. (2007) (MEA07, green) as well as the instrumental data compiled by Usoskin et al. (2011) (US11, violet). The latter was used for normalisation and extension of our Φ reconstruction over recent decades. Note that all values of Φ are normalised to the LIS of Castagnoli and Lal (1980) according to Herbst et al. (2010). The dotted line in the lowest panel (usually not distinguishable from the solid line) shows Φ as calculated with the alternative production model of Kovaltsov et al. (2012).

Northern Hemisphere data are applied globally (Fig. 12, dashed line). Due to the lower Q in the normalisation period from 1937 to 1950 AD (see Fig. 8, dashed line), the Φ record during the Holocene is shifted downward by approximately 140 MeV for INT09 compared to CIRC/BIO; the same normalisation of Φ to the Forbush data is applied. Then, the solar activity for recent decades appears unusually high compared to Holocene values in the INT09 case.

3.4 Reconstructed total solar irradiance

We apply the reconstruction of Φ in combination with Eqs. (3) and (4) to reconstruct total solar irradiance (Fig. 14). Uncertainties in TSI are again estimated using a Monte Carlo approach, and considering uncertainties in Φ and in the parameters of the analytical relationship (but not the $\pm 0.4\,\mathrm{W\,m^{-2}}$ in the TSI–B_r relationship), TSI is expressed as

deviation from the solar cycle minimum in 1986, here taken to be $1365.57\,\mathrm{W\,m^{-2}}$. We note that recent measures suggest a slight downward revision of the absolute value of TSI by a few per mil (Kopp and Lean, 2011); this hardly effects reconstructed TSI anomalies. The irradiance reduction during the Maunder Minimum is $0.85 \pm 0.16\,\mathrm{W\,m^{-2}}$ (1685 AD) compared to the solar cycle 22 average value of $1365.9\,\mathrm{W\,m^{-2}}$. This is a reduction in TSI of 0.62 ± 0.11 ‰.

Changes in TSI can be expressed as radiative forcing (RF), which is given by $\Delta\mathrm{TSI} \times \frac{1}{4} \times (1 - A)$, where A is the earth's mean albedo (~ 0.3). A reduction of $0.85\,\mathrm{W\,m^{-2}}$ corresponds to a change in RF of about $0.15\,\mathrm{W\,m^{-2}}$ only. This is more than an order of magnitude smaller than the current radiative forcing due to the anthropogenic CO_2 increase of $1.8\,\mathrm{W\,m^{-2}}$ ($5.35\,\mathrm{W\,m^{-2}}\,\ln(390\,\mathrm{ppm}/280\,\mathrm{ppm})$). This small reduction in TSI and RF is a direct consequence of the small
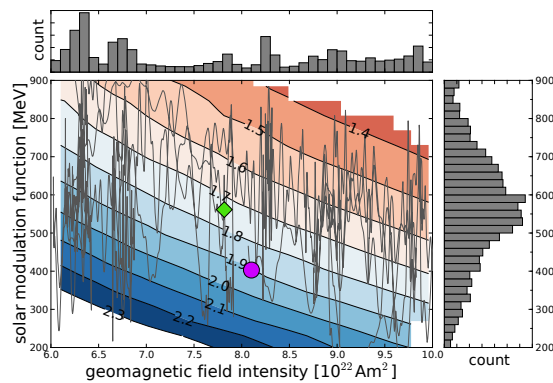
Fig. 13. The absolute radiocarbon production rate plotted as a function of the solar modulation parameter Φ and VADM. Yearly values of the smoothed Q record are used (with a cutoff period of 20 yr as in Fig. 10). The path taken by the model in this (Φ, VADM)-space is indicated by the thin grey line. The circle shows the value of Φ for the normalisation period 1937–1950 as reported by Usoskin et al. (2011). The diamond shows the average production rate over the entire Holocene. On the sides of the figure, two histograms are displayed showing the relative occurrence of certain VADM (top panel) and Φ (right panel) values, ~ 565 MeV being the median modulation potential during the Holocene.

slope in the relationship between TSI and the interplanetary magnetic field as suggested by Fröhlich (2009). Applying the relationships between TSI and Φ suggested by Shapiro et al. (2011) yields changes almost an order of magnitude larger in TSI and RF (right scale in Fig. 14).

We compare our newly produced TSI record with two other recently published reconstructions based on radionuclide production, Vieira et al. (2011) (VEA11) and Steinhilber et al. (2012) (SEA12). For the last millennium, the data from Delaygue and Bard (2011) (DB11) is shown for completeness. During three grand minima in the last millennium, i.e. the Wolf, Spörer and Maunder minima, SEA12 shows plateau-like values, apparently caused by a truncation of the Φ record to positive values. Also VEA11 suggests lower values during these minima compared to our reconstructions, but in general the differences in the TSI reconstructions are small, in particular when compared to the large TSI variations suggested by Shapiro et al. (2011).

Well-known solar periodicities in TSI contain the Hallstatt (2300 yr), Eddy (1000 yr), Suess (210 yr) and Gleissberg cycle (70–100 yr) as also discussed by Wanner et al. (2008) and Lundstedt et al. (2006). These periodicities are also present in our reconstruction (Fig. 15), as well as the long-term modulation of approximately 6000 yr (Xapsos and Burke, 2009) (not shown). A wavelet (Morlet) power spectrum indicates that the power associated with the different cycles fluctuated somewhat during the Holocene.

We test the predictability of TSI given by its periodic nature to extrapolate insolation changes up to 2300 AD. The extrapolation is calculated by fitting an autoregressive model (AR(p)) of order p, applying Burg's method (Kay, 1988) for parameter optimisation (Fig. 15c). The order of the model is the number of past time steps (i.e. years) used to fit the model to the time series. We note that the spectrum of TSI is not strictly stationary (Fig. 15b), limiting the confidence in forecasting future changes in TSI. We forecast TSI in the historical period (dashed lines in Fig. 15c) to test to which degree TSI changes can be considered as an AR(p) process. Obviously, not all changes are matched in the historic period, although the present high values of TSI seems to be predictable based on past TSI changes. Common to all extrapolations is the decreasing TSI in the next 10–20 yr to a magnitude comparable to 1900 AD. Towards 2200 AD, all three extrapolations show again increasing TSI.

3.5 Changes in global mean surface air temperature from total solar irradiance variability

We translate our new TSI record as well as two earlier reconstructions (VEA11, SEA12) into past changes in SAT using the Bern3D-LPJ model. We follow the same protocol as in Sect. 2.2. Two transient simulations were performed for each TSI reconstruction: in one simulation TSI is kept constant at its mean value, in the other simulation the actual TSI reconstruction is applied. ΔSAT was then computed as the difference between the two simulations, normalised to ΔSAT $= 0\,°$C in 2005 AD. As shown in Fig. 16, the reconstructions yield rather small temperature changes attributed to solar forcing with $|\Delta$SAT$|$ less than 0.15 °C at any time during the Holocene. Compared to VEA12 and SEA12, our TSI reconstruction results in less negative and more positive values in ΔSAT before 1900 AD as expected from the TSI record. No considerable TSI-induced long-term temperature trend is simulated. Applying our TSI reconstruction based on the Shapiro et al. (2011) scaling (green line and right scale in Fig. 16) translates into SAT changes ≈ 6 times larger than the other reconstructions.

We note that our energy balance model does not take into account spectral changes and changes in ultraviolet (UV) radiation, and thus related heating or cooling of the stratosphere by the absorption of UV by ozone and other agents (Gray et al., 2010).

4 Summary and conclusions

In the present study the Holocene evolution of cosmogenic radiocarbon (^{14}C) production is reconstructed using a state of the art Earth system model of intermediate complexity and the IntCal09/SHCal04 radiocarbon records. Then this production record is used in combination with reconstructions of the geomagnetic field to reconstruct the solar modulation

potential Φ. In further steps, total solar irradiance is reconstructed using recently proposed relationships between Φ and TSI, and variations in TSI were translated into temperature anomalies. The uncertainty arising from uncertainties in input data, model parametrisation for the glacial termination, and model parameter values are propagated through the entire chain from production to solar modulation to TSI using Monte Carlo and sensitivity simulations as well as Gaussian error propagation.

The Bern3D-LPJ model is used to estimate radiocarbon production from the IntCal09/SHCal04 radiocarbon records. The model features a 3-D dynamic ocean component with an ocean sediment model and an interactive marine biological cycle, a 2-D atmosphere and a dynamic global vegetation model component. The model is able to reproduce the observation-based distributions of carbon and radiocarbon within the ocean as well as approximate the evolution of atmospheric CO_2 during the past 21 kyr. The explicit representation of dissolved inorganic carbon and dissolved inorganic radiocarbon and the biological cycle in a 3-D dynamic setting is a step forward compared to the often applied perturbation approach with the box diffusion model of Oeschger et al. (1975) or the outcrop model of Siegenthaler (1983) (Vieira et al., 2011; Usoskin and Kromer, 2005; Solanki et al., 2004; Muscheler et al., 2005b). These models underestimate by design the inventory of dissolved inorganic carbon in the ocean due to the neglect of the marine biological cycle. Thus, the marine radiocarbon inventory and implied cosmogenic production is also underestimated. The Bern3D-LPJ carbon–climate model is forced with reconstructed changes in orbital parameters, ice sheet extent influencing surface albedo, and natural and anthropogenic variations in greenhouse gas concentrations as well as sulfate aerosol forcings and climate variations, thereby taking into account the influence of climatic variations on the cycling of carbon and radiocarbon.

Our production rate estimates can be compared to independent estimates obtained with models that compute production of cosmogenic nuclides in the atmosphere by simulating the interaction of incoming high energy particles with atmospheric molecules (Masarik and Beer, 1999, 2009). Masarik and Beer (2009) suggests a production of 2.05 ± 0.2 atoms $cm^{-2}\,s^{-1}$ for a solar modulation potential of 550 MeV. The radiocarbon budget analysis yields a lower production of 1.71 atoms $cm^{-2}\,s^{-1}$ and for the same Φ. The Holocene mean ^{14}C production depends on variations in Φ and the geomagnetic field and is estimated to 1.77 atoms $cm^{-2}\,s^{-1}$.

An open question was by how much uncertainties in the carbon cycle processes leading to the deglacial CO_2 rise affect estimates of the radiocarbon production. To this end, two alternative, bounding scenarios for the deglacial CO_2 rise were applied in addition to a control simulations with constant climate and ocean circulation. We show that uncertainties in the processes responsible for the reconstructed CO_2 and $\Delta^{14}C$ variations over the glacial termination translate into an uncertainty of the order of 5 % in the absolute magnitude of the production in the early Holocene, but only to small uncertainties in decadal to centennial production variations. This uncertainty in millennial average production due to the memory of the system to earlier changes vanishes over the Holocene and becomes very small ($< 1\,\%$) in recent millennia. Although a detailed process understanding of the termination, e.g. the cause of the "mystery interval" (Broecker and Barker, 2007), is not required to reconstruct radiocarbon production in the Holocene, the decreasing trend in atmospheric radiocarbon over the glacial termination must be taken into account.

Small differences between simulations that include Holocene climate change and the control run with no climate change are found. A caveat is that our 2-D atmospheric energy and moisture balance model does not represent important features of climate variability such as interannual and decadal atmospheric modes. However, the available evidence and the generally good agreement between ^{14}C-based and independent solar proxy reconstructions suggest that atmospheric radiocarbon and inferred production are relatively insensitive to typical Holocene climate variations.

A prominent excursion in the early Holocene Northern Hemisphere climate is the 8.2 kyr BP event with a decrease in Greenland air temperature by about 3 K within a few decades (Kobashi et al., 2007). A reduction in North Atlantic Deep Water formation related to a spike in meltwater input has been proposed to have occurred with this event (Ellison et al., 2006; Hoffman et al., 2012). This 8.2 kyr event is not represented in our model setup, and a possible atmospheric radiocarbon signal from changing ocean circulation (e.g. Matsumoto and Yokoyama, 2013) would be erroneously attributed to a change in production. Vonmoos et al. (2006) compared solar modulation estimated from ^{10}Be versus ^{14}C. Deviations between the two reconstructions are not larger during the 8.2 kyr event than during other early Holocene periods. Similarly, the different reconstructions shown in Fig. 12 do not point to an exceptionally large imprint of the 8.2 kyr event on inferred solar modulation and thus on radiocarbon production.

Solar modulation potential Φ is computed using the relationship between radiocarbon production, the geomagnetic dipole (Korte et al., 2011), and Φ from the models of Masarik and Beer (1999) and Kovaltsov et al. (2012). A key step is the normalisation of the ^{14}C-derived Φ record to the Forbush instrumental observations over the period 1937 to 1950 AD. Atmospheric $\Delta^{14}C$ is heavily contaminated after 1950 by atomic bomb tests, preventing a reliable extraction of the natural production signal. In the mid-20th century, atmospheric $\Delta^{14}C$ and its interhemispheric gradient is influenced by the early signals of fossil fuel combustion and land use. Our spatially resolved model allows us to treat interhemispheric concentration differences and land use explicitly. We show that reconstructions in Φ that rely on the Northern Hemisphere $\Delta^{14}C$ record only are biased towards low values during the
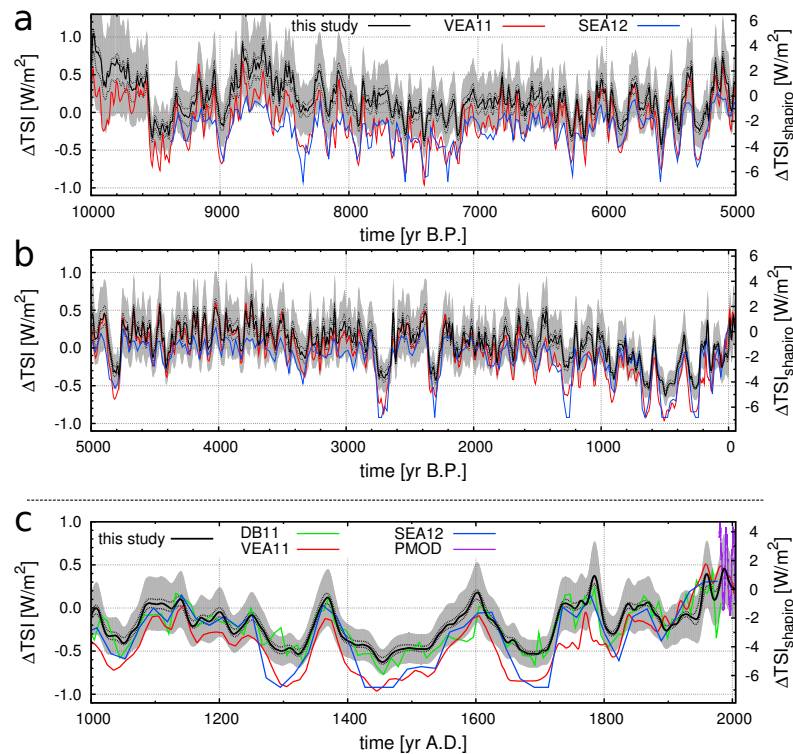
Fig. 14. (a, b) Total solar irradiance deviation from solar cycle minimum value in 1986 (assumed to 1365.57 W m^{-2}) calculated in this study (black with grey 1σ error, left y axis), and the reconstructions by Vieira et al. (2011) (VEA11, red) and Steinhilber et al. (2012) (SEA12, blue). The dotted lines indicate the uncertainty introduced by random errors from the Δ^{14}C history alone excluding any systematic errors. **(c)** Magnification of the last 1000 yr; in addition to VEA11 and SEA12 the data of Delaygue and Bard (2011) (DB11, green) is shown as well as the composite record from the Physikalisch-Meteorologisches Observatorium Davos (PMOD). The DB11 record has been aligned to the other records by adding an offset of 0.5 W m^{-2}. The right y axis shows the corresponding TSI variations when applying the Φ–TSI scaling of Shapiro et al. (2011) to our Φ history.

Holocene. To our knowledge, the Φ record by Usoskin et al. (2007) is based on Q from Usoskin and Kromer (2005) and thus on the Northern Hemisphere radiocarbon record only. Their values are systematically lower than ours and their best estimates are in general outside our 1σ confidence band during the last 7 kyr. The Φ record by Steinhilber et al. (2008) shows in general values below our confidence range during the period 7 to 3 kyr BP, while the two reconstructions agree on average during the more recent millennia. Agreement with respect to decadal to centennial variability is generally high among the different reconstructions. However, notable exceptions exist. For example, the reconstruction by Steinhilber et al. (2008) suggests a strong negative fluctuation between 8 and 7.8 kyr BP, not seen in the ^{14}C-derived records.

We reevaluated the claim by Solanki et al. (2004) that the recent sun is exceptionally active. As earlier studies (Muscheler et al., 2007; Steinhilber et al., 2008), we conclude that recent solar activity is high but not unusual in the

context of the Holocene. Φ was estimated to be on average at 650 MeV during the last 25 yr by Steinhilber et al. (2008) for a reference Local Interstellar Spectrum (LIS) of Castagnoli and Lal (1980). We find an average Φ for the Holocene (10 to 0 kyr BP) of 555 MeV. Solar activity in our decadally smoothed record is during 28 % of the time higher than the modern average of 650 MeV and during 39 % of the time higher than 600 MeV, used to define periods of high activity by Steinhilber et al. (2008) (Fig. 13). This may be compared to corresponding values of 2 and 15 % by Steinhilber et al. (2008). In contrast to earlier reconstructions, our record suggests that periods of high solar activity ($>$ 600 MeV) were quite common not only in recent millennia, but throughout the Holocene.

Our reconstruction in Φ can be used to derive a range of solar irradiance reconstructions using published methods. Shapiro et al. (2011) suggest that variations in spectral and thus total solar irradiance are proportional to variation in Φ.
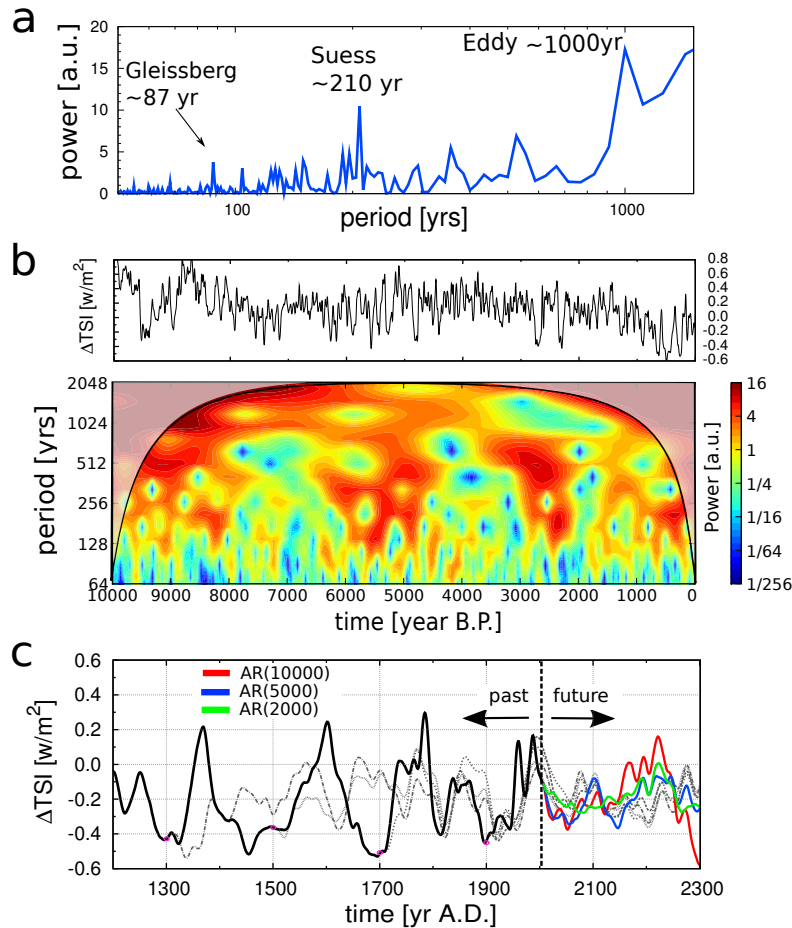
Fig. 15. (a) Power spectrum of our TSI record up to periodicities of 2000 yr. The most dominant periodicities correspond to the Gleissberg, Suess and Eddy cycles. **(b)** Wavelet power spectrum calculated with a Morlet wavelet with $\log_2$ periodicity axis and colour shading. **(c)** Forecasting of the solar irradiance using an autoregressive model of order p (AR(p)) fitted using Burg's method. Before fitting the time series, a high-pass filter (1000 yr) has been applied in order to remove low-frequency trends. The dashed lines show forecasts with the AR(5000) model starting at year 1300, 1500, 1700 and 1900 AD (magenta dots). Coloured lines show forecasts starting in 2005 AD for different orders of the AR model.

Their analysis suggests a high scaling of Φ with TSI and a Maunder Minimum reduction in TSI compared to the present solar minimum by about 0.4 %. This is significantly larger than the reduction suggested in other recent reconstructions (Steinhilber et al., 2012; Vieira et al., 2011), but within the range of TSI variations explored in earlier climate model studies (Ammann et al., 2007; Jansen et al., 2007). Here, we further converted Φ into TSI using the nonlinear equations used by Steinhilber et al. (2008). This yields small variations in TSI and a Maunder Minimum reduction in TSI compared to recent solar minima of only 0.62 ‰. The resulting overall range in TSI is about $1.2\,\mathrm{W\,m^{-2}}$. Future extension of TSI using autoregressive modelling suggests a declining

solar activity in the next decades towards average Holocene conditions.

We applied different TSI reconstructions to estimate variations in global mean surface air temperature (SAT) due to TSI changes only. We stress that these SAT anomalies are due to TSI variations only and do not include SAT variations due to other drivers such as orbital forcing, natural and anthropogenic greenhouse gas concentration variations, or changes in the extent and the albedo of ice sheets. The results suggest that there were several periods in the Holocene were TSI-related SAT anomalies were larger than for year 2000 AD. In particular, several warm anomalies occurred in the period from 5500 to 3600 BP. Temperature anomalies
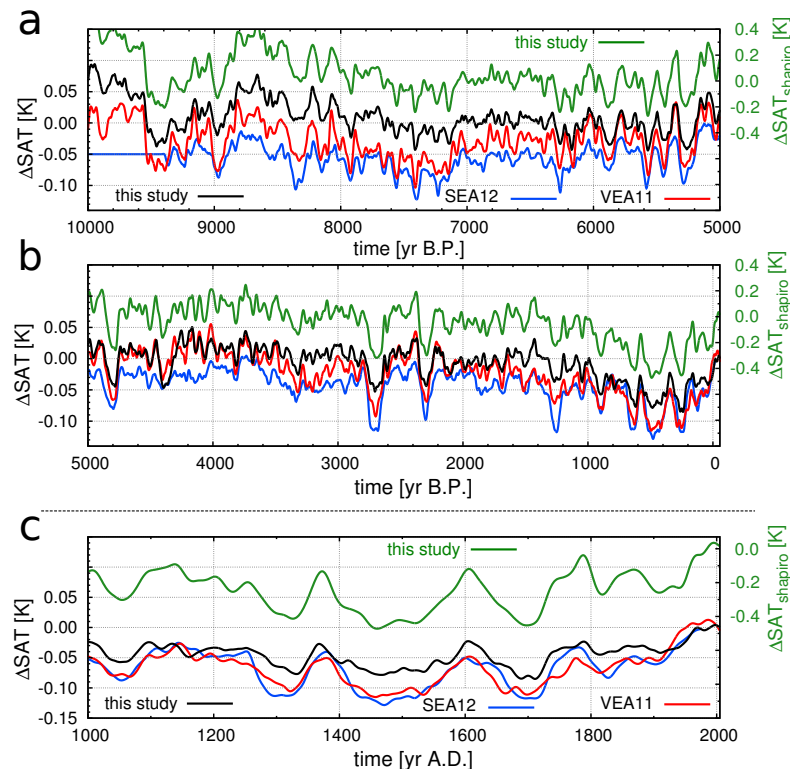
Fig. 16. **(a, b)** Simulated changes in SAT as a response to different TSI forcings: this study (black), VEA11 (red) and SEA12 (blue), left y axis. The green line (right y axis) shows the simulated SAT changes by a solar variation based on our Φ history but converted to TSI using the method of Shapiro et al. (2011). The anomalies were calculated as the difference between two transient simulations, one with all forcings and the other with the same forcings but solar forcing taken to be constant. The last 1000 yr are shown again in **(c)**. All lines show smoothing splines with a cutoff period of 30 yr.

are comparable to twentieth century anomalies in the period from 200 BC to 600 AD. In contrast, the TSI reconstruction of Steinhilber et al. (2012) implies that SAT anomalies due to TSI changes were below current values almost during the entire Holocene. In conclusion, our reconstruction of the radiocarbon production rate and the solar modulation potential, as well as the implied changes in solar irradiance, provide an alternative for climate modellers.

Appendix A

Estimation of uncertainties

A1   Assessment of uncertainties in the ^{14}C production record

There are several potential sources of error entering the calculation of the production rate, summarised in Fig. A1. As already discussed in detail in the main text, the uncertain

deglacial carbon cycle changes translate into an uncertainty in Q, especially in the early Holocene. To account for this, we use the arithmetic mean of BIO and CIRC as our best guess Q reconstruction and the difference between them as our uncertainty range, which is around 4.5 % in the early Holocene and drops below 1 % at 5000 kyr BP.

In addition, also the uncertainty of the IntCal09/SHCal04 record translates into an error of the production record. 100 radiocarbon histories were randomly generated with Gaussian-distributed Δ^{14}C values at each point in time of the record, varied within 1σ uncertainty as (shown in Fig. 2b) on their original time grid (5 yr spacing). For each realisation of the Δ^{14}C history, the transient simulation with Bern3D-LPJ was repeated and the resulting Q smoothed. The 1σ range from the 100 smoothed records (Fig. A1b) is of the order of 4–5 %, decreasing towards preindustrial times to 1.5 %.

During 1930–1950, this error increases again rapidly (hardly visible in Fig. A1b) to 10 % because the atmospheric carbon inventory increases at a high rate. Therefore, rather
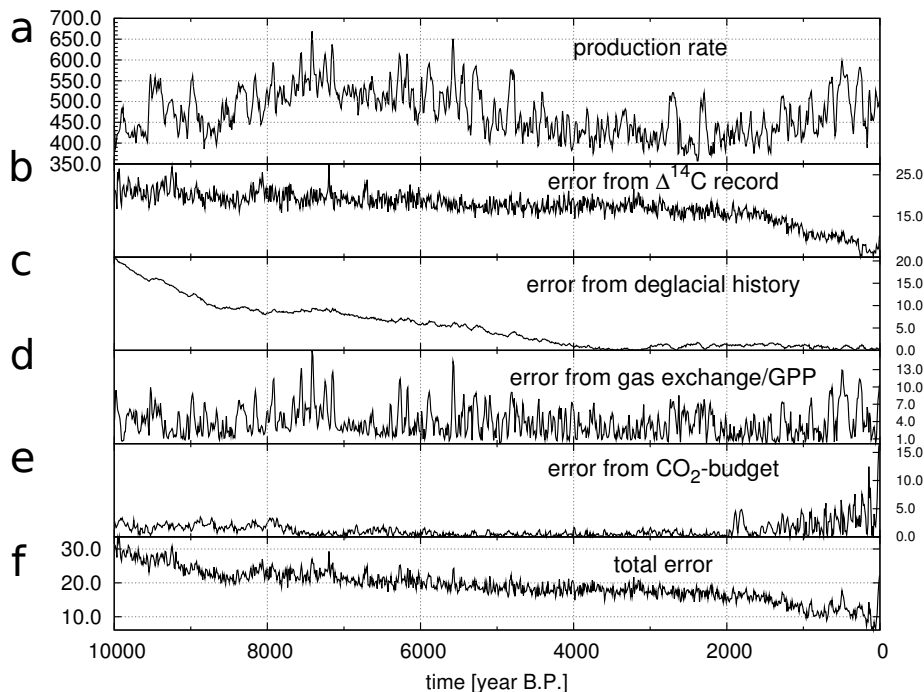
Fig. A1. Assessment of uncertainties in our production rate record in mol yr^{-1}. **(a)** Radiocarbon production rate (arithmetic mean of CIRC and BIO); **(b)** the uncertainty stemming from the pre-Holocene carbon cycle evolution calculated as the absolute difference between results from simulations BIO and CIRC; **(c)** the smoothed 1σ error from the Δ^{14}C record (as shown in Fig. 2b) is calculated by a Monte Carlo approach including 100 individual simulations; and **(d)** the uncertainty in air–sea and air–land fluxes deduced by sensitivity experiments. The total error in production **(e)** varies between 30 and 5 mol yr^{-1}, corresponding to a relative error of $\sim$ 6 to 1.5 %. The bulk uncertainty in the average level of Q resulting form an uncertain ocean (and land) inventory is not included in this calculation. We estimate this uncertainty to be $\sim$ 15 %.

small errors in Δ^{14}C of $\sim$ 1 ‰ translate into rather big uncertainties in the change of the atmospheric radiocarbon inventory, and thus into the production rate.

The air–sea flux of radiocarbon is the dominant flux out of the atmosphere with approximately 430 mol yr^{-1}. We assess its variations by nominally changing the air–sea gas-exchange rate within $\pm$15 % (Müller et al., 2008). Two additional runs were performed in which the seasonally and spatially varying gas exchange rates of the standard setup were increased/decreased everywhere by 15 %. In analogy, uncertainties in the flux into the land biosphere were assessed by varying the gross primary productivity of the model by $\pm$15 %. In these two experiments, differences in the total ^{14}C inventory were subtracted to get the uncertainties in the fluxes alone; the effect of the inventory is discussed separately. These errors in $^{14}F_{as} + {}^{14}F_{ab}$ vary together with changes in the atmospheric Δ^{14}C signature. The error from the uncertainty in the combined air-to-sea and air-to-land ($^{14}F_{as} + {}^{14}F_{ab}$) fluxes is smaller than 2.5 % of the production at any time (Fig. A1d). It is important to note that the

uncertainty in gas exchange and GPP do not alter the absolute value of Q, but change the amplitude in the variations of Q.

Uncertainties are also related to the ^{14}C signature associated with the carbon flux applied to close the atmospheric CO_2 budget ($^{14}F_{budget}$ in Eq. 1). For example, the missing carbon sink process could be due to a slow down of the oceanic thermohaline circulation (THC) or a growth of land vegetation: two processes with different isotopic signatures. We assume that this signature varies between $\pm$200 ‰ relative to the contemporary atmosphere. The associated error in the production is in general small with peaks of 1–2 % (Fig. A1e). However, towards 1950 AD, where the anthropogenic influence leads to increasing CO_2 levels, the uncertainty reaches up to 4 % as the model simulates a too-weak oceanic/land sink and/or too-high emissions.

We estimate the total standard deviation by quadratic error addition, $\sigma_Q = \sqrt{\sum \sigma_{Q,i}^2}$, to be $\sim$ 6 % during the early Holocene, decreasing to 1.5–2.5 % towards preindustrial times (Fig. A1f). The total uncertainty in the early Holocene
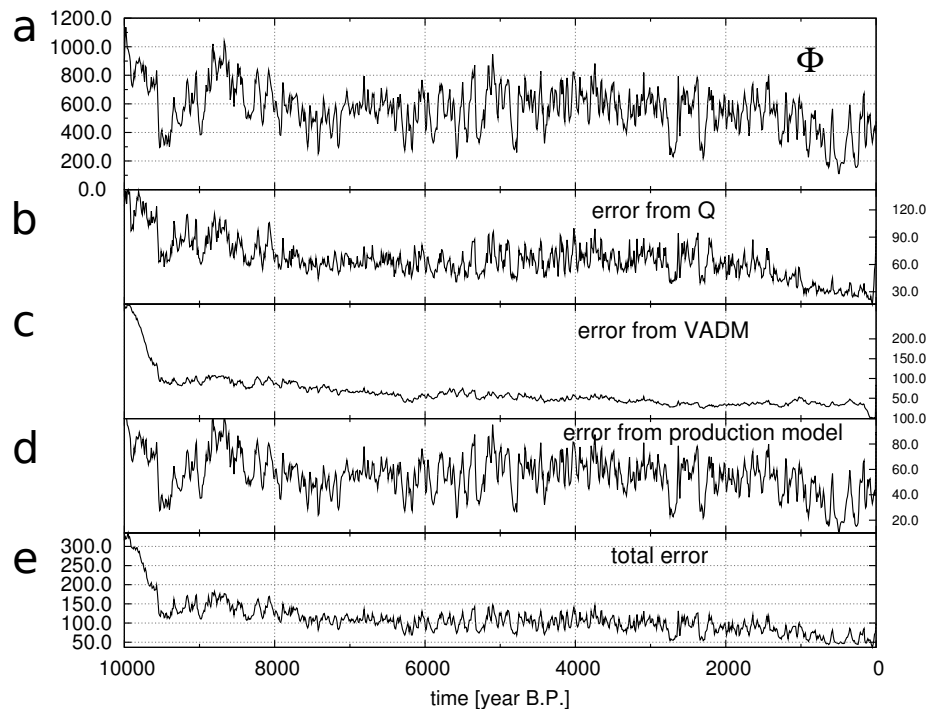
Fig. A2. Assessment of uncertainties in the solar modulation potential Φ in MeV. **(a)** Best estimate of Φ (mean of the Monte Carlo simulations), **(b)** uncertainty in Φ from uncertainties in the radiocarbon production Q, **(c)** from the uncertainty in the VADM reconstruction by Korte et al. (2011), **(d)** the uncertainty in the model to convert production into Φ, and **(e)** total 1σ uncertainty in the MC calculation.

is dominated by the uncertainty in the Δ^{14}C input data and the deglacial history. These two sources of error decrease towards preindustrial times. In the first half of the last century, uncertainties increase again mainly associated with the anthropogenic CO_2 increase. This increasing uncertainty towards 1950 AD ($\sim$ 9 %) is important when normalising reconstructed solar modulation to the recent instrumental records.

As noted in the main text, the 1σ error is estimated to be 15 % for the ocean ^{14}C inventory (R. Key, personal communication, May 2013) and for the total ^{14}C inventory. This potential systematic bias is not included in the uncertainty band of Q as it would not change the temporal evolution.

A2   Propagation of uncertainties from Q to Φ and ΔTSI

Next, the uncertainty calculation of Φ and of ΔTSI is discussed (grey bands in Figs. 12 and 14). Three general sources of uncertainty in Φ are considered: the uncertainty in Q, the uncertainty in VADM and finally the error of the production rate simulations (i.e. the slope of Φ/Q) assumed to be 10 %. Using Monte Carlo calculations, we varied the different sources of uncertainty individually in every year to assess the propagation of errors. In Fig. A2b–d the individual

1σ errors of this calculation are shown. The total error in Φ varies then between 300 MeV (early Holocene) and 70 MeV (preindustrial). All three components of error contribute to approximately equal parts to the total uncertainty.

The possible bias introduced by the normalisation is not included in this figure. This would add another $\sim$ 130 MeV uncertainty to the average level of Φ (but not on its temporal evolution). Note that any constant systematic offset in Q would not translate into an offset in the solar modulation potential as Q is normalised before converting to Φ.

Similarly, the uncertainty in the change in TSI as reconstructed with the use of Eqs. (3) and (4) is calculated (Fig. A3b and c). The 1σ error of Φ is taken into account as well as the uncertainties in Eq. (4) and of the exponent α in Eq. (3) (± 0.3) (Steinhilber et al., 2009). The error in the reference value of TSI (1264.64 W m^{-2} in Eq. 4) does not affect relative changes in TSI, but its absolute level. The total 1σ uncertainty in ΔTSI ranges between 0.2 and 0.8 W m^{-2} (Fig. A3d), to equal part stemming from the error in Φ and the conversion model.

More than half of the uncertainty in TSI is of systematic nature and related to the Φ–TSI relationship (Fig. A3c). More specifically, the slope of the linear relationship between
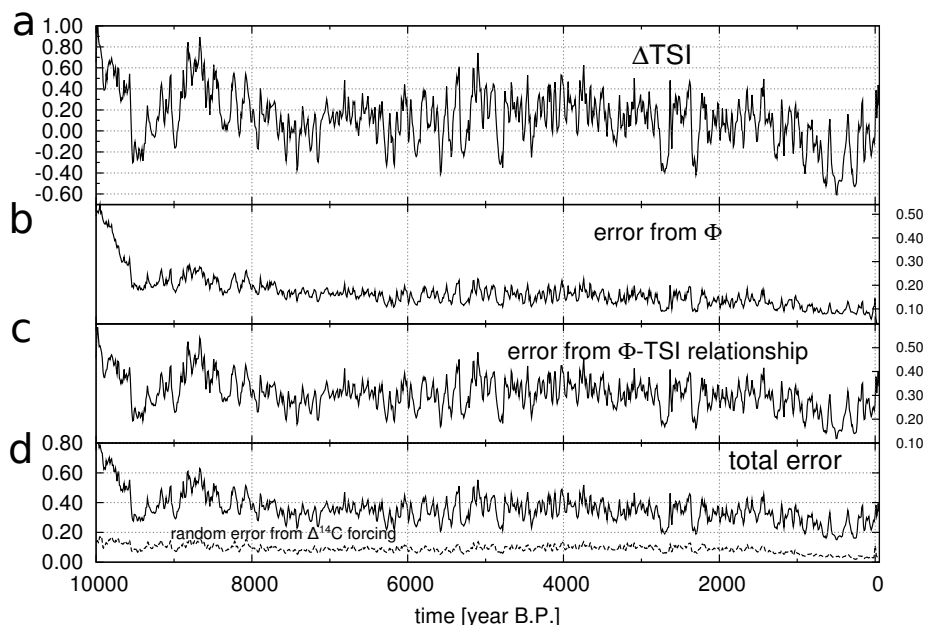
Fig. A3. Assessment of uncertainties in the ΔTSI reconstruction in $\mathrm{W\,m}^{-2}$. **(a)** ΔTSI (mean of the Monte Carlo simulations), **(b)** the uncertainty in ΔTSI from the error of Φ, **(c)** from the uncertainty in the TSI–B_r relationship, and **(d)** when considering all uncertainties in the MC calculation. Errors are 1σ uncertainties. The dashed line shows the uncertainty introduced by random errors propagated from the Δ^{14}C history excluding any systematic errors.

the interplanetary magnetic field and TSI (Eq. 3) is highly uncertain with 0.38 ± 0.17 units. A lower slope would correspond to correspondingly lower amplitude variations in TSI and a larger slope to larger amplitudes in TSI, while the temporal structure of the reconstruction would remain unchanged. To distinguish between random and systematic errors, we provide the uncertainty related to the random uncertainty in the radiocarbon data and the total uncertainty arising from both systematic and random errors in panel d of Fig. A3.

Supplementary material related to this article is available online at: http://www.clim-past.net/9/1879/ 2013/cp-9-1879-2013-supplement.zip.

Edited by: L. Skinner

References

Adkins, J., Griffin, S., Kashgarian, M., Cheng, H., Druffel, E., Boyle, E., Edwards, R., and Shen, C.: Radiocarbon dating of deep-sea corals, Radiocarbon, 44, 567–580, 2002.

Ammann, C. M., Joos, F., Schimel, D. S., Otto-Bliesner, B. L., and Tomas, R. A.: Solar influence on climate during the past millennium: results from transient simulations with the NCAR Climate System Model, P. Natl. Acad. Sci. USA, 104, 3713–3718, doi:10.1073/pnas.0605064103, 2007.

Anderson, R. F., Ali, S., Bradtmiller, L. I., Nielsen, S. H. H., Fleisher, M. Q., Anderson, B. E., and Burckle, L. H.: Wind-driven upwelling in the Southern Ocean and the deglacial rise in atmospheric CO_2, Science, 323, 1443–1448, doi:10.1126/science.1167441, 2009.

Andres, R., Fielding, D., Marland, G., Boden, T., Kumar, N., and Kearney, A.: Carbon dioxide emissions from fossil-fuel use, 1751–1950, Tellus B, 51, 759–765, doi:10.1034/j.1600-0889.1999.t01-3-00002.x, 1999.

Antonov, J. I., Seidov, D., Boyer, T. P., Locarnini, R. A., Mishonov, A. V., Garcia, H. E., Baranova, O. K., Zweng, M. M., and Johnson, D. R.: World Ocean Atlas 2009, Vol. 2: Salinity, NOAA Atlas NESDIS 68, US Government Printing Office, Washington, D.C., 2010.

R. Roth and F. Joos: A reconstruction of radiocarbon production and total solar irradiance   **1905**

Bard, E., Raisbeck, G., Yiou, F., and Jouzel, J.: Solar modulation of cosmogenic nuclide production over the last millennium: comparison between C-14 and Be-10 records, Earth Planet. Sc. Lett., 150, 453–462, doi:10.1016/S0012-821X(97)00082-4, 1997.

Bard, E., Raisbeck, G., Yiou, F., and Jouzel, J.: Solar irradiance during the last 1200 years based on cosmogenic nuclides, Tellus B, 52, 985–992, doi:10.1034/j.1600-0889.2000.d01-7.x, 2000.

Bauer, J. E., Williams, P. M., and Druffel, E. R. M.: ^{14}C activity of dissolved organic carbon fractions in the north-central Pacific and Sargasso Sea, Nature, 357, 667–670, doi:10.1038/357667a0, 1992.

Beer, J., Andrée, M., Oeschger, H., Stauffer, B., Balzer, R., Bonani, G., Stoller, C., Suter, M., Wölfli, W., and Finkel, R. C.: Temporal ^{10}Be variations in ice, Radiocarbon, 25, 269–278, 1983.

Berger, A. L.: Long-term variations of daily insolation and quaternary climatic changes, J. Atmos. Sci., 35, 2362–2367, 1978.

Bouttes, N., Paillard, D., Roche, D. M., Brovkin, V., and Bopp, L.: Last Glacial Maximum CO_2 and δ^{13}C successfully reconciled, Geophys. Res. Lett., 38, L02705, doi:10.1029/2010GL044499, 2011.

Broecker, W. and Barker, S.: A 190‰ drop in atmosphere's Δ^{14}C during the "Mystery Interval" (17.5 to 14.5 kyr), Earth Planet. Sc. Lett. 256, 90–99, doi:10.1016/j.epsl.2007.01.015, 2007.

Brovkin, V., Ganopolski, A., Archer, D., and Rahmstorf, S.: Lowering of glacial atmospheric CO_2 in response to changes in oceanic circulation and marine biogeochemistry, Paleoceanography, 22, PA4202, doi:10.1029/2006PA001380, 2007.

Brovkin, V., Ganopolski, A., Archer, D., and Munhoven, G.: Glacial CO_2 cycle as a succession of key physical and biogeochemical processes, Clim. Past, 8, 251–264, doi:10.5194/cp-8-251-2012, 2012.

Bryan, S. P., Marchitto, T. M., and Lehman, S. J.: The release of ^{14}C-depleted carbon from the deep ocean during the last deglaciation: evidence from the Arabian Sea, Earth Planet. Sc. Lett., 298, 244–254, doi:10.1016/j.epsl.2010.08.025, 2010.

Burke, A. and Robinson, L. F.: The Southern Ocean's role in carbon exchange during the last deglaciation, Science, 335, 557–561, doi:10.1126/science.1208163, 2012.

Castagnoli, G. and Lal, D.: Solar modulation effects in terrestrial production of carbon-14, Radiocarbon, 22, 133–158, 1980.

Clark, P. U., Shakun, J. D., Baker, P. A., Bartlein, P. J., Brewer, S., Brook, E., Carlson, A. E., Cheng, H., Kaufman, D. S., Liu, Z., Marchitto, T. M., Mix, A. C., Morrill, C., Otto-Bliesner, B. L., Pahnke, K., Russell, J. M., Whitlock, C., Adkins, J. F., Blois, J. L., Clark, J., Colman, S. M., Curry, W. B., Flower, B. P., He, F., Johnson, T. C., Lynch-Stieglitz, J., Markgraf, V., McManus, J., Mitrovica, J. X., Moreno, P. I., and Williams, J. W.: Global climate evolution during the last deglaciation, P. Natl. Acad. Sci. USA, 109, E1134–E1142, doi:10.1073/pnas.1116619109, 2012.

Crowley, T. J.: Causes of climate change over the past 1000 years, Science, 289, 270–277, doi:10.1126/science.289.5477.270, 2000.

Delaygue, G. and Bard, E.: An Antarctic view of beryllium-10 and solar activity for the past millennium, Clim. Dynam., 36, 2201–2218, doi:10.1007/s00382-010-0795-1, 2011.

De Pol-Holz, R., Keigwin, L., Southon, J., Hebbeln, D., and Mohtadi, M.: No signature of abyssal carbon in intermediate waters off Chile during deglaciation, Nat. Geosci., 3, 192–195, doi:10.1038/ngeo745, 2010.

Edwards, N. R. and Marsh, R.: Uncertainties due to transport-parameter sensitivity in an efficient 3-D ocean-climate model, Clim. Dynam., 24, 415–433, doi:10.1007/s00382-004-0508-8, 2005.

Ellison, C. R. W., Chapman, M. R., and Hall, I. R.: Surface and deep ocean interactions during the cold climate event 8200 years ago, Science, 312, 1929–1932, doi:10.1126/science.1127213, 2006.

Elsig, J., Schmitt, J., Leuenberger, D., Schneider, R., Eyer, M., Leuenberger, M., Joos, F., Fischer, H., and Stocker, T. F.: Stable isotope constraints on Holocene carbon cycle changes from an Antarctic ice core, Nature, 461, 507–510, doi:10.1038/nature08393, 2009.

Enting, I. G.: On the use of smoothing splines to filter CO_2 data, J. Geophys. Res., 92, 10977–10984, doi:10.1029/JD092iD09p10977, 1987.

Farquhar, G. D., Caemmerer, S. V., and Berry, J. A.: A biochemical-model of photosynthetic CO_2 assimilation in leaves of C-3 species, Planta, 149, 78–90, 1980.

Feely, R., Sabine, C., Lee, K., Berelson, W., Kleypas, J., Fabry, V., and Millero, F.: Impact of anthropogenic CO_2 on the $CaCO_3$ system in the oceans, Science, 305, 362–366, doi:10.1126/science.1097329, 2004.

Francey, R., Allison, C., Etheridge, D., Trudinger, C., Enting, I., Leuenberger, M., Langenfelds, R., Michel, E., and Steele, L.: A 1000-year high precision record of δ^{13}C in atmospheric CO_2, Tellus B, 51, 170–193, doi:10.1034/j.1600-0889.1999.t01-1-00005.x, 1999.

Franois, R., Altabet, M. A., Yu, E.-F., Sigman, D. M., Bacon, M. P., Frank, M., Bohrmann, G., Bareille, G., and Labeyrie, L. D.: Contribution of Southern Ocean surface-water stratification to low atmospheric CO_2 concentrations during the last glacial period, Nature, 389, 929–935, doi:10.1038/40073, 1997.

Fröhlich, C.: Evidence of a long-term trend in total solar irradiance, Astron. Astrophys., 501, L27–L30, doi:10.1051/0004-6361/200912318, 2009.

Galbraith, E. D., Jaccard, S. L., Pedersen, T. F., Sigman, D. M., Haug, G. H., Cook, M., Southon, J. R., and Francois, R.: Carbon dioxide release from the North Pacific abyss during the last deglaciation, Nature, 449, 890–893, doi:10.1038/nature06227, 2007.

Gehlen, M., Bopp, L., Emprin, N., Aumont, O., Heinze, C., and Ragueneau, O.: Reconciling surface ocean productivity, export fluxes and sediment composition in a global biogeochemical ocean model, Biogeosciences, 3, 521–537, doi:10.5194/bg-3-521-2006, 2006.

Gerber, S., Joos, F., Brugger, P., Stocker, T. F., Mann, M. E., Sitch, S., and Scholze, M.: Constraining temperature variations over the last millennium by comparing simulated and observed atmospheric CO_2, Clim. Dynam., 20, 281–299, doi:10.1007/s00382-002-0270-8, 2003.

Gleeson, L. and Axford, W.: Solar modulation of galactic cosmic rays, Astrophys. J., 154, 1011–1026, doi:10.1086/149822, 1968.

Gray, L. J., Beer, J., Geller, M., Haigh, J. D., Lockwood, M., Matthes, K., Cubasch, U., Fleitmann, D., Harrison, G., Hood, L., Luterbacher, J., Meehl, G. A., Shindell, D., van Geel, B., and White, W.: Solar influences on climate, Rev. Geophys., 48, RG4001, doi:10.1029/2009RG000282, 2010.

Griffies, S. M.: The Gent–Williams skew flux, J. Phys. Oceanogr., 28, 831–841, doi:10.1175/1520-0485(1998)028<0831:TGMSF>2.0.CO;2, 1998.

Hambaryan, V. V. and Neuhäuser, R.: A galactic short gamma-ray burst as cause for the ^{14}C peak in AD 774/5, Mon. Not. R. Astron. Soc., doi:10.1093/mnras/sts378, 430, 32–36, 2013.

Hansell, D. A., Carlson, C. A., Repeta, D. J., and Schlitzer, R.: Dissolved organic matter in the ocean a controversy stimulates new insights, Oceanography, 22, 202–211, 2009.

Heinze, C., Maier-Reimer, E., Winguth, A. M. E., and Archer, D.: A global oceanic sediment model for long-term climate studies, Global Biogeochem. Cy., 13, 221–250, 1999.

Herbst, K., Kopp, A., Heber, B., Steinhilber, F., Fichtner, H., Scherer, K., and Matthiä, D.: On the importance of the local interstellar spectrum for the solar modulation parameter, J. Geophys. Res., 115, D00I20, doi:10.1029/2009JD012557, 2010.

Hodell, D. A., Venz, K. A., Charles, C. D., and Ninnemann, U. S.: Pleistocene vertical carbon isotope and carbonate gradients in the South Atlantic sector of the Southern Ocean, Geochem. Geophy. Geosy., 4, 1–19, doi:10.1029/2002GC000367, 2003.

Hoffman, J. S., Carlson, A. E., Winsor, K., Klinkhammer, G. P., LeGrande, A. N., Andrews, J. T., Strasser, J. C.: Linking the 8.2 ka event and its freshwater forcing in the labrador sea, Geophys. Res. Lett., 39, L18703, doi:10.1029/2012GL053047, 2012.

Hughen, K., Baillie, M., Bard, E., Beck, J., Bertrand, C., Blackwell, P., Buck, C., Burr, G., Cutler, K., Damon, P., Edwards, R., Fairbanks, R., Friedrich, M., Guilderson, T., Kromer, B., McCormac, G., Manning, S., Ramsey, C., Reimer, P., Reimer, R., Remmele, S., Southon, J., Stuiver, M., Talamo, S., Taylor, F., van der Plicht, J., and Weyhenmeyer, C.: Marine04 marine radiocarbon age calibration, 0–26 cal kyr BP, Radiocarbon, 46, 1059–1086, 2004.

Jackson, A., Jonkers, A. R. T., and Walker, M. R.: Four centuries of geomagnetic secular variation from historical records, Philos. T. Roy. Soc. A, 358, 957–990, doi:10.1098/rsta.2000.0569, 2000.

Jansen, E., Overpeck, J., Briffa, K. R., Duplessy, J.-C., Joos, F., Masson-Delmotte, V., Olago, D., Otto-Bliesner, B., Peltier, W. R., Rahmstorf, S., Ramesh, R., Raynaud, D., Rind, D., Solomina, O., Villalba, R., and Zhang, D.: Palaeoclimate, in: Climate Change 2007: The Physical Science Basis. Working Group I Contribution to the Fourth Assessment Report of the Intergovernmental Panel on Climate Change, edited by: Solomon, S., Qin, D., Manning, M., Chen, Z., Marquis, M., Averyt, K. B., Tignor, M., and Miller, H. L., Cambridge University Press, 433–497, 2007.

Joos, F. and Spahni, R.: Rates of change in natural and anthropogenic radiative forcing over the past 20,000 years, P. Natl. Acad. Sci. USA, 105, 1425–1430, doi:10.1073/pnas.0707386105, 2008.

Joos, F., Prentice, I. C., Sitch, S., Meyer, R., Hooss, G., Plattner, G.-K., Gerber, S., and Hasselmann, K.: Global warming feedbacks on terrestrial carbon uptake under the Intergovernmental Panel on Climate Change (IPCC) emission scenarios, Global Biogeochem. Cy., 15, 891–907, 2001.

Joos, F., Gerber, S., Prentice, I. C., Otto-Bliesner, B. L., and Valdes, P. J.: Transient simulations of Holocene atmospheric carbon dioxide and terrestrial carbon since the Last Glacial Maximum, Global Biogeochem. Cy., 18, GB2002, doi:10.1029/2003GB002156, 2004.

Jungclaus, J. H., Lorenz, S. J., Timmreck, C., Reick, C. H., Brovkin, V., Six, K., Segschneider, J., Giorgetta, M. A., Crowley, T. J., Pongratz, J., Krivova, N. A., Vieira, L. E., Solanki, S. K., Klocke, D., Botzet, M., Esch, M., Gayler, V., Haak, H., Raddatz, T. J., Roeckner, E., Schnur, R., Widmann, H., Claussen, M., Stevens, B., and Marotzke, J.: Climate and carbon-cycle variability over the last millennium, Clim. Past, 6, 723–737, doi:10.5194/cp-6-723-2010, 2010.

Kalnay, E., Kanamitsu, M., Kistler, R., Collins, W., Deaven, D., Gandin, L., Iredell, M., Saha, S., White, G., Woollen, J., Zhu, Y., Chelliah, M., Ebisuzaki, W., Higgins, W., Janowiak, J., Mo, K., Ropelewski, C., Wang, J., Leetmaa, A., Reynolds, R., Jenne, R., and Joseph, D.: The NCEP/NCAR 40-year reanalysis project, B. Am. Meteorol. Soc., 77, 437–471, doi:10.1175/1520-0477(1996)077<0437:TNYRP>2.0.CO;2, 1996.

Kay, S. M.: Modern Spectral Estimation: Theory and Application, Prentice-Hall, Englewood Cliffs, N.J., 1988.

Key, R. M., Kozyr, A., Sabine, C. L., Lee, K., Wanninkhof, R., Bullister, J. L., Feely, R. A., Millero, F. J., Mordy, C., and Peng, T.-H.: A global ocean carbon climatology: results from Global Data Analysis Project (GLODAP), Global Biogeochem. Cy., 18, GB4031, doi:10.1029/2004GB002247, 2004.

Klein Goldewijk, K.: Estimating global land use change over the past 300 years: the HYDE database, Global Biogeochem. Cy., 15, 417–433, 2001.

Klein Goldewijk, K. and van Drecht, G.: HYDE3: current and historical population and land cover, in: Integrated Modelling of Global Environmental Change, An Overview of IMAGE 2.4., edited by: Bouwman, A. F., Kram, T., and Klein Goldewijk, K., Netherlands Environmental Assessment Agency (MNP), Bilthoven, the Netherlands, 2006.

Knudsen, M. F., Riisager, P., Donadini, F., Snowball, I., Muscheler, R., Korhonen, K., and Pesonen, L. J.: Variations in the geomagnetic dipole moment during the Holocene and the past 50 kyr, Earth Planet. Sc. Lett., 272, 319–329, doi:10.1016/j.epsl.2008.04.048, 2008.

Kobashi, T., Severinghaus, J. P., Brook, E. J., Barnola, J.-M., and Grachev, A. M.: Precise timing and characterization of abrupt climate change 8200 years ago from air trapped in polar ice, Quaternary Sci. Rev., 26, 1212–1222, doi:10.1016/j.quascirev.2007.01.009, 2007.

Köhler, P., Fischer, H., Munhoven, G., and Zeebe, R.: Quantitative interpretation of atmospheric carbon records over the last glacial termination, Global Biogeochem. Cy., 19, GB4020, doi:10.1029/2004GB002345, 2005.

Kopp, G. and Lean, J. L.: A new, lower value of total solar irradiance: evidence and climate significance, Geophys. Res. Lett., 38, L01706, doi:10.1029/2010GL045777, 2011.

Korte, M., Constable, C., Donadini, F., and Holme, R.: Reconstructing the Holocene geomagnetic field, Earth Planet. Sc. Lett., 312, 497–505, doi:10.1016/j.epsl.2011.10.031, 2011.

Kovaltsov, G. A., Mishev, A., and Usoskin, I. G.: A new model of cosmogenic production of radiocarbon ^{14}C in the atmosphere, Earth Planet. Sc. Lett., 337–338, 114–120, doi:10.1016/j.epsl.2012.05.036, 2012.

Krakauer, N. Y., Randerson, J. T., Primeau, F. W., Gruber, N., and Menemenlis, D.: Carbon isotope evidence for the latitudinal distribution and wind speed dependence of the air–sea gas transfer velocity, 7th International Carbon Dioxide Conference (CO_2), Boulder, CO, 25–30 September 2005, Tellus B, 58, 390–417, doi:10.1111/j.1600-0889.2006.00223.x, 2006.

Kwon, E. Y., Primeau, F., and Sarmiento, J. L.: The impact of remineralization depth on the air–sea carbon balance, Nat. Geosci., 2, 630–635, doi:10.1038/ngeo612, 2009.

Lambert, F., Delmonte, B., Petit, J. R., Bigler, M., Kaufmann, P. R., Hutterli, M. A., Stocker, T. F., Ruth, U., Steffensen, J. P., and Maggi, V.: Dust-climate couplings over the past 800,000-years from the EPICA Dome C ice core, Nature, 452, 616–619, doi:10.1038/nature06763, 2008.

Lean, J.: Evolution of the Sun's spectral irradiance since the Maunder Minimum, Geophys. Res. Lett., 27, 2425–2428, doi:10.1029/2000GL000043, 2000.

Lisiecki, L. E. and Raymo, M. E.: A Pliocene-Pleistocene stack of 57 globally distributed benthic δ^{18}O records, Paleoceanography, 20, PA1003, doi:10.1029/2004PA001071, 2005.

Locarnini, R. A., Mishonov, A. V., Antonov, J. I., Boyer, T. P., Garcia, H. E., Baranova, O. K., Zweng, M. M., and Johnson, D. R.: World Ocean Atlas 2009, Vol. 1: Temperature, NOAA Atlas NESDIS 68, US Government Printing Office, Washington, D.C., 2010.

Lockwood, M.: Solar change and climate: an update in the light of the current exceptional solar minimum, P. Natl. Acad. Sci. USA, 466, 303–329, doi:10.1098/rspa.2009.0519, 2010.

Lockwood, M.: Solar influence on global and regional climates, Surv. Geophys., 33, 503–534, doi:10.1007/s10712-012-9181-3, 2012.

Lockwood, M. and Owens, M. J.: Centennial changes in the heliospheric magnetic field and open solar flux: the consensus view from geomagnetic data and cosmogenic isotopes and its implications, J. Geophys. Res., 116, A04109, doi:10.1029/2010JA016220, 2011.

Lundstedt, H., Liszka, L., Lundin, R., and Muscheler, R.: Long-term solar activity explored with wavelet methods, Ann. Geophys., 24, 769–778, doi:10.5194/angeo-24-769-2006, 2006.

Luo, C., Mahowald, N. M., and del Corral, J.: Sensitivity study of meteorological parameters on mineral aerosol mobilization, transport, and distribution, J. Geophys. Res., 108, 4447, doi:10.1029/2003JD003483, 2003.

MacFarling Meure, C., Etheridge, D., Trudinger, C., Steele, P., Langenfelds, R., van Ommen, T., Smith, A., and Elkins, J.: Law Dome CO_2, CH_4 and N_2O ice core records extended to 2000 years BP, Geophys. Res. Lett., 33, L14810, doi:10.1029/2006GL026152, 2006.

Mahowald, N. M., Muhs, D. R., Levis, S., Rasch, P. J., Yoshioka, M., Zender, C. S., and Luo, C.: Change in atmospheric mineral aerosols in response to climate: last glacial period, preindustrial, modern, and doubled carbon dioxide climates, J. Geophys. Res., 111, D10202, doi:10.1029/2005JD006653, 2006.

Marchal, O.: Optimal estimation of atmospheric ^{14}C production over the Holocene: paleoclimate implications, Clim. Dynam., 24, 71–88, doi:10.1007/s00382-004-0476-z, 2005.

Marchitto, T. M., Lehman, S. J., Ortiz, J. D., Fluckiger, J., and van Geen, A.: Marine radiocarbon evidence for the mechanism of deglacial atmospheric CO_2 rise, Science, 316, 1456–1459, 2007.

Masarik, J. and Beer, J.: Simulation of particle fluxes and cosmogenic nuclide production in the Earth's atmosphere, J. Geophys. Res., 104, 12099–12111, doi:10.1029/1998JD200091, 1999.

Masarik, J. and Beer, J.: An updated simulation of particle fluxes and cosmogenic nuclide production in the Earth's atmosphere, J. Geophys. Res., 114, D11103, doi:10.1029/2008JD010557, 2009.

Matsumoto, K.: Biology-mediated temperature control on atmospheric $p$$CO_2$ and ocean biogeochemistry, Geophys. Res. Lett., 34, L20605, doi:10.1029/2007GL031301, 2007.

Matsumoto, K. and Yokoyama, Y.: Atmospheric Δ^{14}C reduction in simulations of Atlantic overturning circulation shutdown Global Biogeochem. Cy., 27, 296–304, doi:10.1002/gbc.20035, 2013.

McCormac, F., Hogg, A., Blackwell, P., Buck, C., Higham, T., and Reimer, P.: SHCal04 Southern Hemisphere calibration, 0–11.0 cal kyr BP, Radiocarbon, 46, 1087–1092, 2004.

Menviel, L. and Joos, F.: Toward explaining the Holocene carbon dioxide and carbon isotope records: results from transient ocean carbon cycle-climate simulations, Paleoceanography, 27, PA1207, doi:10.1029/2011PA002224, 2012.

Menviel, L., Joos, F., and Ritz, S.: Simulating atmospheric CO_2, ^{13}C and the marine carbon cycle during the Last Glacial-Interglacial cycle: possible role for a deepening of the mean remineralization depth and an increase in the oceanic nutrient inventory, Quaternary Sci. Rev., 56, 46–68, doi:10.1016/j.quascirev.2012.09.012, 2012.

Miyake, F., Nagaya, K., Masuda, K., and Nakamura, T.: A signature of cosmic-ray increase in ad 774–775 from tree rings in Japan, Nature, 486, 240–242, doi:10.1038/nature11123, 2012.

Monnin, E., Steig, E. J., Siegenthaler, U., Kawamura, K., Schwander, J., Stauffer, B., Stocker, T. F., Morse, D. L., Barnola, J.-M., Bellier, B., Raynaud, D., and Fischer, H.: Evidence for substantial accumulation rate variability in Antarctica during the Holocene, through synchronization of CO_2 in the Taylor Dome, Dome C and DML ice cores, Earth Planet. Sc. Lett., 224, 45–54, doi:10.1016/j.epsl.2004.05.007, 2004.

Müller, S. A., Joos, F., Edwards, N. R., and Stocker, T. F.: Water mass distribution and ventilation time scales in a cost-efficient, three-dimensional ocean model, J. Climate, 19, 5479–5499, doi:10.1175/JCLI3911.1, 2006.

Müller, S. A., Joos, F., Edwards, N. R., and Stocker, T. F.: Modeled natural and excess radiocarbon: sensitivities to the gas exchange formulation and ocean transport strength, Global Biogeochem. Cy., 22, GB3011, doi:10.1029/2007GB003065, 2008.

Muscheler, R., Beer, J., Kubik, P. W., and Synal, H.-A.: Geomagnetic field intensity during the last 60,000 years based on ^{10}Be and ^{36}Cl from the Summit ice cores and ^{14}C, Quaternary Sci. Rev., 24, 1849–1860, 2005a.

Muscheler, R., Joos, F., Muller, S. A., and Snowball, I.: Climate: how unusual is today's solar activity?, Nature, 436, E3–E4, doi:10.1038/nature04045, 2005b.

Muscheler, R., Joos, F., Beer, J., Müller, S. A., Vonmoos, M., and Snowball, I.: Solar activity during the last 1000 yr inferred from radionuclide records, Quaternary Sci. Rev., 26, 82–97, doi:10.1016/j.quascirev.2006.07.012, 2007.

Muscheler, R., Kromer, B., Bjorck, S., Svensson, A., Friedrich, M., Kaiser, K. F., and Southon, J.: Tree rings and ice cores reveal ^{14}C calibration uncertainties during the Younger Dryas, Nat. Geosci., 1, 263–267, doi:10.1038/ngeo128, 2008.

Naegler, T. and Levin, I.: Closing the global radiocarbon budget 1945–2005, J. Geophys. Res.-Atmos., 111, D12311, doi:10.1029/2005JD006758, 2006.

Najjar, R. G., Orr, J., Sabine, C. L., and Joos, F.: Biotic-HOWTO, Internal OCMIP Report, Tech. rep., LSCE/CEA Saclay, Gif-sur-Yvette, France, 1999.

Oeschger, H., Siegenthaler, U., Schotterer, U., and Gugelmann, A.: A box diffusion model to study the carbon dioxide exchange in nature, Tellus, 27, 168–192, 1975.

Orr, J. and Najjar, R. G.: Abiotic-HOWTO, Internal OCMIP Report, Tech. rep., LSCE/CEA Saclay, Gif-sur-Yvette, France, 1999.

Parekh, P., Joos, F., and Müller, S. A.: A modeling assessment of the interplay between aeolian iron fluxes and iron-binding ligands in controlling carbon dioxide fluctuations during Antarctic warm events, Paleoceanography, 23, PA4202, doi:10.1029/2007PA001531, 2008.

Peltier, W. R.: Ice age paleotopography, Science, 265, 195–201, 1994.

Peltier, W. R.: Global glacial isostasy and the surface of the ice-age Earth: the ICE-5G (VM2) model and GRACE, Annu. Rev. Earth Pl. Sc., 32, 111–149, doi:10.1146/annurev.earth.32.082503.144359, 2004.

Reader, M. C. and Boer, G. J.: The modification of greenhouse gas warming by the direct effect of sulphate aerosols, Clim. Dynam., 14, 593–607, 1998.

Reimer, P. J., Baillie, M. G. L., Bard, E., Bayliss, A., Beck, J. W., Blackwell, P. G., Ramsey, C. B., Buck, C. E., Burr, G. S., Edwards, R. L., Friedrich, M., Grootes, P. M., Guilderson, T. P., Hajdas, I., Heaton, T. J., Hogg, A. G., Hughen, K. A., Kaiser, K. F., Kromer, B., McCormac, F. G., Manning, S. W., Reimer, R. W., Richards, D. A., Southon, J. R., Talamo, S., Turney, C. S. M., van der Plicht, J., and Weyhenmeye, C. E.: IntCal09 and Marine09 radiocarbon age calibration curves, 0–50,000 years cal BP, Radiocarbon, 51, 1111–1150, 2009.

Ritz, S. P., Stocker, T. F., and Joos, F.: A coupled dynamical ocean-energy balance atmosphere model for paleoclimate studies, J. Climate, 24, 349–75, doi:10.1175/2010JCLI3351.1, 2011.

Sarmiento, J. L. and Gruber, N.: Ocean Biogeochemical Dynamics, Chapt. 8: Carbon Cycle, Princeton University Press, 318–358, 2006.

Schmidt, G. A., Jungclaus, J. H., Ammann, C. M., Bard, E., Braconnot, P., Crowley, T. J., Delaygue, G., Joos, F., Krivova, N. A., Muscheler, R., Otto-Bliesner, B. L., Pongratz, J., Shindell, D. T., Solanki, S. K., Steinhilber, F., and Vieira, L. E. A.: Climate forcing reconstructions for use in PMIP simulations of the last millennium (v1.0), Geosci. Model Dev., 4, 33–45, doi:10.5194/gmd-4-33-2011, 2011.

Schmidt, G. A., Jungclaus, J. H., Ammann, C. M., Bard, E., Braconnot, P., Crowley, T. J., Delaygue, G., Joos, F., Krivova, N. A., Muscheler, R., Otto-Bliesner, B. L., Pongratz, J., Shindell, D. T., Solanki, S. K., Steinhilber, F., and Vieira, L. E. A.: Climate forcing reconstructions for use in PMIP simulations of the Last Millennium (v1.1), Geosci. Model Dev., 5, 185–191, doi:10.5194/gmd-5-185-2012, 2012.

Schmitt, J., Schneider, R., Elsig, J., Leuenberger, D., Lourantou, A., Chappellaz, J., Köhler, P., Joos, F., Stocker, T. F., Leuenberger, M., and Fischer, H.: Carbon isotope constraints on the deglacial CO_2 rise from ice cores, Science, 336, 711–714, doi:10.1126/science.1217161, 2012.

Scholze, M., Kaplan, J. O., Knorr, W., and Heimann, M.: Climate and interannual variability of the atmosphere-biosphere $^{13}CO_2$ flux, Geophys. Res. Lett., 30, 1097, doi:10.1029/2002GL015631, 2003.

Schrijver, C. J., Livingston, W. C., Woods, T. N., and Mewaldt, R. A.: The minimal solar activity in 2008–2009 and its implications for long-term climate modeling, Geophy. Res. Lett., 38, L06701, doi:10.1029/2011GL046658, 2011.

Shackleton, N.: Climate change across the hemispheres, Science, 291, 58–59, doi:10.1126/science.10.1126/SCIENCE.1057253, 2001.

Shapiro, A. I., Schmutz, W., Rozanov, E., Schoell, M., Haberreiter, M., Shapiro, A. V., and Nyeki, S.: A new approach to the long-term reconstruction of the solar irradiance leads to large historical solar forcing, Astron. Astrophys., 529, A67, doi:10.1051/0004-6361/201016173, 2011.

Siegenthaler, U.: Uptake of excess CO_2 by an outcrop-diffusion model of the ocean, J. Geophys. Res., 88, 3599–3608, 1983.

Singarayer, J. S. and Valdes, P. J.: High-latitude climate sensitivity to ice-sheet forcing over the last 120 kyr, Quaternary Sci. Rev., 29, 43–55, doi:10.1016/j.quascirev.2009.10.011, 2010.

Sitch, S., Smith, B., Prentice, I., Arneth, A., Bondeau, A., Cramer, W., Kaplan, J., Levis, S., Lucht, W., Sykes, M., Thonicke, K., and Venevsky, S.: Evaluation of ecosystem dynamics, plant geography and terrestrial carbon cycling in the LPJ dynamic global vegetation model, Global Change Biol., 9, 161–185, doi:10.1046/j.1365-2486.2003.00569.x, 2003.

Skinner, L. C., Fallon, S., Waelbroeck, C., Michel, E., and Barker, S.: Ventilation of the deep Southern Ocean and deglacial CO_2 rise, Science, 328, 1147–1151, 2010.

Solanki, S., Usoskin, I., Kromer, B., Schussler, M., and Beer, J.: Unusual activity of the Sun during recent decades compared to the previous 11,000 years, Nature, 431, 1084–1087, 2004.

Spahni, R., Joos, F., Stocker, B. D., Steinacher, M., and Yu, Z. C.: Transient simulations of the carbon and nitrogen dynamics in northern peatlands: from the Last Glacial Maximum to the 21st century, Clim. Past Discuss., 8, 5633–5685, doi:10.5194/cpd-8-5633-2012, 2012.

Steinacher, M.: Modeling Changes in the Global Carbon Cycle-Climate System, Ph. D. thesis, University of Bern, 2011.

Steinhilber, F., Abreu, J. A., and Beer, J.: Solar modulation during the Holocene, Astrophys. Space Sci. T., 4, 1–6, doi:10.5194/astra-4-1-2008, 2008.

Steinhilber, F., Beer, J., and Fröhlich, C.: Total solar irradiance during the Holocene, Geophys. Res. Lett., 36, L19704, doi:10.1029/2009GL040142, 2009.

Steinhilber, F., Abreu, J. A., Beer, J., and McCracken, K. G.: Interplanetary magnetic field during the past 9300 years inferred from cosmogenic radionuclides, J. Geophys. Res., 115, A01104, doi:10.1029/2009JA014193, 2010.

R. Roth and F. Joos: A reconstruction of radiocarbon production and total solar irradiance 1909

Steinhilber, F., Abreu, J. A., Beer, J., Brunner, I., Christl, M., Fischer, H., Heikkilä, U., Kubik, P. W., Mann, M., Mc-Cracken, K. G., Miller, H., Miyahara, H., Oerter, H., and Wilhelms, F.: 9,400 years of cosmic radiation and solar activity from ice cores and tree rings, P. Natl. Acad. Sci. USA, 109, 5967–5971, doi:10.1073/pnas.1118965109, 2012.

Stocker, B. D., Strassmann, K., and Joos, F.: Sensitivity of Holocene atmospheric CO_2 and the modern carbon budget to early human land use: analyses with a process-based model, Biogeosciences, 8, 69–88, doi:10.5194/bg-8-69-2011, 2011.

Strassmann, K. M., Joos, F., and Fischer, G.: Simulating effects of land use changes on carbon fluxes: past contributions to atmospheric CO_2 increases and future commitments due to losses of terrestrial sink capacity, Tellus B, 60, 583–603, doi:10.1111/j.1600-0889.2008.00340.x, 2008.

Stuiver, M. and Polach, H. A.: Discussion: reporting of ^{14}C data, Radiocarbon, 3, 355–363, 1977.

Sweeney, C., Gloor, E., Jacobson, A. R., Key, R. M., McKinley, G., Sarmiento, J. L., and Wanninkhof, R.: Constraining global air-sea gas exchange for CO_2 with recent bomb ^{14}C measurements, Global Biogeochem. Cy., 21, GB2015, doi:10.1029/2006GB002784, 2007.

Tagliabue, A., Bopp, L., Roche, D. M., Bouttes, N., Dutay, J.-C., Alkama, R., Kageyama, M., Michel, E., and Paillard, D.: Quantifying the roles of ocean circulation and biogeochemistry in governing ocean carbon-13 and atmospheric carbon dioxide at the last glacial maximum, Clim. Past, 5, 695–706, doi:10.5194/cp-5-695-2009, 2009.

Tarnocai, C., Canadell, J. G., Schuur, E. A. G., Kuhry, P., Mazhitova, G., and Zimov, S.: Soil organic carbon pools in the northern circumpolar permafrost region, Global Biogeochem. Cy., 23, GB2023, doi:10.1029/2008GB003327, 2009.

Thompson, S. L. and Warren, S. G.: Parameterization of outgoing infrared radiation derived from detailed radiative calculations, J. Atmos. Sci., 39, 2667–2680, 1982.

Thornalley, D. J. R., Barker, S., Broecker, W. S., Elderfield, H., and McCave, I. N.: The deglacial evolution of North Atlantic deep convection, Science, 331, 202–205, doi:10.1126/science.1196812, 2011.

Tschumi, T., Joos, F., and Parekh, P.: How important are Southern Hemisphere wind changes for low glacial carbon dioxide? A model study, Paleoceanography, 23, PA4208, doi:10.1029/2008PA001592, 2008.

Tschumi, T., Joos, F., Gehlen, M., and Heinze, C.: Deep ocean ventilation, carbon isotopes, marine sedimentation and the deglacial CO_2 rise, Clim. Past, 7, 771–800, doi:10.5194/cp-7-771-2011, 2011.

Usoskin, I. G. and Kromer, B.: Reconstruction of the ^{14}C production rate from measured relative abundance, Radiocarbon, 47, 31–37, 2005.

Usoskin, I. G., Solanki, S. K., and Kovaltsov, G. A.: Grand minima and maxima of solar activity: new observational constraints, Astron. Astrophys., 471, 301–309, doi:10.1051/0004-6361:20077704, 2007.

Usoskin, I. G., Bazilevskaya, G. A., and Kovaltsov, G. A.: Solar modulation parameter for cosmic rays since 1936 reconstructed from ground-based neutron monitors and ionization chambers, J. Geophys. Res., 116, A02104, doi:10.1029/2010JA016105, 2011.

Usoskin, I. G., Kromer, B., Ludlow, F., Beer, J., Friedrich, M., Kovaltsov, G. A., Solanki, S. K., and Wacker, L.: The AD 775 cosmic event revisited: the Sun is to blame, Astron. Astrophys., 552, L3, doi:10.1051/0004-6361/201321080, 2013.

Vecsei, A. and Berger, W. H.: Increase of atmospheric CO_2 during deglaciation: constraints on the coral reef hypothesis from patterns of deposition, Global Biogeochem. Cy., 18, GB1035, doi:10.1029/2003GB002147, 2004.

Vieira, L. E. A., Solanki, S. K., Krivova, N. A., and Usoskin, I.: Evolution of the solar irradiance during the Holocene, Astron. Astrophys., 531, A6, doi:10.1051/0004-6361/201015843, 2011.

Vonmoos, M., Beer, J., and Muscheler, R.: Large variations in Holocene solar activity: constraints from ^{10}Be in the Greenland Ice Core Project ice core, J. Geophys. Res., 111, A10105, doi:10.1029/2005JA011500, 2006.

Wang, Y.-M., Lean, J. L., and Sheeley Jr., N. R.: Modeling the Sun's magnetic field and irradiance since 1713, Astrophys. J., 625, 522–538, 2005.

Wanner, H., Beer, J., Crowley, T. J., Cubasch, U., Flückiger, J., Goosse, H., Grosjean, M., Joos, F., Kaplan, J. O., Küttel, M., Solomina, O., Stocker, T. F., Tarasov, P., Wagner, M., and Widmann, M.: Mid- to Late Holocene climate change: an overview, Quaternary Sci. Rev., 27, 1791–1828, doi:10.1016/j.quascirev.2008.06.013, 2008.

Watson, R.: IPCC Special Report: Land Use, Land Use Change, and Forestry, Summary for Policymakers, Tech. rep., Cambridge University Press, New York, 2000.

Weaver, A. J., Eby, M., Wiebe, E. C., Bitz, C. M., Duffy, P. B., Ewen, T. L., Fanning, A. F., Holland, M. M., MacFadyen, A., Wang, H. X., and Yoshimori, M.: The UVic Earth System Climate Model: model description, climatology, and applications to past, present and future climates, Atmos. Ocean, 39, 361–428, 2001.

Xapsos, M. and Burke, E.: Evidence of 6000 year periodicity in reconstructed sunspot numbers, Sol. Phys., 257, 363–369, doi:10.1007/s11207-009-9380-3, 2009.

Yang, S., Odah, H., and Shaw, J.: Variations in the geomagnetic dipole moment over the last 12000 years, Geophys. J. Int., 140, 158–162, doi:10.1046/j.1365-246x.2000.00011.x, 2000.

Yu, Z., Loisel, J., Brosseau, D. P., Beilman, D. W., and Hunt, S. J.: Global peatland dynamics since the Last Glacial Maximum, Geophys. Res. Lett., 37, L13402, doi:10.1029/2010GL043584, 2010.

4.2   Supplementary material to: A reconstruction of radiocarbon production and total solar irradiance from the Holocene ^{14}C and CO$_2$ records: implications of data and model uncertainties

4.2.1   The carbon cycle response to changes in the remineralization profile of organic matter

In this section the response of the carbon cycle to changes in the remineralization profile of particulate organic matter (POM) is discussed. This profile was altered in Roth & Joos (2013) in order to force the model in a LGM state compatible with observed atmospheric CO$_2$. The implication of glacial-interglacial remineralization changes in the context of CO$_2$ and δ^{13}C is further discussed in Menviel et al. (2012). The other mechanism invoked in Roth & Joos (2013), i.e. the change in surface ocean wind stress, has already been discussed in detail by Tschumi et al. (2011).

Kwon et al. (2009) pointed out the high sensitivity of atmospheric CO$_2$ to changes in the depth where organic matter remineralizes and speculated for a possible role of this mechanism to explain G-IG CO$_2$ changes. Kwon et al. (2009) used an OCMIP-type biogeochemistry model similar to that incorporated into the Bern3D ocean model, where remineralization in the water column is parametrized according a power-law know as the "Martin-curve" (Martin et al., 1987):

$$F_{\text{PO}_4}(z) = \int\limits_{z'=z_e}^{0} (1-\sigma)\Gamma_{\text{new}}(z')dz' \left(\frac{z}{z_e}\right)^{-\alpha} \text{ for } z > z_e. \tag{4.1}$$

Here, $F_{\text{PO}_4}(z)$ is the flow of organic matter at depth z, 1-σ the fraction of the new production (Γ_{new}) which is exported out of the euphotic zone at $z_e = 75$ m. The exponent α defines the shape of the curve: a high value of α shoals while a low α deepens the depth at which organic matter is remineralized. The default configuration is $\alpha = 0.9$ in the Bern3D model. The stated numbers are valid for the Bern3D model, the model of Kwon et al. (2009) uses slightly different values.

In contrast to the model used by Kwon et al. (2009), the Bern3D ocean model is coupled to a sediment model. i.e. an "open" model subject to burial-weathering dynamics. The sensitivity of atmospheric CO$_2$ to varying α is found to be even more pronounced in the coupled ocean-sediment model, making α a powerful tuning-knob to alter CO$_2$ as applied in Menviel et al. (2012) as well as in Roth & Joos (2013).

In the following, sensitivity runs are discussed where α is set to discrete values for preindustrial background conditions of the carbon cycle-climate system with CO$_2$ set to 278 ppm during the spinup. The same experiments have also been conducted with a setup where the sediment model was deactivated to mimic the model invoked by Kwon et al. (2009).

We now focus on the experiment where α has been set to 0.8, this corresponds an increase in the depth where $F_{\text{PO}_4}(z)/F_{\text{PO}_4}(z_e)$ is reduced to 1/e (e-folding depth) of 262 m, i.e. +34 m compared to the control experiment ($\alpha = 0.9$). Figure 4.1 shows the resulting equilibrium anomalies w.r.t. the control simulation for PO$_4$, DIC, Alk and (potential) pCO$_2$ in a transect through the Atlantic, Southern Ocean and Pacific.

Without sediment module, the oceans PO$_4$ inventory is conserved and a deepening of the remineralization depth leads to a steepening of the gradient in PO$_4$ and DIC as more POM reaches the deep ocean. At the same time, Alk is slightly increased at shallow depths as less POM is remineralized near the surface ocean (POM remineralization consumes Alk). These changes in DIC and Alk lead to a reduction in surface ocean pCO$_2$ and thus atmospheric CO$_2$.

Figure 4.1: Comparison of anomalies of oceanic PO_4, DIC, Alk and (potential) pCO_2 from the perturbation run ($\alpha = 0.8$) w.r.t. the control run ($\alpha = 0.9$). Anomalies are calculated after $40\,$kyr and shown as a transect through the Atlantic, Southern Ocean and Pacific. The left column shows the results in the setup where no sediment model was coupled to the ocean model, while the right column shows the corresponding results in the coupled ocean-sediment model.

In the setup with sediment model, downward fluxes of POM (and $CaCO_3$) are not remineralized at the seafloor, but deposited on the model's sediment layer and may get completely buried after some thousand years. This organic matter sedimentation is a sink for ocean tracers: an enhanced burial of POM leads to an transient imbalance between burial and weathering of PO_4, DIC and Alk. Global integrated fluxes are presented in Fig. 4.2. Although the export production of POM decreases as a result of the limited nutrient availability, the loss of carbon due to seafloor POM sedimentation, is increased. On the other hand, also the $CaCO_3$ cycle is affected as the lysocline deepens (not shown). Despite the deepened lysocline, the $CaCO_3$ burial rates are not enhanced because the reduced rate of export production overcompensates for the larger volume of water oversaturated w.r.t. calcite.

Both the reduced $CaCO_3$ and the increased POM burial rates lead to a transiently positive oceanic Alk budget as weathering exceeds burial. For DIC, this imbalance is less pronounced as changes $CaCO_3$ and POM partly compensates. This increase in mean oceanic Alk, and thus the decrease in seawater pCO_2, is clearly visible in Fig. 4.1.

To summarize: the change of α leads to an much stronger perturbation in the ocean's carbonate system in an open model: this is because the sustained imbalance between weathering and burial rates of DIC and Alk, overcompensating the counteracting effect of a net removal of nutrients from the ocean.

Now the response in atmospheric CO_2 is quantified for a wider range of choices for α. In Figure 4.3a, the time-evolution of those variables is presented again compared to a closed system. The change in atmospheric CO_2 is 4–7 times higher in the setup with sediments compared to the setup without sediments due to the aforementioned processes. As most of the changes in CO_2 can be attributed to the weathering-burial imbalance, the involved timescales are relatively long with an e-folding timescale, that is the time where 63% of the final anomaly is reached, of $\approx 7000 \, \text{yr}$. Compared to this, the corresponding timescale in the closed system is only $\approx 650 \, \text{yr}$!

Can we also expect a drastic change in atmospheric $\Delta^{14}C$? As shown in Fig. 4.3b, the changes are modest with only 30‰ (i.e. 3%) change for $\alpha = 0.9 \to 0.8$ compared to the 24% change in CO_2. This can be explained with the fact that atmospheric $\Delta^{14}C$ is primarily controlled by the rate of which ^{14}C is transported away from the atmosphere, e.g. by air-sea gas-exchange and subsequent mixing in the deep ocean by advection and diffusion. The high rate of ^{14}C transport through the upper ocean due to the strong gradient in ^{14}R between the atmosphere and the deep ocean is dominant compared to the relatively weak biological pump. In addition, the system has only a limited "memory" due to the radioactive decay, i.e. longterm imbalances
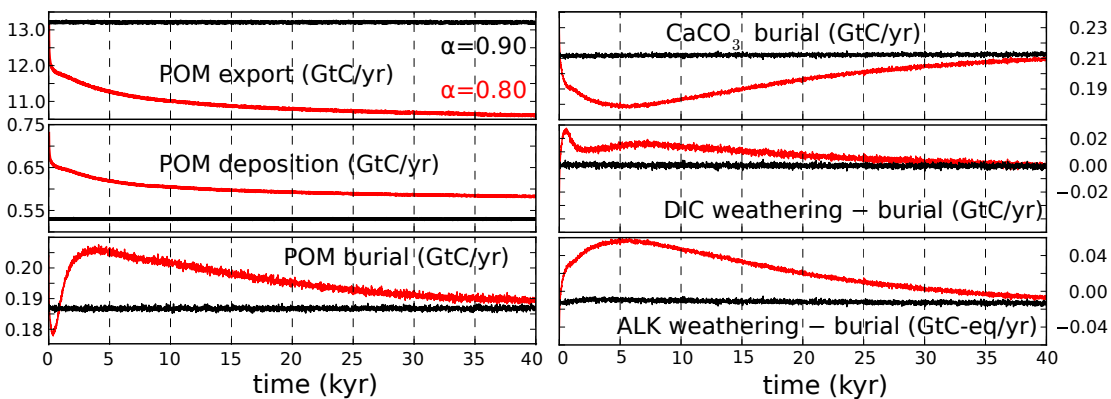

Figure 4.2: Globally integrated export, deposition and burial fluxes for the control run ($\alpha = 0.9$, black) and the perturbation experiment ($\alpha = 0.8$, red). The imbalance between weathering and burial of DIC and Alk accumulating over many $10 \, \text{kyr}$ leads to strong changes in atmospheric CO_2 shown in Fig. 4.3.

between ^{14}C (in POM, and $CaCO_3$) do not accumulate long enough to generate a large response in atmospheric $\Delta^{14}C$.

In fact, the changes in atmospheric $\Delta^{14}C$ shown in Fig. 4.3b are mainly a result of the reduced CO_2 levels: given the constant rate of ^{14}C production, a lower atmospheric ^{12}C inventory increases $^{12}C/^{14}C$ and thus $\Delta^{14}C$. But the changes in $\Delta^{14}C$ are not proportional to changes in CO_2; increased air-sea gas exchange driven by increased ^{14}R removes most of the perturbation and leave only $\approx 1/10$ of the anomaly in the atmosphere.

Figure 4.3: Equilibrium response of atmospheric CO_2 **(a)** and $\Delta^{14}C$ of CO_2 **(b)** for a range of values for α (0.9 being the base case). Black lines show the response in the setup with sediment module system, while the blue lines show the same experiments conducted without sediment model.

4.3 Production rate estimation for the spike in $\Delta^{14}C$ of CO_2 in 774/775 AD

Miyake et al. (2012) found an increase in the annual values atmospheric $\Delta^{14}C$ measured in Japanese tree-ring (i.e. $\approx 12‰$ within a single year, shown in the upper panel of Fig. 4.5). The question arises how energetic the incoming protons were to cause this sharp increase. If this energy is know, the event could be attributed to a certain cause (e.g. whether it's of solar origin or not). This energy can be calculated if the ^{14}C production rate can be reconstructed for this event. Different recent publications came up with very different estimates for Q and thus a different interpretation on the possible causes of the 774/775 AD event. Here an estimate to constrain Q during this events with the Bern3D model is presented.

Well mixed atmosphere

As a starting point, we assume the atmosphere to be well mixed, i.e. the (radio)carbon concentration is everywhere the same within the atmosphere (i.e. horizontally and vertically)[1].

---

[1]This corresponds to the setup used in Roth & Joos (2013) where decadal changes in Q were examined.

Thus, the atmosphere can be approximated by one box. This is only justified if variations in atmospheric $\Delta^{14}C$ are small compared to the mixing timescale within the atmosphere.

The production of radiocarbon can then be estimated by solving the atmospheric budget equation for ^{14}C:

$$Q = {}^{14}F_{as} + {}^{14}F_{ab} + \lambda^{14}N_a + {}^{14}\dot{N}_a \quad . \tag{4.2}$$

Given an atmospheric $\Delta^{14}C$ and CO_2 history, the atmospheric ^{14}C inventory (^{14}N) can be calculated. The fluxes from/to the ocean and land biosphere ($^{14}F_{as}$ and $^{14}F_{ab}$) have to be calculated with a carbon cycle model. Here, $^{14}\dot{N}_a$ denotes the time-derivative of $^{14}N_a$. The decay of ^{14}C within the atmosphere with the decay constant $\lambda = 1/8267\,\mathrm{yr}^{-1}$ is small and could be neglected.

The (vertically) well-mixed representation of the atmosphere is used in Roth & Joos (2013). However, this model is not applicable for strong interannual changes in prescribed $\Delta^{14}C$ due to the finite mixing timescales within the atmosphere.

2-box atmosphere

For changes in the production rate on timescales comparable (or shorter) than the atmospheric mixing timescale (i.e. 1–3 yr), the assumption of a well mixed atmosphere is not justified anymore. In such a case, the atmosphere has to be represented by a (at least) two box model with separate boxs for the stratosphere and the troposphere.

The stratospheric and tropospheric reservoirs (having subscripts s and t, respectively) are assumed to contain 15% and 85% of the total atmospheric carbon and the exchange timescale, i.e. the stratospheric-tropospheric exchange (STE) flux, is parametrized by an effective exchange parameter k_{STE} which is defined as the inverse timescale on which the stratospheric carbon inventory exchanges with the troposphere (i.e. $k_{\mathrm{STE}} = N_s/F_{\mathrm{STE}}$). The production of ^{14}C takes place by a fraction X_s in the stratosphere and X_t in the troposphere, i.e. $Q_s = X_sQ$ and the total production rate then reads $Q = Q_s + Q_t$. Estimates for X_s range from 0.5 Masarik & Beer (1999) to 0.7 (Usoskin et al., 2013). The two separate atmospheric budget equations read:

$$\begin{align}
{}^{14}\dot{N}_s &= Q_s - {}^{14}F_{st} - \lambda^{14}N_s \tag{4.3}\\
{}^{14}\dot{N}_t &= Q_t + {}^{14}F_{st} - \lambda^{14}N_t - {}^{14}F_{as} - {}^{14}F_{ab}, \tag{4.4}
\end{align}$$

where $^{14}F_{st}$ is the net flux from the stratosphere to the troposphere, which is given by:

$$^{14}F_{st} = k_{\mathrm{STE}} \cdot N_s({}^{14}R_s - {}^{14}R_t). \tag{4.5}$$

These equations are solved for Q by:

1. The tropospheric budget equation is solved for $Q = Q_s/X_s$ using $^{14}N_t$ from tree-ring data and $^{14}F_{st}$ from the last timestep. $^{14}F_{as}$ and $^{14}F_{ab}$ are prescribed from an existing Bern3D simulation with prescribed annual tree-ring $\Delta^{14}C$.

2. The stratospheric budget equation is solved for $^{14}N_s$ (and thus for $^{14}R_s$) by prescribing Q from step 1.

3. Calculate new fluxes $^{14}F_{st}$ based on updated $^{14}R_s$ and $^{14}R_t$.

4. Restart with step 1.

Note that in the following, $^{14}F_{ab}$ is calculated with the 4-box land-biosphere model from Siegenthaler & Oeschger (1987); the LPJ model is only coupled once per year with the Bern3D and therefore intra-annual variations of $\Delta^{14}C$ can not be applied. This setup is sketched in Fig. 6.1. Atmospheric CO_2 is assumed to remain constant[2] at 278 ppm.
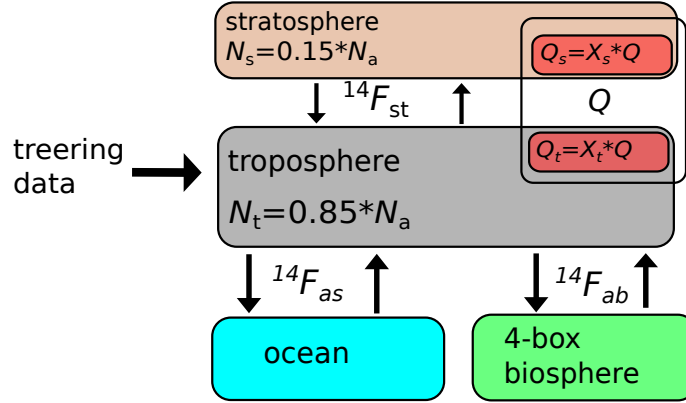
Figure 4.4: Setup of the 2-box atmosphere model coupled to the Bern3D and the 4-box land-biosphere model of Siegenthaler & Oeschger (1987).

Sensitivity experiments

The production rate has been calculated for different parameters and is presented in Fig. 4.5b. As expected, the choice of the STE timescale k and the relative fractions of the production rate in the stratosphere has the biggest influence on the diagnosed Q. As a comparison, the 1-box atmospheric model (which can be reproduced by choosing a very strong stratopshere-troposphere coupling, i.e. a high k_{STE}) is also included in Fig. 4.5. The 1-year running average of Q is peaking at around $4.3\,\text{atoms}\,\text{cm}^{-2}\,\text{s}^{-1}$, while all runs calculated with the 2-box model yield a higher Q.

As visible in Fig. 4.5, the peak production rate is higher for high values of X_s and $1/k_{STE}$, peaking at a maximum of $\approx 9\,\text{atoms}\,\text{cm}^{-2}\,\text{s}^{-1}$; more than 5 fold increase in the longterm mean Q. Note that some combinations of parameters require Q to become negative after the sharp $\Delta^{14}C$ increase after 775 AD. This can be understood by the fact the signal of the increased Q has not fully propagate from the stratosphere into the troposphere: there is still a high excess ^{14}C downward flux from the stratosphere to the troposphere which is not seen in the data; they suggest a stabilizing or even declining $\Delta^{14}C$ after 776 AD (Fig. 4.5a).

Note that we tried to reproduce the results from Usoskin et al. (2013) (green line in Fig. 4.5) using the same atmospheric parameters as they did. With these parameters, our estimated Q of $\approx 6.2\,\text{atoms}\,\text{cm}^{-2}\,\text{s}^{-1}$ is still larger than the $4.1\,\text{atoms}\,\text{cm}^{-2}\,\text{s}^{-1}$ stated in Usoskin et al. (2013). There seem to be quite some differences in the air-sea/biosphere fluxes in the two models?

A plausible range for Q

An 1000 member Monte-Carlo simulation was set up in order to estimate a range of plausible 1-year peak ^{14}C production. To do so, the tree-ring $\Delta^{14}C$ data were randomly varied in each year, using a Gaussian random number. The parameters $1/k_{STE}$ and X_s were perturbed in a similar manner (2 ± 1 years and 0.6 ± 0.2, respectively) between subsequent Monte-Carlo iterations[3]. The corresponding random numbers were picked within a 1σ interval around the best-guess

---

[2]Therefore N_a remains constant as well.

[3]But they remained constant in time.

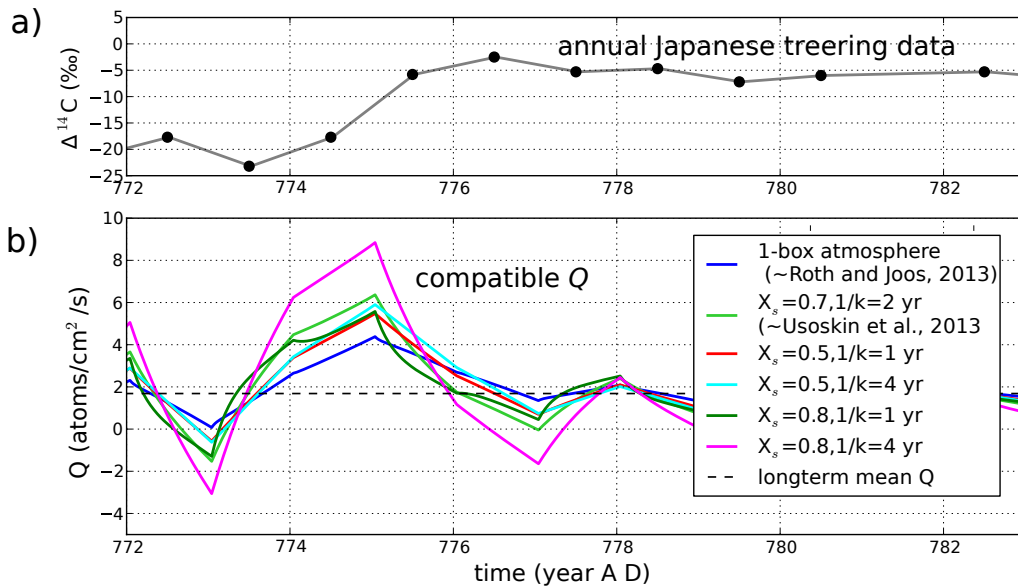**Figure 4.5:** **(a)** Annually resolved atmospheric Δ^{14}C from Japanese trees. **(b)** 1 year running average of the diagnosed production rate using different parameters for the 2-box model. The dashed line indicates the level of the longterm mean Q.

parameters. The uncertainty of the Δ^{14}C data was translated to air-sea air-biosphere fluxes calculated by the Bern3D model by applying the same relative errors to these fluxes multiplied by a gross air-sea flux (and NPP, respectively) of $60\,\mathrm{Gt\,C\,yr}^{-1}$. The uncertainty introduced by these fluxes is rather small, as they do not strongly depend on the slope of the Δ^{14}C curve.

The result of this analysis is shown in Fig. 4.6a, where the median and the 90% confidence interval is shown. The 5, 50 and 95 percentiles of the peak production rate are 3.8, 5.6 and $8.8\,\mathrm{atoms\,cm}^{-2}\,\mathrm{s}^{-1}$. In a subsequent step, all timeseries containing negative values of Q (in the running average) were rejected, as there is no physical explanation for a negative production rate. Recalculating the statistics again on the constrained ensemble yields the lower panel in Fig. 4.6. The corresponding 5, 50 and 95 percentiles of the peak production rate are then 3.8, 4.7 and $6.4\,\mathrm{atoms\,cm}^{-2}\,\mathrm{s}^{-1}$ and shown in Fig. 4.6b. The median estimate is thus not much larger than the corresponding result of the 1-box model ($4.3\,\mathrm{atoms\,cm}^{-2}\,\mathrm{s}^{-1}$).

We therefore conclude that the proposed $20\,\mathrm{atoms\,cm}^{-2}\,\mathrm{s}^{-1}$ by Miyake et al. (2012) are an overestimation, in agreement with the conclusions drawn by Usoskin et al. (2013). A production rate of more than $6.4\,\mathrm{atoms\,cm}^{-2}\,\mathrm{s}^{-1}$ sustained over one year seems unlikely. Note that we used the assumption that the tree-ring data are representative for the entire troposphere. If there are interhemispheric gradients within Δ^{14}C the estimated production rate may be different. Also, the 2-box model used here is a crude simplification. The spatially resolved production and transport of ^{14}C should be incorporated in an AGCM for future studies.

4.4   Pre-Holocene radiocarbon dynamics

The dynamics of the pre-Holocene atmospheric Δ^{14}C-history raises several questions: i) how levels of Δ^{14}C as high as 600‰ be reconciled, and ii) what is the cause of the abrupt changes in Δ^{14}C during the deglaciation (e.g. during the "Mystery Interval" $\sim$17.5–14.5 kyr ago, (Denton et al., 2006)). In the following, some aspects of i) are to be discussed, namely what the influence of different reconstructions of past Q on Δ^{14}C, and the steady-state contribution of the carbon cycle and climate state to variations of atmospheric Δ^{14}C.
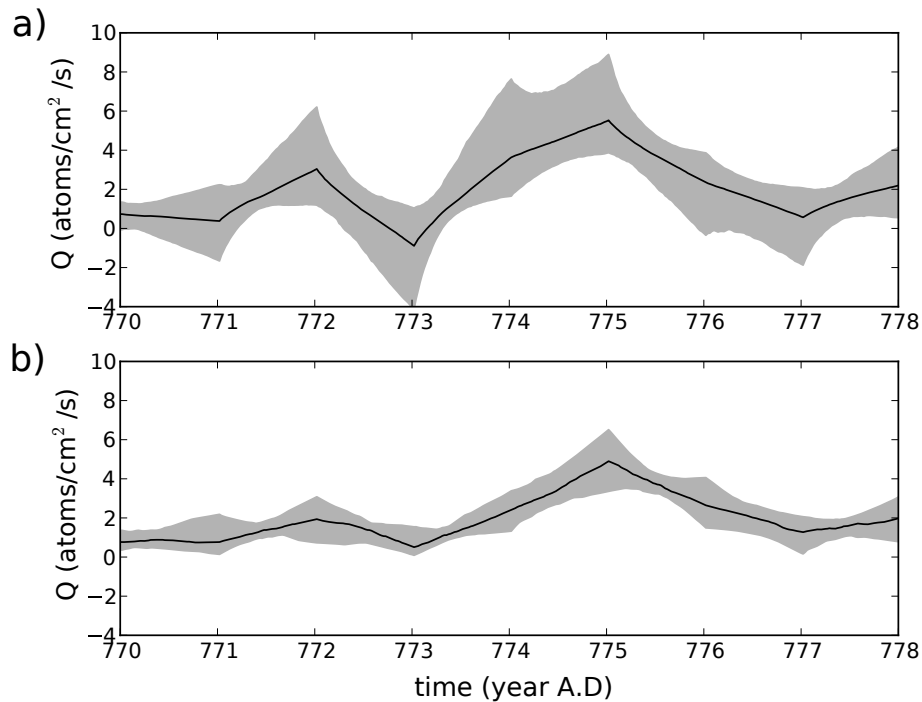
Figure 4.6: (a) Median (black line) and 5%-95% confidence interval (gray shading) of the unconstrained ensemble-reconstruction of Q and **(b)** the same for the constrained ensemble, in which models with negative Q have been rejected.

One of the problems we face when studying this time period is that reconstructions of atmospheric $\Delta^{14}C$ are less robust than during the Holocene, where $\Delta^{14}C$ can be reconstructed from ancient trees. Several datasets are available and have been used in the past as a benchmark for models: the IntCal09 dataset (Reimer et al., 2009) which is a composite of mainly marine proxies. The main problem with these proxies is the reservoir-age effect: as the marine proxies (e.g. corals) represent the $\Delta^{14}C$ of surface waters, a oceanic surface reservoir age has be estimated which is then subtracted from these data to get atmospheric $\Delta^{14}C$. Often a constant surface reservoir age is assumed which is probably not true during changes of global ocean circulation.

Recently, the stalagmite data of Hoffmann et al. (2010) and the newly available lake sediment data from the lake Suigetsu (Bronk Ramsey et al., 2012), as well as new data from the new Hulu-Cave (Southon et al., 2012) came available which are not affected by this issue. These presumably more robust datasets have now been incorporated in IntCal13 (Reimer et al., 2013) and displayed in Fig. 4.7b. In contrast to IntCal09, the new data show generally lower $\Delta^{14}C$ values before 25 kyr BP and a less steep drop during the "Mystery Interval". The average $\Delta^{14}C$ level from 40–28 kyr BP decreased from 580‰ in IntCal09 to 482‰ in IntCal13, on the other hand LGM levels of $\Delta^{14}C$ slightly increased from 418 to 455‰.

The high glacial $\Delta^{14}C$ levels and the apparent incompatibility between ^{14}C an ^{10}Be data suggested that a large fraction of this discrepancy had to be caused by changes in the global carbon cycle (Muscheler et al., 2004). A study, in which where a multi-box model is used, concluded that the carbon-cycle's contribution to high atmospheric $\Delta^{14}C$ levels did not exceed +110‰ and therefore glacial $\Delta^{14}C$ levels as high as 700‰ can not be explained, as the contribution by ^{14}C production rate changes do not fill the missing "gap" (Köhler et al., 2006). Here, this statement is revisited in the light of new available proxy data and results from a more sophisticated carbon cycle-climate model.

How does Q influence atmospheric $\Delta^{14}C$? Let Q_{mod} be the modern production rate which

is compatible with a $\Delta^{14}C = 0‰$ atmosphere. If we now set $Q = 2 \cdot Q_{mod}$, atmospheric ^{14}C concentrations will also double in the long run (i.e. $\Delta^{14}C$ increases to $1000‰$). The reason for this is that a doubling of Q_{mod} leads to a ^{14}C production that exceeds the decay in the (radio-)carbon reservoirs. As the loss of ^{14}C is proportional to is inventory, a new equilibrium is only given at the time where the ^{14}C inventory itself is doubled.

The timescales for the model response to such step-changes in Q are a combination of the lifetime of ^{14}C ($\tau = 8267\,yr$) and the exchange-timescales between the exchanging reservoirs: for a reduction of Q, $\Delta^{14}C$ of the total carbon in the system decreases proportional to $e^{-t/\tau}$, while the timescale of the atmospheric response cannot be expressed by a single timescale. The e-folding timescale of the atmospheric $\Delta^{14}C$ change in such an experiment turns out to be $\sim 6000\,yr$, that is, comparable to the half-life of ^{14}C. In other words: if the variations in Q are very slow, the response in $\Delta^{14}C$ can be easily estimated, but variations in Q faster than $\sim 10\,kyr$ need to be translated in $\Delta^{14}C$ by a model.

The main cause of these elevated $\Delta^{14}C$ is thought to be the result of a weakened geomagnetic shielding, leading to a higher rate of radiocarbon production. This is especially pronounced during the Laschamp event around $\sim 40\,kyr$ BP where the geomagnetic field was shortly reversed. But yet, the available reconstructions differ in the magnitude and timing of past ^{14}C production rate changes.

A set of available reconstructions of Q are shown in Fig. 4.7a. We consider the production rates based on the NAPIS-75 paleointensity stack (Laj et al., 2002) and the GLOPIS–75 paleointensity stack (Laj et al., 2013)[4] In addition, two production rate estimates are based on the ^{10}Be-flux too the Greenland ice sheet, one is taken from Muscheler et al. (2004), while the other has been provided by J. Beer and F. Steinhilber (denoted as Steinhilber/Beer). Note that the record from Laj et al. (2002) is on the GRIP timescale while to other 3 are synchronized to the GISP2 age scale.

Before the reconstructions were applied to the Bern3D model, they have been normalized to the modern production rate, that is the amount of ^{14}C production needed to compensate the loss of ^{14}C in the preindustrial spinup due to decay and burial. For further usage, the so-constructed timeseries can be used as a multiplier for the steady-state production rate in the Bern3D model as diagnosed during the spinup. The reconstruction have not been smoothed for the following experiments, they are only smoothed in Fig. 4.7a for visualization purpose.

To study the contribution of varying Q, the following experiments were set up: a preindustrial spinup of the Bern3D model has been performed including sediment and 4-box biosphere models. Atmospheric CO_2 had been fixed at $278\,ppm$ and $\Delta^{14}C$ at $0‰$. Then, the model was then integrated forward in time with interactive $\Delta^{14}C$ from $60\,kyr$ BP to $0\,kyr$ BP either with the transient production rate given in the reconstructions or, if these do not reach back that far, the first Q datapoint available. The interval from 60–$50\,kyr$ BP is again considered as a spinup and is not further discussed here. In general, the $\Delta^{14}C$ level at which the carbon cycle is spun up is not crucial in the long term as initial conditions are to be "forgotten" after $\sim 10\,kyr$ due to the limited memory in the ^{14}C-cycle[5].

As we are interested in the low-frequency variations of $\Delta^{14}C$, a smoothing spline filter (Enting, 1987) with a cut-off period of $1\,kyr$ is applied to the simulated history of $\Delta^{14}C$. Although the Q timeseries have been normalized to modern values, the interactive $\Delta^{14}C$ may be different from $0‰$ at $0\,kyr$ BP (because the value of $\Delta^{14}C$ also depends on its history). To make the simulations comparable, the resulting $\Delta^{14}C$ histories have been shifted to $0‰$ in $0\,kyr$ BP. The introduced error is small due to rather linear behavior of the system in terms of $\Delta^{14}C$ response.

---

[4]This record had to be converted to a production rate first. We used the ^{14}C-production model of Kovaltsov et al. (2012) under the assumption that the solar intensity remained at Holocene levels.
[5]This is e.g. shown in Fig. 8 in Köhler et al. (2006).
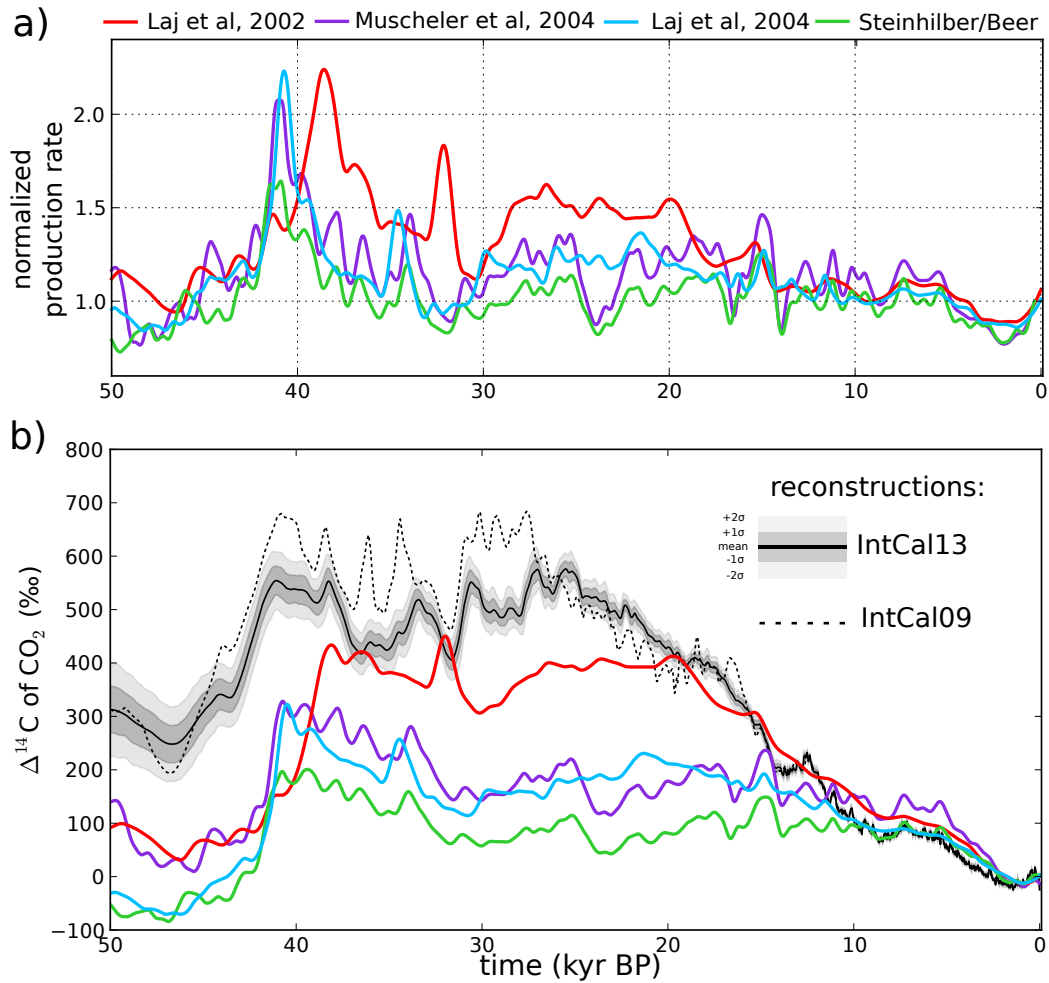
Figure 4.7: **(a)** The different ^{14}C production rate reconstructions used to force the Bern3D model. **(b)** The modeled responses of atmospheric Δ^{14}C, compared observed atmospheric Δ^{14}C reconstructions (black lines and shading) from Reimer et al. (2009, IntCal09) and Reimer et al. (2013, IntCal13).

The results of these experiments are shown in Fig. 4.7b and compared to the IntCal09 and IntCal13 datasets (Reimer et al., 2009, 2013). There is obviously (still) a considerable gap between the best-guess observed and modeled history of atmospheric Δ^{14}C prior to the LGM: the offset is $\approx$300–500‰ except for the production rate estimate of Laj et al. (2002), which yields significantly higher Δ^{14}C values. The difference between the modeled Δ^{14}C and the IntCal13 dataset ($\Delta\Delta^{14}$C) from 21–10 kyr BP is shown in Fig. 4.8. During the LGM, the model-data offset in Δ^{14}C is 70–390‰. Two fast drops in Δ^{14}C and coincident increase in CO_2, namely after Heinrich event 1 (H1, i.e. the "Mystery Interval") and during the Younger Dryas (YD) are highlighted in Fig. 4.8. Especially the fast drop following H1 was intensively discussed in the literature (Denton et al., 2006; Broecker & Barker, 2007; Hain et al., 2011; Huiskamp & Meissner, 2012) as it is interpreted as oceanic outgassing of an old (i.e. low in Δ^{14}C) watermass, which could not be located so far.

The results shown in Fig. 4.7b indicate that, depending on the production rate reconstruction, the drop in Δ^{14}C is actually smaller than the 190‰ discussed in the literature ($\sim$100‰ and $\sim$140‰ for the reconstructions of Laj et al. (2002) and Laj et al. (2013), respectively).
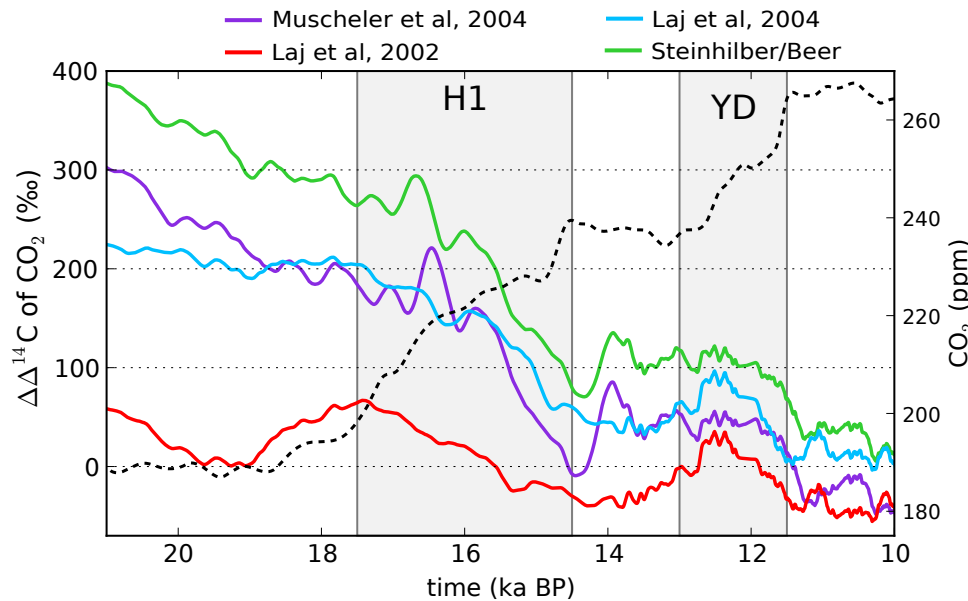
Figure 4.8: Difference between observed (IntCal13, (Reimer et al., 2013)) and modeled Δ^{14}C between 21–10 kyr BP.

Contribution of carbon-cycle changes

Could this gap of 300–500‰ in atmospheric Δ^{14}C during the LGM been explained by changes in the global carbon cycle? In order to assess this question, the following experiments have been conducted: from a preindustrial spinup with Δ^{14}C $= 0$‰ and atmospheric CO_2 set to 278 ppm (experiment PI), LGM boundary conditions are applied, these include:

Physics:

- orbital configuration,

- radiative forcings of GHGs CO_2, CH_4 and N_2O,

- ice-sheet albedo,

- and freshwater relocation from ocean to the ice sheets.

Carbon cycle:

- Fe-fertilization of the marine primary production,

- the land-biosphere carbon stocks are reduced by 500 Gt C.

We chose LGM conditions because they serve for an upper limit of the carbon cycle contributions: glacial conditions were most "extreme" at the LGM. In this configuration, the model is integrated for 30 kyr using the modern ^{14}C production rate. This experiment is denoted as LGM$_{std}$ in Fig. 4.9. Atmospheric CO_2 stabilizes at 260 ppm and does obviously not coincide with the observed ~185 ppm (Petit et al., 1999), simulated atmospheric Δ^{14}C stays close to 0‰. The negligible change in Δ^{14}C is the result of compensating effects: slowed ocean circulation and more widespread sea ice would increase Δ^{14}C, but the modeled increase of the total carbon inventory in the atmosphere-ocean-sediment system of ~3000 Gt C decreases Δ^{14}C, as the constant production has to replace more decay of ^{14}C.

A similar approach has then applied as in Roth & Joos (2013): the model is forced to LGM-compatible CO_2 levels invoking two different mechanism: in LGM_{bio}, the remineralization depth of organic matter is increased while in the experiment LGM_{circ}, global windstress is reduced. In best agreement with LGM CO_2 data ($\sim$185 ppm) are the experiments where α as been set to 0.75 and global windstress is reduced by 40%, respectively. Only these two realizations are discussed in the following.
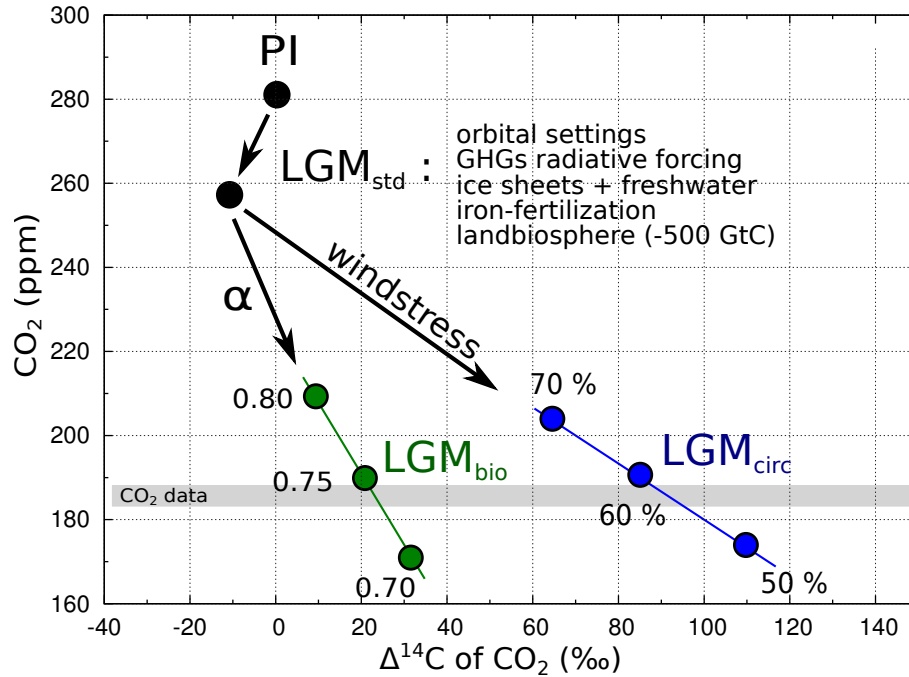
Figure 4.9: Changes in CO_2 and $\Delta^{14}C$ when applying different forcings on the climate and carbon cycle, while keeping the production rate at modern values. Maximum $\Delta^{14}C$ changes due to LGM carbon cycle and climate conditions do not exceed $\approx$80‰ for compatible CO_2 levels of $\sim$185 ppm in the Bern3D model. As explained in the main text, these changes roughly scale with the background production rate which was higher during the LGM by 0–50%, depending on the reconstructions used.

The model response is evaluated after 50 kyr and sketched in the (CO_2,$\Delta^{14}C$)-space in Fig. 4.9. As expected, atmospheric $\Delta^{14}C$ in LGM_{bio} is hardly affected as the surface-to-deep mixing of ^{14}C is not altered. The only change is the slightly deeper transport of POC-14 tending to lower atmospheric $\Delta^{14}C$ values. The small net increase in $\Delta^{14}C$ from -10‰ in LGM_{std} to +20‰ is primarily a result of the low atmospheric CO_2 levels. The other extreme is the strongly reduced ocean mixing (the AMOC is e.g. shut down) in LGM_{circ}, leading to large ocean top-to-bottom reservoir ages (Roth & Joos, 2013) and as a result an atmospheric anomaly in $\Delta^{14}C$ of $\sim$80‰.

The two experiments yielding $\Delta^{14}C$ of 20–80‰ were conducted using the modern production rate of ^{14}C. Köhler et al. (2006) showed that carbon-cycle induced changes in $\Delta^{14}C$ actually scale with the background production rate. In other words: in a setup where the Q is doubled, equilibrium $\Delta^{14}C$ would approach 1000‰ and carbon-cycle induced changes would then be as high as $\sim$40–160‰. LGM estimates for Q range from by 0% (Steinhilber/Beer) to 50% (Laj et al., 2002) above modern values, depending on the reconstructions used. To conclude: our model simulations suggest that changes in the carbon cycle during the LGM did not contribute more than 80%×1.5 = 120‰, which is in agreement with Köhler et al. (2006). LGM $\Delta^{14}C$ could therefore been brought into agreement with data only by applying the Q reconstruction of Laj et al. (2002).

On the other hand, a problem emerges when using the production rate reconstruction of Laj et al. (2002) is used: differences between observed and modeled $\Delta^{14}C$ are much higher prior to

the LGM ($\sim$ +200%) than during the LGM ($\sim$ +60‰) although carbon-cycle induced changes are expected to reach their maximum during the LGM.

To summarize: although glacial atmospheric Δ^{14}C have recently been corrected to lower values, their is still a large discrepancy between production-rate induced Δ^{14}C and observed Δ^{14}C for most of the Q reconstructions available, leaving a too-high fraction of the difference to be explained by the glacial carbon cycle.

Bibliography

Broecker, W. & Barker, S., 2007. A 190 ‰ drop in atmosphere's Δ^{14}C during the "Mystery Interval" (17.5 to 14.5 kyr), *Earth Planet. Sci. Lett.*, 256(1–2), 90–99.

Bronk Ramsey, C., Staff, R. A., Bryant, C. L., Brock, F., Kitagawa, H., van der Plicht, J., Schlolaut, G., Marshall, M. H., Brauer, A., Lamb, H. F., Payne, R. L., Tarasov, P. E., Haraguchi, T., Gotanda, K., Yonenobu, H., Yokoyama, Y., Tada, R., & Nakagawa, T., 2012. A Complete Terrestrial Radiocarbon Record for 11.2 to 52.8 kyr B.P., *Science*, 338(6105), 370–374.

Denton, G. H., Broecker, W. S., & Alley, R. B., 2006. The mystery interval 17.5 to 14.5 kyrs ago, *PAGES news*, 14, 14–16.

Enting, I. G., 1987. On the use of smoothing splines to filter CO_2 data, *J. Geophys. Res.*, 92(D9), 10977–10984.

Hain, M. P., Sigman, D. M., & Haug, G. H., 2011. Shortcomings of the isolated abyssal reservoir model for deglacial radiocarbon changes in the mid-depth Indo-Pacific Ocean, *Geophys. Res. Lett.*, 38(4), L04604.

Hoffmann, D. L., Beck, J. W., Richards, D. A., Smart, P. L., Singarayer, J. S., Ketchmark, T., & Hawkesworth, C. J., 2010. Towards radiocarbon calibration beyond 28 ka using speleothems from the Bahamas, *Earth Planet. Sci. Lett.*, 289(1–2), 1–10.

Huiskamp, W. N. & Meissner, K. J., 2012. Oceanic carbon and water masses during the Mystery Interval: A model-data comparison study, *Paleoceanography*, 27(4), PA4206.

Köhler, P., Muscheler, R., & Fischer, H., 2006. A model-based interpretation of low-frequency changes in the carbon cycle during the last 120,000 years and its implications for the reconstruction of atmospheric ^{14}C, *Geochem. Geophys. Geosyst.*, 7(11), Q11N06.

Kovaltsov, G. A., Mishev, A., & Usoskin, I. G., 2012. A new model of cosmogenic production of radiocarbon ^{14}C in the atmosphere, *Earth Planet. Sci. Lett.*, 337–338(0), 114–120.

Kwon, E. Y., Primeau, F., & Sarmiento, J. L., 2009. The impact of remineralization depth on the air-sea carbon balance, *Nature Geosci.*, 2(9), 630–635.

Laj, C., Kissel, C., Mazaud, A., Michel, E., Muscheler, R., & Beer, J., 2002. Geomagnetic field intensity, North Atlantic Deep Water circulation and atmospheric Δ^{14}C during the last 50 kyr, *Earth Planet. Sci. Lett.*, 200(1–2), 177–190.

Laj, C., Kissel, C., & Beer, J., 2013. *High Resolution Global Paleointensity Stack Since 75 kyr (GLOPIS-75) Calibrated to Absolute Values*, pp. 255–265, American Geophysical Union.

Martin, J. H., Knauer, G. A., Karl, D. M., & Broenkow, W., 1987. VERTEX: Carbon cycling in the northeast Pacific.

Masarik, J. & Beer, J., 1999. Simulation of particle fluxes and cosmogenic nuclide production in the Earth's atmosphere, *J. Geophys. Res.*, 104, 12099–12111.

Menviel, L., Joos, F., & Ritz, S., 2012. Simulating atmospheric CO_2, ^{13}C and the marine carbon cycle during the Last Glacial-Interglacial cycle: possible role for a deepening of the mean remineralization depth and an increase in the oceanic nutrient inventory, *Quaternary Sci. Rev.*, 56(0), 46–68.

Miyake, F., Nagaya, K., Masuda, K., & Nakamura, T., 2012. A signature of cosmic-ray increase in AD 774-775 from tree rings in Japan, *Nature*, 486(7402), 240–242.

Muscheler, R., Beer, J., Wagner, G., Laj, C., Kissel, C., Raisbeck, G. M., Yiou, F., & Kubik, P. W., 2004. Changes in the carbon cycle during the last deglaciation as indicated by the comparison of ^{10}Be and ^{14}C records, *Earth Planet. Sci. Lett.*, 219(3–4), 325–340.

Petit, J. R., Jouzel, J., Raynaud, D., Barkov, N. I., Barnola, J.-M., Basile, I., Bender, M., Chappellaz, J., Davis, M., Delaygue, G., Delmotte, M., Kotlyakov, V. M., Legrand, M., Lipenkov, V. Y., Lorius, C., PEpin, L., Ritz, C., Saltzman, E., & Stievenard, M., 1999. Climate and atmospheric history of the past 420,000 years from the Vostok ice core, Antarctica, *Nature*, 399(6735), 429–436.

Reimer, P., Bard, E., Bayliss, A., Beck, J., Blackwell, P., Ramsey, C. B., Grootes, P., Guilderson, T., Haflidason, H., Hajdas, I., Hatté, C., Heaton, T., Hoffmann, D., Hogg, A., Hughen, K., Kaiser, K., Kromer, B., Manning, S., Niu, M., Reimer, R., Richards, D., Scott, E., Southon, J., Staff, R., Turney, C., & van der Plicht, J., 2013. IntCal13 and Marine13 Radiocarbon Age Calibration Curves 0–50,000 Years cal BP, *Radiocarbon*, 55(4).

Reimer, P. J., Baillie, M. G. L., Bard, E., Bayliss, A., Beck, J. W., Blackwell, P. G., Ramsey, C. B., Buck, C. E., Burr, G. S., Edwards, R. L., Friedrich, M., Grootes, P. M., Guilderson, T. P., Hajdas, I., Heaton, T. J., Hogg, A. G., Hughen, K. A., Kaiser, K. F., Kromer, B., McCormac, F. G., Manning, S. W., Reimer, R. W., Richards, D. A., Southon, J. R., Talamo, S., Turney, C. S. M., van der Plicht, J., & Weyhenmeye, C. E., 2009. IntCal09 and Marine09 radiocarbon age calibration curves, 0–50,000 years cal BP, *Radiocarbon*, 51(4), 1111–1150.

Roth, R. & Joos, F., 2013. A reconstruction of radiocarbon production and total solar irradiance from the Holocene ^{14}C and CO_2 records: implications of data and model uncertainties, *Clim. Past*, 9(4), 1879–1909.

Siegenthaler, U. & Oeschger, H., 1987. Biospheric CO_2 emissions during the past 200 years reconstructed by deconvolution of ice core data, *Tellus B*, 39B(1–2), 140–154.

Southon, J., Noronha, A. L., Cheng, H., Edwards, R. L., & Wang, Y., 2012. A high-resolution record of atmospheric 14c based on hulu cave speleothem h82, *Quaternary Sci. Rev.*, 33(0), 32 – 41.

Tschumi, T., Joos, F., Gehlen, M., & Heinze, C., 2011. Deep ocean ventilation, carbon isotopes, marine sedimentation and the deglacial CO_2 rise, *Clim. Past*, 7(3), 771–800.

Usoskin, I. G., Kromer, B., Ludlow, F., Beer, J., Friedrich, M., Kovaltsov, G. A., Solanki, S. K., & Wacker, L., 2013. The AD775 cosmic event revisited: the Sun is to blame, *A&A*, 552, L3.

Chapter 5

The response of the Earth system to a CO_2 emission pulse

5.1 Foreword

The impulse response function of atmospheric CO_2 (IRF_{CO_2}), i.e. the temporal evolution of the airborne-fraction of a CO_2 after a pulse emission, serves as a basis for the calculation of the global warming potential (GWP) of CO_2. The GWP of CO_2 is of special importance as CO_2 serves as the reference gas for the calculation of GWPs of other greenhouse gases. As for the Forth Assessment Report (AR4) of the Intergovernmental Panel on Climate Change (IPCC) (Forster et al., 2007), IRF_{CO_2} was only based on a single model[1], there was need to follow a multi-model approach in order to update IRF_{CO_2} and the absolute global warming potential (AGWP) of CO_2 for IPCC's AR5 released in 2013.

In 2012, an effort was started in order to update IRF_{CO_2}. Several modeling groups[2] agreed to run a set of well-defined simulations with their models of various complexities. The experimental protocol which has been distributed to the contributing groups can be found in Appendix E and `http://www.climate.unibe.ch/~joos/IRF_Intercomparison/protocol.html`.

The outcome of this study is presented in the following chapter. The results were further used in Chap. 8 of IPCC's AR5 (Myhre et al., 2013), for which I acted as a "Contributing Author".

---

[1]i.e. on an earlier version of the Bern-model
[2]`http://www.climate.unibe.ch/~joos/IRF_Intercomparison/participants.html`

5.2 Carbon dioxide and climate impulse response functions for the computation of greenhouse gas metrics: a multi-model analysis

F. Joos, R. Roth, J. S. Fuglestvedt, G. P. Peters, I. G. Enting, W. von Bloh, V. Brovkin, E. J. Burke, M. Eby, N. R. Edwards, T. Friedrich, T. L. Frölicher, P. R. Halloran, P. B. Holden, C. Jones, T. Kleinen, F. T. Mackenzie, K. Matsumoto, M. Meinshausen, G.-K. Plattner, A. Reisinger, J. Segschneider, G. Shaffer, M. Steinacher, K. Strassmann, K. Tanaka, A. Timmermann, and A. J. Weaver

Atmospheric
Chemistry
and Physics

Carbon dioxide and climate impulse response functions for the computation of greenhouse gas metrics: a multi-model analysis

F. Joos[1,2], R. Roth[1,2], J. S. Fuglestvedt[3], G. P. Peters[3], I. G. Enting[4], W. von Bloh[5], V. Brovkin[6], E. J. Burke[7], M. Eby[8], N. R. Edwards[9], T. Friedrich[10], T. L. Frölicher[11,1], P. R. Halloran[7], P. B. Holden[9], C. Jones[7], T. Kleinen[6], F. T. Mackenzie[12], K. Matsumoto[13], M. Meinshausen[5,14], G.-K. Plattner[1], A. Reisinger[15], J. Segschneider[6], G. Shaffer[16,17], M. Steinacher[1,2], K. Strassmann[1,2], K. Tanaka[18], A. Timmermann[10], and A. J. Weaver[8]

[1]Climate and Environmental Physics, Physics Institute, University of Bern, Bern, Switzerland
[2]Oeschger Centre for Climate Change Research, University of Bern, Bern, Switzerland
[3]Center for International Climate and Environmental Research – Oslo (CICERO), P.O. Box 1129 Blindern, 0318 Oslo, Norway
[4]MASCOS, 139 Barry St, The University of Melbourne, Vic 3010, Australia
[5]Potsdam Institute for Climate Impact Research, P.O. Box 601203, 14412, Potsdam, Germany
[6]Max Planck Institute for Meteorology, Bundesstr. 53, 20146 Hamburg, Germany
[7]Met Office Hadley Centre, FitzRoy Road, Exeter, EX1 3PB, UK
[8]School of Earth and Ocean Sciences, University of Victoria, Victoria, British Columbia, Canada
[9]The Open University, Environment, Earth and Ecosystems, Milton Keynes, UK
[10]International Pacific Research Center, School of Ocean and Earth Science and Technology, University of Hawaii, 1680 East-West Rd. Honolulu, HI, USA
[11]AOS Program, Princeton University, Princeton, NJ, USA
[12]Department of Oceanography, School of Ocean and Earth Science and Technology, University of Hawaii, Honolulu, Hawaii, 96822, USA
[13]Department of Earth Sciences, University of Minnesota, Minneapolis, MN, USA
[14]School of Earth Sciences, The University of Melbourne, VIC, Australia
[15]New Zealand Agricultural Greenhouse Gas Research Centre, Palmerston North 4442, New Zealand
[16]Department of Geophysics, University of Concepcion, Chile
[17]Niels Bohr Institute, University of Copenhagen, Copenhagen, Denmark
[18]Institute for Atmospheric and Climate Science, ETH Zurich, Zurich, Switzerland

Correspondence to: F. Joos (joos@climate.unibe.ch)

Abstract. The responses of carbon dioxide (CO_2) and other climate variables to an emission pulse of CO_2 into the atmosphere are often used to compute the Global Warming Potential (GWP) and Global Temperature change Potential (GTP), to characterize the response timescales of Earth System models, and to build reduced-form models. In this carbon cycle-climate model intercomparison project, which spans the full model hierarchy, we quantify responses to emission pulses of different magnitudes injected under different conditions. The CO_2 response shows the known rapid decline in the first few decades followed by a millennium-scale tail. For a 100 Gt-C emission pulse added to a constant CO_2 concentration of 389 ppm, $25 \pm 9\%$ is still found in the atmosphere after 1000 yr; the ocean has absorbed $59 \pm 12\%$ and the land the remainder ($16 \pm 14\%$). The response in global mean surface air temperature is an increase by $0.20 \pm 0.12\,°C$ within the first twenty years; thereafter and until year 1000, temperature decreases only slightly, whereas ocean heat content and sea level continue to rise. Our best estimate for the Absolute Global Warming Potential, given by the time-integrated

response in CO_2 at year 100 multiplied by its radiative efficiency, is $92.5 \times 10^{-15}\,\mathrm{yr\,W\,m^{-2}}$ per kg-CO_2. This value very likely (5 to 95 % confidence) lies within the range of (68 to 117) $\times 10^{-15}\,\mathrm{yr\,W\,m^{-2}}$ per kg-CO_2. Estimates for time-integrated response in CO_2 published in the IPCC First, Second, and Fourth Assessment and our multi-model best estimate all agree within 15 % during the first 100 yr. The integrated CO_2 response, normalized by the pulse size, is lower for pre-industrial conditions, compared to present day, and lower for smaller pulses than larger pulses. In contrast, the response in temperature, sea level and ocean heat content is less sensitive to these choices. Although, choices in pulse size, background concentration, and model lead to uncertainties, the most important and subjective choice to determine AGWP of CO_2 and GWP is the time horizon.

1 Introduction

Emissions of different greenhouse gases (GHGs) and other agents that force the climate to change are often compared by simplified metrics in economic frameworks, emission trading and mitigation schemes, and climate policy assessments. The Global Warming Potential (GWP) introduced by the Intergovernmental Panel on Climate Change (IPCC) in 1990 (Shine et al., 1990), is the most widely used emission metric. GWPs are applied for emission reporting under the United Nations Framework Convention on Climate Change (UN-FCCC, 2002) and in the emission basket approach of the legally-binding Kyoto Protocol (UNFCCC, 1998) to compare emissions of different GHGs and to compute the so called "CO_2-equivalent" emissions. The initial Kyoto Protocol covered emissions of carbon dioxide (CO_2), methane (CH_4), nitrous oxide (N_2O), sulphur hexafluoride (SF_6), hydrofluorocarbons (HCFs) and perfluorocarbons (PFCs) in the first commitment period (2008–2012). The Doha Amendment to the Kyoto Protocol covers emissions in a second commitment period of 2013–2020 and nitrogen trifluoride (NF_3) is added to the basket of greenhouse gases. The GWP compares the radiative forcing (Forster et al., 2007) integrated over a time period caused by the emission of 1 kg of an agent relative to the integrated forcing caused by the emissions of 1 kg CO_2. As CO_2 is used as a reference gas in the GWP definition, any changes in the computation of the radiative influence of CO_2 affect the GWP of any other agent.

The purpose of this study is to compute the response in atmospheric CO_2, in ocean and land carbon, global mean surface air temperature, ocean heat uptake and sea level change to a pulse-like (i.e., instantaneous) emission of CO_2 into the atmosphere. Best estimates for the mean and the 5 to 95 % confidence range are provided for the Absolute Global Warming Potential (AGWP) and the Absolute Global Temperature change Potential (AGTP) introduced by Shine et al. (2005). We analyse the responses of fifteen carbon cycle-

climate models, covering the full model hierarchy, and including two large ensembles of simulations by two of the models constrained with observations as well as an ensemble of runs of a box model substituting for a suite of more complex models. This allows us to address model-related uncertainties by investigating within-model and between-model differences. Uncertainties related to the size of the emission pulse, the atmospheric and climatic background conditions or the choice of the future scenario, and the carbon cycle-climate feedback are assessed in sensitivity simulations. Results are also compared to CO_2 response functions as published in the IPCC First (FAR) (Shine et al., 1990), Second (SAR) (Schimel et al., 1996), and Fourth Assessment Report (AR4) (Forster et al., 2007).

A reevaluation of the CO_2 response appears timely as (i) past GWP calculations applied results from a single model and (ii) the atmospheric and climatic conditions influencing the CO_2 response continue to change with time. The GWP adopted for the first commitment period of the Kyoto protocol (2008–2012) (UNFCCC, 1997, 1998) and used for reporting under the UNFCCC (UNFCCC, 2002) are given by the SAR (Schimel et al., 1996) and based on the CO_2 response of the Bern model (Bern-SAR), an early generation reduced-form carbon cycle model (Joos et al., 1996). Its behaviour was compared to other carbon cycle models in Enting et al. (1994) and it was found to be a middle of the range model. The GWP provided in the AR4 (Forster et al., 2007) relies on the CO_2 response from the Bern2.5CC (here Bern2.5D-LPJ) Earth System Model of Intermediate Complexity (EMIC) (Plattner et al., 2008). More recently, the Conference of the Parties serving as the meeting of the Parties to the Kyoto Protocol decided (UNFCCC, 2011b, a) that the GWP from the AR4 should be used for the second commitment period of the Kyoto Protocol and the Conference also noted in its decision that metrics are still being assessed by IPCC in the context of its Fifth Assessment Report (AR5). A much broader set of models covering the whole model hierarchy from reduced-form models, to EMICs, to comprehensive Earth System Models (ESMs) are now available.

The redistribution of additional CO_2 emissions among the major carbon reservoirs in the Earth System depends on previous emissions and on climate. In addition, radiative forcing of CO_2 depends logarithmically on its own concentration. The response functions are calculated by modelling the response to a pulse emission added to a given concentration and climate state, but these background conditions have changed and will continue to change. For example, the concentration of atmospheric CO_2 continued to increase from 354 ppm in 1990, to 378 ppm at the time of the preparation of the IPCC AR4 report to 389 ppm in 2010 (Conway and Tans, 2012). Such changes in the background concentration cause both the radiative forcing and the response function to change, but the changes partially cancel leading to smaller changes in the AGWP (Caldeira and Kasting, 1993; Reisinger et al., 2011).

Additional uncertainties are of a fundamental nature as any metric to compare greenhouse gas emissions represents a crude simplification. Different forcing agents are distinct and have distinct impacts on climate and the Earth system. Differences include different atmospheric perturbation lifetimes ranging from weeks to many millennia, different regional and vertical distributions within the atmosphere and thus different influences on the energy fluxes within the atmosphere and to the Earth's surface, different indirect effects such as confounding impacts on the lifetimes of other GHGs (Prather and Hsu, 2010).

A complication is the complex and regionally and temporally distinct relationship between anthropogenic emissions, atmospheric abundances, radiative forcing, climate change and impacts and damages on socio-economic and natural systems. Other metrics have been proposed in addition to GWP such as global temperature change potential (GTP) (Shine et al., 2005; Fuglestvedt et al., 2010), the integrated temperature change potential (iGTP) (Peters et al., 2011; Azar and Johansson, 2012; Gillett and Matthews, 2010), the TEMPerature proxy index (TEMP) (Tanaka et al., 2009a), global damage potentials (GDP) (Kandlikar, 1995), global cost potentials (GCP) (Tol et al., 2012; Manne and Richels, 2001) and the Cost-Effective Temperature Potential (CETP) (Johansson, 2012). These metrics compare, for equal mass emissions of two GHGs, the global average surface air temperature change at a given point in time (GTP), the relative damages (GDP), or the ratio of the shadow price of a gas to the shadow price of CO_2 when a given climate change target is achieved at least cost (GCP). TEMP is defined so that it provides a best fit to the temperature trajectory of a given period and CETP is based on an approximation of the GCP. Uncertainties generally increase along the cause-effect chain from emissions to impacts (Prather et al., 2009) and there is a trade-off for the selection of metrics between completeness and complexity versus simplicity and transparency, implying the necessity of subjective judgments (Fuglestvedt et al., 2003; Plattner et al., 2009; Tanaka et al., 2010).

While the GWP is a proxy for climate impacts, non-climatic effects are not captured by the GWP or similar metrics. Air pollutants, such as ozone, aerosols, nitrogen oxides, carbon monoxide, or volatile organic compounds, influence human health and ecosystems directly. Anthropogenic CO_2 emissions cause not only global warming, but also ocean acidification by the uptake of excess CO_2 (Orr et al., 2005; Joos et al., 2011; Friedrich et al., 2012) – a threat to coral reefs, marine ecosystems, and related economic sectors (Gattuso et al., 2011).

The different perturbation timescales imply that near-term effects of short-lived agents must be compared with the persistent effects of long-lived agents if a metric is to be defined. Attempts involve the restriction to a distinct time horizon for the numerical evaluation of the metric (traditionally 20, 100 or 500 yr for GWP) or the application of discounting rates, typically giving little weight to effects in the more distant future. In summary, any metric used to compare emissions of GHGs and other agents involves subjective choices and value judgments and represents a considerable simplification (e.g., Tanaka et al., 2010; Fuglestvedt et al., 2003; Boucher, 2012).

2 Emission metrics and impulse response functions

2.1 Global warming potential

The Global Warming Potential is based on the time-integrated radiative forcing due to a *pulse* emission of a unit mass of gas at nominal time, $t = 0$. It can be given as an Absolute Global Warming Potential for gas x (AGWP$_x$) or as a dimensionless value by dividing the AGWP$_x$ by the AGWP of a reference gas, usually CO_2. The GWP is thus defined as:

$$\text{GWP}_x(\text{TH}) == \frac{\text{AGWP}_x(\text{TH})}{\text{AGWP}_{CO_2}(\text{TH})} \tag{1}$$

and the AGWP by:

$$\text{AGWP}_x(\text{TH}) = \int_0^{\text{TH}} \text{RF}_x(t)dt = \int_0^{\text{TH}} A_x \cdot \text{IRF}_x(t)dt, \tag{2}$$

where $\text{RF}_x(t)$ is the radiative forcing at time t caused by the emission pulse released at time $t = 0$. TH is the time horizon of choice over which the radiative forcing is integrated. For the GWP used by the UNFCCC and in the Kyoto Protocol, a time horizon TH of 100 yr is applied, though this choice lacks a scientific basis (Shine et al., 1990).

Forster et al. (2007) (Table 2.14, p. 212) report the GWP of many gases and for different time horizons. A problem related to reporting GWP only is that each update in AGWP$_{CO_2}$ affects the reported GWP values of all other gases. This could be easily avoided by reporting Absolute Global Warming Potentials in addition to GWP.

The radiative forcing, RF$_x$, of gas x can be written as the product of its radiative efficiency, A_x, and the perturbation in its abundance or burden, IRF$_x$. A_x is defined as the radiative forcing per kg increase in atmospheric burden of gas x. IRF$_x(t)$ is the impulse response function (IRF) or Green's function. IRF$_x$ represents the time-dependent abundance of gas x caused by the additional emission of one kg of gas x at time 0. In other words, the IRF$_x(t)$ is the fraction of the enhancement in concentration due to the added emission pulse remaining in the atmosphere at time t. For sufficiently small emissions and approximately constant background conditions the radiative efficiency, A_x, can be approximated as time-invariant.

The radiative forcing by a perturbation in the atmospheric burden of CO_2, ΔN_{CO_2}, relative to a reference burden , $N_{CO_2,0}$, is parameterized following (Myhre et al., 1998):

$$\text{RF}_{CO_2}(\Delta N_{CO_2}) = 5.35\,\text{W}\,\text{m}^{-2}\ln\left(\frac{N_{CO_2,0} + \Delta N_{CO_2}}{N_{CO_2,0}}\right). \tag{3}$$

This yields for small perturbations:

$$\mathrm{RF}_{\mathrm{CO}_2}(\Delta \mathrm{CO}_2(t)) = 5.35\,\mathrm{W\,m}^{-2}\frac{\Delta N_{\mathrm{CO}_2}}{N_{\mathrm{CO}_2,0}} = A_{\mathrm{CO}_2} \cdot \Delta N_{\mathrm{CO}_2}$$

for $\Delta \mathrm{N}_{\mathrm{CO}_2} \to 0$ \hfill (4)

Thus in the limit of a small perturbation, the radiative efficiency of CO$_2$ is $5.35\,\mathrm{W\,m}^{-2}$ divided by the constant reference burden and is thus itself a constant and time-invariant.

It is convenient to describe the IRF$_\mathrm{x}$ by exponential functions (Prather, 2007; Maier-Reimer and Hasselmann, 1987; Aamaas et al., 2012).

$$\mathrm{IRF}_{\mathrm{x}}(t) = a_{\mathrm{x},0} + \sum_{i=1}^{n} a_{\mathrm{x},i} \cdot \exp\left(\frac{-t}{\tau_{\mathrm{x},i}}\right) \text{ for } t \geq 0. \tag{5}$$

The unitless coefficients $a_{\mathrm{x},i}$ represent a fraction that is associated with a certain nominal timescale $\tau_{\mathrm{x},i}$ and their sum, including $a_{\mathrm{x},0}$, equals 1. $a_{\mathrm{x},0}$ is the fraction of emissions that remains permanently in the atmosphere. In turn the AGWP for gas x is:

$$\mathrm{AGWP}_{\mathrm{x}}(\mathrm{TH}) = A_{\mathrm{x}} \cdot a_{\mathrm{x},0} \cdot \mathrm{TH}$$
$$+ A_{\mathrm{x}} \sum_{i=1}^{n} a_{\mathrm{x},i} \cdot \tau_{\mathrm{x},i} \left(1 - \exp\left(\frac{-\mathrm{TH}}{\tau_{\mathrm{x},i}}\right)\right). \tag{6}$$

AGWP increases with increasing time horizon TH. It approaches a constant value for TH several times larger than the largest perturbation timescale of gas x and if $a_{\mathrm{x},0}$ is equal zero. Then, the AGWP becomes the product of the "steady-state" life time of a perturbation, $\tau_{x,\mathrm{SS}}$, (Prather, 2007) and the radiative efficiency, i.e., $\mathrm{AGWP}_{\mathrm{x}} = A_{\mathrm{x}}\tau_{x,\mathrm{SS}}$. The steady-state perturbation lifetime is the weighted sum over all timescales ($\tau_{\mathrm{x},\mathrm{SS}} = \Sigma\, a_{\mathrm{x},i}\tau_{\mathrm{x},i}$). This implies that a change in the integration horizon from, for example, 100 yr to 1000 yr has no impact on the AGWP of gases with up to decadal perturbation timescales such as methane, but AGWP continues to increase with TH for long-lived gases such as CO$_2$, N$_2$O, or SF$_6$. Consequently, the GWP of gases with a short life time generally decreases with increasing time horizon and the variation in GWP values with time horizon only reflects properties of the reference gas CO$_2$. For instance, the GWP values for CH$_4$, which has an adjustment time of approximately 12 yr, decrease with increasing time horizon (except for time horizons of a few years only), since GWP is defined with the (increasing) integrated RF of CO$_2$ in the denominator. As TH increases past the adjustment time of CH$_4$, the development in GWP$_{\mathrm{CH}_4}$ with time horizon is purely controlled by the development in AGWP$_{\mathrm{CO}_2}$ (Aamaas et al., 2012). For long-lived gases (e.g. N$_2$O, SF$_6$) the development in GWP is controlled by both the increasing integrals of the radiative forcing by the long-lived gas and CO$_2$. In conclusion, the GWP depends strongly on the behavior of the reference gas and sensitively on the (subjective) choice of the time horizon (see e.g., Shine, 2009).

Most GHGs are involved in complex chemical reactions in the atmosphere and are transported within the atmosphere. A local perturbation in one species invokes perturbations elsewhere on a range of timescales and often involving many other species. The chemistry-transport system can be linearized and represented with the help of eigenvalue decomposition following Prather, 2007. Then, it becomes clear that the perturbation timescales $\tau_{\mathrm{x},i}$ represent the (negative inverse) eigenvalues characterizing the leading chemical modes of gas x.

CO$_2$ is, unlike most other agents, not destroyed by chemical reactions in the atmosphere or deposited on the earth surface, but redistributed within the major carbon reservoirs atmosphere, ocean, land biosphere involving multiple timescales for exchange among and for overturning within these reservoirs. A substantial fraction of the initial perturbation by the emission pulse remains in the atmosphere and the ocean for millennia. This fraction is only removed by ocean-sediment interactions and interactions with the weathering and burial cycle of carbon involving timescales from many millennia to hundred thousand years (Archer et al., 2009).

The continuum of timescales involved in the redistribution of CO$_2$ can be approximated in practice by a few timescales only. It is usually sufficient to consider three to four terms in the sum in Eq. (5). Then the coefficients $a_{\mathrm{CO}_2,i}$ and $\tau_{\mathrm{CO}_2,i}$ have no direct process-based meaning, but are fitting parameters chosen to represent a given model-based IRF$_{\mathrm{CO}_2}$. The IRF of a model is normally computed by calculating the response to a pulse-like perturbation. In our case, the IRF for atmospheric CO$_2$ is computed within the suite of carbon cycle-climate models by monitoring the simulated decrease of an initial atmospheric CO$_2$ perturbation due to a pulse-like CO$_2$ release into the model atmosphere. Similarly, IRFs for surface temperature, ocean heat uptake, sea level rise or any other variable of interest are obtained by monitoring its simulated evolution after the initial perturbation.

The IRFs or Green's functions computed in this study are also useful to characterize the carbon cycle-climate models. The theoretical justification is that IRFs represent a complete characterization of the response of a linear system to an external perturbation. For CO$_2$, the value of the IRF at any particular time is the fraction of the initially added carbon which is still found in the atmosphere. In a linear approximation, the change in atmospheric CO$_2$ inventory at time t can be represented as the sum of earlier anthropogenic emissions, e, at time t' multiplied by the fraction still remaining airborne after time $t - t'$, IRF$_{\mathrm{CO}_2}(t - t')$:

$$\mathrm{CO}_2(t) = \int_{t_0}^{t} e(t') \cdot \mathrm{IRF}_{\mathrm{CO}_2}(t - t')\mathrm{d}t' + \mathrm{CO}_2(t_0), \tag{7}$$

where CO$_2(t_0)$ is the atmospheric CO$_2$ inventory at a time when the system was in (approximate) steady state. The IRF is thus a first-order approximation how excess anthropogenic carbon is removed from the atmosphere by a particular model.

Non-linearities in the carbon cycle-climate system, however, limit the accuracy of the above equation substantially. The IRF_{CO_2} is not an invariant function, but depends on the magnitude of the carbon emissions (Maier-Reimer and Hasselmann, 1987). Non-linearities arise from the non-linearity of the carbonate chemistry in the ocean, from changes in ocean circulation with global warming that affect the surface-to-deep transport of excess anthropogenic CO_2 as well as from other effects such as non-linear dependencies of terrestrial productivity or soil overturning rates on climate and atmospheric CO_2. It has been shown that the atmospheric response, as simulated with a comprehensive model, is better approximated using oceanic and terrestrial impulse response functions that include major non-linearities of the carbon cycle (Joos et al., 1996; Meyer et al., 1999). In conclusion, the IRF and thus also the AGWP for CO_2 depends on the details of the experimental setup (background concentration, pulse size) as well as on the characteristics of the carbon cycle-climate model used for its determination.

2.2 Global temperature change potential

The GWP has been critiqued from several angles (e.g., Shine, 2009; O'Neill, 2000) and an important critique is that the AGWP does not directly translate into a well-known climate response. The Global Temperature change Potential (GTP) was developed as an alternative (Shine et al., 2005). The Absolute Global Temperature change Potential (AGTP) is the change in global mean surface temperature, ΔT, at time TH in response to a pulse emission, e, of one unit of agent x at time $t = 0$. It corresponds to $IRF_{T,x}$, the impulse response of temperature, T, to a unit emission of agent x:

$$AGTP_x(TH) = \frac{\Delta T(TH)}{e_x(t=0)}. \tag{8}$$

The Global Temperature change Potential, GTP_x, is the AGTP of x compared to that of CO_2:

$$GTP_x(TH) = \frac{AGTP_x(TH)}{AGTP_{CO_2}(TH)} \tag{9}$$

The AGTP is often written as convolution integral of the radiative forcing:

$$AGTP_x(TH) = \int_0^{TH} RF_x(t) \cdot R(TH - t)dt, \tag{10}$$

where $R(t)$ is the temporally displaced response in T to a δ-function change in radiative forcing at time $t = 0$. R is influenced by the uncertain properties of the global climate system such as the climate sensitivity, the heat capacity of the lower atmosphere-earth surface system, and by the rate of ocean heat uptake.

In most previous work (Fuglestevedt et al., 2010), the AGTP has been estimated from the convolution of the RF_x

with R_T (Eq. 10), where the RF_x and R often come from different models that are likely not consistent in terms of ocean heat and carbon uptake (for example, the RF_{CO_2} is from the Bern-SAR model and the R is from HadCM3). It is also possible to estimate $AGTP_{CO_2}$ and IRF_{T,CO_2} directly from a climate-carbon cycle model in response to a pulse emission. This is done in this study with the suite of carbon-cycle climate models. Apart from the box models, these models feature a consistent treatment of heat and carbon transport. Following similar logic, it is possible to derive similar expressions for the time-integrated GTP, ocean heat content, and sea level rise. Recent research has shown that the GWP and the time-integrated GTP are numerically similar over a range of time horizons, other than for very short lived species like black carbon (Peters et al., 2011; Azar and Johansson, 2012).

3 Model description and experimental setup

An open call was directed to the carbon cycle-climate modelling community to participate in this IRF_{CO_2} intercomparison project (Joos et al., 2012). A common protocol defines model setup, requested simulations (Table 1), and output and it is given as a Supplement. The procedure corresponds to that for the calculation of the IRF_{CO_2} for the IPCC SAR (Enting et al., 1994) and the IPCC AR4. In addition, output was also requested for the change in global mean surface air temperature as well as ocean heat content, and steric sea level rise. This allows us to derive the impulse response functions for temperature, ocean heat content and steric sea level rise to an emission pulse of CO_2 and correspondingly the AGWP and AGTP for CO_2 and similar metrics for ocean heat content and steric sea level rise.

Results from fifteen models were submitted (Tables 2 and 3) and these are briefly described and referenced in the Appendix A. The models include three comprehensive Earth System Models (HADGEM2-ES, MPI-ESM, NCAR CSM1.4), seven Earth System Models of Intermediate Complexity (EMICs), and four box-type models (ACC2, Bern-SAR, MAGICC, TOTEM). Many of these EMICs also participated in three model intercomparsion projects targeted to study the evolution of the climate and the carbon cycle over the historical period (Eby et al., 2012) and under different future scenarios (Zickfeld et al., 2012) and to explore the evolution of the North Atlantic Meridional Overturning Circulation scenarios (Weaver et al., 2012). The EMICs are of varying complexity and include either a 3-dimensional dynamic ocean (Bern3D-LPJ, GENIE, LOVECLIM, MESMO, Uvic-2.9), a 2-dimensional dynamic ocean (Bern2.5D-LPJ, Climber2.4-LPJmL), or a box-type ocean (DCESS). Nine models include a Dynamic Global Vegetation Model (HADGEM2-ES, MPI-ESM, Bern2.5-LPJ, Bern3D-LPJ, Climber2.4-LPJmL, GENIE, LOVE-CLIM, MESMO, UVic-2.9), one model a spatially-resolved

Table 1. Overview on main simulations. All simulations are started from a preindustrial state.

Simulation	Model setup
	PD100, standard impulse
run 1	Atmospheric CO$_2$ prescribed to follow the historical evolution up to year 2010 and kept at 389 ppm thereafter. Compatible emissions are diagnosed. Non-CO$_2$ and land use forcing constant after 2010.
run 2	Model is forced with diagnosed emissions from run 1 and atmospheric CO$_2$ is computed. Other forcings as in run 1.
run 3	Setup as in run 2. An emission pulse of 100 GtC is added in 2015 AD
	PI100 and PI5000 preindustrial impulses
run 4	Control simulation under preindustrial conditions and freely evolving CO$_2$
run 5	As run 4. An emission pulse of 100 GtC is added in year 10
run 6	As run 4. An emission pulse of 5000 GtC is added in year 10

terrestrial carbon cycle with prescribed vegetation distribution (NCAR CSM1.4) and five models (ACC2, Bern-SAR, DCESS, MAGGIC6, TOTEM) a box-type biosphere with a simple logarithmic dependency of NPP on CO$_2$. Land use and land use changes and their impacts on the carbon cycle and biophysical forcing are explicitly included as internal part of the model in five models (HADGEM2-ES, MPI-ESM, Bern3D-LPJ, GENIE, UVic-2.9). One model (Bern3D-LPJ, ensemble version) also includes a representation of peatlands and permafrost processes and corresponding carbon stocks (Tarnocai et al., 2009). The equilibrium climate sensitivity of the models ranges between 1.5 to 5.7 °C for a nominal doubling of atmospheric CO$_2$. Eight models include an ocean-sediment and weathering/burial module to address long-term (multi-millennial) carbon cycle changes. However, here we restrict the time horizon to 1000 yr and do not provide results for the multi-millennial CO$_2$ evolution. The models used to compute IRF$_{CO_2}$ for the SAR (Bern-SAR) and for the AR4 (Bern2.5-LPJ) as used by the UNFCCC are included for traceability of results.

The "standard" setup corresponds to a pulse input of 100 GtC added to a constant background concentration of 389 ppm. The emission pulse is equivalent to a mean atmospheric change of 47.10 ppm when using a unit conversion factor of 2.123 GtC ppm^{-1} (Enting et al., 1994). Recently, the factor to convert ppm into mol was slightly revised to 0.1765 ($\pm$5 %) Pmol ppm^{-1} (Prather et al., 2012); this yields a conversion factor of 2.120 GtC ppm^{-1} (0.1765 Pmol ppm^{-1} × 12.01 gC mol^{-1}) when assuming that CO$_2$ is distributed evenly in the atmosphere as done here. For current emissions, the increase in the stratosphere lags the tropospheric increase and a 1 ppm change in the troposphere may corresponds to a mean atmospheric change that is about 1 to 2 % lower. In the following these uncertainties of order 2 % are neglected. Three simulations are performed

to determine the "standard" IRF from individual models. An example figure showing results from these three simulations in terms of atmospheric CO$_2$ can be found in the protocol added in the Supplement.

In run 1, a model is forced with historical concentration up to a reference year (here $t_{ref} = 2010$) and then concentration is kept fixed thereafter at a constant value (here CO$_{2,ref} = 389$ ppm). A data file with the reconstructed distribution of atmospheric CO$_2$ over the period 850 to 2010 AD was distributed to all groups. The model emissions, that are compatible with the prescribed CO$_2$ evolution, are diagnosed from the simulated change in total carbon inventory (prescribed atmospheric change plus modelled ocean and terrestrial carbon uptake and any imbalance in the weathering/burial cycle).

In run 2, a model is forced with the diagnosed emissions obtained from run 1 with the same model. Run 2 serves for control purposes only and was not provided for the MPI-ESM and NCAR CSM1.4 model as CPU time was lacking. In run 3, the same forcing and setup as in run 2 is applied, but in addition 100 GtC are added instantaneously to the atmosphere five years after the reference year (here in 2015.0). The normalised IRF is then approximately:

$$\text{IRF}_{CO_2}(t = t_{model} - 2015.0) = (CO_2(t_{model}) - CO_{2,ref})/$$

$$(100\,\text{GtC}/2.123\,\text{GtC}\,\text{ppm}^{-1}) \text{ for } t_{model} \geq 2015$$

The general advice in the protocol was to include non-CO$_2$ forcing and land use area changes to the extent possible. Non-CO$_2$ forcing as well as land use area are kept constant at 2010 level after 2010. While the total radiative forcing is kept constant in run 1 and 2 after 2010, the climate is evolving freely. The response to a 100 GtC pulse obtained from run 1 to 3 for a present day (PD) background is also termed "PD100" and represents our standard case.

In addition to these standard experiments, groups were also asked to provide results for emissions pulses of 100 GtC

F. Joos et al.: A multi-model analysis   **2799**

Table 2. Characterization of the climate models: physical components, ΔT_{2x} denotes the equilibrium climate sensitivity for a nominal doubling of CO_2. ΔT_{2x} reported here for the Bern3D-LPJ, CLIMBER2, DCESS, LOVECLIM, MESMO1.0, UVic2.9 are those determined by doubling preindustrial CO_2 in a simulation over 1000 yr (Eby et al., 2012).

Model	Atmosphere Ocean and Sea ice	Land surface	ΔT_{2x} (Celsius)	
ACC2	Land-ocean energy balance model	Diffusion model, simple sea-ice correction factor	Simple land surface albedo parameterization	4.04
Bern-SAR	1-box	upwelling-diffusion-entrainment model	n/a	n/a
Bern2.5D-LPJ (or Bern2.5CC)	1-D (zonally and vertically averaged) energy moisture-balance model, $7.5° \times 15°$	2-D friction-geostrophic circulation model with thermodynamic sea ice; 3 ocean basins, connected in Southern Ocean, $7.5° \times 15°$, 14 vertical levels	n/a	3.2
Bern3D-LPJ	2-D energy-moisture balance model; $10° \times (3–19)°$	3-D friction-geostrophic circulation model with sea ice; $10° \times (3–19)°$, 32 levels	1-layer soil temperature, no soil moisture storage, river routing	3.3
CLIMBER-2-LPJmL	3-D statistical-dynamical model; $10° \times 51°$, 10 layers	2-D friction-geostrophic circulation model with sea ice; 2.5°, 21 levels	1-layer soil temperature, 2-layer soil hydrology, snow cover, river routing	3.0
DCESS	2-box energy-moisture balance model	2-box parameterized circulation and exchange, no explicit sea ice; 55 levels	No explicit soil temperature and moisture calculation	2.8
GENIE	2-D energy-moisture balance model; $10° \times (3–19)°$	3-D friction-geostrophic circulation model with sea ice; $10° \times (3–19)°$, 16 levels	1-layer soil temperature, bucket soil moisture model, river routing	4.0 ± 0.8
HADGEM2-ES	3-D GCM, 38 vertical levels, N96 (1.25×1.875 degree) resolution	3-D ocean GCM, 1-degree, increasing to 1/3 degree at equator. 40 vertical levels	MOSES-2: tiled land-surface with 4-layer soil temperature and hydrology, river routing.	4.58
LOVECLIM 1.1	3-D quasi-geostrophic circulation model; $5.6° \times 5.6°$, 3 levels	3-D primitive equation circulation model with sea ice; $3° \times 3°$, 20 levels	1-layer soil temperature, bucket soil moisture model, river routing	1.5
MAGICC6	4-box energy-balance model.	2 hemispheric columns, upwelling-diffusion-entrainment, 50 levels, simple sea-ice correction factor.	Simple land surface albedo parameterization; soil temperature/moisture only parameterized for permafrost area.	1.9 to 5.7 (Average 2.88)
MESMO 1.0	2-D energy-moisture balance model; $10° \times (3–19)°$	3-D friction-geostrophic circulation model with sea ice; $10° \times (3–19)°$, 16 levels	1-layer soil temperature, bucket soil moisture model, river routing	3.7
MPI-ESM	ECHAM6 3D GCM T63L47	MPIOM 3-D primitive equation GCM + sea ice GR15L40 grid	JSBACH: tiled land-surface, 5-layer soil temperature, 1-layer hydrology, HD river routing model	3.4
NCAR CSM1.4	CCM3 T31, L18	NCOM $3.6° \times (0.8 - 1.8°)$, 25 levels with sea ice	LSM T31	2.0
TOTEM	n/a	n/a	n/a	n/a
UVic 2.9	2-D energy-moisture balance model; $1.8° \times 3.6°$	3-D primitive equation circulation model with dynamic & thermodynamic sea ice $1.8° \times 3.6°$, 19 levels	1-layer soil temperature, complex soil moisture model, river routing	3.6

(run 5, case PI100) and 5000 GtC (run 6, PI5000) added to a preindustrial (PI) background. A preindustrial control simulation with constant boundary conditions and freely evolving CO_2 was also requested (run 4). 5000 GtC is of the same order as available conventional (coal, oil, gas) fossil carbon resources and has been used in past pulse experiments (e.g., Archer et al., 2009; Eby et al., 2009). This experiment is thus indicative of the long-term consequences for burning all conventional fossil resources. The influence of different background CO_2 concentrations is quantified by comparing the

standard run with the 100 GtC pulse added to the preindustrial CO_2 concentration.

Sensitivity simulations with one model (Bern3D-LPJ, see figures in protocol in tbe Supplement) for PD100 suggest that the simulated response is insensitive to the inclusion of non-CO_2 forcing and whether the emissions pulse is released at the beginning of the year or distributed over one year. On the other hand, the simulated IRF_{CO_2} is about 0.02 higher if anthropogenic land use is explicitly included compared to

Table 3. Characterization of the carbon cycle models.

Model	Land Carbon Cycle	Land use (LU) (LU area data and anthropogenic LU classes	Marine Biogeochemistry & Ecosystem	Sediment/ Weathering
ACC2	4-box, ß-factor (CO_2 fertilization) and $Q10$ temperature sensitivity of soil respiration)	n/a	4-box global atmosphere-ocean, temperature-sensitive carbonate chemistry	n/a
BernSAR	4-box, ß-factor (CO_2 fertilization)	n/a	n/a (perturbation approach)	n/a
Bern2.5D-LPJ (or Bern2.5CC)	Dynamic Vegetation Model, 9 Plant Functional Types, multiple-litter/soil pools, $3.75° \times 2.5°$	n/a	Prognostic export production, P, DIC, DOC, (POC), ALK, O_2, no ecosystem	n/a
Bern3D-LPJ	Dynamic Vegetation Model, 9 Plant Functional Types, multiple-litter/soil pools, $3.75° \times 2.5°$	Hyde 3.1 3 LU classes, products	Prognostic export production, P, Fe, Si, DIC, DOC, POC ALK, O_2, no ecosystem	yes/diagnosed
CLIMBER2-LPJmL	Dynamic Vegetation Model 9 Plant Functional Types, 12 Crop Functional Types, $0.5° \times 0.5°$	Landuse dataset 1700–2005 (Portman et al., 2008; Fader et al., 2010)	Prognostic export production, P, DIC, DOC, POC, ALK, O_2, NPZD ecosystem	yes/yes
DCESS	4-box, ß-factor (CO_2 fertilization) and $Q10$ temperature sensitivity of soil respiration	n/a	Prognostic export production, P, O_2, POC PIC, DIC and ALK, no ecosystem	yes/yes
GENIE	Efficient Numerical Terrestrial Scheme (ENTS). 1 Plant Functional Type; $10° \times (3–19)°$	PMIP3 (800–1699), CMIP5 (1500–2005) 1 LU class	Prognostic export production, P, Fe, DIC, DOC, POC, ALK, O_2, no ecosystem	yes/diagnosed
HADGEM2-ES	TRIFFID Dynamic global vegetation model, with 5 PFTs. Half-hourly carbon fluxes from vegetation physiology and soil respiration. 4-pool soil carbon model.	Hurtt et al. (2011) harmonized; Anthropogenic agricultural fraction	DiatHadOCC	n/a
LOVECLIM1.1	Dynamic Vegetation Model 2 Plant Functional Types; $5.6° \times 5.6°$	n/a	Prognostic P, DIC, POC, DOC, ALK, O_2, export production/no ecosystem	preservation/no
MAGICC6	4-box global carbon cycle model, calibrated towards 9 C4MIP carbon cycle model's pools and fluxes.	n/a.	n/a (perturbation approach)	n/a.
MESMO 1.0	Efficient Numerical Terrestrial Scheme (ENTS). 1 Plant Functional Type; $10° \times (3–19)°$	n/a	Prognostic export production, P, Fe, Si, N, DIC, DOC,POC, ALK, no ecosystem	n/a
MPI-ESM	JSBACH:, 3 living, 4 litter, 1 slow soil carbon pool, dynamical vegetation, 12 PFTs	Prescribed 1994 distribution of agricultural land	Full carbonate chemistry, NPZD type ecosystem, PO_4, NO_3, Fe colimitation of biological production	yes/diagnosed
NCAR CSM1.4	CASA prescribed veg. distribution	n/a	Modified OCMIP-2 with prognostic export	n/a
TOTEM	Global carbon-nitrogen-phosphorus cycle model, explicit treatments of rivers, erosion, fertilizer appl.	n/a	Global carbon-nitrogen-phosphorus cycle model, explicit treatments of coastal zone	param./ parameterized
UVic 2.9	Dynamic Vegetation Model, 5 Plant Functional Types, $3.6° \times 1.8°$, 3 carbon pools per PFT, 1 soil carbon pool	Hyde 3.1, 2 grass PFTs used for agriculture, LUC carbon split evenly to soil and atmosphere	NPZD, 2 nutrient and 2 phytoplankon classes, prognostic PO_4, NO_3, O_2, DIC, ALK, denitrification	yes/diagnosed

a simulation with natural vegetation only as less carbon is taken up on the converted land.

Three of the participating modeling groups delivered results from an ensemble of simulations. The GENIE group reported results from an ensemble with 69 members where model parameters where varied within uncertainties. The 69-member ensemble was derived from a set of around 1500 simulations combined with a statistical modelling and fil-

tering procedure applying eight preindustrial climatic constraints (Holden et al., 2013). The 69 member ensemble was reduced to 20 members by requiring a plausible present-day CO_2 concentration in an emission-forced simulation over the industrial period and beyond. Here, median and 5 % to 95 % intervals from these 20 different model setups are reported.

The 69-member ensemble has an ensemble-averaged CO_2 concentration of 404 ± 50 ppm (mean ± 1 sdv) at 2000 AD,

compared to 370 ppm measured at Mauna Loa. CO_2 is on average lowered to 364 ± 14 ppm at 2000 AD in the reduced set. The cases that give the better agreement with observed CO_2 have the larger land uptake through the model's CO_2 fertilization mechanism. Gross primary productivity in GE-NIE increases by 27 ± 18 % (mean ± 1 sdv) in the full set and by 39 ± 17 % in the reduced set for a doubling of the atmospheric CO_2 concentration and considering fertilization only.

The MAGICC model version 6.3 has been run in 171 different parameter settings that emulate 19 AOGCMs and 9 coupled climate-carbon cycle models from the Coupled Model Intercomparison Project Three (CMIP3) and the Coupled Carbon Cycle Climate Model Intercomparison Project (C4MIP). The application of this model to simulate IRFs has been described in (Reisinger et al., 2010).

The Bern3D-LPJ model was run in 1069 different setups selected from a 5000-member ensemble following a Bayesian approach. Nineteen key model parameters are varied. These are related to terrestrial and ocean carbon and heat exchange, uncertainties in anthropogenic radiative forcing, and the transient and equilibrium climate sensitivity of the model. The 5000 member ensemble is constrained by a large set of observation-based data including estimates for surface air temperature change, ocean heat uptake, atmospheric CO_2 change and ocean and land carbon uptake rates, seven physical and biogeochemical 3-D ocean tracer fields, and land carbon stocks and fluxes.

Additional sensitivity simulations were carried out with the standard setup of the Bern3D-LPJ model. These include a series of runs with emission pulses ranging from 10 to 10 000 GtC added to a preindustrial background. These simulations are used to demonstrate the dependency of the IRF on the magnitude of emissions. The model was also run in a mode where climate was kept constant for emission pulses of 100 and 5000 GtC. These simulations allow us to quantify the impact of carbon-cycle climate feedbacks on the IRF_{CO_2} within the Bern3D-LPJ model.

The pulse size of 100 GtC applied in the standard simulation (run 3) is larger than the pulse size of 10 GtC applied to determine the IRF_{CO_2} in the Bern-SAR model for the SAR and the pulse of 40 GtC applied in the Bern2.5D-LPJ for the AR4. The choice of the larger pulse size is to improve signal-to-noise ratio in the simulated response. The simple Bern-SAR model does not feature any internal variability and so a small pulse size still permits us to compute its response reliably. In contrast, the Bern2.5D-LPJ used in the AR4 and even more the ESM used in this study feature considerable internal variability in atmospheric CO_2 and climate that would mask the response to a small emission pulse.

Model output was smoothed to remove short-term variability using a spline-fit method (Enting, 1987). A cut-off period is chosen as input parameter to the spline routine such that the amplitude of a sine wave with this period is attenuated by 50 %. The results from run 3 are subtracted from the

control run (run 2; run 1 for MPI-ESM and NCAR CSM1.4). The resulting response is smoothed using cut-off periods of 4, 20, 50, 250, and 500 yr for the periods from year 0 to 10, from year 10 to 50, from year 50 to 100, from year 100 to 300 and year 300 to 1000, respectively. The response of all models to the 100 GtC pulse added to a 389 ppm background was smoothed in this way for consistency. This treatment has virtually no effect on results from box-models and from EMICs with small or absent internal variability and on the integrated IRF_{CO_2} that is used to compute the AGWP and GWP.

The multi-model mean IRF_{CO_2} and responses in other quantities are fitted by a sum of exponentials:

$$\text{IRF}(t) = a_0 + \sum_{i=1}^{3} a_i \cdot \exp\left(\frac{-t}{\tau_i}\right) \text{ for } 0 \leq t \leq 1000 \text{ yr} \quad (11)$$

For IRF_{CO_2} the conditions is applied that the sum of the coefficients a_i equals 1 and for the other variables (e.g., surface air temperature, ocean heat content, steric sea level rise) that the sum equals zero. We suggest to use numerical values as obtained by these fits for the multi-model mean in future studies. Note that the fits only apply for the period from 0 to 1000 yr. We use the values from the fits as our best estimates.

The responses as simulated by individual models were also fitted using Eq. (11). The coefficients (a_i, τ_i) are tabulated in the Supplement for all models and for the responses in CO_2. Results of the fits are compared with the model output in a complementary figure in the Supplement.

4 Results

4.1 Impulse response functions and absolute global warming potentials for CO_2

The evolution of the IRF_{CO_2} (Fig. 1a) shows a rapid decrease in the first few years after the emission pulse and then a continued but slow decline. It reaches a fraction of 0.60 ± 0.14 ($\pm$ two sdv) at year 20 and 0.41 ± 0.13 at year hundred. In other words, while 40 % of the initial atmospheric CO_2 perturbation is on model-average removed from the atmosphere within 20 yr, it takes additional 80 yr to mitigate the next 19 % of the perturbation. At year 1000, more than 25 % (± 9 %) of the perturbation is still airborne. This evolution is consistent with earlier model results (Maier-Reimer and Hasselmann, 1987; Cao et al., 2009; Siegenthaler and Joos, 1992; Sarmiento et al., 1992; Enting et al., 1994; Archer et al., 2009; Eby et al., 2009). It is also consistent with our understanding of the carbon cycle as two-way transfers of carbon between reservoirs with different timescales (Prentice et al., 2001; Denman et al., 2007; Oeschger et al., 1975; Broecker et al., 1980).

The time-integrated IRF_{CO_2} (Fig. 1b), and thus $AGWP_{CO_2}$, increases continuously with time and there is no sign of approaching a steady state value at year 1000. The time-integrated IRF_{CO_2} for the individual models is

Table 4. Time-integrated airborne fraction for different time horizons in units of years and corresponding uncertainty ranges. Multiplication with 1.77×10^{-15} W m^{-2} kg-CO$_2^{-1}$ yields the Absolute Global Warming Potential (AGWP) for CO_2. Values in parentheses for the Bern3D-LPJ, GENIE, and MAGICC6 ensembles represent median and 5 % to 95 % confidence range. The median for each of these models is included in the multi-model mean; reference setup of the Bern3D-LPJ is not included. The errors of the multi-model mean represent ±two standard deviations. Our best estimate for the mean is the value from the fit to the multi-model mean and the best estimate for the 5 to 95 % confidence range is the average range from the different methods centered at the mean.

Time Horizon	20 yr	50 yr	100 yr	500 yr	1000 yr
	Time-integrated IRF$_{CO_2}$ (yr)				
NCAR CSM1.4	13.8	27.8	46.6	n/a	n/a
HadGEM2-ES	14.7	30.9	53.3	n/a	n/a
MPI-ESM	14.5	29.2	48.8	n/a	n/a
Bern3D-LPJ (reference)	15.4	34.3	61.9	241	417
Bern3D-LPJ ensemble	15.1	32.7	57.6	205	n/a
	(14.0–16.0)	(28.9–36.0)	(48.9–65.6)	(160–265)	n/a
Bern2.5D-LPJ	13.9	29.7	51.1	163	283
CLIMBER2-LPJ	13.0	26.8	49.2	181	306
DCESS	14.6	31.8	56.3	199	329
GENIE ensemble	13.6	28.9	50.5	173	n/a
	(10.9–17.6)	(21.7–41.4)	(38.3–77.9)	(143.68–271)	n/a
LOVECLIM	13.5	27.9	45.3	170	280
MESMO	15.1	33.6	61.1	238	410
UVic2.9	13.7	29.5	53.0	209	376
ACC2	13.7	27.9	46.5	151	252
Bern-SAR	14.0	29.0	48.9	161	270
MAGICC6 ensemble	14.0	29.6	51.8	199	n/a
	(12.0–16.1)	(23.6–35.7)	(40.0–64.2)	(148–233)	n/a
TOTEM2	16.9	38.3	66.6	180	281
multi-model mean	14.3 ± 1.8	30.2 ± 5.7	52.4 ± 11.3	186 ± 48	308 ± 94
	Uncertainty ranges (yr)				
multi-model range	3.6	11.3	22.6	96	189
Bern3D-LPJ	2.1	7.2	16.7	105	n/a
GENIE	6.7	19.8	39.5	128	172
MAGICC6	4.1	12.1	24.2	85	n/a
Linear Progamming	n/a	n/a	24.0	n/a	n/a
Average of ranges	4.1	12.6	25.8	103	180
in % of multi-model mean	28.8	41.6	49.1	56	58
	Best estimates for time-integrated IRF$_{CO_2}$ (yr)				
mean	14.2	30.3	52.4	184	310
5–95 % confidence range	(12.2–16.3)	(24.0–36.6)	(39.5–65.2)	(132–235)	(220–400)
	Best estimates for AGWP of CO_2 (10^{-15} yr W m^{-2} kg-CO$_2^{-1}$)				
mean	25.2	53.5	92.5	324	548
5–95 % confidence range	(20.7–29.6)	(41.1–65.8)	(67.9–117)	(228–421)	(380–716)

tabulated in Table 4. The multi-model mean increases from 14.3 ± 1.8 yr (mean ± 2 sdv) at year 20, to 30.2 ± 5.7 at year 50, to 52.4 ± 11.3 at year 100, to 186 ± 48 at year 500, and to 308 ± 94 at year 1000.

The multi-model mean IRF$_{CO_2}$ over the first 1000 yr is fitted by a sum of exponentials and the coefficients for IRF$_{CO_2}$ and for other responses are given in Table 5. We note that the time-integrated IRF$_{CO_2}$ as calculated with this fit is the same for a time horizon of 100 yr and slightly different for the time horizons of 20, 50, 500, and 1000 yr than those the multi-model mean values (the values from the fit are: 14.2 yr, 30.3 yr, 52.4 yr, 184 yr, 310 yr). We use these values from the fit as our best estimates in Table 4.

Uncertainty ranges across models and from model ensembles: there are uncertainties in the IRF$_{CO_2}$ and the AGWP$_{CO_2}$. The range in integrated IRF$_{CO_2}$ across all models

Table 5. Coefficients to fit multi-model mean responses to a pulse emission of 100 GtC following Equation 11 in the main text and for $0 < t < 1000$ yr. The mean relative error of the fit is given in percent. The error is calculated from annual values as the average of the absolute differences between fit (f) and multi-model mean (m) divided by the multi-model mean ($1/N \sum (m - f)/m$). Multiplication by $(12/(100 \times 44 \times 10^{12}))$ yields the change per kg-CO_2 for ocean and land carbon storage, surface air temperature (SAT), time-integrated SAT (iSAT), steric sea level rise (SSLR), and ocean heat content (OHC). The timescales τ_i are given in years and units of a_i are indicated in parentheses in the first column.

	rel. error	a_0	a_1	a_2	a_3	τ_1	τ_2	τ_3
IRF_{CO_2}	0.6	0.2173	0.2240	0.2824	0.2763	394.4	36.54	4.304
Ocean (GtC)	0.6	60.29	−26.48	−17.45	−16.35	390.5	100.5	4.551
Land (GtC)	1.3	17.07	332.1	−334.1	−15.09	74.76	70.31	6.139
SAT (°C)	1.8	0.1383	0.05789	−0.06729	−0.1289	264.0	5.818	0.8062
iSAT (°C yr)	1.8	3934	−4432	777.7	−280.0	16 080	2294	1144
SSLR (cm)	1.5	5.259	−3.789	−0.9351	−0.5350	581.7	75.71	5.963
OHC (10^{22} J)	1.0	42.63	−32.86	−6.589	−3.182	420.4	54.82	6.340

is 40 to 65 yr at year hundred. This is comparable to the 5–95 % interval ranging from 40 to 64 yr for the MAGICC6 ensemble that emulates a number of carbon-climate models. The 5–95 % confidence interval for the Bern3D-LPJ ensemble, constrained with a broad set of observations, is 49 to 66 yr at year 100 and somewhat smaller than the model range. The ensemble interval from the GENIE model is larger than the other ranges at year 100; the time-dependence of this ensemble was constrained only by preindustrial to modern CO_2 change. At year 20 and 50, the situation with regard to uncertainties ranges is qualitatively similar as for year 100. However, the 5–95 % confidence range for the MAGICC6 ensemble is smaller than the range across all models at year 500, whereas the width of the confidence range is larger than that of the model range for the observation-constrained Bern3D-LPJ and GENIE ensembles. This may suggest that observational-constraints as applied in the Bern3D-LPJ narrow the uncertainty range for a time horizon of up to 100 yr.

An alternative, linear programming approach: an alternative approach is to constrain the uncertainty in IRF_{CO_2} by assuming a linear carbon system and constraining the IRF_{CO_2} with estimates of the 20th century airborne fraction of CO_2. If we consider the uncertainty in the integrated response, then clearly if IRF_{CO_2} lies between 0 and 1, the integral to time TH will lie between 0 and TH, regardless of the form of the function IRF_{CO_2}. However not all functions have physically reasonable behaviour and not all functions will be consistent with the 20th century pattern of emissions and concentrations. Including such considerations can narrow the range of possible values of the integrated response. Finding the maximum and minimum possible values of the integral (and the functions that give these extrema) is a problem in mathematical optimisation that can be analysed using the calculus of variations. If the constraints are linear, then the discretised form of the optimisation can be expressed as a problem in linear programming for which well-established computational techniques are available (Press et al., 1986). Such an

approach to analysing the carbon cycle response was introduced earlier (Enting and Mansbridge, 1987).

For the present study we consider functions with IRF_{CO_2} $(t = 0) = 1$, IRF_{CO_2} $(t) \geq 0$, d/dt IRF_{CO_2} $(t) \leq 0$, and d^2/dt^2 IRF_{CO_2} $(t) \geq 0$, and which give behavior consistent with observations for the 20th century. This last condition is expressed in terms of the 20th century cumulative airborne fraction γ. If we take γ as known precisely then we find that for TH $= 100$ yr, the integrated response is constrained to lie in the range 39.7 to 52.4 yr. The implication is that regardless of the model structure, no linear model that exhibits the dissipative behaviour expressed by the constraints on the derivatives, can have an integrated response that lies outside this range. This range of 13 yr is thus an upper bound on the amount of uncertainty that can arise from differences in model structure (and termed "structural uncertainty", Enting et al., 2012).

If, however, it is acknowledged that the 20th century cumulative airborne fraction is not known precisely, mainly because of uncertainties in land-use emissions (Stocker et al., 2011), then a wider class of response functions and a wider range of integrals is possible. Constraining the airborne fraction to lie in the range 0.5 ± 0.05 gives the range 33.6 to 57.6 yr for possible values of the integral for TH $= 100$ yr. This expanded range of uncertainty is a combination of the "structural uncertainty" described above, and a "calibration uncertainty" arising from uncertainties in the calibration data (Enting et al., 2012).

Since we are primarily concerned with the range rather than the specific value, the 20th century constraint has been approximated in terms of carbon emissions that grew exponentially over 150 yr with a timescale of 50 yr (emissions are proportional to $\exp(t/(50\,\text{yr}))$). This is a truncation of the expression for the airborne fraction in terms of the Laplace transform of the response (Enting, 1990). In principle, the same approach can be used for TH $= 20$ yr but because the 20 yr timescale is less representative of 20th
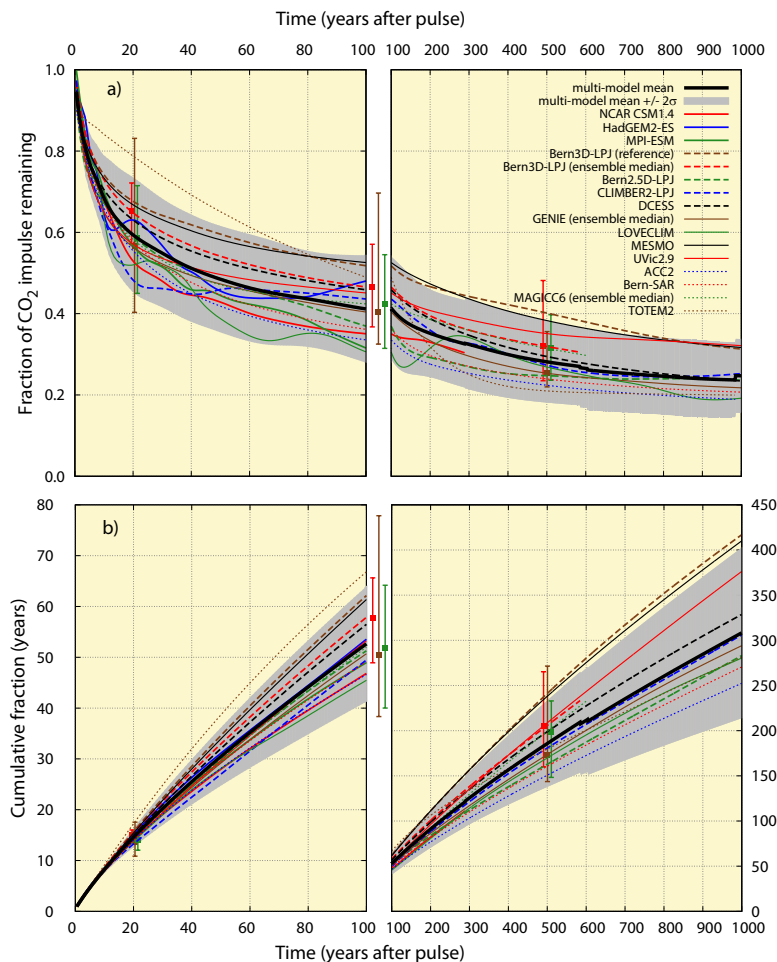
Fig. 1. (a) The evolution of the impulse response function for CO$_2$, IRF$_{CO_2}$, for an emission pulse of 100 GtC added to an atmospheric background concentration of 389 ppm (PD100) for a range of Earth System Models (thick solid), EMICs (dashed and thin solid), and reduced-form models (dotted). The multi-model mean, computed by giving each available model equal weight, and the corresponding ±two standard deviation range is shown by the black solid line and the grey shading. Note that not all models were run to year 1000 and thus the number of models included in the average changes with time. For three models, Bern3D-LPJ (red), GENIE (brown) and MAGICC (green), an ensemble of simulations is available and the ensemble median and 5 to 95 % confidence intervals are given by error bars for year 20, 100, and 500. Only the ensemble medians are included in the multi-model mean and range. **(b)** Same as **(a)** but for the time-integrated IRF$_{CO_2}$.

century changes, the "calibration" constraint does little to constrain the range of uncertainty for the integral.

5–95 % confidence range: in conclusion, different approaches to estimate the uncertainty in the integrated IRF$_{CO_2}$ for a time horizon of 100 yr yield comparable results. Taken together, these approaches yield an average uncertainty range of 26 yr or of 49 % for the 100-yr integrated response (Table 4). We assume that this average range represents approximately a 5–95 % confidence range and that it is symmetrically distributed around the multi-model mean to arrive at our

best estimates for the mean and 5–95 % confidence range for the time-integrated IRF$_{CO_2}$.

The MAGICC and Bern3D-LPJ ensemble ranges are roughly symmetrically distributed around the median for time horizons of 20, 50, and 100 yr and skewed, but in different directions, for 500 yr. These results tend to support the assumption that the uncertainty range is symmetric around the best estimate, though the ensemble range from the GENIE model is skewed towards high values.

F. Joos et al.: A multi-model analysis

Absolute Global Warming Potential: multiplying the time-integrated IRF_{CO_2} with the radiative efficiency of CO_2, A_{CO_2}, yields the Absolute Global Warming Potential, $AGWP_{CO_2}$. Here, A_{CO_2} is computed for an atmospheric background of 389 ppm and in the limit of a small perturbation by using the derivative of the simplified radiative forcing expression of (Myhre et al., 1998) (Eqs. 3 and 4 and converting ppm into kg-CO_2): $A_{CO_2} = 5.35$ W m^{-2} $(389\text{ ppm})^{-1} \times (2.123 \times 10^{12}$ kg-C ppm$^{-1})^{-1} \times$ (12 kg-C/44 kg-CO_2) $= 1.77 \times 10^{-15}$ W m^{-2} kg-CO_2^{-1}.

The uncertainty in the radiative efficiency of CO_2 is given as $\pm 10\%$ in the IPCC TAR and AR4 (90 % confidence interval; see page 140 of Forster et al., 2007) and guided by the spread in published estimates. An uncertainty of $\pm 10\%$ translates to an uncertainty range of 20 %. The overall uncertainty in $AGWP_{CO_2}$ is only slightly larger than that for IRF_{CO_2} as the uncertainty in A_{CO_2} is much smaller than that of the time integrated IRF_{CO_2}. Assuming quadratic error propagation, the uncertainty range in $AGWP_{CO_2}(TH = 100\text{ yr})$ is 53 % ($\sqrt{(0.49^2 + 0.2^2)} = 0.53$) compared to 49 % of the integrated IRF_{CO_2} (Table 4). Our best estimate for the $AGWP_{CO_2}$ is a mean value of 92.5×10^{-15} yr W m^{-2} kg-CO_2^{-1} and a 5–95 % confidence range of $(68$ to $117) \times 10^{-15}$ yr W m^{-2} kg-CO_2^{-1} for a time horizon of 100 yr. In IPCC uncertainty language (Solomon et al., 2007), it is very likely that the $AGWP_{CO_2}$ for a time horizon of 100 yr is within a range of $(68$ to $117) \times 10^{-15}$ yr W m^{-2} kg-CO_2^{-1}.

4.2 Response in surface air temperature and AGTP, ocean heat uptake and steric sea level rise

The response in radiative forcing to the 100 GtC pulse (equivalent to 47.1 ppm) corresponds to a step increase by 0.61 W m^{-2} at year 0, followed by a decrease to 0.26 W m^{-2} at year 100 and to 0.16 W m^{-2} at year 1000. These values are computed from the multi-model mean IRF_{CO_2} with the help of Eq. (3) and for a reference mixing ratio of 389 ppm $(RF(t) = 5.35$ W m^{-2} ln((389 ppm + $IRF_{CO_2}(t) \times 47.1$ ppm)/389 ppm)). What magnitude in the SAT response is to be expected from this forcing? The equilibrium response in global mean surface air temperature (SAT) to these forcing values are 0.49 °C (year 0), 0.21 °C (year 100) and 0.13 °C (year 1000) when assuming for illustrative purposes a typical mid-range climate sensitivity of 3 °C for a nominal doubling of CO_2.

The multi-model mean response in SAT to the 100 GtC pulse emission (Fig. 2a, Tables 6 and 7) is an increase by 0.20 ± 0.12 °C within the first 20 yr. Afterwards, SAT remains almost constant until year 100. This evolution is a consequence of the delayed response in SAT to the initial increase in radiative forcing as it takes time to heat the surface layers of the ocean with its large heat capacity and heat exchange with the deep ocean. After year 100, SAT is generally closer to steady state with the simulated radiative forcing and
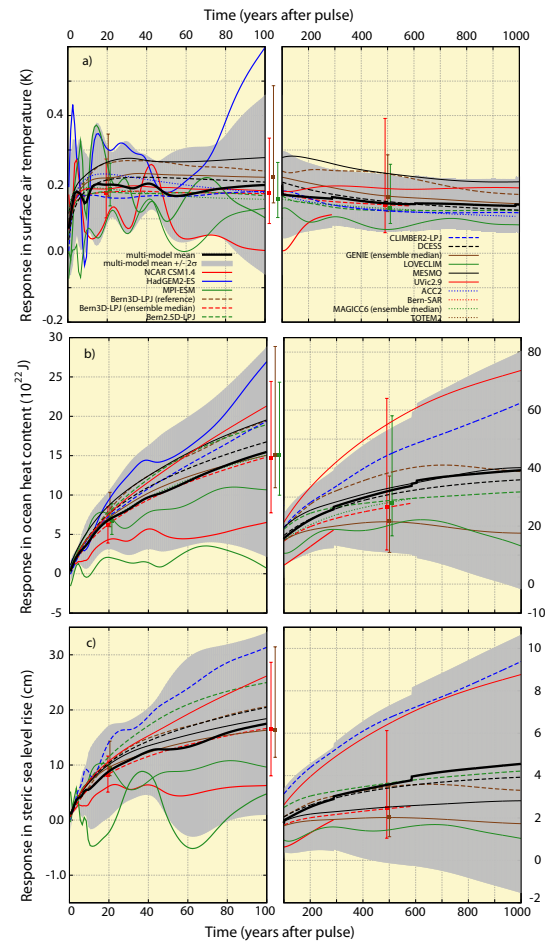

Fig. 2. As Fig. 1 but for the perturbation in global mean surface air temperature **(a)**, in ocean heat content **(b)**, and in steric sea level rise **(c)**. Results are for a CO_2 emission pulse of 100 GtC added to a current CO_2 concentration of 389 ppm (PD100). We note that the signal-to-noise ratio is small for the models that feature a dynamic atmosphere (HadGEM2-ES, MPI-ESM, NCAR-CSM1.4, and LOVECLIM) and the plotted evolutions for these models represent both the forced response and a contribution from the models' internal (unforced) climate variability. Small abrupt changes in the multi-model mean and confidence range arise from a change in the number of model simulations; different groups run their model over different periods, pending on CPU availability.

decreases slowly to 0.14 ± 0.08 °C by year 1000. Our best estimates for the mean and 5 to 95 % uncertainty ranges in SAT changes and AGTP for CO_2 are tabulated for a range of time horizons in Table 6. For a time horizon of 100 yr, AGTP of CO_2 is 0.49×10^{-15} °C per kg-CO_2 and the estimated 5 to 95 % confidence range is $(0.05$ to $0.92) \times 10^{-15}$ °C per kg-CO_2.

Fuglestvedt et al. (2010) applied the analytical response functions for CO$_2$ as given in the AR4 and the analytical response function for temperature to a change in radiative forcing (R) by Boucher and Reddy (2008) to estimate AGTP$_{CO_2}$ to 0.68, 0.58 and 0.51 $\times 10^{-15}$ °C per kg-CO$_2$ for time horizons of 20, 100, and 500 yr respectively. These values are higher than our best estimates of 0.52, 0.49 and 0.40 $\times 10^{-15}$ °C per kg-CO$_2$, but well within the 5 to 95 % confidence range (Table 6). The different values are explained by the difference in temperature responses and less due to the differences in IRF$_{CO_2}$.

The response in SAT is fairly smooth in most EMICs and box models and the response in SAT is well defined in these models. However, the models that feature a dynamic atmosphere (HadGEM2-ES, MPI-ESM, NCAR CSM1.4, LOVECLIM) show strong interannual-to-decadal variability in SAT of several tenths of a degree Celsius both in the control and in the pulse simulation. We note that the three Earth System Models were run over the first 100 yr only. This internal variability of the more comprehensive models makes the extraction of the response in SAT challenging for these models and a well-defined separation of the forced response from the models' internal variability is not achieved when relying on single simulations. For example HadGEM2-ES shows a positive variation in annual SAT values of several tenths of a degree Celsius towards the end of the simulation in the standard pulse experiment. This yields a difference in SAT of about 0.4 °C between the smoothed HadGEM2-ES response and the multi-model mean response near year 100 (Fig. 2). This indicates that it is difficult to extract the temperature response for use in GTP from comprehensive models when they are forced with a pulse of modest size as applied here. Excluding the four models with dynamic atmosphere from the averaging has a relatively small effect on the multi-model mean SAT and deviations are well within the uncertainty range.

The response in ocean heat content (OHC) and steric sea level rise (SSLR) is on multi-century timescales (Fig. 2b, c, Table 8). The responses in these quantities are in general much smoother than for SAT as they mainly reflect the time-integrated, cumulative perturbation in air-sea heat fluxes. Multi-model SSLR is 1.8 ± 1.7 cm (± 2 sdv) at year 100 and 4.6 ± 6.1 cm at year 1000 in response to the 100 GtC pulse. The median in SSLR response in the Bern3D-LPJ ensemble is close to the multi-model mean at year 100, while the 5 to 95 % confidence interval ranges from 0.7 to 2.8 cm and is thus smaller than the multi-model range.

The multi-model response in OHC for the 100 GtC pulse reaches $15 \pm 13 \times 10^{22}$ J by year 100 and $40 \pm 41 \times 10^{22}$ J by year 1000. The upper and lower extreme cases in the multi-model ensemble are the ESMs: the MPI-ESM and NCAR CSM1.4 on the low side and the HadGEM2-ES on the high side. This indicates that the responses in globally aggregated values do not depend on the type of model, e.g., ESM versus EMIC. The 5 to 95 % interval in OHC of the MAG-
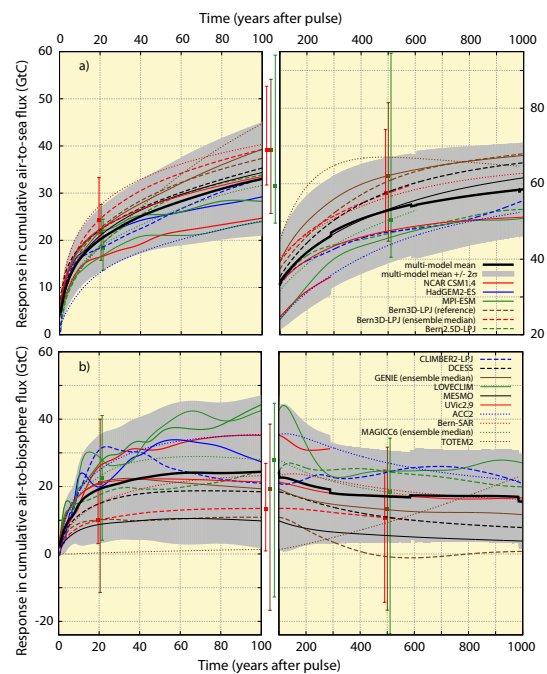

Fig. 3. As Fig. 1, but for the time-integrated perturbation in air-to-sea **(a)** and air-to-land biosphere carbon fluxes **(b)**. Results are for a CO$_2$ emission pulse of 100 GtC added to a present day CO$_2$ concentration of 389 ppm (PD100).

ICC ensemble and of the observation-constrained Bern3D-LPJ ensemble is smaller at year 100 and comparable to the model range at year 500.

In conclusion, AGTP of CO$_2$ varies much less than AGWP for time horizons between 20 and 1000 yr. However, relative uncertainties (e.g., in percent of the mean value) in the estimates of AGTP are much larger than those for AGWP, as also inferred with a box model ensemble by Reisinger et al. (2010), and relative uncertainties in the response in ocean heat content and steric sea level rise are also larger than for AGWP.

4.3 Response in ocean and land carbon

The carbon that is removed from the atmosphere is taken up by the ocean and the land biosphere (Fig. 3). In the first decade, both the ocean and the land contribute substantially to removing the atmospheric carbon perturbation. Land and ocean absorb on multi-model mean close to 20 GtC during the first 20 yr after the emission. The ocean continues to absorb carbon from the atmosphere and the multi-model perturbation in the ocean carbon inventory is 20 ± 7 GtC by year 20, 33 ± 12 GtC by year 100 and 59 ± 12 GtC by year 1000. In other words, 59 % of the emission pulse (multi-

Table 6. Response in global mean surface air temperature to an emission pulse of 100 GtC added to an atmospheric concentration of 389 ppm.

Time Horizon	20 yr	50 yr	100 yr	500 yr	1000 yr
	temperature response (°C)				
NCAR CSM1.4	0.10	0.14	0.01	n/a	n/a
HadGEM2-ES	0.31	0.18	0.59	n/a	n/a
MPI-ESM	0.27	0.09	0.10	n/a	n/a
Bern3D-LPJ (reference)	0.26	0.26	0.24	0.23	0.17
Bern3D-LPJ ensemble	0.18	0.18	0.17	0.14	n/a
	(0.10–0.27)	(0.10–0.30)	(0.09–0.33)	(0.06–0.39)	n/a
Bern2.5D-LPJ	0.18	0.17	0.17	0.13	0.13
CLIMBER2-LPJ	0.16	0.17	0.18	0.12	0.11
DCESS	0.21	0.22	0.21	0.15	0.12
GENIE ensemble	0.22	0.23	0.22	0.16	n/a
	(0.17–0.35)	(0.17–0.46)	(0.15–0.49)	(0.12–0.29)	n/a
LOVECLIM	0.09	0.06	0.13	0.07	0.08
MESMO	0.26	0.27	0.28	0.23	0.2
UVic2.9	0.19	0.19	0.18	0.19	0.19
ACC2	0.23	0.21	0.18	0.12	n/a
Bern-SAR	n/a	n/a	n/a	n/a	n/a
MAGICC6 ensemble	0.19	0.17	0.16	0.13	n/a
	(0.14–0.26)	(0.12–0.27)	(0.10–0.26)	(0.09–0.26)	n/a
TOTEM2	n/a	n/a	n/a	n/a	n/a
multi-model mean	0.20±0.12	0.17±0.11	0.20±0.26	0.14±0.08	0.14±0.08
	Uncertainty ranges (°C)				
Multi-model range	0.24	0.21	0.52	0.17	0.16
Bern3D-LPJ	0.17	0.21	0.25	0.33	n/a
GENIE	0.18	0.28	0.34	0.16	0.13
MAGICC6	0.12	0.15	0.16	0.17	n/a
Average of ranges	0.18	0.21	0.32	0.21	0.14
in % of multi-model mean	90	123	160	144	101
	Best estimates for temperature response (°C)				
mean	0.19	0.19	0.18	0.15	0.14
5–95 % confidence range	(0.10–0.28)	(0.09–0.30)	(0.02–0.34)	(0.05–0.26)	(0.07–0.21)
	Best estimates for AGTP of CO_2 (10^{-15} °C kg-CO_2^{-1})				
mean	0.52	0.51	0.49	0.40	0.38
5–95 % confidence range	0.27–0.76	0.24–0.81	0.05–0.92	0.13–0.70	0.19–0.57

model average) has been transferred to the ocean by year 1000 (Fig. 3a)

In contrast, the land perturbation remains fairly constant after a few decades up to year 100 and decreases thereafter in most models. On multi-model average, the land has sequestered 19 ± 16 GtC by year 20, 23 ± 20 GtC by year 100 and 16 ± 14 GtC by year 1000. It is interesting to note that the three ensembles include also cases where the land loses carbon to the atmosphere in response to the 100 GtC emission pulse (Fig. 3b). In these model realizations, the climate change resulting from an emission pulse forces a carbon loss from land ecosystems that is larger than the positive impacts of elevated atmospheric CO_2. This loss is likely predomi-

nantly driven by accelerated turnover of soil and litter carbon in response to warming (Joos et al., 2001).

The response in ocean carbon inventory to an emission pulse is relatively well understood. Ocean uptake is mainly driven by physico-chemical processes and uptake rates are governed by the quantitatively well-understood carbonate chemistry in surface waters and by the rates of surface-to-deep transport. The latter are constrained by the distribution of transient tracers such as CFCs and bomb-produced radiocarbon in the thermocline (Key et al., 2004). In early generation carbon cycle models such as the Bern-SAR model only these physico-chemical processes were included. This first-order response is modified by other processes such as ocean warming and changes in ocean circulation and

Table 7. Response in time-integrated global mean surface air temperature to an emission pulse of 100 GtC added to an atmospheric concentration of 389 ppm.

Time Horizon	20 yr	50 yr	100 yr	500 yr	1000 yr
	time-integrated temperature response (°C yr)				
NCAR CSM1.4	2.53	7.36	10.6	n/a	n/a
HadGEM2-ES	4.24	12.4	30.3	n/a	n/a
MPI-ESM	3.83	8.84	19.1	n/a	n/a
Bern3D-LPJ (reference)	4.11	12.1	24.5	121	219
Bern3D-LPJ ensemble	3.20	8.61	17.3	79.7	n/a
	(2.1–4.6)	(5.1–13.5)	(9.5–29.3)	(38–175)	n/a
Bern2.5D-LPJ	3.15	8.40	17.1	71.0	133
CLIMBER2-LPJ	3.05	7.96	16.5	74.2	134
DCESS	3.38	9.96	20.6	89.8	158
GENIE ensemble	3.77	10.54	21.6	96.6	n/a
	(3.0–5.2)	(8.2–17.5)	(17–42)	(76–195)	n/a
LOVECLIM	0.22	3.46	7.83	36.8	80.8
MESMO	4.41	12.5	26.0	129	236
UVic2.9	3.40	9.17	18.5	94.8	189
ACC2	3.99	10.55	20.0	76.9	n/a
Bern-SAR	n/a	n/a	n/a	n/a	n/a
MAGICC6 ensemble	3.64	8.96	17.2	74.4	n/a
	(2.7–4.7)	(6.6–12.7)	(12–26)	(49–129)	n/a
TOTEM2	n/a	n/a	n/a	n/a	n/a
multi-model mean	3.29±2.03	9.13±4.45	18.7±11.1	82.2±44.5	158±91
	Uncertainty ranges (°C yr)				
Multi-model range	4.06	8.9	22.1	89.1	182
Bern3D-LPJ	2.52	8.34	19.8	137	n/a
GENIE	2.13	9.27	24.7	119	184
MAGICC6	2.00	6.11	14.4	80.4	n/a
Average of ranges	2.68	8.16	20.3	106	183
in % of multi-model mean	81.4	89.3	108	130	116
	Best estimates for time-integrated temperature response (°C yr)				
mean	3.31	8.67	17.4	82.2	155
5–95 % confidence range	(2.0–4.7)	(4.6–12.7)	(7.3–27.6)	(29–135)	(64–247)
	Best estimates for time-integrated AGTP of CO_2 (10^{-15} °C yr kg-CO_2^{-1})				
mean	9.03	23.6	47.6	224	424
5–95 % confidence range	5.37–12.7	12.5–34.8	20.0–75.2	79.0–369	174–673

Table 8. Response in ocean heat content and steric sea level rise to an emission pulse of 100 GtC added to an atmospheric concentration of 389 ppm. Multiplication by $(12/(100 \times 44 \times 10^{12}))$ yields the change per kg-CO_2.

Time Horizon	20 yr	50 yr	100 yr	500 yr	1000 yr
	Best estimates for steric sea level rise (cm)				
mean	0.86	1.30	1.82	3.65	4.58
5–95 % confidence range	(0.37–1.35)	(0.45–2.14)	(0.59–3.05)	(1.17–6.14)	(0.98–8.17)
	Best estimates for ocean heat content change (10^{22} J)				
mean	6.59	10.8	15.7	32.6	39.6
5–95 % confidence range	(4.06–9.11)	(5.3–16.3)	(6.2–25.1)	(12.3–53.0)	(13.8–65.3)

marine biogeochemistry (Plattner et al., 2001; Sarmiento et al., 1998; Joos et al., 1999).

The response of the land biosphere carbon inventory is associated with considerable uncertainties. It is currently not clear whether the land will continue to act as a strong carbon sink or whether climate change will lead to a loss of land carbon that overwhelms the potentially positive influence of elevated atmospheric CO_2 and nitrogen input on net primary productivity and carbon stocks. This limited understanding is reflected in the large uncertainty range. We estimate the 5 to 95 % confidence range for the response in land carbon inventory to 45 GtC at year 100. For comparison, the corresponding uncertainty range for the ocean inventory is 29 GtC.

In conclusion, carbon uptake by the land biosphere is about equally important for the evolution of IRF_{CO_2} as uptake by the ocean during the first two decades after the release. Subsequently, the ocean becomes the dominant carbon sink. The uncertainty range of the terrestrial and oceanic carbon inventories remain substantial over the 1000 yr analysis period.

4.4 Influence of background conditions, pulse size, and carbon cycle-climate feedback

4.4.1 Background conditions

The response in atmospheric CO_2 and cumulative air-to-sea and air-to-land carbon fluxes depends sensitively on the background conditions (Fig. 4). Ten out of fifteen models were also used to run the simulations where a 100 GtC emission pulse is added to preindustrial (PI) in addition to present day (PD) conditions. For these models, the time integrated IRF_{CO_2} at year 100 ranges between 34 and 47 yr for the PI100 case and between 45 and 62 yr for the PD100 case. The lower CO_2 perturbation for PI100 is generally due to a higher uptake by both the ocean and the land biosphere and is consistently lower for PI than PD conditions for all individual models.

The responses in SAT, OHC, and SSLR are similar for PI100 and PD100. This is due to two compensating effects (Caldeira and Kasting, 1993; Wuebbles et al., 1995; Reisinger et al., 2011). The time-integrated CO_2 response decreases by roughly 23 % from PD to PI conditions. On the other hand, the radiative forcing per unit change in atmospheric CO_2 increases by 39 % from PD to PI conditions. The range in time-integrated forcing at year 100 is then almost identical (32 to 43 yr W m^{-2} for PI100 versus 29 to 40 yr W m^{-2} for PD100).

The ocean uptake capacity regulated by the carbonate chemistry decreases with increasing CO_2 and warmer climate conditions are generally associated with a lower solubility of CO_2 and a more sluggish surface-to-deep transport (Joos et al., 1999; Roy et al., 2011). As expected, the model range in cumulative air-to-sea flux is smaller for PD (24 to 40 GtC) than for PI (32 to 47 GtC) conditions and

at year 100. The ocean carbon uptake is consistently lower for PD than PI conditions in all models during the first hundred years. In the long-run, the time-integrated ocean uptake becomes larger for PD100 than PI100 in the Bern3D-LPJ model. This is likely related to the large difference in the land carbon responses (~ 26 GtC at year 500) between the PI100 and PD100 cases in this model.

The land carbon uptake in the model depends on factors such as the spatio-temporal evolution of net primary productivity (NPP) under changing CO_2 and climate and the change in soil and litter carbon turnover rates with changing climate conditions. It is beyond the scope of this paper to discuss the processes affecting land carbon stocks in detail for the range of models. The response in land carbon inventory to changes in CO_2 and climate is complex and regionally distinct. Generally, the models react with an increase in NPP to increasing atmospheric CO_2. Temperature and precipitation changes can have both positive and negative effects on NPP, while most models assume that soil and litter turnover rates increase approximately exponentially with increasing temperatures.

The response in land carbon inventory at year 100 ranges between 21 and 36 GtC for PI100 compared to 10 to 42 GtC for PD100. The model spread is thus considerably smaller for the PI100 than for the PD100 case. The response is not consistent among models. LOVECLIM shows a higher land carbon uptake under PD than PI conditions, NCAR CSM1.4 and DCESS show similar changes, whereas most models simulate a reduced land uptake for PD100 compared to PI100.

The response for temporally varying background conditions is in addition explored with one model (Bern3D-LPJ) for illustrative purposes. Emissions of CO_2 and non-CO_2 agents are prescribed to follow those from the Representative Concentration Pathways RCP2.6, RCP4.5, RCP6.0 and RCP8.5 in the control setup. The same procedure was applied to determine the IRF as in the standard setup. However, forcing (CO_2, non-CO_2, aerosoles,landuse area) was extended based on the RCPs until year 2300 as described in Zickfeld et al. (2012). After year 2300, the forcing is extended until year 3010 by using 2300 values. The pulse was released in year 2010 instead of 2015 as in the 389 ppm background scenario. The evolution of IRF_{CO_2} (Fig. 5a) is relatively similar between the standard case (389 ppm background) and RCP2.6, but very different for the three other RCP cases. IRF_{CO_2} decreases in all cases to about 70 % in the first two decades after the pulse. Then, it continues to decrease for the standard and the RCP2.6 cases, whereas IRF_{CO_2} increases again in the other cases as atmospheric CO_2 and global warming continues to rise in these scenarios. For RCP8.5, the pulse fraction remaining airborne is still well above 80 % at year 1000. The time-integrated IRF_{CO_2} evaluated at year 100 is 62 yr for the 389 ppm background and 66, 68, 69 and 75 yr for RCP2.6, RCP4.5, RCP6.0, and RCP8.5, respectively. The resulting perturbation in radiative forcing is evaluated as difference in forcing between the control without pulse and the
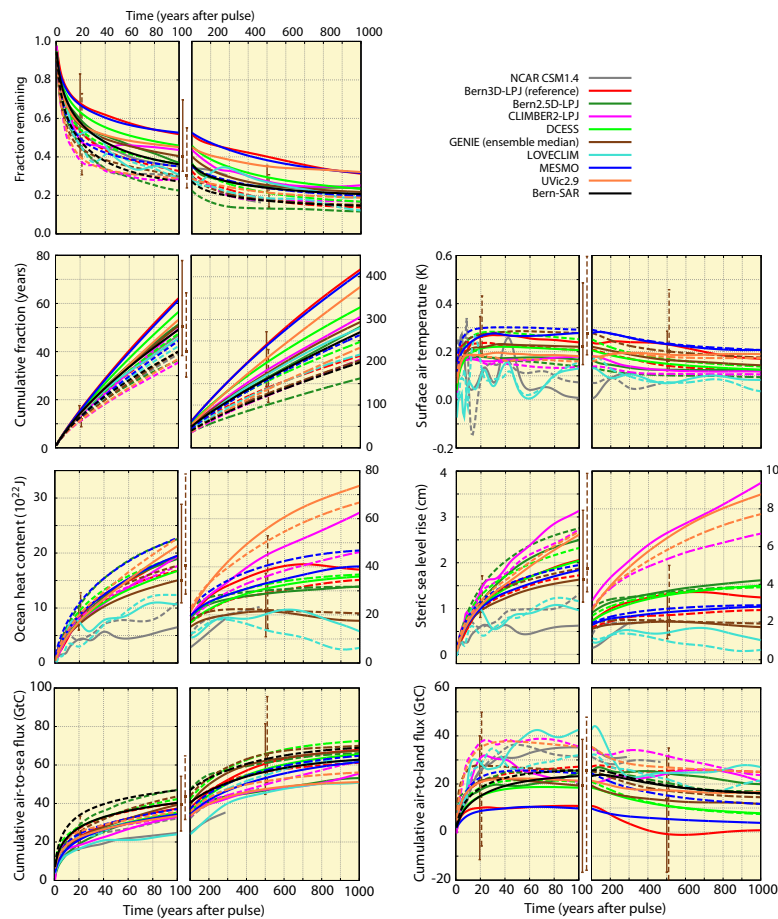
Fig. 4. Influence of the background conditions on the climate-carbon cycle response to a pulse emission of $100\,\mathrm{GtC}$ into the atmosphere. Solid lines are for current conditions ($CO_{2,\mathrm{ref}} = 389\,\mathrm{ppm}$, PD100) and dashed lines for preindustrial conditions ($CO_{2,\mathrm{ref}} \sim 280\,\mathrm{ppm}$, PI100).

corresponding pulse run and using the non-linear Eq. (3). AGWP range between 105 and $85 \times 10^{-15}\,\mathrm{yr\,W\,m^{-2}\,kg}$-$CO_2^{-1}$ for the five cases and at year 100. The RCP8.5 case, although featuring the largest time-integrated IRF_{CO_2}, has the smallest AGWP of the five cases as the radiative efficiency decreases with higher CO_2 concentration.

4.4.2 Pulse size

We next turn to the case where $5000\,\mathrm{GtC}$ were released into the atmosphere (PI5000) (Fig. 6). The $5000\,\mathrm{GtC}$ pulse run was carried out with 10 models. With this higher input, a considerably greater proportion of CO_2 remains in the atmosphere, compared to the release of $100\,\mathrm{GtC}$ (PI100). For the PI5000 simulation, the integral of IRF_{CO_2} through to year 100 is about double that from the PI100 simulation. In other words, the time integrated IRF_{CO_2} depends sensitively on the

pulse size. In particular the ocean uptake of carbon per unit carbon emitted is substantially smaller for the PI5000 than PI100 case.

As for pulse sizes of $100\,\mathrm{GtC}$, the SAT increases rapidly within the first two decades after the pulse and remains high for the centuries to follow, while ocean heat content and steric sea level rise increase more gradually. The simulated SAT at year 100 per unit carbon emission is roughly $40\,\%$ smaller in the PI5000 than the PI100 case (0.05 to $1.7\,^{\circ}\mathrm{C}$ versus 0.08 to $0.3\,^{\circ}\mathrm{C}$ per $100\,\mathrm{GtC}$). Similarly, the responses in ocean heat content and steric sea level rise are smaller per unit emission for the larger pulse. This smaller climate response per unit emission is a consequence of the smaller time-integrated forcing per unit emissions for larger pulses. The time-integrated radiative forcing at year 100 is smaller by $39\,\%$ for PI5000 than for PI100. The decrease in radiative
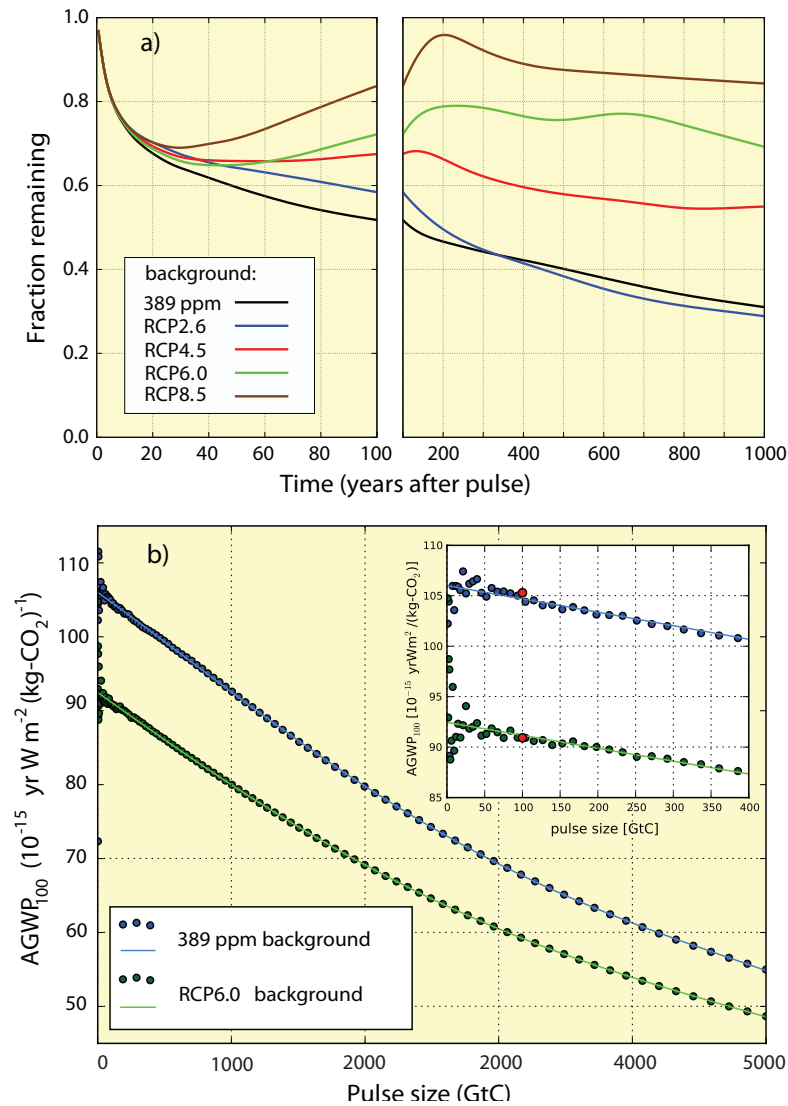
Fig. 5. (a) IRF_{CO_2} for different background conditions as simulated with the Bern3D-LPJ model (reference). Carbon emissions and emissions of other agents, and land use maps are prescribed following those of the Representative Concentration Pathways. In the runs without pulse, atmospheric CO_2 is projected to reach 421, 538, 670, 936 ppm by 2100 and 360, 543, 752, 1962 ppm by year 3000 and for RCP2.6, RCP4.5, RCP6, and RCP8.5 respectively. The IRF_{CO_2} for the standard setup with a constant CO_2 background of 389 ppm is shown by the black line. (b) $AGWP_{CO_2}$ versus pulse size for two different background conditions. Circles represent results from individual simulations and the lines fits through the results. The standard pulse size of 100 GtC is indicated by red circles.

efficiency (Eq. 3) more than compensates for the larger time-integrated IRF_{CO_2} in PI5000 than PI100.

Next, the influence of the pulse size on the Absolute Global Warming Potential of CO_2 at year 100 is investigated in more detail (Fig. 5b). Specifically, we ask how representative is the $AGWP_{CO_2}$ as determined with a pulse in-

put of 100 GtC in our standard setup for the limiting case of an infinitely small pulse. The pulse size was varied between 1 GtC and 5000 GtC in the Bern3D-LPJ both for constant background conditions of 389 ppm as well as for the RCP6.0 case. $AGWP_{CO_2}(t = 100 \, \text{yr})$ is plotted versus pulse size in Fig. 5b. A polynomial fit through the data points yields

a continuous relationship between pulse size and AGWP over the range from 0 to 5000 GtC. The results show that $AGWP_{CO_2}(t = 100 \text{ yr})$ for an infinitely small pulse is only about 1.2 % higher than for a pulse size of 100 GtC. Results also show that internal climate variability affect the computed $AGWP_{CO_2}$ significantly for small pulses of a few GtC only in the Bern3D-LPJ. This is evidenced by the scatter in results for small pulses. In conclusion, the $AGWP_{CO_2}$ values tabulated in Table 4 are a good approximation for the limiting case of infinitely small carbon additions or removals to the atmosphere.

4.4.3   Carbon cycle-climate feedbacks

The influence of the carbon cycle-climate feedbacks is investigated with the Bern3D-LPJ model for emission pulses of 100 and 5000 GtC added to preindustrial conditions (Fig. 7). Results are compared between a setup where climate varies in response to an emission pulse and a setup where climate is kept invariant at preindustrial conditions and for a range of pulse sizes. The time-integrated IRF_{CO_2} at year 20, 50, 100, 500, and 1000 is 5 %, 10 %, 13 %, 13 %, 8 % lower for the 100 and 4 %, 9 %, 15 %, 33 %, 40 % lower for the 5000 GtC pulses if the carbon cycle-climate feedback is suppressed. The reductions in the time-integrated IRF_{CO_2} due to the carbon cycle-climate feedback are similar to the effects of reducing the pulse size from 5000 GtC to about 2000 GtC and from 100 GtC to 10 GtC, respectively (Fig. 7).

In summary, IRF_{CO_2} and its time integral is lower for preindustrial than present day background conditions and for smaller compared to larger emission pulses. On the other hand, the ocean uptake per unit emission decreases with increasing background CO_2 concentrations (and related warmer climate conditions) and increasing pulse sizes. The responses in SAT, ocean heat content and steric sea level rise show little differences between the two 100 GtC cases and a smaller response per unit emission for larger pulse sizes. The time-integrated IRF_{CO_2} and thus the AGWP depend also on the carbon cycle-climate feedback. However, the most important factor that determines the time-integrated IRF_{CO_2} and AGWP is the choice of time horizon.

5   Discussion and conclusion

We have reassessed the response of the coupled carbon cycle-climate system to an emission pulse of carbon for present day CO_2 and climate conditions using a suite of models of various complexity. The multi-model mean response in atmospheric CO_2 was fitted by an analytical function (sum of exponentials) for easy use by others. A novel element of the study is a thorough assessment of uncertainties in the simulated responses based on the spread of the multi-model ensemble and of three ensembles with individual models as well as using a linear programming approach constrained by

Table 9. Sensitivity of GWP on the time horizon TH and the perturbation life time of a gas.

Gas/TH		20 yr	50 yr	100 yr	500 yr	1000 yr
	life time (yr)	ratio of GWP(TH) to GWP(TH = 100)				
CH_4	12	2.98	1.71	1.00	0.28	0.17
N_2O	114	1.01	1.05	1.00	0.48	0.29
SF_6	3200	0.74	0.87	1.00	1.33	1.48

observations. These different approaches to estimate the uncertainty in the integrated IRF_{CO_2} yield comparable results. We also quantified the sensitivity of the responses to the magnitude of the emission pulse and the atmospheric and climatic background conditions. The influence of the climate-carbon cycle feedback on results was investigated within one model. A recent study investigates how differences among the IRFs impact the estimates of GWP and GTP (Olivie and Peters, 2012).

It is important to update the AGWP and AGTP of CO_2 and to assess their uncertainty since CO_2 is the reference gas in GWP and GTP calculations. It therefore exerts a significant control on the GWP and GTP of any other gas. We find that that the absolute global warming potential (AGWP) of CO_2 for a time horizon of 100 yr is 92.5×10^{-15} yr W m^{-2} per kg-CO_2 with a 5 to 95 % confidence range of $(68$ to $117) \times 10^{-15}$ yr W m^{-2} per kg-CO_2 (Table 4). Although, the ocean absorbs most of the emission pulse, the uncertainty in the perturbation of the land carbon inventory (in absolute units) is larger than for the perturbation in the ocean carbon inventory. This is related to different responses of the land biosphere models to changes in atmospheric CO_2 and climate and reflects our incomplete knowledge on these terrestrial processes.

There are also uncertainties related to the experimental setup. The time-integrated CO_2 impulse response at year 100 is about twice as large for an emission pulse of 5000 GtC compared to our standard pulse size of 100 GtC. An emission of 5000 GtC is an extreme case in the context of Global Warming Potential (GWP), though within reach when burning all fossil resources. Such large pulses are also used in other studies to assess the evolution in the CO_2 perturbation over several centuries and up to 10 000 yr (Archer et al., 2009; Eby et al., 2009). These studies also find a long-lasting perturbation in atmospheric CO_2. A more modest increase of the pulse size from 100 GtC to 1000 GtC yields an increase in the time-integrated CO_2 impulse response, used to compute AGWP and GWP, by one third. The influence of the carbon-cycle climate feedback is found to be of order 10 % to 20 % on the time integrated CO_2 impulse response and the AGWP of CO_2. The magnitude of this effect varies across models (Friedlingstein et al., 2006; Gillett and Matthews, 2010). The carbon-cycle climate feedback was not included in the IRF of CO_2 derived with the Bern-SAR model, but is included in the
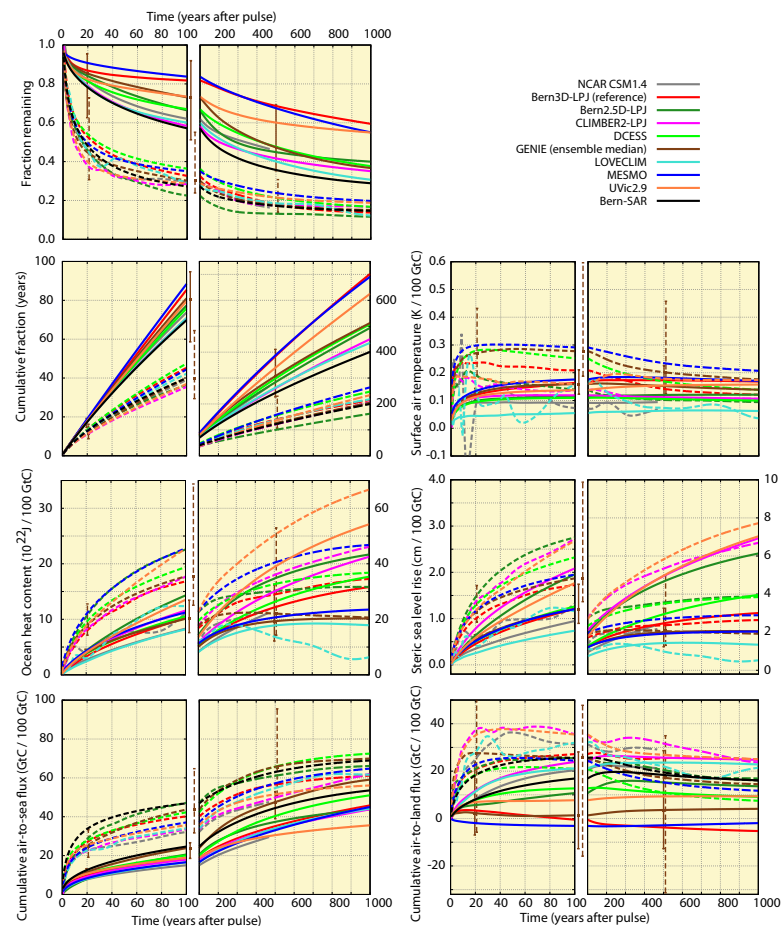
Fig. 6. Response of the carbon cycle-climate system to a pulse emission of 5000 GtC (solid, PI5000) and 100 GtC (dashed, PI100) added to the atmosphere under preindustrial conditions. The responses in surface air temperature, ocean heat content, steric sea level rise, and in carbon fluxes for PI5000 are scaled by a factor of 50 for a better comparison with the 100 GtC pulse.

Bern model versions as used in the TAR and AR4 and corresponding IRFs. A potential inconsistency in GWP can arise if climate feedbacks are included in the calculation of IRF_{CO_2} and $AGWP_{CO_2}$, but not in the calculation of the gas under consideration. Although, choices in pulse size, background concentration, and model lead to considerable uncertainties in AGWP and GWP, the most important variable is the time horizon (Table 9).

The subjective choice of the time horizon has a much larger influence on the range in absolute global warming potential of CO_2 and in the global warming potential of most other agents than uncertainties associated with the computation of these values for a given time horizon. The uncertainty in AGWP (in units of yr W m^{-2} per kg-CO_2) can be mapped to a range in the time horizon (in units of year). For a time horizon of 100 yr, the lower and upper bound of the 5–95 % confidence range of the AGWP for CO_2 correspond to the multi-model mean value of AGWP evaluated at the time horizon of 68 yr and 135 yr. This range of 67 yr, stemming from uncertainties in the carbon cycle-climate model response, is much smaller than the differences resulting from the subjective choice of alternative time horizons; in the AR4 IPCC report (Table 2.14, p. 212 in Forster et al., 2007) GWP are tabulated for illustrative time horizons of 20, 100, and 500 yr. Table 9 illustrates how the GWP of methane, nitrous oxide, and sulphur hexafluoride calculated with a single e-fold decay of 12 yr, 114 yr and 3200 yr changes with the choice of time horizon. For example, one could select a time horizon of 1000 yr instead of 100 yr in the UNFCCC process and thereby account somewhat more explicitly for the
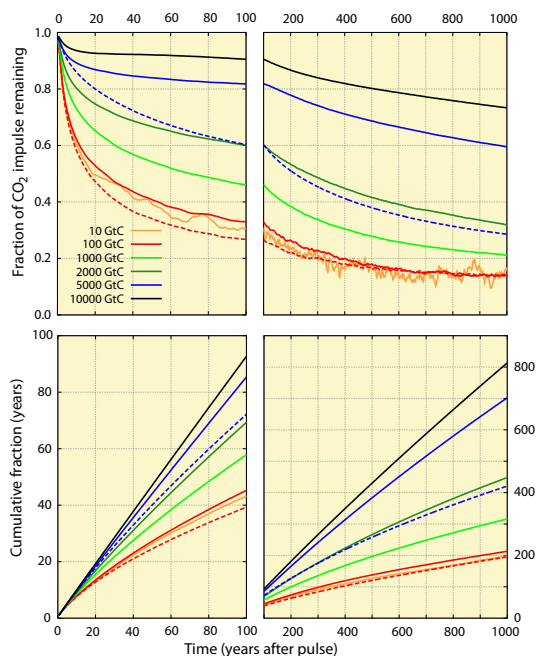
Fig. 7. Influence of pulse size and climate-carbon cycle feedback on the response in atmospheric CO_2 and the time-integrated IRF_{CO_2} as simulated with the Bern3D-LPJ model (standard setup). Pulse emissions, ranging from 10 to 10 000 GtC in the individual simulations, are added to the atmosphere under preindustrial conditions. Dashed lines represent simulations where climate was kept constant in the model.

long timescales involved in the Earth System. In this case, the GWP for methane would be more than 5 times smaller and only 17 % (13 to 24 %; 5 to 95 % confidence range considering uncertainty in IRF_{CO_2} only) of that for 100 yr. The GWP for N_2O would be more than 3 times smaller and only 29 % (23 to 41 %) of that for 100 yr, whereas the GWP for SF_6 would be about 48 % (15 % to 110 %) larger than that for a time horizon of 100 yr. On the other hand, selecting a time horizon of 20 yr instead of 100 yr yields a three times larger GWP for methane. A strong influence of the time horizon is also found for GTP and time-integrated GTP (Peters et al., 2011).

The IPCC presented impulse response functions of CO_2, IRF_{CO_2}, in its major assessment reports. Figure 8 shows how IRF_{CO_2} has changed from the IPCC First Assessement Report (FAR), to the Second Assessment Report (SAR), to the Fourth Assessement Report (AR4) and compares these responses with the results of this study. IRF_{CO_2} was not updated in the Third Assessment Report. Differences in the IRF_{CO_2} are relatively small. The higher initial airborne fraction published in the FAR is related to the application of an atmosphere-ocean model with a neutral land biosphere,

whereas in subsequent reports the land biosphere model absorbs a considerable fraction of the initial emission pulse during the first few decades. The responses published in the SAR and the AR4 are lower than the multi-model model mean response of this study. This is predominantly due to the smaller pulse size and lower CO_2 background in the SAR and AR4 setup. The time-integrated IRF_{CO_2} for the AR4 (Bern2.5D-LPJ) and SAR (Bern-SAR) models under the setup of this study (Table 4) are with 49 and 51 yr only slightly lower than the multi-model mean of 52 yr at year 100. We do not find indications that there are systematic differences in IRF_{CO_2} between models of different complexities such as EMICs and comprehensive Earth System Models.

In addition to the Absolute Global Warming Potential, we have also quantified the Absolute Global Temperature change Potential and corresponding responses in ocean heat content and steric sea level rise by directly applying the suite of carbon cycle-climate models. The uncertainty in these responses is much larger than the uncertainty in the IRF_{CO_2} and the AGWP of CO_2. This is mainly a consequence of the large range in the climate sensitivity of the different models (Table 2) and their ocean heat uptake efficiency. More general, uncertainties increase along the cause-effect chain from emissions to atmospheric abundance to radiative forcing to climate change. In addition, it is difficult to extract the temperature signal from a relatively small CO_2 emission pulse from results of comprehensive ESM as these models feature considerable interannual-to-decadal temperature variability. Larger pulse sizes and/or running ensembles instead of single simulations would improve signal-to-noise ratio. Intercomparison studies that look into the responses of non-CO_2 agents might further improve the quantification of metrics and their uncertainties. Yet fundamental issues will remain. Different forcing agents are distinct and any simple metric intended to compare forcing agents relies on subjective choices.

CO_2 continues to dominate anthropogenic warming. For the current crop of emission scenarios from the integrated assessment community (Weyant et al., 2006; Van Vuuren et al., 2008), the contribution of CO_2 to the anthropogenic warming by 2100 is estimated using an emission-driven climate model to be 58 to 76 % of that of all greenhouse gases together (Strassmann et al., 2009). Independent from the choice of emission metric, the long life time of the anthropogenic CO_2 perturbation implies that anthropogenic emissions of CO_2 must be reduced if greenhouse gas forcing and anthropogenic climate change are to be stabilized (Siegenthaler and Oeschger, 1978).
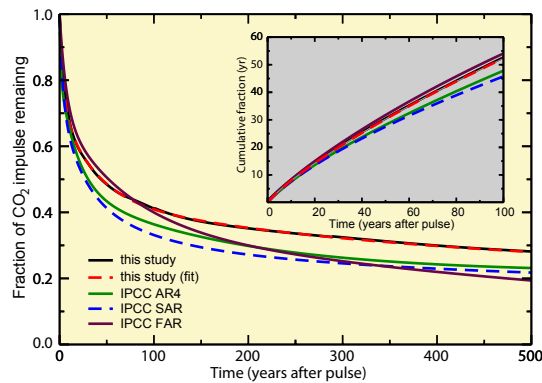
Fig. 8. The impulse response function for CO_2 (IRF_{CO_2}) as used to compute GWP in the IPCC First (FAR), Second (SAR) and Fourth (AR4) Assessment Report and from this study. The red curve is a fit to the multi-model mean shown in black. The inset shows the time-integrated IRF_{CO_2} for the first 100 yr after the emission pulse.

Appendix A

Model descriptions

ACC2: the Aggregated Carbon Cycle, Atmospheric Chemistry and Climate model (ACC2) (Tanaka et al., 2007; Tanaka, 2008) consists of a box model of the global carbon cycle, simple parameterizations of the atmospheric chemistry, and a land-ocean energy balance model. Most relevant to this study is the carbon cycle component, which is a four-layer atmosphere-ocean box model coupled with a four-reservoir land biosphere box model (Sect. 2.1 of Tanaka, 2008). The saturation of the ocean CO_2 uptake under rising atmospheric CO_2 concentration is dynamically reproduced by the thermodynamic equilibrium for carbonate species. The CO_2 fertilization effect is parameterized by the β factor. The temperature sensitivity of the soil respiration is modeled through the $Q10$ parameter. The land and ocean CO_2 uptake is influenced by the temperature change. Values of uncertain parameters (including the β factor and the $Q10$ parameter) are estimated based on an inverse estimation setup (Sect. 3 of Tanaka, 2008), in which a large number of parameters are simultaneously optimized by using associated historical observations and prior parameter estimates including their uncertainties from year 1750 to 2000 (Tables 3.1 and 3.2 of Tanaka, 2008). Parameter values estimated through the inverse estimation are consistently used in projections beyond 2000. The simplified process representations in ACC2 allow one to perform a sensitivity analysis for the CO_2 response under various sets of assumptions. ACC2 has been applied to several studies (Tanaka et al., 2009a, b, 2012).

Bern-SAR: this model was applied to calculate the CO_2 impulse response function as used for the Global Warming

Potentials of IPCC 1994 report on Radiative Forcing, the IPCC Second Assessment Report and the Kyoto Protocol. The Bern model (Siegenthaler and Joos, 1992; Joos et al., 1996) is designed to compute the uptake of anthropogenic carbon by land and ocean. It links a well-mixed atmosphere with the High-Latitude Exchange/Interior Diffusion-Advection(HILDA) ocean model and a 4-box representation of the land biosphere (Siegenthaler and Oeschger, 1987). Model parameters of the box-diffusion-type ocean model were determined such that the model reproduces the oceanic distribution of natural and bomb-produced radiocarbon. Net primary production on land increases with the natural logarithm of CO_2 and the scaling factor ($\beta = 0.27$) was chosen in order to close the atmospheric CO_2 budget in the early nineties.

Bern2.5D-LPJ: this model was used to calculate the CO_2 impulse response function for the IPCC AR4 report (Forster et al., 2007, p. 213). Here, the same code version as in the AR4 was used and subsequent updates of the land biosphere component (LPJ) are not included. The Bern2.5D-LPJ (or Bern2.5CC in Plattner et al., 2008) reduced complexity climate model includes components describing (1) the physical climate system, (2) the cycling of carbon and related elements, and (3) a module to calculate concentrations of non-CO_2 greenhouse gases and radiative forcing by atmospheric CO_2, non-CO_2 greenhouse gases, and aerosols (Plattner et al., 2008). The ocean physical component is the zonally averaged, three-basin circulation model of Stocker et al. (1992), coupled to a zonally and vertically averaged atmospheric energy balance model, including an active hydrological cycle (Schmittner and Stocker, 1999). The ocean biogeochemical component includes a simple prognostic description of the cycles of carbon, carbon isotopes, oxygen, and carbon-related tracers (Marchal et al., 1998; Joos et al., 1999; Plattner et al., 2001). The terrestrial biosphere component is the Lund-Potsdam-Jena (LPJ) dynamic global vegetation model at $3.75° \times 2.5°$ resolution as used by Joos et al. (2001); Gerber et al. (2003) and described in detail by Sitch et al. (2003). Vegetation is represented by nine plant functional types. Fertilization of plants by increasing atmospheric CO_2 concentrations is modeled according to a modified Farquhar scheme (Farquhar et al., 1980; Haxeltine and Prentice, 1996). The module designed to calculate radiative forcing by atmospheric CO_2, non-CO_2 greenhouse gases, and aerosols is based on work summarized in Fuglestvedt and Berntsen (1999) and Joos et al. (2001). The climate sensitivity is 3.2 K for a nominal doubling of CO_2.

Bern3D-LPJ: Bern3D-LPJ is an Earth System Model of Intermediate Complexity with a fully coupled carbon cycle and components that represent the ocean and sea ice, ocean sediments, the atmosphere, and the terrestrial biosphere. The ocean component is a seasonally forced three-dimensional frictional geostrophic global ocean model (Edwards et al., 1998) with a resolution of 36×36 boxes in the horizontal direction and 32 vertical layers (Müller et al., 2006). Marine

biogeochemical cycles are implemented following OCMIP-2 (Najjar and Orr, 1999; Orr et al., 1999; Najjar et al., 2007) with the addition of prognostic formulations for biological productivity and the cycling of iron, silica, ^{13}C and ^{14}C (Parekh et al., 2008; Tschumi et al., 2008), as well as a sedimentary component (Tschumi et al., 2011; Gehlen et al., 2006; Heinze et al., 1999). The atmosphere is represented by a single-layer energy and moisture balance model with the same horizontal resolution as the ocean component (Ritz et al., 2011). The CO_2 forcing is calculated after (Myhre et al., 1998) and the model is tuned to simulate an equilibrium climate sensitivity of 3 °C. Other greenhouse gases and volcanic aerosols are prescribed as global radiative forcing, while tropospheric sulphate aerosols are taken into account by changing the surface albedo locally (Steinacher, 2011; Reader and Boer, 1998). The climate sensitivity is 3 K for a nominal doubling of CO_2. The terrestrial biosphere component is based on the Lund-Potsdam-Jena (LPJ) Dynamic Global Vegetation Model at 3.75° × 2.5° resolution (Joos et al., 2001; Sitch et al., 2003). Vegetation is represented by 12 plant functional types and CO_2 fertilization is modeled according to the modified Farquhar scheme (Farquhar et al., 1980; Haxeltine and Prentice, 1996). The model has recently been extended with modules to account for land use (Strassmann et al., 2008; Stocker et al., 2011), peatlands and permafrost dynamics (Gerten et al., 2004; Wania et al., 2009a, b), and land surface albedo (Steinacher, 2011). The LPJ component is driven by global mean CO_2 concentrations and changes in surface air temperature relative to a reference period by scaling global mean surface temperature change simulated by the Bern3D with spatial patterns of precipitation and temperature (Steinacher, 2011; Stocker et al., 2011).

CLIMBER2-LPJmL: CLIMBER2-LPJml (Kleinen et al., 2010) consists of the Earth System Model of Intermediate Complexity (EMIC) CLIMBER2, coupled to the dynamic global vegetation model (DGVM) LPJmL. CLIMBER2 (Petoukhov et al., 2005) consists of a 2.5-dimensional statistical-dynamical atmosphere with a resolution of roughly 51° (longitude) by 10° (latitude), a zonally averaged ocean resolving three basins with a latitudinal resolution of 2.5°, and a sea ice model. CLIMBER2 also contains oceanic biogeochemistry, a model for marine biota, and a sediment model (Archer, 1996; Brovkin et al., 2002, 2007). Weathering rates scale to runoff from the land surface. To this EMIC we have coupled the DGVM LPJmL (Sitch et al., 2003; Bondeau et al., 2007; Fader et al., 2010; Portmann et al., 2008) in order to investigate land surface processes at a significantly higher resolution of 0.5 × 0.5°. Agricultural land use is included in this version of LPJ. Monthly anomalies from the climatology of the climate fields are passed to LPJ, where they are added to climate patterns based on the Climatic Research Unit CRU-TS climate data set (New et al., 2000). The carbon flux between atmosphere and land surface is determined from the annual change in the LPJ carbon pools, and employed in CLIMBER2 to de-

termine the CO_2 concentration. Biogeochemical feedbacks are thus determined by the combination of CLIMBER2 and LPJmL, while biogeophysical effects are solely determined by CLIMBER2. The climate sensitivity is 3 K.

DCESS: the DCESS model consists of fully coupled modules for the atmosphere, ocean, ocean sediment, land biosphere and lithosphere (Shaffer et al., 2008). The model geometry consists of one hemisphere, divided into two 360° × 52° zones. Long term climate sensitivity has been calibrated to 3 °C. The atmosphere component considers radiation balance, heat and gas exchanges with other modules, and meridional transport of heat and water vapor between low-mid latitude and high latitude zones. The ocean component is 270° wide and extends from the equator to 70° latitude. Both ocean sectors are divided into 55 layers with 100 m vertical resolution. Each layer is assigned an ocean sediment section, with width determined from observed ocean depth distributions. Sea ice and snow cover are diagnosed from estimated atmospheric temperature profiles. Circulation and mixing are prescribed, with values calibrated from observations as in the HILDA model (Shaffer and Sarmiento, 1995). Biogenic production of particulate organic matter in the ocean surface layer depends on phosphate availability but with lower efficiency in the high latitude zone. The calcite to organic carbon rain ratio depends on surface layer temperature. The ocean sediment component considers calcium carbonate dissolution as well as oxic-anoxic organic matter remineralisation. The land biosphere component includes leaves, wood, litter and soil. Here, it has been modified to include prescribed land use change carbon losses, distributed in proportion to the initial inventory sizes of the module components. With this change, the model CO_2 fertilization factor, originally 0.65, has been recalibrated to 0.37. Finally, the lithosphere component considers outgassing and climate-dependent weathering of carbonate and silicate rocks, as well as rocks containing old organic carbon and phosphorus. The atmospheric methane module was not used here.

GENIE: the GENIE-1 physical model comprises the 3-D frictional geostrophic ocean model GOLDSTEIN, with a resolution of 36 × 36 boxes in the horizontal direction and 16 vertical levels, coupled to a 2-D energy moisture balance atmosphere and a thermodynamic-dynamic sea-ice model (Edwards and Marsh, 2005). Recent developments (Marsh et al., 2011) include the incorporation of stratification-dependent mixing, a more general equation of state through a parameterization of thermobaricity, and improvements to the representation of fixed wind forcing. The land surface component is ENTS, a dynamic model of terrestrial carbon storage (Williamson et al., 2006) with a relatively simple implementation of spatiotemporal land use change. Ocean chemistry is modeled with BIOGEM (Ridgwell et al., 2007), including iron limitation (Annan and Hargreaves, 2010), and is coupled to the sediment model SEDGEM with fixed weathering, diagnosed during the model spin-up to simulated observed ocean alkalinity (Ridgwell and Hargreaves, 2007). All GE-

NIE results are derived from ensembles applying the same 20-member parameter set. The selected parameters were filtered from a 100-member, 28-parameter pre-calibrated ensemble, constrained for plausible present-day CO_2 concentrations.

HadGEM2-ES: HadGEM2-ES (Collins et al., 2011) couples interactive ocean biogeochemistry, terrestrial biogeochemistry and dust, interactive tropospheric chemistry and aerosol components into an update of the physical model HadGEM1. The physical model contains a 40 level 1×1 degree, moving to 1/3rd degree at the equator ocean, and a 38 level 1.875×1.25 atmosphere (The HadGEM2 Development Team, 2011). HadGEM2-ES has been set-up and used to perform all of the CMIP5 simulations as described by Jones et al. (2011). The ocean biogeochemistry uses the Diat-HadOCC model an update of HadOCC (Palmer and Totterdell, 2001), now simulating diatom and non-diatom phytoplankton functional types, a single zooplankton, and cycling of nitrogen, silica and iron. Diat-HadOCC is coupled to other earth system components through the model's physics, iron supplied through dust, air-sea exchange of CO_2 and oceanic emission of dimethylsulphide. The terrestrial carbon cycle is represented by the MOSES2 land surface scheme (Essery et al., 2003) which simulates exchange of water, energy and carbon between the land surface and the atmosphere, and the TRIFFID dynamic global vegetation model (Cox, 2001) which simulates the coverage and competition between 5 plant functional types (broadleaf tree, needleleaf tree, C3 and C4 grass and shrub) and 4 non-vegetated surface types (bare soil, urban, lakes and land-ice).

LOVECLIM: the Earth system model of intermediate complexity LOVECLIM (version 1.1) (Menviel et al., 2008) links the ECBilt atmosphere, the CLIO sea-ice ocean model and a bucket model for land hydrology with the VECODE dynamic vegetation model and the LOCH ocean carbon model. The atmosphere model (ECBilt) is a spectral T21 model, based on quasigeostrophic equations with 3 vertical levels and a horizontal resolution of about 5.625×5.625 degree. Ageostrophic forcing terms are estimated from the vertical motion field and added to the prognostic vorticity equation and thermodynamic equation.

The sea ice-ocean component (CLIO) (Goosse et al., 1999) consists of a primitive equation ocean general circulation model with 3×3 degree resolution on a partly rotated grid in the North Atlantic. CLIO uses a free surface and is coupled to a thermodynamic-dynamic sea ice model (Fichefet and Maqueda, 1997). In the vertical there are 20 unevenly spaced levels. Mixing along isopycnals, diapycnal mixing, as well as the effect of mesoscale eddies on transports and mixing and downsloping currents at the bottom of continental shelves are parameterized (Goosse et al., 2010). The ocean, atmosphere and sea ice components model are coupled by exchange of momentum, heat and freshwater fluxes. The hydrological cycle over land is closed by a bucket model for soil moisture and simple river runoff scheme. The global dynamic terrestrial vegetation is modeled using VECODE (Brovkin et al., 1997). Annual mean values of precipitation and temperature are communicated to the vegetation from the atmospheric model. On the basis of these mean values the evolution of the vegetation cover described as a fractional distribution of desert, tree, and grass in each land grid cell is calculated once a year. In the current version, only land albedo (as seen by the atmospheric model) outside the ice sheets is changed by VECODE. LOCH is a three-dimensional global model of the oceanic carbon cycle with prognostic equations for dissolved inorganic carbon, total alkalinity, phosphate, dissolved and particulate organic matter, oxygen and silicates (Goosse et al., 2010; Menviel et al., 2008). The phytoplankton growth is a function of temperature, light and phosphate concentration. The sink term depends on grazing and mortality. Although phytoplankton biomass is a prognostic variable it is not subject to advective transports. Remineralization below the euphotic zone (0–120 m) is a function of oxygen concentrations. Anoxic remineralization can occur in oxygen-depleted areas but is less efficient. The export production is accompanied by the export of opal assuming a constant silicate-to-phosphate ratio. Furthermore $CaCO_3$ (calcite and aragonite) shells are formed as a function of phytoplankton growth. The dissolution of shells occurs in the deepest ocean layer. LOCH is coupled to CLIO, using the same time step. Biogeochemical tracers that are subject to advection and mixing are advected and mixed using the same circulation field and mixing parameters respectively as in CLIO.

MAGICC6: MAGICC is a reduced-complexity climate model with an upwelling-diffusive-entrainment ocean and is coupled to a simple carbon cycle model including CO_2 fertilization and temperature feedback parameterizations of the terrestrial biosphere and oceanic uptake. MAGICC version 6 has been calibrated to AOGCMs (Meehl et al., 2007) and carbon cycle models (Friedlingstein et al., 2006) used in the Fourth IPCC Assessment Report (see Meinshausen et al., 2011a and b for details). Varying the parameters in MAGICC to emulate AOGCM/C4MIP model combinations allows to explore the climate response space in terms of concentrations, radiative forcing, and hemispheric land/ocean surface air temperatures spanned by the range of complex climate models. This version of MAGICC6 was also used to produce harmonized GHG concentrations for the new set of Representative Concentration Pathways (Meinshausen et al., 2011b). For this intercomparison, we used a set of 19 AOGCM calibrations and 9 coupled climate-carbon cycle model calibrations.

MESMO: MESMO version 1 (Matsumoto et al., 2008) is based on the C-GOLDSTEIN ocean model (Edwards and Marsh, 2005). It consists of a frictional geostrophic 3-D ocean circulation model coupled to a dynamic-thermodynamic sea ice model and atmospheric model of energy and moisture balance. Ocean production is based on prognostic nutrient uptake kinetics of phosphate and nitrate with dependence on light, mixed layer depth,

temperature, and biomass. Interior ocean ventilation is well calibrated against natural radiocarbon on centennial timescale and against transient anthropogenic tracers on decadal timescales. Here MESMO1 is coupled to a simple prognostic land biosphere model (Williamson et al., 2006) that calculates energy, moisture, and carbon exchanges between the land and the atmosphere. Prognostic variables include vegetation and soil carbon as well as land surface albedo and temperature.

MPI-ESM: the fully comprehensive Earth System Model MPI-ESM of the Max-Planck-Institute for Meteorology in Hamburg, Germany consists of the atmospheric model ECHAM6 (here in T63L47 resolution) with land surface model JSBACH (Raddatz et al., 2007). Each land grid cell is divided into tiles covered with 8 natural and 4 anthropogenic PFTs; vegetation model in JSBACH includes an efficient module for vegetation dynamics (Brovkin et al., 2009). Anthropogenic land use is predetermined. The physical ocean model is MPIOM, which further includes a sea-ice model (Marsland et al., 2003) on a nominal 1.5° grid with higher resolution in the North Atlantic. Marine biogeochemistry is represented by the Hamburg Ocean carbon cycle HAMOCC 5.1 which operates on the same grid as MPIOM and includes the full carbonate chemistry and a NPZD type model of the biological pump (Maier-Reimer et al., 2005; Maier-Reimer, 1993). MPI-ESM is used here in the same version that is employed for the CMIP5 experiments "MPI-ESM-LR". CO_2 is allowed to float freely between the model's carbon reservoirs (i.e., atmosphere, land, and ocean) depending on the state of the compartments and climate-carbon cycle feedbacks are simulated by the model.

NCAR CSM1.4: the physical core of the Climate System Model of the National Centre for Atmospheric Research (NCAR CSM1.4-carbon) (Doney et al., 2006; Fung et al., 2005) is a modified version of the NCAR CSM1.4 coupled physical model, consisting of ocean, atmosphere, land and sea ice components integrated via a flux coupler without flux adjustments. Atmospheric CO_2 is treated as a prognostic variable whose balance is determined by exchange fluxes with the land and ocean. The ocean model includes a derivate of the OCMIP-2 (Ocean Carbon-Cycle Model Intercomparison Project Phase 2) ocean biogeochemistry model (Najjar et al., 2007) with prognostic formulations for marine biological production. The main processes of the organic and inorganic carbon cycle within the ocean and air-sea CO_2 flux are included. A parameterization of the marine iron cycle (Doney et al., 2006) considers atmospheric dust deposition/iron dissolution, biological uptake, vertical particle transport and scavenging. Prognostic variables in the ocean include phosphate, dissolved inorganic carbon, alkalinity, oxygen, and dissolved organic phosphorus. The land carbon module combines the NCAR Land Surface Model with a modified version of the terrestrial biogeochemical Carnegie-Ames-Stanford Approach (CASA; Randerson et al., 1997) providing full coupling of energy (via dynamic leaf

phenology and hence albedo), water (via transpiration), and carbon cycles of the atmosphere and land. CASA follows the life cycles of plant functional types from carbon assimilation via photosynthesis, to mortality and decomposition, and the return of CO_2 to the atmosphere via respiration. NPP is allocated to leafs, roots, and wood with preferred allocation to roots during water-limited conditions and to wood/leaves during light-limited conditions. There are nine soil carbon pools. The transfer rates between them and to the atmosphere are sensitive to soil temperature and soil moisture saturation. The land model does not include other land surface processes that affect atmosphere-biosphere interactions such as an explicit nitrogen cycle, fires and other disturbances, herbivory, dynamic vegetation cover, or anthropogenic land cover change.

TOTEM2: TOTEM2 (Ver et al., 1999; Mackenzie et al., 2011) is a global biogeochemical model of the life-essential elements carbon, nitrogen, and phosphorus. The model comprises thirteen reservoirs: the atmosphere; six terrestrial reservoirs (living biota, humus, inorganic soil, continental soilwater, shallow groundwater, and lakes); three coastal-zone reservoirs (organic matter, water, and sediments); and three open ocean reservoirs (organic matter, surface water, and deep water). The coupling of the individual cycles is achieved by the average C:N:P ratios associated with oceanic and terrestrial photosynthesis (Redfield ratios), autorespiration on land and in ocean waters, humus formation, and sedimentation of organic matter in the coastal zone and open ocean. We make a simplifying assumption that these biologically mediated coupling processes apply over many different species and environments, and occur with the same global mean elemental ratios on the decadal to century timescale. All the transfer processes between the model reservoirs are represented by linear or nonlinear equations describing reaction mechanisms and physical transport processes. The model has been shown to reproduce well the atmospheric CO_2 concentration for the past 300 yr (Ver et al., 1999).

UVic ESCM: the UVic ESCM version 2.9 (Eby et al., 2009) consists of a primitive equation 3-D ocean general circulation model coupled to a dynamic-thermodynamic sea-ice model and an atmospheric energy-moisture balance model with dynamical feedbacks (Weaver et al., 2001). The model conserves heat, moisture, and carbon between components to machine precision without flux adjustments. The land surface and terrestrial vegetation components are represented by a simplified version of the Hadley Centre's MOSES land-surface scheme coupled to the dynamic vegetation model TRIFFID (Meissner et al., 2003). Land carbon fluxes are calculated within MOSES and are allocated to vegetation and soil carbon pools (Matthews et al., 2004). Ocean carbon is simulated by means of an OCMIP-type inorganic carbon-cycle model and a NPZD marine ecosystem model with two nutrients (PO_4 and NO_3), two phytoplankton classes, and prognostic denitrification (Schmittner and Galbraith, 2008). Sediment processes are represented using an oxic-

only model of sediment respiration (Archer, 1996). Terrestrial weathering is diagnosed from the net sediment flux during spin-up and held fixed at the steady state pre-industrial value for transient simulations. The model was spun up with boundary conditions from the year 1800 for more than 10 000 yr.

Supplementary material related to this article is available online at: http://www.atmos-chem-phys.net/13/2793/2013/acp-13-2793-2013-supplement.pdf.

Edited by: M. Heimann

References

Aamaas, B., Peters, G. P., and Fuglestvedt, J. S.: A synthesis of climate-based emission metrics with applications, Earth Syst. Dynam. Discuss., 3, 871–934, doi:10.5194/esdd-3-871-2012, 2012.

Annan, J. D. and Hargreaves, J. C.: Efficient identification of ocean thermodynamics in a physical/biogeochemical ocean model with an iterative Importance Sampling method, Ocean Modell., 32, 205–215, doi:10.1016/j.ocemod.2010.02.003, 2010.

Archer, D.: A data-driven model of the global calcite lysocline, Global Biogeochem. Cy., 10, 511–526, doi:10.1029/96gb01521, 1996.

Archer, D., Eby, M., Brovkin, V., Ridgwell, A., Cao, L., Mikolajewicz, U., Caldeira, K., Matsumoto, K., Munhoven, G., Montenegro, A., and Tokos, K.: Atmospheric Lifetime of Fossil Fuel Carbon Dioxide, Annu. Rev. Earth Planet. Sci., 37, 117–134, doi:10.1146/annurev.earth.031208.100206, 2009.

Azar, C. and Johansson, D. J. A.: On the relationship between metrics to compare greenhouse gases – the case of IGTP, GWP and SGTP, Earth Syst. Dynam., 3, 139–147, doi:10.5194/esd-3-139-2012, 2012.

Bondeau, A., Smith, P. C., Zaehle, S., Schaphoff, S., Lucht, W., Cramer, W., Gerten, D., Lotze-Campen, H., MÜLler, C., Reichstein, M., and Smith, B.: Modelling the role of agriculture for the 20th century global terrestrial carbon balance, Glob. Change Biol., 13, 679–706, 2007.

Boucher, O.: Comparison of physically- and economically-based CO_2-equivalences for methane, Earth Syst. Dynam., 3, 49–61, doi:10.5194/esd-3-49-2012, 2012.

Boucher, O. and Reddy, M. S.: Climate trade-off between black carbon and carbon dioxide emissions, Energy Policy, 36, 193–200, 2008.

Broecker, W. S., Peng, T.-H., and Engh, R.: Modelling the carbon system, Radiocarbon, 22, 565–598, 1980.

Brovkin, V., Ganopolski, A., and Svirezhev, Y.: A continuous climate-vegetation classification for use in climate-biosphere studies, Ecol. Modell., 101, 251–261, doi:10.1016/s0304-3800(97)00049-5, 1997.

Brovkin, V., Bendtsen, J., Claussen, M., Ganopolski, A., Kubatzki, C., Petoukhov, V., and Andreev, A.: Carbon cycle, vegetation, and climate dynamics in the Holocene: Experiments with the CLIMBER-2 model, Global Biogeochem. Cy., 16, 1139, 1131–1113, doi:10.1029/2001GB001662, 2002.

Brovkin, V., Ganopolski, A., Archer, D., and Rahmstorf, S.: Lowering of glacial atmospheric CO_2 in response to changes in oceanic circulation and marine biogeochemistry, Paleoceanography, 22, PA4202, doi:10.1029/2006pa001380, 2007.

Brovkin, V., Raddatz, T., Reick, C. H., Claussen, M., and Gayler, V.: Global biogeophysical interactions between forest and climate, Geophys. Res. Lett., 36, L07405, doi:10.1029/2009gl037543, 2009.

Caldeira, K. and Kasting, J. F.: Insensitivity of global warming potentials to carbon dioxide emission scenarios, Nature, 366, 251–253, 1993.

Cao, L., Eby, M., Ridgwell, A., Caldeira, K., Archer, D., Ishida, A., Joos, F., Matsumoto, K., Mikolajewicz, U., Mouchet, A., Orr, J. C., Plattner, G.-K., Schlitzer, R., Tokos, K., Totterdell, I., Tschumi, T., Yamanaka, Y., and Yool, A.: The role of ocean transport in the uptake of anthropogenic CO_2, Biogeosciences, 6, 375–390, doi:10.5194/bg-6-375-2009, 2009.

Collins, W. J., Bellouin, N., Doutriaux-Boucher, M., Gedney, N., Halloran, P., Hinton, T., Hughes, J., Jones, C. D., Joshi, M., Liddicoat, S., Martin, G., O'Connor, F., Rae, J., Senior, C., Sitch, S., Totterdell, I., Wiltshire, A., and Woodward, S.: Development and evaluation of an Earth-System model – HadGEM2, Geosci. Model Dev., 4, 1051–1075, doi:10.5194/gmd-4-1051-2011, 2011.

Conway, T. and Tans, P. P.: Globally averaged marine surface annual mean data, NOAA/ESRL www.esrl.noaa.gov/gmd/ccgg/trends/, 2012.

Cox, P. M.: Description of the TRIFFID dynamic global vegetation model, Met Office, UK, 2001.

Denman, K. L., Brasseur, G., Chidthaisong, A., Ciais, P., Cox , P., Dickinson, R. E., Hauglustaine, D., Heinze, C., Holland, E., Jacob, D., Lohmann, U., Ramachandra, S., da Silva Dias, P. L., Wofsy, S., and Zhang, X.: Couplings between changes in the climate system and biogeochemistry, in: Climate Change 2007: The Physical Science Basis. Contribution of Working Group I to the Fourth Assessment Report of the Intergovernmental Panel on Climate Change, edited by: Solomon, S., Qin, D., Manning, M., Chen, Z., Marquis, M., Averyt, K. B., Tignor, M., and Miller, H. L., Cambridge University Press, Cambridge United Kingdom and New York, NY, USA, 498–587, 2007.

Doney, S. C., Lindsay, K., Fung, I., and John, J.: Natural variability in a stable, 1000-year global coupled climate-carbon cycle

simulation, J. Climate, 19, 3033–3054, 2006.

Eby, M., Zickfeld, K., Montenegro, A., Archer, D., Meissner, K. J., and Weaver, A. J.: Lifetime of Anthropogenic Climate Change: Millennial Time Scales of Potential CO$_2$ and Surface Temperature Perturbations, J. Climate, 22, 2501–2511, doi:10.1175/2008jcli2554.1, 2009.

Eby, M., Weaver, A. J., Alexander, K., Zickfeld, K., Abe-Ouchi, A., Cimatoribus, A. A., Crespin, E., Drijfhout, S. S., Edwards, N. R., Eliseev, A. V., Feulner, G., Fichefet, T., Forest, C. E., Goosse, H., Holden, P. B., Joos, F., Kawamiya, M., Kicklighter, D., Kienert, H., Matsumoto, K., Mokhov, I. I., Monier, E., Olsen, S. M., Pedersen, J. O. P., Perrette, M., Philippon-Berthier, G., Ridgwell, A., Schlosser, A., Schneider von Deimling, T., Shaffer, G., Smith, R. S., Spahni, R., Sokolov, A. P., Steinacher, M., Tachiiri, K., Tokos, K., Yoshimori, M., Zeng, N., and Zhao, F.: Historical and idealized climate model experiments: an EMIC intercomparison, Clim. Past Discuss., 8, 4121–4181, doi:10.5194/cpd-8-4121-2012, 2012.

Edwards, N. R. and Marsh, R.: Uncertainties due to transport-parameter sensitivity in an efficient 3-D ocean-climate model, Clim. Dynam., 24, 415–433, doi:10.1007/s00382-004-0508-8, 2005.

Edwards, N. R., Willmott, A. J., and Killworth, P. D.: On the role of topography and wind stress on the stability of the thermohaline circulation, J. Phys. Oceanogr., 28, 756–778, 1998.

Enting, I. G.: On the use of smoothing splines to filter CO$_2$ data, J. Geophys. Res., 92, 10977–10984, 1987.

Enting, I. G.: Ambiguities in the calibration of carbon cycle models, Inverse Problems, 6, L39–L46, 1990.

Enting, I. G. and Mansbridge, J. V.: The incompatibility of ice-core CO$_2$ data with reconstructions of biotic CO$_2$ sources, Tellus, 39B, 318–325, 1987.

Enting, I. G., Wigley, T. M. L., and Heimann, M.: Future Emissions and Concentrations of Carbon Dioxide: Key Ocean/Atmosphere/Land analyses, CSIRO, Division of Atmospheric Research, 1–118, 1994.

Enting, I. G., Rayner, P. J., and Ciais, P.: Carbon Cycle Uncertainty in REgional Carbon Cycle Assessment and Processes (REC-CAP), Biogeosciences, 9, 2889–2904, doi:10.5194/bg-9-2889-2012, 2012.

Essery, R. L. H., Best, M. J., Betts, R. A., Cox, P. M., and Taylor, C. M.: Explicit representation of subgrid heterogeneity in a GCM land-surface scheme, J. Hydrometeorol., 43, 530–543, 2003.

Fader, M., Rost, S., Müller, C., Bondeau, A., and Gerten, D.: Virtual water content of temperate cereals and maize: Present and potential future patterns, J. Hydrol., 384, 218–231, doi:10.1016/j.jhydrol.2009.12.011, 2010.

Farquhar, G. D., von Caemmerer, S., and Berry, J. A.: A biochemical model of photosynthetic CO$_2$ assimilation in leaves of C3 species, Planta, 149, 78–90, 1980.

Fichefet, T. and Maqueda, M. A. M.: Sensitivity of a global sea ice model to the treatment of ice thermodynamics and dynamics, J. Geophys. Res., 102, 12609–12646, doi:10.1029/97jc00480, 1997.

Forster, P., Ramaswamy, V., Artaxo, P., Berntsen, T., Betts, R., Fahey, D. W., Haywood, J., Lean, J., Lowe, D. C., Myhre, G., Nganga, J., Prinn, R., Raga, G., Schulz, M., and Van Doorland, R.: Changes in Atmospheric Constitutents and in Radiative Forcing, in: Climate Change 2007: The Physical Science Basis. Contribution of Working Group I to Fourth Assessment Report of the Intergovernmental Panel on Climate Change, edited by: Solomon, S., Qin, D., Manning, M., Chen, Z., Marquis, M., Averyt, K. B., Tignor, M., and Miller, H. L., Cambridge United Kingdom and New York, NY, USA, New York, NY, USA, 129–234, 2007.

Friedlingstein, P., Cox, P., Betts, R., Bopp, L., von Bloh, W., Brovkin, V., Doney, S., Eby, M., Fung, I., Govindasamy, B., John, J., Jones, C., Joos, F., Kato, T., Kawamiya, M., Knorr, W., Lindsay, K., Matthews, H. D., Raddatz, T., Rayner, R., Reick, C., Roeckner, E., Schnitzler, K.-G., Schnur, R., Strassmann, K., Thompson, S., Weaver, A. J., Yoshikawa, C., and Zeng, N.: Climate-carbon cycle feedback analysis, results from the C4MIP model intercomparison, J. Climate, 19, 3337–3353, 2006.

Friedrich, T., Timmermann, A., Abe-Ouchi, A., Bates, N. R., Chikamoto, M. O., Church, M. J., Dore, J. E., Gledhill, D. K., Gonzalez-Davila, M., Heinemann, M., Ilyina, T., Jungclaus, J. H., McLeod, E., Mouchet, A., and Santana-Casiano, J. M.: Detecting regional anthropogenic trends in ocean acidification against natural variability, Nature Clim. Change, 2, 167–171, 2012.

Fuglestvedt, J. S. and Berntsen, T.: A simple model for scenario studies of changes in global climate, Working Paper, Center for International Climate and Environmental Research, Oslo, 1999:2, 1999.

Fuglestvedt, J., Berntsen, T., Godal, O., and Sausen, R.: Metrics of climate change: Assessing radiative forcing and emission indices, Climatic Change, 267–331, 2003.

Fuglestvedt, J. S., Shine, K. P., Berntsen, T., Cook, J., Lee, D. S., Stenke, A., Skeie, R. B., Velders, G. J. M., and Waitz, I. A.: Transport impacts on atmosphere and climate: Metrics, Atmos. Environ., 44, 4648–4677, doi:10.1016/j.atmosenv.2009.04.044, 2010.

Fung, I., Doney, S. C., Lindsay, K., and John, J.: Evolution of carbon sinks in a changing climate, P. Natl. Acad. Sci., 102, 11201–11206, 2005.

Gattuso, J. P., Bijma, J., Gehlen, M., Riebesell, U., and Turley, C.: Ocean acidification: knowns, unknowns, and perspectives, in: Ocean Acidification, edited by: Gattuso, J. P. and Hansson, L., Oxford University Press, Oxford, 291–311, 2011.

Gehlen, M., Bopp, L., Emprin, N., Aumont, O., Heinze, C., and Ragueneau, O.: Reconciling surface ocean productivity, export fluxes and sediment composition in a global biogeochemical ocean model, Biogeosciences, 3, 521–537, doi:10.5194/bg-3-521-2006, 2006.

Gerber, S., Joos, F., Brugger, P., Stocker, T. F., Mann, M. E., Sitch, S., and Scholze, M.: Constraining temperature variations over the last millennium by comparing simulated and observed atmospheric CO$_2$, Clim. Dynam., 20, 281–299, 2003.

Gerten, D., Schaphoff, S., Haberlandt, U., Lucht, W., and Sitch, S.: Terrestrial vegetation and water balance – hydrological evaluation of a dynamic global vegetation model, J. Hydrol., 286, 249–270, 2004.

Gillett, N. P. and Matthews, H. D.: Accounting for carbon cycle feedbacks in a comparison of the global warming effects of greenhouse gases, Environ. Res. Lett., 5, 1–6, doi:10.1088/1748-9326/5/3/034011, 2010.

Goosse, H., Deleersnijder, E., Fichefet, T., and England, M. H.: Sensitivity of a global coupled ocean-sea ice model to the

parameterization of vertical mixing, J. Geophys. Res., 104, 13681–13695, doi:10.1029/1999jc900099, 1999.

Goosse, H., Brovkin, V., Fichefet, T., Haarsma, R., Huybrechts, P., Jongma, J., Mouchet, A., Selten, F., Barriat, P.-Y., Campin, J.-M., Deleersnijder, E., Driesschaert, E., Goelzer, H., Janssens, I., Loutre, M.-F., Morales Maqueda, M. A., Opsteegh, T., Mathieu, P.-P., Munhoven, G., Pettersson, E. J., Renssen, H., Roche, D. M., Schaeffer, M., Tartinville, B., Timmermann, A., and Weber, S. L.: Description of the Earth system model of intermediate complexity LOVECLIM version 1.2, Geosci. Model Dev., 3, 603–633, doi:10.5194/gmd-3-603-2010, 2010.

Haxeltine, A. and Prentice, I. C.: A general model for the light use efficiency of primary production, Funct. Ecol., 10, 551–561, 1996.

Heinze, C., Maier-Reimer, E., Winguth, A. M. E., and Archer, D.: A global oceanic sediment model for long-term climate studies, Global Biogeochem. Cy., 13, 221–250, 1999.

Holden, P. B., Edwards, N. R., Gerten, D., and Schaphoff, S.: A model-based constraint on CO_2 fertilisation, Biogeosciences, 10, 339–355, doi:10.5194/bg-10-339-2013, 2013.

Hurtt, G. C., Chini, L. P., Frolking, S., Betts, R. A., Feddema, J., Fischer, G., Fisk, J. P., Hibbard, K., Houghton, R. A., Janetos, A., Jones, C. D., Kindermann, G., Kinoshita, T., Klein Goldewijk, K., Riahi, K., Shevliakova, E., Smith, S., Stehfest, E., Thomson, A., Thornton, P., Vuuren, D. P., and Wang, Y. P.: Harmonization of land-use scenarios for the period 1500–2100: 600 years of global gridded annual land-use transitions, wood harvest, and resulting secondary lands, Climatic Change, 109, 117–161, doi:10.1007/s10584-011-0153-2, 2011.

Johansson, D.: Economics- and physical-based metrics for comparing greenhouse gases, Climatic Change, 110, 123–141, doi:10.1007/s10584-011-0072-2, 2012.

Jones, C. D., Hughes, J. K., Bellouin, N., Hardiman, S. C., Jones, G. S., Knight, J., Liddicoat, S., O'Connor, F. M., Andres, R. J., Bell, C., Boo, K.-O., Bozzo, A., Butchart, N., Cadule, P., Corbin, K. D., Doutriaux-Boucher, M., Friedlingstein, P., Gornall, J., Gray, L., Halloran, P. R., Hurtt, G., Ingram, W. J., Lamarque, J.-F., Law, R. M., Meinshausen, M., Osprey, S., Palin, E. J., Parsons Chini, L., Raddatz, T., Sanderson, M. G., Sellar, A. A., Schurer, A., Valdes, P., Wood, N., Woodward, S., Yoshioka, M., and Zerroukat, M.: The HadGEM2-ES implementation of CMIP5 centennial simulations, Geosci. Model Dev., 4, 543–570, doi:10.5194/gmd-4-543-2011, 2011.

Joos, F., Bruno, M., Fink, R., Siegenthaler, U., Stocker, T. F., and LeQuere, C.: An efficient and accurate representation of complex oceanic and biospheric models of anthropogenic carbon uptake, Tellus B, 48, 397–417, 1996.

Joos, F., Plattner, G. K., Stocker, T. F., Marchal, O., and Schmittner, A.: Global warming and marine carbon cycle feedbacks an future atmospheric CO_2, Science, 284, 464–467, 1999.

Joos, F., Prentice, I. C., Sitch, S., Meyer, R., Hooss, G., Plattner, G. K., Gerber, S., and Hasselmann, K.: Global warming feedbacks on terrestrial carbon uptake under the Intergovernmental Panel on Climate Change (IPCC) emission scenarios, Global Biogeochem. Cy., 15, 891–908, 2001.

Joos, F., Frölicher, T. L., Steinacher, M., and Plattner, G.-K.: Impact of climate change mitigation on ocean acidification projections, in: Ocean Acidification, edited by: Gattuso, J. P., and Hansson, L., Oxford University Press, Oxford, 273-289, 2011.

Joos, F., Roth, R. Fuglestvedt, J. S., and Peters, G. P.:CO_2 pulse response function for the calculation of Global Warming Potentials: a multi-model analysis: http://www.climate.unibe.ch/~joos/IRF_Intercomparison/ (last access: July 2012), 2012.

Kandlikar, M.: The relative role of trace gas emissions in greenhouse abatement policies, Energy Policy, 23, 879–883, 1995.

Key, R. M., Kozyr, A., Sabine, C. L., Lee, K., Wanninkhof, R., Bullister, J. L., Feely, R. A., Millero, F. J., Mordy, C., and Peng, T. H.: A global ocean carbon climatology: Results from Global Data Analysis Project (GLODAP), Global Biogeochem. Cy., 18, GB4031, doi:10.1029/2004GB002247, 2004.

Kleinen, T., Brovkin, V., von Bloh, W., Archer, D., and Munhoven, G.: Holocene carbon cycle dynamics, Geophys. Res. Lett., 37, L02705, doi:10.1029/2009GL041391, 2010.

Mackenzie, F. T., De Carlo, E. H., and Lerman, A.: Coupled C, N, P, and O biogeochemical cycling at the land-ocean interface, in: Treatise on Estuarine and Coastal Science, edited by: Wolanski, E. and McLusky, D. S., Academic Press, Waltham, 317–342, 2011.

Maier-Reimer, E.: Geochemical cycles in an ocean general circulation model. Preindustrial tracer distributions, Global Biogeochem. Cy., 7, 645–677, doi:10.1029/93gb01355, 1993.

Maier-Reimer, E. and Hasselmann, K.: Transport and storage of CO_2 in the ocean – an inorganic ocean-circulation carbon cycle model, Clim. Dynam., 2, 63–90, 1987.

Maier-Reimer, E., Kriest, I., Segschneider, J., and Wetzel, P.: The Hamburg ocean carbon cycle model HAMOCC5.1 Technical description, Release 1.1, Max-Planck-Institut für Meteorologie, Hamburg, 2005.

Manne, A. S. and Richels, R. G.: An alternative approach to establishing trade-offs among greenhouse gases, Nature, 410, 675–677, 2001.

Marchal, O., Stocker, T. F., and Joos, F.: Impact of oceanic reorganizations on the ocean carbon cycle and atmospheric carbon dioxide content, Paleoceanography, 13, 225–244, 1998.

Marsh, R., Müller, S. A., Yool, A., and Edwards, N. R.: Incorporation of the C-GOLDSTEIN efficient climate model into the GENIE framework: "eb_go_gs" configurations of GENIE, Geosci. Model Dev., 4, 957–992, doi:10.5194/gmd-4-957-2011, 2011.

Marsland, S. J., Haak, H., Jungclaus, J. H., Latif, M., and Röske, F.: The Max-Planck-Institute global ocean/sea ice model with orthogonal curvilinear coordinates, Ocean Modell., 5, 91–127, doi:10.1016/s1463-5003(02)00015-x, 2003.

Matsumoto, K., Tokos, K. S., Price, A. R., and Cox, S. J.: First description of the Minnesota Earth System Model for Ocean biogeochemistry (MESMO 1.0), Geosci. Model Dev., 1, 1–15, doi:10.5194/gmd-1-1-2008, 2008.

Matthews, H. D., Weaver, A. J., Meissner, K. J., Gillett, N. P., and Eby, M.: Natural and anthropogenic climate change: incorporating historical land cover change, vegetation dynamics and the global carbon cycle, Clim. Dynam., 22, 461–479, doi:10.1007/s00382-004-0392-2, 2004.

Meehl, G. A., Stocker, T. F., Collins, W. D., Friedlingstein, P., Gaye, A. T., Gregory, J. M., Kitoh, A., Knutti, R., Murphy, J. M., Noda, A., Raper, S. C. B., Watterson, I. G., J., W. A., and Zhao, Z.-C.: Global Climate Projections, in: Climate Change 2007: The Physical Science Basis. Contribution of Working Group I to Fourth Assessment Report of the Intergovernmental Panel on Climate Change, edited by: Solomon, S., Qin, D., Manning, M., Chen, Z.,

Marquis, M., Averyt, K. B., Tignor, M., and Miller, H. L., Cambridge United Kingdom and New York, NY, USA, New York, NY, USA, 747–845, 2007.

Meinshausen, M., Raper, S. C. B., and Wigley, T. M. L.: Emulating coupled atmosphere-ocean and carbon cycle models with a simpler model, MAGICC6 – Part 1: Model description and calibration, Atmos. Chem. Phys., 11, 1417–1456, doi:10.5194/acp-11-1417-2011, 2011a.

Meinshausen, M., Smith, S. J., Calvin, K., Daniel, J. S., Kainuma, M. L. T., Lamarque, J.-F., Matsumoto, K., Montzka, S. A., Raper, S. C. B., Riahi, K., Thomson, A., Velders, G. J. M., and van Vuuren, D. P. P.: The RCP greenhouse gas concentrations and their extensions from 1765 to 2300, Climatic Change, 109, 213–241, doi:10.1007/s10584-011-0156-z, 2011b.

Meissner, K. J., Weaver, A. J., Matthews, H. D., and Cox, P. M.: The role of land surface dynamics in glacial inception: a study with the UVic Earth System Model, Clim. Dynam., 21, 515–537, doi:10.1007/s00382-003-0352-2, 2003.

Menviel, L., Timmermann, A., Mouchet, A., and Timm, O.: Climate and marine carbon cycle response to changes in the strength of the Southern Hemispheric westerlies, Paleoceanography, 23, PA4201, doi:10.1029/2008pa001604, 2008.

Meyer, R., Joos, F., Esser, G., Heimann, M., Hooss, G., Kohlmaier, G., Sauf, W., Voss, R., and Wittenberg, U.: The substitution of high-resolution terrestrial biosphere models and carbon sequestration in response to changing CO$_2$ and climate, Global Biogeochem. Cy., 13, 785–802, 1999.

Müller, S. A., Joos, F., Edwards, N. R., and Stocker, T. F.: Water mass distribution and ventilation time scales in a cost-efficient, three-dimensional ocean model, J. Climate, 19 5479–5499, doi:10.1175/JCLI3911.1, 2006.

Myhre, G., Highwood, E. J., Shine, K. P., and Stordal, F.: New estimates of radiative forcing due to well mixed greenhouse gases, Geophys. Res. Lett., 25, 2715–1718, 1998.

Najjar, R. G. and Orr, J. C.: OCMIP-2 Biotic-HOWTO: http://www.ipsl.jussieu.fr/OCMIP/, 1999.

Najjar, R. G., Jin, X., Louanchi, F., Aumont, O., Caldeira, K., Doney, S. C., Dutay, J. C., Follows, M., Gruber, N., Joos, F., Lindsay, K., Maier-Reimer, E., Matear, R. J., Matsumoto, K., Monfray, P., Mouchet, A., Orr, J. C., Plattner, G. K., Sarmiento, J. L., Schlitzer, R., Slater, R. D., Weirig, M. F., Yamanaka, Y., and Yool, A.: Impact of circulation on export production, dissolved organic matter, and dissolved oxygen in the ocean: Results from Phase II of the Ocean Carbon-cycle Model Intercomparison Project (OCMIP-2), Global Biogeochem. Cy., 21, GB3007, doi:10.1029/2006GB002857, 2007.

New, M., Hulme, M., and Jones, P.: Representing Twentieth-Century Space-Time Climate Variability. Part II: Development of 1901–96 Monthly Grids of Terrestrial Surface Climate, J. Climate, 13, 2217–2238, doi:10.1175/1520-0442(2000)013¡2217:rtcstc¿2.0.co;2, 2000.

O'Neill, B. C.: The Jury is Still Out on Global Warming Potentials, Climatic Change, 44, 427–443, doi:10.1023/a:1005582929198, 2000.

Oeschger, H., Siegenthaler, U., Schotterer, U., and Gugelmann, A.: A box diffusion model to study the carbon dioxide exchange in nature, Tellus, 27, 170–192, 1975.

Olivié, D. J. L. and Peters, G. P.: The impact of model variation in CO$_2$ and temperature impulse response functions on

emission metrics, Earth Syst. Dynam. Discuss., 3, 935–977, doi:10.5194/esdd-3-935-2012, 2012.

Orr, J. C., Najjar, R. G., Sabine, C., and Joos, F.: OCMIP-2 Abiotic-HOWTO: http://www.ipsl.jussieu.fr/OCMIP/phase2/simulations/Abiotic/HOWTO-Abiotic.html (last access: July 2012), 1999.

Orr, J. C., Fabry, V. J., Aumont, O., Bopp, L., Doney, S. C., Feely, R. A., Gnanadesikan, A., Gruber, N., Ishida, A., Joos, F., Key, R. M., Lindsay, K., Maier-Reimer, E., Matear, R., Monfray, P., Mouchet, A., Najjar, R. G., Plattner, G. K., Rodgers, K. B., Sabine, C. L., Sarmiento, J. L., Schlitzer, R., Slater, R. D., Totterdell, I. J., Weirig, M. F., Yamanaka, Y., and Yool, A.: Anthropogenic ocean acidification over the twenty-first century and its impact on calcifying organisms, Nature, 437, 681–686, 2005.

Palmer, J. R. and Totterdell, I. J.: Production and export in a global ocean ecosystem model, Deep Sea Res. I, 48, 1169–1198, 2001.

Parekh, P., Joos, F., and Müller, S. A.: A modeling assessment of the interplay between aeolian iron fluxes and iron-binding ligands in controlling carbon dioxide fluctuations during Antarctic warm events, Paleoceanography, 23, PA4202, 4201–4214, doi:10.1029/2007PA001531, 2008.

Peters, G. P., Aamaas, B., Berntsen, T., and Fuglestvedt, J. S.: The integrated global temperature change potential (iGTP) and relationships between emission metrics, Environ. Res. Lett., 6, 044021, doi:10.1088/1748-9326/6/4/044021, 2011.

Petoukhov, V., Claussen, M., Berger, A., Crucifix, M., Eby, M., Eliseev, A. V., Fichefet, T., Ganopolski, A., Goosse, H., Kamenkovich, I., Mokhov, I. I., Montoya, M., Mysak, L. A., Sokolov, A., Stone, P., Wang, Z., and Weaver, A. J.: EMIC Intercomparison Project (EMIP-CO$_2$): comparative analysis of EMIC simulations of climate, and of equilibrium and transient responses to atmospheric CO$_2$ doubling, Clim. Dynam., 25, 363–385, doi:10.1007/s00382-005-0042-3, 2005.

Plattner, G. K., Joos, F., Stocker, T. F., and Marchal, O.: Feedback mechanisms and sensitivities of ocean carbon uptake under global warming, Tellus B, 53, 564–592, 2001.

Plattner, G.-K., Knutti, R., Joos, F., Stocker, T. F., von Bloh, W., Brovkin, V., Cameron, D., Driesschaert, E., Dutkiewicz, S., Eby, M., Edwards, N. R., Fichefet, T., Hargreaves, J. C., Jones, C. D., Loutre, M. F., Matthews, H. D., Mouchet, A., Mueller, S. A., Nawrath, S., Price, A., Sokolov, A., Strassmann, K. M., and Weaver, A. J.: Long-term climate commitments projected with climate – carbon cycle models, J. Climate, 21, 2721–2751, 2008.

Plattner, G.-K., Stocker, T., Midgley, P., and Tignor, M.: IPCC Expert Meeting on the Science of Alternative Metrics: Meeting Report, IPCC Working Group I, Technical Support Unit, Bern, Switzerland, 2009.

Portmann, F., Siebert, S., Bauer, C., and Döll, P.: Global Data Set of Monthly Growing Areas of 26 Irrigated Crops, Institute of Physical Geography, University of Frankfurt, Frankfurt am Main, Germany, 2008.

Prather, M. J.: Lifetimes and time-scales in atmospheric chemistry, Philos. T. Roy. Soc. A, 365, 1705–1726, 2007.

Prather, M. J. and Hsu, J.: Coupling of Nitrous Oxide and Methane by Global Atmospheric Chemistry, Science, 330, 952–954, 2010.

Prather, M. J., Penner, J. E., Fuglestvedt, J. S., Kurosawa, A., Lowe, J. A., Höhne, N., Jain, A. K., Andronova, N., Pinguelli, L., Pires de Campos, C., Raper, S. C. B., Skeie, R. B., Stott, P. A., van Aardenne, J., and Wagner, F.: Tracking uncertainties in the causal

chain from human activities to climate, Geophys. Res. Lett., 36, L05707, doi:10.1029/2008gl036474, 2009.

Prather, M. J., Holmes, C. D., and Hsu, J.: Reactive greenhouse gas scenarios: Systematic exploration of uncertainties and the role of atmospheric chemistry, Geophys. Res. Lett., 39, L09803, doi:10.1029/2012gl051440, 2012.

Prentice, I. C., Farquhar, G. D., Fasham, M. J., Goulden, M. I., Heimann, M., Jaramillo, V. J., Kheshgi, H. S., LeQuéré, C., Scholes, R. J., and Wallace, D. W. R.: The carbon cycle and atmospheric CO_2, in: Climate Change 2001: The Scientific Basis, Contribution of Working Group I to the Third Assessment Report of the Intergovernmental Panel on Climate Change, edited by: Houghton, J. T., Ding, Y., Griggs, D. J., Noguer, M., van der Linden, P. J., Dai, X., Maskell, K., and Johnson, C. A., Cambridge University Press, Cambridge, United Kingdom and New York, NY, USA, 183–237, 2001.

Press, W. H., Teukolsky, S. A., Vetterling, W. T., and Flannery, B. P.: Numerical Recipes, Cambridge University Press, Cambridge UK, 1986.

Raddatz, T., Reick, C., Knorr, W., Kattge, J., Roeckner, E., Schnur, R., Schnitzler, K. G., Wetzel, P., and Jungclaus, J.: Will the tropical land biosphere dominate the climate-carbon cycle feedback during the twenty-first century?, Clim. Dynam., 29, 565–574, doi:10.1007/s00382-007-0247-8, 2007.

Randerson, J. T., Thompson, M. V., Conway, T. J., Fung, I. Y., and Field, C. B.: The contribution of terrestrial sources and sinks to trends in the seasonal cycle of atmospheric carbon dioxide, Global Biogeochem. Cy., 11, 535–560, 1997.

Reader, M. C. and Boer, G. J.: The modification of greenhouse gas warming by the direct effect of sulphate aerosols, Clim. Dynam., 14, 593–607, doi:10.1007/s003820050243, 1998.

Reisinger, A., Meinshausen, M., Manning, M., and Bodeker, G.: Uncertainties of global warming metrics: CO_2 and CH_4, Geophys. Res. Lett., 37, L14707, doi:10.1029/2010GL043803, 2010.

Reisinger, A., Meinshausen, M., and Manning, M.: Future changes in global warming potentials under representative concentration pathways, Environ. Res. Lett., 6, 024020, doi:10.1088/1748-9326/6/2/024020, 2011.

Ridgwell, A. and Hargreaves, J. C.: Regulation of atmospheric CO_2 by deep-sea sediments in an Earth system model, Global Biogeochem. Cy., 21, GB2008, doi:10.1029/2006gb002764, 2007.

Ridgwell, A., Hargreaves, J. C., Edwards, N. R., Annan, J. D., Lenton, T. M., Marsh, R., Yool, A., and Watson, A.: Marine geochemical data assimilation in an efficient Earth System Model of global biogeochemical cycling, Biogeosciences, 4, 87–104, doi:10.5194/bg-4-87-2007, 2007.

Ritz, S. P., Stocker, T. F., and Joos, F.: A coupled dynamical ocean-energy balance atmosphere model for paleoclimate studies, J. Climate, 24, 349–375, 2011.

Roy, T., Bopp, L., Gehlen, M., Schneider, B., Cadule, P., Frölicher, T., Segschneider, J., Tjiputra, J., Heinze, C., and Joos, F.: Regional impacts of climate change and atmospheric CO_2 on future ocean carbon uptake:A multi-model linear feedback analysis, J. Climate, 24, 2300–2318, doi:10.1175/2010JCLI3787.1, 2011.

Sarmiento, J. L., Orr, J. C., and Siegenthaler, U.: A perturbation simulation of CO_2 uptake in an ocean general circulation model, J. Geophys. Res., 97, 3621–3645, 1992.

Sarmiento, J. L., Hughes, T. M. C., Stouffer, R. J., and Manabe, S.: Simulated response of the ocean carbon cycle to anthropogenic

climate warming, Nature, 393, 245–249, 1998.

Schimel, D., Alves, D., Enting, I. G., Heimann, M., Joos, F., Raynaud, D., Wigley, T. M. L., Prather, M., Derwent, R., Ehhalt, D., Fraser, P., Sanhueza, E., Zhou, X., Jonas, P., Charlson, R., Rhode, H., Sadasivan, S., Shine, K. P., Fouquart, Y., Ramaswamy, V., Solomon, S., Srinivasan, J., Albritton, D., Derwent, R., Isaksen, I., Lal, M., and Wuebbles, D.: Radiative Forcing of Climate Change, in: Climate Change 1995: The Science of Climate Change. Contribution of WGI to the Second Assessment Report of the Intergovernmental Panel on Climate Change, edited by: Houghton, J. T., Meira Filho, L. G., Callander, B. A., Harris, N., Kattenberg, A., and Maskell, K., Cambridge University Press, New York, 65–131, 1996.

Schmittner, A. and Galbraith, E. D.: Glacial greenhouse gas fluctuations controlled by ocean circulation changes, Nature, 456, 373–376, doi:10.1038/nature07531, 2008.

Schmittner, A. and Stocker, T. F.: The stability of the thermohaline circulation in global warming experiments, J. Climate, 12, 1117–1133, 1999.

Shaffer, G. and Sarmiento, J. L.: Biogeochemical cycling in the global ocean 1. A new, analytical model with continuous vertical resolution and high-latitude dynamics, J. Geophys. Res., 100, 2659–2672, doi:10.1029/94jc01167, 1995.

Shaffer, G., Malskær Olsen, S., and Pepke Pedersen, J. O.: Presentation, calibration and validation of the low-order, DCESS Earth System Model (Version 1), Geosci. Model Dev., 1, 17–51, doi:10.5194/gmd-1-17-2008, 2008.

Shine, K.: The global warming potential-the need for an interdisciplinary retrial, Climatic Change, 467–472, 2009.

Shine, K., Fuglestvedt, J., Hailemariam, K., and Stuber, N.: Alternatives to the Global Warming Potential for Comparing Climate Impacts of Emissions of Greenhouse Gases, Climatic Change, 68, 281–302, doi:10.1007/s10584-005-1146-9, 2005.

Shine, K. P., Derwent, R. G., Wuebbles, D. J., and Morcrette, J.-J.: Radiative Forcing of Climate, in: Climate Change: The IPCC Scientific Assessment, edited by: Houghton, J. T., Jenkins, G. J., and Ephraums, J. J., Cambridge University Press, Cambridge, United Kingdom and New York, NY, USA, 41–68, 1990.

Siegenthaler, U. and Joos, F.: Use of a Simple-Model for Studying Oceanic Tracer Distributions and the Global Carbon-Cycle, Tellus B, 44, 186–207, 1992.

Siegenthaler, U. and Oeschger, H.: Predicting future atmospheric carbon dioxide levels, Science, 199, 388–395, 1978.

Siegenthaler, U. and Oeschger, H.: Biospheric CO_2 emissions during the past 200 years reconstructed by deconvolution of ice core data, Tellus, 46B, 103–142, 1987.

Sitch, S., Smith, B., Prentice, I. C., Arneth, A., Bondeau, A., Cramer, W., Kaplan, J. O., Levis, S., Lucht, W., Sykes, M. T., Thonicke, K., and Venevsky, S.: Evaluation of ecosystem dynamics, plant geography and terrestrial carbon cycling in the LPJ dynamic global vegetation model, Glob. Change Biol., 9, 161–185, 2003.

Solomon, S., Qin, D., Manning, M., Alley, R., Berntsen, T., Bindoff, N. L., Chen, Z., Chidthaisong, A., Gregory, J., Hegerl, G., Heimann, M., Hewitson, B., Hoskins, B., Joos, F., Jouzel, J., Kattsov, V., Lohmann, U., Matsuno, T., Molina, M., Nicholls, N., Overpeck, J., Raga, G., Ramaswamy, V., Ren, J., Rusticucci, M., Somerville, R., Stocker, T. F., Stouffer, R. J., Whetton, P., Wood, R. A., and Wratt, D.: Technical Summary, in:

Climate Change 2007: The Physical Science Basis, Contribution of Working Group I to the Fourth Assessment Report of the Intergovernmental Panel on Climate Change, edited by: Solomon, S., Qin, D., Manning, M., Chen, Z., Marquis, M., Averyt, K. B., Tignor, M., and Miller, H. L., Cambridge University Press, Cambridge United Kingdom and New York, NY, USA, 19–91, 2007.

Steinacher, M.: Modeling changes in the global carbon cycle-climate system, PhD, Philosophisch-naturwissenschaftliche Fakultät, University of Bern, Bern, 212 pp., 2011.

Stocker, B. D., Strassmann, K., and Joos, F.: Sensitivity of Holocene atmospheric CO_2 and the modern carbon budget to early human land use: analyses with a process-based model, Biogeosciences, 8, 69–88, doi:10.5194/bg-8-69-2011, 2011.

Stocker, T. F., Wright, D. G., and Mysak, L. A.: A Zonally Averaged, Coupled Ocean Atmosphere Model for Paleoclimate Studies, J. Climate, 5, 773–797, 1992.

Strassmann, K. M., Joos, F., and Fischer, G.: Simulating effects of land use changes on carbon fluxes: past contributions to atmospheric CO_2 increases and future commitments due to losses of terrestrial sink capacity, Tellus B, 60B, 583–603, 2008.

Strassmann, K. M., Plattner, G. K., and Joos, F.: CO_2 and non-CO_2 radiative forcing agents in twenty-first century climate change mitigation scenarios, Clim. Dynam., 33, 737–749, 2009.

Tanaka, K.: Inverse Estimation for the Simple Earth System Model ACC2 and Its Applications, Ph.D., Universität Hamburg, Hamburg, 296 pp., 2008.

Tanaka, K., Kriegler, E., Bruckner, T., Hooss, G., Knorr, W., and Raddatz, T.: Aggregated Carbon Cycle, Atmospheric Chemistry, and Climate Model (ACC2) – description of the forward and inverse modes, Max Planck Institute for Meteorology, Hamburg, 188, 2007.

Tanaka, K., O'Neill, B., Rokityanskiy, D., Obersteiner, M., and Tol, R.: Evaluating Global Warming Potentials with historical temperature, Climatic Change, 96, 443–466, doi:10.1007/s10584-009-9566-6, 2009a.

Tanaka, K., Raddatz, T., O'Neill, B. C., and Reick, C. H. I.: Insufficient forcing uncertainty underestimates the risk of high climate sensitivity, Geophys. Res. Lett., 36, L16709, doi:10.1029/2009GL039642, 2009b.

Tanaka, K., Peters, G. P., and Fuglestvedt, J. S.: Policy Update: Multicomponent climate policy: why do emission metrics matter?, Carbon Management, 1, 191–197, doi:10.4155/cmt.10.28, 2010.

Tanaka, K., Berntsen, T., Fuglestvedt, J. S., and Rypdal, K.: Climate Effects of Emission Standards: The Case for Gasoline and Diesel Cars, Environ. Sci. Technol., 46, 5205–5213, doi:10.1021/es204190w, 2012.

Tarnocai, C., Canadell, J. G., Schuur, E. A. G., Kuhry, P., Mayhitova, G., and Zimov, S.: Soil organic carbon pools in the northern circumpolar permafrost region, Global Biogeochem. Cy., 23, 1–11, 2009.

The HadGEM2 Development Team: Martin, G. M., Bellouin, N., Collins, W. J., Culverwell, I. D., Halloran, P. R., Hardiman, S. C., Hinton, T. J., Jones, C. D., McDonald, R. E., McLaren, A. J., O'Connor, F. M., Roberts, M. J., Rodriguez, J. M., Woodward, S., Best, M. J., Brooks, M. E., Brown, A. R., Butchart, N., Dearden, C., Derbyshire, S. H., Dharssi, I., Doutriaux-Boucher, M., Edwards, J. M., Falloon, P. D., Gedney, N., Gray, L. J., Hewitt, H. T., Hobson, M., Huddleston, M. R., Hughes, J., Ineson, S., Ingram, W. J., James, P. M., Johns, T. C., Johnson, C. E., Jones, A.,

Jones, C. P., Joshi, M. M., Keen, A. B., Liddicoat, S., Lock, A. P., Maidens, A. V., Manners, J. C., Milton, S. F., Rae, J. G. L., Ridley, J. K., Sellar, A., Senior, C. A., Totterdell, I. J., Verhoef, A., Vidale, P. L., and Wiltshire, A.: The HadGEM2 family of Met Office Unified Model climate configurations, Geosci. Model Dev., 4, 723–757, doi:10.5194/gmd-4-723-2011, 2011.

Tol, R., Berntsen, T., O'Neill, B. C., Fuglestvedt, J. S., and Shine, K. P.: A unifying framework for metrics for aggregating the climate effect of different emissions, Environ. Res. Lett., 7, 1–8, 10.1088/1748-9326/7/4/044006, 2012.

Tschumi, T., Joos, F., and Parekh, P.: How important are Southern Hemisphere wind changes for low glacial carbon dioxide? A model study, Paleoceanography, 23, PA4208, doi:10.1029/2008PA001592, 2008.

Tschumi, T., Joos, F., Gehlen, M., and Heinze, C.: Deep ocean ventilation, carbon isotopes, marine sedimentation and the deglacial CO_2 rise, Clim. Past, 7, 771–800, doi:10.5194/cp-7-771-2011, 2011.

UNFCCC, FCCC/CP/1997/7 decision 4/CP.5, Guidelines for the preparation of national communications from Parties included in Annex I to the Convention. Secretary of the United Nations Framework Convention on Climate Change, Bonn, Germany: http://unfccc.int/resource/docs/cop5/07.pdf, 1997.

UNFCCC, FCCC/CP/1997/7/Add.1, Methodological issues related to the Kyoto Protocol, Secretary of the United Nations Framework Convention on Climate Change, Bonn, Germany: http://unfccc.int/resource/docs/cop3/07a01.pdf, 1998.

UNFCCC, FCCC/CP/2002/7/Add.2 Decision 17/CP.8, Guidelines for the preparation of national communications from Parties not included in Annex I to the Convention. Secretary of the United Nations Framework Convention on Climate Change, Bonn, Germany: http://unfccc.int/resource/docs/cop8/07a02.pdf#page=2, 2002.

UNFCCC, FCCC/CP/2011/9/Add.2, Decision 15/CP.17, Revision of the UNFCCC reporting guidelines on annual inventories for Parties included in Annex I to the Convention. Secretary of the United Nations Framework Convention on Climate Change, Bonn, Germany: http://unfccc.int/resource/docs/2011/cop17/eng/09a02.pdf#page=23, 2011a.

UNFCCC, FCCC/KP/CMP/2011/10/Add.1, decision 4/CMP.7, Greenhouse gases, sectors and source categories, common metrics to calculate the carbon dioxide equivalence of anthropogenic emissions by sources and removals by sinks, and other methodological issues. Secretary of the United Nations Framework Convention on Climate Change, Bonn, Germany: http://unfccc.int/resource/docs/2011/cmp7/eng/10a01.pdf#page=23, 2011b.

Van Vuuren, D. P., Meinshausen, M., Plattner, G.-K., Joos, F., Strassmann, K. M., Smith, S. J., Wigley, T. M. L., Raper, S. C. B., Riahi, K., de la Chesnaye, F., den Elzen, M., Fujino, J., Jiang, K., Nakicenovic, N., Paltsev, S., and Reilly, J. M.: Temperature increase of 21st century mitigation scenarios, P. Natl. Acad. Sci. USA, 105, 15258–15262, 2008.

Ver, L. M. B., Mackenzie, F. T., and Lerman, A.: Biogeochemical responses of the carbon cycle to natural and human perturbations; past, present, and future, American Journal of Science, 299, 762–801, 1999.

Wania, R., Ross, I., and Prentice, I. C.: Integrating peatlands and permafrost into a dynamic global vegetation model: 1. Evaluation and sensitivity of physical land surface processes, Global

F. Joos et al.: A multi-model analysis   **2825**

Biogeochem. Cy., 23, GB3014, doi:10.1029/2008gb003412, 2009a.

Wania, R., Ross, I., and Prentice, I. C.: Integrating peatlands and permafrost into a dynamic global vegetation model: 2. Evaluation and sensitivity of vegetation and carbon cycle processes, Global Biogeochem. Cy., 23, GB3015, doi:10.1029/2008gb003413, 2009b.

Weaver, A. J., Eby, M., Wiebe, E. C., Bitz, C. M., Duffy, P. B., Ewen, T. L., Fanning, A. F., Holland, M. M., MacFadyen, A., Matthews, H. D., Meissner, K. J., Saenko, O., Schmittner, A. H. W., and Yoshimori, M.: The UVic Earth System Climate Model: Model description, climatology and application to past, present and future climates, Atmos.-Ocean, 39, 361–428, 2001.

Weaver, A. J., Sedlácek, J., Eby, M., Alexander, K., Crespin, E., Fichefet, T., Philippon-Berthier, G., Joos, F., Kawamiya, M., Matsumoto, K., Steinacher, M., Tachiiri, K., Tokos, K., Yoshimori, M., and Zickfeld, K.: Stability of the Atlantic meridional overturning circulation: A model intercomparison, Geophys. Res. Lett., 39, L20709, doi:10.1029/2012gl053763, 2012.

Weyant, J. R., de la Chesnaye, F. C., and Blanford, G. J.: Overview of emf-21: Multigas mitigation and climate policy, Energy Journal, 27, 1–32, 2006.

Williamson, M. S., Lenton, T. M., Shepherd, J. G., and Edwards, N. R.: An efficient numerical terrestrial scheme (ENTS) for Earth system modelling, Ecol. Modell., 198, 362–374, doi:10.1016/j.ecolmodel.2006.05.027, 2006.

Wuebbles, D. J., Jain, A. K., Patten, K. O., and Grant, K. E.: Sensitivity of direct global warming potentials to key uncertainties, Climatic Change, 29, 265–297, 1995.

Zickfeld, K., Eby, M., Weaver, A. J., Crespin, E., Fichefet, T., Goosse, H., Edwards, N. R., Holden, P. B., Eliseev, A. V., Mokhov, I. I., Feulner, G., Kienert, H., Perrette, M., Schneider von Deimling, T., Forest, C. E., Joos, F., Spahni, R., Steinacher, M., Kawamiya, M., Tachiiri, K., Kicklighter, D., Monier, E., Schlosser, A., Sokolov, A. P., Matsumoto, K., Tokos, K., Olsen, S. M., Pedersen, J. O. P., Shaffer, G., Ridgwell, A., Zeng, N., and Zhao, F.: Long-term Climate Change Commitment and Reversibility: An EMIC Intercomparison, J. Climate, in press, 2012.

5.2.1   Technical informations

In this section some technical details are discussed, namely the preprocessing of the data in the model ensemble as well as the smoothing of the timeseries.

Data preprocessing

Although clearly specified in the experimental protocol, some modeling groups did not strictly apply the requested procedure of the pulse injection. Some pulses were released too early or too late, or the pulse was emitted during the year instead of at the beginning of the year. There were also groups which provided instantaneous values instead of annual mean values, therefore a regridding on a mid-year time-grid has been applied which approximates well annual mean values. These factors led to the problem that IRF_{CO_2} of the individual models did not reach its maximum in 2015, i.e. the first years after the pulse release. The time axes were then shifted so all that all models showed a maximum IRF_{CO_2} in the annual mean of 2015 (i.e. denoted as "2015.5" or "0.5 yr after the pulse"). The result of this procedure is shown in Fig. 5.1.
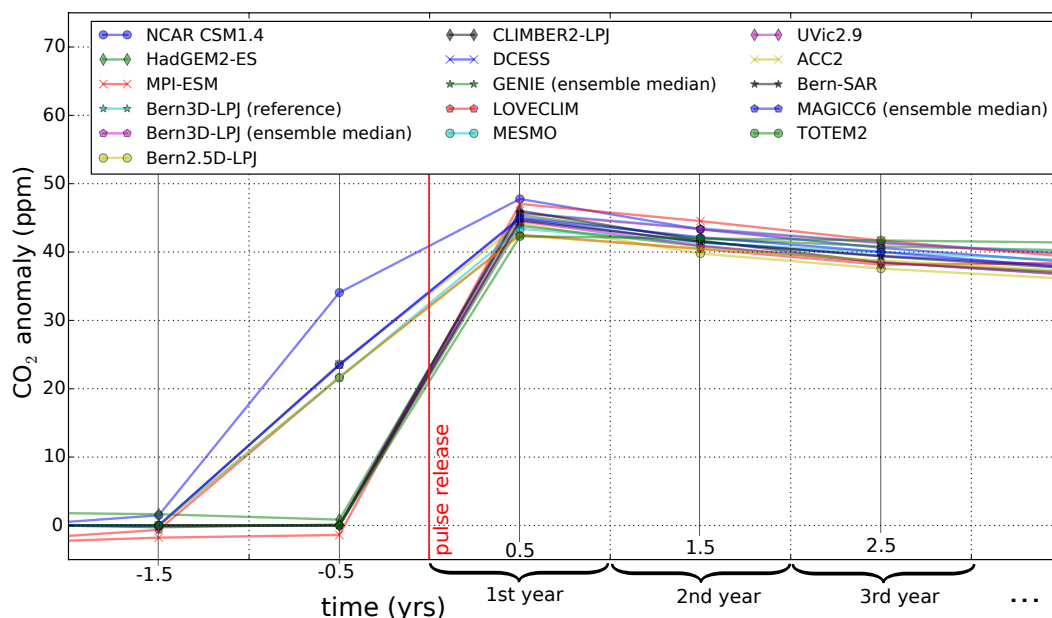

Figure 5.1: Alignment of the timeseries: the data has been aligned such that the maximum annual mean airborne fraction is in the first year after the pulse release, corresponding to the year "0.5" on the annual-mean time grid (i.e. year 2015.5 AD in the PD100 experiment).

Smoothing of the IRFs

After the alignment of the timeseries, different smoothing techniques have been tested and evaluated. The idea behind this is that variability in the model response should be removed without influencing the actual model response. The problem is that IRF_{CO_2} declines very fast shortly after the pulse injection. A normal filter (having a fixed "width") would be either too strong in the first years or ineffective afterwards. Therefore a filter has been designed based on smoothing splines (Enting, 1987) which has different cut-off periods, i.e. a short period at the beginning and a long period thereafter. Combining 5 different timescales with cut-off periods of 4, 20, 50, 250 and 500 yr for the period from year 0 to 10, 10 to 50, 50 to 100, 100 to 300 and 300 to 1000, respectively. The effect of this filter is demonstrated in Fig. 5.2 for the 4 models showing the highest internal variability. The other model's response (i.e. most EMICs) are

already smooth enough such that the filter has no visible effect on the IRF_{CO_2}. As a comparison, a smoothing spline with a single cut off (50 yr) is shown in Fig. 5.2 (blue dashed line).
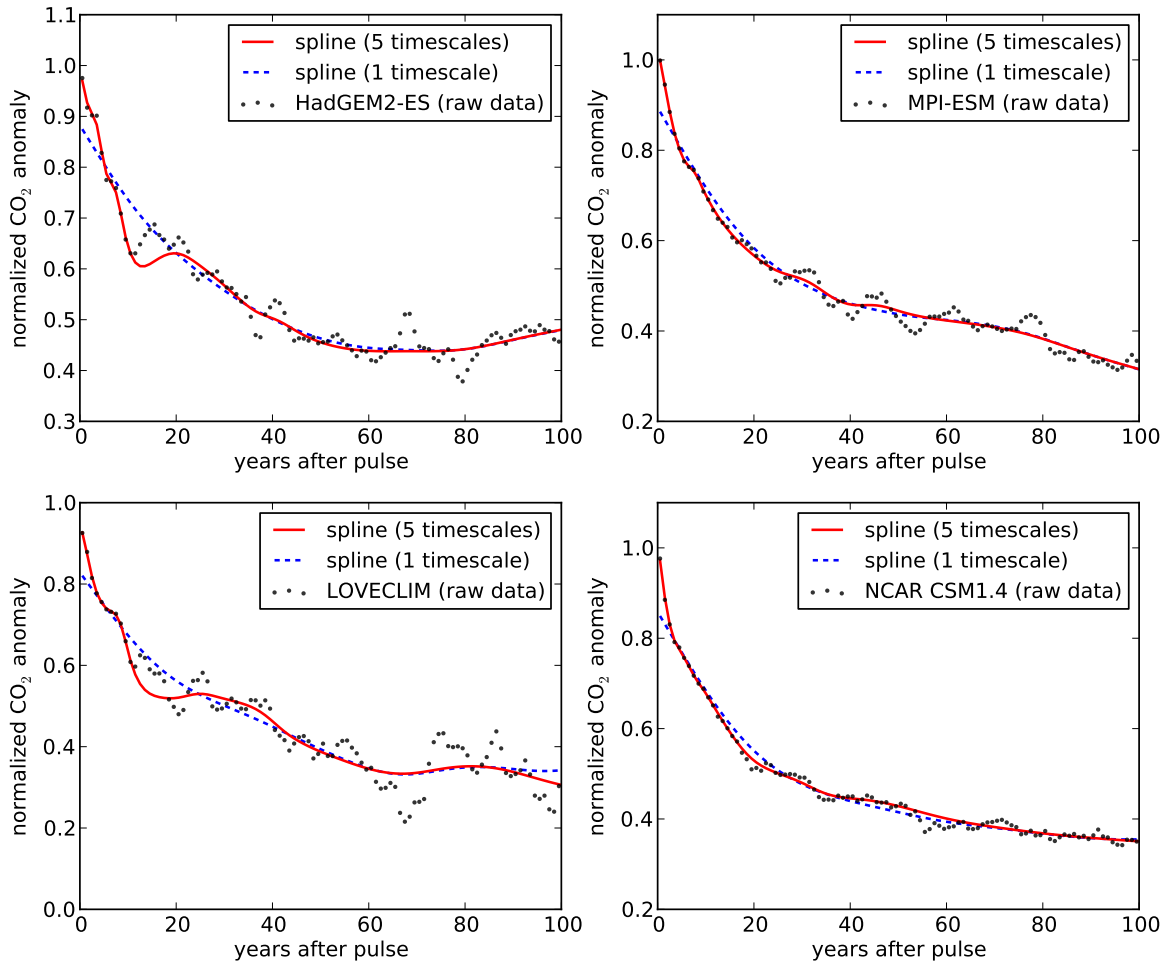

Figure 5.2: Filtering of the model output of the normalized CO_2 perturbation at the example of 4 models having a high variability. Black dots: raw data, blue dashed line: smoothing spline with only one timescale (50 yr cut off) and red: the filter based on smoothing splines with 5 different smoothing timescales as used in Joos et al. (2013).

5.2.2 Supplementary results to: Carbon dioxide and climate impulse response functions for the computation of greenhouse gas metrics: a multi-model analysis

The content of this section (5.2.2) is partially identical with the supplementary informations to Joos et al. (2013).

Fitting of IRF_{CO_2}

The IRF_{CO_2} of the individual models as well as the multi-model mean IRF_{CO_2} are fitted with simple analytical expressions. This has the advantage that the models can be "emulated" (e.g. in IAMs) just by using an analytical expressions and the corresponding fit parameters.

Responses in CO_2 for the $100\,Gt\,C$ emission pulse added to a constant background of 389 ppm (PD100 case) are fitted by a sum of exponentials:

$$IRF_{CO_2}(t) = a_0 + \sum_{i=1}^{3} a_i \cdot \exp\left(\frac{-t}{\tau_i}\right) \qquad \text{for } 0 \leq t \leq \text{nryears} \tag{5.1}$$

For IRF_{CO_2} the constraints are applied that the $\sum_{i=0}^{3} a_i = 1$ and $a_i > 0 \quad \forall i$. This ensures that IRF_{CO_2} is 1 for $t = 0$. The same equation was also used to fit the responses of the other variables (cumulative F_{as} and F_{ab}, SAT, iSAT, SSLR and OHC) but using only the side condition $a_0 = -\sum_{i=1}^{3} a_i$. This ensures that the IRF is 0 for $t = 0$ and can exceed 1 (as their IRFs are not normalized).

Note that the fits only apply to the period from 0 to nryears, where nryears is the number of available output $\leq 1000\,yr$.
The mean relative error, mre (reported in ‰) is calculated from annual values:

$$\text{mre} = \frac{1}{\text{nryears}} \sum_{i=1}^{\text{nryears}} \frac{|f_i - m_i|}{m_i} \cdot 1000‰ \tag{5.2}$$

where f_i are the annual data from the fit and m_i from the model output.

Optimization procedure

The model results (CO_2, SAT, SSLR, ...) are fitted using a least-square optimization module from Scipy (Jones et al., 2001). `Scipy.optimize.leastsq` is a wrapper around `MINPACK`'s lmdif and lmder algorithms to be used in Python. As the function to be minimized (i.e. the rhs of Eq. 5.1) is 7-dimensional, the global optimum is not trivial to find especially if IRF_{CO_2} is "noisy" due to internal variability of GCMs. Additional information on the fitting procedure including an example script to fit the multi-model mean CO_2 response is provided in Appendix F.

In Tab. 5.1, the fitting coefficients of all participating models are listed; the comparison between raw data (i.e. yearly model output) and fitted response is shown in Fig. 5.3

The effect of the climate-carbon feedback

An additional experiment has been set up with the Bern3D-LPJ model in order to quantify the contribution of the climate-carbon feedback, that is the effect of the warming induced by the air-borne CO_2 pulse on the ocean- and land-uptake of CO_2. Although IRF_{CO_2} mainly characterizes the model's carbon-concentration feedback (β, see Chap. 1), IRF_{CO_2} is also influenced by the climate-carbon feedback (γ).
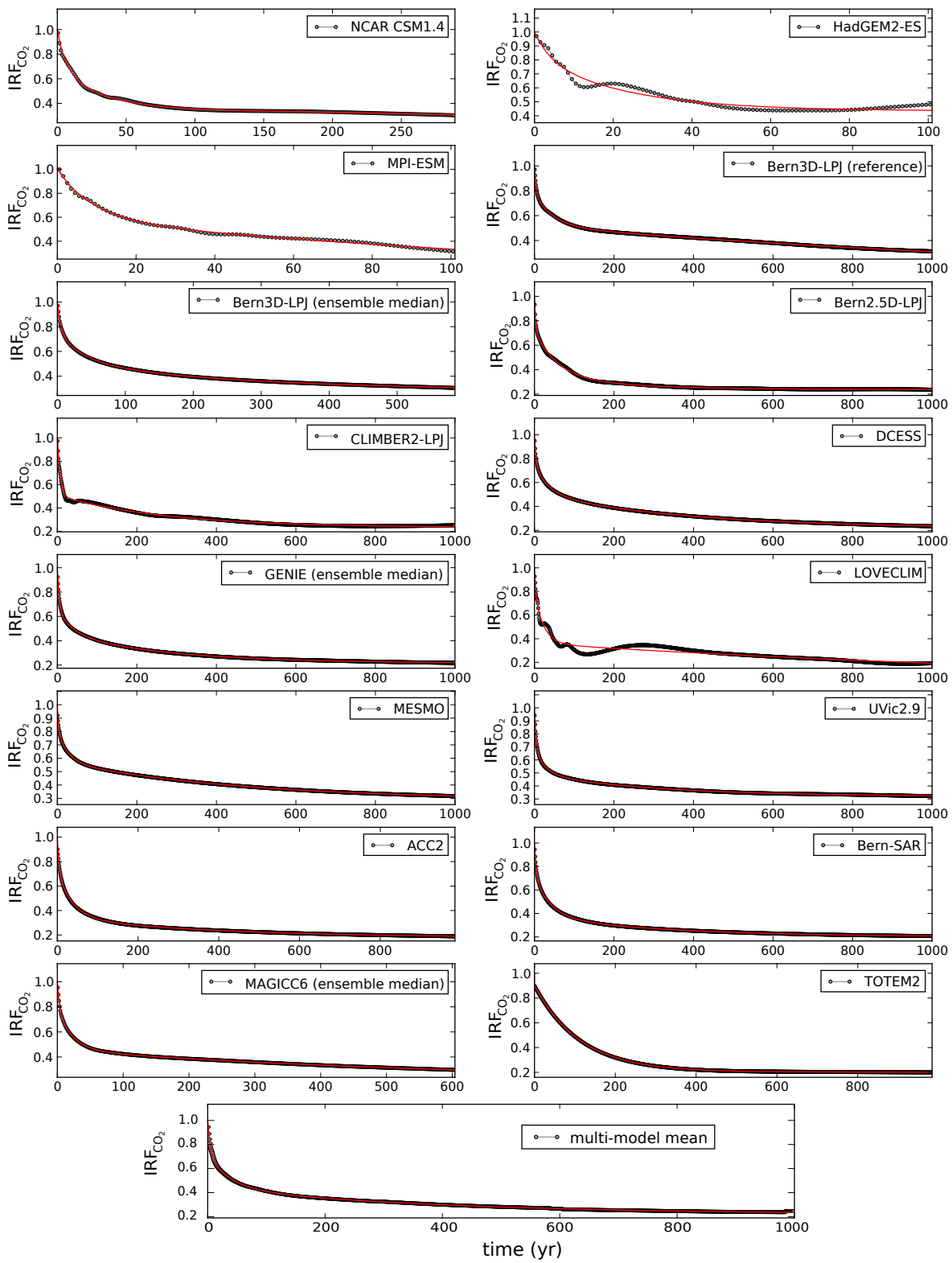
Figure 5.3: Responses in IRF$_{CO_2}$ from individual models (black) and corresponding fits (red).

model	nryears	mre	a_0	a_1	a_2	a_3	τ_1	τ_2	τ_3
NCAR CSM1.4	289	11	2.94E-007	3.67E-001	3.54E-001	2.79E-001	1.69E+003	2.84E+001	5.32E+000
HadGEM2-ES	101	40	4.34E-001	1.97E-001	1.89E-001	1.80E-001	2.31E+001	2.31E+001	3.92E+000
MPI-ESM	101	16	1.25E-007	5.86E-001	1.83E-001	2.31E-001	1.78E+002	9.04E+000	8.99E+000
Bern3D-LPJ (reference)	1000	5	6.35E-010	5.15E-001	2.63E-001	2.22E-001	1.96E+003	4.58E+001	3.87E+000
Bern3D-LPJ (ensemble)	585	3	2.80E-001	2.38E-001	2.38E-001	2.44E-001	2.76E+002	3.85E+001	4.93E+000
Bern2.5D-LPJ	1000	9	2.36E-001	9.87E-002	3.85E-001	2.80E-001	2.32E+002	5.85E+001	2.59E+000
CLIMBER2-LPJ	1000	20	2.32E-001	2.76E-001	4.90E-001	2.58E-003	2.73E+002	6.69E+000	6.69E+000
DCESS	1000	4	2.16E-001	2.91E-001	2.41E-001	2.52E-001	3.80E+002	3.63E+001	3.40E+000
GENIE (ensemble)	1000	5	2.15E-001	2.49E-001	1.92E-001	3.44E-001	2.70E+002	3.93E+001	4.31E+000
LOVECLIM	1000	58	8.54E-008	3.61E-001	4.50E-001	1.89E-001	1.60E+003	2.17E+001	2.28E+000
MESMO	1000	1	2.85E-001	2.94E-001	2.38E-001	1.83E-001	4.54E+002	2.50E+001	2.01E+000
UVic2.9	1000	4	3.19E-001	1.75E-001	1.92E-001	3.15E-001	3.05E+002	2.66E+001	3.80E+000
ACC2	985	4	1.78E-001	1.65E-001	3.80E-001	2.77E-001	3.86E+002	3.69E+001	3.72E+000
Bern-SAR	1000	3	1.99E-001	1.76E-001	3.45E-001	2.79E-001	3.33E+002	3.97E+001	4.11E+000
MAGICC6 (ensemble)	604	1	2.05E-001	2.53E-001	3.32E-001	2.10E-001	5.96E+002	2.20E+001	3.00E+000
TOTEM2	984	2	7.18E-006	2.03E-001	7.00E-001	9.74E-002	8.58E+004	1.12E+002	1.58E-002
multi-model mean	1000	6	2.17E-001	2.24E-001	2.82E-001	2.76E-001	3.94E+002	3.65E+001	4.30E+000

Table 5.1: Coefficients to fit model responses in CO_2 (IRF_{CO_2}) for the PD100 case. The mean relative error (mre) is given in permil.

This is of interest because for the IRFs of other GHGs, this feedback is normally not included: in a "ideal" experiment for a substance X, a pulse emission of X would trigger an ocean and land loss of carbon as $\gamma < 0$ (Arora et al., 2013) and the total radiative forcing (and thus GWP) of X would by the sum of the direct RF of X plus the indirect RF stemming from the liberated CO_2. In practise, this climate-carbon feedback is not included for non-CO_2 gases and therefore their GWP is underestimated.

As expected, the results with the Bern3D-LPJ show that the additional warming hampers the CO_2 removal from the atmosphere (Fig. 5.4), especially due to enhanced SST and lower CO_2 solubility in the ocean and higher soil turnover rates on land. The resulting coefficients for the IRF_{CO_2} fit are tabulated in Tab. 5.2. The effect of climate-carbon feedbacks on AGWP is discussed in Sect. 4.4.3 in Joos et al. (2013)
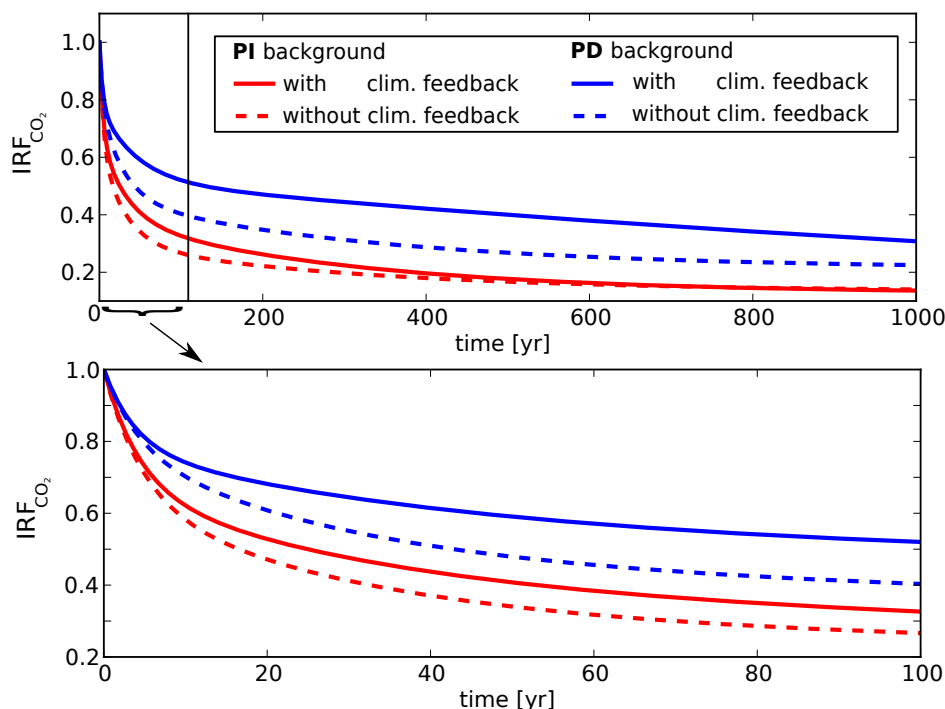

Figure 5.4: Top: comparison of IRF_{CO_2} of the 100 Gt C pulse for a setup with (solid) and without (dashed) climate-carbon feedback for present day (PD) and preindustrial (PI) conditions for the first 1000 years after the pulse release. **Bottom**: same for the first 100 years.

	nryears	mre	a_0	a_1	a_2	a_3	τ_1	τ_2	τ_3
PI100									
With climate feedback	1000	4	1.27E-001	2.61E-001	2.91E-001	3.22E-001	3.03E+002	3.16E+001	4.24E+000
Without climate feedback	1000	3	1.33E-001	1.66E-001	3.45E-001	3.55E-001	3.13E+002	3.00E+001	4.60E+000
PD100									
With climate feedback	1000	5	6.35E-010	5.15E-001	2.63E-001	2.22E-001	1.96E+003	4.58E+001	3.87E+000
Without climate feedback	1000	0.02	2.12E-001	2.44E-001	3.36E-001	2.07E-001	3.36E+002	2.79E+001	4.06E+000

Table 5.2: Coefficients to fit model responses in CO_2 (IRF_{CO_2}) for the PI100 and PD100 cases with and without climate feedbacks and for the Bern3D-LPJ(reference). The mean relative error (mre) is given in permil.

Conservation of carbon

Next it is checked how the participating models perform in terms of conservation of the emitted carbon. Figure 5.5 shows the evolution of the total pulse-carbon (C_{pulse}) in the system, i.e.

$$C_{pulse}(t) = \Delta CO_2(t) \times 2.123 + \sum_{t'=0}^{t} \Delta F_{as}(t') + \sum_{t'=0}^{t} \Delta F_{ab}(t') \tag{5.3}$$

where Δ denotes the anomaly in the pulse experiment w.r.t. the control-run and t the time since the pulse has been injected. Ideally, $C_{pulse}(t) = 100\,Gt\,C$ for $t > 0$ but most models show some discrepancy of a few %. The Bern3D-LPJ (as well as other models) shows a characteristic decline in the first 5–10 years. The reason for this seem to be the asynchronous calculation between fluxes and inventories within the model time-stepping: in a given timestep, the atmospheric transport-equation considers F_{as} based on ΔpCO_2 of the last timestep, but for the diagnostic of the annual mean F_{as} the updated values are used. This is especially a problem in the first years when F_{as} changes most between two timesteps. We note that this is solely a problem in the diagnostics of the model, as carbon is conserved in the model between individual timesteps.
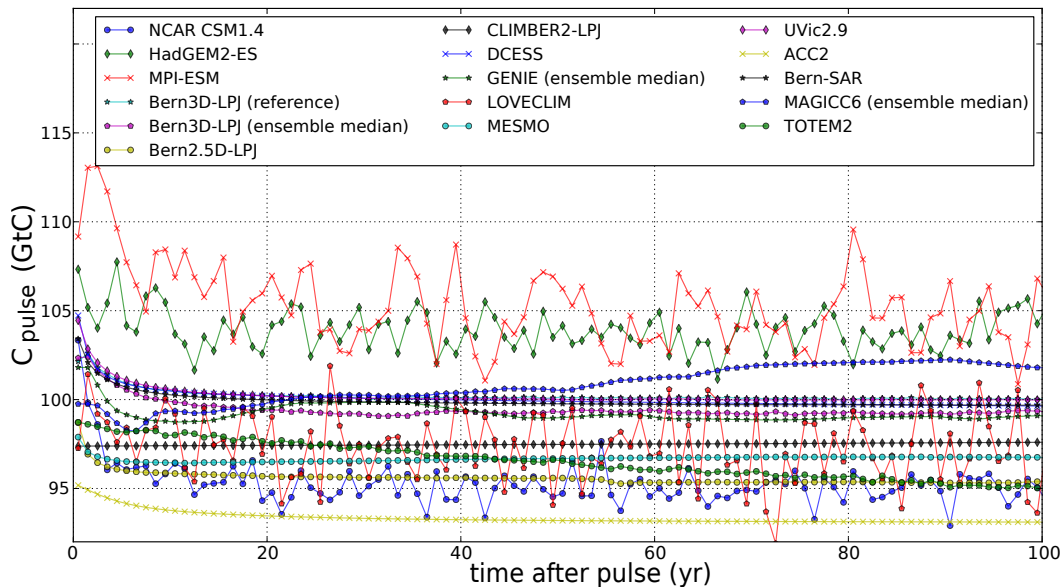

Figure 5.5: Conservation of carbon in the $100\,Gt\,C$ PD experiment for all model using the *unsmoothed* timeseries for the first 100 years after the pulse release.

5.3 Longterm response to a CO$_2$ pulse: the role of the weathering feedback

The Bern3D-LPJ, as well as most other models participating in Joos et al. (2013) do not include a weathering feedback, that is, a climate-dependent weathering/riverine input of tracers. This is justified as these processes are thought to play an important role only on multi-millennia timescales (see e.g. Archer et al., 2009, for a review). However, this feedback is crucial because it is the mechanism which ultimately neutralizes[3] (anthropogenic) CO$_2$ perturbations (Archer et al., 2009).

In this, section the "0D" (i.e. globally averaged) implementation of the carbonate- and silicate-weathering feedbacks as proposed in Colbourn et al. (2013) are incorporated in the Bern3D-LPJ and tested by the means of an instantaneous release of $1000\,\mathrm{Gt\,C}$ and $5000\,\mathrm{Gt\,C}$ of CO$_2$. The effect on IRF$_{\mathrm{CO_2}}$ and the AGWP$_{\mathrm{CO_2}}$ is then quantified.

In a first step, the given weathering rates as determined from the global sedimentation budget during a spinup have to be attributed to certain processes, namely the pathway in which they re-enter the atmosphere-ocean system after they have been buried at the seafloor. As the model of Colbourn et al. (2013) only considers the inorganic burial-weathering cycle, the organic cycle (subscript org) and inorganic contributions to the weathering rates have first to be separated in the Bern3D. We can then write the steady-sate weathering fluxes of DIC (F_{DIC}) and alkalinity (F_{Alk}):

$$
\begin{aligned}
F_{\mathrm{DIC}} &= F_{\mathrm{CaCO_3}}^{\mathrm{burial}} + F_{\mathrm{POC}}^{\mathrm{burial}} && (5.4)\\
&= F_{\mathrm{volc}} + F_{\mathrm{CaCO_3}}^{\mathrm{weathering}} + F_{\mathrm{org}}^{\mathrm{weathering}} && (5.5)
\end{aligned}
$$

$$
\begin{aligned}
F_{\mathrm{Alk}} &= 2 \cdot F_{\mathrm{CaCO_3}}^{\mathrm{burial}} + \mathcal{R}_{\mathrm{Alk:P}} \cdot F_{\mathrm{POC}}^{\mathrm{burial}} && (5.6)\\
&= 2 \cdot F_{\mathrm{CaSiO_3}}^{\mathrm{weathering}} + 2 \cdot F_{\mathrm{CaCO_3}}^{\mathrm{weathering}} + \mathcal{R}_{\mathrm{Alk:P}} \cdot F_{\mathrm{org}}^{\mathrm{weathering}}, && (5.7)
\end{aligned}
$$

where the subscripts CaCO$_3$ and CaSiO$_3$ denotes carbonate and silicate weathering processes, F_{volc} the volcanic emissions of CO$_2$ and $\mathcal{R}_{\mathrm{Alk:P}}$ the Redfield ratio of alkalinity in organic matter (being set to -16/117 in the Bern3D). The weathering fluxes are then allowed to vary as a function of the steady-state fluxes (subscript 0), atmospheric temperature (SAT) and atmospheric CO$_2$:

$$
F_{\mathrm{CaCO_3}}^{\mathrm{weathering}} = \overbrace{F_{\mathrm{CaCO_3},0}}^{\text{steady state weathering rate}} \cdot \overbrace{(1 + k_{\mathrm{Ca}} \cdot (\mathrm{SAT\text{-}SAT_0}))}^{\text{temperature feedback}}
$$
$$
\cdot \underbrace{(1 + k_{\mathrm{run}} \cdot (\mathrm{SAT\text{-}SAT_0}))}_{\text{runoff feedback}} \cdot \underbrace{2\frac{\mathrm{CO_2}}{\mathrm{CO_{2,0}}}/(1.0 + \frac{\mathrm{CO_2}}{\mathrm{CO_{2,0}}})^{\epsilon_p}}_{\text{productivity feedback}} \qquad (5.8)
$$

$$
F_{\mathrm{CaSiO_3}}^{\mathrm{weathering}} = \overbrace{F_{\mathrm{CaSiO_3},0}}^{\text{steady state weathering rate}} \cdot \overbrace{e^{k_{\mathrm{T}} \times (\mathrm{SAT\text{-}SAT_0})}}^{\text{temperature feedback}}
$$
$$
\cdot \underbrace{(1 + k_{\mathrm{run}} \cdot (\mathrm{SAT\text{-}SAT_0}))^{\epsilon_r}}_{\text{runoff feedback}} \cdot \underbrace{2\frac{\mathrm{CO_2}}{\mathrm{CO_{2,0}}}/(1.0 + \frac{\mathrm{CO_2}}{\mathrm{CO_{2,0}}})^{\epsilon_p}}_{\text{productivity feedback}}, \qquad (5.9)
$$

---

[3]Without a weathering feedback from the lithosphere, the airborne fraction of CO$_2$ emissions will always stabilize on a level > 0, even with ocean-sediments interactions are included by the model.

with a best-guess set of parameters as suggested in Colbourn et al. (2013): $k_{\text{Ca}} = 0.049$, $k_{\text{run}} = 0.025$, $k_{\text{T}} = 0.09$, $\epsilon_p = 0.4$ and $\epsilon_r = 0.65$. Note that for simplicity, the productivity and runoff-feedbacks have been parametrized as a function of global mean temperature and CO$_2$.

Application of the model

The experimental setup corresponds to the preindustrial (PI) setup in Joos et al. (2013) except that the LPJ model was not activated in order to make the model computationally more efficient. First, fluxes have to be attributed to different processes: The organic cycle is given by the amount of PO$_4$ buried in the spinup and is $0.187\,\text{Gt}\,\text{C}\,\text{yr}^{-1}$. The inorganic contributions are then set to $0.101\,\text{Gt}\,\text{C}\,\text{yr}^{-1}$, $0.105\,\text{Gt}\,\text{C}\,\text{yr}^{-1}$ and $0.107\,\text{Gt}\,\text{C}\,\text{yr}^{-1}$ for $F_{\text{CaSiO}_3}^{\text{weathering}}$, $F_{\text{CaCO}_3}^{\text{weathering}}$ and F_{volc} to close the models DIC and Alk budgets given by Eqs. 5.5 and 5.7[4]. Note that the constraint $F_{\text{volc}} = F_{\text{CaSiO}_3}$ given in Colbourn et al. (2013) could not be exactly fulfilled without violating the total tracer budget in the Bern3D.

Different setups of the model have then been forced with a 1000 Gt C and a 5000 Gt C pulse release to examine the effect of the CaCO$_3$ and CaSiO$_3$ weathering parametrization. The standard setup with sediment interactions but with constant weathering rates as used in Joos et al. (2013) is denoted as SED. SED+CA is the setup with CaCO$_3$ weathering feedback, SED+SI with CaSiO$_3$ feedback and SED+CA+SI with both feedbacks active. In addition, a setup without sediment model was run (CLO). Climate is allowed to change during the experiment depending to the radiative forcing of the airborne pulse-CO$_2$ according to Myhre et al. (1998). In all open setups, the weathering rate related to the organic cycle is set constant, but it is suggested that changes in e.g. the PO$_4$ weathering rate should also be taken into account in the future.

Results

First, we focus on the ocean's DIC and Alk budgets and inventories which are displayed in Fig. 5.6. Note that on such long timescales model drift becomes apparent, especially in the inventories. To correct for drift, a 20 kyr control simulation was run for all the setups which was then used to fit a linear trend to the drift. This trend was then subtracted from the perturbation experiments. In the experiment SED, weathering rates are kept constant. Seafloor CaCO$_3$ is dissolved as a response to the increased ocean pH and shoaling of the lysocline (not shown). This pulse of CaCO$_3$ dissolution and transient imbalance between weathering and sedimentation leads to a net increase in the Alk inventory. After $\sim$50 kyr the oceanic Alk budget — given by *deposition* − *redissolution* at the ocean-sediment interface — is balanced again. But both DIC and Alk inventories stabilize on a higher level than before the pulse, leaving a finite airborne fraction of CO$_2$ (e.g. Archer et al., 1998; Tschumi, 2009) which is shown in Fig. 5.7. In the same figure, the CO$_2$ response of the closed system is shown. Without CaCO$_3$-neutralization the inventory of Alk is conserved as air-sea gas exchange of CO$_2$ does not alter Alk (because CO$_2$ is not charged). This leads to a higher airborne fraction in CLO than SED. The airborne fraction itself is a function of the pulse size due to the non-linear carbonate chemistry in the seawater.

When activating the CaCO$_3$ weathering feedback, both F_{Alk} and F_{DIC} increase in a 2:1 ratio according to the parametrizations given in Eq. 5.8. This has only a minor influence on the carbonate system although $\text{CO}_3^{2-} \approx \text{Alk–DIC}$ is increased, but overall the depth of the lysocline does not change significantly compared to SED. The airborne fraction of CO$_2$ stays finite at a slightly lower value than SED.

Which process allows the system to relax back in the original state? The answer is somewhat counter-intuitive: the experiment SED+SI leads to higher Alk sedimentation rates by increasing the Alk weathering input, but not the DIC input. This additional Alk flux deepens the lysocline such that after $\sim$20 kyr the sedimentation of Alk and DIC exceed the weathering input. In other

---

[4]The solution of the budget eqautions are not unique, there are other possible combinations of fluxes.

words: the increased Alk weathering flux does remove Alk from the ocean in the long run. This leads to a relaxation of all variables to their initial values after ∼300–500 kyr. Activating both feedbacks as in SED+CA+SI leads to an increase in the Alk and DIC weathering rates of ≈2:1 and does not differ much from SED+SI. This clearly highlights the importance of the silicate weathering feedback in regulating atmospheric CO$_2$ on geological timescales.
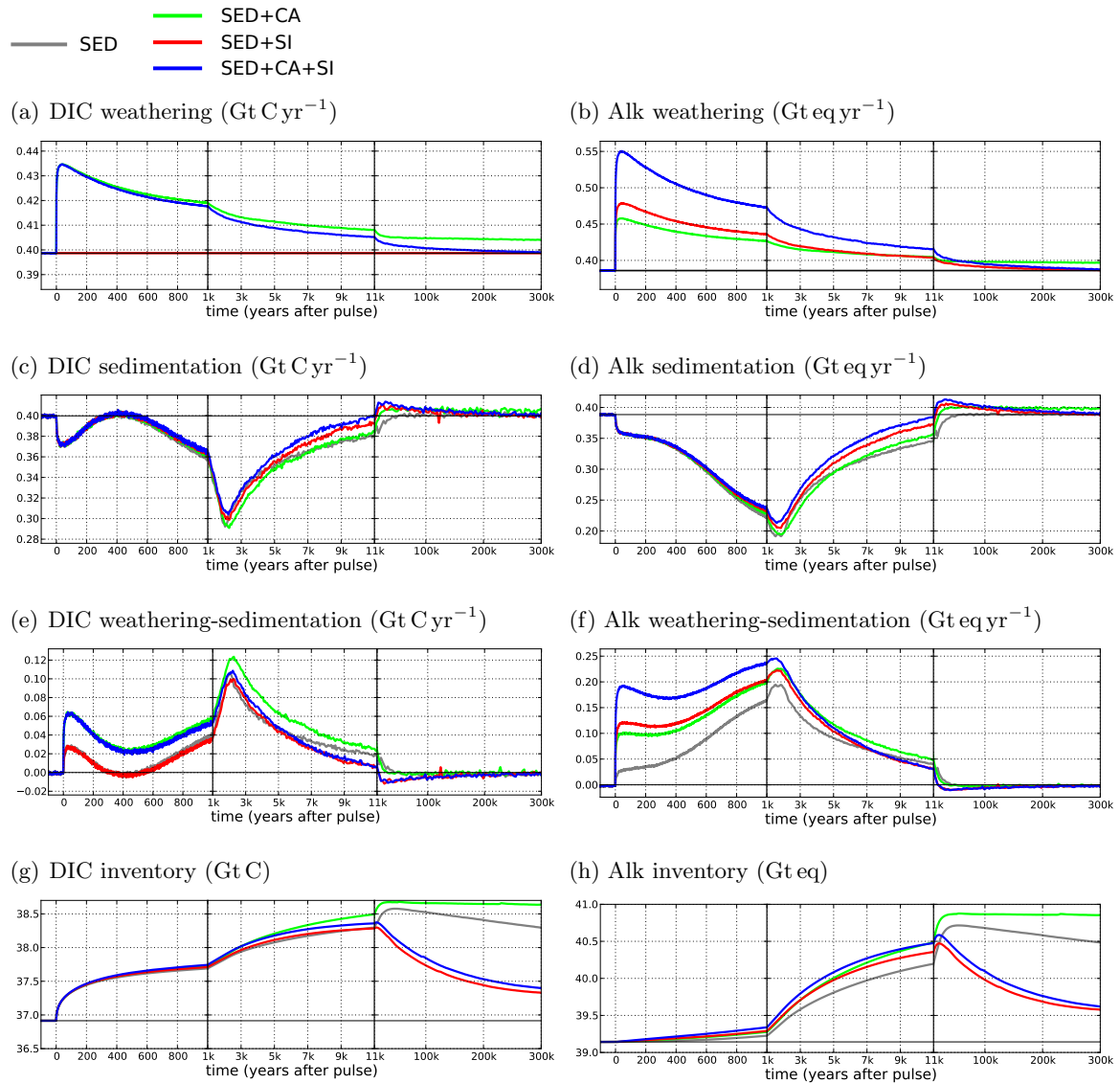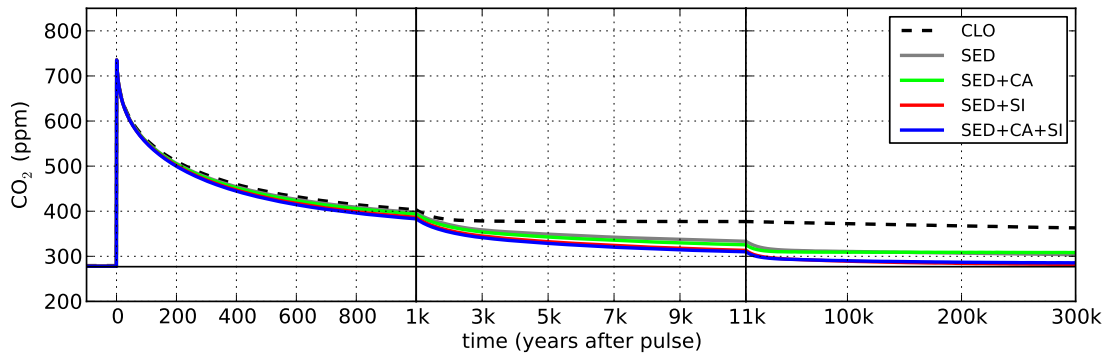

Figure 5.6: Ocean-sediment response to a 1000 Gt C pulse for DIC **(a,c,e,g)** and Alk **(b,d,f,h)** for different setups: open system without weathering feedback (SED), with CaCO$_3$ weathering feedback (SED+CA), with CaSiO$_3$ weathering feedback (SED+SI) and with both feedbacks (SED+CA+SI). Sedimentation is computed as *deposition − redissolution* at the ocean-sediment interface and temporarily different from the sedimentation-flux. The baseline fluxes are indicated by a black horizontal line.

What are the consequences of this for IRF$_{CO_2}$ and time-integrated IRF$_{CO_2}$ (and thus AGWP)? In Table 5.3 the corresponding values are listed for the time horizons 100 yr, 1,000 yr and 10,000 yr. The stated changes are given relative to SED, which is the setup used in Joos et al. (2013) ("Bern3D-LPJ (reference)"). Due to the long timescales involved in the weathering feedback, the 100 yr IRF$_{CO_2}$ and AGWP of the SED+CA+SI experiment are only marginally different from SED. For longer horizons, the differences become apparent with e.g. a 5.3% reduction of AGWP$_{1000}$ and the AGWP$_{10000}$ is even reduced by 23% when taken the weathering-feedback

into account. Note that the values in Tab. 5.3 slightly differ from those of the PI100 experiment in Joos et al. (2013) as the experimental setup is not identical. It must be stressed that these numbers only represent the tested 0D parametrization with only one parameter set. As shown by Colbourn et al. (2013), the application of the spatially resolved weathering model (2D) gives e.g. a rather different response, as well as other parameter combinations of the 0D-parametrization.

(a) 1000 Gt C pulse:

(b) 5000 Gt C pulse:
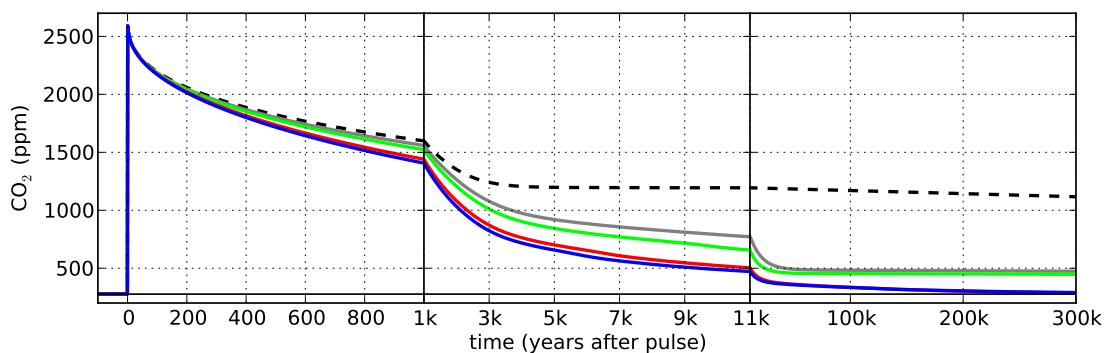
Figure 5.7: Atmospheric CO_2 response to a 1000 Gt C **(a)** and 5000 Gt C **(b)** emission pulse for different setups: closed system (CLO), open system without weathering feedback (SED), with $CaCO_3$ weathering feedback (SED+CA), with $CaSiO_3$ weathering feedback (SED+SI) and with both feedbacks (SED+CA+SI).

time horizon	100 yr	1000 yr	10000 yr
	IRF_{CO_2}		
CLO	0.593 (+0.94%)	0.263 (+4.0%)	0.208 (+71%)
SED	0.588	0.253	0.121
SED+CA+SI	0.580 (-1.3%)	0.223 (-12%)	0.072 (-41%)
	time-integrated IRF_{CO_2} (yr)		
CLO	70.3 (+0.59%)	396 (+2.1%)	2300 (+29%)
SED	69.9	388	1780
SED+CA+SI	69.5 (-0.57%)	367 (-5.3%)	1370 (-23%)

Table 5.3: IRF_{CO_2} and time-integrated IRF_{CO_2} of the 1000 Gt C pulse experiment for 3 different time horizons. The percentage changes given in parenthesis are relative to SED. To get the AGWP, the time-integrated IRF_{CO_2} has to be multiplied with $1.77 \cdot 10^{-15} \, W \, m^{-2} \, kg\text{-}CO_2^{-1}$.

Bibliography

Archer, D., Eby, M., Brovkin, V., Ridgwell, A., Cao, L., Mikolajewicz, U., Caldeira, K., Matsumoto, K., Munhoven, G., Montenegro, A., & Tokos, K., 2009. Atmospheric Lifetime of Fossil Fuel Carbon Dioxide, *Ann. Rev. Earth and Planet. Sci.*, 37(1), 117–134.

Archer, D., Kheshgi, H., & Maier-Reimer, E., 1998. Dynamics of fossil fuel CO2 neutralization by marine CaCO3, *Global Biogeochem. Cy.*, 12(2), 259–276.

Arora, V. K., Boer, G. J., Friedlingstein, P., Eby, M., Jones, C. D., Christian, J. R., Bonan, G., Bopp, L., Brovkin, V., Cadule, P., Hajima, T., Ilyina, T., Lindsay, K., Tjiputra, J. F., & Wu, T., 2013. Carbon–Concentration and Carbon–Climate Feedbacks in CMIP5 Earth System Models, *J. Climate*, 26(15), 5289–5314.

Colbourn, G., Ridgwell, A., & Lenton, T. M., 2013. The Rock Geochemical Model (RokGeM) v0.9, *Geosci. Model Dev.*, 6(5), 1543–1573.

Enting, I. G., 1987. On the use of smoothing splines to filter CO_2 data, *J. Geophys. Res.*, 92(D9), 10977–10984.

Forster, P., Ramaswamy, V., Artaxo, P., Berntsen, T., Betts, R. A., Fahey, D. W., Haywood, J., Lean, J., Lowe, D. C., Myhre, G., Nganga, J., Prinn, R., Raga, G., Schulz, M., & Dorland, R. V., 2007. Chapter 2: Changes in atmospheric constituents and in radiative forcing, in *Climate Change 2007: The Physical Science Basis. Contribution of Working Group I to the Fourth Assessment Report of the Intergovernmental Panel on Climate Change*, eds Solomon, S., Qin, D., Manning, M., Chen, Z., Marquis, M., Averyt, K., Tignor, M., & Miller, H., Cambridge Univ. Press, United Kingdom and New York, NY, USA.

Jones, E., Oliphant, T., Peterson, P., et al., 2001. SciPy: Open source scientific tools for Python.

Joos, F., Roth, R., Fuglestvedt, J. S., Peters, G. P., Enting, I. G., von Bloh, W., Brovkin, V., Burke, E. J., Eby, M., Edwards, N. R., Friedrich, T., Frölicher, T. L., Halloran, P. R., Holden, P. B., Jones, C., Kleinen, T., Mackenzie, F. T., Matsumoto, K., Meinshausen, M., Plattner, G.-K., Reisinger, A., Segschneider, J., Shaffer, G., Steinacher, M., Strassmann, K., Tanaka, K., Timmermann, A., & Weaver, A. J., 2013. Carbon dioxide and climate impulse response functions for the computation of greenhouse gas metrics: a multi-model analysis, *Atmos. Chem. Phys.*, 13(5), 2793–2825.

Myhre, G., Highwood, E. J., Shine, K. P., & Stordal, F., 1998. New estimates of radiative forcing due to well mixed greenhouse gases, *Geophys. Res. Lett.*, 25(14), 2715–2718.

Myhre, G., Shindell, D., Bréon, F.-M., Collins, W., Fuglestvedt, J., Huang, J., Koch, D., Lamarque, J.-F., Lee, D., Mendoza, B., Nakajima, T., Robock, A., G., S., Takemura, T., & Zhang, H., 2013. Chapter 8: Anthropogenic and Natural Radiative Forcing, in *Climate Change 2013: The Physical Science Basis. Working Group I Contribution to the Fifth Assessment Report of the Intergovernmental Panel on Climate Change*, Final Draft, 7. June 2013.

Tschumi, T., 2009. *Modeling the Ocean's Contribution to Past and Future Changes in Global Carbon Cycling*, PhD thesis, University of Bern.

Chapter 6

Future terrestrial greenhouse-gas feedbacks

6.1 Multiple greenhouse-gas feedbacks from the land biosphere under future climate change scenarios

Benjamin D. Stocker*, Raphael Roth*, Fortunat Joos, Renato Spahni, Marco Steinacher, Soenke Zaehle, Lex Bouwman, Xu-Ri and Iain Colin Prentice

* equally contributing authors

Multiple greenhouse-gas feedbacks from the land biosphere under future climate change scenarios

Benjamin D. Stocker[1,2]*, Raphael Roth[1,2], Fortunat Joos[1,2], Renato Spahni[1,2], Marco Steinacher[1,2], Soenke Zaehle[3], Lex Bouwman[4,5], Xu-Ri[6] and Iain Colin Prentice[7,8]

Atmospheric concentrations of the three important greenhouse gases (GHGs) CO_2, CH_4 and N_2O are mediated by processes in the terrestrial biosphere that are sensitive to climate and CO_2. This leads to feedbacks between climate and land and has contributed to the sharp rise in atmospheric GHG concentrations since pre-industrial times. Here, we apply a process-based model to reproduce the historical atmospheric N_2O and CH_4 budgets within their uncertainties and apply future scenarios for climate, land-use change and reactive nitrogen (Nr) inputs to investigate future GHG emissions and their feedbacks with climate in a consistent and comprehensive framework[1]. Results suggest that in a business-as-usual scenario, terrestrial N_2O and CH_4 emissions increase by 80 and 45%, respectively, and the land becomes a net source of C by AD 2100. N_2O and CH_4 feedbacks imply an additional warming of 0.4–0.5 °C by AD 2300; on top of 0.8–1.0 °C caused by terrestrial carbon cycle and Albedo feedbacks. The land biosphere represents an increasingly positive feedback to anthropogenic climate change and amplifies equilibrium climate sensitivity by 22–27%. Strong mitigation limits the increase of terrestrial GHG emissions and prevents the land biosphere from acting as an increasingly strong amplifier to anthropogenic climate change.

At present, the terrestrial biosphere is mitigating anthropogenic climate change by acting as a carbon (C) sink, compensating about 30% of global CO_2 emissions from fossil and land-use sources[2]. In contrast, 44–73% of global nitrous oxide (N_2O) emissions[3,4] and 24–43% of global methane (CH_4) emissions[5], both potent GHGs, originate from land ecosystems and partly offset the cooling effect of C uptake by the land. Terrestrial N_2O and CH_4 emissions, henceforth termed eN_2O and eCH_4, are enhanced in a warm climate[6,7] and under high atmospheric CO_2 concentrations (cCO_2; ref. 8). The associated feedback loop amplifies anthropogenic climate change and is reflected in palaeo records on glacial–interglacial and centennial timescales[9,10]. However, despite its potential importance[6] there is yet a lack of studies investigating combined multiple GHG feedbacks between terrestrial ecosystems and climate.

The strength of feedbacks between land and climate is determined by the sensitivity of the forcing agents (here: eN_2O; eCH_4; terrestrial C storage, ΔC; and Albedo change) to the drivers (climate and cCO_2), and the radiative efficiency of the respective forcing agent. Earlier quantifications of terrestrial GHG

feedbacks have relied on observational data and land-only models to derive the sensitivities, multiplied by the radiative efficiency[6,7,9–11]. Here, we assess multiple feedbacks from terrestrial ecosystems in a coupled Earth system model of intermediate complexity and follow a quantification framework commonly applied to measure the strength of physical climate feedbacks[1,12] (Fig. 1 and Methods). Applying future scenarios of N-deposition and N-fertilizer application in agriculture allows us to assess their impact on eN_2O and related feedbacks.

We start the discussion by exploring to which extent a process-based land biosphere model is able to reproduce the observation-based evolution of atmospheric N_2O and CH_4 concentrations (cN_2O, cCH_4) over the industrial period. Addressing the historical atmospheric GHG budgets serves as a test for the sensitivity of simulated GHG emissions to the combination of climate, cCO_2 and external forcings. LPX-Bern[13–18] is applied here to simulate the coupled cycling of carbon and nitrogen and the emissions of GHGs from agricultural and natural land and from peat. Site-scale evaluations of this model have been presented earlier[7,15–20]. For this test, we force LPX-Bern with observational data for climate[21], cCO_2 (ref. 22), Nr (N deposition[23] plus mineral N fertilizer inputs[24]) and anthropogenic land-use area change and combine simulated emissions with independent emission data from remaining sources to assess atmospheric budgets (see Methods and Supplementary Fig. S1).

For eN_2O, we confirm earlier results[24] showing that the simulated emission increase in the second half of the twentieth century matches measured concentrations (Fig. 2a). Experiments with incomplete driving factors perform worse at reproducing the observed rate of increase in the past four decades. The increase in atmospheric N_2O before AD 1920 is not captured, although an increasing manure source is prescribed. Climatic changes after the late-nineteenth-century temperature minimum are a potential driver not represented in the applied CRU climate forcing data[21].

The twentieth-century increase in cCH_4 is dominated by changes in prescribed sources (see Methods). Simulated changes in eCH_4 from boreal peatlands, inundated areas (natural and anthropogenic) and wet mineral soils remain comparably small over the industrial period. The magnitudes of these fluxes were scaled individually to match results of an atmospheric CH_4 transport inversion[19]. The small model response to twentieth-century climatic variations is consistent with the measured

[1]Climate and Environmental Physics, Physics Institute, University of Bern, 3012 Bern, Switzerland, [2]Oeschger Center for Climate Change Research, University of Bern, 3012 Bern, Switzerland, [3]Max Planck Institute for Biogeochemistry, Department for Biogeochemical Systems, 07745 Jena, Germany, [4]Department of Earth Sciences, Geochemistry, Faculty of Geosciences, Utrecht University, 3508 TA Utrecht, The Netherlands, [5]PBL Netherlands Environmental Assessment Agency, PO Box 303, 3720 AH Bilthoven, The Netherlands, [6]Laboratory of Tibetan Environment Changes and Land Surface Processes, Institute of Tibetan Plateau Research, Chinese Academy of Sciences, Beijing 100101, China, [7]Department of Biological Sciences, Macquarie University, North Ryde, New South Wales 2109, Australia, [8]Grantham Institute for Climate Change and Division of Ecology and Evolution, Imperial College, Silwood Park, Ascot SL5 7PY, UK. *e-mail: beni@climate.unibe.ch.
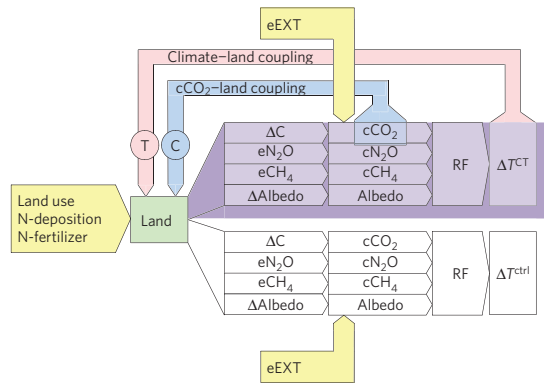
LETTERS

Figure 1 | Schematic of feedback loops and model set-up. Representing the fully coupled (purple background, superscript CT) and the control (uncoupled, white background, superscript ctrl) simulations. The evolution of land-use area and reactive nitrogen addition (N-deposition and N-fertilizer) is a prescribed input to the land model and the evolution of non-land biosphere-related, external emissions (eEXT) of N_2O, CO_2, CH_4 and other forcing agents (aerosols, precursors, CFCs, SF_6 and so on) is a prescribed input to the atmosphere module in both the coupled and uncoupled set-up as indicated by the yellow panels. The land model (green) simulates changes in land carbon stocks (ΔC) and the related net land-to-atmosphere CO_2 flux, terrestrial emissions of N_2O and CH_4 (eN_2O, eCH_4) and land surface Albedo changes (ΔAlbedo). These simulated changes, in combination with eEXT, yield the simulated atmospheric concentrations (cCO_2, cN_2O, cCH_4) and the surface Albedo, cause a radiative forcing (RF) and affect climate, here represented by the global mean temperature (ΔT), which scales spatial climate change anomaly patterns in Bern3D-LPX. Note that the prescribed emissions of reactive gases (CO, VOC, NO_x) affect cCH_4. Note also that even in the control set-up (ctrl), land use and Nr affect terrestrial GHG emissions, and eEXT is added and ΔT^{ctrl} is not zero. In the fully coupled set-up (CT), changes in the drivers, climate and cCO_2 relative to their pre-industrial state are communicated to the land model, whereas the land model sees none of these changes in the control set-up. In cCO_2–land coupled (C) and climate–land coupled (T) simulations only changes in one driver are communicated to the land model (see Supplementary Fig. S16). Results shown in Figs 4 and 5 are obtained by the set-up of the Bern3D-LPX model shown in here. In offline simulations for which results are shown in Figs 2 and 3, cCO_2 and climate change are not simulated, but prescribed (see Supplementary Fig. S17).

Figure 2 | Simulated and observed concentrations. a,b, Observed and simulated cN_2O (**a**) and cCH_4 (**b**). Observational N_2O data (grey) is from refs 22,33. Measurement precision ($\pm 1\sigma$) is given by vertical bars. The dashed grey line is a 200-yr cutoff spline through observational data. Observational CH_4 point data (grey) are from ref. 22 and represent Southern Hemispheric concentrations. The solid grey line (NEEM) is derived from Northern Hemispheric firn air data and includes seasonal variability[34]. The dashed grey line is a spline of observational Southern Hemisphere data. Simulation results (red) are from offline experiments where changes in climate, cCO_2 and Nr inputs are prescribed (standard), or where climate is held at pre-industrial levels (no climate change), cCO_2 is held constant at pre-industrial levels (no cCO_2) or Nr is held at pre-industrial levels (no Nr, see Supplementary Table S2). An oceanic N_2O source (3.3 Tg $N_2O - N$ yr^{-1}) and a constant geological CH_4 source (38 Tg CH_4 yr^{-1}), tuned to match RCP data in year AD 1900, are included.

atmospheric CH_4 record, but the small signal prevents any firm evaluation of the modelled sensitivity of eCH_4 to climate change (Fig. 2b). In conclusion, the model produces realistic global results for eN_2O and eCH_4 under plausible forcing.

Next, we assess the sensitivity of terrestrial GHG emissions to future climate, cCO_2, Nr and their combination for a stringent climate mitigation scenario that maintains the possibility of reaching the two-degree target (Representative Concentration Pathway (RCP) 2.6; ref. 25) and a high-emission/business-as-usual scenario (RCP8.5; ref. 26). Scenarios for land use, N-fertilizer and N-deposition each consistently follow socio-economic developments in the respective RCP (model inputs described in Supplementary Section S2). Climate is prescribed for each RCP using Climate Model Intercomparison Project 5 (CMIP5) output from ensemble simulations of five comprehensive climate models. This allows us to assess the influence of uncertainties in the climate evolution and in the scenario choice. Prescribed cCO_2, global temperatures and Nr inputs stabilize in RCP2.6, whereas in RCP8.5, they increase throughout the twenty-first century.
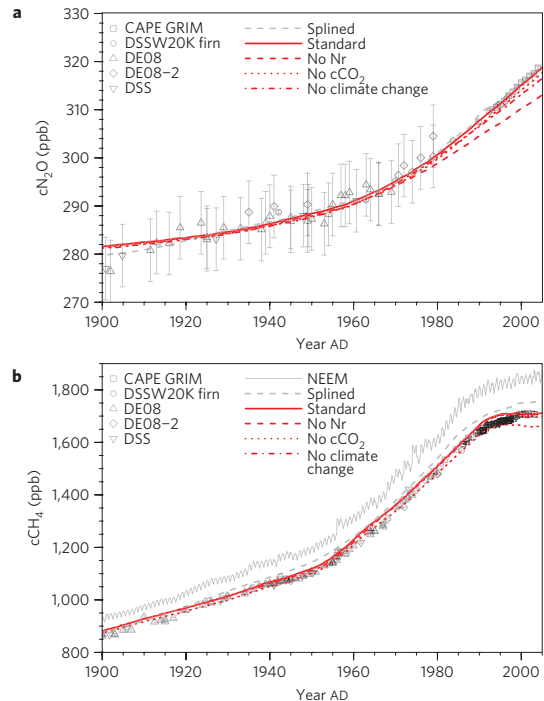
The combination and interactions of global warming, cCO_2 and external forcings (land-use change and anthropogenic Nr inputs) drive eN_2O up from a preindustrial level of 6.9 to 9.0 Tg N_2O–N yr^{-1} by today and to 9.8–11.1 (RCP2.6) and 14.2–17.0 Tg N_2O–N yr^{-1} by AD 2100 (RCP8.5, Fig. 3a). In RCP8.5, only 14–21% of this increase is due to external forcings alone (Fig. 3a, right panel, 'ctrl' stripe) Climate change and rising cCO_2 are responsible for the remaining amplification. Without Nr inputs, the amplification is reduced by 24–32% (Fig. 3a, right panel, empty bars).

eN_2O is governed by denitrification of reactive N in the soil, not taken up by the plant. Given sufficient nutrient availability, high cCO_2 tends to increase plant productivity, which ultimately feeds litter and soil decomposition. Warmer soil temperatures accelerate decomposition, making nutrients available for plant uptake but also increasing substrate availability for denitrification and eN_2O. Increased loads of reactive nitrogen from atmospheric deposition and on fertilized agricultural land are prone to temperature-driven denitrification, leaching to water streams and loss as N_2O. In our RCP8.5 simulations, the fraction of Nr inputs to
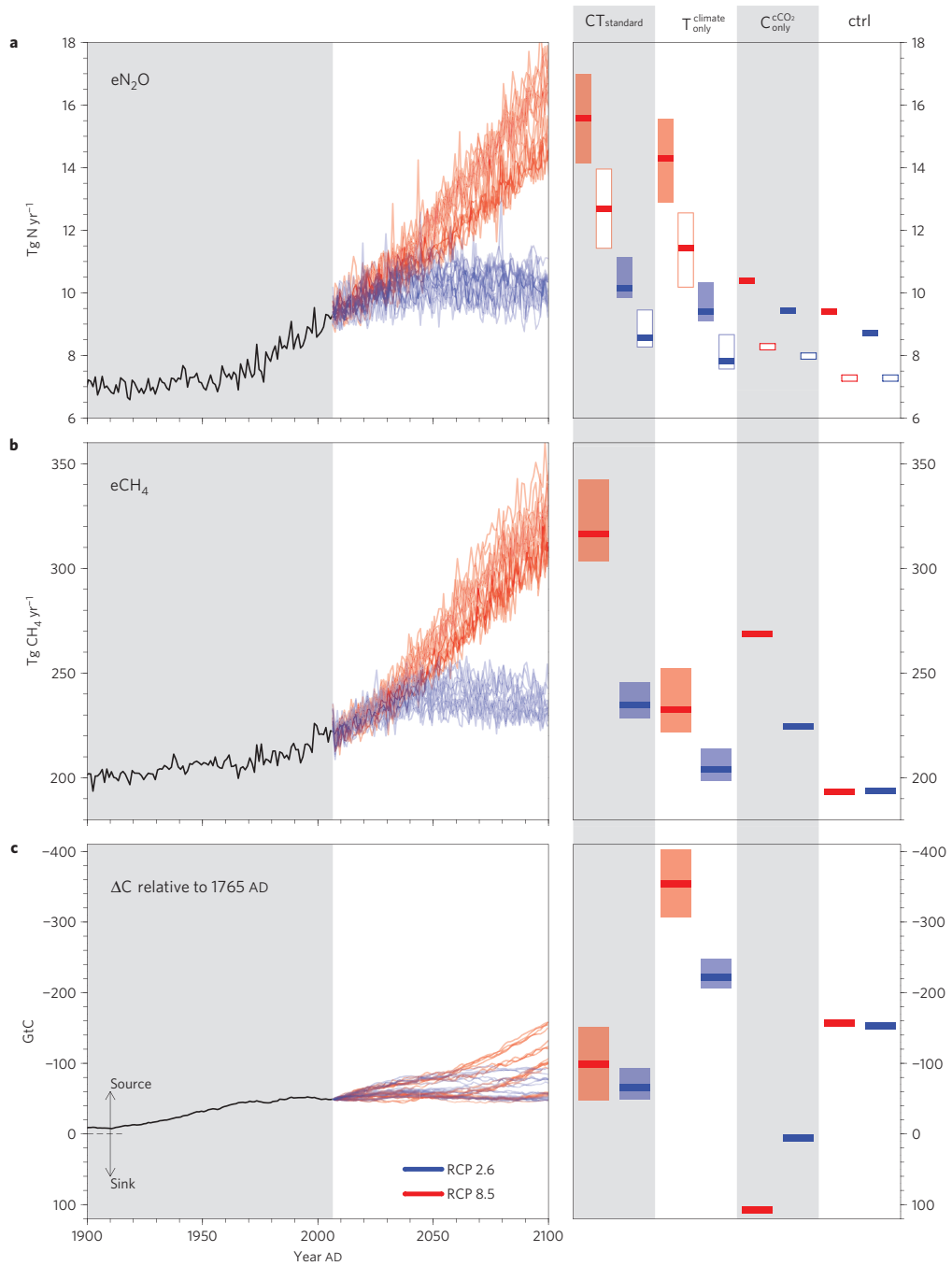
LETTERS

Figure 3 | Future emissions. a–c, N_2O emissions from terrestrial ecosystems and from leached N in water streams (**a**), terrestrial CH_4 emissions (**b**), and change in terrestrial C storage since AD 1765 (**c**; including land-use change) for the historical period (black), and the twenty-first century for RCP2.6 (blue) and RCP8.5 (red). Minimum, mean and maximum at the end of the twenty-first century (mean over AD 2090–2100) for emissions and C storage change for different set-ups are given by the bars in the right panel. Empty bars represent ranges of N_2O emissions in simulations with Nr inputs held at pre-industrial levels. Effects of Nr inputs on CH_4 emissions and ΔC are negligible and are thus not shown. The spread of emissions arises from different prescribed patterns of future climate change from different CMIP5 climate models. Results are from offline simulations.
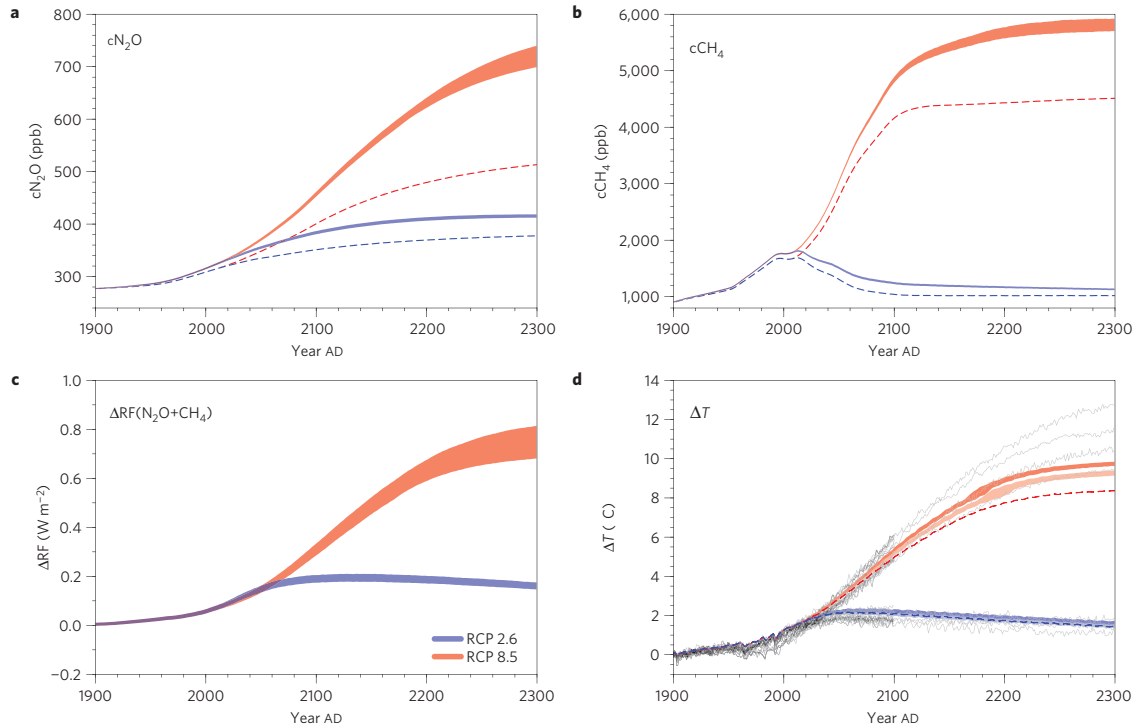
Figure 4 | Future concentrations, radiative forcing and global mean temperature. a,b, Simulated cN_2O (**a**) and cCH_4 (**b**) in the fully coupled (ranges) and the control (dashed lines) simulations for RCP2.6 (blue) and RCP8.5 (red). Results are from online simulations. Higher concentrations in the fully coupled simulations are due to amplified emissions in response to changes in both climate and cCO_2. **c,** Additional radiative forcing due the higher cN_2O and cCH_4 in the fully coupled simulation compared with the control simulation. Changes in cCH_4 concentrations affect stratospheric cH_2O and cO_3. Resulting radiative forcings are included in $RF(CH_4)$. **d,** Global mean temperature change in the control simulation (dashed line), the fully coupled simulation (upper range), and the fully coupled simulation without changes in eN_2O and eCH_4 affecting climate (lower, pale-coloured range) for RCP2.6 (blue) and RCP8.5 (red). Grey lines represent ΔT as simulated by the ensemble of CMIP5 models applied.

agricultural soil lost as N_2O is enhanced by 43–78% by AD 2100 owing to the interaction of Nr inputs with climate change and cCO_2 (see Supplementary Fig. S13). Such effects thus impede the application of Intergovernmental Panel on Climate Change (IPCC) N_2O emission factors to derive anthropogenic N_2O emissions from Nr inputs[27].

eCH_4 rises from 221 Tg CH_4 yr^{-1} at present to 228–245 in RCP2.6 and to 303–343 Tg CH_4 yr^{-1} in RCP8.5. eCH_4 is modelled as a fraction of soil C decomposition under anaerobic soil conditions in mineral soils and is explicitly simulated with production, oxidation and vertical transport in peatlands[17,18]. High cCO_2 ultimately enhances decomposition and affects soil moisture through water-use efficiency. It is thus the main driver of the eCH_4 increase in RCP8.5 (Fig. 2b and Supplementary Information). eCH_4 from boreal peatlands experiences the strongest increase in RCP8.5 (+120–200%). However, climate change at high northern latitudes is subject to substantial uncertainties as evidenced by the spread in CMIP5 model results. This also implies a wide range of simulated ΔC, with climate from models featuring a strong polar warming amplification yielding the largest C losses. Decline in seasonal snow cover and vegetation shifts in response to a warmer climate entail effects on surface Albedo mostly causing an further positive feedback (see Supplementary Fig. S15).

To capture the entire feedback loops between climate and land (Fig. 1), we apply the Bern3D-LPX Earth system model of intermediate complexity[28,29]. The model is forced by anthropogenic

emissions, land-use change and Nr inputs. Atmospheric GHG concentrations, radiative forcing, climate change and GHG release from land ecosystems are simulated and evolve interactively.

The response of eN_2O and eCH_4 to climate and cCO_2 adds to direct anthropogenic emissions and further amplifies atmospheric concentrations. The associated additional radiative forcing (ΔRF) amplifies the temperature increase by 0.4–0.5 °C by AD 2300 in RCP8.5 (Fig. 4). ΔRF broadly scales with ΔT and is thus smaller in RCP2.6. The proportionality between ΔT and ΔRF represents the strength of the feedback and is captured by the feedback factor r (see Supplementary Equation S6).

Applying a comprehensive set of simulations following the emission pathways associated with RCP8.5 and RCP2.6 and using a formalism commonly applied to physical climate feedbacks, we quantify individual feedback factors for each forcing agent mediated by the land model and for each driver of the land response (Fig. 5).

The total land climate feedback is 0.11–0.16 (0.22–0.24) W m^{-2} K^{-1} in 2100 (2300) AD and thus about an order of magnitude smaller than other physical climate feedbacks. The negative feedback arising from cCO_2 effects on ΔC (CO_2-fertilization) dominates at present but declines thereafter owing to eco-physiological saturation (see Supplementary Fig. S9) and the declining radiative efficiency of cCO_2 under high concentrations. In the long term, this negative feedback is largely compensated by the positive feedback from a warmer climate ($r_{\Delta C}^T$), and thus the
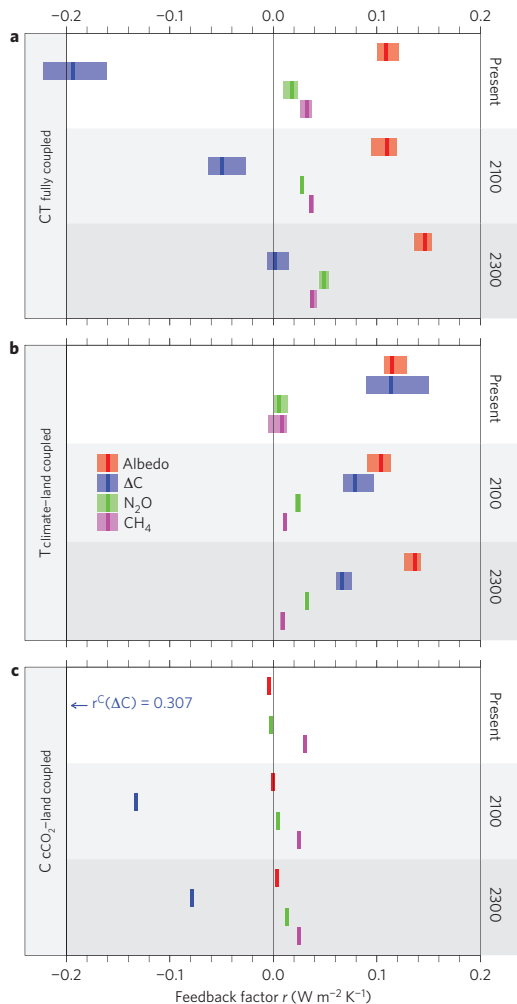
Figure 5 | Feedback factors. a–c, Feedback factors in fully coupled simulations (r_i^{CT}, with $i = \Delta C, eN_2O, eCH_4, \Delta Albedo$; **a**), in climate–land coupled simulations (r_i^T; **b**) and in cCO$_2$–land coupled simulations (r_i^C; **c**). Values are for present (mean of AD 2000–2010), 2100 (mean of 2095–2105) and 2300 (mean of 2290–2300). Rectangles represent minimum (left edge), maximum (right edge) and mean (middle line) of values derived from simulations with different climate change anomaly patterns from the five CMIP5 models applied. Results are from online RCP8.5 simulations. Feedback factors evaluated from RCP2.6 are given in Supplementary Fig. S21.

net feedback ($r_{\Delta C}^{CT}$) is small. The positive feedback from Albedo change remains effective and becomes the strongest positive land feedback in response to changes in climate by AD 2300. eN$_2$O and eCH$_4$ induce positive feedbacks in both climate–land and cCO$_2$–land coupled simulations, but their magnitude is smaller. Generally, non-ΔC feedbacks do not exhibit declining trends and increasingly affect the climate response to anthropogenic forcing in the long run. In addition, effects of C–N interactions, sensitivity of peatland C-storage and land-use change—features not represented in last-generation terrestrial biosphere models presented in the IPCC AR4 (ref. 5)—each tend to enhance the total land feedback r_{land} in our

model on long timescales and under high radiative forcings as in RCP8.5 (see Supplementary Fig. S18).

Limiting the rise in cCO$_2$ and climate change (RCP2.6) maintains a regime where the negative feedback from cCO$_2$-fertilization remains effective and the total land feedback is broadly neutral (Supplementary Fig. S21). Results also illustrate how reducing Nr inputs limits the amplification of eN$_2$O under future climate and thus mitigates the positive associated feedback.

Climate sensitivity is conventionally defined as the temperature change in response to a doubling of cCO$_2$ (+2.9 °C in Bern3D-LPX). Here, we quantify the effective climate sensitivity including land biogeochemical and land Albedo feedbacks in response to sustained radiative forcing of 3.7 W m^{-2}, corresponding to 2 × cCO$_2$, but allowing cCO$_2$ to evolve interactively. Climate sensitivity is increased from 2.8 °C (control set-up) to 3.2–3.3 °C (+15–20%) when land C stock and Albedo feedbacks are included and to 3.4–3.5 °C (+22–27%) when also feedbacks from eN$_2$O and eCH$_4$ are simulated (see Supplementary Fig. S7). Compared with a conventionally defined climate sensitivity, which commonly includes feedbacks from terrestrial Albedo changes, this is an amplification of 16–21%. Earth system models representing only carbon cycle and Albedo feedbacks, including a number of CMIP5 models, may thus underestimate the potential of land-based processes to amplify climate change through positive feedbacks.

Feedback strengths are subject to relatively large uncertainties associated with the representation of processes governing the sensitivity of terrestrial GHG emissions to climate and cCO$_2$. Values of feedback factors reported here are at the lower end of the range previously reported[1,6,7] where multiple agent interactions have not been accounted for. In our simulations, feedback uncertainties introduced by disagreement about climate change patterns are ±17% (AD 2100). Processes not represented in LPX-Bern (for example, changes in biogenic volatile organic carbon emissions and wetland extent) have the potential to further revise the total land feedback towards more positive values.

By applying an Earth system model, representing terrestrial biogeochemical cycling explicitly and interactively, we establish a consistent link between small-scale processes, with altered substrate availability and environmental conditions affecting denitrification and methane production, to the large scale, with amplified eCH$_4$ and eN$_2$O inducing positive land–climate feedbacks in a high-emission/business-as-usual scenario for the twenty-first century. The land biosphere is shifted from a regime where negative feedbacks from higher cCO$_2$ compensate smaller positive feedbacks from eN$_2$O and eCH$_4$ today to a state where non-ΔC feedbacks exert an increasingly strong additional warming in the future. These results suggest that land ecosystem feedbacks in addition to those directly related to carbon storage should be included in the next generation of comprehensive Earth system models.

Methods

Terrestrial processes are simulated with the LPX-Bern 1.0 model (Land surface processes and exchanges, Bern version 1.0), which unifies representations for natural[13], agricultural[14,20] and peatland[15,17,18] coupled C and N (ref. 16) dynamics and predicts the release/uptake of CO$_2$, N$_2$O and CH$_4$. The model version applied here uses a vertically resolved soil hydrology/heat diffusion scheme as a previous LPX version[30], but does not include the comprehensive fire scheme of ref. 30.

To assess the historical budgets and project GHG emissions under RCP2.6 and RCP8.5, we apply LPX in offline mode, where climate and atmospheric CO$_2$ concentration are prescribed (simulations termed offline). For the feedback quantification, LPX is coupled to the Bern3D Earth system model of intermediate complexity and land GHG emissions are prescribed, whereas atmospheric GHG concentrations, radiative forcing and climate change are calculated online (simulations termed online). Bern3D simulates three-dimensional dynamics of ocean heat and CO$_2$ uptake[28], ocean biogeochemistry, and includes a two-dimensional Earth surface energy balance[29].

In both set-ups, inputs prescribed to LPX are N-deposition[23], mineral N-fertilization[24], croplands, pastures and urban areas, fixed lateral extent of

LETTERS

peatland areas and seasonally inundated wetlands. The historical N-fertilization data set is extended to AD 2100 in consistency with the RCP scenarios[25,26] (see Supplementary Information for complete references of input data).

In offline mode, temperature, precipitation and cloud cover are prescribed from CRU TS 3.1 (ref. 21) for the historical period and from the CMIP5 outputs for AD 2005–2100. As input to LPX, we selected outputs from five CMIP5 models (HadGEM2-ES, MPI-ESM-LR, IPSL-CM5A-LR, MIROC-ESM, CCSM4) covering a wide range of uncertainty with respect to model climate sensitivity and polar amplification and providing required climate variables for the RCP2.6 and RCP8.5 simulations (total 32 experiments, see Supplementary Table S1). CMIP5 data were offset-corrected to match the CRU data at present (mean of AD 1996–2005). In online mode, a spatial pattern per unit temperature change, derived for each CMIP5 model, is scaled by the global mean temperature change (ΔT) simulated online by Bern3D. To assess uncertainties, all offline simulations are performed for each CMIP5 model; all online simulations are performed for each anomaly pattern.

N_2O emissions from rivers are modelled as a constant fraction (0.6%) of leached nitrate. This yields a flux of 0.65 Tg N_2O–N yr^{-1} in AD 1900, increasing to 0.8 Tg N_2O–N yr^{-1} in 2005 AD. Simulated terrestrial emissions of CO_2, N_2O and CH_4 are complemented with other sources not simulated by LPX and an additional flux to close the pre-industrial atmospheric budget (see Supplementary Fig. S6). For the historical period, we use data for N_2O emissions not simulated by LPX as presented in ref. 24, but extend records in consistency with the RCP scenarios[25,26]. To close the pre-industrial atmospheric budget, we use an oceanic source of 3.3 Tg N_2O–N yr^{-1} increasing by 3.3% until 2005 AD in line with changes in total reactive Nr in the surface ocean due to atmospheric deposition[31].

For prescribed non-LPX CH_4 emissions we use total anthropogenic CH_4 emissions from the RCP database as they do not include any sources explicitly simulated by LPX. The pre-industrial atmospheric budget, based on Southern Hemisphere records, is closed by a geological source of 38 Tg CH_4 yr^{-1}, held constant thereafter.

Atmospheric concentrations are calculated using a simplified atmospheric chemistry model[32] to simulate variations in the lifetime of GHGs and using prescribed emissions of other reactive gases from the RCP database (VOC, NO_x, CO). Ocean biogeochemistry operates in all online simulations and affects cCO_2, but interactive ocean N_2O emissions are neglected. The radiative forcing of all agents affected by variations of terrestrial GHG emissions are simulated online in Bern3D after ref. 32. Radiative forcing from other agents (aerosols, HFCs, CFCs) is prescribed from the RCP database.

Feedbacks are evaluated following the framework outlined for climate–carbon cycle feedbacks in ref. 1 and schematically illustrated in Fig. 1. External radiative forcings are acting on the system without being affected by the state of the system, for example GHG emissions from fossil-fuel combustion, anthropogenic land-use change, nitrogen fertilizer application and so on. These affect the Earth energy balance with a radiative forcing F. In the absence of any feedbacks from terrestrial GHG emissions and Albedo change, that is, the land model does not see any changes in climate or cCO_2, this would lead to an increase in global mean temperature ΔT^{ctrl}. Positive (negative) feedbacks from land (λ_{land}) amplify (attenuate) this response and lead to a higher (lower) temperature change ΔT^i:

$$F = \lambda_0 \cdot \Delta T^{\text{ctrl}} \qquad (1)$$

$$F = (\lambda_0 + \lambda^i_{\text{land}}) \cdot \Delta T^i \qquad (2)$$

λ_0 is the sum of all non-land feedbacks (black-body, sea ice-Albedo, lapse rate, water vapour feedbacks and so on). Here, land feedbacks summarize effects from all forcing agents: changes in terrestrial C storage (ΔC), eN_2O, eCH_4 and Albedo ($\lambda^i_{\text{land}} \approx \lambda^i_{\Delta C} + \lambda^i_{CH_4} + \lambda^i_{N_2O} + \lambda^i_{\text{Albedo}}$). They can be evaluated with respect to their drivers in a climate–land coupled ($i = T$, Fig. 1), a cCO_2–land coupled ($i = C$) or a fully coupled simulation ($i = CT$) and are related as $\lambda^{CT} \approx \lambda^C + \lambda^T$. We refer to feedback factors as $r = -\lambda$, so that positive feedbacks have positive values and vice versa.

References

1. Gregory, J. M., Jones, C. D., Cadule, P. & Friedlingstein, P. Quantifying carbon cycle feedbacks. *J. Clim.* **22,** 5232–5250 (2009).
2. Canadell, J. G. *et al.* Contributions to accelerating atmospheric CO_2 growth from economic activity, carbon intensity, and efficiency of natural sinks. *Proc. Natl Acad. Sci. USA* **104,** 18866–18870 (2007).
3. Hirsch, A. *et al.* Inverse modelling estimates of the global nitrous oxide surface flux from 1998–2001. *Glob. Biogeochem. Cycles* **20,** GB1008 (2006).
4. Davidson, E. A. The contribution of manure and fertilizer nitrogen to atmospheric nitrous oxide since 1860. *Nature Geosci.* **2,** 659–662 (2009).
5. Denman, K. L. *et al.* in *IPCC Climate Change 2007: The Physical Science Basis* (eds Solomon, S. *et al.*) Ch. 7 (Cambridge Univ. Press, 2007).
6. Arneth, A. *et al.* Terrestrial biogeochemical feedbacks in the climate system. *Nature Geosci.* **3,** 525–532 (2010).
7. Xu-ri Prentice, I. C., Spahni, R. & Niu, H. S. Modelling terrestrial nitrous oxide emissions and implications for climate feedback. *New Phytol.* **2,** 472–88 (2012).
8. Van Groenigen, K. J., Osenberg, C. W. & Hungate, B. A. Increased soil emissions of potent greenhouse gases under increased atmospheric CO_2. *Nature* **475,** 214–216 (2011).
9. Khalil, M. A. K. & Rasmussen, R. A. Climate-induced feedbacks for the global cycles of methane and nitrous oxide. *Tellus B* **41B,** 554–559 (1989).
10. Torn, M. S. & Harte, J. Missing feedbacks, asymmetric uncertainties, and the underestimation of future warming. *Geophys. Res. Lett.* **33,** L10703 (2006).
11. Frank, D. C. *et al.* Ensemble reconstruction constraints on the global carbon cycle sensitivity to climate. *Nature* **463,** 527–530 (2010).
12. Knutti, R. & Hegerl, G. C. The equilibrium sensitivity of the Earth's temperature to radiation changes. *Nature Geosci.* **1,** 735–743 (2008).
13. Sitch, S. *et al.* Evaluation of ecosystem dynamics, plant geography and terrestrial carbon cycling in the LPJ dynamic global vegetation model. *Glob. Change Biol.* **9,** 161–185 (2003).
14. Strassmann, K. M., Joos, F. & Fischer, G. Simulating effects of land use changes on carbon fluxes: Past contributions to atmospheric CO_2 increases and future commitments due to losses of terrestrial sink capacity. *Tellus B* **60,** 583–603 (2008).
15. Wania, R., Ross, I. & Prentice, I. C. Integrating peatlands and permafrost into a dynamic global vegetation model: 2. Evaluation and sensitivity of vegetation and carbon cycle processes. *Glob. Biogeochem. Cycles* **23** (2009).
16. Xu-Ri, & Prentice, I. C. Terrestrial nitrogen cycle simulation with a dynamic global vegetation model. *Glob. Change Biol.* **14,** 1745–1764 (2008).
17. Spahni, R., Joos, F., Stocker, B. D., Steinacher, M. & Yu, Z. C. Transient simulations of the carbon and nitrogen dynamics in northern peatlands: from the Last Glacial Maximum to the twenty first century. *Clim. Past Discuss.* **8,** 5633–5685 (2012).
18. Zürcher, S., Spahni, R., Joos, F., Steinacher, M. & Fischer, H. Impact of an 8.2-kyr-like event on methane emissions in northern peatlands. *Biogeosci. Discuss.* **9,** 13243–13286 (2012).
19. Spahni, R. *et al.* Constraining global methane emissions and uptake by ecosystems. *Biogeosciences* **8,** 1643–1665 (2011).
20. Stocker, B. D., Strassmann, K. & Joos, F. Sensitivity of Holocene atmospheric CO_2 and the modern carbon budget to early human land use: Analyses with a process-based model. *Biogeosciences* **8,** 69–88 (2011).
21. Mitchell, T. D. & Jones, P. D. An improved method of constructing a database of monthly climate observations and associated high-resolution grids. *Int. J. Climatol.* **25,** 693–712 (2005).
22. MacFarling Meure, C. *et al.* Law Dome CO_2, CH_4 and N_2O ice core records extended to 2000 years BP. *Geophys. Res. Lett.* **33,** L14810 (2006).
23. Lamarque, J-F. *et al.* Global and regional evolution of short-lived radiatively-active gases and aerosols in the representative concentration pathways. *Climatic Change* **109,** 191–212 (2011).
24. Zaehle, S., Ciais, P., Friend, A. D. & Prieur, V. Carbon benefits of anthropogenic reactive nitrogen offset by nitrous oxide emissions. *Nature Geosci.* **4,** 601–605 (2011).
25. Van Vuuren, D. P. *et al.* RCP2.6: Exploring the possibility to keep global mean temperature increase below 2 °C. *Climatic Change* **109,** 95–116 (2011).
26. Riahi, K. *et al.* RCP 8.5-A scenario of comparatively high greenhouse gas emissions. *Climatic Change* **109,** 33–57 (2011).
27. De Klein, C. *et al.* in *IPCC Guidelines for National Greenhouse Gas Inventories* Vol. 4 (eds Eggleston, H., Buendia, L., Miwa, K., Ngara, T. & Tanabe, K.) Ch. 11 (IGES, 2006).
28. Müller, S. A., Joos, F., Edwards, N. R. & Stocker, T. F. Water mass distribution and ventilation timescales in a cost-efficient, three-dimensional ocean model. *J. Clim.* **19,** 5479–5499 (2006).
29. Ritz, S. P., Stocker, T. F. & Joos, F. A coupled dynamical ocean energy balance atmosphere model for paleoclimate studies. *J. Clim.* **24,** 349–375 (2011).
30. Prentice, I. C. *et al.* Modelling fire and the terrestrial carbon balance. *Glob. Biogeochem. Cycles* **25,** GB3005 (2011).
31. Suntharalingam, P. *et al.* Quantifying the impact of anthropogenic nitrogen deposition on oceanic nitrous oxide. *Geophys. Res. Lett.* **39,** L07605 (2012).
32. Joos, F. *et al.* Global warming feedbacks on terrestrial carbon uptake under the Intergovernmental Panel on Climate Change (IPCC) emission scenarios. *Glob. Biogeochem. Cycles* **15,** 891–907 (2001).
33. Langenfelds, R. *et al.* in *Baseline Atmospheric Program Australia* (eds Cainey, J., Derek, N. & Krummel, P.) 55–56 (Bureau of Meteorology and CSIRO Atmospheric Research, 2004).
34. Buizert, C. *et al.* Gas transport in firn: Multiple-tracer characterization and model intercomparison for NEEM, Northern Greenland. *Atmos. Chem. Phys.* **12,** 4259–4277 (2012).

NATURE CLIMATE CHANGE DOI: 10.1038/NCLIMATE1864

LETTERS

Additional information

Supplementary information is available in the online version of the paper. Reprints and permissions information is available online at www.nature.com/reprints. Correspondence and requests for materials should be addressed to B.D.S.

6.2 Supplementary material

This section (6.2) provides supplementary information not provided in the main text of the article *Multiple greenhouse gas feedbacks from the land biosphere under future climate change scenarios*. This section is a shortened and reformatted version of the online supplementary informations to Stocker et al. (2013) with a focus on the coupled Bern3D-LPX simulations (i.e. the "online" simulations). The published study (Stocker et al., 2013) as presented in the previous section is referred to as the *main article* in the following.
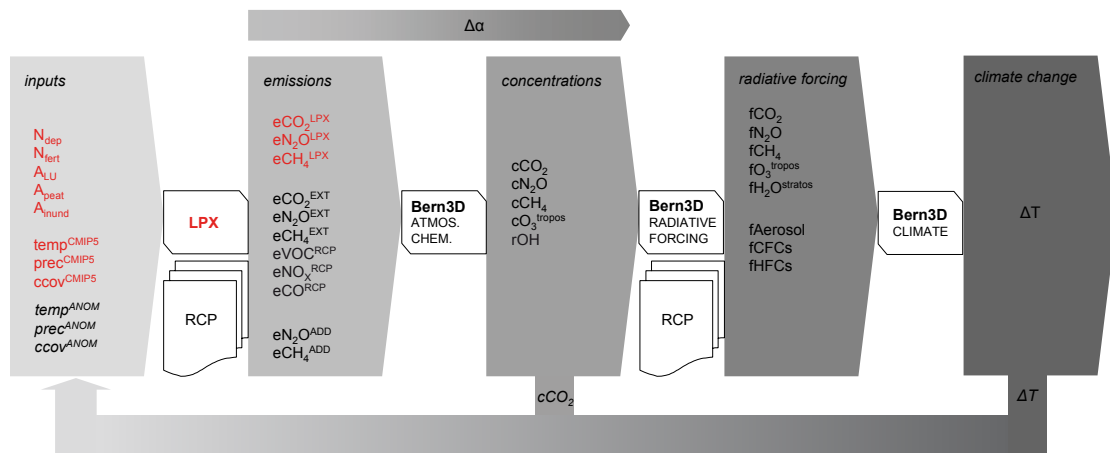
6.2.1 Input data

Figure 6.1: Model setup: inputs and model components.

Figure 6.1 illustrates the model setup: which variables are prescribed to individual model components and which are simulated interactively. The naming of variables introduced here is followed throughout this document. Components in red represent the model parts used for the "offline" simulations (see Methods, main article). Inputs prescribed to LPX-Bern 1.0 are N-deposition (N_{dep}) from Lamarque et al. (2011), mineral N-fertilization (N_{fert}) from Zaehle et al. (2011), distribution of croplands, pastures and urban areas (A_{LU}) from Hurtt et al. (2006), fixed distribution of peatland areas (A_{peat}) and seasonally inundated wetlands (A_{inund}) from Tarnocai et al. (2009). In offline mode, monthly temperature, precipitation and cloud cover are prescribed from the CMIP5 outputs ($temp^{CMIP5}$, $prec^{CMIP5}$, $ccov^{CMIP5}$). In online mode, a spatial pattern per unit temerature change ($temp^{ANOM}$, $prec^{ANOM}$, $ccov^{ANOM}$, derived for each CMIP5 model used, is scaled by the global mean temperature change simulated online by Bern3D (ΔT), see Sect. 6.2.1). Simulated terrestrial emissions (eCO_2^{LPX}, eN_2O^{LPX}, eCH_4^{LPX}) are complemented with other sources not simulated by LPX (eCO_2^{EXT}, eN_2O^{EXT}, eCH_4^{EXT}) and an additional flux to close the atmospheric budget in 1900 AD (eN_2O^{ADD}, eCH_4^{ADD}). Atmospheric concentrations (cCO_2, cN_2O, cCH_4, cO_3^{tropos}, rOH) are calculated online in Bern3D using a simplified atmospheric chemistry model (ATMOS. CHEM) of Joos et al. (2001)) to simulate variations in the life time of CH_4 and using prescribed emissions of reactive gases from the RCP database ($eVOC^{RCP}$, $eNOX^{RCP}$, eCO^{RCP}). cCO_2 evolves as a result of the coupled oceanic and terrestrial C cycle and is communicated back to LPX where it affects plant photosynthesis. The radiative forcing of all agents affected by variations of terrestrial GHG emissions (fCO_2, fN_2O, fCH_4, fO_3^{tropos}, $fH_2O^{stratos}$) are simulated online in Bern3D after Joos et al. (2001) (Bern3D RADIATIVE FORCING). Radiative forcing from other agents (fAerosol, fCFCs, fHFCs) are prescribed directly from the RCP database. The global mean temperature increase (ΔT) is calculated by Bern3D using a two-dimensional representation of the Earth

energy balance (Ritz et al., 2011) and a three-dimensional physical ocean model (Müller et al., 2006). The top arrow represents the communication of land albedo changes ($\Delta\alpha$) from LPX to the radiative component of Bern3D. The bottom arrow visualizes the feedback from simulated cCO_2 and ΔT on LPX. Land surface albedo changes in response to vegetation changes and snow cover are simulated based on Otto et al. (2011) and are described in Steinacher (2011).

Climate

In offline mode, monthly climate data is prescribed to LPX. CMIP5 climate output for surface temperature, precipitation, and cloud cover is applied for all RCP2.6 and RCP8.5 experiments. To correct CMIP5 model output for bias w.r.t. the present-day CRU climatology (Mitchell & Jones, 2005), 2-D climate fields (coordinates x and y) are anomalized as follows:

$$\mathrm{CMIP5}^*_{x,y}(t) = \mathrm{CMIP5}_{x,y}(t) - \overline{\mathrm{CMIP5}_{x,y}} + \overline{\mathrm{CRU}_{x,y}} , \tag{6.1}$$

where $\mathrm{CMIP5}_{x,y}(t)$ is the original and $\mathrm{CMIP5}^*_{x,y}(t)$ is the offset-corrected CMIP5 climate variable field (surface temperature, precipitation, cloud cover) defined for $t =$ 2005–2100 (2300) AD. Bars denote the mean over the years 1996–2005 AD. In online mode, a spatial pattern per unit temperature change, derived for each CMIP5 model and each month is scaled by the global mean temperature change (ΔT) simulated online by the energy balance model (EBM) component of the Bern3D model. Temperature and precipitation anomaly patterns are illustrated in Figs. 6.2 and 6.3. All online experiments are repeated for all 5 different anomaly pattern; this serves as an uncertainty estimate.

N fertilizer input

Mineral N fertilizer (N_{fert}) is assumed to be added to croplands only. N_{fert} inputs on pastures, as well as N inputs from manure are not simulated explicitly. Tracking C and N mass flow from harvest on agricultural land to soil application of animal manure and recycling of crop residues, with denitrification, volatilization, and N_2O emissions along the pathway, is beyond the scope of the present study. N_2O emissions from manure are prescribed instead (see section below).

Four equal doses of mineral N-fertilizer are added during the vegetation period to the soil nitrate and ammonium pool with a constant respective split of 1:7. For the historical period (1765–2005 AD), N_{fert} data is from Zaehle et al. (2011) (ZAE11), based on country-wise ammonium plus nitrate data from the FAO statistical database (1960–2005) (FAOSTAT, 2009). For years 1910–1960, an exponential increase was assumed.

For the years 2005–2100 AD, spatial N_{fert} data provided by the IAM groups (RCP8.5:Riahi et al. (2011), pers. comm. K. Riahi, January 2012; RCP2.6: van Vuuren et al. (2011); Bouwman et al. (2009), pers. comm. L. Bouwman, April 2012) is used to scale the 2005 AD-field from ZAE11 for each continent separately. Thereby, the relative increase in the total amount of annual N_{fert} inputs in each continent is conserved from the original data delivered by the IAM groups, while the spatial pattern within each continent is conserved from the data of ZAE11 in year 2005 AD. This scaling can be described by

$$N_i^{\mathrm{RCP}}(t) = N_i^{\mathrm{ZAE11}}(t = 2005) \cdot \frac{\sum\limits_{\forall i \in k} N_i^{\mathrm{RCP-orig}}(t)}{\sum\limits_{\forall i \in k} N_i^{\mathrm{RCP-orig}}(t = 2005)} \quad \forall \quad \text{continents } k, \tag{6.2}$$

where $N_i^{\mathrm{RCP}}(t)$ is the harmonized RCP N_{fert} scenario at the spatial index i, $N_i^{\mathrm{ZAE11}}(t = 2005)$ is the spatialized field of ZAE11 in year 2005 AD. $N_i^{\mathrm{RCP-orig}}(t)$ is the original spatialized RCP scenario data for each time t and grid cell i. The sum over all grid cells i belonging to continent k is used to scale $N_i^{\mathrm{ZAE11}}(t = 2005)$. For RCP8.5, the scaling factor is corrected to guarantee that the total N_{fert} input in 2100 and in each continent is identical as in the original data.
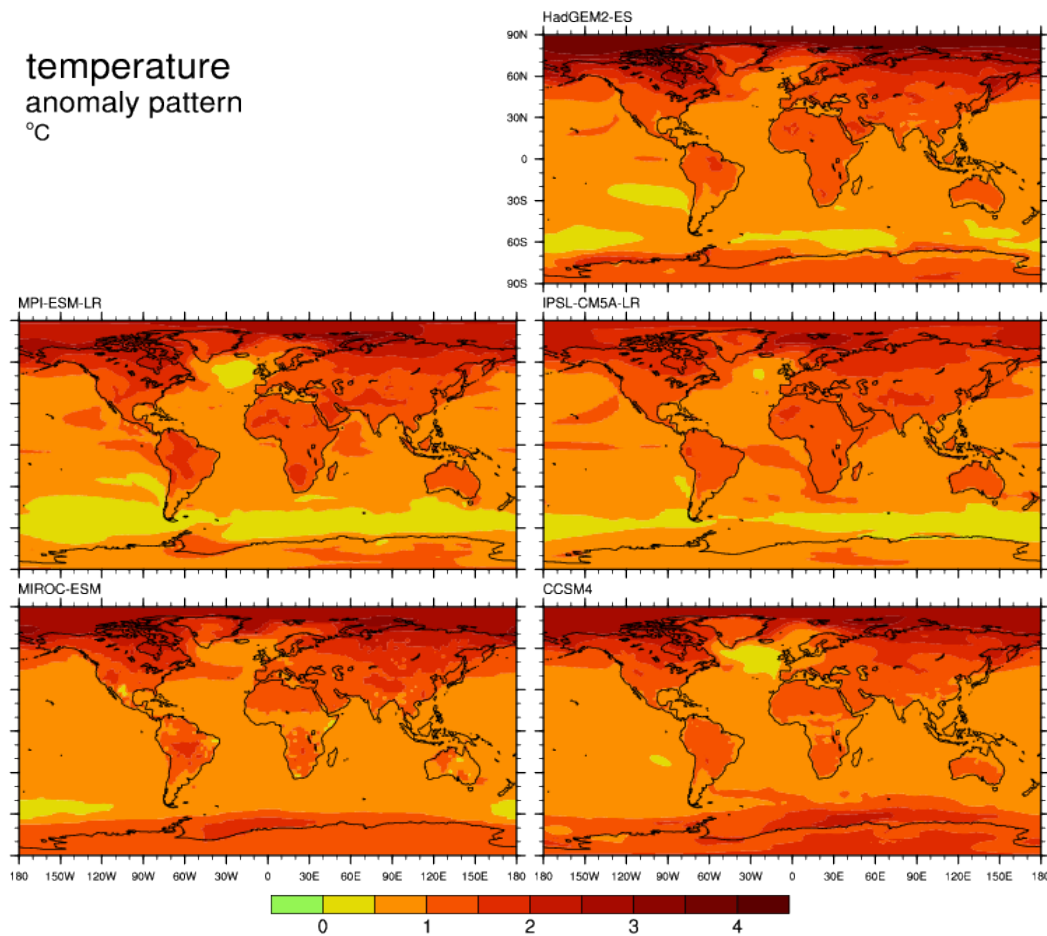
Figure 6.2: Annual mean temperature anomaly patterns per $1\,^\circ$C global temperature change used for coupled simulations $[^\circ\text{C}\,(\text{global mean}\,^\circ\text{C})^{-1}]$. Note that values above 1 represent locations where regional temperature change is larger than on global average.

N deposition

Annual fields for atmospheric NHx and NOy deposition are from Lamarque et al. (2011), generated by an atmospheric chemistry/transport model and provided for the historical period as well as for RCP scenarios of the 21st century. NHx and NOy are added to the ammonium and nitrate pool in LPX along with daily precipitation. For the present study, we treat N deposition as an external forcing, meaning that it is not affected by climate or CO_2. The assessment of a feedback between climate and CO_2, emissions of NO, NO_2 and NH_3 from soils, atmospheric transport and chemical reactions, deposition and radiative forcing is beyond the present study. We summarize the sum of N deposited and N_{fert} as "reactive N inputs" (Nr).

Land use change

Anthropogenic land use change (LU) is treated as an external forcing (see Fig. 1 in the main article) and is prescribed also in the "ctrl" online and offline simulations. LU is prescribed as maps for each year from Hurtt et al. (2006). Resulting CO_2 emissions from deforestation are simulted by the model. A thorough description can be found in previous publications (Strassmann et al., 2008; Stocker et al., 2011). Note that LU also has indirect effects by changing the C sink capacity under rising cCO_2(Strassmann et al., 2008). This is reflected in a stronger negative feedback factor $r_{\Delta C}^{C}$ (Fig. 6.8) when the model is set up without accounting for LU (simulation DyNrPt in Table 6.2).
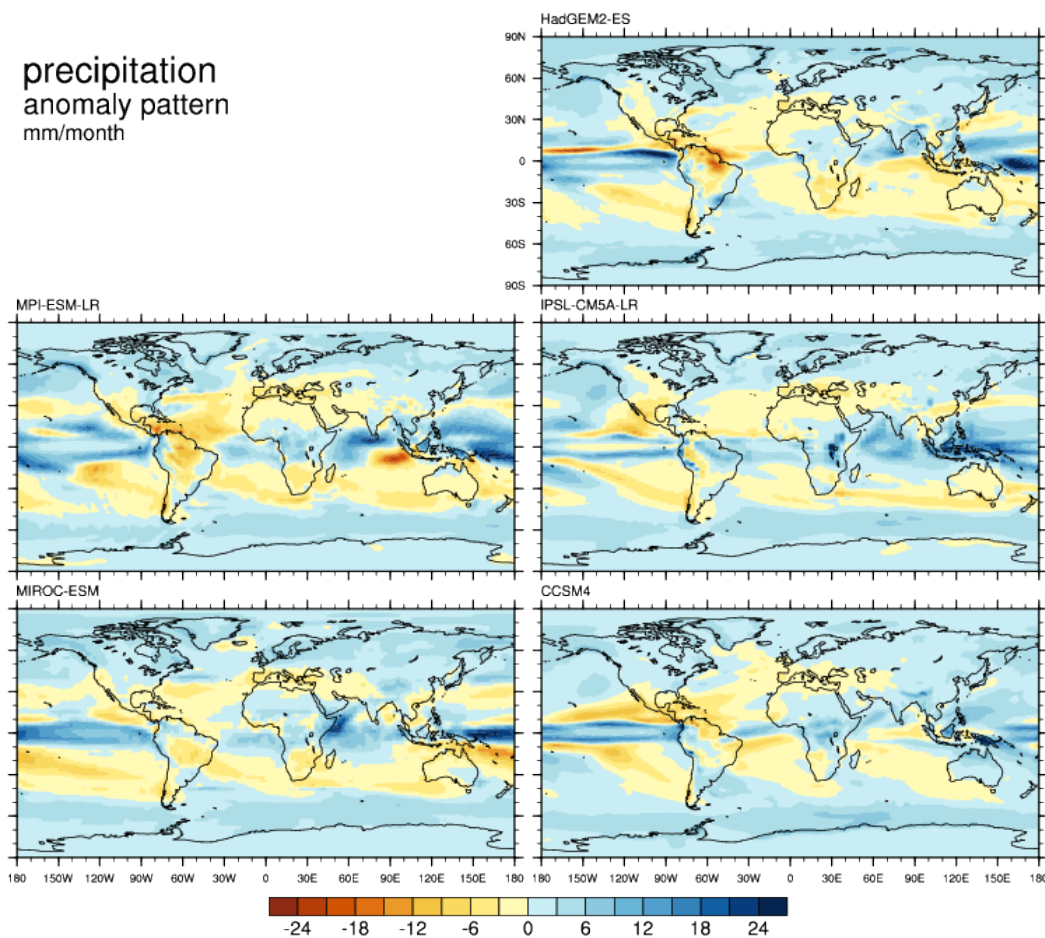
Figure 6.3: Annual mean precipitation anomaly patterns per $1\,^\circ$C global temperature change used for coupled simulations [mm month^{-1} (global mean $^\circ$C)$^{-1}$].

N_2O and CH_4 emissions not simulated by LPX

For eN$_2$O$^{\text{EXT}}$ we use historical emission data for domestic/industrial sources, fire, and manure as described in Zaehle et al. (2011). Domestic/industrial emissions were derived from van Aardenne et al. (2001) giving a flux of $1.2\,\text{Tg}\,N_2\text{O-N}\,\text{yr}^{-1}$ in 2005 AD. The biomass burning estimate ($0.5\,\text{Tg}\,N_2\text{O-N}\,\text{yr}^{-1}$ in 2005 AD) is from Davidson (2009). Manure-N_2O flux is taken as a fraction of global manure-N input yielding $2.2\,\text{Tg}\,N_2\text{O-N}\,\text{yr}^{-1}$ in 2005 AD. To extend N_2O emissions to 2100 AD, we scale the total of domestic/industrial plus fire plus manure emissions in year 2005 AD with the relative increase in the sum of respective categories in each RCP scenario. RCP emission data are consistent with the economical, demographic, and political development in the respective RCP scenarios as simulated by Integrated Assessment Modeling.

To complete the N_2O budget and reproduce the atmospheric concentration for pre-industrial conditions, we tuned the oceanic source to $3.3\,\text{Tg}\,N_2\text{O-N}\,\text{yr}^{-1}$ (eN$_2$O$^{\text{ADD}}$ in Fig. 6.1). This is in agreement with the broad range of available estimates (1.2–$5.8\,\text{Tg}\,N_2\text{O-N}\,\text{yr}^{-1}$, e.g. Hirsch et al., 2006; Denman et al., 2007; Rhee et al., 2009). The oceanic source is scaled by 3.3% between 1850 and 2005 AD with the scaling factor following the increase in atmospheric N deposition. This increase reflects the increase in reactive N in oceans due to atmospheric deposition (Suntharalingam et al., 2012). After 2005 AD, the oceanic source is held constant in all scenarios.

Non-soil CH_4 emissions are taken from the RCP database (2009). These include emissions from biomass burning and wet rice cultivation which are not explicitly simulated by LPX. To close the atmospheric CH_4 budget and reproduce the atmospheric concentration in 1900 AD, we
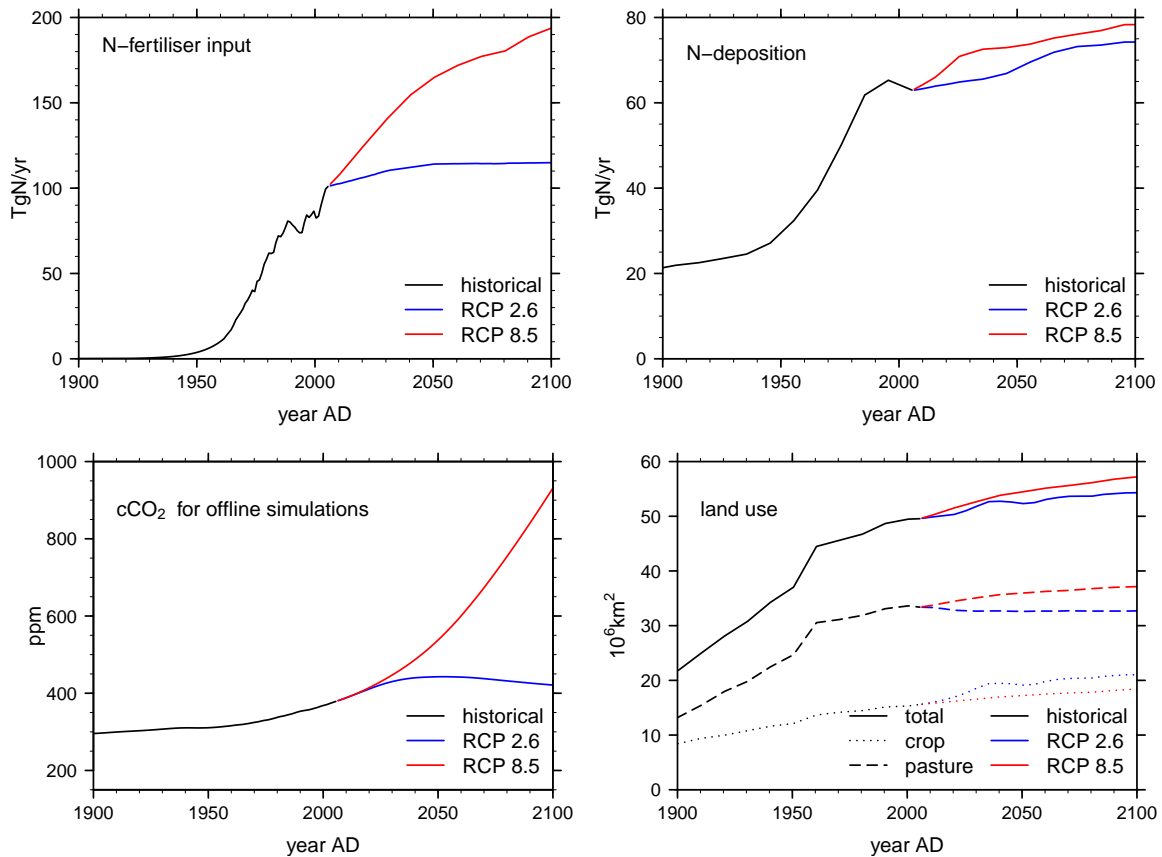
Figure 6.4: Top left: global mineral nitrogen fertilizer input (N_{fert}) [Tg N yr^{-1}] for the historical period (black), RCP2.6 (blue) and RCP8.5 (red). **Top right:** global atmospheric N deposition from Lamarque et al. (2011) [Tg N yr^{-1}] for the historical period (black), RCP2.6 (blue) and RCP8.5 (red). **Bottom left:** atmospheric CO_2 concentration as prescribed in offline simulations for the historical period (black), RCP2.6 (blue) and RCP8.5 (red). **Bottom right:** global land use area from Hurtt et al. (2006) [Tg N yr^{-1}] for the historical period (black), RCP2.6 (blue) and RCP8.5 (red).

tuned the additional prescribed source (representing geological and small oceanic sources) to $38\,\mathrm{Tg\,CH_4\,yr^{-1}}$ (eCH$_4^{\mathrm{ADD}}$ in Fig. 6.1). This is based on a data spline of southern-hemisphere atmospheric records as provided by the RCP database (2009).

6.2.2 Simulation protocol and feedback quantification

Feedback formalism

Our framework to quantify feedbacks between land and climate follows the formalism applied in physical climate science as presented, e.g., in Roe (2009) and Gregory et al. (2009). The latter also address feedbacks between climate and the carbon cycle. Here, we extend this concept to other radiative agents (eCH$_4$, eN$_2$O and albedo) mediated by the terrestrial biosphere and affected by environmental conditions (climate; and atmospheric CO_2 concentrations, cCO$_2$). We start with a brief introduction into the feedback formalism. Consider the Earth's climate to be a system responding to a radiative forcing F with a radiative response H, so that in equilibrium, the net energy flux into the system N is zero and no warming or cooling occurs.

$$N = F - H \,,\ N = 0 \ \Rightarrow\ F = H \tag{6.3}$$

Observations confirm that H can be linearized with respect to the temperature change ΔT (Gregory et al., 2009), so that

$$F = \lambda \cdot \Delta T \tag{6.4}$$

λ is the climate feedback factor given in $\mathrm{W\,m^{-2}\,K^{-1}}$ and is equal to the inverse of the climate sensitivity factor. λ is thus the basic quantity to describe the temperature change of the climate system in response to a given radiative forcing. However, λ summarizes all feedbacks operating. To quantify an individual feedback, we define a reference system, in which the feedback of interest is not operating. The most basic reference system is to consider the Earth as a Black Body. Here, we chose the reference system to repesent the ocean-atmosphere climate system without any interaction with the land. This is the control simulation (termed "ctrl"), in which the radiative forcing F leads to a temperature change ΔT^{ctrl} (see Fig. 4 in the main article, bottom right, dashed line).

$$\Delta T^{\mathrm{ctrl}} = \frac{F}{\lambda_0} \tag{6.5}$$

λ_0 is the sum of all non-land feedbacks operating in the control simulation (the Black Body response or Planck feedback (BB), water vapor (WV), ice-albedo (α), lapse rate (LR), cloud (CL), etc. $\lambda_0 = \lambda_{\mathrm{BB}} + \lambda_{\mathrm{WV}} + \lambda_\alpha + \lambda_{\mathrm{LR}} + \lambda_{\mathrm{CL}} + \ldots$. Note, that the radiative forcing F depends on the reference system chosen. Note also that in our reference system, the land is still affected by external forcings (land use, Nr inputs), which leads to terrestrial GHG emissions and albedo change, eventually affecting ΔT^{ctrl}.

When a feedback is included, the system adjusts to a different temperature ΔT because it now "sees" an additional radiative forcing (ΔF) triggered by the feedback. E.g. a warmer climate stimulates terrestrial N_2O emissions which increase its atmospheric concentration and lead to additionally absorbed energy due to its greenhouse effect. Let us look at "land" as a feedback element in the climate system interacting via a multitude of feedbacks. We summarize these as λ_{land}. With the additional radiative forcing from all land feedbacks written as $\Delta F = r_{\mathrm{land}} \cdot \Delta T$ we get

$$\lambda_0 \cdot \Delta T = F + r_{\mathrm{land}} \cdot \Delta T \ . \tag{6.6}$$

With $r = -\lambda$ we get the form presented in the paper (Eq.2)

$$F = (\lambda_0 + \lambda_{\mathrm{land}}) \, \Delta T \ . \tag{6.7}$$

This illustrates that the additional radiative forcing per degree temperature change (r) caused by the feedback of interest is equal to the negative of the feedback factor λ. Equations (6.5) and (6.7) are combined to derive λ using a control simulation ("ctrl") and a fully coupled simulation ("CT", see Table 6.1). Equation (6.6) can be rewritten as

$$\Delta T = \frac{F}{\lambda_0} + \frac{r}{\lambda_0} \, \Delta T \ , \tag{6.8}$$

illustrating that the feedback arises because a fraction $f = \frac{r}{\lambda_0}$ of the system output ΔT is fed back into the input. We can take a different perspective and characterize the effect of a feedback with the gain factor $G = \frac{\Delta T}{\Delta T^{\mathrm{ctrl}}}$. By combining Eqs. (6.5) and (6.6), the gain factor becomes

$$G = \frac{\Delta T}{\Delta T^{\mathrm{ctrl}}} = \frac{\frac{F}{\lambda_0 - \lambda_0 f}}{\frac{F}{\lambda_0}} = \frac{\lambda_0}{\lambda_0 - \lambda_0 f} = \frac{1}{1 - f} \tag{6.9}$$

Note that $f = \frac{r}{\lambda_0}$ is often referred to as the "feedback factor", but not here, where the feedback factor is $\lambda = -r$. The advantage of the formulation of Eqs. (6.6) and (6.7) is that individual feedbacks can be added to derive their combined effect.

$$\lambda_0 \cdot \Delta T = F + \Delta T \sum_i r_i \ , \tag{6.10}$$

or in the form presented in the paper

$$F = (\lambda_0 + \sum_i \lambda_i)\, \Delta T \;. \tag{6.11}$$

Note that $f = \frac{1}{\lambda_0} \sum_i r_i$ and that $G \neq \sum_i G_i$.

Model setups

So far, we have been looking at feedbacks arising simply "from land". However, a multitude of processes affecting climate are operating in terrestrial ecosystems. One way is to decompose the total land feedback into contributions from individual *forcing agents* (eN$_2$O, eCH$_4$, ΔC, and Δalbedo):

$$\lambda_{\mathrm{land}} = \lambda_{\Delta\mathrm{C}} + \lambda_{\mathrm{CH_4}} + \lambda_{\mathrm{N_2O}} + \lambda_{\Delta\mathrm{albedo}} + \delta \tag{6.12}$$

δ is a non-linearity term. To isolate individual λs, the model has to be set up, where only the respective feedback is operating. In practice, we prescribe the time series of global terrestrial emissions from the control run for all non-operating forcing agents. In the case of albedo, we prescribe the monthly two-dimensional field from the control run. Table 6.1 provides a full account of all model setups applied.

A further decomposition of λ_{land} can be done by *drivers* of land feedbacks. Not only climate (superscript "T") but also atmospheric cCO$_2$ (superscript "C") affects terrestrial GHG emissions and albedo. We quantify its effects in the same framework.

$$\lambda_{\mathrm{land}} = \lambda^{\mathrm{C}} + \lambda^{\mathrm{T}} + \delta \equiv \lambda^{\mathrm{CT}} \tag{6.13}$$

Simulations where only changes of the respective driver is communicated to the land model (see also Fig. 1 in the main article) are used to quantify λ^{T} and λ^{C}. In "climate-coupled" simulations, only feedbacks arising from the sensitivity of forcing agents to climate are taken into account and lead to a temperature change ΔT^{T}:

$$F = (\lambda_0 + \lambda^{\mathrm{T}})\, \Delta T^{\mathrm{T}} \;, \tag{6.14}$$

In "cCO$_2$-coupled" simulation, the land sees only changes in cCO$_2$ and the system attains a temperature ΔT^{C}:

$$F = (\lambda_0 + \lambda^{\mathrm{C}})\, \Delta T^{\mathrm{C}} \;, \tag{6.15}$$

Additionally, we quantify the modification of feedbacks by the individual effects of C-N interactions, peatland C dynamics (Spahni et al., 2013), anthropogenic land use change (Strassmann et al., 2008), and Nr inputs. Respective feedback factors are quantified identically but with LPX not simulating respective features (see Tab. 6.2). This requires the full set of coupled as well as "ctrl" simulations for each setup. Due to non-linearities in the system, the "expansion" with respect to the full setup (by turning one of each feature *off* in an individual setup) is preferred over an expansion w.r.t. the "null"-setup (by turning only one of each feature *on*). To quantify the modification by C-N interactions, results from a carbon-only version of LPX are used.

To assess the sensitivity of terrestrial GHG emissions to different drivers and to capture the effects of the range of climate projections in different CMIP5 models, we use LPX in an offline mode (see Fig. 6.1) and only evaluate emissions (Fig. 3 in the main article).

Table 6.1: Couplings overview. Columns ΔCO_2 and ΔT indicate which *drivers* are communicated to the land model LPX. Columns cCO_2, cCH_4, cN_2O, and $\Delta\alpha$ indicate whether variations in the respective forcing agent affect the climate module in Bern3D ($\checkmark$) or if the climate module responds to variations in respective agents prescribed from the control run ("ctrl").

name	ΔT	ΔCO_2	cCO_2	cCH_4	cN_2O	$\Delta\alpha$
control:						
ctrl	0	0	$\checkmark$	$\checkmark$	$\checkmark$	$\checkmark$
fully coupled:						
CT	1	1	$\checkmark$	$\checkmark$	$\checkmark$	$\checkmark$
cCO_2-land coupled:						
C	0	1	$\checkmark$	$\checkmark$	$\checkmark$	$\checkmark$
climate-land coupled:						
T	1	0	$\checkmark$	$\checkmark$	$\checkmark$	$\checkmark$
fully coupled - single agent:						
CT-ΔCO_2	1	1	$\checkmark$	ctrl	ctrl	ctrl
CT-ΔCH_4	1	1	ctrl	$\checkmark$	ctrl	ctrl
CT-ΔN_2O	1	1	ctrl	ctrl	$\checkmark$	ctrl
CT-$\Delta\alpha$	1	1	ctrl	ctrl	ctrl	$\checkmark$
fully coupled - CO_2/albedo only:						
CT-ΔCO_2-$\Delta\alpha$	1	1	$\checkmark$	ctrl	ctrl	$\checkmark$

6.2.3 Supplementary results

Terrestrial C balance

Changes in terrestrial C storage (ΔC) as illustrated in Fig. 6.5 are the result of external forcings (land use change, Nr) and the impact of changes in climate and cCO_2. At high northern latitudes, temperature increase acts to relieve the limitation of plant growth by temperature and low nutrient availability and leads increased C storage, while at lower latitudes, warmer temperatures generally reduce soil C storage by enhancing soil C decomposition. The C balance of forest biomes (boreal and tropical) is sensibly affected by vegetation dynamics responding to water stress, exceedance of bioclimatic limits, etc. and exhibits abrupt transitions (collapse of vegetation) leading to a sharp decline in primary productivity and C storage.

Equilibrium climate sensitivity

Climate sensitivity is conventionally defined as the temperature response to a doubling of cCO_2, thus not involving slowly adjusting biogeochemical feedbacks (Knutti & Hegerl, 2008). Here, we assess climate sensitivity to a sustained radiative forcing of $3.7\,\mathrm{W\,m^{-2}}$, corresponding to a nominal doubling of preindustrial CO_2 levels. Note that the climate sensitivity is inversely proportional to the sum of all feedbacks $1/(\lambda_0 + \lambda_{\mathrm{land}})$. Bern3D is tuned to yield a conventionally defined sensitivity of $\sim 2.9\,^{\circ}\mathrm{C}$. We assess results for *(i)* a simulation with interactive land biosphere and all feedbacks operating (setup like "CT-LuDyNrPt") *(ii)* a simulation with interactive land biosphere where only feedbacks from albedo and terrestrial C storage are operating (setup like "CT-ΔCO_2-$\Delta\alpha$") and *(iii)* a simulation without land-climate interactions (simulation setup like "ctrl-LuDyNrPt", Tab. 6.1, see Fig. 6.6). The coupled Bern3D-LPX model is run for 2000 simulation years. All boundary conditions (Nr inputs, land use, initial atmospheric CO_2, initial climatology) are set to preindustrial values. We chose to compare the fully coupled simulation "CT-LuDyNrPt" with "CT-ΔCO_2-$\Delta\alpha$" because the latter represents a setup commonly represented by latest-generation Earth system models (e.g., CMIP5 models).

In our simulations, feedbacks from terrestrial C storage and albedo amplify the equilibrium
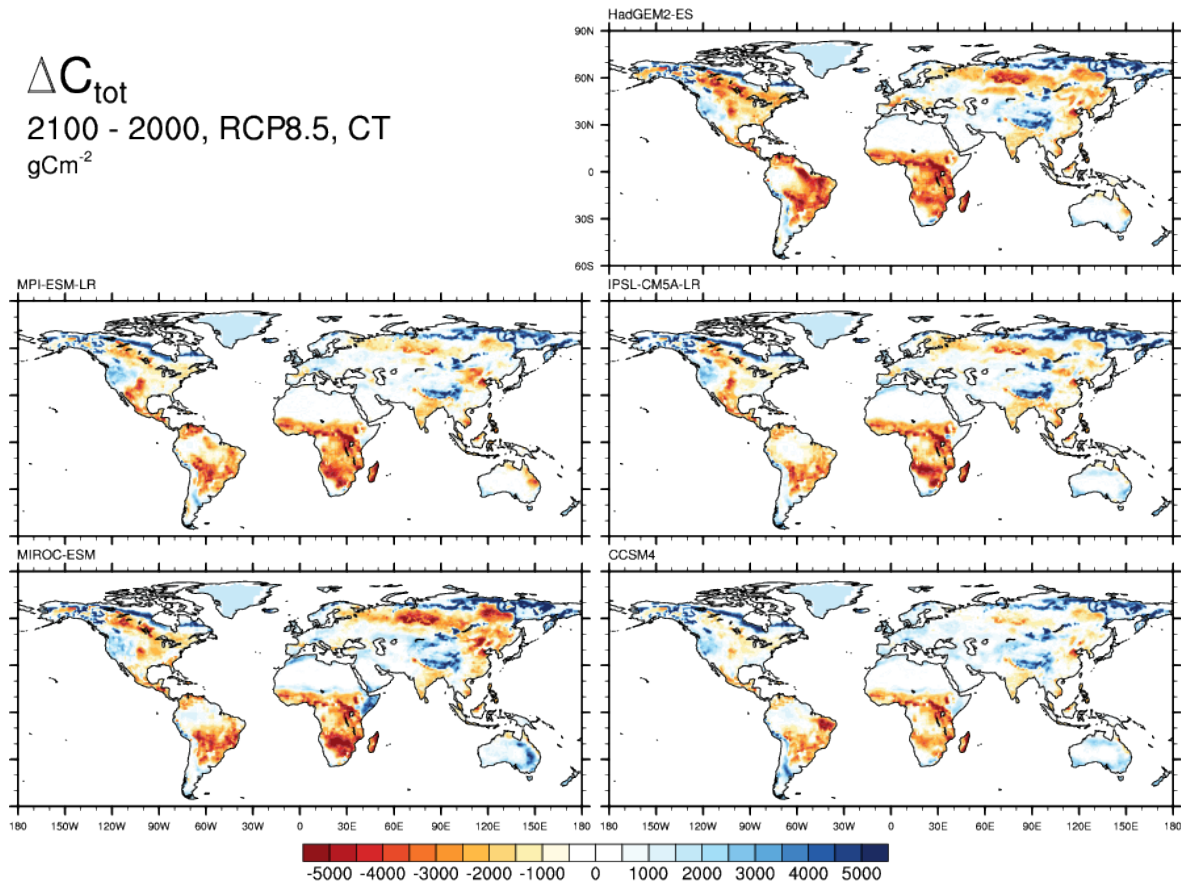
Figure 6.5: ΔC_{tot}, change in total (vegetation, litter, soil) terrestrial C storage [$gC\,m^{-2}$], 2100–2000 AD, in RCP8.5, from offline simulation "CT", and based on different CMIP5 climates. Differences are taken from the means of the years 2006 to 2011 AD and 2095 to 2100 AD. Brown colors represent C release from the terrestrial biosphere.

temperature increase by 0.4–0.5 °C, while the combination of all simulated land-climate interactions finally results in 3.4–3.5 °C warming, 0.6–0.7 °C (or 22–27%) above the 2.8 °C warming when only non-land climate feedbacks are operating (see Fig. 6.6).

Values for λ_{land} reported here are somewhat higher than derived from the RCP8.5 simulations as presented in the article. Differences are likely linked to total C in the system. In RCP8.5 fossil fuel combustion adds C and stimulates C storage on land, acting as a negative feedback. Applying present-day boundary conditions would enhance the positive feedback from N_2O due to higher Nr loads in soils. Assumptions regarding the state of land use used for the equilibrium assessment further influence results. This scenario-dependence of any feedback quantification may be interpreted as favouring the use of scenarios with consistent future developments in land use and emissions of GHGs and other forcing agents.

Attribution of feedbacks to scenario background and model setup

In order to deduce the scenario-dependency of the feedback factors, all simulations listed in Tab. 6.1 have been repeated using the RCP2.6 scenario as a background (instead of RCP8.5). RCP2.6 being a low scenario in terms of temperature and CO_2, the resulting RF-feedback from the land biosphere is also much smaller than under the RCP8.5 background (see Fig. 6.7). But as the feedback factors are normalized to global mean ΔT, these effects almost cancel out except for the non-linearity in the climate-land interactions. As shown in the left column of Fig. 6.8, feedback factors in the T-coupled setup are very similar to the corresponding feedback factors in the RCP8.5 setup (Fig. 5 in the main article). The most striking difference is the sustained
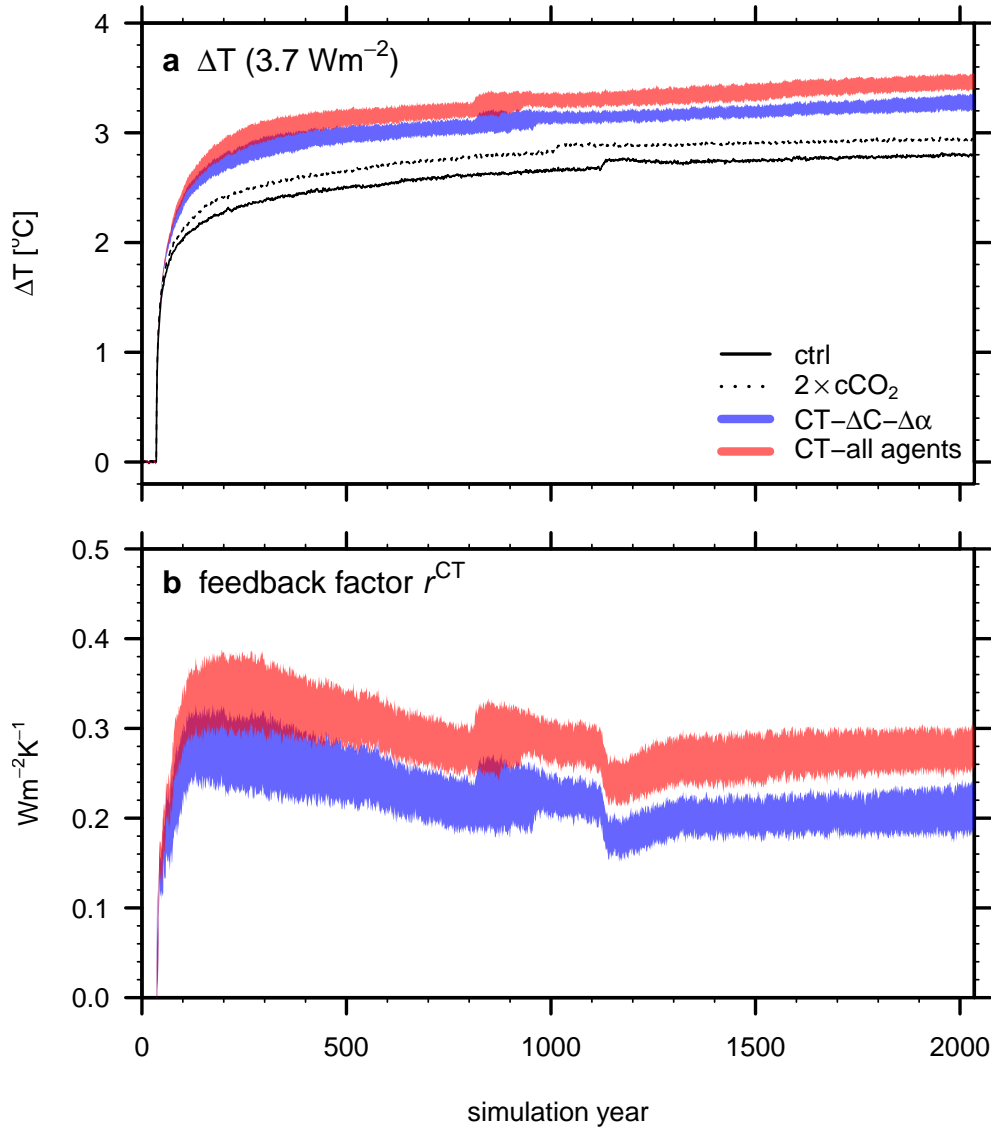
Figure 6.6: **(a)** Global mean temperature increase in response to a radiative forcing of $3.7\,\mathrm{W\,m^{-2}}$. The black curve represents the "ctrl" simulation, where no feedbacks from land are accounted for. The dotted black curve represents the temperature change in response to a doubling of atmospheric cCO_2, the "conventionally defined" climate sensitivity as referred to in the main article. The blue range represents a setup where only terrestrial feedbacks from ΔC and albedo are accounted for. The red range represents a setup where also eN_2O and eCH_4 are operating (see also Tab. 6.1). The difference between the red and blue range is due to effects from terrestrial eN_2O and eCH_4. The range of temperature response arises from the sensitivity to different climate change patterns. Abrupt temperature changes (e.g., "ctrl" in simulation year 1100) are due to abrupt transitions in ocean convection and associated temperature mixing. **(b)** Total land-climate feedback factor (λ_{land}) with colors representing the same setups as in the upper panel. All external forcings of the land (land use, Nr) and initial state (cCO_2) are preindustrial conditions.

negative feedback of CO_2 in RCP2.6 up to 2300 AD, making the total land-feedback smaller.

We also quantify the modification of feedbacks by the individual effects of C-N interactions, peatland C dynamics, anthropogenic land use change and Nr inputs. Respective feedback factors are quantified identically but with LPX not simulating respective features (see Tab. 6.2). This requires the full set of coupled as well as "ctrl" simulations for each setup. Due to non-linearities in the system, the "expansion" with respect to the full setup (by turning one of each feature *off* in an individual setup) is preferred over an expansion w.r.t. the "null-"setup (by turning only one of each feature *on*). To quantify the modification by C-N interactions, results from a carbon-only version of LPX are used.

name	LU	DyN	N_{dep}	N_{fert}	peat
LuDyNrPt	1	1	1	1	1
LuDyNr	1	1	1	1	0
LuDyNPt	1	1	0	0	1
LuPt	1	0	0	0	1
DyNrPt	0	1	1	1	1

Table 6.2: Features overview. Model features, variably turned on ("1") and off ("0") are: anthropogenic land use change (LU), interactive carbon-nitrogen cycling (DyN), N-deposition (N_{dep}), N-fertilization (N_{fert}), and C-N dynamics/CH_4 emissions on peatlands (peat). For the model setup with DyN turned off, the carbon-only version of LPX was used.

The results of these simulations are shown in the right column of Fig. 6.8, where feedback factors are shown for the different setups. We find that differences in the model setup generally overlap within the range of uncertainty, which gives some confidence in the results: feedback factors do obviously not sensitively depend on a certain model component.
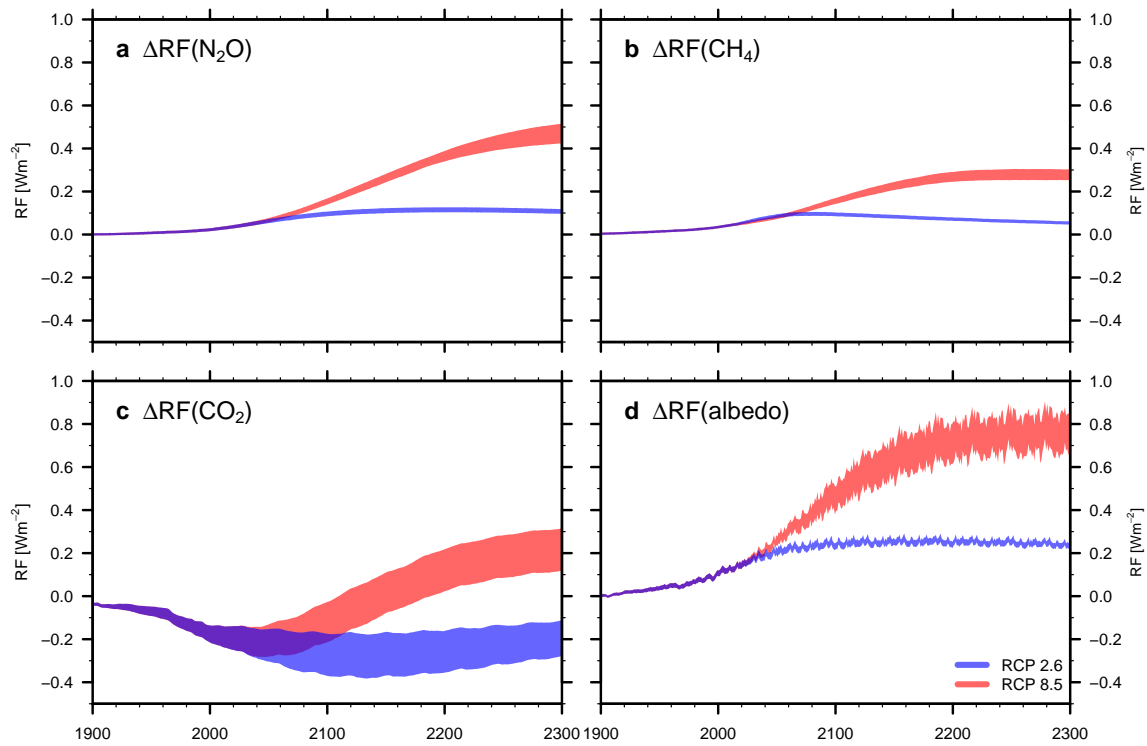
Figure 6.7: Additional radiative forcing due the higher N_2O (**a**), CH_4 (**b**), CO_2 (**c**), and albedo (**d**) in the fully coupled simulation compared to the ctrl simulation both for the RCP2.6 (blue) and RCP8.5 scenarios (red). ΔRF is caused by terrestrial feedbacks. Note that changes in cCH_4 concentrations affect stratospheric cH_2O and cO_3 and hence invoke an indirect radiative forcing. Resulting radiative forcings are included in $RF(CH_4)$. The sum $\Delta RF(N_2O+CH_4)$ is presented in Fig. 4 in the main article (bottom left).

feedback factors for the RCP2.6 background
feedback factors for different model setups
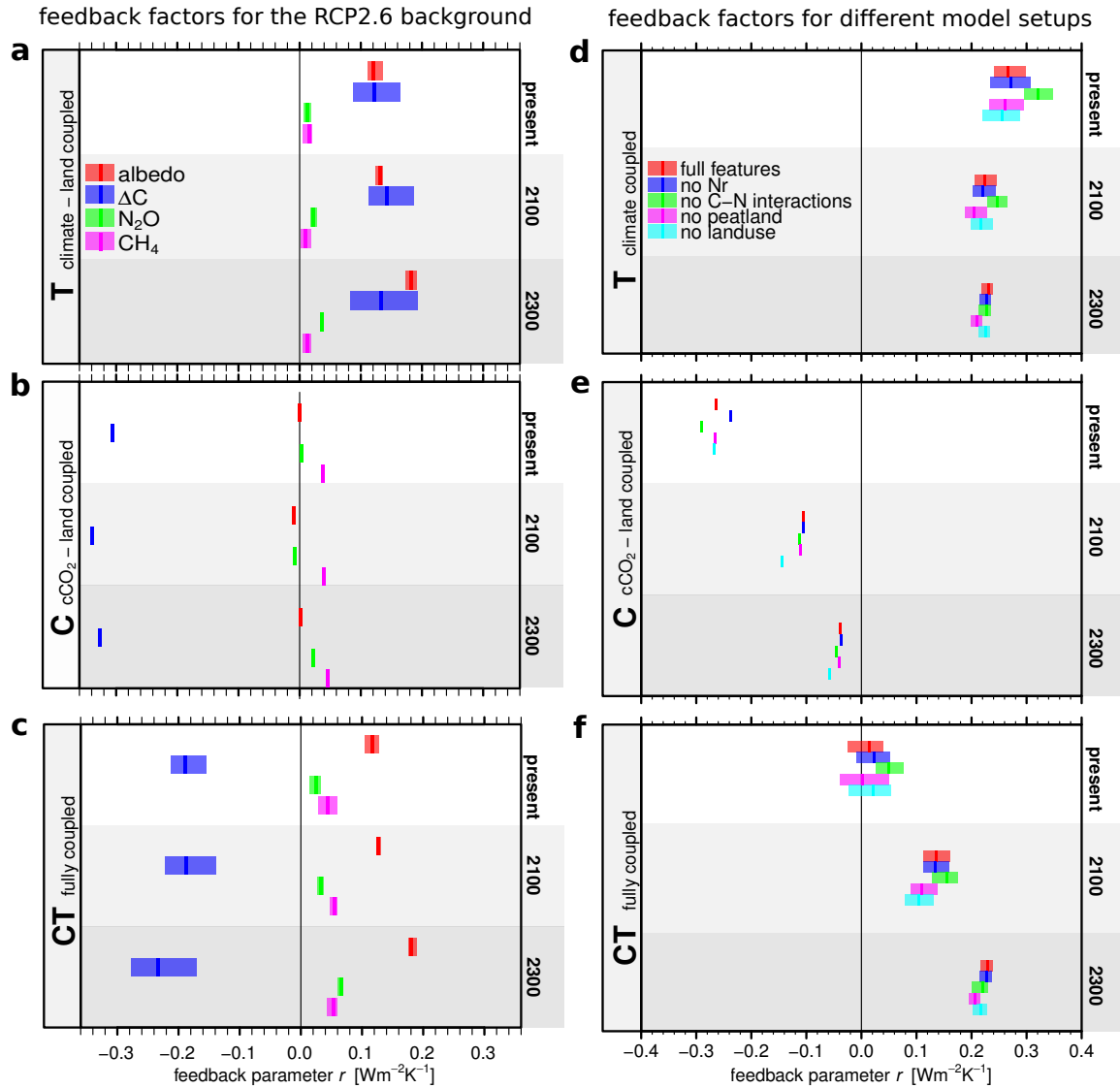

Figure 6.8:
Left: feedbacks factors evaluated from RCP2.6. **(a)** Feedback factors in climate-land coupled simulations r_i^T. **(b)** Feedback factors in cCO$_2$-land coupled simulations r_i^C. **(c)** Feedback factors in fully coupled simulations r_i^{CT}, with $i = CO_2, N_2O, CH_4$, albedo. Rectangles represents minimum (left edge), maximum (right edge), and mean (middle line) of values derived from simulations with different climate change anomaly patterns from the five CMIP5 models applied. The feedbacks are quantified at three time periods: present (mean of 2000-2010 AD), 2100 (mean of 2095–2105), and 2300 (mean of 2290–2300).
Right: feedback factors r^T **(d)**, r^C **(e)**, r^{CT} **(f)** evaluated by model features. Feedback factors represent the combined feedbacks from all forcing agents (eCO$_2$, eN$_2$O, eCH$_4$, and albedo).

Bibliography

Bouwman, A. F., Beusen, A. H. W., & Billen, G., 2009. Human alteration of the global nitrogen and phosphorus soil balances for the period 1970-2050, *Global Biogeochem. Cy.*, 23.

Davidson, E. A., 2009. The contribution of manure and fertilizer nitrogen to atmospheric nitrous oxide since 1860, *Nature Geosci.*, 2(9), 659–662.

Denman, K. L., Brasseur, G., Chidthaisong, A., Ciais, P., Cox, P. M., Dickinson, R. E., Hauglustaine, D., Heinze, C., Holland, E., Jacob, D., Lohmann, U., Ramachandran, S., da Silva Dias, P. L., Wofsy, S. C., & Zhang, X., 2007. Couplings between changes in the climate system and biogeochemistry, in *Climate Change 2007: The Physical Science Basis. Working Group I Contribution to the Fourth Assessment Report of the Intergovernmental Panel on Climate Change*, pp. 499–588, eds Solomon, S., Qin, D., Manning, M., Chen, Z., Marquis, M., Averyt, K. B., Tignor, M., & Miller, H. L., Cambridge University Press, Cambridge, United Kingdom and New York, NY, USA.

FAOSTAT, 2009. Resourcesstat: Fertilisers, Website, Available from http://faostat.fao.org; accessed 08/12/2009.

Gregory, J. M., Jones, C. D., Cadule, P., & Friedlingstein, P., 2009. Quantifying carbon cycle feedbacks, *J. Climate*, 22(19), 5232–5250.

Hirsch, A., Michalak, A., Bruhwiler, L., Peters, W., Dlugokencky, E., & Tans, P., 2006. Inverse modeling estimates of the global nitrous oxide surface flux from 1998-2001, *Global Biogeochem. Cy.*, 20(1), GB1008.

Hurtt, G. C., Frolking, S., Fearon, M. G., Moore, B., Shevliakova, E., Malyshev, S., Pacala, S. W., & Houghton, R. A., 2006. The underpinnings of land-use history: three centuries of global gridded land-use transitions, wood-harvest activity, and resulting secondary lands, *Glob. Change Biol.*, 12, 1208–1229.

Joos, F., Prentice, I. C., Sitch, S., Meyer, R., Hooss, G., Plattner, G.-K., Gerber, S., & Hasselmann, K., 2001. Global warming feedbacks on terrestrial carbon uptake under the Intergovernmental Panel on Climate Change (IPCC) emission scenarios, *Global Biogeochem. Cy.*, 15(4), 891–907.

Knutti, R. & Hegerl, G. C., 2008. The equilibrium sensitivity of the earth's temperature to radiation changes, *Nature Geosci.*, 1(11), 735–743.

Lamarque, J.-F., Kyle, G., Meinshausen, M., Riahi, K., Smith, S., Vuuren, D., Conley, A., & Vitt, F., 2011. Global and regional evolution of short-lived radiatively-active gases and aerosols in the Representative Concentration Pathways, *Climatic Change*, 109, 191–212.

Mitchell, T. D. & Jones, P. D., 2005. An improved method of constructing a database of monthly climate observations and associated high-resolution grids, *Int. J. Climatol.*, 25(6), 693–712.

Müller, S. A., Joos, F., Edwards, N. R., & Stocker, T. F., 2006. Water mass distribution and ventilation time scales in a cost-efficient, three-dimensional ocean model, *J. Climate*, 19(21), 5479–5499.

Otto, J., Raddatz, T., & Claussen, M., 2011. Strength of forest-albedo feedback in mid-holocene climate simulations, *Clim. Past Discuss.*, 7, 809–840.

RCP database, 2009. RCP database, version 2.0.5, Website, Available from http://www.iiasa.ac.at/web-apps/tnt/RcpDb/ accessed 27/10/2011.

Rhee, T. S., Kettle, A. J., & Andreae, M. O., 2009. Methane and nitrous oxide emissions from the ocean: A reassessment using basin-wide observations in the Atlantic, *J. Geophys. Res.-Atmos.*, 114, D12304.

Riahi, K., Rao, S., Krey, V., Cho, C., Chirkov, V., Fischer, G., Kindermann, G., Nakicenovic, N., & Rafaj, P., 2011. RCP 8.5-A scenario of comparatively high greenhouse gas emissions, *Climatic Change*, 109(1-2, SI), 33–57.

Ritz, S. P., Stocker, T. F., & Joos, F., 2011. A coupled dynamical ocean-energy balance atmosphere model for paleoclimate studies, *J. Climate*, 24(2), 349–75.

Roe, G., 2009. Feedbacks, timescales, and seeing red, *Ann. Rev. Earth and Planet. Sci.*, 37(1), 93–115.

Spahni, R., Joos, F., Stocker, B. D., Steinacher, M., & Yu, Z. C., 2013. Transient simulations of the carbon and nitrogen dynamics in northern peatlands: from the Last Glacial Maximum to the 21st century, *Clim. Past*, 9, 1287–1308.

Steinacher, M., 2011. *Modeling changes in the global carbon cycle-climate system*, PhD thesis, University of Bern.

Stocker, B. D., Strassmann, K., & Joos, F., 2011. Sensitivity of Holocene atmospheric CO_2 and the modern carbon budget to early human land use: analyses with a process-based model, *Biogeosciences*, 8(1), 69–88.

Stocker, B. D., Roth, R., Joos, F., Spahni, R., Steinacher, M., Zaehle, S., Bouwman, L., Xu-Ri, & Prentice, I. C., 2013. Multiple greenhouse-gas feedbacks from the land biosphere under future climate change scenarios, *Nature Clim. Change*, 3(7), 666–672.

Strassmann, K. M., Joos, F., & Fischer, G., 2008. Simulating effects of land use changes on carbon fluxes: past contributions to atmospheric CO_2 increases and future commitments due to losses of terrestrial sink capacity, *Tellus B*, 60(4), 583–603.

Suntharalingam, P., Buitenhuis, E., Le Quere, C., Dentener, F., Nevison, C., Butler, J. H., Bange, H. W., & Forster, G., 2012. Quantifying the impact of anthropogenic nitrogen deposition on oceanic nitrous oxide, *Geophy*, 39.

Tarnocai, C., Canadell, J. G., Schuur, E. A. G., Kuhry, P., Mazhitova, G., & Zimov, S., 2009. Soil organic carbon pools in the northern circumpolar permafrost region, *Global Biogeochem. Cy.*, 23(2), GB2023.

van Aardenne, J., Dentener, F., Olivier, J., Goldewijk, C., & Lelieveld, J., 2001. A 1°×1° resolution data set of historical anthropogenic trace gas emissions for the period 1890-1990, *Global Biogeochem. Cy.*, 15(4), 909–928.

van Vuuren, D. P., Stehfest, E., den Elzen, M. G. J., Kram, T., van Vliet, J., Deetman, S., Isaac, M., Goldewijk, K. K., Hof, A., Beltran, A. M., Oostenrijk, R., & van Ruijven, B., 2011. RCP2.6: exploring the possibility to keep global mean temperature increase below 2 °C, *Climatic Change*, 109(1-2, SI), 95–116.

Zaehle, S., Ciais, P., Friend, A. D., & Prieur, V., 2011. Carbon benefits of anthropogenic reactive nitrogen offset by nitrous oxide emissions, *Nature Geosci.*, 4(9), 601–605.

Chapter 7

Outlook

The modeling work presented in this study can be continued and improved in several ways. With the recently updated ocean model, some of the published experiments should be repeated, e.g. LGM simulations. Especially experiments focusing on the response of the Southern Ocean are worthwhile to conduct (e.g. deglaciation), as the high-latitude regions are now considerably better resolved in the model. In addition, as the coupled Bern3D-LPJ is now capable to simulate the three major greenhouse gases CO_2, N_2O and CH_4 (Spahni et al., 2011; Stocker et al., 2013), more sensitivity experiments should be performed.

A similar experiment as performed by Goldstein et al. (2003) has been set up with the newest version of the Bern3D-LPJ: an attempt to model a Younger-Dryas type abrupt climate event. Figure 7.1 shows a promising (preliminary) result at the example of the N_2O response during such an freshwater experiment. These simulations were performed using the updated version of the Bern3D ocean component.
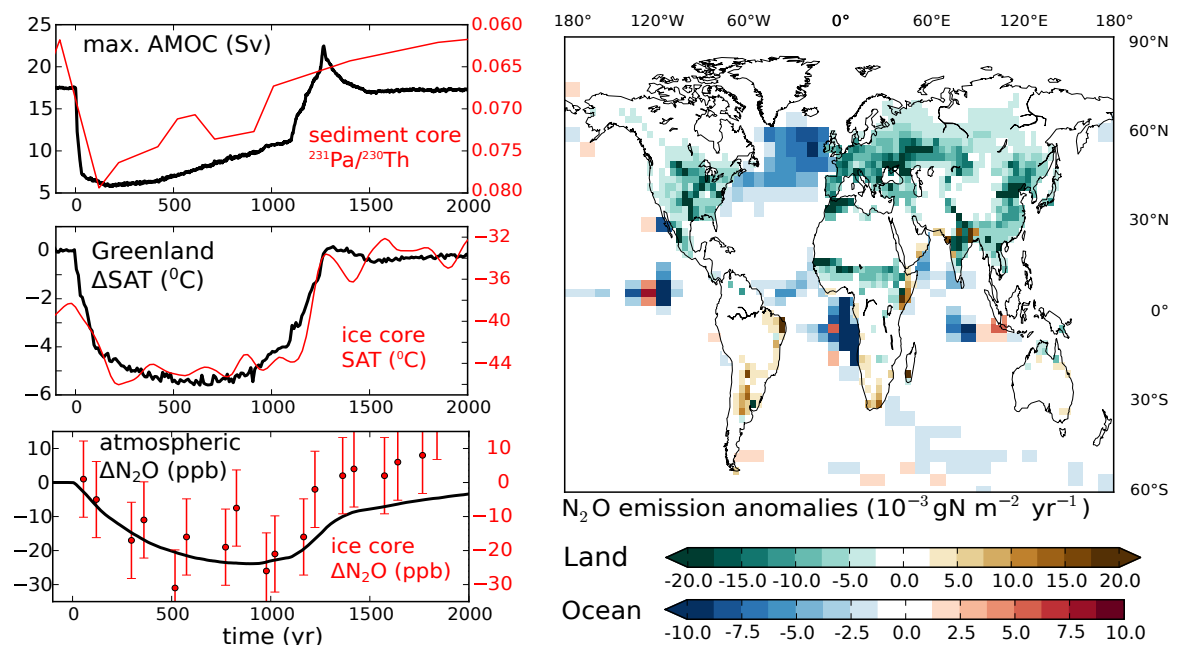
Figure 7.1: **Left**: response of the meridional overturning circulation to the $\sim$1000 yr lasting freshwater perturbation in the North Atlantic and as a result, a strong cooling over Greenland. The atmospheric drop in N_2O concentration of $\sim$20-25 ppb is a result of the combined ocean and land response. ^{231}Pa/^{230}Th data are from McManus et al. (2004), Greenland temperature from Kindler et al. (2013) and N_2O from Schilt et al. (2010). **Right**: a snapshot of oceanic and terrestrial N_2O emission anomalies taken at year 500 (note the different colorscales).

The simulation of multiple GHGs (and their isotopes) could also be performed in a transient way, e.g. over one or multiple glacial cycles. Peatland and permafrost dynamics should be included in such simulation, as they have so far only been studied with the land-only component (Spahni et al., 2013). Currently, the development of a dynamic peatland module is ongoing: instead of prescribed present-day peatland areas, the model dynamically calculates the wetland extent according to topography, climate and runoff. In analogue, circulation proxies such as $\delta^{13}C$, $\Delta^{14}C$, $^{231}Pa/^{230}Th$ and ϵ_{Nd} (Rempfer et al., 2011) should be used in the future in order to constrain the modeled ocean dynamics to available paleo-records.

With such multi-proxy approaches, the number of constraints increases, but also the number of degrees of freedom. I therefore see the need for data-assimilation methods applicable for transient simulations. The idea behind this is as follows: given a set of temporally and spatially sparse proxy-data, e.g. from ice and sediment cores, the model's forcings (and responses) that fits best has to be determined. This could be realized in a particle-filter approach (Dubinkina & Goosse, 2013), or by an inverse modeling technique as applied by Heinze & Hasselmann (1993). The first approach seems problematic, as it already assumes the processes and feedbacks resolved by the model are (potentially) sufficient to explain the observed data. In addition, the internal variability in the Bern3D is rather small due to the prescribed atmospheric dynamics, therefore small perturbation would not lead to a significantly different evolution of the model.

The second approach allows to include a set of (partially) unknown forcings (and parametrizations of feedbacks), such as freshwater inputs, changes in the marine biology, ocean stratification changes etc. The solution, that is the best fitting combination of forcings, could either be found by running the model in a probabilistic mode (Steinacher et al., 2013), e.g. minimizing the model-data mismatch every 1 kyr. Alternatively, impulse response functions for all forcings could be calculated with the full model and subsequently the best solution determined using the linearized response and mathematical minimization techniques.

But first, the Bern3D ocean component needs some major improvement in order to be able to simulate the glacial carbon cycle. Here I see two main issues: firstly, the biogeochemistry module is too simple. For example the remineralization and redissolution profiles are prescribed and as a consequence, they do not respond to changes of local seawater temperature and chemistry. Secondly, the physical component shows a relatively high numerical diffusion, linked to the coarse vertical resolution on the deep ocean. This is probably one of the causes why glacial ocean gradients of salt, carbon and $\Delta^{14}C$ are not steep enough, and therefore the ocean stratification is too weak in order to reproduce glacial CO_2 and $\Delta^{14}C$ levels.

In terms of ^{14}C production rate reconstructions, the next step would be to invoke 3-D atmosphere models in order to resolve the spatial distribution and transport of ^{14}C (and/or ^{10}Be) within the atmosphere. In this case, also short-term $\Delta^{14}C$ variations as reconstructed from tree-rings (Miyake et al., 2012, 2013) could be related to changes in solar activity or changes in the GCR influx. But reconstructions further back in time (i.e. pre-Holocene) seem not feasible so far, as reconstructions of past $\Delta^{14}C$ and geomagnetic field strength are too uncertain. In addition, the carbon cycle state is less constrained before the relatively stable Holocene.

Bibliography

Dubinkina, S. & Goosse, H., 2013. An assessment of particle filtering methods and nudging for climate state reconstructions, *Clim. Past*, 9(3), 1141–1152.

Goldstein, B., Joos, F., & Stocker, T. F., 2003. A modeling study of oceanic nitrous nitrous oxide during the Younger Dryas cold period, *Geophys. Res. Lett.*, 30(2), 1092.

Heinze, C. & Hasselmann, K., 1993. Inverse multi-parameter modelling of paleo–climate carbon cycle indices, *Quaternary Res.*, 40, 281–296.

Kindler, P., Guillevic, M., Baumgartner, M., Schwander, J., Landais, A., & Leuenberger, M., 2013. NGRIP temperature reconstruction from 10 to 120 kyr b2k, *Clim. Past Discuss.*, 9(4), 4099–4143.

McManus, J. F., Francois, R., Gherardi, J.-M., Keigwin, L. D., & Brown-Leger, S., 2004. Collapse and rapid resumption of Atlantic meridional circulation linked to deglacial climate changes, *Nature*, 428(6985), 834–837.

Miyake, F., Nagaya, K., Masuda, K., & Nakamura, T., 2012. A signature of cosmic-ray increase in AD 774-775 from tree rings in Japan, *Nature*, 486(7402), 240–242.

Miyake, F., Masuda, K., & Nakamura, T., 2013. Another rapid event in the carbon-14 content of tree rings, *Nat. Commun.*, 4, 1748.

Rempfer, J., Stocker, T. F., Joos, F., Dutay, J.-C., & Siddall, M., 2011. Modelling Nd-isotopes with a coarse resolution ocean circulation model: Sensitivities to model parameters and source/sink distributions, *Geochim. Cosmochim. Ac.*, 75, 5927–5950.

Schilt, A., Baumgartner, M., Schwander, J., Buiron, D., Capron, E., Chappellaz, J., Loulergue, L., Schüpbach, S., Spahni, R., Fischer, H., & Stocker, T. F., 2010. Atmospheric nitrous oxide during the last 140,000 years, *Earth Planet. Sci. Lett.*, 300(1-2), 33–43.

Spahni, R., Wania, R., Neef, L., van Weele, M., Pison, I., Bousquet, P., Frankenberg, C., Foster, P. N., Joos, F., Prentice, I. C., & van Velthoven, P., 2011. Constraining global methane emissions and uptake by ecosystems, *Biogeosciences*, 8(6), 1643–1665.

Spahni, R., Joos, F., Stocker, B. D., Steinacher, M., & Yu, Z. C., 2013. Transient simulations of the carbon and nitrogen dynamics in northern peatlands: from the Last Glacial Maximum to the 21st century, *Clim. Past*, 9, 1287–1308.

Steinacher, M., Joos, F., & Stocker, T. F., 2013. Allowable carbon emissions lowered by multiple climate targets, *Nature*, 499, 197–201.

Stocker, B. D., Roth, R., Joos, F., Spahni, R., Steinacher, M., Zaehle, S., Bouwman, L., Xu-Ri, & Prentice, I. C., 2013. Multiple greenhouse-gas feedbacks from the land biosphere under future climate change scenarios, *Nature Clim. Change*, 3(7), 666–672.

Appendix A

Structure of the Bern3D-LPJ code

Figure A.1 shows the structure of subroutine calls in the fully coupled atmosphere-ocean-sediment-landbiosphere setup of the Bern3D model (as of ∼2012). The main part of the code, i.e. the loop over timesteps, is highlighted in red. The subroutine names are given in blue, while in black a short description of the subroutine is given. Note that not all diagnostic routines are listed in Fig. A.1 but indicated in green.
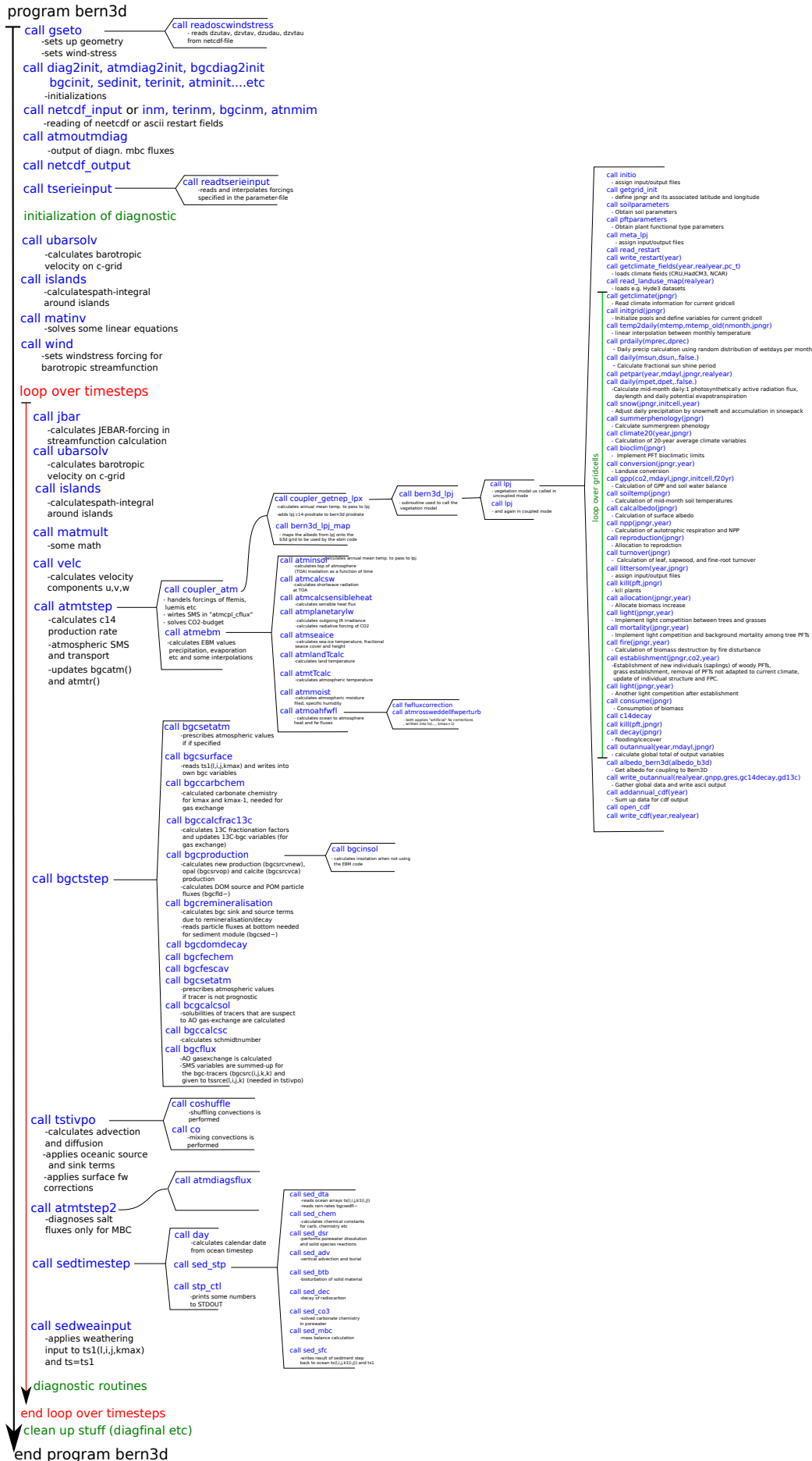
Figure A.1: Flowchart of Bern3D-LPJ subroutine calls for revision numbers **r1948** (Bern3D) and **r1701** (LPJ).

Appendix B

Bern3D grid overview

The grid of the `41×40` version of the ocean component is depicted in Fig. B.1. The colorcode indicates the bathymetry (blue=shallow, red=deep). The index of the depth-level of each water column is labeled within each box. Note that the indices of the vertical axis are flipped in the output ($\mathtt{k}_{\mathrm{output}}$) w.r.t. the source code ($\mathtt{k}_{\mathrm{code}}$). The horizontal tracer-grid (t-grid) is shown, given by the indices $\mathtt{i}$ (longitude) and $\mathtt{j}$ (latitude). The indices and coordinates of the velocity-grid (u-grid) is labeled by numbers only.

Figure B.1: The horizontal grid of the **41×40** setup of the Bern3D ocean, atmosphere and sediment components.
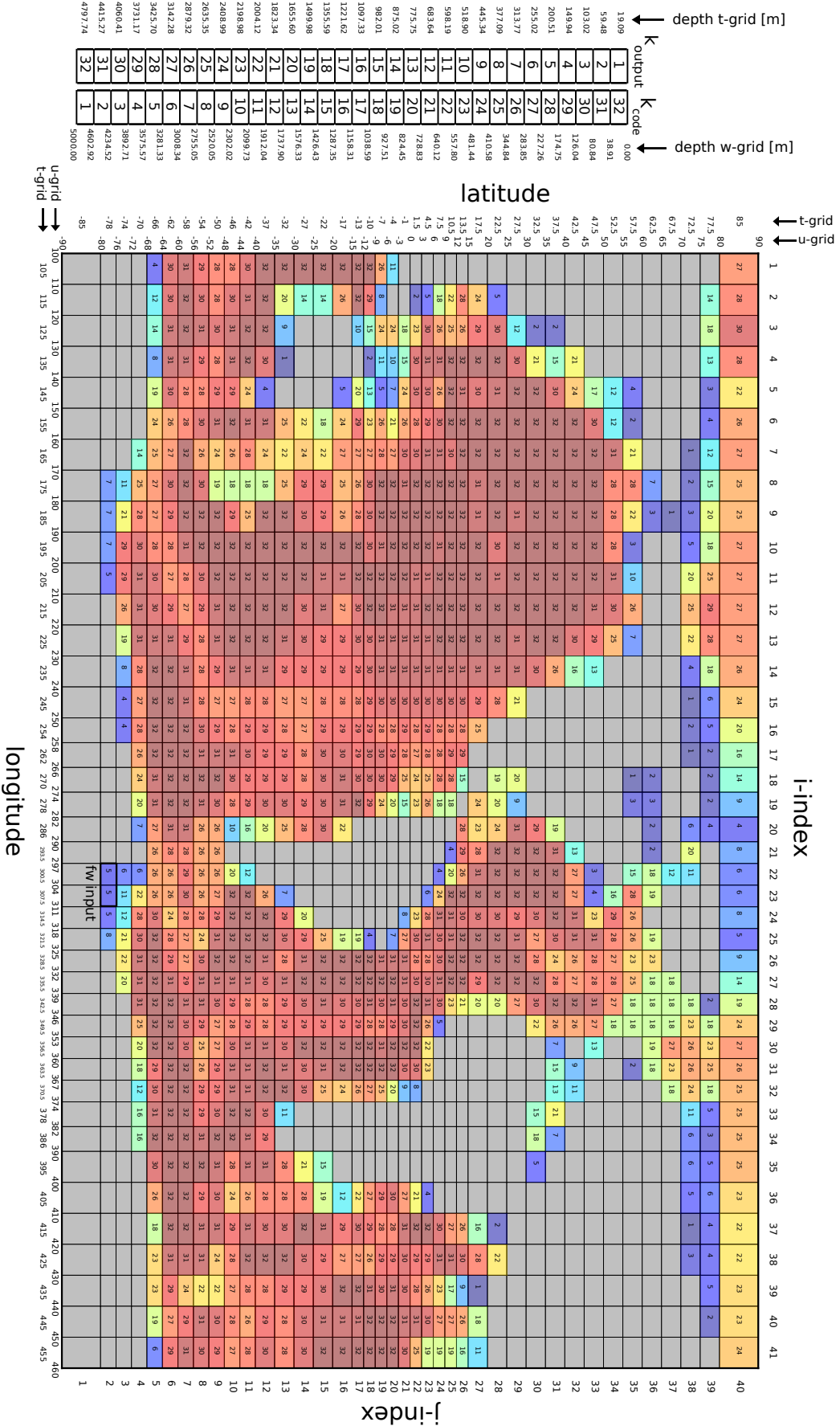
Appendix C

An attempt to optimize the fundamental ocean parameters

For the new model in the 41×40 setup, the ocean parameters have been set to their original values (i.e. the values from the 36×36 setup) except for an ad-hoc doubling of the diapycnal diffusivity. Applying these, the parameters of the EBM were adjusted by "bare eye", i.e. comparing to observations without applying a quantitative metric by S. Ritz. To test whether a better set of ocean parameters can be found, 7 key parameters were varied in a probabilistic approach: isopycnal diffusivity (k_I), diapycnal diffusivity (k_D), Gent-McWilliams diffusivity (κ), windstress scaling (α), gas-exchange scaling ($k_{\mathrm{scale}}^{\mathrm{gas}}$), inverse minimum drag (λ) and Southern Ocean freshwater removal (fw$_{\mathrm{SO}}$). The standard values of these parameters are listed in the first row of Tab. C.1. One thousand parameter sets were generated using Latin Hypercube sampling on truncated normal distributions.

Each model was then spun up under 1765 AD conditions and a subsequent transient simulations until 2000 AD including the tracers T, S, DIC, DIC-14 and CFC-11 and prescribing the atmospheric boundary conditions. The model results were then compared to observational gridded datasets for temperature and salinity (WOA09) and bottle data for Δ^{14}C and CFC-11 (GLODAP) which were remapped on the Bern3D grid using area-weighted regridding. The total model-data bias is further expressed by a normalized root-mean-squared error (nRMSE):

$$\mathrm{nRMSE} = \sum_{\mathrm{constrains}} \left(\frac{1}{\#\mathrm{ocean\ cells}} \cdot \sum_{\mathrm{ocean\ cells}} \frac{(\mathrm{model\text{-}obs})^2}{\sigma_{\mathrm{obs}}^2} \right)^{1/2}, \qquad (\mathrm{C.1})$$

where σ_{obs}^2 is used to normalize the different variables having totally different absolute values (and therefore biases). The binned nRMSE is shown in Fig. C.1 as a function of parameter values, the red vertical line indicating the standard parameter set. In general, k_D and α are the most relevant parameters determine the circulation while $k_{\mathrm{scale}}^{\mathrm{gas}}$ largely determines the radiocarbon inventories. Due to the strong interdependencies of the parameters (e.g. k_D and α), it is not possible to deduce an optimal parameter set from this statistics alone (this would only be possible if the parameters were completely independent). But it can already be seen here that the standard parameter set performs relatively well.

In a subsequent step, the 5 best performing ensemble members were picked and spun-up again with the full biogeochemistry and sediment modules. Note that the above defined metric is a common but somewhat arbitrary choice. In the following, the best 5 members were deduced by calculating the average rank of all 4 constraints as listed in Tab. C.1. In contrast to the nRMSE, the normalization issue is completely obsolete as all constraints are weighted equally. This metric also ensures that these 5 model do perform well in fulfilling all constraints. The Taylor diagram
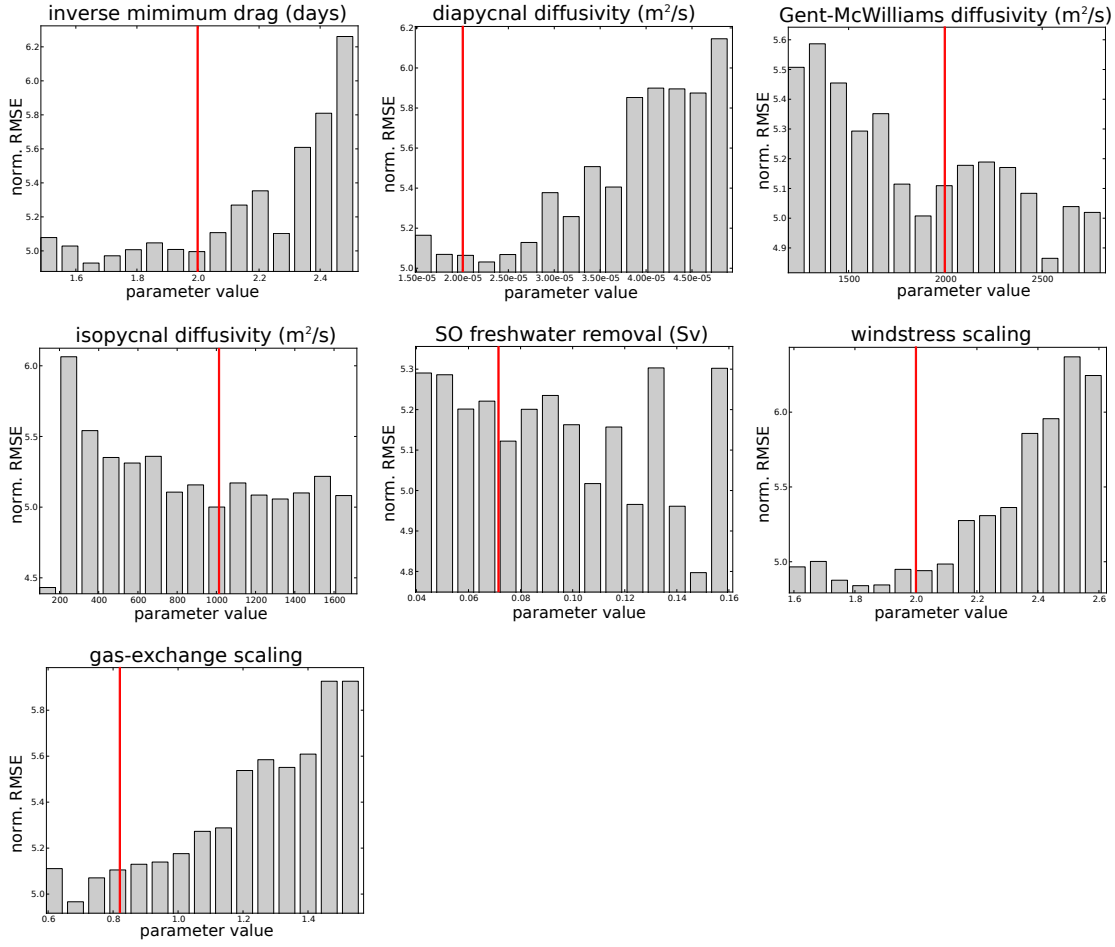
Figure C.1: Normalized RMSE for the different parameter combining the 4 constraint temperature, salinity, radiocarbon and CFC-11. The red line indicates the standard parameter set.

model	parameter average rank	k_D (m²/s)	k_I (m²/s)	κ (m²/s)	α (−)	$k_{\mathrm{scale}}^{\mathrm{gas}}$ (−)	λ (days)	fw$_{\mathrm{SO}}$ (Sv)
STD	−	2.00e-05	1.00e+03	2.00e+03	2.00	0.810	2.00	0.0700
1st	21	3.28e-05	1.64e+03	2.37e+03	1.85	1.02	1.63	0.0705
2nd	47	2.36e-05	1.46e+03	2.75e+03	1.84	1.13	2.04	0.104
3rd	61	1.76e-05	1.70e+03	2.41e+03	2.28	0.842	2.04	0.0766
4th	64	3.20e-05	1.67e+03	2.25e+03	1.77	0.880	2.00	0.0691
5th	66	2.20e-05	1.56e+03	2.28e+03	2.15	0.822	2.07	0.0608

Table C.1: Standard model parameters and 5 best performing models from the 1000 ensemble members.
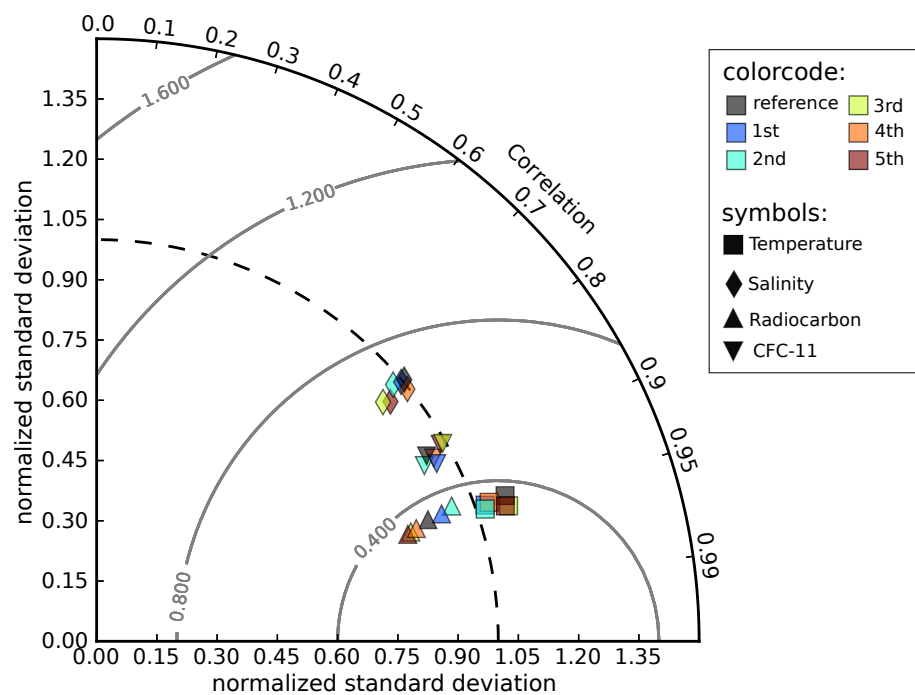
Figure C.2: Taylor-diagram showing normalized standard deviation and correlation for the standard run and 5 of the best performing ensemble members. Global tracer fields were used to generate the statistics where tracer concentrations where weighted by gridbox volumes.

shown in Fig. C.2 summarizes the performance. In addition to the observational constraints, uptake rates of anthropogenic CO_2, meridional heat transport and equatorial upwelling (nutrient trapping) were studied and the standard model performed well. Obviously, the standard model is hard to beat given the structural limitations of the model. As a consequence, the standard ocean parameters as listed in Tab. C.1 were kept for the new model as we could not find a solid reason to change them.

The final changes in parameters (w.r.t. Ritz et al., 2011) for the ocean and EBM modules are listed in Tab. 2.3 in the main text.

Bibliography

Ritz, S. P., Stocker, T. F., & Joos, F., 2011. A coupled dynamical ocean-energy balance atmosphere model for paleoclimate studies, *J. Climate*, 24(2), 349–75.

Appendix D

Deepwater formation in the new Bern3D ocean component

Regions of deepwater formation, that is the locations where surface water sink to the deep ocean, are of great importance as they largely control the atmosphere-ocean partitioning of tracers as they control their deep ocean storage. Tracers such as e.g. temperature and noble gases are conserved once they leave the atmosphere-ocean interface. Therefore, deep ocean temperatures are defined by the temperature of some few specific surface gridcells, especially in a coarse-resolution model such as the Bern3D.

Unfortunately, the standard model diagnostics (vertical velocity, number and depth of convection events) do not allow direct insight which cells contribute most to the formation of deepwater. To overcome this problem, a sophisticated experiment was set up: for every surface ocean cell (i',j'), the following dye-tracer experiment was performed:

$$
\text{tr\_dye(i,j)} \xrightarrow[\tau=30\,\text{d}]{\text{restoring}} \begin{cases} 1 & \text{if i=i' and j=j'} \\ 0 & \text{otherwise} \end{cases} \tag{D.1}
$$

In (other) words: at one surface grid cell (i',j'), the dye tracer is restored towards 1, while in all other surface grid cells, the tracer is restored to 0. In the ocean interior, the dye tracers behaves like a passive tracers and is only subject to advection, convection and diffusion , i.e. without any sources or sinks.

Each of the 1159 simulations was then equilibrated for 3000 yr using this boundary condition. Note that the ocean is not completely equilibrated after this integration time, but the errors are supposedly small regarding the computation cost of some thousand years. Note that the choice of a restoring timescale of 30 days is arbitrary. The whole ocean tracer inventory below 1000 m is then calculated for every surface gridcell. The result of this exercise if summarized in Fig. D.1a. The same procedure is repeated but integrating the Atlantic and Pacific ocean alone (Figs. D.1b-c).

Globally, 50% of the global ocean interior is filled by 26 cells (7 cells fill 20%), most pronounced in the North Atlantic and in the Southern Ocean along Antarctica. Especially the gridcells in the Southern Ocean are prone to sea-ice cover, some of them even year-round. This has implications both for the solubility of gases which sink partially undersaturated in these regions as well as for nutrients which are not utilized under the ice and sink to the deep as preformed nutrients. This fact is also of interest when using noble-gas ratios as proxy for the mean ocean temperature: the sea-ice cover decouples the noble-gas from the temperature signals as discussed in e.g. Ritz et al. (2011b).

The Atlantic ocean is primarily filled by northern sourced NADW. The southern-sourced water makes only a small fraction as the AABW is comparably weak (2 Sv) in the Bern3D. Most of the Pacific interior originates from the Southern Ocean deepwater formation regions, with a minor contribution from NADW transported by the ACC to the east.
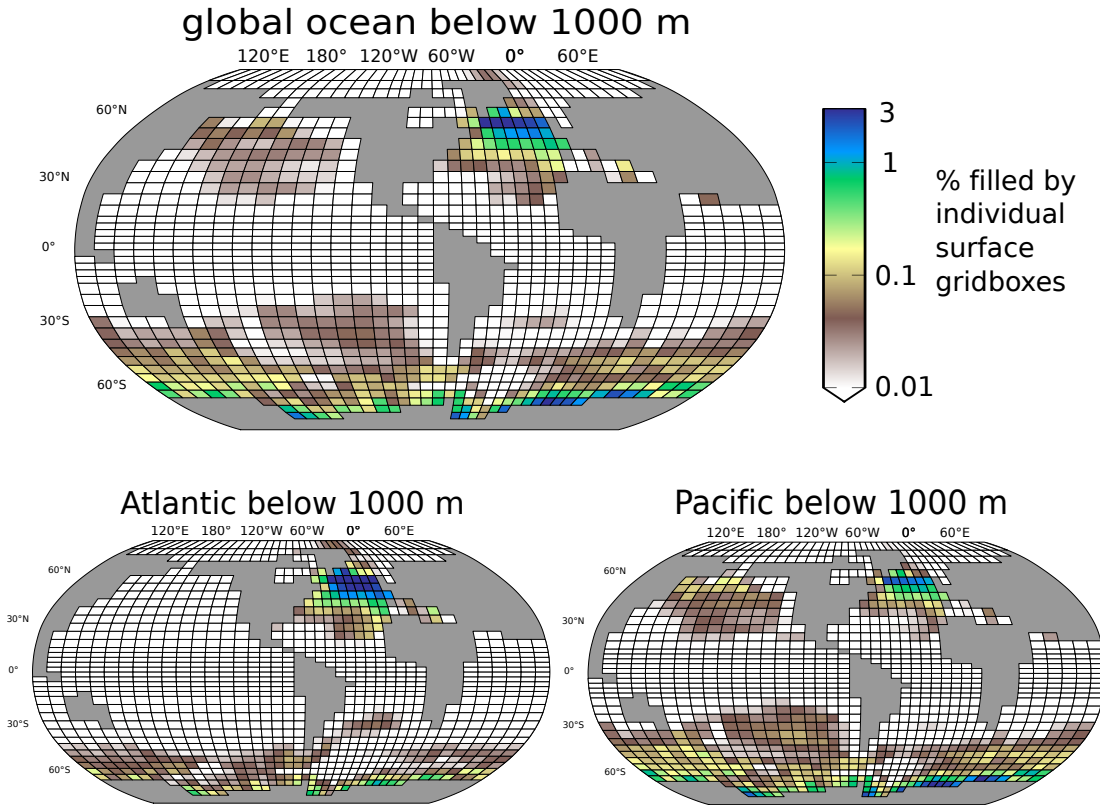

Figure D.1: Visualization of the 1159 individual dye-tracer experiments. The color-code indicates the volume of the ocean deeper than 1000 m filled by that certain surface cell. Note the strongly nonlinear color mapping. 50% of the global ocean interior is filled by only 26 cells.

Appendix E

The impulse response intercomparison project: the experimental protocol

In the following section the experimental protocol distributed among to groups is shown. Note that this is a slightly re-formatted version of the original protocol. The original protocol including the tabulated values for the CO_2 forcing can be found in the (online) supplementary material to Joos et al. (2013) and under `http://www.climate.unibe.ch/~joos/IRF_Intercomparison/protocol.html`.

The experimental protocol (V1.1)

Global warming potentials (GWP) of different gases are used as a metric to compare emissions of various greenhouse gases in the Kyoto Basket approach. The response in atmospheric CO_2 to an instantaneous release of carbon into the atmosphere, the atmospheric CO_2 impulse response function (IRF), is used for the computation of global warming potentials (GWP) and global temperature change potential (GTP, Shine et al., 2005). The goal of this exercise is to determine the atmospheric CO_2 impulse response function (IRF) by a suite of carbon-cycle climate models to explore model-model differences. Results will be written up for publication in a peer-reviewed journal in spring 2012 (IPCC AR5 WG1 deadline is summer 2012) in order to be available for calculations of GWPs in IPCC AR5. The results will also be useful for metrics and simplified climate models in other contexts.

Model requirements
The model must be able to compute the redistribution of anthropogenic carbon among the principal carbon reservoirs atmosphere, land biosphere, and ocean. Further compartments such as ocean sediments may also be included. Preferentially, the model simulates changes in climate in response to CO_2 radiative forcing and includes a representation of the relevant carbon cycle-climate feedbacks.

Model runs: overview
The scenario setup is inspired by the calculation of the IRF function as done for the Second Assessment Report (SAR) and as used in the Kyoto GWP with the Bern SAR model version and as repeated in preparation of the Fourth Assessment. The setup relies on that described in Enting, Wigley, Heimann, CSIRO Division of Atmospheric Research. Technical Paper No 31, 1994:

Three simulations are performed:
(a) The model is forced with historical concentration up to a reference year (here tref=2010) and

then concentration are kept fixed thereafter at a constant value (here CO2,ref=389 ppm). The allowed emission are calculated from the change in total inventory (prescribed atmospheric change plus modeled ocean and terrestrial uptake)

(b) A simulation with prescribed emissions from (a) (or concentration prescribed up to the reference year and emissions prescribed thereafter)

(c) same as (b) but an impulse of carbon, here of 100 Gt C, added instantaneously to the atmosphere five years after the reference year (here in 2015).

The normalized IRF is then approximately:

IRF(t=tmodel-2015.0) = (CO$_2$ (tmodel)-CO$_2$,ref)/(100 Gt C/2.123 Gt C/ppm)   for tmodel > 2015

Model runs: detailed description
A) CO$_2$ background concentration of 389 ppm

1. PresCO2_389ppm: The simulation starts from preindustrial conditions. Atmospheric CO$_2$ is prescribed and compatible emissions (=change in all carbon reservoirs) diagnosed. Atmospheric CO$_2$ is prescribed to follow the historical evolution up to year 2010. After 2010, the concentration is kept fixed at the value of 389.0 ppm. The diagnosed emissions should be written frequently (at least annually); these will be used to drive the model in run 2 and 3. An input file with the historical concentrations is provided (file name: `co2ccn_irf_850_2010_v1.0.dat`). A restart file may be written in 2010 to start simulation 2 and 3 in 2010.

2. PresEmiss_389ppm: run 2 may either start in 2010 as a continuation of run 1 or at the same preindustrial initial conditions used in run 1. Atmospheric CO$_2$ is evolving freely. Diagnosed emissions from run PresCO2_389ppm are used to force the model. (Expected result: the computed CO$_2$ evolution should be close to the evolution prescribed in run PresCO2_389ppm, see Fig. E.1).

3. PresEmiss100_389ppm: Atmospheric CO$_2$ is evolving freely. Diagnosed emissions from run PresCO2_389ppm are used to force the model as in run PresEmiss_389ppm. In addition, 100 Gt C are released at the beginning of year 2015. (Expected results: Atmospheric CO$_2$ will increase by 47.1032 ppm above the background concentration (389 ppm) in 2015 and then slowly decline over the coming decades, see Fig. E.1)

Remarks:

–It is crucial that the carbon pulse will be added to a constant background concentration of 389 ppm for comparability (roughly 2010 value).

–Run 1 (PresCO2_389ppm): An existing run or setup from the CMIP or EMIC Intercomparison projects may be used up to a concentration of 389 ppm.

–Run 3 (PresEmiss100_389ppm): The atmospheric CO$_2$ concentration should be increased at the beginning of year 2015 by 47.1032 ppm (100 Gt C/2.123 Gt C/ppm) in all atmospheric grid cells.

–Non-CO$_2$ forcing agents should be included to the extent possible. Non-CO2 forcing should be kept constant at 2010 level after 2010 (or at the year at which 389 ppm CO$_2$ is reached).

–Land use and land use changes should be included to the extent possible. Land use area should be kept constant at 2010 level after 2010.
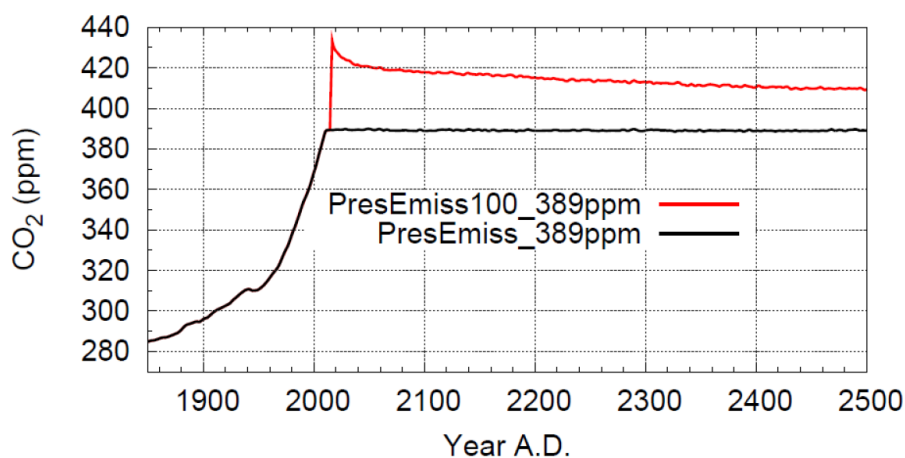
Figure E.1: Simulated evolution of atmospheric CO_2 for runs 2 and 3 (PresEmiss_389ppm PresEmiss100_389ppm). 100 Gt C are instantaneously released at the beginning of year 2015 in simulations PresEmiss100_389ppm (red) in addition to the emissions prescribed in run PresEmiss_389ppm (black). Prescribed emissions were diagnosed from a run in which atmospheric CO_2 was prescribed to follow the observed evolution until 2010 and kept constant at 389 ppm after 2010.
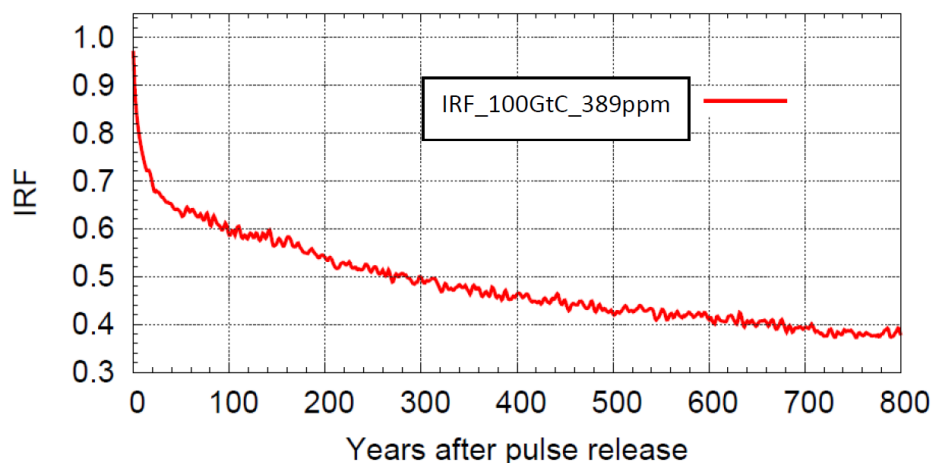
Figure E.2: CO_2 impulse response function (IRF_{CO_2}) as obtained from the difference of the runs shown in Fig E.1. The IRF is normalized by the size of the pulse input. Time is shifted such that year 0 corresponds to the time when the pulse of 100 Gt C was released into the atmosphere.
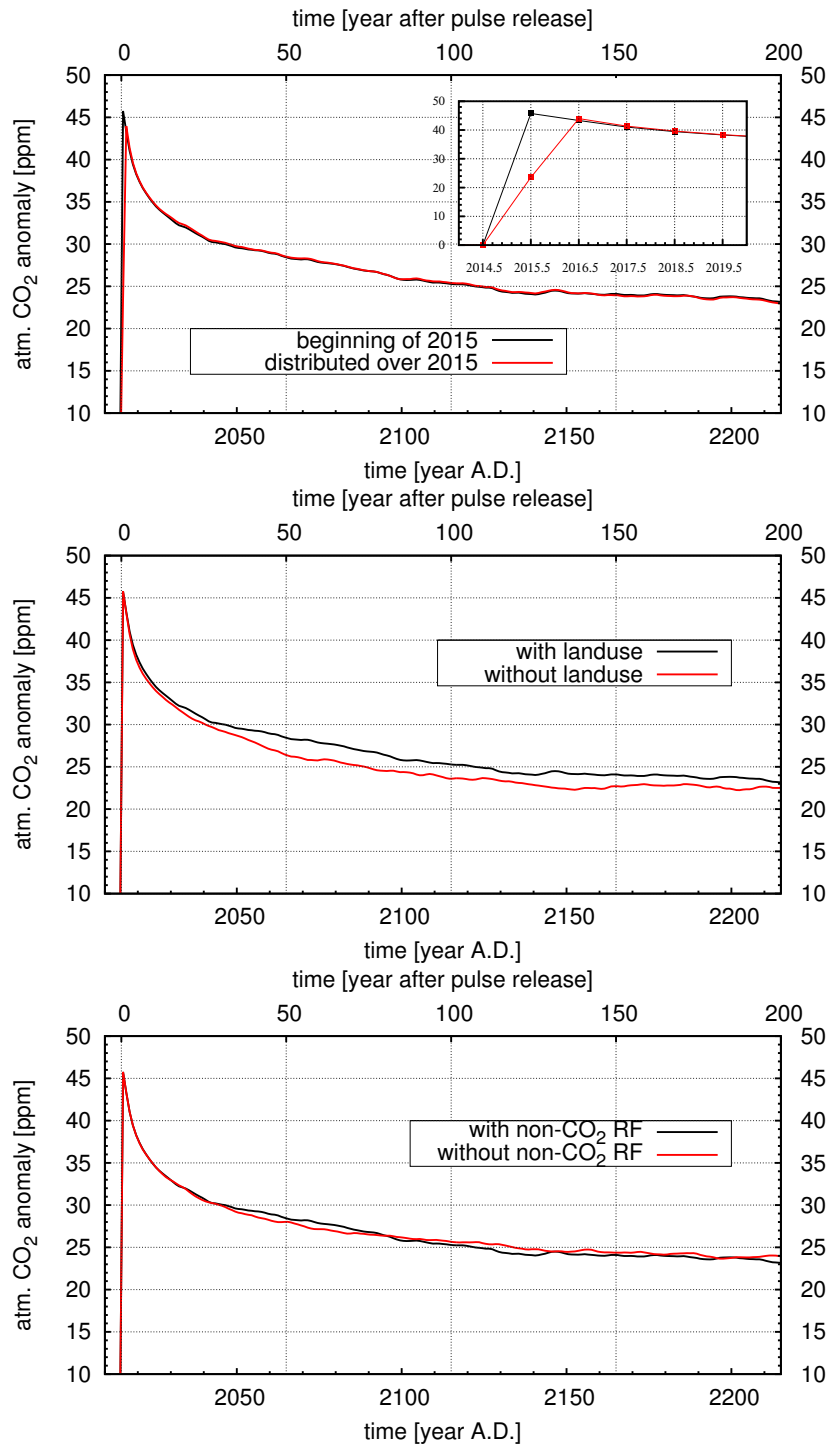
Figure E.3: Differences in Impulse Response Function computed with the Bern3D-LPX model for different model setups. Top: Results from simulations with and without anthropogenic land use. Middle: Results from simulations with and without non-CO$_2$ forcings. Bottom: Release of pulse emissions at the beginning of the year versus a release of 100 Gt C over one year. Note that the Bern3D-LPX model considers CO$_2$ to be well mixed in the atmosphere. Thus differences in IRF may be larger for models that feature atmospheric carbon transport.

–If CPU time is an issue and if a group is sure that CO_2 remains at a constant value with the emissions diagnosed in run#1, run#2 may be skipped. This may only apply to ESMs and it is strongly recommended to perform run #2 to avoid problems with model drift.

B) Preindustrial Set

Runs 4 to 5 start from preindustrial conditions

5. CTRL: Control simulation with constant boundary conditions and freely evolving atm. CO_2

6. PI100: Freely evolving atm. CO_2. 100 Gt C are released into the atmosphere during year 10 of the control simulation and then continued. (Expected result: atm CO_2 will increase from the preindustrial value of around 280 ppm by about 45 ppm to 325 ppm in year 10. Afterwards, the CO_2 concentration will then decrease due to uptake by the ocean and the land biosphere).

7. PI5000: as PI100, but 5000 Gt C are released instead of 100 Gt C

Remark: an available control simulation may be used to minimize work

Resulting IRF

We will use your results to compute impulse response functions for CO_2 and other variables:

a) IRF_100GtC_389ppm: The difference in atm. CO_2 of run PresEmiss100_389ppm and PresEmiss_389ppm divided by the pulse size of 47 ppm will yield the (normalized) IRF for a background concentration of 389 ppm and a pulse size of 100 Gt C (see Fig. E.2)

b) IRF_100GtC_PI: The difference in atm. CO_2 of run PI100 and CTRL will yield the IRF for preindustrial background conditions and a pulse size of 100 Gt C

c) IRF_5000GtC_PI: The difference in atm. CO_2 of run PI5000 and CTRL will yield the IRF for preindustrial background conditions and a pulse size of 5000 Gt C

Duration of runs

Preferentially, simulations are run for 2000 years after the pulse release until a complete equilibrium between atmosphere-ocean-land biosphere is re-established. If this is not feasible, runs of shorter duration are also welcome. Usually models are close to equilibrium after 1000 years. Global Warming Potentials for which the IRFs will be used were tabulated in past IPCC reports for 500, 100, and 20 years. A time horizon of 100 years is used in the Kyoto protocol.

A minimum of 100 years after the pulse release is requested.

Models that include ocean sediments and/or weathering and that are cost-efficient enough may also be run over many millennia (e.g. 100 ka).

Priority of runs

The top priority is to get results needed to compute the IRF for a background concentration of 389 ppm (IRF_100Gt C _389ppm). For this, runs 1, 2, and 3 are required.

Alternative: If computing requirements are too high for run 1 to 3, please provide at least results for runs 4 and 5 (PI100, CTRL).

Conversion factor Gt C to ppm

Please use a conversion factor of 2.123 Gt C per ppm

Preindustrial condition

It is up to the researcher to define the exact preindustrial state and the exact evolution how to reach the 2010 atmospheric CO_2 value of 389 ppm. However, model runs should start before 1900 AD and concentration should be kept fixed at a value of 389 ppm a few years before and during the pulse release. The idea is that the carbon pulse is added for the same background concentration of 389 ppm in all models.

Other forcings

Non-CO2 forcings and land use are preferentially included in run 1 to 3; keep non-CO2 forcing and land use area constant after 2010 at the level of year 2010. A suitable set of forcing is provided by the EMIC Intercomparison Project (`http://climate.uvic.ca/EMICAR5/forcing`).

Output

ASCII files with global mean values, provide at least 5 significant digits for each run.

a) File name: `RUNNAME_MODELNAME_Modelversion_startyear_endyear.dat`, e.g.
   "`PresCO2_2010_Bern3D--LPX_v1.0_1750_4015.dat`" for run 1 with the Bern3D–LPX model,
   version 1.0 and simulation starting at 1750 AD and ending at 4015

b) Header:
   - start each comment line with: #
   - indicate run name
   - provide contact address
   - indicate model name and version and model components included
   - indicate climate sensitivity of model
   - conversion factor used to convert $Gt\,C$ into ppm and/or pulse size in ppm
   - description of non-CO2 forcing applied
   - indicate whether tabulated data show annual averages or instantaneous values
   - column headers with units

c) Tabulated data including year, global mean values of atmospheric CO_2 in ppm (CO2atm),
   global mean net air-to-sea carbon flux in $Gt\,C$ per year (Fas,net), global mean net air-to-land
   carbon flux in $Gt\,C$ per year (Fab,net), global mean surface temperature in Celsius (T) ,
   global mean sea level rise in cm (SLR), ocean heat content in Joule (Heat):

   `# year CO2atm [ppm] Fas,net [Gt C yr`$^{-1}$` ] Fab,net [Gt C yr`$^{-1}$` ] T [deg Celsius] SLR[cm] Heat[J]`

A text file in ASCII describing the model, model resolution, model components, climate sensitivity, and appropriate references. File name: `MODELNAME_Modelversion_description.txt`. Include contact address. It is assumed that groups will store more output individually than just the few global numbers that we ask for as output. It is anticipated that the runs may be very useful to diagnose response patterns for a wide range of variables. In additions to IRFs for CO_2, temp, and sea level, one may also want to analyze pH, precip, etc.

Deadlines

Please let us know by 15 December 2011 whether you plan to contribute and submit the runs until 15 February 2012 to joos@climate.unibe.ch and roth@climate.unibe.ch

Appendix F

Fitting of CO$_2$ IRFs

Some additional information is given here how to fit IRF$_{CO_2}$ as applied in Joos et al. (2013). The timeseries of the preprocessed and normalized CO$_2$ response have been fitted using Eq. 5.1. To avoid SciPy's (Jones et al., 2001) minimization routine being stuck in a local optimum (which in turn depends on the initial guess), a brute-force approach has been applied: The fit is repeated N times with randomly generated (uniformly distributed) initial guesses within reasonable limits. Finally, the solution with the smallest squared error is chosen. Note that this Monte Carlo-type approach is only necessary for 4–5 of the models fitted for Joos et al. (2013), but despite increased computational cost it is not a problem to apply it by default. A self-running version of the used Python program is shown in the following. This program reproduces the fitting-parameters of the multi-model mean IRF$_{CO_2}$ given in Tab. 5 of Joos et al. (2013):

```python
#!/usr/bin/env python
import matplotlib
import numpy as np
import matplotlib.pyplot as plt
import os
import sys
from math import exp

from scipy.optimize import leastsq

#ignore overflow warnings, happens when error-functions
#get too large
np.seterr(over='ignore')

############### LOCAL FUNCTIONS ###################

def affitfunc(p, x):
    """
    the IRF fitting function for CO2, 3 timescales, a0=sum(a1+a2+a3)
    used by affit(), see below

    input: p : array of lenght 7 containing the parameters
            Note: p[0],p[1],p[2],p[3] are the a_i's  : i=0..3
                    p[4],p[5],p[6] are the tau_i's: i=1..3
            x : timegrid
    """

    #copy input array because we change it due to the side-condition below
    a = np.zeros(7)
    a = p

    #side condition: a0+a1+a2+a3=1.0
    a[0] = 1.0 - a[1:4].sum()

    return a[0] + a[1]*np.exp(-x/a[4]) + a[2]*np.exp(-x/a[5]) + a[3]*np.exp(-x/a[6])


def affit(in_time, in_af, shake=False):
    """
    the IRF fitting function for CO2, 3 timescales

    input: in_time: timegrid
    input: in_af  : the data to fit

    retuns:
            x: the optimized parameter set

            Note: x[0],x[1],x[2],x[3] are the a_i's  : i=0..3
                    x[4],x[5],x[6] are the tau_i's: i=1..3
```

```
                 sumsqerr: sum of squared error
        """

        if len(in_time)!=len(in_af):
                raise ValueError('time and data np.arrays have different dimensions')

        #the function to np.minimize, i.e. the deviation between
        #the data and the function to fit
        def errfunc(p, x, y):
            err=(affitfunc(p, x) - y)
            # blow up error function when side-constraints are violated
            punish=1.0e2
            #supress negative a_i's
            if p[0:4].min()<=0.0:
                return err*punish
            #supress extremly small timescales
            if p[4:].min()<0.01:
                return err*punish
            else:
                return err

        #only fit the valid data,
        # i.e. np.where the data is non NaN:
        start_data=np.min(np.where(np.isfinite(in_af)))
        end_data=np.max(np.where(np.isfinite(in_af)))
        data_fit=in_af[start_data:end_data]
        time_fit=in_time[start_data:end_data]

        while True:
            #initial guess
            if shake:
                a0 = np.array([
                                np.random.uniform(0.0,0.5),      #a0
                                np.random.uniform(0.0,0.5),      #a1
                                np.random.uniform(0.0,0.5),      #a2
                                np.random.uniform(0.0,0.5),      #a3
                                np.random.uniform(100,2000),    #tau 1
                                np.random.uniform(10,200),      #tau 2
                                np.random.uniform(0.01,10)]     #tau 3
                             )
            else:
                a0=[0.25,0.25,0.25,0.25,1000,100,1]

            x,cov_x,infodict,mesg,ier=leastsq(errfunc, a0[:],args=(time_fit, data_fit),full_output=True)
            sumsqerr=((infodict['fvec']**2).sum())

            # accept fits with reasonable results,
            #else reject and retry with slighlty different initial guess
            if (sumsqerr/len(data_fit))<data_fit.mean():
                break

        return x,sumsqerr

def affunc(p, x):
    """
    the IRF fitting function for CO2, 3 timescales, only used for visualization of the results

    input: p : array of lenght 7 containing the parameters
            Note: p[0],p[1],p[2],p[3] are the a_i's  : i=0..3
                  p[4],p[5],p[6] are the tau_i's: i=1..3
           x : timegrid
    """
    return p[0] + p[1]*np.exp(-x/p[4]) + p[2]*np.exp(-x/p[5]) + p[3]*np.exp(-x/p[6])




############## MAIN PROGRAM ##################

#fit multi model mean CO2 response, results from:
#http://www.climate.unibe.ch/~roth/IRF_Intercomparison/IRF_PD100.zip

CO2_PD100=np.loadtxt('IRF_PD100_SMOOTHED_CO2.dat')
#number of years to fit: 1000 yrs
nryears = 1000

#select multi-model mean and slice
time = CO2_PD100[0:nryears,0]
IRF  = CO2_PD100[0:nryears,17]/100.*2.123

#number of monte-carlo iterations
nrmonte=500

#fine time grid (only for visualizing the fit-function)
finetime=np.arange(0.0,nryears+0.1,0.1)

#initialize arrays
pars       =np.zeros((7,nrmonte))
sumsqerror =np.zeros(nrmonte)

#now do the monte-carlo fitting:
for monte in range(nrmonte):
    pars[:,monte],sumsqerror[monte]=affit(time,IRF,shake=True)

#pick the best fit, i.e. the one with the lowest sum of squared errors
best=np.where(sumsqerror==np.nanmin(sumsqerror))[0][0]
opt=pars[:,best]
```

```python
# only carry on a certain number of significant digits
# such that plots and errors are consistent
# with tabulated numbers, use 4 significant digits
opt_trunc=np.zeros((len(opt)))
for i in range(len(opt)):
    opt_trunc[i]=float("%.4g" %opt[i])


#display optimized parameters
#note that the order of i is arbitrary,
#only pairings of a_i and tau_i is important
print "a_0    ",opt_trunc[0]
print
print "a_1    ",opt_trunc[1]
print "tau_1 ",opt_trunc[4]
print
print "a_2    ",opt_trunc[2]
print "tau_2 ",opt_trunc[5]
print
print "a_3    ",opt_trunc[3]
print "tau_3 ",opt_trunc[6]
print

#mean relative error:
diff=(np.abs((IRF[0:nryears]-affunc(opt_trunc,time[0:nryears]))/IRF[0:nryears])).mean()

print "mre   ",diff*1000

#plot the fit-curve
plt.figure(figsize=(7,5))
plt.plot(time,IRF,marker='o',markersize=3.0,label='rawdata',color='0.6')
plt.plot(finetime,affunc(opt_trunc,finetime),color='red',label='fit')
plt.xlim([0.0,nryears])
plt.ylim([0.1,1.05])
plt.savefig('fit.pdf',bb_inches='tight')
```

Bibliography

Jones, E., Oliphant, T., Peterson, P., et al., 2001. SciPy: Open source scientific tools for Python.

Joos, F., Roth, R., Fuglestvedt, J. S., Peters, G. P., Enting, I. G., von Bloh, W., Brovkin, V., Burke, E. J., Eby, M., Edwards, N. R., Friedrich, T., Frölicher, T. L., Halloran, P. R., Holden, P. B., Jones, C., Kleinen, T., Mackenzie, F. T., Matsumoto, K., Meinshausen, M., Plattner, G.-K., Reisinger, A., Segschneider, J., Shaffer, G., Steinacher, M., Strassmann, K., Tanaka, K., Timmermann, A., & Weaver, A. J., 2013. Carbon dioxide and climate impulse response functions for the computation of greenhouse gas metrics: a multi-model analysis, *Atmos. Chem. Phys.*, 13(5), 2793–2825.

Acknowledgements

I would like to thank Fortunat Joos, Hubertus Fischer and Thomas Stocker for giving me the opportunity for this PhD thesis in Bern, and Victor Brovkin for being the external referee.

A great thank goes to

... Johannes Rempfer, Basil Neff, Beni Stocker, Cevahir Kiliç, Eveline Lehmann, Flavio Lehner, Marco Steinacher, Niklaus Merz, Patrik Pfister, Sarah Egglestone, Sonja Keel and Stefan Ritz. Because of you, I enjoyed to go to work day after day

... Gianna, Marco, Patrik and Sarah for proofreading parts of the thesis.

... Doris Rätz, Susanne Nydegger, Kay Bieri and René Bleisch for the excellent administrative work and technical assistance

A special thank to one of the reasons why I came to Bern:

... without you, this thesis would probably not exist!

.. and finally, I like to thank my beloved **Bettina Feddern** for the wonderful past 3 years in Bern, it was great!

Publications

Papers published (ordered by date):

[1] Steiner, P., **Roth, R.**, Gnecco, E., Baratoff, A., Maier, S., Glatzel, T., & Meyer, E., 2009. Two-dimensional simulation of superlubricity on nacl and highly oriented pyrolytic graphite, *Phys. Rev. B*, 79, 045414.

[2] Steiner, P., **Roth, R.**, Gnecco, E., Glatzel, T., Baratoff, A., & Meyer, E., 2009. Modulation of contact resonance frequency accompanying atomic-scale stick-slip in friction force microscopy, *Nanotechnology*, 20(49), 495701.

[3] **Roth, R.**, Glatzel, T., Steiner, P., Gnecco, E., Baratoff, A., & Meyer, E., 2010. Multiple slips in atomic-scale friction: An indicator for the lateral contact damping, *Tribol., Lett.*, 39(1), 63–69.

[4] Steiner, P., **Roth, R.**, Gnecco, E., Baratoff, A., & Meyer, E., 2010. Angular dependence of static and kinetic friction on alkali halide surfaces, *Phys. Rev. B*, 82, 205417.

[5] Fessler, G., Zimmermann, I., Glatzel, T., Gnecco, E., Steiner, P., **Roth, R.**, Keene, T. D., Liu, S.-X., Decurtins, S., & Meyer, E., 2011. Orientation dependent molecular friction on organic layer compound crystals, *Appl. Phys. Lett.*, 98(8), 083119.

[6] Gnecco, E., **Roth, R.**, & Baratoff, A., 2012. Analytical expressions for the kinetic friction in the prandtl-tomlinson model, *Phys. Rev. B*, 86, 035443.

[7] **Roth, R.** & Joos, F., 2012. Model limits on the role of volcanic carbon emissions in regulating glacial-interglacial CO_2 variations, *Earth Planet. Sci. Lett.*, 329–330(0), 141–149.

[8] Joos, F., **Roth, R.**, Fuglestvedt, J. S., Peters, G. P., Enting, I. G., von Bloh, W., Brovkin, V., Burke, E. J., Eby, M., Edwards, N. R., Friedrich, T., Frölicher, T. L., Halloran, P. R., Holden, P. B., Jones, C., Kleinen, T., Mackenzie, F. T., Matsumoto, K., Meinshausen, M., Plattner, G.-K., Reisinger, A., Segschneider, J., Shaffer, G., Steinacher, M., Strassmann, K., Tanaka, K., Timmermann, A., & Weaver, A. J., 2013. Carbon dioxide and climate impulse response functions for the computation of greenhouse gas metrics: a multi-model analysis, *Atmos. Chem. Phys.*, 13(5), 2793–2825.

[9] **Roth, R.** & Joos, F., 2013. A reconstruction of radiocarbon production and total solar irradiance from the Holocene ^{14}C and CO_2 records: implications of data and model uncertainties, *Clim. Past.*, 9(4), 1879–1909.

[10] Stocker, B. D., **Roth, R.**, Joos, F., Spahni, R., Steinacher, M., Zaehle, S., Bouwman, L., Xu-Ri, & Prentice, I. C., 2013. Multiple greenhouse-gas feedbacks from the land biosphere under future climate change scenarios, *Nature Clim. Change*, 3(7), 666–672.

Papers submitted:

[11] **Roth, R.**, Fajardo, O., Mazo, J., Meyer, E. and & Gnecco, E., 2013. Atomic-scale friction reduction caused by in-plane vibrations, submitted to *Appl. Phys. Lett.*

[12] Gehlen, L., Seferian, R., Jones, D., Roy, T., **Roth, R.**, Barry, J., Bopp, L., Doney, S., Dunne, J., Heinze, C., Joos, F., Orr, J., Resplandy, L., Segschneider, J., & Tjiputra, J., 2013. Deep North Atlantic biodiversity threatened by future pH reductions, submitted to *Nature*

[13] Usoskin, I., Hulot, G., Gallet, Y., **Roth, R.**, Licht, A., Joos, F., Kovaltsov, G.A. & Thébault, E., 2013. Evidence for distinct solar dynamo modes in past solar activity, submitted to *Nature Geosci.*

Papers in preparation:

[14] Bauska, T., Joos, F., **Roth, R.**, Ahn, J., Mix, A., & Brook, E., 2013. Pre-industrial atmospheric carbon dioxide controlled by land carbon during the last millennium, in prep. for *Nature*

Erklärung

gemäss Art. 28 Abs. 2 RSL 05

Name/Vorname: Raphael Roth

Matrikelnummer: 03-050-929

Studiengang: Physik

                  Bachelor ☐   Master ☐   Dissertation ☒

Titel der Arbeit: Modeling forcings and responses in the global carbon cycle
-climate system: Past, present and future

Leiter der Arbeit: Prof. Dr. Fortunat Joos

Ich erkläre hiermit, dass ich diese Arbeit selbständig verfasst und keine anderen als die angegebenen Quellen benutzt habe. Alle Stellen, die wörtlich oder sinngemäss aus Quellen entnommen wurden, habe ich als solche gekennzeichnet. Mir ist bekannt, dass andernfalls der Senat gemäss Artikel 36 Absatz 1 Buchstabe o des Gesetzes vom 5. September 1996 über die Universität zum Entzug des auf Grund dieser Arbeit verliehenen Titels berechtigt ist.

Bern, 14. November 2013

Curriculum vitæ

Personal Data

Name	Raphael Roth
Date of birth	November 29, 1983
Place of origin	Basel (BS)

Education

1990–1995	Primary School, Rodersdorf, Switzerland
1995–1999	Secondary School, Bättwil, Switzerland
1999–2002	Matura Type E (Economy & Law) at Gymnasium Oberwil, Switzerland
2003–2006	Bachelor in Physics at the University of Basel, Switzerland (subsidiary subjects: Astronomy/Astrophysics)
2006–2008	Master in Physics at the University of Basel, Switzerland (Thesis advisor: Prof. Dr. Ernst Meyer)
2009–2010	Travel: Cycling through Latin America in 9 months
2010–2013	Ph. D. thesis at the division of Climate and Environmental Physics, Physics Institute, University of Bern, Switzerland (Thesis advisor: Prof. Dr. Fortunat Joos)

Conferences and Workshops

2008	Jahrestagung Swiss Physical Society (SPS) Geneva, Switzerland (Poster)
2009	Physics of Tribology : 428th WE–Heraeus Seminar, Bad Honnef, Germany (Talk)
2010	Parallel Programming Workshop at Swiss National Supercomputing Centre (CSCS), Manno, Switzerland
2010	Past4Future WP3.1 workshop, Hamburg, Germany (Talk)
2011	Workshop on "Earth System Models of Intermediate Complexity", Potsdam, Germany
2011	INQUA 2011, Bern, Switzerland
2011	NCCR Climate Plenary Meeting, Zürich, Switzerland (Talk)
2012	3rd International Conference on Earth System Modelling, Hamburg, Germany (Poster)
2013	EGU General Assembly, Vienna, Austria (PICO)
2013	Global Change Day, Bern, Switzerland (Poster)
2013	Seminar of "Climate and Environmental Physics", Bern, Switzerland (invited Talk)
2013	Conference on Isotopes, Bern, Switzerland (Poster)